DOE/CS/40158-20

DOE/ID/12702

ENERGY

INERT ANODES FOR ALUMINUM SMELTING

Final Report
For the Period
29 September 1980 – 30 September 1985

J. D. Weyand
S. P. Ray
F. W. Baker
D. H. DeYoung
G. P. Tarcy

February 1986

Aluminum Company of America
Alcoa Laboratories
Alcoa Center, PA 15069

Prepared for the U.S. Department of Energy
Idaho Operations Office, Idaho Falls, ID
Under Contract Number DE-FC07-80CS40158
Sponsored by the Office of the Assistant Secretary for
Conservation and Renewable Energy
Office of Industrial Programs
Washington D.C.

U. S. DEPARTMENT OF ENERGY
IDAHO OPERATIONS OFFICE

DISCLAIMER

This book was prepared as an account of work sponsored by an agency of the United States Government. Neither the United States Government nor any agency thereof, nor any of their employees, makes any warranty, express or implied, or assumes any legal liability or responsibility for the accuracy, completeness, or usefulness of any information, apparatus, product or process disclosed, or represents that its use would not infringe privately owned rights. References herein to any specific commercial product, process, or service by trade name, trademark, manufacturer, or otherwise, does not necessarily constitute or imply its endorsement, recommendation, or favoring by the United States Government or any agency thereof. The views and opinions of authors expressed herein do not necessarily state or reflect those of the United States Government or any agency thereof.

DOE/CS/40158-20

INERT ANODES FOR ALUMINUM SMELTING

Final Report
For the Period
29 September 1980 – 30 September 1985

J. D. Weyand
D. H. DeYoung
S. P. Ray
G. P. Tarcy
F. W. Baker

February 1986

Aluminum Company of America
Alcoa Laboratories
Alcoa Center, PA 15069

Prepared for the U.S. Department of Energy
Idaho Operations Office, Idaho Falls, ID
Under Contract Number DE-FC07-80CS40158
Sponsored by the Office of the Assistant Secretary for
Conservation and Renewable Energy
Office of Industrial Programs
Washington D.C.

DISCLAIMER

This report was prepared as an account of work sponsored by an agency of the United States Government. Neither the United States Government nor any agency thereof, nor any of their employees, makes any warranty, express or implied, or assumes any legal liability or responsibility for the accuracy, completeness, or usefulness of any information, apparatus, product, or process disclosed, or represents that its use would not infringe privately owned rights. Reference herein to any specific commercial product, process, or service by trade name, trademark, manufacturer, or otherwise, does not necessarily constitute or imply its endorsement, recommendation, or favoring by the United States Government or any agency thereof. The views and opinions of authors expressed herein do not necessarily state or reflect those of the United States Government or any agency thereof.

DISCLAIMER

Portions of this document may be illegible in electronic image products. Images are produced from the best available original document.

NOTICE

This report was prepared as an account of work sponsored by an agency of the United States Government under a cost-sharing Cooperative Agreement with the Aluminum Company of America. The United States Government, agencies and employees thereof, and the Aluminum Company of America make no warranty, expressed or implied, to assume any legal liability or responsibility for any third party's use or the results of such use of any information, apparatus, product, or process disclosed in this report or represents that its use by such third party would not infringe privately owned rights.

Do not disseminate this report further until patent clearance is obtained through the U.S. Department of Energy Patent Counsel.

ABSTRACT

The use of nonconsumable or inert anodes for replacement of consumable carbon anodes in Hall electrolysis cells for the production of aluminum has been a technical and commercial goal of the aluminum industry for many decades. This report summarizes the technical success realized in the development of an inert anode that can be used to produce aluminum of acceptable metal purity in small scale Hall electrolysis cells.

The inert anode material developed consists of a cermet composition containing the phases: copper, nickel ferrite and nickel oxide. This anode material has an electrical conductivity comparable to anode carbon used in Hall cells, i.e., 150 $ohm^{-1}cm^{-1}$. Metal purity of 99.5 percent aluminum has been produced using this material. The copper metal alloy present in the anode is not removed by anodic dissolution as does occur with cermet anodes containing a metallic nickel alloy. Solubility of the oxide phases in the cryolite electrolyte is reduced by: (1) saturated concentration of alumina, (2) high nickel oxide content in the $NiO\text{-}NiFe_2O_4$ composition, (3) lowest possible cell operating temperature, (4) additions of alkaline or alkaline earth fluorides to the bath to reduce solubilities of the anode components, and (5) avoiding bath contaminants such as silica. Dissolution rate measurements indicate first-order kinetics and that the rate limiting step for dissolution is mass transport controlled.

Fabrication procedures were developed to successfully manufacture commercial size inert anodes for application in pilot and commercial size Hall cells. The process flow sheet consists of selection of the reactive raw materials; dry blending; calcination and reaction of the raw materials to make nickel ferrite, nickel oxide and copper alloy in the powder; powder attrition; spray drying the powder; green compaction; green machining; and densification by sintering. Anodes up to 35 x 30 x 20 cm have been manufactured. Thermal, electrical, physical and mechanical properties of oxide and cermet anodes have been determined.

Several connection methods have been developed between the nickel buss and the cermet inert anode to provide an electrical conduction path and mechanical strength to hold the electrode in place during electrolysis. These connections can be classified as diffusion weld, graded sintered metal, mechanical and high temperature brazed.

Commercial size cermet inert anodes have been tested in a 2500-ampere bench size cell. Anodes for this cell were designed using finite element methods and the measured properties. Methods were developed to heat, transfer and place inert anodes into the operating cell without thermal or mechanical shock failures occurring. The 2500-ampere cell was successfully operated up to 21 days with inert anodes by control of the alumina content in the bath and temperature in the cell.

FOREWORD

This final technical report summarizes the work completed during 1980 September 29 to 1985 September 30 on the cost-sharing Cooperative Agreement DE-FC07-80CS40158 between the U.S. Department of Energy and the Aluminum Company of America. Program management and technical monitoring are provided by the Office of Industrial Programs, the Department of Energy, under the direction of Mr. R. L. Sheneman, Dr. W. H. Thielbahr and Mr. M. J. McMonigle.

The United States Government, agencies and employees thereof, and the Aluminum Company of America make no warranty, expressed or implied, or assume any legal liability or responsibility for any third party's use or the results of such use of any information, apparatus, product or process disclosed in this report or represent that its use by such third party would not infringe privately owned rights.

Acknowledgment is given to Dr. R. A. Rapp, Ohio State University; Dr. H. U. Anderson, University of Missouri-Rolla; Dr. D. A. Payne, University of Illinois; R. C. Bradt, Pennsylvania State University; Dr. E. B. Yeager, Case Western Reserve University; and Dr. J. Thonstad, University of Trondheim, Norway for their valuable technical assistance.

The program was conducted by the Alcoa Laboratories organization of Alcoa. F. W. Baker was Program Manager; S. P. Ray, D. H. DeYoung, J. D. Weyand and G. P. Tarcy were the Principal Investigators. Other colleagues of the Aluminum Company of America who made significant contributions to this program include S. C. Byrne, P. A. Foster, G. E. Graddy, R. W. Gunkel, T. R. Hornack, S. C. Jacobs, N. Jarrett, L. K. King, A. V. Pajerski, F. E. Phelps, R. C. Rolf, R. C. Schoener, E. H. Rogers, J. L. Schuster, K. M. Tomaswick and R. D. Wiltzius.

TABLE OF CONTENTS

NOTICE
ABSTRACT
FOREWARD

I. SUMMARY
A. Background
B. Objective
C. Scope
D. Approach
E. Technical Progress and Results
1. Inert Anode Material Development
a. Compositional Development
b. Corrosion Studies
c. Electrochemical Studies
d. Material Properties
2. Anode Fabrication Studies
a. Raw Material Selection
b. Powder Preparation
c. Consolidation Studies
3. Anode-Stub Connection Design, Testing and Evaluation
F. Conclusions
G. Recommendations

II. INTRODUCTION 1

III. PHASE I - INERT ANODE MATERIAL DEVELOPMENT 3
A. Compositional Development. 4
1. Objective. 4
2. Introduction 4
a. Review of Previous Work. 4
b. Review of Previous Alcoa Work. 6
1) Refractory Metals. 7
2) Borides, Nitrides, and Carbides. 7
3) Noble Metals 7
4) High Temperature Corrosion Resistant Alloys. . . 8
5) Coatings on Conducting Materials 8
6) Mixed Oxides 8
7) Coatings on Semiconductors 11
8) Cermet Anodes and Alloys 14
3. Experimental Techniques. 14
a. Fabrication of Oxides. 14
b. Fabrication of Coatings. 15
c. Fabrication of Cermets 16
d. Electrical Conductivity Measurements 16
e. Hall Cell Evaluation of Inert Anodes 18
4. Results and Discussions. 20
a. Hall Cell Tests. 20
b. Oxidation Characteristics. 33
c. Marker Experiments 36
d. Effect of Hall Cell Operating Conditions on Performance of Ni-$NiFe_2O_4$ Inert Anodes. . . . 38

e. "See Through" Hall Cell Operation. 49
f. Effect of Bare Carbon Sidewall on Inert Anode Performance. 51
g. Improved Cermet. 51
1) Microstructural Evaluation 63
2) Electrical Properties. 82
3) Effect of Electrolyte Composition on Performance. 96
4) Effect of Cathode Area on Performance. 99
h. Other Compositions 99
B. Inert Anode Corrosion Studies. 109
1. Objective. 109
2. Introduction 109
3. Part A. Solubility Measurements 111
a. Literature Review. 111
b. Experimental Method. 111
c. Results and Discussion 118
1) Effects of Temperature and Bath Composition. . . 118
a) Solubilities 118
b) Enthalpy of dissolution. 126
c) Comparison to other thermodynamic data . . . 133
d) Na_3AlF_6-Fe_2O_3-NiO phase diagram. 134
2) Effects of Bath Additives. 140
a) Effect of SiO_2 additions 140
b) Effect of CaF_2 additions 141
c) Effect of MgF_2 additions 146
d) Effect of LiF additions. 146
e) Effect of ZrO_2 additions 150
f) Effect of combined additions of basic fluorides. 161
3) Alternate Anode Materials. 171
a) New materials. 171
b) Doped nickel ferrite 189
c) Suggestions for further work 199
4) Implications to Hall Cell Operation. 201
d. Conclusions from Solubility Measurements 203
4. Part B. Rate Measurements 205
a. Literature Review. 205
b. Scope of Work. 207
c. Experimental Methods 208
1) General. 208
2) Sample Fabrication 210
3) Experiments Under Oxidizing Conditions 214
4) Experiments with Polarized Anodes, No Aluminum Present 214
5) Experiments with Aluminum Metal Pads 217
6) Experiments to Test Effect of Carbon/Al_4C_3 . . . 219
7) Effect of Sampling Depth on Concentrations in Bath. 220
d. Results and Discussion 221
1) Experiments Under Oxidizing Conditions 221
a) Analysis of data 221
b) Results. 229
2) Experiments with Polarized Anodes, Copper Cathodes 240

a) Analysis of data 240
b) Results. 246
3) Experiments with Aluminum Metal Pads 252
a) Analysis of data 252
b) Results. 264
4) Effect of Carbon/Al_4C_3 on Dissolution Rate . . . 276
a) Analysis of data 276
b) Results. 279
5) Results for Differing Anode-Compositions 284
a) All-oxide material (5324). 284
b) Cu cermet (5324 + 17% Cu). 290
c) Single crystal $NiFe_2O_4$ 290
e. Conclusions from Rate Measurements 296
C. Electrochemical Studies. 297
1. Objective. 297
2. Introduction 297
3. Experimental Procedures. 298
a. Electrochemical Characterization 298
b. Long Term Testing. 303
c. Voltage Characteristics of the 2500-Ampere Cell. . . 305
1) Materials. 305
a) Cell design. 305
b) Reference electrode design 307
c) Reference electrode manipulator. 307
4. Corrosion and Passivation of Cermet Inert Anodes 312
a. Electrochemical Corrosion Study. 312
b. Discussion on Porous Electrode 319
c. Development of an Improved Cermet. 321
d. Parameters Affecting the Passivation 327
e. Parameters not Affecting the Passivation 331
f. Conclusions. 335
5. Long Term Testing of the Improved Cermet 336
a. Introduction 336
b. Results and Discussion 337
1) Internal Oxidation of the Metal Phase. 338
2) Aluminum Metal Purity. 341
3) Anode Dissolution Rates. 355
a) Anode Connection Integrity 368
6. Voltage Characteristics of the 2500-Ampere Cell. 371
a. Introduction 371
b. Results and Discussion 372
1) Anode EMF and Overvoltage. 372
2) Anode Connection and Cermet Voltage Drop 375
3) Electrolyte Voltage Drop 376
4) Bubble Layer Ohmic Losses. 382
5) Cathode Drop and Muck. 383
6) Externals. 384
c. Conclusions. 384
D. Properties of Fabricated Inert Anodes. 386
1. Objective. 386
2. Introduction 386
3. Mechanical Properties. 389
a. Strength 389

1) Effect of Materials, Surface Preparation and Temperature 390
2) Effect of Porosity on Cermet Inert Anode Strength. 390
3) Effect of Hall Cell Exposure Time on Inert Anode Strength. 393
b. Weibull Modulus. 396
c. Fracture Toughness 398
d. Young's Modulus. 401
e. Other Mechanical Properties. 405
4. Thermal Properties 405
a. Thermal Expansion. 405
b. Thermal Conductivity 408
5. Other Properties 409

IV. PHASE II - ANODE FABRICATION STUDIES. 412
1. Objective. 412
2. Introduction 412
3. Experimental Procedures. 416
a. Compositions and Materials 416
b. Powder Preparation 416
c. Consolidation Studies. 421
d. Process Flow Diagram Investigations. 421
e. Property Evaluations 423
4. Results and Discussion 423
a. Raw Material Selection 424
1) Fe_2O_3. 424
2) Fe_3O_4. 425
3) NiO. 429
4) Fe 429
5) Ni and Cu. 434
b. Powder Preparation 434
c. Consolidation Studies. 443
1) Green Compaction and Binder Selection Studies. . 443
2) Pressureless Sintering Studies 449
3) Pressure Sintering 453
d. Fabrication Process Methods. 456
e. Microstructural and Physical Property Evaluations. . 458
5. Conclusions. 467

V. PHASE III - ANODE-STUB CONNECTION, DESIGN, TESTING, AND EVALUATION
1. Objectives 468
2. Introduction 468
3. Anode Connection Designs and 60-A Cell Testing 469
4. 2500-Ampere Hall Cell Design and Testing 476
a. Anode Preheat. 481
b. Anode Transfer and Early Life in the Cell. 481
c. Cell Operation with Inert Anodes 494
5. Results and Discussions. 496
6. Evaluation of Inert Anodes Tested in the 2500-Ampere Cell 504
7. Conclusions and Recommendations. 508

VII. REFERENCES 510

LIST OF TABLES

Page

1. Properties of Pertinent Oxides. 10
2. Oxide Semiconductors. 12
3. Spinel. 13
4. Summary of Fabricated Anodes Tested in Bench-Scale Hall Cell 17
5. Summary of Bench-Scale Hall Cell Tests. 24
6. Summary of Bench-Scale Hall Cell Tests with Cermet Anodes 28
7. Bench-Scale Hall Cell with Cermet Anodes Tested in a 1.1 Ratio Bath with 5 wt.% CaF_2 and 5 wt.% Al_2O_3 29
8. Oxidation Experiments in Air. 34
9. Oxidation Experiments in Air at 960°C 35
10. Effect of Bath Ratio on the Performance of Inert Anodes 39
11. Effect of Al_2O_3 Concentration on Decomposition Voltage at 1250 K. 44
12. Effect of Bath Composition on the Performance of Inert Anodes. 46
13. Properties of Various Bath Compositions 48
14. Effect of Bath Composition on Anode Performance 50
15. Effect of Bare Graphite Sidewall on Inert Anode Performance 54
16. Hall Cell Results 61
17. Analyses of Metallic Phases from Anode Sample at End of 30-hour Test. 64
18. Fabrication of Inert Anode Compositions for Bench-Scale Hall Cell Test by Sintering in Argon Atmosphere. 65
19. Fabrication of Inert Anode Compositions for Electrical Conductivity Measurements 67
20. Metal Particle Size Analyses in Sintered Inert Anodes 85

21. Analysis of Metal Grains in 5324 Cu-Cermet Compositions 86

22. Electrical Conductivity of 5324 Cu-Cermet Anodes. 89

23. Hall Cell Test Results, Effect of Bath Composition on Anode Performance of 5324 Cu Anodes 98

24. Bench-Scale Hall Cell Tests with NiO-Cu, Fe_2O_3-Cu, and Cu-Fe-Ni Alloy Inert Anodes. 101

25. Solubility of Fe_2O_3 in Na_3AlF_6-Al_2O_3 Melts at 1000°C 135

26. Solubility of NiO in Na_3AlF_6-Al_2O_3 Melts at 1000°C 136

27. Solubility of $NiFe_2O_4$ in Na_3AlF_6-10% Al_2O_3 at 1000°C 137

28. Analyzed Mg Concentration in Bath to Which 8.0 wt.% MgF_2 was Added. 149

29. High Basic Fluoride Melts Used for Solubility Measurements. . . 162

30. Sample Analyses for High Basic Fluoride Baths 170

31. Solubilities for Oxides in Cryolite - 5% Al_2O_3 Bath at 960°C 173

32. Free Energy of Formation of Some Double Oxides. 174

33. Formation of New Materials. 175

34. X-ray Diffraction Results and Densities for Cobalt-Based Materials 176

35. X-ray Diffraction Results and Densities for Chromium-Based Materials 177

36. Raw Materials Used for Cobalt and Chromium Oxides 178

37. Compositions of Doped Nickel Ferrites 190

38. Chemical Formulas for Doped Nickel Ferrites 192

39. Raw Materials Used for Doped Nickel Ferrites. 193

40. X-ray Diffraction of Al, Mg, Zn and Li Doped Nickel Ferrites Which Were Presintered in Air at 1125°C for 24 hours. 195

41. Proposed Alternate Materials Program. 200

42. Candidate Materials for Solubility and Dissolution Rate Tests 202

43. Materials Used for Chemical Corrosion Measurements. 212

44. Dissolution Rate Constants for 6846 Ni-Cermet Inert Anodes in Bath Under an Air Atmosphere 230

45. Effect of Test Time on the Dissolution Rate Constants for 6846 Ni-Cermet Inert Anodes in Bath Under an Air Atmosphere 231

46. Mean Rate Constants for Dissolution of 6846 Ni-Cermet Materials in Bath Under Oxidizing Conditions, Experiments R43-R48. 239

47. Average Accumulaton Rates of Inert Anode Constituents in Bath and Copper Cathodes 243

48. Dissolution Rate Constants from Experiments with Copper Cathodes 247

49. Analysis of Skim from Experiments with Metal Pads 257

50. Dissolution Rate Constants from Experiments with Aluminum Metal Pads 265

51. Dissolution Rate Constants from High Alumina, High Temperature Experiments 273

52. Dissolution Rate Constants from Experiments with Carbon or Aluminum Carbide Additions. 281

53. Dissolution Rate Constants for 5324 Inert Anode Material. . . . 286

54. Dissolution Rate Constants for Cu-Cermet (5324 + 17% Cu) Material. 291

55. Electrochemical Corrosion Result of Metal and Alloys. 323

56. Metal Purity Results for Long Term Tested Cu-NiO-$NiFe_2O_4$ Inert Anodes. 345

57. Voltage Characteristics of an Inert Anode Hall Cell 373

58. Relative Comparison of the Effect of Metal Phase Oxidation on the Anode and Connection Voltage Drop of 6846 Material 374

59. Comparison of Inert Anode and Carbon Anode Systems. 385

60. Properties of Fabricated Inert Anodes 388

61. Thermal Expansion - Inert Anode Compositions. 406

62. Spray Drying Conditions to Produce 6846 Inert Anode Powder for Pressing. 419

63. Inert Anode Raw Material Powder Properties - Oxides 426

64. Inert Anode Raw Material Powder Properties - Metals 431

65. Cermet Fabrication Studies by Reaction Sintering. 438

66. Powder Characterizaton - Agglomerated Powders 440

67. Organic Binder - Inert Anode
Green Compact Strength Evaluation. 447

68. Density and Phase Amounts in
Cermet Anodes by Image Analysis. 460

69. Calculated Stresses in Inert Anode
Resulting from Thermal Gradients 488

70. Material Properties Used in Finite Element Analyses 490

71. Stresses in Anode 492

72. MOR Strength of Inert Anode 6846. 493

73. Data Collected from 2500-A Cell 495

LIST OF FIGURES

		Page
1.	Schematic of Bench-Scale Hall Cell.	19
2.	Photomicrograph of Fabricated Mixed Oxide Anode	21
3.	Electrical Conductivity of 5324 Anode Composition	22
4.	Backscattered Picture of Reaction Sintered Cermet Anode - 39.7 wt.% Fe, 60.3 wt.% NiO.	25
5.	X-ray Images for Ni, Fe and Oxygen Corresponding to Figure 4.	26
6.	Anode 013084 (Interior) Backscattered Electron Image and X-ray Images for Fe, Ni and Oxygen	31
7.	Anode 013084 (Bottom) Backscattered Electron Image and X-ray Images for Fe, Ni, O, F, Na and Al	32
8.	Anode 010383 - Schematic Representation of Areas Analyzed by Electron Probe	41
9.	AlF_3 Activity as a Function of AlF_3 Concentration in $NaF-AlF_3$ Melts at Various Temperatures.	43
10.	Schematic of See-Through Electrolytic Cell.	52
11.	Anode 011083 - Cell Volts vs. Current at Start-up	53
12.	Anode 011083 - Cell Volts vs. Current after 24 hours Operation	55
13.	Schematic Cross Section of Anode Showing Reacted Areas. . .	56
14.	Anode 011785 Backscattered and X-ray Images After Hall Cell Test	62
15.	Anode 578656: 95 wt.% 5324 + 5 wt. Cu Photomicrographs. .	68
16.	Anode 57864: 90 wt.% 5324 + 10 wt.% Cu Photomicrographs. .	69
17.	Anode 578655: 85 wt.% 5324 + 15 wt.% Cu Photomicrographs .	70
18.	Anode 578667: 95 wt.% 5324 + 5 wt.% Cu Photomicrographs. .	72
19.	Anode 578668: 90 wt.% 5324 + 10 wt.% Cu Photomicrographs .	73
20.	Anode 578669: 85 wt.% 5324 + 15 wt.% Cu Photomicrographs .	74

21. Anode 578674: 84 wt.% 5324 + 16 wt.% Cu Photomicrographs . 75

22. Anode 578676: 83 wt.% 5324 + 17 wt.% Cu Photomicrographs . 76

23. Anode 578686: 95 wt.% 5324 + 5 wt.% Cu Photomicrographs. . 77

24. Anode 578684: 90 wt.% 5324 + 10 wt.% Cu Photomicrographs . 78

25. Anode 578685: 85 wt.% 5324 + 15 wt.% Cu Photomicrographs . 79

26. Anode 578682: 84 wt.% 5324 + 16 wt.% Cu Photomicrographs . 80

27. Anode 578683: 83 wt.% 5324 + 17 wt.% Cu Photomicrographs . 81

28. Anode 568654: 5 wt.% 1 μm Cu, Chord Size Distribution. . . 83

29. Anode 568676: 17% Composition, 10 μm Cu, Chord Size Distribution. 84

30. Electrical Conductivity of 6846 Reaction Sintered Cermet Composition (94-2) 87

31. Electrical Conductivity of 5324 + Cu-Cermet Anode Material at 960°C; Conductivity vs. wt.% Copper. 90

32. Electrical Conductivity of 5324 + Cu-Cermet Anode Material at 960°C; Conductivity vs. volume % Copper. 91

33. Electrical Conductivity of 83 wt.% 5324 + 17 wt.% Cu. . . . 92

34. Electrical Conductivity of Anode Material 5324 + Cu 95

35. Electrical Conductivity of 5324 + 5 wt.% Cu; Comparison of Labortory Milled vs. Un-milled Powders. 97

36. Schematic of Reduced Cathode Area Hall Cell 100

37. Anode 031485: 80 wt.% NiO, 20 wt.% Cu; Positions for Microprobe Analysis. 103

38. Sample 031485: Backscattered and X-ray Images, Position 4 105

39. Anode 051485: 84.2 wt.% Cu, 1.3 wt.% Fe, 14.5 wt.% Ni, Schematic After Hall Cell Test 107

40. Anode 051485: Backscattered and X-ray Images, Area 1 . . . 108

41. Experimental Apparatus for Solubility Measurements. 112

42. Bath Analyses Illustrating Time Needed for Equilibrium of Fe_2O_3 with Melt 115

43. Bath Analyses Illustrating Time Needed for Equilibrium of NiO with Melt 116

44. Approach to Solubilities From Lower and Higher Temperatures 117

45. Analysis of Melts From Selected Experiments for Bath Ratio and Al_2O_3 119

46. Solubility of Fe_2O_3 in $NaF-AlF_3-CaF_2-Al_2O_3$ Melts. 120

47. Solubility of NiO in $NaF-AlF_3-CaF_2-Al_2O_3$ Melts. 121

48. Solubility of $NiFe_2O_4$ in $NaF-AlF_3-CaF_2-Al_2O_3$ Melts. 122

49. Effect of Al_2O_3 Concentration in the Melt on Solubility of Fe_2O_3 124

50. Effect of Al_2O_3 Concentration in Melt on Solubility of NiO 125

51. Effect of Bath Ratio on Solubility of Fe_2O_3 127

52. Effect of Bath Ratio on Solubility of NiO 128

53. Least-squares Fit of Fe_2O_3 Solubility Data. 130

54. Least-squares Fit of NiO Solubility Data. 131

55. Least-squares Fit of $NiFe_2O_4$ Solubility Data. 132

56. Calculated Isothermal Section for $Fe_2O_3-NiO-(NaF-AlF_3-Al_2O_3)$ Pseudo Ternary System at 960°C 139

57. Effect of SiO_2 on Solubility of Fe_2O_3 in $NaF-AlF_3-CaF_2-Al_2O_3$ Melts with 0.9 Bath Ratio. 142

58. Effect of SiO_2 on Solubility of Fe_2O_3 in $NaF-AlF_3-CaF_2-Al_2O_3$ Melts. 143

59. Effect of CaF_2 on Solubility of Fe_2O_3 in $NaF-AlF_3-CaF_2-Al_2O_3$ Melts. 144

60. Effect of CaF_2 on Solubility of NiO in $NaF-AlF_3-CaF_2-Al_2O_3$ Melts Containing wt.% CaF_2 145

61. Effect of MgF_2 on Solubility of Fe_2O_3 in $NaF-AlF_3-CaF_2-Al_2O_3$ Melts Containing 1.3 wt.% CaF_2 147

62. Effect of MgF_2 on Solubility of NiO in $NaF-AlF_3-CaF_2-Al_2O_3$ Melts Containing 1.3 wt.% CaF_2 148

63. Effect of LiF on Solubility of Fe_2O_3 in $NaF-AlF_3-CaF_2-Al_2O_3$ Melts Containing 1.3 wt.% CaF_2 151

64. Effect of LiF on Solubility of NiO in $NaF-AlF_3-CaF_2-Al_2O_3$ Melts Containing 1.3 wt.% CaF_2 152

65. Effect of ZrO_2 on Solubility of NiO in $NaF-AlF_3-CaF_2-Al_2O_3$ Melts Containing 1.3 wt.% CaF_2 153

66. Effect of ZrO_2 on Solubility of Fe_2O_3 in $NaF-AlF_3-CaF_2-Al_2O_3$ Melts Containing 1.3 wt.% CaF_2 154

67. Solubility of ZrO_2 in $NaF-AlF_3-CaF_2-Al_2O_3-ZrO_2$ Melts Containing Small Amounts of NiO or Fe_2O_3 and 1.3 wt.% Caf_2 156

68. Solubility of Fe_2O_3 in $NaF-AlF_3-CaF_2-Al_2O_3-ZrO_2$ Melts With 0.9 Bath Ratio. 157

69. Solubility of Fe_2O_3 in $NaF-AlF_3-CaF_2-Al_2O_3-ZrO_2$ Melts With 1.3 Bath Ratio. 158

70. Solubility of NiO in $NaF-AlF_3-CaF_2-Al_2O_3-ZrO_2$ Melts With 0.9 Bath Ratio. 159

71. Solubility of NiO in $NaF-AlF_3-CaF_2-Al_2O_3-ZrO_2$ Melts with 1.3 Bath Ratio. 160

72. Effect of Combined Additions of CaF_2, MgF_2 and LiF on Solubility of NiO in $NaF-AlF_3-Al_2O_3$ Melts 163

73. Effect of Combined Additions of CaF_2, MgF_2 and LiF on Solubility of Fe_2O_3 in $NaF-AlF_3-Al_2O_3$ Melts 164

74. Effect of Combined Additions of CaF_2, MgF_2 and LiF on Solubility of NiO in $NaF-AlF_3-Al_2O_3$ Melts 166

75. Effect of Combined Additions of CaF_2, MgF_2 and LiF on Solubility of Fe_2O_3 in $NaF-AlF_3-Al_2O_3$ Melts 167

76. Effect of Combined Additions of CaF_2, MgF_2 and LiF on Solubility of NiO in $NaF-AlF_3-Al_2O_3$ Melts 168

77. Effect of Combined Additions of CaF_2, MgF_2 and LiF on Solubility of Fe_2O_3 in $NaF-AlF_3-Al_2O_3$ Melts 169

78. Iron Solubility from Cobalt-Nickel Ferrites in Hall Cell Bath. 180

79. Cobalt Solubility from Cobalt-Nickel Ferrites in Hall Cell Bath. 181

80. Nickel Solubility from Cobalt-Nickel Ferrites in Hall Cell Bath. 182

81. Solubility of $Co_xNi_{1-x}Fe_2O_4$ in Hall Cell Bath Containing 6.5 wt.% Al_2O_3, 1.3 wt.% CaF_2. 184

82. Bath Analyses for Dissolution of $CoCr_2O_4$ During Solubility Experiments. 185

83. Bath Analyses for Dissolution of $NiCr_2O_4$ During Solubility Experiments. 186

84. Chromium Concentrations in Bath Resulting from the Dissolution of Several Chromium Oxide Materials 187

85. Distance Between 311 Plains for Doped $NiFe_2O_4$ Sintered in Air at 1450°C. 194

86. Solubility of Doped Nickel Ferrites in Hall Cell Bath . . . 197

87. Solubilities of Zn and Li Doped Nickel Ferrite Compared to the Solubility of $NiFe_2O_4$. 198

88. Schematic Diagram of Rotating Disk Apparatus for Dissolution Rate Measurements. 209

89. Anode Assembly Used for Dissolution Rate Measurements . . . 211

90. Schematic Diagram of Cell for Dissolution Measurements of Polarized Anodes Without Aluminum Pads. 215

91. Floating Metal Reference Electrode. 216

92. Cell for Measurements of Dissolution Rates of Inert Anodes with a Metal Pad in System. 218

93. Variation of Bath Analysis with Depth During Experiment R80. 222

94. Dissolution of Ni Cermet (6846) Inert Anode Material from a Rotating Disk at 780 rpm 223

95. Nickel Dissolution from Ni Cermet (6846) Inert Anodes in an $NaF-AlF_3-CaF_2-Al_2O_3$ Melt. 224

96. Iron Dissolution from Ni Cermet (6846) Inert Anodes in an $NAf-AlF_3-CaF_2-Al_2O_3$ Melt. 225

97. Dissolution Data for Experiment No. R29 Plotted According to Integrated Rate Equation for Mass Transport-Controlled Dissolution. 227

98. Dissolution Data Plotted According the Integrated Form of the Rate Equation for Mass Transport-Controlled Dissolution. 228

99. Dissolution Rate Constants for Ni Cermet (6846) Anode Material in Bath Under Air Atmosphere. 233

100. Effect of Bath Composition and Temperature on Dissolution Rate Constants for Ni Cermet (6846). . . . 235

101. Effect of Bath Ratio on Dissolution Rate Constants for Ni Cermet (6846) 236

102. Bath Analysis for Experiment R81, Ni Cermet (6846). 242

103. Dissolution Data from Experiment R81 Plotted According to the Integrated, First Order Rate Equation. 245

104. Effect of Current Density on Dissolution Rate Constants from Tests with Solid Copper Cathodes-6.5% Al_2O_3 (Saturated) 248

105. Effect of Current Density on Dissolution Rate Constants Determined from Tests with Solid Copper Cathodes-4.5% Al_2O_3. 249

106. Dissolution Rate Constants from Experiments with Copper Cathodes, Bath Saturated with Al_2O_3 250

107. Dissolution Rate Constants from Experiments with Copper Cathodes, Bath Not Saturated with Al_2O_3 251

108. Bath Analysis for Experiment R64, Ni Cerment (6846), Bath Contained 6.5% Al_2O_3 253

109. Metal Pad Analysis for Experiment R64 254

110. Cross Section of Bath from Experiment R55 Illustrating Layer of Gray Skim. 255

111. Iron Distribution for Dissolution Experiments with Metal Pads Present in the Cell 258

112. Nickel Distribution for Dissolution Experiments with Metal Pads Present in the Cell 259

113. Total Weight of Impurities Dissolved in the Aluminum Metal Pad in Experiment R64. 262

114. Dissolution Data from Experiment R64 Plotted According to the Integrated, First Order Rate Equation. Bath Composition was 6.5% Al_2O_3. . . . 263

115. Dissolution Rate Constants for Iron for Ni Cermet (6846) Inert Anodes at 960°C. Bath Composition Contained 6.5 wt.% Al_2O_3 266

116. Dissolution Rate Constants for Nickel for Ni Cermet (6846) Inert Anodes at 960°C. Bath Composition Contained 6.5 wt.% Al_2O_3 267

117. Rate Constants for Dissolution of Ni Cermet (6846) Inert Anodes at 960°C. Bath Composition Contained 6.5 wt.% Al_2O_3 269

118. Comparison of Iron Dissolution Rate Constants for Ni Cermet (6846) from Tests With and Without an Aluminum Metal Pad. 271

119. Composition of Nickel Dissolution Rate Constants for Ni Cermet (6846) from Tests With and Without an Aluminum Metal Pad. 272

120. Dissolution Rate Constants for Iron in the High Temperature-High Alumina Bath Compared to Those With a Standard Bath. Ni Cermet (6846). 274

121. Dissolution Rate Constants for Nickel in the High Temperature-High Alumina Bath Compared to Those With a Standard Bath. Ni Cermet (6846). 275

122. Comparison of k x C_s Which is Proportional to the Total Dissolution Rate for High Temperature-High Alumina Bath to that for Standard Bath. 277

123. Quantities of Iron and Nickel Plated Onto the Cathodically Polarized Graphite Rods in Experiment R88. 278

124. Distribution of Impurities Dissolving From Anode in Experiments Designed to Determine the Effects of Carbon and Al_4C_3 on Anode Dissolution 280

125. Effects of Carbon and Aluminum Carbide Additions to Bath, and Effect of Suspending a Cathodically Polarized Graphite Rod in Bath on Dissolution Rate Constant for Iron 283

126. Effects of Carbon and Aluminum Carbide Additions to Bath, and Effect of Suspending a Cathodically Polarized Graphite Rod in Bath on Dissolution Rate Constant for Nickel 285

127. Comparison of the Dissolution Rate Constants for the All Oxide (5324) Material and Ni Cermet (6846) Material. Anodes were Unpolarized. . 287

128. Comparison of the Dissolution Rate Constants for All Oxide (5324) Material and Ni Cermet (6846) Material. 289

129. Comparison of the Dissolution Rate Constants for Cu Cermet (5324 + 17% Cu) and the Ni Cermet (6846) Material. 292

130. Single Crystal $NiFe_2O_4$ with Pt Connection 294

131. Comparison of Dissolution Rate Constants for Single Crystal $NiFe_2O_4$ to Polycrystalline Ni Cerment (6846). 295

132. Cell Design for Electric Chemical Corrosion Study and Material Screening 299

133. Cell Design for Long Term Testing of Inert Anodes 300

134. Schematic of 2500-A Hall Cell 306

135. Design of Reference Electrode for Voltage Characterization of 2500-A Cell. 308

136. Design of Anode Voltage Drop Probe. 309

137. Schematic Representation of Voltage Probe Manipulator . . . 311

138. Cross Section of Ni-$NiFe_2O_4$ Cerment (6846) After 96 Hours in 60-A Cell. 313

139. Linear Sweep Voltammograms of Ni-$NiFe_2O_4$ Cermet and Pt Working Electrode. 315

140. Linear Sweep Voltammograms of Ni-$NiFe_2O_4$ Cermet (6846) and All-Oxide (5324) Anodes. 317

141. Voltammogram Plotted in a Tafel Format for Cermet 6846 Anode. 318

142. Voltammograms of Cu and Ni Metal Anodes 324

143. Microprobe Comparison of Various Metal Phases in 6846 Cermet Anodes 325

144. Comparison of Voltammograms for Cermet Anode Materials Displayed in a Tafel Format. 328

145. Internal Penetration of Electrolyte Into Cermet Anode With a Decreased Al_2O_3 Concentration 330

146. Cross Section of 6846 Cermet Anodes Following Electrolysis in 60-A Cell. 332

147. Microprobe Analyses Showing Importance of Metal Phase Composition and Geometry on Internal Penetration of Electrolyte Into Anode 334

148. Cross Sections of 5324 + Cu Anode Material Following Electrolysis in 60-A Cell. 339

149. Thickness of Oxidized Zone on 6846 Cermet Anodes. 340

150. Aluminum Metal Contamination vs. Electrolysis Time for Test 2-165 Hours 343

151. Aluminum Metal Contamination vs. Electrolysis Time for Test 3-264 Hours 344

152. Ratio of Cu/Ni in Aluminum vs. Electrolysis Time. Test 2-165 Hours 348

153. Ratio of Cu/Ni in Aluminum vs. Electrolysis Time. Test 3-264 Hours 349

154. Ratio of Fe/Cu in Aluminum vs. Electrolysis Time. Test 2-165 Hours 351

155. Ratio of Fe/Cu in Aluminum vs. Electrolysis Time. Test 3-264 Hours 352

156. Ratio of Fe/Ni in Aluminum vs. Electrolysis Time. Test 2-165 Hours 353

157. Ratio of Fe/Ni in Aluminum vs. Electrolysis Time. Test 3-264 Hours 354

158. Total Weight of Fe in Aluminum vs. Time. Test 2-165 Hours. 360

159. Total Weight of Ni in Aluminum vs. Time. Test 2-165 Hours. 361

160. Total Weight of Cu in Aluminum vs. Time. Test 2-165 Hours. 362

161. Total Weight of Fe in Aluminum vs. Time. Test 3-264 Hours. 363

162. Total Weight of Ni in Aluminum vs. Time. Test 3-264 Hours. 364

163. Total Weight of Cu in Aluminum vs. Time. Test 3-264 Hours. 365

164. Electrolyte Contamination vs. Time. Test 2-165 Hours. 369

165. Electrolyte Contamination vs. Time. Test 3-264 Hours. 370

166. Inert Anode Inner Electrode Space Voltage Scan - Cell Current 2800-A 378

167. Inert Anode Inner Electrode Space Voltage Scan - Cell Current 3400-A 379

168. Graphite Anode Inner Electrode Space Voltage Scan - Cell Current 2700-A 380

169. 3-Point MOR Strength of 6846 Cermet Bars vs. Raw Materials Used, Temperature and Surface Finish . . 391

170. 3-Point MOR Strength of 5324 Oxide Inert Anode Bars 392

171. 4-Point MOR Strength of Cermet Inert Anode vs. Porosity . . 394

172. 3-Point MOR Strength of Inert Anode 6846 Cermet vs. Exposure Time and Location in Hall Cell. 395

173. Modulus of Rupture Data (3-pt.) for 94-12 6846 Cermet Bars at 20 and 1000°C. 397

174. Inert Anode Strength, MOR-4 pt. for Reaction Sinter and Calcine-Sinter Processed Material 399

175. Inert Anode Strength, MOR-4 pt. for Metal Added to 5324 Oxide Processed Materials. 400

176. Fracture Toughness of 5324 and 6846 Cermet Bars vs. Temperature 402

177. Fracture Toughness of Inert Anode Material vs. Metallic Phase Content. 403

178. Young's Moduli of 6846 Cermet and 5324 Oxide Anode Bars vs. Temperature. 404

179. Thermal Expansion-Inert Anode Compositions. 407

180. Measured Thermal Diffusivity of Oxide and Cermet Inert Anodes. 410

181. Calculated Thermal Conductivity of Oxide and Cermet Inert Anodes. 411

182. $NiO-Fe_2O_3$ Phase Diagram 414

183. Oxide Inert Anode Fabrication Process 415

184. Ni-O-Fe System at 1000°C. 417

185. Closed System Spray Dryer Schematic 420

186. Possible Process Flow Paths for Production of Inert Anodes 422

187. Fe_2O_3 Raw Materials (Pfizer and Sidmar) 427

188. Fe_3O_4 Raw Materials (Pfizer). 428

189. NiO Raw Materials 430

190. Microstructure (200X) of Reaction Sintered Inert Anode Using Coarse 74-Micron Median Diameter Fe Powder . . . 432

191. Microstructure (400X) of Reaction Sintered Inert Anode Material Using 21-Micron Median Diameter Fe Powder . . 433

192. Fe Raw Materials. 435

193. Ni Raw Materials. 436

194. Cu Raw Materials. 437

195. Closed System Spray-Dryed 6846 Powder-94-2 Mix Unreacted. . 441

196. Spray-Dryed 6846 Powder Using Atomizer Wheel and Pressure Nozzle 442

197. Spray-Dryed NiO and Fe_3O_4 Oxides Using Two Fluid Nozzle . . 444

198. Diametral Strength Tests on Green Compacts Pressed Wet and Dry with Binder Additions. 446

199. Inert Anode Powder Compaction Curves. 448

200. Expansion-Sintering Curves for Reaction-Sintered and Calcined-Sintered Inert Anode Powder Compacts. . . 451

201. Density vs. Sintering Temperature for Reaction-Sintered, As-blended, or Calcined-Ground Inert Powder Compacts. 452

202. Bulk Density of Inert Anode vs. Partial Pressure of Oxygen During Sintering. 454

203. Density of Cermet Anodes vs. Ni or Cu Alloy Content for Several Manufacturing Methods. 455

204. Preferred Inert Anode Manufacturing Process Flow Sheet. . . 457

205. Photograph of Pilot Size Anodes for 2500-A Cell 459

206. Microstructure and Physical Properties of Oxide Composition 5324 After Hot Isostatic Pressing at 1100°C 462

207. Microstructure and Physical Properties of Cermet Composition 6846 After Calcination, Cold Pressing, Sintering and Hot Isostatic Pressing at 1100°C 463

208. Microstructure and Physical Properties of Cermet Composition 6846 After Hot Isostatic Pressing at 1100°C 464

209. Microstructure of Cermet Anodes Fabricated by Addition of Grade 123-Ni Metal 25324 Oxide Powder, Cold Pressing and Sintering. 465

210. Fractured and Polished Surfaces of 5324 + 20% Cu Composition 466

211. Photograph of 60-A Bench Scale Reduction Cell 471

212. Anode 6846 Composition, Test 96, 96 Hours in 60-A Cell. . . 472

213. Micrographs of Anode 6846 Composition After 96 Hours in 60-A Cell. 473

214. Micrograph of Test 1A-96, Top of Billet, Below Diffusion Weld. 474

215. Test 1A-96, 96 Hours, Bottom of Exposed Billet. 475

216. Photograph of 2500-A Hall Cell. 477

217. Materials of Construction for Diffusion Welded Pilot Anodes for 2500-A Cell. 479

218. Materials of Construction for Pilot Sized Anode Utilizing Mechanical Connection for 2500-A Cell. . . 480

219. Photograph of 4-Anode Assembly. 482

220. Anode Preheat Furnace 483

221. Thermocouple Locations for Simulated Inert Anode Transfer 485

222. Delta-T Through Anode Wall. 486

223. Delta-T Along Anode Length. 487

224. Comparison of Analytical and Experimental Temperatures in Anodes. 489

225. Alumina Concentration in Bath for 12 Day Run. 497

226. Alumina Concentration in Bath for 21 Day Run. 498

227. Bath Ratio as Determined by Pyrotitration for 12 Day Run 499

228. Bath Ratio as Determined by Pyrotitration for 21 Day Run 500

229. Comparison of Bath Ratio Determination by Pyrotitration to the Determination by X-ray Diffractions. 501

230. Metal Analysis During 12 Day Run. 502

231. Metal Analysis During 21 Day Run. 503

232. Cross Section of 6846 (94-2) Anode As-fabricated. 505

233. Cross Section of 6846 (94-2) Anode Tested 21 Days in 2500-A Cell. 506

234. Cross Section of 6846 Cermet Anode (Mechanical Connection) After 185 Hours in 2500-A Cell 507

INERT ANODES FOR ALUMINUM SMELTING

I. SUMMARY

A. Background

The Bayer-Hall-Heroult Process for the production of primary aluminum has dominated the industry since its inception. In this process, Al_2O_3 obtained through the Bayer Process is electrolyzed in a Hall-Heroult cell in a cryolite bath at approximately 1250 K according to the reaction

$$Al_2O_3 + 3/2\ C \rightarrow 2\ Al + 3/2\ CO_2 \qquad (1)$$

Although 0.33 kilogram of carbon is theoretically required for each kilogram of aluminum produced according to reaction (1), nearly 0.5 kilogram of carbon per kilogram of aluminum is actually consumed because of losses due to air burning, back reaction of CO_2 with aluminum and formation of CO at the anode. Because of metal purity considerations, only petroleum coke is used at present. For the U.S. aluminum industry, the carbon consumption is nearly 2.27×10^6 metric tons per year.

The use of inert anodes (long lasting anodes that would not affect metal quality) in a Hall-Heroult cell employs the reaction

$$Al_2O_3 \rightarrow 2\ Al + 3/2\ O_2 \qquad (2)$$

The major consequence of replacing carbon anodes with long-lived anodes of another material is that a huge quantity of petroleum coke (2.27×10^6 metric tons per year for U.S. industry) and its energy content is saved. A substantial energy benefit results from approximately 75% lower polarization voltage. The use of inert anodes also may allow lower anode-cathode distance (ACD) to be maintained. The theoretical power requirement employing an inert anode according to Equation (2) is 9.24 kWh/kg of aluminum produced compared to 6.33 kWh/kg of aluminum produced for reaction (1). However, lower polarization and carbon savings lead to approximately 5.4% decrease in overall energy with no changes in A-C distance. If, however, the A-C distance could be reduced to 1.9 cm from the present 4.4 cm, e.g., by avoiding the thermal

upset in setting cold new carbon anodes, a 23% decrease in energy requirement would be achieved. Additional savings may result from oxygen produced at the anode, lowered energy for pollution control, and possibly improved current efficiency.

As presently perceived, the specific criteria which an anode must meet include: a) high electronic conductance comparable to carbon anodes at operating temperature, b) low reactivity with bath, or oxygen, or reduced species present in the electrolyte, c) relatively low cost and ready availability, d) ability to produce commercial purity aluminum, e) ability to be fabricated into large shapes, f) stable electrical connections, and g) adequate mechanical strength.

The concept of using inert anodes in the electrowinning of aluminum is as old as the Hall-Heroult process. Hall's original patents refer to the use of platinum and copper as nonconsumable anodes. Although Hall recognized the possible advantages of inert anodes and spent considerable effort in their development, an acceptable inert anode material eluded the inventor. On January 20, 1911, in an address to the American Chemical Society, the American Electrochemical Society and the Society of Chemical Industry, Hall said his work on inert anodes "delayed a successful result (other improvements in the overall smelting process) for a year or two." An inert anode for aluminum smelting has continued to remain elusive.

In the past, work on inert anodes has concentrated on two classes of materials, ceramics oxide and metals (1,2). The oxide ceramics had low solubility in molten cryolite, but generally possessed low electrical conductivity. This low conductivity dictated thin electrodes which required extremely low corrosion rates. On the other hand, the metal electrodes had excellent electrical conductivity. However, except for the noble metals (e.g., Pt) the metal anodes were unstable with respect to oxygen. The oxide layers that formed also tended to spall. Neither the ceramic electrodes nor metal electrodes investigated in these studies proved satisfactory as inert anodes.

However, the results generated, reports issued (3-13), and patents allowed

(14-16), during the course of the present cooperative program have shown that a cermet anode containing NiO, $NiFe_2O_4$ oxide phases and a Cu-Ni-Fe alloy metallic phase can be used successfully as an inert anode for the production of aluminum. These results will be presented in the following sections of this report.

B. Objective

The objective of this program was to develop an inert anode to replace carbon anodes in Hall cells used for the production of aluminum. Successful selection, fabrication, and operation of inert anodes will produce metal of acceptable quality, operate for significant lengths of time (six months or more), and result in an energy savings over present Hall cell operations.

C. Scope

The primary thrusts of the program are to develop an inert (non-consumable) anode material, evaluate its corrosion resistance, physical, and mechanical properties; fabricate anode shapes for small- and large-scale Hall cell testing; develop an electrical-mechanical connection to the anode bus; and evaluate anode performance in large-scale bench or pilot Hall cells.

D. Approach

Original objectives of the program were approached by conducting the following phases:

1. Phase I - Anode Material Development
2. Phase II - Anode Fabrication Development
3. Phase III - Connection Design and Testing

E. Technical Progress and Results

Technical progress and results for the cooperative program are summarized in the following section. The cooperative program was begun September 29, 1980, and continued until September 30, 1985.

1. Inert Anode Material Development

a. Compositional Development

A mixed oxide anode containing $Ni_xFe_{3-x}O_4$ and $Ni_yFe_{1-y}O$ phases has been evaluated for use in Hall-Heroult cells for electrolytic production of aluminum. The anode has poor electrical conductivity (~0.8 $ohm^{-1}cm^{-1}$ at 1000°C) and poor thermal shock properties. The anode has been used in a bench scale Hall cell to produce aluminum containing 0.15-0.4 wt% Fe and 0.02-0.09 wt.% Ni. A corrosion rate of ~$2x10^{-4}$ cm/h has been calculated from a number of test results.

The electrical conductivity and thermal shock properties are dramatically improved in cermet anodes in which Fe (metal), and nickel and iron oxides are made to react to form an interwoven network of Ni,Fe alloy in an oxide matrix. Bench-scale Hall cell tests on a number of cermet anodes showed relatively low levels of iron and nickel (0.02-0.10 wt.% Ni and 0.11-0.5 wt.% Fe) in the aluminum product. If the alumina feed is stopped, the anode corrodes more rapidly and the aluminum produced shows much higher levels of Ni and Fe. This Ni-nickel ferrite cermet material degrades by loss of Ni-Fe metal phase and electrolyte penetration. Anodic dissolution is involved in degrading the material.

A cermet material in which Ni-Fe alloy is replaced by Cu-Ni-Fe alloy performs significantly better. This material does not degrade with time, and apparently forms a passive layer which prevents loss of the metallic phase. Anodes of this material produced aluminum containing 0.03-.07 wt.% Ni, 0.26-0.34 wt.% Fe, and 0.05-0.12 wt.% Cu. The 17 wt.% Cu-containing cermet has a conductivity of ~90 ohm^{-1} cm^{-1}.

b. Corrosion Studies

Solubility data in cryolite-alumina melts has been gathered on the principal oxide phases present in the fabricated inert anode

compositions investigated during this contract. The oxides Fe_2O_3, NiO, and $NiFe_2O_4$ are increasingly soluble in cryolite as the Al_2O_3 content decreases in the melt. The solubility of $NiFe_2O_4$ is lower than the solubilities of its simple oxides. The solubility of NiO is less than Fe_2O_3. Based on these results and free energy calculations, ferrite based inert anodes should be operated at the lowest possible temperatures in electrolyte with near saturated alumina content, and the anode composition should be formulated with excess NiO.

The effects of additions of SiO_2, CaF_2, MgF_2, LiF, or ZrO_2 to the cryolite melt on the solubilities of Fe_2O_3 were determined. SiO_2 increased the solubility of Fe_2O_3, while the additions of CaF_2, MgF_2, and LiF decreased the solubilities of Fe_2O_3 and NiO in cryolite. These additives are only useful as long as the alumina solubility is not significantly reduced. The addition of ZrO_2 decreased the solubility of NiO but did not change the solubility of Fe_2O_3.

The solubilities of cobalt oxide, cobalt ferrite, and cobalt-nickel ferrite were measured in cryolite and were found to be as high or higher than iron-nickel ferrite. Several chrome oxided based materials were checked for solubility and results, generally, were higher than the iron-nickel ferrit.

Experiments with additions of Al, Mg, Li, and Zn dopants to the inert anode composition did not result in decreased solubilities.

Rotating disk experiments were used to determine the rates of dissolution of inert anodes. Dissolution was shown to proceed by first-order kinetics. Mass transport is indicated as the rate limiting step.

The dissolution rate constant vs. polarization, current, dissolved reduced species, and additions of carbon or Al_4C_3 were determined. An increase in current increased the dissolution rate constant. Additions of carbon or Al_4C_3 to the bath did not increase the dissolution rates of the anodes.

c. Electrochemical Studies

Ray (16) introduced the concept of a cermet inert anode containing approximately 70% $NiFe_2O_4$/NiO ceramic and 30% Ni metal. The nickel metal was intertwined throughout the ceramic base as a so-called wormy structure. The $NiFe_2O_4$ had low chemical solubility in cryolite, imparting a high degree of dimensional stability to the anode. The nickel metal provided high electrical conductivity (300 ohm^{-1} cm^{-1}) and improved mechanical properties such as resistance to thermal shock.

Conceptually, this cermet solved several problems of past material. The cermet was highly conductive and fairly inexpensive; therefore, an anode having a thickness of several inches with a long but finite life was acceptable. In practice, several problems remained, the most significant being that the corrosion rate of the metal phase greatly exceeded the corrosion rate of the ceramic oxide phases. Although the primary failure mechanism of the first cermet anode material was the rapid corrosion rate of the metal phase, poor aluminum metal quality and rapid anode material loss were also significant problems. Another major problem was failure of the anode connection. This was most often due to the rapid corrosion of the metal phase. Occasionally a connection failure not related to the corrosion process would also occur. All of the above problems were apparent when the Ni-cermet anode was scaled-up and tested.

Performance targets were set for each stage of testing of new inert anode materials that had to be met before the next stage of testing was attempted. The improved Cu-cermet anode displayed no signs of accelerated corrosion, nor any signs of the other problems when 2.5 cm diameter anodes were tested at 6 A for 30 hours (11). The improved cermet, therefore, passed the performance targets set for the 30-hour test. This mandated testing the material's performance in a more rigorous test, the 60-A cell. The following targets were set for the 60-A cell program: (1) internal oxidation rate of less than 8.7 cm/yr, (2) anode dissolution rate less than 6.6 cm/yr, (3) aluminum

metal purity >99.5% based on inert anode constituents, and (4) connection integrity that showed no signs of being affected by the electrolysis process. The improved Cu-cermet anode met or exceeded all of the performance targets. Three 60-A cell tests were performed with the improved cermet material.

Although material development was the primary goal of the inert anode program, the operation of inert anode cells at reduced interelectrode distances would provide the primary benefit of the inert anode. The benefit would be realized by reduced ohmic loss in the cell. This reduced ohmic loss was to be tested directly on a 20000-A pilot cell, but the 20000-A cell was never operated. The largest cell operated during the inert anode program was a 2500-A cell. The reduced ohmic loss could not be determined directly due to the thermal imbalance of the 2500-A cell at small anode-to-cathode distances. An indirect method of determining the voltage characteristic of a cell was first described by Haupin (17). A modification has been developed for the voltage characterization of the 2500-A cell. The 2500-A cell, with similar designs for both inert anodes and carbon anodes, was operated at higher voltages with the inert anodes than with the carbon anodes. The higher voltages are proposed due to increased ohmic losses in the electrolyte due to an emulsion of fine oxygen bubbles. The increased decomposition energy to produce oxygen instead of CO_2 is compensated by decreased ohmic losses in the anode.

d. Inert Anode Material Properties

Mechanical properties including modulus of rupture (MOR), fracture toughness, and Young's modulus, were measured for the 5324 nickel ferrite oxide, 6846 Ni-nickel ferrite cermet, Ni-nickel ferrite cermet (Ni + 5324), and Cu-nickel ferrite cermet (Cu + 5324) inert anode compositions. The mean MOR strengths were 104 MPa for Cu-nickel ferrite, 110 MPa for 6846 reaction sintered Ni-nickel ferrite, 166 MPa for 5324 nickel ferrite, and 190 MPa for Ni-nickel ferrite inert anode materials. MOR values were determined in four-point flexure on 3 x 4 x 45 mm test bars with a 20 mm upper and a 40 mm lower span.

Fracture toughness ranged from 1.9 for the 5324 nickel ferrite oxide composition to 5.4 MPa $m^{1/2}$ for Ni-nickel ferrite cermet compositions. Fracture toughness increases with increased metal content as expected. Young's modulus, measured by determination of resonance frequencies, were 155 GPa for 5324 nickel ferrite, 146 GPa for lower density 6846 Ni-nickel ferrite, 145 GPa for Cu-nickel ferrite, and 173 GPa for a higher density 6846 Ni-nickel ferrite composition.

The thermal properties of thermal expansion and thermal conductivity were determined for inert anode materials. The coefficients of thermal expansion for nickel ferrite, Ni-nickel ferrite cermet, and Cu-nickel ferrite cermet are fairly high and were measured as 11.9, 14.2, and 14.4 cm/cm/°C x 10^{-6} to 1000°C, respectively. The thermal conductivity for the 5324 nickel ferrite composition was determined to be 0.026 W/cm K, and that of the 6846 Ni-nickel ferrite cermet was 0.05 W/cm K at 1000°C.

Microstructural determinations on the oxide (5324) and the cermet (6846) inert anodes showed that the metal content was less than 3 up to 28 wt.%, respectively. The Cu-nickel cermet had a metallic content of 20 wt.% after fabrication. Porosity levels ranged from 1 to 5 percent.

The electrical conductivity of the semiconductor nickel 5324 ferrite oxide inert anode was 0.9 $(ohm\text{-}cm)^{-1}$ at 1000°C. The electrical conductivity of the 6846 Ni-nickel ferrite cermet was measured as high as 380 $(ohm\text{-}cm)^{-1}$ at 1000°C, whereas the Cu-nickel ferrite cermet material had a lower electrical conductivity, 89 $(ohm\text{-}cm)^{-1}$ at 1000°C, because of its lower metal content.

2. Anode Fabrication Studies

Fabrication studies were conducted on the various inert anode compositions to determine the optimum process flow sheet that would be technically feasible and commercially available for the manufacturing of inert anodes.

a. Raw Material Selection

Selection of the raw materials used in the fabrication of inert anodes is important because densification is dependent upon the fineness and reactivity of the powders. Finer powders produce a more homogeneous microstructure with finer grain size in the oxide and metal phases and a smaller amount of porosity.

The iron oxides used can be either hematite, Fe_2O_3, or magnetite, Fe_3O_4. They must be of high purity, with an agglomerate size of less than 10 microns with a submicron crystallite size.

The nickel oxide used should be "green" because this material is stoichiometric and was found to be reactive and produced denser inert anodes than did the "black" variety of nickel oxide. The NiO raw material agglomerate and crystallite sizes should be similar to those stated above for iron oxide.

The metal powders used in the fabrication of inert anodes should have a median particle size of 20 microns or less to insure densification, and a homogeneous distribution of fine metallic grains in the inert anode microstructure for optimum electrical conductivity and low levels of porosity.

b. Powder Preparation

Fabrication of large inert anodes for commercial size Hall cell evaluation required the development of powder process methods that would allow the manufacture of these large shapes without laminations, voids, cracks, density gradients, or other defects that could lead to catastrophic failure during use. Agglomeration of the raw materials was necessary to produce a powder that would flow readily into pressing dies and then could be pressed into green shapes without laminations or other pressing defects. Raw materials were processed through spray dryers to produce large agglomerated particles (>100 microns). Closed system spray drying was used with an organic fluid

carrier, isopropyl alcohol, and a polyvinyl butyral binder in combination with the Fe-NiO-Fe_3O_4 raw material combination to prevent oxidation of the free Fe metal during processing. It was learned that open spray dryers can be used to prepare agglomerated particles after the raw materials have been prereacted to produce metal phases that will not oxidize during spray drying. The liquid carrier in this case was water used with a polyvinyl alcohol binder to agglomerate the powder. It was also determined that the preferred powder mixture could be prepared by spray drying the 5324 calcined nickel ferrite oxide composition and then mixing it with Ni or Cu metal powder prior to pressing. Mixtures of spray dried oxides and Ni or Cu metal were successfully pressed into large inert anode shapes. The amount of binder necessary to produce agglomerated particles of sufficient strength for handling was determined to be 1 to 2 percent.

c. Consolidation Studies

Several consolidation processes were evaluated during the contact including cold pressing and sintering, hot pressing, and HIP'ing. The preferred method, that resulted in the maximum fabricated density, was the cold pressing and sintering method. Green powder compacts were pressed at 140 to 170 MPa. Sintering was conducted in controlled atmosphere furnaces where the partial pressure of oxygen was controlled in the 10^{-4} to 10^{-5} range by the use of a flowing argon cover gas. Sintering temperatures of 1350°C were used for the 6846 Ni-nickel ferrite and 1300°C for the Cu-nickel ferrite compositions with hold times of 2 hours for small samples and 4 hours for large anode shapes. Densities of up to 99 percent of theoretical could be obtained by the cold press sinter of calcined powder method. The reaction sinter method produces densities of about 91 percent of theoretical. The use of HIP'ing to enhance the density of reaction sintered compacts was partially successful in that densities were increased from 91 to 96 percent of theoretical. Hot pressing of inert anode compositions was not successful because of reduction of the oxide phases to metal in the presence of graphite dies and punches during the process conditions.

3. Anode-Stub Connection, Design, Testing and Evaluation

a. Anode Connection Studies

A diffusion welding technique was found to be most effective for attaching the cermet anode to the nickel stub material producing a mechanically strong joint with good electrical conductivity. Diffusion welds were made by reducing the inner surface of the anode to be joined with a reductant such as carbon, and diffusion welding by heating the nickel stub and reduced inert anode surface together to 1000°C and holding for several hours under nominal 0.4 MPa pressure. The performance of this diffusion welded joint was excellent in short-term testing in the 60-A cell with respect to electrical conductivity and strength. However, stability of the joint was suspect for long-term performance in Hall cell environments due to bath penetration, nickel stub corrosion, void creation and creep. Tests in the larger 2500-A cell for time periods of up to 21 days demonstrated that the performance of the connection was directly related to the corrosion resistance of the 6846 cermet material.

Bath penetration due to corrosion resulted in objectionable dissolution of anode material and ultimate failure of the connection. Several different connection designs including graded cermet-to-metal, plasma sprayed coatings, brazed alloys and mechanical designs were investigated late in the program in an attempt to extend connection life permitting longer term testing of the cermet anode material.

Mechanically sound connections were obtained by grading mixtures of nickel metal with 6846 cermet composition and increasing nickel content metal layers until the last layer is 100 percent nickel. These layers and anode powder were isostatically pressed together, sintered and diffusion welded to nickel stubs.

Graded layers were also produced by plasma spraying mixtures of inert anode powder with nickel metal powder resulting in a 100 percent nickel surface which can then be diffusion welded to the nickel stub.

A flask anode design incorporating a mechanical connection between the nickel stub and the anode was evaluated in an attempt to raise the anode-to-stub connection interface above bath level, and develop a bath freeze line in the thicker bottomed anode. These attempts were unsuccessful as liquid bath was found to penetrate above bath level during electrolysis in the 2500-A cell. While the mechanical connection performed well, sensitivity of the flask design to thermal shock was demonstrated by cracking of one anode when crust was removed, and insulation then replaced too quickly around the anode.

b. Structural Design

Analytical studies were conducted on both the diffusion welded and the newer flask anode designs to establish preheat and transfer practices for placement of the anode in the 2500-A cell. Procedures were developed to minimize thermal gradients during heat-up and operation, establish steady state preheat temperatures and protect the anode during transfer. Finite element models of the anode were used to study effects of stub depth and undercut geometry at the cylindrical corner of the connection recess well and optimize anode design.

Tensile testing of an anode with the mechanical connection showed that loads in excess of 70 MPa could be applied without failure. The force necessary to break bath crust after long-term cell operation was conducted, demonstrating that the mechanical connection and anode design will allow operation without failure due to expected mechanical and thermal stresses.

Finite element analysis comparison studies of inert anodes made from all-oxide 5324 and cermet 6846 compositions were performed. Mechanical property data including Weibull modulus were used. Radial and circumferential stresses for the all-oxide anode are 25 to 30 percent higher than for the cermet material. The longitudinal stresses are 40 to 50 percent higher. It is thought that either type of anode material could be operated in a Hall cell with proper design and cell operating conditions.

c. 2500-A Cell Testing

The 2500-A pilot cell program successfully demonstrated our ability to fabricate anodes and connection assemblies on a pilot sized scale and to preheat and transfer these assemblies to molten bath. Optimum inert anode performance was obtained by maintaining bath ratio at 1.15 at a temperature of 960°C, bath temperature at 960°C and Al_2O_3 content at or near saturation levels.

2500-A cell testing of the 6846 cermet material demonstrated that this composition is not acceptable as a stable anode. Service life of the inert anode assemblies using the 6846 composition with either diffusion welds or mechanical connections was limited to three weeks. Connections failed because of bath penetration and hot corrosion of the nickel stub and weld area. Metal purity analysis showed the presence of 0.8% Fe and 0.4% Ni by weight. Dissolution rates as determined by physical measurements of the anodes before and after service were determined to range between 12 and 48 cm per year from the anode radius.

d. Autopsy Investigations of 6846 Cermet Anodes

Microstructural, mechanical, chemical and X-ray phase analyses of 6846 composition inert anodes before and after testing showed that this material undergoes major changes in all of these properties that are detrimental for long service life in the Hall cell environment. The nickel metal phase is depleted, porosity is substantially increased, the oxide phase composition is changed and strength of the material is reduced to about one-third of the original amount. Improved cermet compositions, as described in other sections of this report, exhibit excellent performance in bench-scale studies with no evidence of objectionable corrosion.

F. Conclusions

1. A semiconducting mixed oxide material containing $Ni_xFe_{1-x}O$ and $Ni_yFe_{3-y}O_4$ phases has been developed and evaluated for use in Hall-Heroult cells as a nonconsumable electrode (inert anode) and was found to produce aluminum metal with nearly acceptable metal purity (0.14-0.4 wt.% Fe and 0.02-0.09 wt.% Ni) and low anode corrosion rates (2×10^{-4} cm/h).

2. The mixed oxide inert anode had an unacceptably low electrical conductivity (0.8 ohm^{-1} cm^{-1} at 1000°C) and poor thermal shock resistance properties.

3. Cermet anodes with a nickel metal phase interwoven in nickel and nickel ferrite oxides were dramatically improved in thermal shock resistance and electrical conductivity (150-300 ohm^{-1} cm^{-1}) properties.

4. Nickel cermet anodes tested in a 1.1 ratio Hall cell bath with 5% CaF_2 and 5% Al_2O_3 contaminated the metal with relatively low levels of iron and nickel (0.11-0.5 wt.% Fe and 0.02-0.1 wt.% Ni).

5. The nickel-nickel oxide-nickel ferrite cermet inert anodes were unstable in the Hall cell electrolyte and with time were penetrated with bath and the nickel alloy metal phase was removed by anodic dissolution.

6. An improved cermet material was developed that consisted of a Ni-Fe-Cu alloy interwoven in nickel-iron and nickel ferrite oxides. This material did not degrade within the testing time; produced an aluminum with 0.03-0.07 wt.% Ni, 0.26-0.34 wt.% Fe, and 0.05-0.12 wt.% Cu, and had a measured electrical conductivity of 90 ohm^{-1} cm^{-1} at 1000°C.

7. The solubilities of Fe_2O_3, NiO, and $NiFe_2O_4$ increase in $NaF-AlF_3-CaF_2$ melts with decreasing concentrations of Al_2O_3 in the melt.

8. The solubility of Fe_2O_3 decreases and the solubility of NiO does not change with a decreasing bath ratio.

9. The solubility of $NiFe_2O_4$ is lower than the solubilities of the simple oxides in the bath.

10. Results of the solubility studies show that Hall cells using nickel ferrite-based inert anodes should be operated at low temperatures, the electrolyte should contain high concentrations of Al_2O_3, and the anode should be formulated with excess NiO.

11. The addition of SiO_2 to the $NaF-AlF_2-Al_2O_3$ melt greatly increases the solubility of Fe_2O_3 while additions of CaF_2, MgF_2, and LiF to the melt decrease the solubility of Fe_2O_3 and NiO.

12. The solubilities of Co_3O_4, $CoFe_2O_4$, Cr_2O_3, $CoCr_2O_4$, and $NiCr_2O_4$ were determined in cryolite melts and were found to be higher than $NiFe_2O_4$.

13. Al, Mg, Zn, and Li dopants were added in solid solution to the nickel ferrite spinel in an attempt to reduce the activities of NiO and Fe_2O_3 in the material. In each case the solubility of Fe increased and the solubility of Ni decreased for the dopants Al, Mg, and Li; therefore, this approach was not successful.

14. A rotating disk system was used to measure the rates of dissolution in cryolite melts in an air atmosphere with no aluminum present. Dissolution proceeded by first-order kinetics and the rate constant was proportional to the square root of the rotational speed indicating mass transport was the rate limiting step for dissolution.

15. Dissolution rates increased with increased current through the anode because of increased stirring caused by increased oxygen evolution.

16. The presence of a dissolved reduced species (metal pad) did not increase the dissolution rate constant for iron and nickel.

17. Continuous additions of carbon or Al_4C_3 to the bath did not increase the dissolution rates of the anodes.

18. This study has demonstrated that a practical and stable metal phase in an oxygen-producing inert anode used for aluminum smelting is achievable. A copper-rich copper-nickel alloy in a $NiFe_2O_4$-NiO ceramic base is stable

because it cathodically protects the copper metal during initial phases of electrolysis, and high alumina concentration in the electrolyte assures the formation of a passivating $CuAl_2$ phase.

19. Experimental techniques using slow-scan linear-sweep voltammetry, galvanostatic polarizations, and microprobe elemental dot map analyses have proven useful to determine the resistance of metals and alloys to anodic dissolution in cryolite-base melts.

20. Measurement and comparison of voltages losses between inert anodes and carbon anodes in a 2500-A cell indicates that the higher decomposition voltage losses (thermodynamic and kinetic) for inert anodes are regained through small voltage losses in the inert anode and in the connection.

21. Economic raw materials are commercially available for the successful fabrication of inert anodes.

22. Traditional ceramic fabrication processes can be used to manufacture inert anodes.

23. The preferred manufacturing method includes the calcination, grinding, and spray drying of oxide powders; addition of metal powder, cold pressing and sintering.

24. Large oxide and cermet inert anode shapes can be manufactured for application in commercial size Hall cells.

25. The strength of oxide and cermet inert anode materials does not decrease substantially until temperatures above the use temperature of 1000°C are reached.

26. The fracture toughness of cermet anodes is about 5 MPa $m^{1/2}$ compared to 2 MPa $m^{1/2}$ for an oxide inert anode.

27. The finite element method was successfully employed for the design of the commercial size inert anodes to minimize mechanical and thermal stresses

that would cause premature failure during Hall cell testing. The measured properties of strength, elastic modulus, thermal expansion, and thermal conductivity were used for the design calculations.

28. Successful inert anode to bus bar electrical-mechanical connections were developed during the contract. These connection methods included: reduction-diffusion weld, graded cermet-to-metal, mechanical and high temperature brazed.

29. Methods were developed to successfully preheat inert anodes and transfer them to the 2500-A Hall cell without failure by thermal shock.

30. Commercial size inert anodes were successfully tested in a self-heated 2500-A Hall cell for periods up to 21 days.

G. Recommendations

1. Work should continue to improve the specific electrical conductivity of the material by optimizing the particle size, morphology and amount of metallic material in the cermet.

2. The effect of electrolyte composition and current density dissolution rates should be evaluated.

3. Anodes degrade if the electrolyte is not nearly saturated with Al_2O_3, so it is important to ensure alumina saturation without "mucking" the cell during large scale operation. Work should be directed towards improving the control of Al_2O_3 level and the bath ratio in the cell.

4. We performed work on a large number of oxides, mixed oxides, cermets, and a few alloys. Some Cu-NiO cermet, NiO-Li_2O anodes show promise and further work should be carried out with these systems.

5. Economic evaluation and design of anode to channel gases should be performed.

6. Analysis of anode life based on electrochemical engineering principles and physico-chemical data should be completed.

7. Additional development work is needed on fabrication of electrode to bus connections. High temperature braze alloy connections should be investigated more thoroughly.

8. Long term stability of the mechanical and braze alloy connections under service conditions need to be established.

9. The viability of the new Cu Ni-ferrite cermet to perform well for extended periods of time should be demonstrated in larger size pilot cells in order to preclude control problems encountered with the relatively small 2500-A cell.

II. INTRODUCTION

The objective of this project was to develop an inert anode and demonstrate improved energy efficiency in aluminum reduction cells.

For industrial aluminum production by the Hall-Heroult Process, the major reaction is:

$$Al_2O_3(s) + 3/2\ C(s) \rightarrow 2Al(\ell) + 3/2\ CO_2(g) \qquad (3)$$

with a reversible decomposition potential of 1.18 V at 1250 K. The theoretical carbon consumption according to Equation (3) is 0.37 kg of carbon for each kilogram of aluminum produced, at 90% current efficiency. However, according to Grjotheim et al. (1), the actual consumption is substantially higher and ranges from 0.42 to 0.55 kg for each kilogram of aluminum produced. Because of metal purity requirements, petroleum coke is the major source for carbon. The excess carbon consumption may be due to "air burning" of exposed parts of anode, dusting due to selective oxidation of binder coke, chemical reaction between carbon dioxide and carbon, and electrochemical evolution of carbon monoxide.

Throughout the U.S. aluminum industry, average electrical power usage is approximately 16 kWh/kg Al (18), although most recently designed cells can operate with lower power consumption. In a conventional Hall-Heroult cell run with consumable carbon anodes and employing equation (3), the theoretical power requirement is 6.33 kWh per kilogram of aluminum produced at 100% current efficiency (19). This includes contributions to heat the reactants to 1250 K, in addition to providing the decomposition energy of Al_2O_3 in presence of carbon. The difference between the theoretical energy and the actual energy consumed is attributed to current inefficiency, ohmic and voltage losses through anode and cathode, their connections, and through the electrolyte, and electrode polarization. In a typical Hall cell, major voltage losses result from the electrical resistance of the bath and from anode polarization. One way of decreasing the bath resistance is to shorten the anode-cathode distance (A-CD). A typical A-C distance is 4.4 cm. In present cells A-C distance may not be decreased because of possible shorting from undulations of the metal

pad. Metal undulation is greatly increased when new anodes are placed in cells because bath freezes around the cold anode causing severe imbalances in current distribution.

The use of inert anodes (long-lasting anodes that would not affect the metal quality adversely) in a Hall-Heroult cell employs the reaction:

$$Al_2O_3 \rightarrow 2Al + 3/2\ O_2 \qquad (4)$$

with a reversible potential of ~2.21 V at 1250 K. In such a process, carbon does not take part in the reaction and a major consequence of replacing carbon anodes is the savings of petroleum coke and its energy content. The use of an inert anode also results in approximately 75% lower polarization voltage. Inert anodes may also lead to compact cell design, low labor intensity, plus production and use of a moderately valuable byproduct oxygen. The theoretical power requirement employing an inert anode according to Equation (4) is 9.24 kWh/kg of aluminum. However, lower polarization and carbon savings may lead to approximately 5% decrease in overall energy (19) with no changes in anode-cathode distance. Additional savings may result with decreased anode-cathode separation.

As presently perceived, the specific criteria which an inert anode must satisfy are (a) high electrical conductance leading to a small voltage drop across the anode, (b) low reactivity with bath or oxygen, (c) relatively low cost and ready availability, (d) ability to produce commercial purity aluminum, (e) ability to be fabricated into large shapes, (f) stable electrical connections and adequate mechanical strength.

III. PHASE I - INERT ANODE MATERIAL DEVELOPMENT

The selection and development of an inert anode material suitable for use in a Hall cell was the largest technical challenge of the cooperative agreement. The major areas of research that constitute the inert anode material development portion of the program include: (a) compositional development, (b) inert anode corrosion studies, (c) electrochemical studies and (d) materials characterization. These areas will be covered in some detail in the following sections of the report.

A. Compositional Development

1. Objective

The specific objectives of the compositional development phase of the project are:

a. To identify and evaluate promising inert anode materials.
b. To determine the effect of Hall cell operating parameters on inert anode performance.
c. To determine the chemical, physical and electrical properties of inert anode materials as needed for compositional development.

2. Introduction

a. Review of Previous Work

Billehaug and Øye (20) reviewed past efforts to develop inert anodes. The criteria of cost and availability of materials, life expectancy and metal contamination that were encountered in the earliest attempts, persist in more recent works to develop an inert anode. However, advances in high temperature materials and semiconductor technology warrant a reexamination of possible materials for inert anodes. Pearson (5) and Grjotheim et al. (1) provided a discussion of attempts to develop inert anode materials.

Belyaev and Studentsov (6) and Belyaev (7) describe one of the earlier attempts to use nonconsumable anodes made out of oxide materials. Belyaev and Studentsov carried out experiments with Fe_3O_4 (magnetite), SnO_2, ZnO, and Co_3O_4. All these materials showed relatively low dissolution but because of higher resistivity compared to carbon anode, high cell voltages (6-9 volts) were noted at the terminals. Analysis also showed that the metal produced was between 97.5 and 94% pure rather than the required 99.7%.

Belyaev (23) studied a number of ferrite materials notably, $NiO{\cdot}Fe_2O_3$,

$Na_2O \cdot Fe_2O_3$, $MgO \cdot Fe_2O_3$, $2CaO \cdot Fe_2O_3$, $SnO_2 \cdot Fe_2O_3$, $Cr_2O_3 \cdot Fe_2O_3$, and $Co_3O_4 \cdot Fe_2O_3$. Solubility of these ferrites ranged from 0.012-0.947% in a cryolite + 5% Al_2O_3 melt according to their data, and conductivity at 1000°C ranged from 0.4-1.8 $ohm^{-1}cm^{-1}$. Electrolysis in a Hall cell led to 96-98% pure metal. The use of an oxygen-ion conducting material--for example, zirconium oxide stabilized with calcium oxide--was suggested as anode material by Marincek (24,25). Later studies show that a large number of known ion-conducting ceramic oxides indicate significant corrosion and cracking problems from thermal shock. CaO- and Y_2O_3-doped ZrO_2, CaO- and TiO_2-doped ZrO_2, CaO-doped CeO_2, and La_2O_3-doped CeO_2 were all found unsatisfactory because of high dissolution (10). In addition, charge transport at the electronic conductor-oxide conductor interface causes oxygen depletion and finally decrepitation, and requires a complicated mode of operation.

In recent years, Yamada and Tadanoi (27) suggested the oxides of the general formula XYO_2, where X stands for a monovalent metal, Y for a trivalent metal, and O for an oxygen atom; oxides of the general formula $X_2Y_2O_7$, where X stands for a trivalent metal, Y for a tetravalent metal; and XYO_4, where X stands for a tri or tetra and Y stands for a penta or tetravalent material as suitable anode materials. For example, it was claimed (12) that an anode containing 60.2% La_2O_3, 33.9% Cr_2O_3, and 5.9% $SrCO_3$ was electrolyzed in a Hall cell with a current efficiency of 95% and a polarized cell potential of 2.2 volts. This would indicate polarization voltage is nearly zero.

Klein (29) and Alder (30) recently have suggested SnO_2-based anodes, essentially more than 80% SnO_2, with additions like CuO and Sb_2O_3. Alder (30) further claimed that corrosion of such anodes can be greatly reduced by using a protective coating along the sides where current density is low. Low O_2 potential on the anode surface presumably exposes SnO_2 to Al, resulting in an aluminothermic reduction of SnO_2 to Sn.

Stender and Trofimenko (31) have described the use of H_2 or CO as a flowing gas in conjunction with a porous inert anode as a means of decreasing the electrical energy for smelting. A porous, electrically conductive and corrosion resistant material is chosen as the electrode --which is placed in a hermetically sealed apparatus, allowing the gas to be blown through at the necessary pressure. Then, if the electrode material is sufficiently well wetted by the electrolyte, three phases are established in the pores: electrolyte/electrode/gas. Under this condition, two reactions can take place: (1) oxidation of the material of the porous electrode or, (2) oxidation of the working gas (e.g., H_2 or CO) during the discharge of O-containing ion. When oxidation of the gas occurs, the porous electrode is unchanged and the anode operating on such a principle is called a gas anode. The basic material requirement is no less stringent under such conditions, and whether there is any net energy saving is questionable. This approach would be advantageous if the energy gained is not offset by the energy used to make CO of H_2.

Alder (32) has suggested that corrosive attack on the parts of the anode surface not protected by a gas curtain or barrier produced by high current density may be limited by a flowing oxidizing gas. Alder (33) has patented a bipolar cell arrangement similar to the Alcoa $AlCl_3$ bipolar cell using SnO_2 base material as anode and graphite as the cathode material. However, there are serious material problems in both the anodic and cathodic sides that need to be solved before this arrangement can be used in practice. For example, because of high sodium ion activity in a fluoride cell, a bare graphite cathode poses problems of intercalation and degradation. On the other hand, bare SnO_2-based material is not stable enough for commercial quality metal or for stable A-C distance. To date, because of these technical and economic reasons, no aluminum producer has successfully reduced the inert anode concept to practice.

b. Review of Previous Alcoa Work

In the following we review the results of investigations carried out

at Alcoa Laboratories. The strategy has been to develop materials that are cost effective and satisfy the criteria mentioned in the previous section. Oxides present the most attractive class of materials. Emphasis is based on materials development using inexpensive and readily available materials. Chromites and ferrites are the most attractive oxides because they are relatively inexpensive, readily available, and show electronic conduction. Materials with spinel, perovskite, and rutile structures can be doped easily with aliovalent ions that fit into these structures and enhance the electronic conductivity by increasing the number of current carriers.

1) Refractory Metals

The high melting point metals such as Mo, W, Zr, Hf, Ti, Cr, Ta, and Nb possess adequate electronic conductivity and possibly low solubilities. However, in tests at Alcoa Laboratories all of them oxidized to nonconducting, volatile and/or soluble species.

2) Borides, Nitrides, and Carbides

Some of these refractories have attractive semiconducting properties and low solubilities in the electrolyte and do not react with oxygen. In tests as anodes at Alcoa Laboratories, they were all oxidized under the conditions of electrolysis and lost conducting properties.

3) Noble Metals

Metals such as Pt, Au, Ag, Pd, and Rh are good electronic conductors and form no stable oxides. However, in contact with aluminum metal, they form alloys of aluminum. When oxygen was continuously discharged on the platinum in tests at Alcoa Laboratories the anode was more stable, but such metals are excluded because of cost.

4) High Temperature Corrosion Resistant Alloys

High temperature corrosion resistant alloys possess adequate electronic conductivity and a number of them have low solubility in a Hall cell electrolyte. In tests at Alcoa Laboratories various commercial high temperature alloys invariably oxidized, degraded, and lost conducting properties.

5) Coating on Conducting Materials

Attempts have been made at the Alcoa Laboratories to use suitable coatings on steel, copper, or graphite. The coating material included electroplated metals and some oxides. However, such attempts have not been successful mainly because the deposited material did not satisfy the stringent material requirements in a Hall bath.

6) Mixed Oxides

The oxides belong to a class of materials that cover a wide range of stability, resistance to further oxidation, solubility in the electrolyte, resistance to fluoride formation and electrical conductivity. If the oxide is soluble in the melt, there is a possibility of the soluble species reacting with the metal pad, e.g.,

$$M_xO_y + 2y/3\ Al = y/3\ Al_2O_3 + xM\ (\text{dissolved in Al}) \qquad (5)$$

This reaction is thermodynamically favorable if the free energy of formation of the oxide (per gram atom of oxygen) is less negative than that of alumina. For a compound less stable than alumina to function as an inert anode, its rate of dissolution, under electrolysis, should be small. Further, a number of oxides may form fluorides by reaction with cryolite (18), e.g.,

$$1/y\ M_xO_y + 2/3\ Na_3AlF_6 = x/y\ MF_{2y/x} + 1/3\ Al_2O_3 + 2\ NaF \qquad (6)$$

These oxides should be avoided. There is also a possibility of other components of electrolyte, e.g., AlF_3, Al_2O_3, CaF_2, reacting with the anode. In practice, the activities of the components have to be considered. For example, consider the reaction:

$$Fe_2O_3(s) + 2\ AlF_3(s) = 2\ FeF_3(s) + Al_2O_3(s) \qquad (7)$$

for which $\Delta G°$ is +65.3 kJ/mole at 1250 K. Assuming the activity of Al_2O_3 is unity and using $3x10^{-3}$ as value for the activity of AlF_3 in a NaF-AlF_3 melt with a bath ratio of 1.1 at 1250 K (standard state is solid AlF_3) (19), one obtains:

$$\frac{a^2_{FeF_3}}{a_{Fe_2O_3}} = 9.1x10^{-6}$$

Thus, Fe_2O_3 is not likely to form FeF_3 to a large extent. The stability of individual oxides may be improved further by compound formation.

Those oxides more stable than alumina, BaO, BeO, CaO, MgO, etc., are generally quite soluble in molten cryolite. Some transition metal oxides in their highest valent state are relatively insoluble in the molten fluoride bath.

Fe_2O_3 and NiO have relatively low solubility in cryolite melts (1) and each oxide is more stable than its fluoride.

Table 1 shows the properties of pertinent oxides. The free energy values at 1250°K per gm atom of oxygen are shown for these oxides. Further, solubility values at 1000°C in cryolite and solubility in a cryolite melt containing 5 wt.% Al_2O_3 are also shown. The electrical conductivity types are also shown. Table 1 shows that from a solubility point of view, Cr_2O_3, Fe_2O_3, NiO, SnO_2, and Co_3O_4 are interesting candidates.

TABLE 1

PROPERTIES OF PERTINENT OXIDES

Oxide	Stability -ΔF1250°K/gatom oxygen -kcal/gatom of oxygen	Solubility Wt.% in Cryolite at ~1000°C	Solubility in 95 Wt.% Na_3AlF_6 + 5 Wt.% Al_2O_3 at ~1000°C Wt.%	Conductivity Type
Al_2O_3	101.9	11		Nonconductor
BaO	105	35.75	22.34	Nonconductor
BeO	113	8.95	6.43	Nonconductor
CaO	121	13	--	Nonconductor
CeO_2		3.4		Nonconductor
CdO	25	5	0.26	Semiconductor
Co_3O_4		.23	--	
Cr_2O_3	64	0.13	0.05	Defect Semiconductor
CuO	10	1.1	0.68	Defect Semiconductor
Fe_3O_4	43			Mixed Valence Semiconductor
Fe_2O_3	39	0.18	0.003	Semiconductor
HfO_2	104	--	--	Nonconductor
MgO	111	11.7	7.02	Nonconductor
Mn_3O_4	61	2.19	1.22	Semiconductor
Na_2O	57	23.0		
NiO	32	0.32	0.18	Defect Semiconductor
SnO_2	38	0.08	0.01	Excess Semiconductor
SrO	111	--	--	Nonconductor
TnO_2	121	>10		Nonconductor
TiO_2	85	4.9	4.2	Excess Semiconductor
V_2O_3	73	>5		Metallic Conductor
V_2O_5	50	0.9	0.21	Semiconductor
Ta_2O_5	78	3.8		Semiconductor
ZnO	50	0.5		Semiconductor
ZrO_2	102	>4		Nonconductor

Table 2 lists the types of oxide compounds evaluated at Alcoa prior to the start of the DOE-Alcoa cooperative program. Through these studies, Fe_2O_3- and NiO-based material and "spinel type material" containing $NiFe_2O_4$ were chosen for further study. Spinel type material, e.g., AB_2O_4 material may contain two types of cations (A and B). In the example shown in Table 3, the A cations occupy the tetrahedral position and B cations the octahedral position. Table 3 shows that the spinel structure has a possibility to substitute a variety of cations and alter properties. Further, stability of mixed oxides is likely to be reflected in lower solubility of individual oxides. During the cooperative program, the major effort was placed on evaluating the materials in the $NiO-Fe_2O_3$ system and particularly a mixed oxide anode containing 51.7 wt.% NiO and 48.3 wt.% Fe_2O_3 (composition 5324). Anodes formed from these materials had excellent "corrosion" properties. However, their electrical and mechanical properties were inadequate. The material had electrical conductivity of less than 0.5 $ohm^{-1}cm^{-1}$ at 1000°C, and larger shapes often tended to crack during testing. Consequently, we tried various additives (cation substitutions) in the basic 5324 composition material.

7) Coatings

Further, coatings of 5324 material on electron conducting substrates were also evaluated. Plasma spraying is a process whereby powdered material introduced into a plasma stream becomes molten and is projected against the surface being coated. Owing to "splat-quenching" of the molten particles on the cool substrate, a coating is built up which consists of many layers of overlapping lenticular particles. As a result of this mode of formation, three important properties must be considered: a) coating-to-substrate adhesion, 2) interconnected porosity, and 3) accumulating stress factors as the coating thickness is increased.

TABLE 2

OXIDE SEMICONDUCTORS

Type	Compound	Dopant	Electron Exchange
MgO	NiO	Li_2O	Ni^{2+},Ni^{3+}
Hematite	Fe_2O_3 Fe_2O_3+ Cr_2O_3	SnO_2 TiO_2	Fe^{2+},Fe^{3+}
Rutile	SnO_2 TiO_2	Sb_2O_5 Ta_2O_5 Nb_2O_5	Sn^{4+},Sn^{3+} Ti^{4+},Ti^{3+}
Perovskite	$LaCrO_3$ $LaFeO_3$ $SrTiO_3$	SrO La_2O_3	Cr^{2+},Cr^{3+} Fe^{3+},Fe^{4+}
Spinel	$NiFe_2O_4$ $ZnFe_2O_4$ $MnFe_2O_4$ $CoFe_2O_4$	MnO_2 TiO_2 SnO_2 ZrO_2 Nb_2P_5 Ta_2O_5 WO_3	Fe^{2+},Fe^{3+} Ni^{2+},Ni^{3+} Mn^{2+},Mn^{3+} Co^{2+},Co^{3+}

TABLE 3

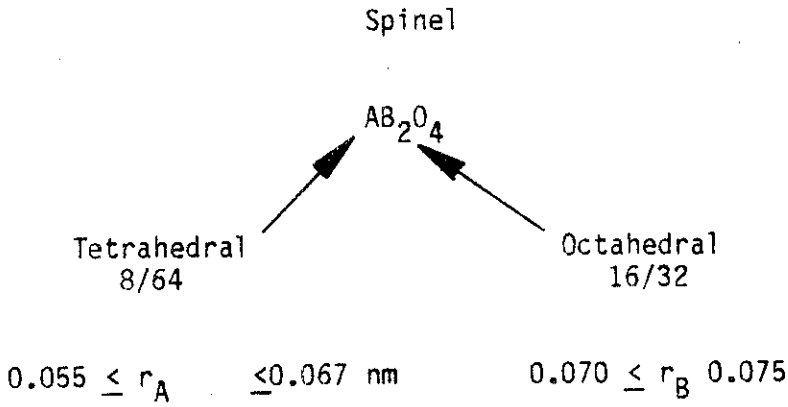
Spinel
AB_2O_4
Tetrahedral
8/64
Octahedral
16/32
$0.055 \leq r_A \leq 0.067$ nm
$0.070 \leq r_B \leq 0.075$
Possibility to substitute
a variety of
cations and alter
properties

In addition, some effort was made to formulate and evaluate other oxide materials as shown in Table 2. In particular, a Fe_2CoO_4 sample was fabricated and evaluated, and several samples in the Fe_2O_3-NiO-Co_3O_4 and Fe_2O_3-Co_3O_4 systems were fabricated. However, no major emphasis was placed on Co_3O_4-containing anodes as thermal shock was found to be a major problem with these oxide anodes.

8) Cermet Anodes and Alloys

We introduced the concept of "cermet anodes" to reduce the problem of poor electrical conductivity and mechanical properties. In addition, we studied a number of metal and alloy anodes. These were formed with the hope to form a protective oxide on anodes. The experiments and results will be described in subsequent sections.

Cermets are a class of material in which both metallic and ceramic components are present. Ideally, these would have the desirable properties of metallic materials as well as those of the ceramics. In the context of its use here, the oxide was found to have the desirable corrosion properties and the metallic materials have the desirable electrical and mechanical properties. By a proper combination we have obtained the desired anode with enhanced electrical conductivity while retaining the desired degree of inertness. We have produced metal oxide-alloy composites by mixing in metallic powder, e.g., Cu with oxide 5324, or by reaction sintering. Reaction sintering leads to displacement reactions in the solid state (35,36).

3. Experimental Techniques

a. Fabrication-Oxides

Experimental mixed oxide compositions were fabricated by milling, powder calcination, or primary sintering, grinding, uniaxial die

pressing and sintering. All materials were reagent grade unless mentioned otherwise. Compositions showing promise during bench scale Hall cell testing because of low dissolution in the electrolyte and desirable metal quality were studied further to improve fabricability. High density and low water absorption are desirable. Through earlier work, anode composition 5324 with 51.7 wt.% NiO and 48.3 wt.% Fe_2O_3 was chosen for scale up and further studies. In addition, parts in the $NiO-Co_3O_4-Fe_2O_3$ and $Fe_2O_3-NiO-Y_2O_3$ and $NiO-Li_2O$ systems were fabricated. Fabricated sample, with 51.7 wt.% NiO and 48.3 wt.% Fe_2O_3, contain 82 wt.% $Ni_xFe_{3-x}O_4$ and 18 vol.% (Ni,Fe) O phases.

Anodes fabricated with 5324 composition were found to have encouraging dissolution and corrosion properties during electrolysis. However, it was found that 5324 anode material has a poor electrical conductivity. Further, difficulties were encountered during scale-up to 7.5-cm diameter sizes. The anodes were too susceptible to cracking, and connection appeared to be a difficult problem with this material. In order to increase the electrical conductivity, various dopants were introduced. However, only marginal improvement was noticed.

b. Fabrication-Coatings

Coatings of 5324 oxide on suitable substrates were examined. 5324 oxide powder was plasma sprayed on carbon, steel, Ni 200 and SS 446 substrates. Stainless steel 446 was chosen as the substrate material because of its favorable thermal expansion match with 5324 oxide. Plasma-sprayed coatings may exhibit interconnected porosity due to their mode of formation. Some efforts were made to make pore-free coatings by use of uniformly sized powders and incorporating a "glassy" additive that tends to fill the voids in the coating. The details of plasma spraying were reported in the first Annual Report (3). However, even in short-time Hall cell tests the coated material did not appear satisfactory.

c. Fabrication-Cermets

Most dramatic improvements in electrical conductivity have been seen when metallic materials were dispersed in a ceramic matrix. Cu, Ni, and Ni-Fe alloys are good materials as dispersions and were identified prior to the start of the cooperative program. Improved electrical conductivity and good weldability were also seen in partially reduced 5324 anode material. In these materials, metals are distributed in a ceramic oxide material. The metal and the oxide must be compatible.

There are a number of ways by which cermets in the Ni-Fe-O system can be prepared. The reaction-sintered cermet material was fabricated by mixing Fe (powder), NiO, and Fe_3O_4 (3,15,16). The powder mix was uniaxially pressed and subsequently sintered in an argon atmosphere. Fe powder was from Quebec Atomet 95, NiO was from ceramic color and chemical, and Fe_3O_4 was Pfizer BK 5000 grade (see Phase II - Anode Fabrication Studies Write-up this report). Reaction sintering led to displacement reactions in the solid state and produced essentially three phases. $Ni_{1-y}Fe_y$ (alloy), $Ni_xFe_{3-x}O_4$ (spinel) and (Ni,Fe) O oxide phases. The copper-containing cermet material was fabricated by mixing copper powder with NiO and Fe_2O_3, uniaxially pressing and sintering. Table 4 shows the details of nickel-nickel ferrite inert anode fabrication, phases present in the product, and electrical conductivity values at 1000°C. The amount of various phases present depends on the starting composition and the atmosphere in which they are sintered. Dalvi and Smeltzer (37) reported the Fe-Ni-O phase diagram at 1000°C.

d. Electrical Conductivity

Electrical conductivity of the mixed oxide (51.7 NiO, 48.3 Fe_2O_3) sample was determined by an AC two-probe technique (38) using a Wayne Kerr Universal Bridge B-224 and spring-loaded electrodes. It is capable of measuring impedances from 10^{-3} ohms to 10^{16} ohms. The bridge operates at 1592 Hz. Four-probe measurement with a Keithley electrometer and a current source was preferred for measuring the electrical conductivity of cermet samples.

TABLE 4

Summary of Fabricated Anodes Tested in Bench-Scale Hall Cell, Anodes Were Pressed at 172 MPa (15 ksi) and Sintered for 14 Hours in Argon

Composition Wt.%									
Fe (metal)	5.86	7.6	8.45	8.91	9.52	12.97	20	20	39.7
NiO	33.34	60.93	56.52	54.14	50.98	34.21	70	60	60.3
Fe_3O_4		31.47	35.03	36.95	39.5	53.0	10	20	
Fe_2O_3	60.80								
Sintering Temp. (°C)	1350	1150	1150	1100	1075	1150	1150	1350	1150
Density (g/cm^3)	5.1	5.0	5.1	5.0	5.0	5.2	4.6	5.4	5.7
X-ray Phases									
Spinel	medium	medium -	medium -	medium -	medium -	medium +	small +	medium	medium
(Ni,Fe)O		medium -	medium -	small +	medium -		small +	trace	
(Ni,Fe) alloy	medium	small -	small -	small +	small +	medium -	medium	medium	medium
Electrical Conductivity at 1000°C, $\Omega^{-1}cm^{-1}$	58	14	22	39	27	115	32	300	955

Electrical conductivity of cermet anodes was measured using the DC four-probe technique (39). After sintering, the pellets were lightly polished and dimensions were measured using a micrometer to within ±0.001 mm. The pellets were pressed between two platinum foils in a spring-loaded quartz assembly. The assembly was kept in a high purity argon atmosphere. The whole assembly was inserted in a Kanthal-wound furnace. Platinum wire spot welded to the two platinum foils in which the sample pellet was sandwiched. The voltage between two points on the sample were measured using a nanovoltmeter. The voltage leads were attached to the sample by making circumferential contact. Specific conductivity was estimated by measuring the voltage and current and by using the usual relationship $\sigma = \ell/RA$, where σ is the specific conductivity in $\Omega^{-1}cm^{-1}$, ℓ the distance between the voltage probes and A, the area of contact in cm^2 calculated from the diameter of the sample.

e. Hall Cell Evaluation of Inert Anodes

The fabricated materials were tested in a bench-scale Hall cell (Figure 1). The anodes were ~2.2 cm diameter and 2.7 cm long. Anodes can be tested in this cell normally for 24-50 hours. Alumina crucibles are used to hold the electrolyte. Alumina was fed to the cell from the hopper shown in Figure 1. The feed was controlled by a timer which can be adjusted depending on current efficiency. Anode connections were made in a groove around the top of the anode. The groove is platinized using a platinum paste (Engelhard 6082). Platinum wire wrapped around the groove served as electrical connection.

The cell is heated by a resistance furnace with temperatures controlled to within ±1°C. Molten aluminum on top of a graphite disk served as the cathode. The graphite disk was immersed in molten aluminum and was attached with a Nickel-200 (Ni-200) rod which serves as the negative lead. The Ni-200 lead was protected from reacting with the aluminum metal or the electrolyte by an alumina sheath. Nickel may contaminate the molten aluminum if this alumina protective

GA 18194.120

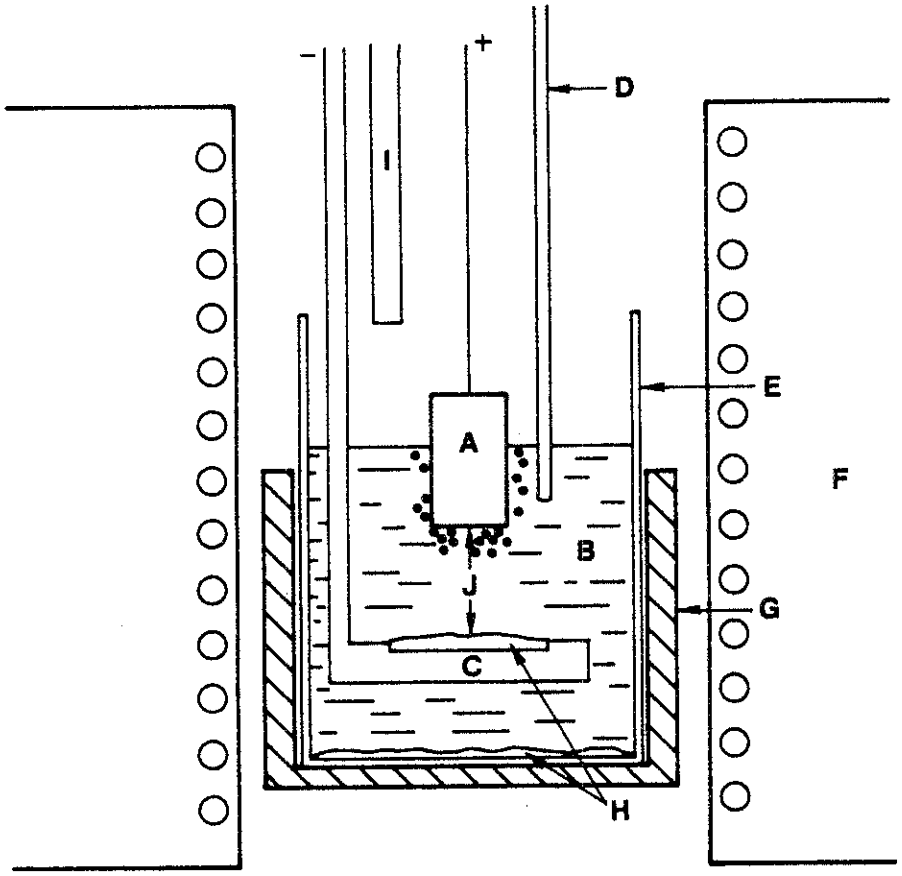

A - Anode
B - Bath
C - Cathode
D - Thermocouple
E - Alumina crucible
F - Furnace
G - Protection crucible
H - Aluminum metal
I - Feeder
J - A-C distance

Bench-Scale Hall Cell
Figure 1

sheath would be destroyed. The cell was operated at ~4 A with an overall anode current density of ~0.3 A/cm^2 or a current density of 1 A/cm^2 based on bottom anode surface area alone. The cell was operated at 960°C with the electrolyte containing NaF and AlF_3 in the weight ratio 1.1:1; the electrolyte also contained 5 wt.% Al_2O_3 and 5 wt.% CaF_2. A chromel-alumel thermocouple protected by an alumina sheath monitored the temperature.

While the above operating conditions were generally used, a number of experiments were carried out to determine the effect of bath ratio, current density, Al_2O_3 content in the bath, and the effect of metal composition in the cermet. See-thru cell tests were carried out to visually examine the bubble pattern with inert anodes as compared to that with carbon anodes. Further inert (Pt) markers were placed on the bottom of some anodes during fabrication, and the positions of the markers were noted to understand the growth mechanism of oxide layers on cermet anodes.

4. Results and Discussions

a. Hall Cell Tests

Figure 2 shows a micrograph of the fabricated mixed oxide anode material. The primary phase in this micrograph is $Ni_xFe_{3-x}O_4$ type spinel, the light dark phase is a (Ni,Fe)O phase, and the dark areas are the pores. Figure 3 shows the electrical conductivity of this material in air, as a function of temperature. Electrical conductivity, σ, is plotted as a function of 1/T°(K) and it is seen that log σ vs. 1/T shows nearly a straight line as expected for a semiconductor material.

The electrical conductivity of this material is rather low, only 0.82 $(ohm\text{-}cm)^{-1}$ at 1000°C, compared to over 200 $ohm^{-1}\text{-}cm^{-1}$ for carbon anodes, presently used. Thus, the use of an inert anode of this material would not be economical because of a large IR drop in the anode even considering the fact that a nonconsumable anode may be

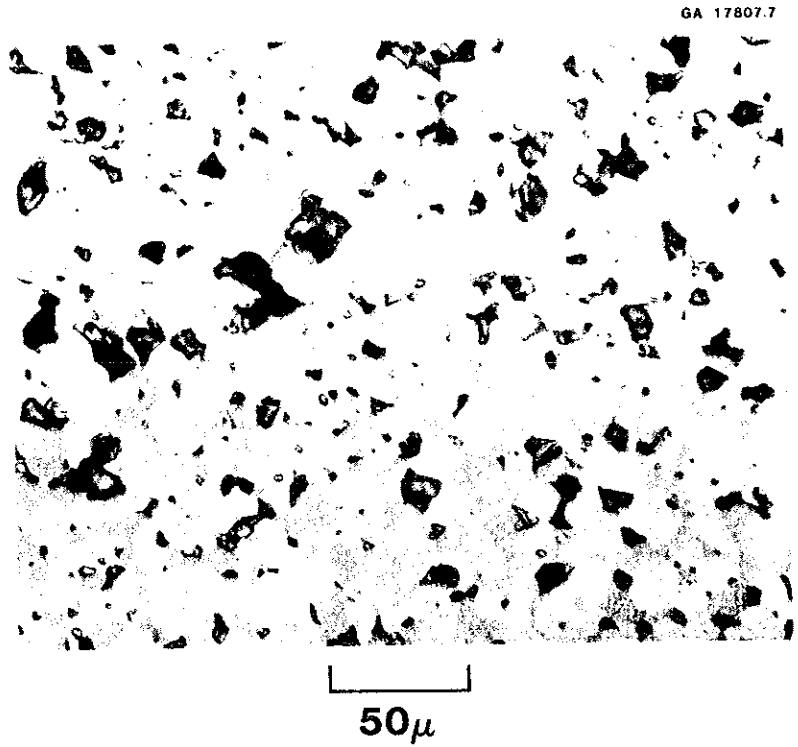

Micrograph of Fabricated Mixed Oxide Anode. The Bulk is $Ni_xFe_{3-x}O_4$ Type Spinel. Light Dark Areas Are $Ni_xFe_{1-x}O$. Dark Areas Are Voids.

Figure 2

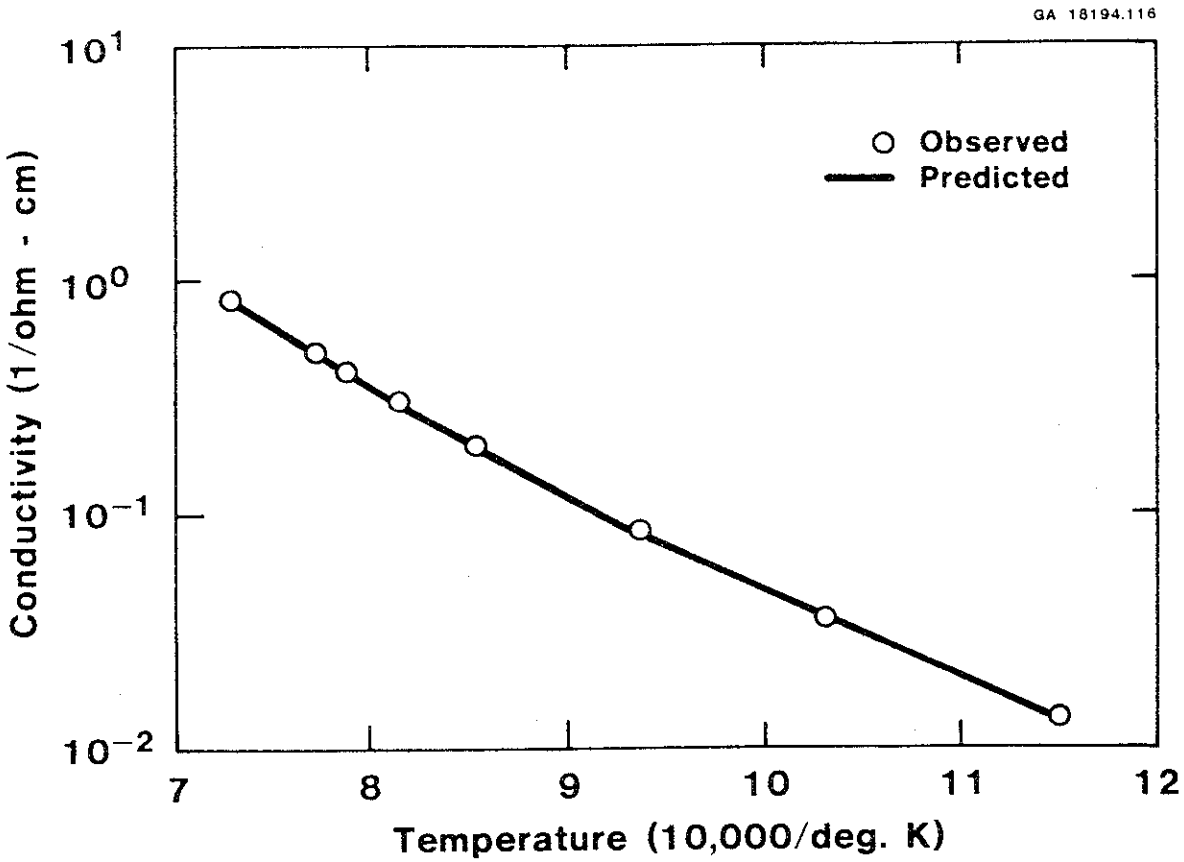

Electrical Conductivity of 5324 Composition All-Oxide Inert Anode

Figure 3

designed to provide a larger ratio of the anode area (A) to the anode length (L), compared to carbon anodes.

Table 5 is a summary of the bench-scale Hall cell tests with a ceramic anode containing 51.7 wt.% NiO and 48.3 wt.% Fe_2O_3. Test results on three anode samples are described. Anode designated A was run first for 25 hours and the same anode was also tested for 24 hours. Anode B was tested four times for a total of 100.5 hours, and Anode C was tested for a total of 81 hours. Small amounts of anode corrosion were noticed at the end of tests lasting over 70 hours. Corrosion rate was calculated from the anode dimension at the end of 100.5 hours test period. The corrosion rate was $\sim 2.2 \times 10^{-4}$ cm/h for Anode B and 1.5×10^{-4} cm/h for Anode C. Analyses of the electrolyte for Ni and Fe at the end of test are shown in Table 5. It appears that the electrolyte is not saturated with respect to iron and nickel oxides.

Figure 4 is a backscattered electron picture of a cermet anode material fabricated from 39.7 wt.% Fe and 60.3 wt.% NiO. Figure 5 shows the corresponding X-ray images for Ni, Fe, and O. It is seen that the material contains essentially two phases: the white area is metallic and contains an (Ni,Fe) alloy; the oxide phase is primarily iron oxide (Fe_3O_4) with a small amount of nickel oxide. The alloy phase is interwoven with the oxide phase. Such interwoven phases are seen in other cermet anodes also.

The electrical conductivity is found to be dependent on the composition and morphology of the product. It should be remembered that the electrical conductivity of a carbon anode is nearly 200 $ohm^{-1}\ cm^{-1}$. A nonconsumable anode with electrical conductivity of only 10 $ohm^{-1}cm^{-1}$ may be usable by proper design of the anode. The electrical conductivity values of these materials are, therefore, very attractive. These materials were also easier to test in a laboratory cell because they appear to have better thermal shock properties than an all-oxide inert anode. The all-oxide-type materials were preheated on top of the cell prior to introduction into the molten salt. The anodes tended to crack or fracture if they were subjected to thermal

TABLE 5

Summary of Bench-Scale Hall Cell Tests
51.7 Wt.% NiO, 48.3 Wt.% Fe_2O_3 Anode, Density 5.1 g/cc,
1.1 Ratio Bath, 5% CaF_2, 5% Al_2O_3

Test No.	Run Time (h)	Total Run (h)	Current Efficiency (%)	Bath Analysis		Metal Analysis		Comments
				Wt.% Ni	Wt.% Fe	Wt.% Ni	Wt.% Fe	
A-1	25		83	0.02	0.04	3.2	0.28	No corrosion of anode, crucible broke. Ni exposed to metal.
A-2	24	49	91	0.02	0.04	0.05	0.17	No measurable change of anode.
B-1	24		96	0.03	0.02	0.02	0.09	No significant change of anode.
B-2	29	53	89	0.03	0.04	0.36	0.40	Possible contamination from thermocouple sheath.
B-3	26.5	79.5	91	0.02	0.03	0.09	0.23	Very small dimensional change.
B-4	21	100.5	80	0.01	0.02	0.06	0.18	Small corrosion noticed, bad connection. 2.2×10^{-4} loss of material based on total run.
C-1	24		91	0.02	0.03	0.05	0.15	No noticeable corrosion.
C-2	25.5	49.5	83	0.02	0.03	0.06	0.27	No noticeable corrosion.
C-3	27	76.5	81	0.02	0.03	0.03	0.19	1.5×10^{-4} cm/h loss (max) based on total run.

GA 17807.4

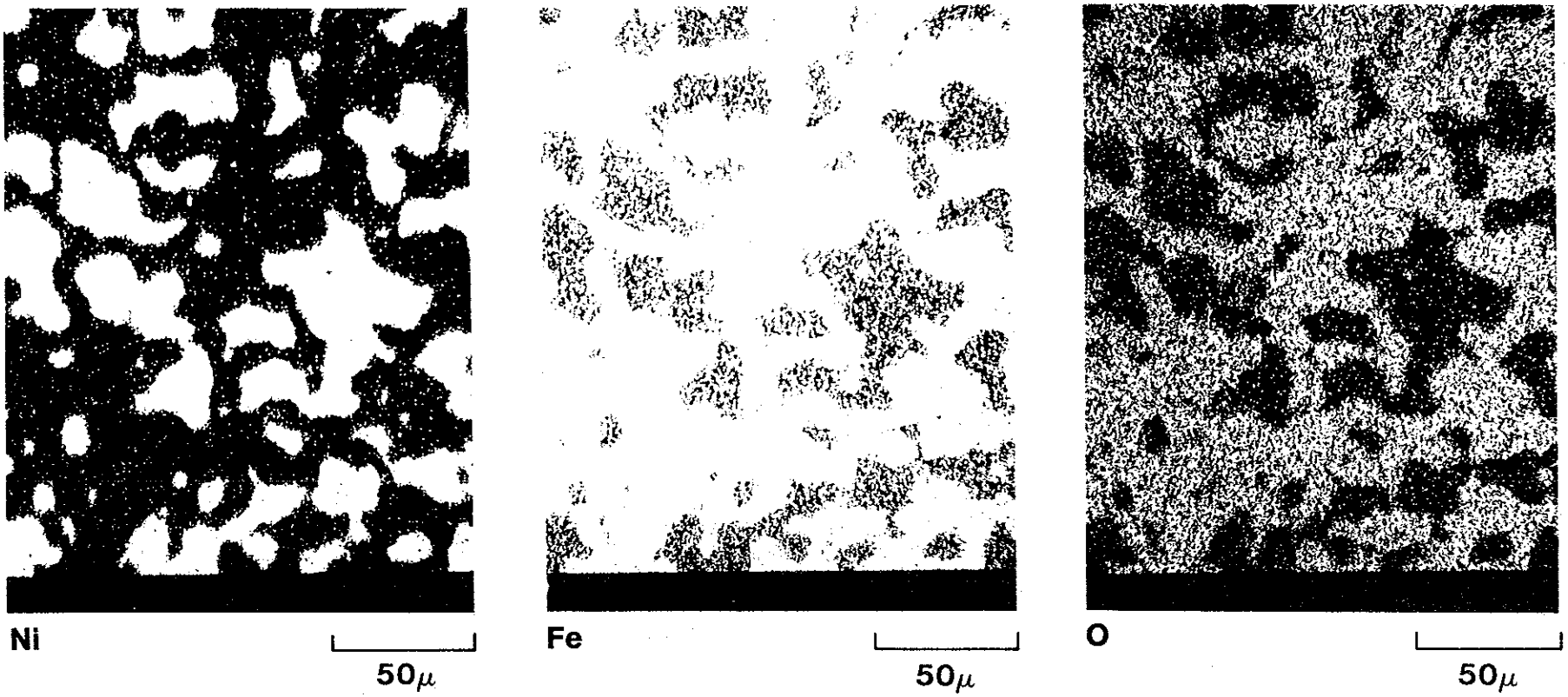

X-Ray Images for Ni, Fe, and Oxygen Corresponding to the Backscattered Electron Picture in Figure 4. Note Metallic Area is Free From Oxygen and Contains Primarily Nickel Metal.

Figure 5

GA 17807.5

50μ

Backscattered Electron Picture of Cermet-Type Anode Fabricated by Reaction-Sintering 39.7 wt % Fe and 60.3 wt % NiO

Figure 4

shock conditions. The cermet anodes required less stringent preheating condition.

Table 6 is a summary of the test results with the cermet anodes. The metal produced during the test is analyzed by emission spectroscopy. The iron and nickel contents indicate the amount of Fe and Ni contained by the aluminum that is produced during the test with these anodes. During a test with the anode fabricated from 9.52 wt.% Fe, 50.98 wt.% NiO, and 39.5 wt.% Fe_3O_4, the feed tube clogged and the alumina level in the area near the anode may have been far below saturation. The anode corroded and the metal contained 0.9 wt.% Fe and 0.4 wt.% Ni. The current efficiency during these tests was calculated from the weight of metal produced during the test.

Table 7 shows the result of tests with a cermet anode fabricated from 8.91 wt.% Fe, 54.14 wt.% NiO, and 36.95 wt.% Fe_3O_4. The anode was run for 19 hours, removed from the cell, cooled, and then tested in a fresh electrolyte for another 28 hours. After test the anode was badly corroded and metal was contaminated with 2.9 wt.% Fe and 0.43 wt.% Ni, apparently because the electrolyte in the vicinity of the anode lacked alumina. The same anode when tested again produced aluminum with only 0.3 wt.% Fe and 0.07 wt.% Ni. A previous test with this anode indicated 0.22 wt.% Fe and 0.05 wt.% Ni (see Table 6). The quality of metal produced and electrical conductivity of some of these anode compositions are very attractive. The current efficiency is generally 70% or higher. In one instance, where alumina feed was stopped, the anode was corroded and the current efficiency was poor.

Volt-amp curves were obtained at various intervals during electrolysis. The polarized cell potential for 51.7 NiO - 48.3 Fe_2O_3 anode was ~2.35 V representing a polarization voltage of approximately 0.15 V, since the equilibrium voltage is 2.2 V. Therefore, for an inert anode the polarization voltage is substantially lower than the 0.4-0.6 V for carbon anodes.

TABLE 6

Summary of Bench-Scale Hall Cell Tests
With Cermet Anodes, Anodes Were Tested in
~1.1 Ratio Bath with 5 Wt.% CaF_2 , 5 Wt.% Al_2O_3

Anode Composition Wt.%				Run Time (h)	Current Efficiency (%)	Metal Analysis		Comments
Fe	NiO	Fe_3O_4	Fe_2O_3			Wt.% Fe	Wt.% Ni	
5.86	33.34		60.80	36	69	0.33	0.02	Some scaling of anode noticed.
7.6	60.93	31.47		23	84	0.14	0.02	
8.45	56.52	35.03		53	90	0.11	0.04	
8.91	54.14	36.95		51	91	0.22	0.05	
9.52	50.98	39.5		20	59	0.9	0.4	Alumina feed stopped.
12.79	34.21	53.01		24	84	0.64	0.05	
20.0	70.0	10.0		23	90	0.21	0.04	
20.0	60.0	20.0		33	88	0.23	0.02	
39.7	60.3			28	80	0.5	0.02	

TABLE 7

Bench-Scale Hall Cell Test with Cermet Anodes Tested in a ~1.1 Ratio Bath with 5 Wt%. CaF_2 and 5 Wt%. Al_2O_3 (Anode Fabricated from 8.91 Wt.% Fe, 54.14 Wt.% NiO and 36.95 Wt.% Fe_3O_4

Anode Density (g/cc)	Run Time (h)	Total Hours	Current Efficiency (%)	Metal Analysis		Comments
				Wt.% Fe	Wt.% Ni	
4.97	19		77	0.5	0.1	Feed stopped.
	28	47	34	2.9	0.43	Anode corroded.
	42	89	89	0.3	0.07	No further significant corrosion.

The anodes develop a mixed oxide layer after testing in a cell. The quality, composition, and morphology of the oxide layer formed and its mechanism of growth are important for long-term use of these materials as anodes for the electrolytic production of aluminum.

Based on the bench-scale Hall cell test results, the electrical conductivity values of the anodes and other factors, the anode composition containing 20 wt.% Fe, 60 wt.% NiO, and 20 wt.% Fe_3O_4 was chosen for further study. The fabricated cermet material contains a metallic phase (nickel with 4-6 wt.% Fe) and oxide phases (nickel-ferrite spinel and nickel-Fe oxide). Figure 6 shows the backscattered electron picture and corresponding X-ray images for Fe, Ni and O from the center of anode 013084. The anode was used for electrolysis for 30 hours in a 1.1 ratio (wt.% NaF/AlF_3) bath at ~960°C. Figure 7 shows the backscattered electron picture and corresponding X-ray images for Fe, Ni, O. F, Na and Al from an area near the bottom part of the tested anode. Figure 6 shows that the cermet anode consists of metallic phase (principally nickel) and oxide phases containing Ni, Fe and oxygen. Figure 7 shows that the area near the bottom of the anode has no free metal and contains a relatively dense oxide containing Ni, Fe and oxygen. Within this dense area, precipitates of iron oxide were also seen. The "dense" layer was followed by "voids" which contain "bath."* The bottom area also contains large amounts of nickel oxide. The "affected layer" after electrolysis amounted to ~0.8 mm near the bottom and ~2.76 mm at the corner. This rate of degradation of material is not acceptable because electrical conductivity of this material without the presence of the "metal phase" is approximately three orders of magnitude lower. Further, the electrolyte penetrates the material and attacks the stub connection with time. Also, undesirable amounts of Fe and Ni are introduced into the metal.

---

*"Bath" refers to the electrolyte that penetrated into the anode. The composition of this material is different from the bulk electrolyte in which the anodes were tested.

GA 17807.3

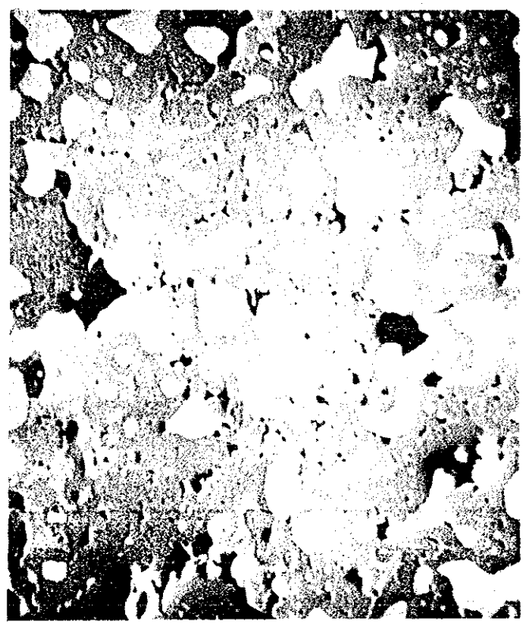

Backscattered

500X

10μ

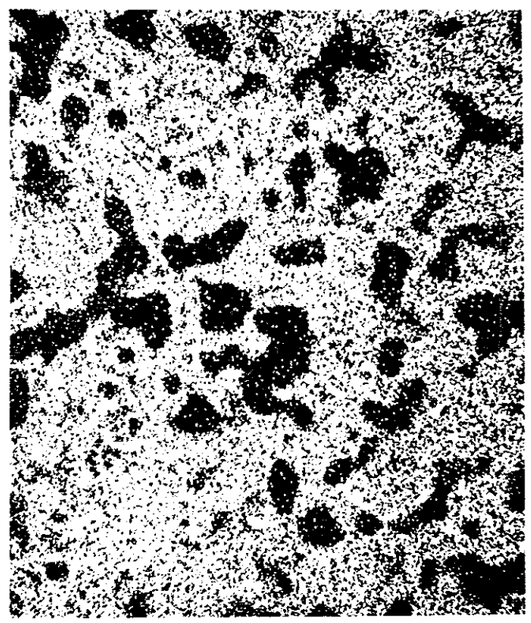

Fe

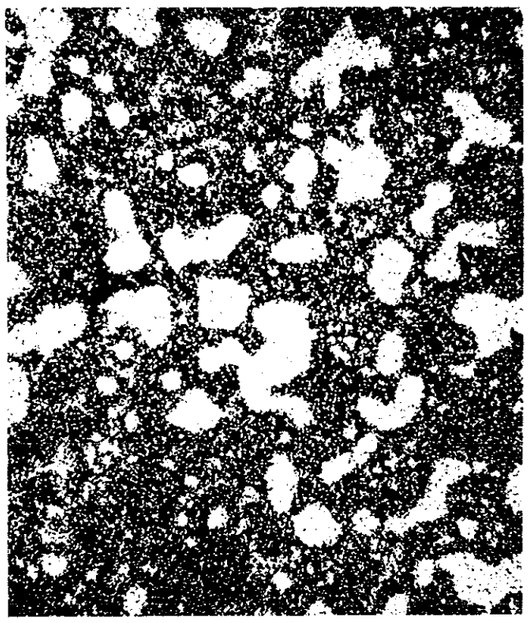

Ni

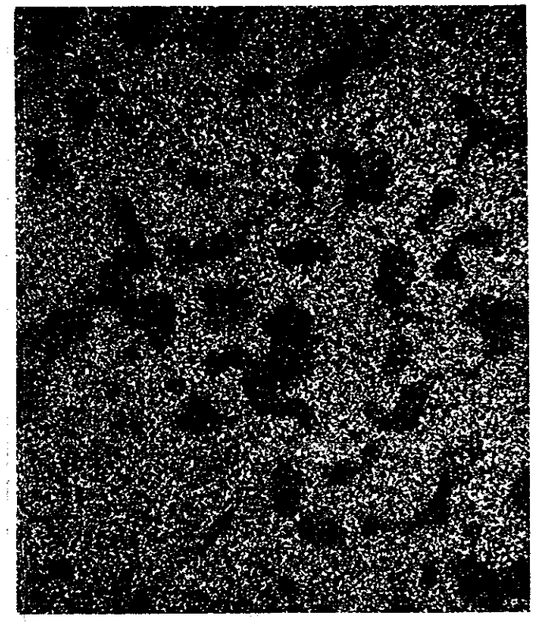

O

Anode 013084 (Interior)
Figure 6

GA 17807.2

Backscattered

Fe

Ni

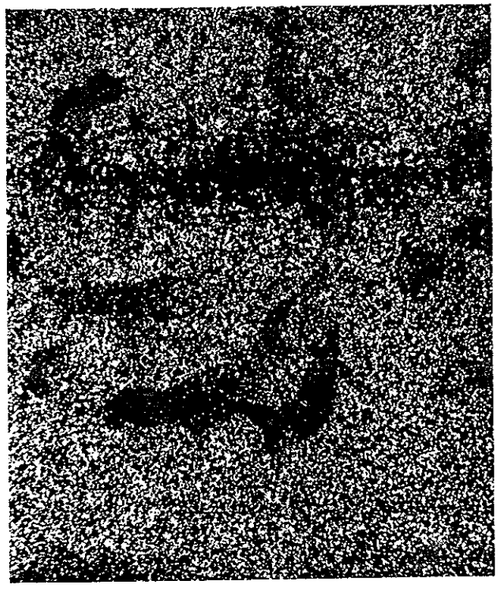

O

F

Na

Al

Anode 013084 (Bottom)
Figure 7

b. Oxidation Characteristics

In order to understand more about the factors affecting the formation of an oxidized layer on inert anodes, specimens from inert anode sample S-N 538928, formed by reaction sintering 20 wt.% Fe, (Quebec Atomet 95), 20% Fe_3O_4 (Pfizer BK 5000) and 60% NiO (Ceramic Color and Chemical), were oxidized in air at 960°C for 3 hours, 21 hours, and 5 days. In addition, anodes containing Al_2O_3 additives (S-N 538946, Fe 20 wt.%, NiO 60 wt.%, Fe_3O_4 18 wt.%, and Al_2O_3 2 wt.%; S-N 539009, 19Fe, 57NiO, $19Fe_3O_4$, and 5 wt.% Al_2O_3; S-N 539010, Fe 18 wt.%, 54NiO, $18Fe_3O_4$, and $10Al_2O_3$) were also oxidized under similar conditions. The results are shown in Table 8. The optical micrograph of the composition 6846 sample before the oxidation experiments shows a "wormy" metallic phase, spinel background (light color), "NiO" (the darker phase), and the void areas (black). After five days of oxidation at 960°C, the same material shows that the dense oxide layer at the bottom contains primarily a spinel phase with little NiO. It is seen that the addition of Al_2O_3 reduces the amount of total affected layer, e.g., 10 wt.% Al_2O_3 addition reduced the oxide layer almost by half.

Some samples were weighed before and after the 960°C oxidation treatment. The exposed surface areas were calculated from initial dimensions. These results are shown in Table 9. The weight gain per unit area (g/cm^2) was plotted vs. time and the oxidation appears to follow a parabolic kinetic. The square of weight gain/area (g^2/cm^4) was plotted vs. time. The parabolic rate constant, K_p, for 19Fe, 57NiO, $19Fe_3O_4$, and 5 wt.% Al_2O_3 sample is $\sim 2.97 \times 10^{-5}$ g^2/cm^4h, and k_p for the sample containing 20 wt.% Fe, 60NiO, $18Fe_3O_4$, and 2 wt.% Al_2O_3 sample is 1.37×10^{-5} g^2/cm^4h.

Oxidation of the samples in air leads to the formation of a spinel layer with some NiO on the anode surface. This layer is followed by a layer rich in NiO with some spinel present. The next layer is believed to be an internally oxidized zone containing NiO, spinel, and a small amount of metallic material. The Al_2O_3-containing samples also contain the dark $(Ni, Fe, Al)_3O_4$ phase.

TABLE 8

Oxidation Experiments in Air

Oxide Layer Thickness in mm After Various Periods of Oxidation Treatment in Air at 960°C

Composition (Wt%)				Layer Thickness (mm)		
Fe	NiO	Fe_3O_4	Al_2O_3	3 h	21 h	120 h
20	60	20		0.02	0.07	0.17
20	60	18	2	<0.02	0.04	0.15
19	57	19	5	<0.02	0.05	0.1-0.15
18	54	18	10	<0.02		0.1

TABLE 9

Oxidation Experiments in Air at 960°C

Composition Wt.%				Time Hrs.	Exposed Surface Area (cm^2)	Weight Gain (g) (x)	x^2 (g^2/cm^4)
Fe	NiO	Fe_3O_4	Al_2O_3*				
19	57	19	5	3	6.4	0.0152	5.66×10^{-6}
19	57	19	5	21	6.77	0.0154	5.15×10^{-6}
19	57	19	5	120	6.21	0.0247	1.58×10^{-5}
20	60	18	2	3	6.94	0.0102	2.16×10^{-6}
20	60	18	2	21	6.75	0.0198	8.58×10^{-6}
20	60	18	2	120	6.85	0.0399	3.38×10^{-5}

*Calcined

The oxidation in service involves both oxidation during electrolysis and oxidation during the heat-up and cool-down periods. The electrolyte is found inside voids, which might enhance oxidation.

c. Marker Experiments

In order to understand the mechanism of oxide growth, anodes with the 6846 composition were fabricated with four small pieces of Pt wire pressed onto the sample. After reaction sintering in an argon atmosphere, the Pt wire markers were exposed at the outer bottom surface of the anode. The anode was used for electrolysis in a bench scale Hall cell for 33 hours, with a bath ratio of 1.1 and containing 5 wt.% Al_2O_3 and 5 wt.% CaF_2. After the electrolysis, no marker wire was visible at the anode surface. The anode was then sectioned and micrographs were taken. Examination at a higher magnification showed that the Pt marker wire was located 0.02 mm within the sample. Another experiment was carried out with a platinum marker wire on the bottom of the 6846 anode. The anode was preheated on top of the bath as usual and then lowered into the electrolyte and electrolysis was carried out. But after only four hours of electrolysis, the crucible cracked and the bath tapped out. The furnace was at an elevated temperature for another 14 hours, at which point the furnace was shut down. The same anode was used for electrolysis again. The anode was preheated on top of the cell and lowered into the electrolyte and electrolysis was carried out for six hours when the bath tapped out. The furnace was kept at 960°C for another ten hours and then shut down. It is estimated that the anode was in an oxidizing environment for about 50 hours. The anode was sectioned and polished. The platinum marker wire was found ~0.1 mm from the bottom.

In addition, another anode was fabricated with rhodium (Rh) powder on the anode bottom. After reaction sintering in an argon atmosphere, the pressed Rh powder was seen exposed. This anode was used for electrolysis but the test was abandoned after 4.5 hours of electrolysis owing to breakage of the Al_2O_3 crucible. The anode was sectioned. However, again the Rh metal was located inside the sample.

The result of the platinum marker experiment suggests that the dense oxide layer on the surface of anode is caused primarily by outward diffusion of cations.

These results, together with the oxidation experiments and the autopsy results, show that upon oxidation the affected area of the sample forms several layers. The outermost layer, formed primarily by cation diffusion, consists of spinel and iron oxide (precipitates). The iron oxide precipitates have not been found in samples oxidized in air. This outermost layer is formed beyond the original anode surface. The next layer contains nickel oxide and spinel. The next layer is the zone of internal oxidation where the spinel, the NiO, and the alloy phases are found.

These zones are not extremely well defined in all samples. In addition, the cavities found in the NiO + spinel layers contain bath material. $(Ni, Al, Fe)_3O_4$-type spinel has been found to form in 6846-samples doped with Al_2O_3.

It is believed that the driving force for cation diffusion through the oxidized layer is the vacancy gradient caused by the variation in oxygen activity. The effect of an oxygen activity gradient and the relative jump frequencies of iron and nickel are such as to preferentially concentrate iron toward the outer interface of the spinel. However, when the concentration becomes too high at a given temperature, iron oxide may precipitate, or iron oxide precipitation may occur when the sample is cooled to a lower temperature, where the solubility of iron oxide in spinel is lower.

At very low oxygen potentials, iron in nickel oxide is present in the form of Fe^{2+} ions. Iron tends to pass from the Fe^{2+} to the Fe^{3+} state at a higher PO_2. NiO cannot incorporate a large amount of Fe^{3+} without creating a large concentration of compensating defects (to maintain the charge neutrality condition). As a result, iron solubility in NiO rapidly decreases at high PO_2. Consequently, Fe is more concentrated at the spinel phase near the high PO_2 side. The

oxidized layer formed during Hall cell testing will also be influenced by diffusion under an electric potential gradient. The oxygen partial pressure equals one atmosphere at the external surface but is only $\sim 4 \times 10^{-11}$ at the unaffected surface.

d. Effect of Operating Conditions (Bath Ratio, Al_2O_3 Level, Temperature) on Performance of Ni-$NiFe_2O_4$ Anodes (6846 Composition)

The rates of all thermally activated processes decrease with a decrease in temperature. Also, solubility of Fe and Ni oxides in the cryolite melt was found to decrease, as expected, with temperature. D. H. DeYoung's studies (40) also showed that solubility of Fe and Ni oxides decreases somewhat with bath ratio. The present studies were aimed at finding out the effect of bath ratios and temperature on anode performance during electrolysis.

Table 10 gives a summary of the results on tests carried out in the temperature range of 825-943°C and with a bath ratio (weight ratio of NaF/AlF_3) of 0.8-1.0. Anode 010383 was used for electrolysis in a bath containing NaF and AlF_3 in the weight ratio of 0.8:1.0. The bath contained 1.2 wt.% CaF_2 and 0.1% MgF_2. The current density considering only the bottom surface area was ~1.0 A/cm^2 but considering the overall surface area, the current density was 0.32 A/cm^2. In a matter of only 2-3 hours, the cell voltage started increasing from a normal of ~4.2 V to over 10 V. The anode was removed at the end of 9 hours and was found to be very badly swollen. The increase in cell voltage was due to increased anode resistance. The current efficiency was very low at only 28.9%. The anode was preoxidized at 800°C for a half-hour before starting the electrolysis. The anode, after the completion of electrolysis experiment, was sectioned, mounted, and polished. Figure 8 is a schematic representation of the areas which were analyzed by electron probe microanalyzer. Area a is practically unaffected after electrolysis. The three phases Ni-Fe alloy, $Ni_xFe_{3-x}O_4$ oxide (spinel) and $Ni_xFe_{1-x}O$ oxides were seen in this area. The dark areas are the voids.

TABLE 10

Effect of Bath Ratio on the Performance of Inert Anodes
60% NiO, 20% Fe, and 20% Fe_3O_4 Anode*

Anode No.	Bath Ratio $\frac{NaF}{AlF_3}$ Wt.%	% Al_2O_3	Run Time (Hrs)	Temp. °C	Current Effeciency %	Metal Analysis Wt.% Fe	Metal Analysis Wt.% Ni	Bath Analysis Wt.% Fe	Bath Analysis Wt.% Ni	Comments
010383	0.8	4.9-6.2	3.0	848	29.0	1.17	0.73	0.02	0.04	Anode badly swelled
011183	0.8	5.2	14.0	823	26.0	0.83	0.34	0.04	0.00	Anode immersed with current on, anode swelled
011283	0.8	4.9	6.0	825	55.2	0.48	0.53	0.01	0.00	Anode preoxidized at 960°C for 24 hours, anode swelled
010483	0.9	4.6	41	885	91.1	1.10	3.8	0.02	0.00	Anode swelled. Nickel contamination from Ni cathode rod; feed tube plugged
010583	<1.0	6.5	18.5	943	86.6	0.56	0.16	0.07	0.01	Anode swelled

*NiO: Ceramic Color and Chemical N-139
Fe: Quebec Atomet 95
Fe_3O_4: Pfizer BK 5000
S.No.: 539346
Feed: Flash Activated Hydrate

Area b represents transition from unaffected to the affected area. Visually, the affected area appears orange-brown in color. Four phases were found in this area. The first phase contained Fe, Ni, and F; the second Ni, Fe, and O; the third Al and F; and the fourth Na, Al, and F. Thus, it is clear that the anode was partially fluorinated.

Areas c and d contained an aluminum fluoride and Ni-Fe-O phases. The micrographs and backscattered electron pictures have been described in Quarterly Report 10 (4).

The phases contained in area e include bath (Na, Al, F), aluminum fluoride, and spinel-type oxide (Ni, Fe, Al, O).

It is seen that nickel and iron fluorides are stable at areas near phase boundaries representing the presence of metal and oxide (Ni/NiO) and its attendent oxygen partial pressure. It is interesting to note the presence of aluminum fluoride in areas b, c, and d and absence of sodium in those areas. This suggests that oxygen was presumably discharged from an aluminum oxyfluoride type complex, leaving the area rich in aluminum and fluorine.

The reaction leading to the formation of oxygen at an inert anode and aluminum at the cathode is governed by the reaction given below:

$$Al_2O_3 \rightarrow 2Al + 3/2\ O_2 \qquad (8)$$

The decomposition voltage at 1250 K with unit activity of alumina is 2.206 V. However, there are competing reactions, e.g.,

$$FeO + AlF_3 \rightarrow FeF_3 + 1/2\ O_2 + Al \qquad (9)$$

with a decomposition voltage of 2.36 V at unit activity of FeO and with $a_{AlF_3} = 1.5 \times 10^{-3}$ at 1250 K. alternatively,

$$3FeO + 2AlF_3 \rightarrow 3FeF_2 + 3/2\ O_2 + 2Al \qquad (10)$$

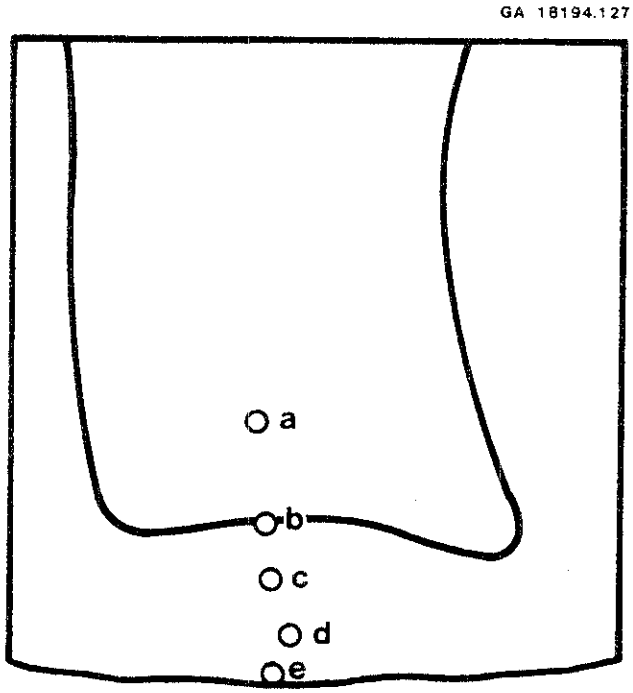

Schematic Representation of the Areas which were Analyzed by Electron Probe Microanalyzer on Anode 010383

Figure 8

with a decomposition voltage of 2.54 V, discharging FeF_2 and oxygen at anode and Al at the cathode ($a_{AlF_3} \simeq 1.5 \times 10^{-3}$, unit activity of FeO). Further,

$$Fe_2O_3 + 2AlF_3 \rightarrow 2Al + 3/2\ O_2 + 2\ FeF_3 \qquad (11)$$

takes place at 2.58 V, and

$$3NiO + 2AlF_3 \rightarrow 3NiF_2 + 3/2\ O_2 + 2Al \qquad (12)$$

occurs at 2.59 V.

The cell reactions (9-12) compete with reaction (4) and will be more favored at high aluminum fluoride activity, at lower temperatures, and with low alumina level, i.e., less than unit activity of alumina. For example, Table 11 shows the cell voltage at various alumina contents at 1250 K. These values will increase even more at lower temperatures. Also, Figure 9 shows a plot of the activity of AlF_3 as a function of the concentration of AlF_3 in $NaF\text{-}AlF_3$ melts at various temperatures (34). It is seen that as the concentration of AlF_3 increases and temperature decreases, the activity of AlF_3 increases. Thus, at 0.8 ratio bath ($x_{AlF_3} = 0.467$ in Figure 9) and 1160 K the activity of AlF_3 is $\sim 1 \times 10^{-2}$ compared to 1.5×10^{-3} at a bath ratio of 1.1 ($x_{AlF_3} = .267$ in Figure 9) at 1250 K. Table 11 shows the alumina activity and decomposition voltage as a function of alumina content. It is clear, therefore, that at lower temperatures and with a low ratio bath and with low alumina in bath there would be an increased tendency for the formation of fluorides. For example, the cell voltage represented by Equation (11) is given by:

$$E = E_o - \frac{RT}{nF} \ln \frac{a_{Al}^2\ a_{O_2}^{3/2}\ a_{FeF_3}^2}{a_{Fe_2O_3} \bullet a_{AlF_3}^2} \qquad (13)$$

GA 18194.124

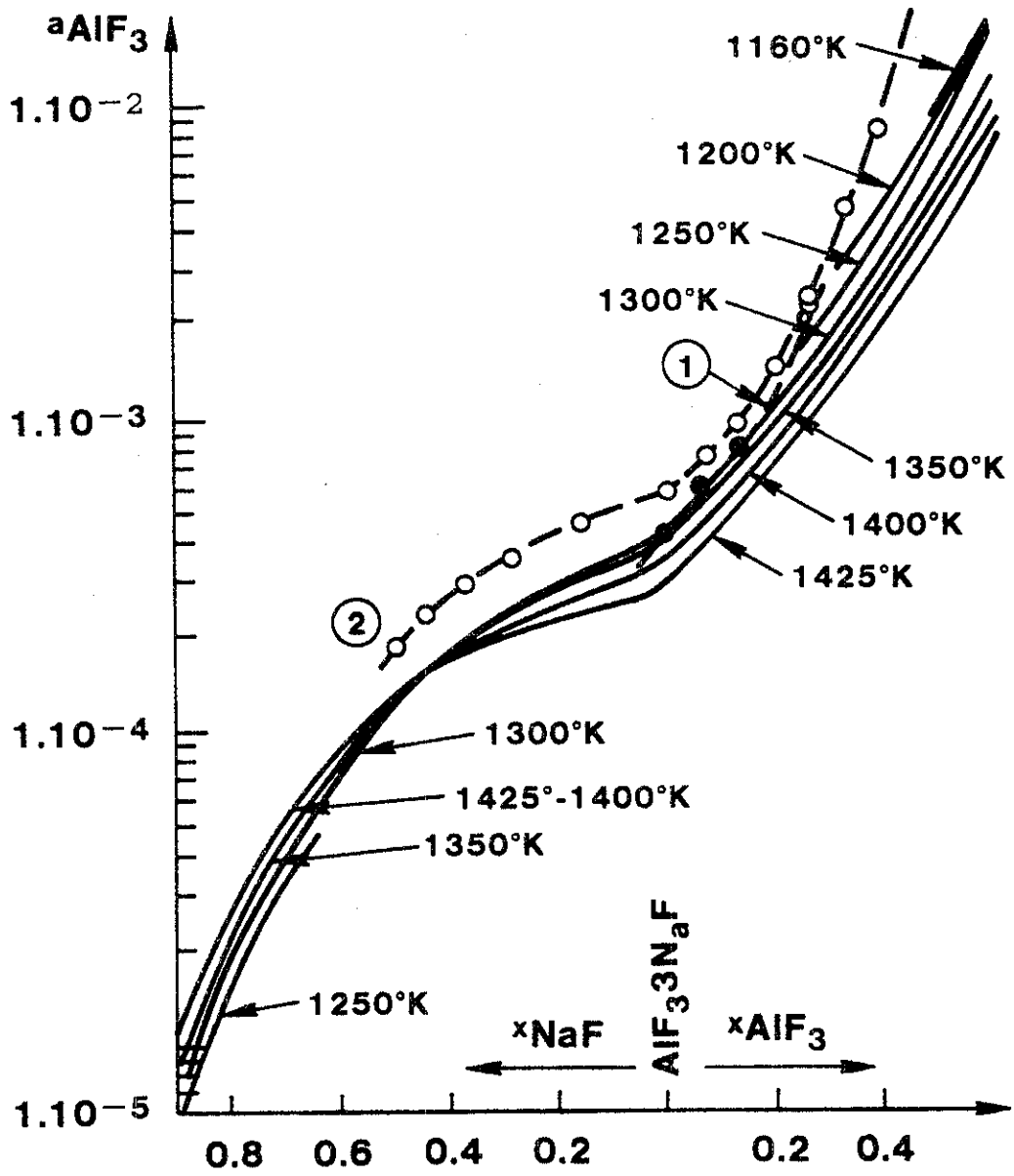

AlF_3 Activity as a Function of AlF_3 Concentration in NaF-AlF_3 Melts at Various Temperatures

Figure 9

TABLE 11

Effect of Al_2O_3 Concentration on
Decomposition Voltage at 1250 K

Wt.% Al_2O_3	$^{x}Al_2O_3$	$^{a}Al_2O_3$ (1)	$-E_{1250}$ Volts
0.5	0.01	0.0001	2.371
1.0	0.020	0.0008	2.334
2.0	0.040	0.0068	2.300
3.0	0.060	0.023	2.274
7.0	0.134	0.257	2.234
11.5	0.211	1.0	2.206

$$(1) \quad {}^{a}Al_2O_3 = \left(\frac{{}^{x}Al_2O_3}{{}^{s}x_{Al_2O_3}} \right)^{3}$$

Thus, the fluoride-forming reactions would be favored at high Fe_2O_3 and AlF_3 activity.

It should be further noted that the iron or nickel metal present in the anode may fluorinate at a voltage lower than that for oxygen production, e.g.,

$$3Ni + AlF_3 \rightleftarrows 3NiF_2 + 2Al \quad (14)$$

or

$$3Fe + 2AlF_3 \rightleftarrows 3FeF_2 + 2Al \quad (15)$$

In order to ascertain that free metal does not come in immediate contact with the AlF_3-containing bath, anode 011283 was preoxidized at 960°C for 24 hours, and an oxidized layer was clearly formed on the surface. However, when this anode was used for electrolysis experiment, the anode also swelled eventually by the formation of fluorides.

Electrolysis on anode 010583 was carried out with a starting bath ratio of ~1.0 and results are shown in Table 10. Surprisingly, analysis of bath at the end of test indicated the ratio to be close to 0.83. This may be in part due to adsorption of Na ions by graphite cathode or absorption of AlF_3 by anode. The temperature was maintained at 943°C. The anode performed better compared to the experiments carried out with 0.8 and 0.9 ratio baths.

V_{ext} values (V_{ext} refers to the cell current-voltage curve extrapolated to zero current) were obtained for some of the experiments described in Table 12. At the start of the experiment, V_{ext} was at 1.76 V for anode 010483 suggesting possible fluorination of metallic materials. After 21 hours the V_{ext} value was at 2.48 V, suggesting oxygen-forming reactions. The overvoltage associated with reactions (3 and 8-12) are very important. Ideally, overvoltage associated with reaction (3) should be low whereas that for reaction

TABLE 12

Effect of Bath Composition on the Performance of Inert Anodes
60 Wt.% NiO, 20% Wt.% Fe, and 20% Wt.% Fe_3O_4*

Anode No.	Density (g/cc)	Bath Ratio $\frac{NaF+LiF}{AlF_3}$ (molar)	Bath Composition - Wt.% CaF_2	MgF_2	LiF	Al_2O_3	Run Time (Hrs)	Temp. °C	Current Effeciency %	Metal Analysis Fe Wt.%	Ni Wt.%	Comments
021783	5.50	2.58-2.8	5.0	0.1	5.0	4.6-<	16	920	16	-	-	Anode swelled. Low Al_2O_3
022283	5.53	2.58-2.8	5.0	0.1	5.0	3.0	23	925	43	1.5	0.39	Cell tapped out. Feed not going in solution
022383	5.53	2.58-2.7	5.0	0.1	5.0	3.0	35	919	79	0.37	0.22	No initial metal pa
030883	5.53	2.58-2.92	5.0	0.1	5.0	3.0	48	919	70	0.79	0.32	Metal pad present
042883	5.53	3.44	7.0	0.1	8.0	3.0	25	945	62	6.4	0.89	Enhanced oxidation
050483		2.89	4.0	0.1	6.0	3.0	31	939	56	5.5	0.48	No dense layer. Large oxidation

*94-2 Powder
NiO: Ceramic Color and Chemical N-139
Fe: Quebec Atomet 95
Fe_3O_4: Pfizer BK 5000

(9-12) should be high so that under normal operation reactions (9-12) are suppressed.

A number of experiments were carried out at a relatively high ratio (1.1 < wt ratio < 1.7). Additives, e.g., LiF, MgF_2, and CaF_2, were added to lower the liquidus temperature. The operating temperature was maintained at a ΔT (operating temperature - liquidus temperature) of 10-20°C.

Table 12 shows the results of experiments carried out with CaF_2 and LiF additions. These bath additives are known to lower the alumina solubility and the data given in Table 13 show that they adversely affect the solution rate of alumina. The operation of the cells was particularly difficult when the maximum alumina solubility was low. Table 13 shows the calculated liquidus temperature for the intended bath compositions and maximum alumina solubility. With these low alumina solubilities and low temperatures, the solution rate of alumina is also very low. However, attempts were made to operate the bench-scale Hall cells under these conditions. These bath compositions had relatively low activity of AlF_3 and hence smaller tendency for the formation of fluorides.

Anode 021783 was operated at a bath ratio of ~1.1 (weight ratio NaF/AlF_3) with 5.0 wt% CaF_2 and LiF. The cell was operated with a TiB_2-AlN composite cathode in a BN crucible without an initial metal pad. The cell voltage started increasing after 6 hours and the bath had crusted up. Apparently, alumina level in the bath was low because some feed fell on top of the crust. The anode was sectioned and examined microscopically and with the help of an electron probe microanalyzer. The anode was practically completely oxidized.

It is believed that a_{AlF_3} was sufficiently high to cause reactions of the type

$$FeO + AlF_3 \rightarrow FeF_3 + 1/2\ O_2 + Al \qquad (9)$$

TABLE 13

Properties of Various Bath Compositions

Bath Ratio ($NaF+AlF_3$) Wt. Ratio	Bath Composition - Wt.%				Liquidus Temperature °C	Operating Temperature °C	Max. Alumina Solubility Wt.%
	CaF_2	MgF_2	LiF	Al_2O_3			
1.1	5.0	0.1	5.0	3.0	909	919-925	4.7 at 924°C
1.35	7.0	0.1	8.0	3.0	931	945	5.3 at 946°C
1.28	4.0	0.1	6.0	3.0	928	943	5.6 at 943°C
1.1	5.0	5.0	4.0	3.0	904	919	3.87 at 919°C
1.22	4.0	4.0	6.0	3.0	902	917	3.7 at 919°C
1.1	5.0	5.0	4.0	3.0	904	919	3.9 at 919°C
1.28	4.0	4.0	6.0	3.0	908		4.21 at 919°C
1.2	2.5	8.0	8.0	2.0		886	3.2 at 906°C

during electrolysis. Further, the primary aluminum forming reaction, Reaction (7), needs a relatively higher voltage at a "low" alumina level. The V_{ext} obtained during the experiment was 2.29 V.

A series of experiments were also carried out with MgF_2 in the bath as well as CaF_2 and LiF. The results of the experiments are summarized in Table 14. The bath compositions were formulated to obtain an operating temperature in the range of 886-920°C. Anode composition 6846 was found to be destroyed under the conditions when the alumina feed tube plugged, even though the test was carried out in an alumina crucible. A major problem is associated with testing the bath compositions where the alumina solubility is low.

In general, operation of cells with modified bath formulations with higher ratio bath and CaF_2, MgF_2, and LiF additives was difficult because of limited alumina solubility at operating temperatures. Tests in a BN crucible resulted in "anode effect," a phenomenon which leads to destruction of an "inert anode" in a bath with very low alumina. Even when tests were carried out in an alumina crucible, if the feed tube plugged the anodes were destroyed. In the future, some tests will be carried out with an alumina shroud around the anode to ensure the availability of alumina.

e. "See-Through Hall Cell Operation"

In order to understand more about factors affecting inert anode performance, a "see-through" bench scale cell with an inert anode and carbon cathode was operated. The cell was lined with quartz and was run for about one hour. The cell was operated with 1.1 ratio bath containing 5 wt.% CaF_2 and 5 wt.% Al_2O_3 at 960°C. A current density of ~0.3 amp/cm^2 on the total exposed surface area or 1 amp/cm^2 on the bottom surface was used. Visual observations and videotape recordings were made. The oxygen bubbles generated during electrolysis were tiny, 0.1-0.5 mm in diameter. The bubbles escaped easily without much coalescence and without violent agitation of electrolyte in the inter-electrode spacing. This suggests high current efficiency and low

TABLE 14

Effect of Bath Composition on Anode Performance
60 Wt.% NiO, 20% Wt.% Fe, and 20% Wt.% Fe_3O_4*

Anode No.	Density (g/cc)	Bath Ratio NaF+LiF / AlF_3 (molar)	Bath Composition - Wt.% CaF_2	MgF_2	LiF	Al_2O_3	Run Time (Hrs)	Temp. °C	Current Effeciency %	Metal Analysis Fe Wt.%	Ni Wt.%	Comments
060783	5.59	3.09	4	4	6	3	48	919	68	3.9	0.6	
061483	5.58	3.13	2.5	8	8.0	2.0	14	886	47	3.1	4.4	Anode destroyed. Fell into bath
061583	5.60	2.52	5.0	5.0	4.0	3.0	7	919	-	-	-	Crucible cracked
062283	5.68	2.5	5.0	5.0	4.0	3.5**	18	919	42	2.8	1.2	Anode swelled
051083		2.92	4.0	4.0	6.0	3.0	46	919	79	3.0	0.45	
050983		3.15	5.0	6.0	6.0	3.0	42	920	52	-	-	Anode destroyed

*94-2 Spray-dried Powder
NiO: Ceramic Color and Chemical N-139
Fe: Quebec Atomet 95
Fe_3O_4: Pfizer BK 5000

**Flash Activated Hydrate (FAH)

overvoltage with inert anode cells. It may be possible to lower the anode-cathode distance without reducing current efficiency. A schematic of the cell is shown in Figure 10.

f. Effect of Bare Carbon Sidewall on Inert Anode Operation

In order to study the effect of carbon on the performance of inert anodes, an experiment was carried out with a bare graphite crucible. This condition may arise if there exists a bare carbon sidewall. Small amounts of carbon dust in bath will not represent this situation. The bare graphite crucible is cathodic and Al_4C_3 is formed on it which has appreciable solubility in bath. Also, anode constituent materials may be reduced there. Table 15 shows the details of operation with this anode. The experiment with this anode was carried out for 32 hours. Figure 11 shows the plot of cell voltage vs. current and extrapolated voltage at zero current at the beginning of the experiment. The value of 2.13 is reasonable, suggesting oxygen evolution. However, at the end of 24 hours of operation the plot of cell voltage vs. current and extrapolated voltage at zero current is given by Figure 12. It is seen that V_{ext} changes to 1.74. This lower value suggests possible formation of CO or CO_2. No metal was produced during this operation. It is believed that the Al_4C_3 formed was dissolved and oxidized near the anode.

g. Improved Cermet

Studies have shown that the 6846-type cermet material containing $Ni_xFe_{3-x}O_4$ (spinel), $Ni_yFe_{1-y}O$, and Ni_zFe_{1-z} alloy provide good electrical conductivity ($1\text{-}3\times10^4$ $ohm^{-1}m^{-1}$) at 1000°C and the material could be inertia, TIG, or diffusion welded after partial reduction. No significant corrosion of the anode was found when these anodes are tested in a 1.1 ratio bath at 960°C, although the metal produced using these anodes contains Fe and Ni in the range of 0.1-0.8 wt.% and 0.01-0.3 wt.%, respectively. An oxidized layer ~2 mm thick can generally be seen on the anode, at the end of a 50-70 hour test. The location of this layer is shown, schematically, in Figure 13.

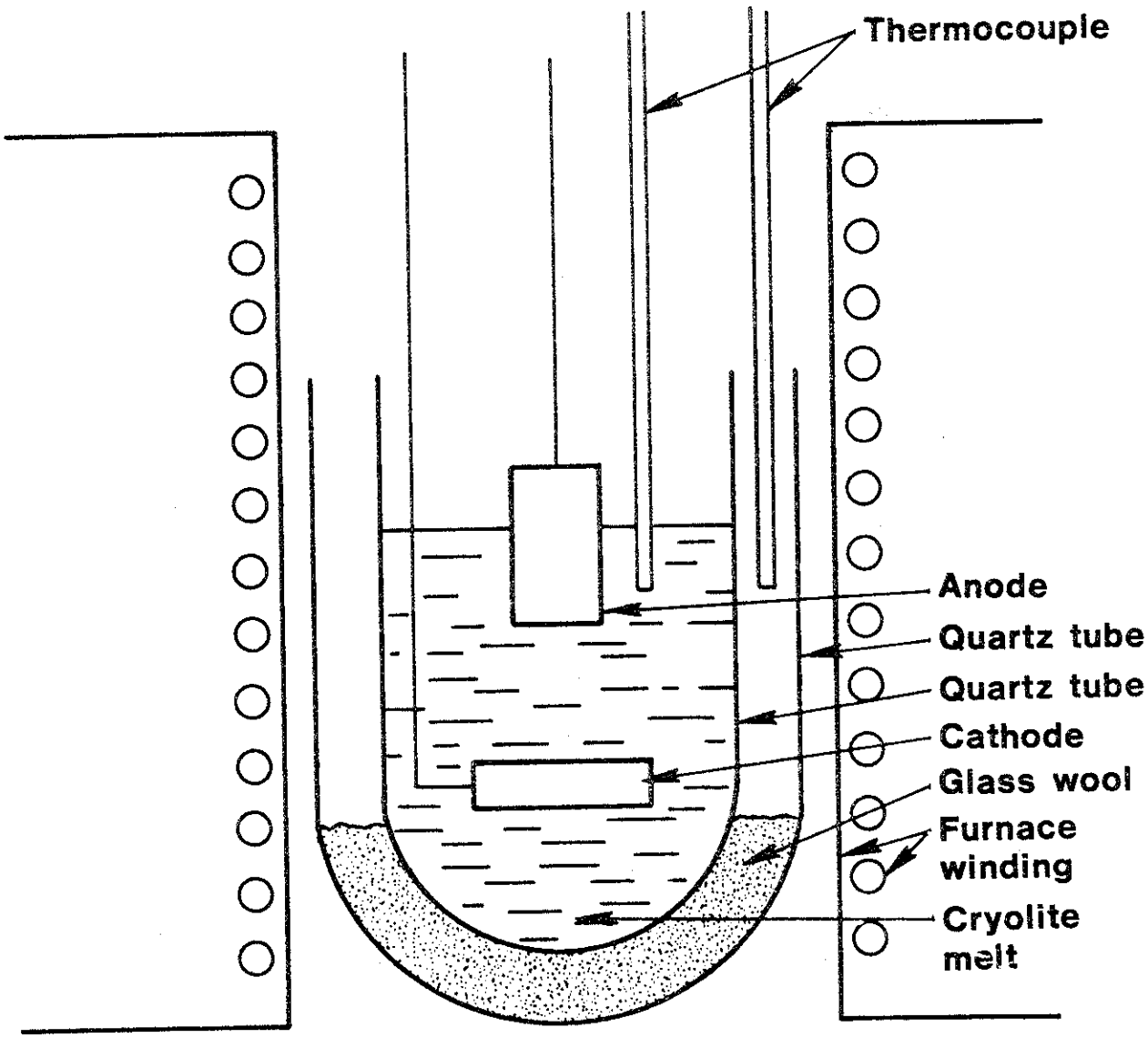

Schematic of a See Through Cell
Figure 10

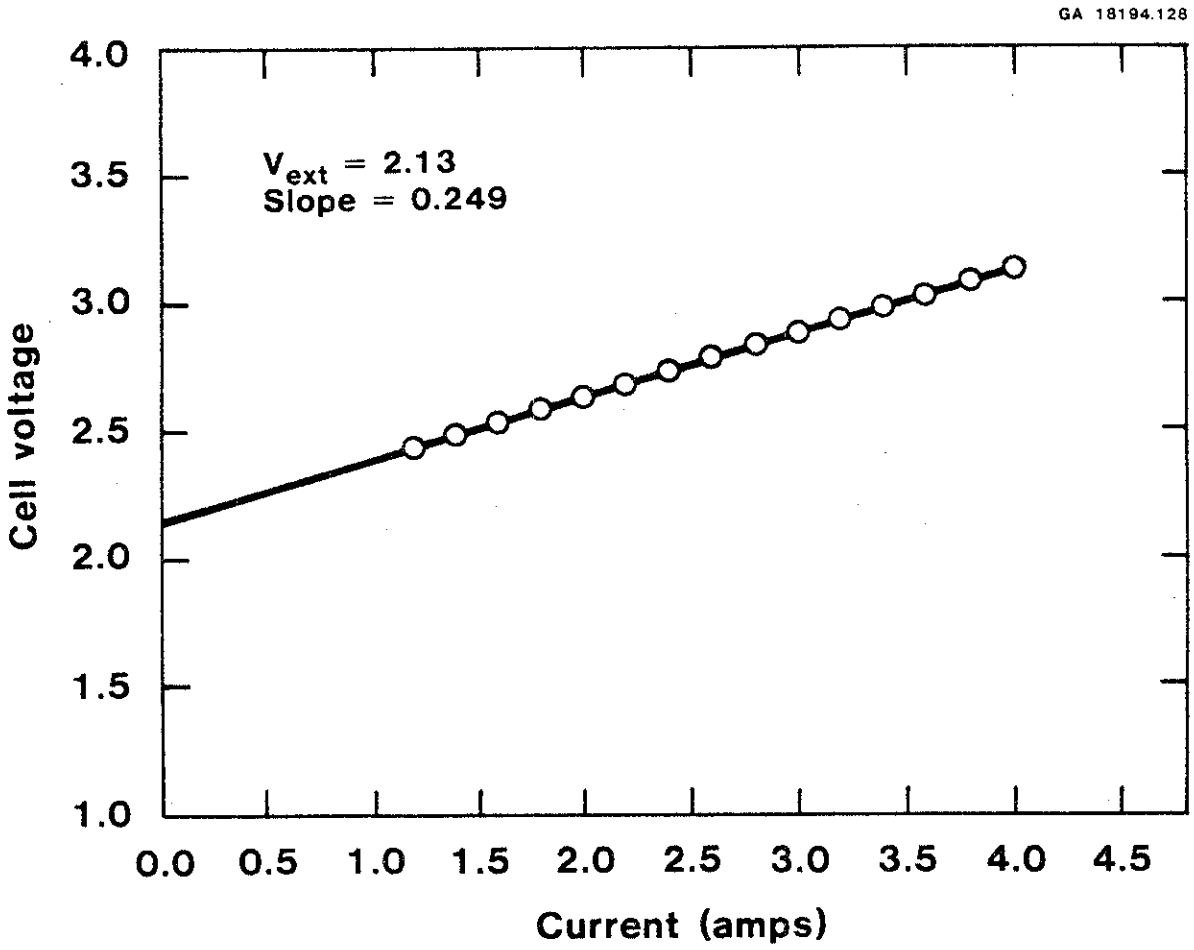

Anode 1-10-83 Start up
S # 539346 Sample 6
Bath ratio - 1.1, + 5 CaF_2 + 5% Al_2O_3

Cell Volts vs. Current for Anode 011083 at Start-up
Figure 11

TABLE 15

Effect of Bare Graphite Sidewall on Inert Anode Performance 94-2, 60 Wt.% NiO, 20 Wt.% Fe_3O_4 20 Wt.% Fe

Anode No.	Bath Ratio (Wt)	% Al_2O_3	Run Time (h)	Current Efficiency (%)	Vext Start (V)	Vext After 24 Hours
011083	1.1	5.0	32	0	2.13	1.74

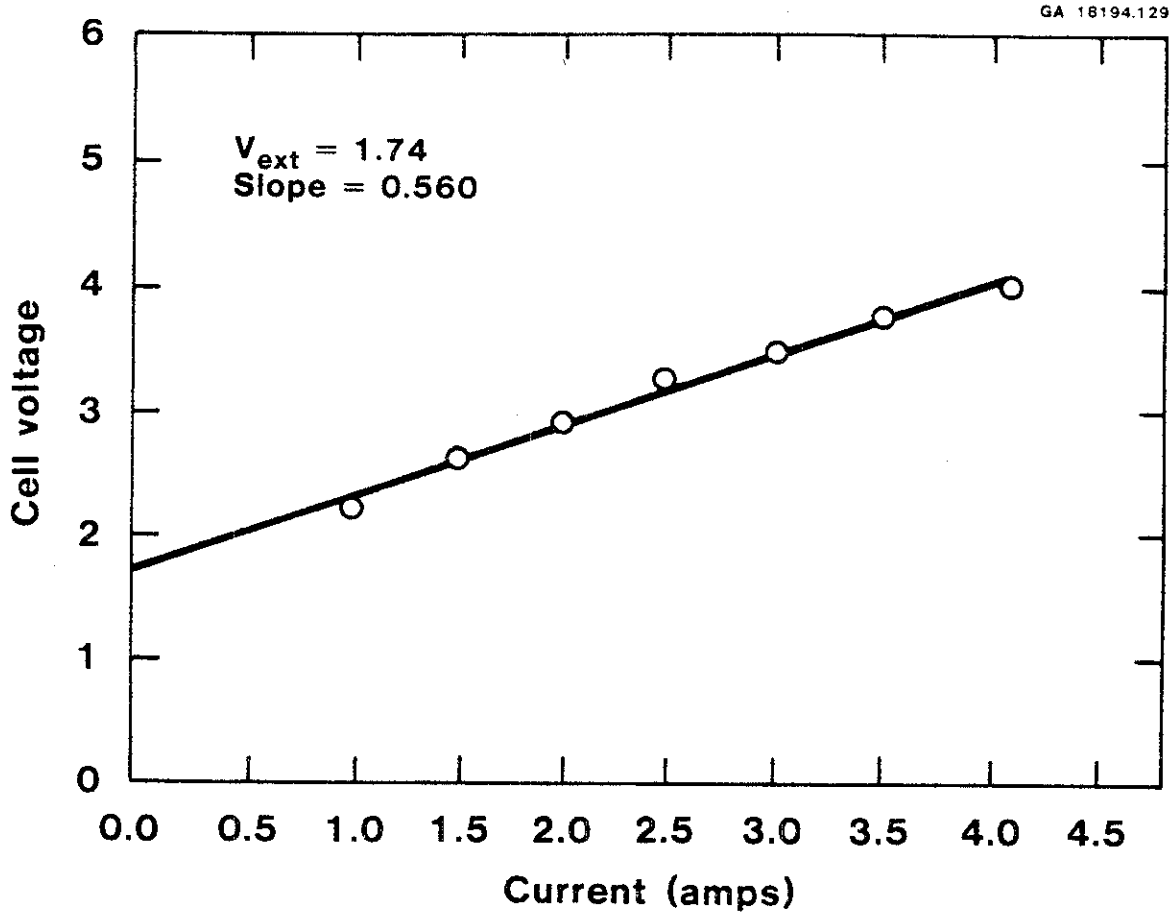

Anode 1-10-83 after 24 hrs run time
S # 539346 Sample 6
Bath ratio - 1.1, + 5 CaF_2 + 5% Al_2O_3

Cell Volts vs. Current for Anode 011083 after 24 Hours of Cell Operation

Figure 12

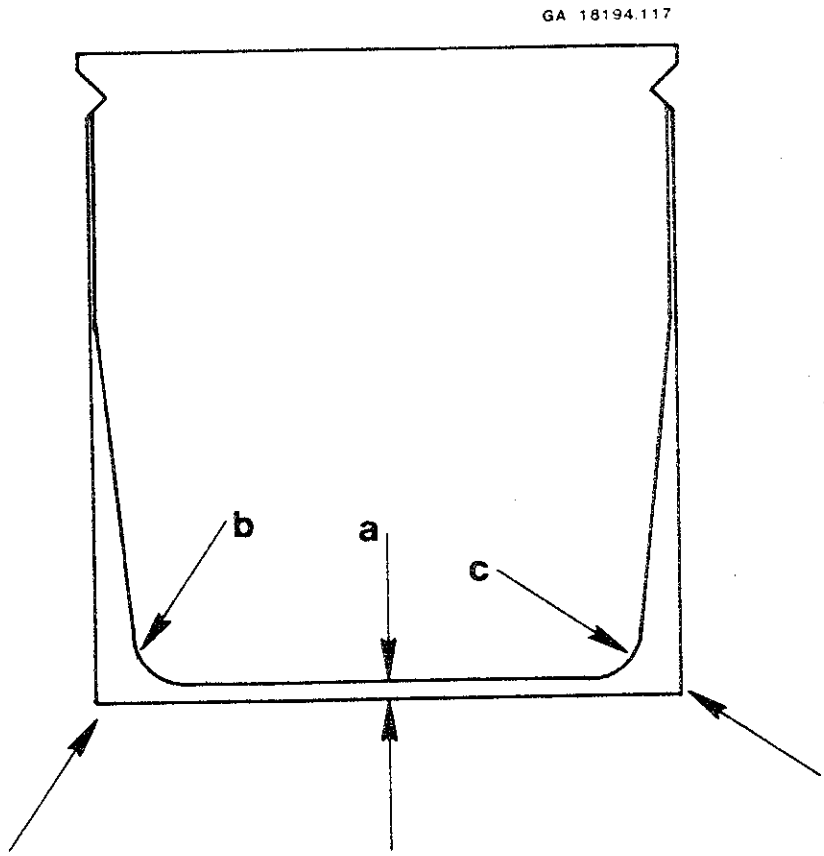

Anode after Test (Bottom and Corner Affected Areas)
Figure 13

The anodes corrode badly when alumina level in the electrolyte is low. The anodes perform best when the alumina level in the electrolyte is close to saturation solubility for the melt. Further, when tests are made with electrolytes containing low ratios (high AlF_3 activity) the anode material was found to swell and degrade by the formation of Fe and Ni fluorides. Additives to the cryolite melt which can lower the operating temperature without increasing the AlF_3 activity have also been tried. It has been found that electrolyte compositions having low alumina solubility and rates of solution lead to the corrosion of anode material by formation of Fe and Ni fluorides which have higher solubility in the electrolyte than the comparable oxides.

The proper operating conditions with this composition appear to be a bath ratio of 1.1-1.15 and a temperature of ~960°C. Metal contamination and the growth of the oxidized layer are major concerns. It has been found that the cermet material oxidizes during operation. The oxidation during its use as an anode or when it is immersed in a bath is more severe compared to the case when the material is left in air or oxygen at a comparable temperature. It appears that bath material inside the anode plays a major role during loss of the metal phase.

The cermet inert anode material may degrade via several mechanisms, e.g., (a) oxidation of the metal phase by air or evolved oxygen, (b) anodic dissolution, (c) loss of material via reaction with reduced species in the melt, (d) porosity generated by electrolyte penetration and subsequent dislodgment of particles, (e) grain boundary attack and (f) loss of material by dissolution of the oxide in the electrolyte.

In practice one or more of these mechanisms may be operative. It has been shown electrochemical investigation that metallic nickel leads to anodic dissolution (10). Further, noble metals like Pt or Pd does not show anodic dissolution. In order to improve the performance of the cermet anodes, several approaches to reduce electrochemical dissolution were pursued. These included:

1) Use of Alternate Metals in the Cermet

Examples are noble metals, such as Pt or Pd, and passivating alloys such as Cu-Ni alloys.

2) Use of Discontinuous Metal Phase

Reaction-sintering the present Ni-Fe-O cermet involves the displacement reaction like $Fe + NiO \rightarrow FeO + Ni$. The nickel metal forms an insitu interwoven network. This network is continuous in three dimensions provided there is sufficient quantity of metal. However, cermets can be produced with a discontinuous metal phase by introducing metal particles (e.g., Ni, Cu, Cu-Ni alloys, Pt, Pd, etc.) in the ceramic matrix. Sintering such metal-oxide mixtures in suitable atmospheres (nonoxidizing) would produce cermets. The electrical conductivity of such cermets would depend on the fraction of metal particles and their size. Reaction-sintering is also possible with CuO. When CuO is introduced in small amounts with NiO, Fe would reduce CuO first and then NiO. Dense cermet anodes were not successfully fabricated by this technique; additional experiments are necessary to evaluate the merits of this approach.

3) Reduce Porosity

Porosity inside the anode leads to degradation of the anode and the connection. The degradation can occur by increased surface area in contact with electrolyte, larger grain dislodgment or increased electrochemical dissolution in porous electrodes. Attempts were made to form dense impervious oxide coatings on cermet anode without success.

4) Freeze Bath

Prevention of bath penetration inside may, in principle, be

accomplished by introducing a component near the pores which would lead to solidification of electrolyte when it enters the pores.

Several composition variations have been tried to see if the molten bath penetration inside the anode could be retarded. Additives to retard bath penetration were chosen from CaF_2, MgF_2, CaO, MgO and also the effect of ZrO_2 additions to the anode have been tested. If the oxidation of the anode is enhanced via molten bath penetration, any effort to reduce molten bath penetration should reduce the size of the "oxidized" layer. CaF_2 and MgF_2 additives were introduced into the 6846 cermet material. These additives are not soluble in the cermet to any large extent and are localized around phase boundaries. These additives are rather high melting compared to the electrolyte. Thus, when small amounts of the electrolyte enter the anode, the electrolyte may freeze in place. The divalent additives like MgO and CaO can go into solid solution to some extent in the ferrite and thus would reduce "NiO" activity in the anode. Further, ZrO_2 additives can also go in partial solid solution. It was found that ZrO_2 and MgF_2 was most effective in reducing the oxidation of the cermet during electrolysis. These results have been described in Quarterly Report No. 15 (9).

If the metal phase is anodically dissolving, one way of reducing that would be to provide a discontinuous metal phase. Several samples were fabricated by adding Nickel powder to a preblended mixture of (51.7 wt.% NiO and 48.3 wt.% Fe_2O_3) oxide powders (5324). Fabrication of anodes by this technique, as opposed to the reaction-sintering technique in which (Fe, NiO, and Fe_3O_4) are reacted during sintering, is likely to provide less continuous metal phase. Further, 5, 10, and 15 wt.% Ni metal was added to these oxides. These anodes also showed significant loss of metal phase and consequent oxide layer.

In addition, several experiments were carried out with $NaFeO_2$ as

an additive to the 6846 cermet material to reduce bath penetration. $NaFeO_2$ was identified as a reaction product when superheated (1400°C) anodes were dropped in molten aluminum contained in a cryolite melt with little Al_2O_3.

Several other experiments were carried out in an effort to develop a dense layer on 6846 anode surface by exposing the anode in $NaFeO_2$ melt and also in an atmosphere containing $NaFeO_2$ and air in the temperature range of 1200-1375°C. Although these results were encouraging, no satisfactory coating for long term use was found.

While the present cermet may be improved by the approaches outlined, the oxide material has a finite rate of corrosion, and efforts should continue to find materials more resistant to attack by the cryolite melt.

The most dramatic improvement in anode performance was provided by addition of Cu to NiO-Fe_2O_3 compositions. It has been reported earlier (41) that addition of copper metal in the NiO-Fe_2O_3 system is desirable.

Copper was added to the oxide composition (5324) containing 51.7 wt.% NiO and 48.3 wt.% Fe_2O_3. Table 16 shows the result of bench-scale Hall cell tests with 5, 10, 15, 16, and 17 wt.% Cu-containing 5324-oxide compositions.

The tests were performed with 1.1 ratio bath with 5 wt.% CaF_2 and at ~960°C. The tests lasted 30 hours of electrolysis at ~1 amp/cm^2 on the anode bottom surface (~0.3 amp/cm^2 on exposed anode surface). The table shows the amounts of Ni, Fe, and Cu found in the aluminum produced during these tests. The anodes were found to be in excellent shape at the end of test. The anodes were sectioned in half, polished and examined microscopically. Microprobe examination was also carried out. Figure 14 shows the backscattered electron picture and corresponding X-ray images for Ni, Fe, Cu, O, Al, Na, and

TABLE 16

Hall Cell Test Results, 1.15 Ratio, 5 Wt.% CaF_2, 960°C

Anode No.	ANODE COMPOSITION WT.% Oxide 5324*	Cu Particle Size(microns)	Density g/cc	Current Efficiency %	Run Time Hrs.	METAL ANALYSIS WT.% Ni	Fe	Cu
021385	95	5 (1)	5.8	83.8	30	0.03	0.29	0.05
022085	95	5 (10)	5.8					
013185	90	10 (1)	5.91	82.2	30	0.04	0.26	0.07
022585	90	10 (10)	5.92	80.6	30	0.07	0.28	0.06
010885	85	15 (1)	5.92	83.8	30	0.05	0.34	0.12
022885	84	16 (10)	6.08	88.7	30	0.03	0.28	0.06
011785	83	17 (10)	6.14	85.1	30	0.05	0.30	0.10

*Oxide 5324 contains spray-dried mixture of 51.7 wt.% NiO and 48.3 wt.% Fe_2O_3.

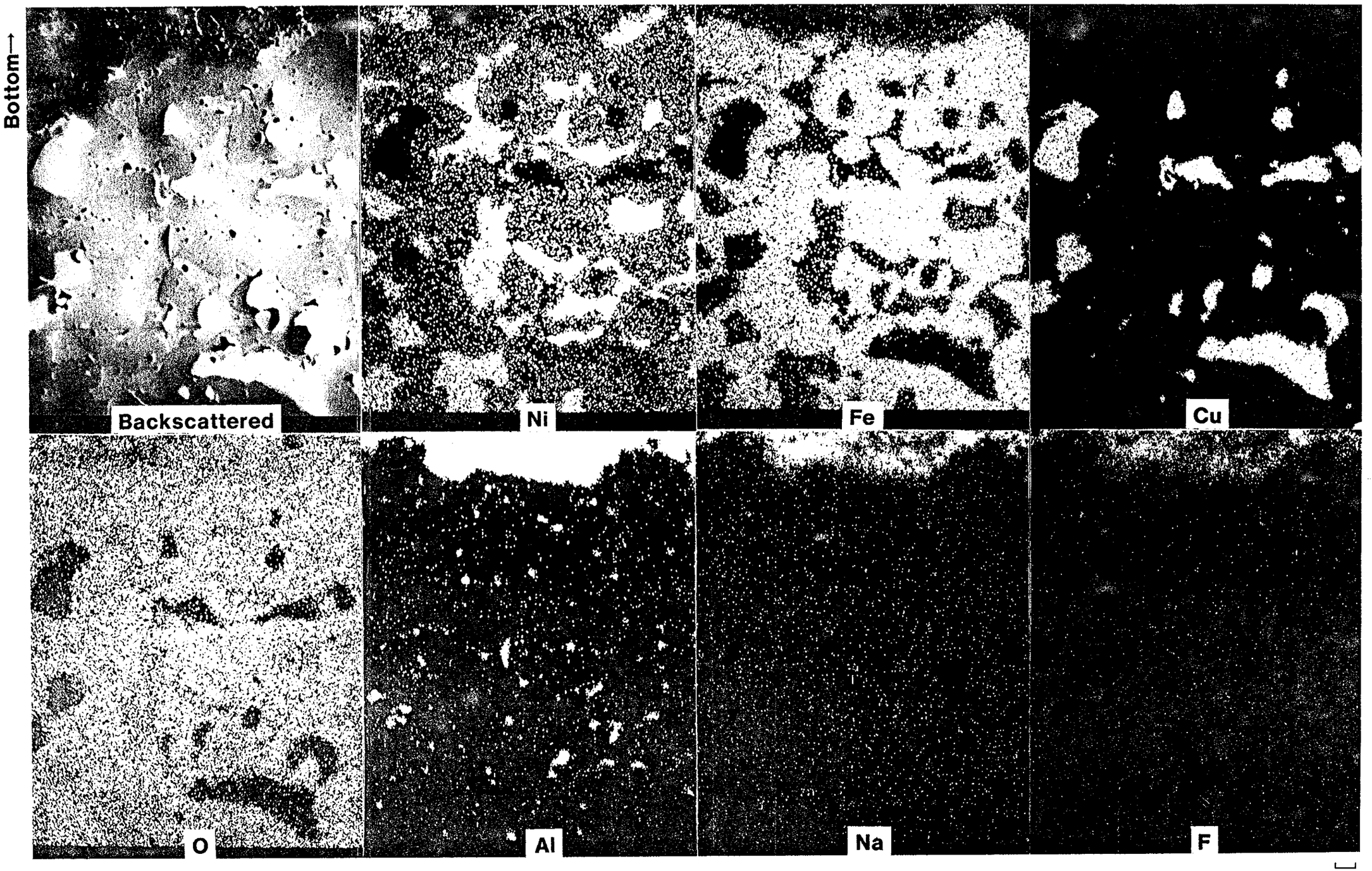

Anode Bottom, Sample 011785 After Hall Cell Test
Figure 14

F from anode 011785 containing 17 wt.% Cu and 83 wt.% oxide (51.7 wt.% NiO-48.3 wt.% Fe_2O_3) after Hall cell test. The top of the picture represents the bottom of the anode and some bath could be seen stuck to the anode (note the presence of Na, Al, and F). No degradation or loss of copper metal is seen deep inside the anode, unlike the nickel-containing cermet material. These positive results were very encouraging, and additional extended tests with this material confirmed these findings.

These studies showed that 5324-Cu anodes perform well in bench-scale Hall cell tests with ~2.5 cm diameter anodes and also in 60-A cell test with ~7.5 cm diameter anodes. These anodes contain Ni_x-$Fe_{3-x}O_4$ (spinel), $Ni_yFe_{1-y}O$ type oxide, and (Ni, Fe, Cu) alloy phases. No substantial dimensional losses of the anodes were found when these anodes were tested in a 1.1 ratio bath at 960°C, although metal produced using these anodes was contaminated with Fe, Ni, and Cu in the range of 0.26-0.34, 0.03-0.07, and 0.05-0.12 wt.%, respectively. No significant oxide layer was seen on the anodes at the end of 30-hour bench scale operation. The metal phase near anode surface was found to be enriched with respect to Cu metal and depleted with respect to the nickel metal phase. Table 17 shows the analyses of metallic phases from 15 wt.% Cu-5324 anode at the end of a 30-hour test.

These results are very encouraging and in sharp contrast with the 6846 anodes containing Ni-Fe alloy metal phase in Ni_x-$Fe_{3-x}O_4$ and $Ni_yFe_{1-y}O$ oxide phases.

1) Microstructural Evaluation of Improved Cermets

Table 18 shows the fabrication details of cermet anodes, approximately 2.5 cm diameter and 2.5-3.2 cm long, containing 5, 10, 15, 16, and 17 wt.% Cu powders added to a calcined oxide mixture 5324 [spray dried powder of composition 51.7 wt.% NiO and 48.3 wt.% Fe_2O_3] (31). The table also shows the results with 20 wt.% Pt in 5324 oxide composition. The addition of greater

TABLE 17

Analyses of Metallic Phases From Anode
(15 Wt.% Cu-5324) Sample at the End of 30 Hour Test

Sample No.	Location		Wt.% Cu	Wt.% Ni	Wt.% Fe	Atom % Cu	Atom % Ni	Atom % Fe
101584	Bottom-Center	1	90.1	8.0	1.8	89.4	8.6	2.0
		2	88.0	10.3	1.6	87.1	11.0	1.9
		3	85.5	12.3	2.3	84.4	13.1	2.5
		4	83.2	14.6	2.0	82.0	15.7	2.3
	Bottom Corner	1	96.6	1.4	2.1	96.1	1.5	2.4
		2	96.5	1.3	2.1	96.3	1.4	2.4
		3	97.3	0.9	1.8	97.0	1.2	1.7
		4	97.4	1.1	1.4	97.1	1.2	1.7
	Interior	1	77.2	20.5	2.2	75.6	21.8	2.5
		2	78.3	20.4	1.2	76.9	21.6	1.4
		3	77.7	20.4	1.8	76.2	21.8	2.0
		4	77.7	20.7	1.5	76.2	22.0	1.8

TABLE 18

Fabrication of Inert Anode Comnpositions for
Bench-Scale Hall Cell Test by
Sintering in Argon Atmosphere

	Composition (Wt.%)		Pressure MPa	Sintering Temp. °C	Sintering Time/Hrs.	Density g/cc
5324	Cu (10 μ)	Pt				
80		20	172	1350	2	6.67
95	5		172	1350	2	5.85
90	10		172	1350	2	5.95
85	15		172	1350	2	6.07
84	16		172	1350	2	6.10
83	17		172	1350	2	6.14

5324: Spray-dried powder composition 51.7 wt.% NiO, 48.3 wt.% Fe_2O_3
Cu: Powder, Alfa

amounts of copper increase the density as expected. These anodes were used to evaluate their performance in bench scale Hall cell tests.

Table 19 lists the fabrication parameters of inert anode compositions used for electrical conductivity measurements. 5324-type oxide compositions were mixed with 1μ or 10μ Cu powder in the amounts of 5, 10, 15, 16, and 17 wt.%. Higher amounts of copper lead to bleed-out of copper beads during sintering. Copper powder was obtained from Alfa Corporation in two nominal size ranges, "1μ" and "10μ." However, there were larger lumps and particles in both of these copper powders. Therefore, it was decided to remove the larger lumps by passing the copper powder through a mesh screen. Screening and storage of copper powder was carried out inside a glove box. The anodes were fabricated to approximately 0.95 cm diameter.

The density of anodes with "10μ" copper powder was found to increase with increasing copper content, as expected. Copper has a density of 8.92 g/cc and 5324-type oxide composition has a calculated density of ~5.7 g/cc. It is, therefore, expected that higher amounts of copper in 5324 would lead to increased density. However, when parts were fabricated with "1μ" powder, the changes in density did not always show this pattern. Surface oxide on smaller particles may have reduced the densification activity of this powder and caused lower sinter densities to occur.

A small piece of the sample fabricated for electrical conductivity measurements was mounted, polished and examined metallographically. Figures 15-17 show the micrographs at 150X and 600X of samples fabricated using as-received nominally "1μ" copper powder as received. Figures 15-17 represent the micro graph with 95, 90, and 85 wt.% 5324 material with 5, 10, and 15 wt.% copper. It is clear from these micrographs that a large number of particles are over 10μ range and some agglomeration of smaller particles is also seen.

TABLE 19

Fabrication of Inert Anode Compositions for Electrical Conductivity Measurements, Sintered in Argon Atmosphere, 172 MPa

Composition Wt.%					Sintering	Sintering	Density
5324	1μ Cu	10μ Cu	1μ Screened	10μ Screened	Temp. °C	Time/Hrs.	g/cc
95	5				1350	2	5.99
90	10				1350	2	5.95
85	15				1350	2	6.01
95			5		1350	2	5.98
90			10		1350	2	5.97
85			15		1350	2	5.97
84			16		1350	2	5.08
83			17		1350	2	6.15
95		5			1350	2	5.96
90		10			1350	2	6.13
85		15			1350	2	6.35
84		16			1350	2	6.35
83		17			1350	2	6.02
95				5	1350	2	5.99
90				10	1350	2	6.12
85				15	1350	2	6.28
84				16	1350	2	6.35
83				17	1350	2	6.40

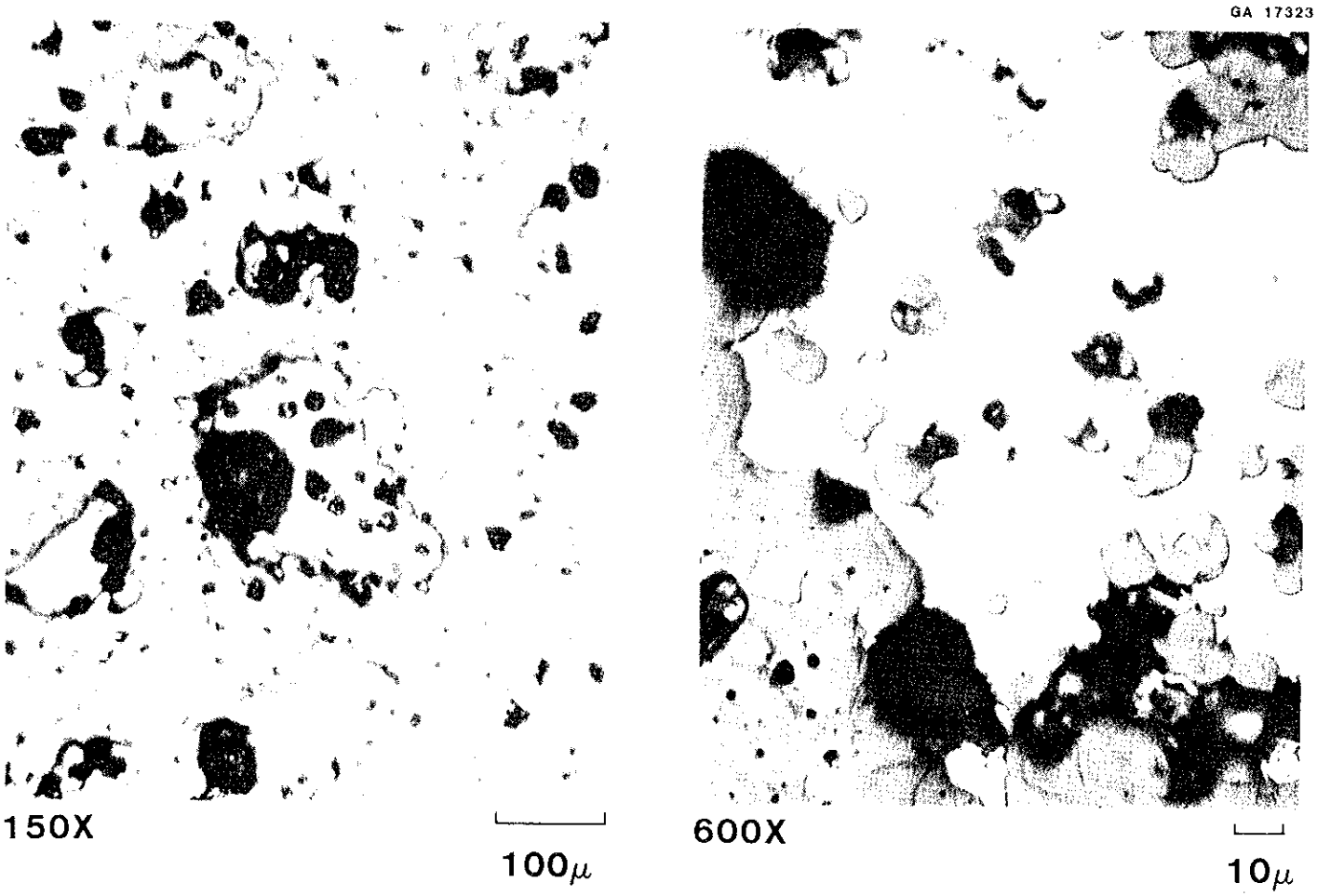

S #578656: 95 Wt. % 5324 + 5 Wt. % Cu
(1μ As Received)
Figure 15

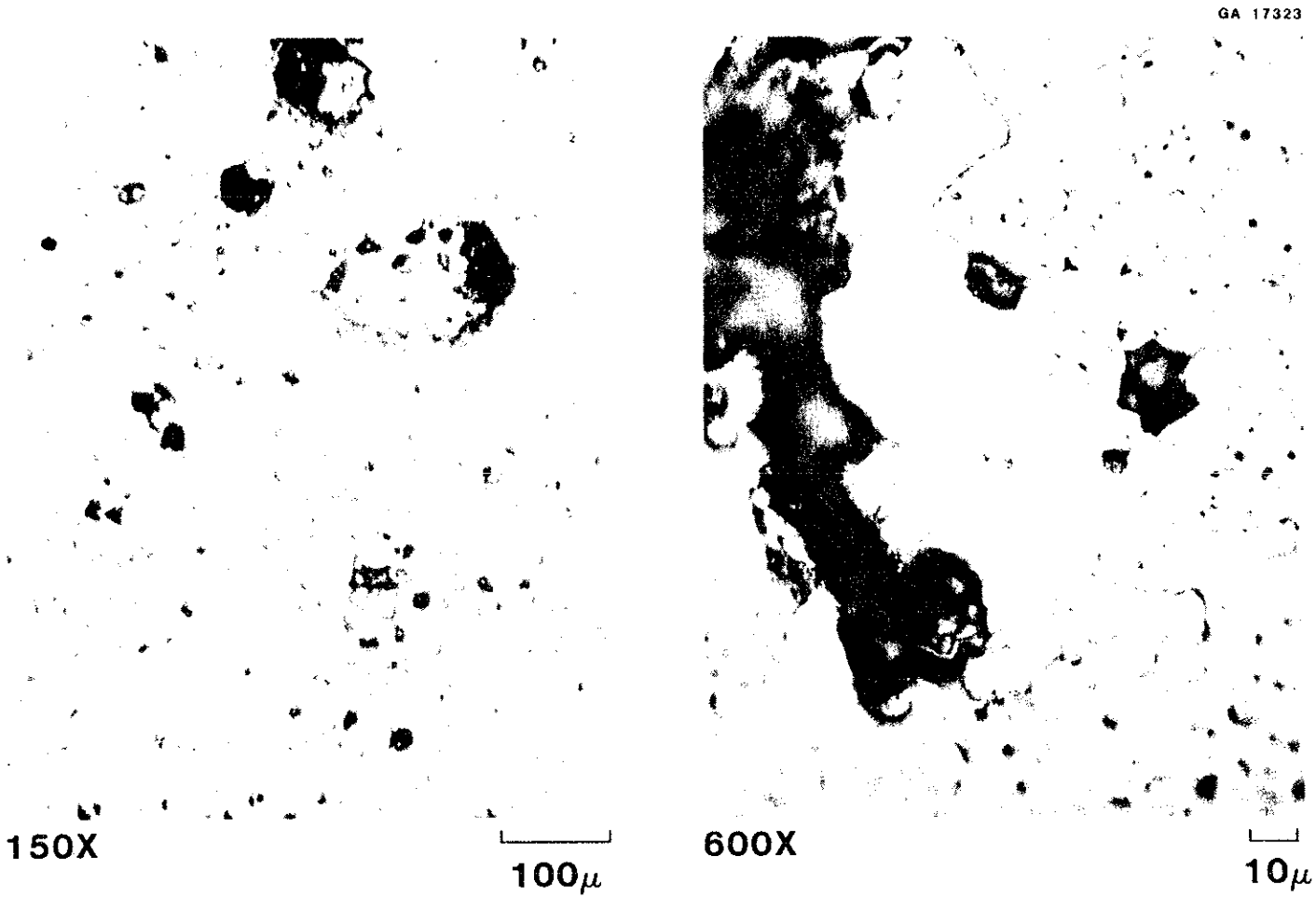

S #57864: 90 Wt. % 5324 + 10 Wt. % Cu
(10μ As Received)
Figure 16

GA 17323

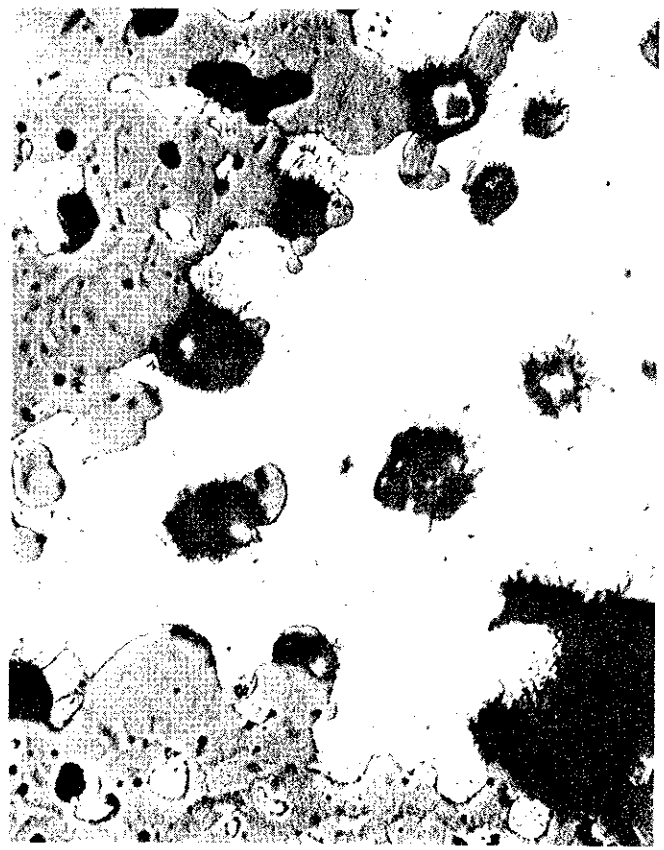

S #578655: 85 Wt. % 5324 + 15 Wt. % Cu
(1μ As Received)
Figure 17

Figures 18-22 represent samples fabricated with 95, 90, 85, 84, and 83 wt.% 5324 material and 5, 10, 15, 16, and 17 wt.% as-received nominally 10μ copper particles. The density of the fabricated parts was found to increase with increasing copper content as expected except for the sample with 17 wt.% Cu which showed more porosity. This batch of samples had relatively low porosities.

Figures 23-27 show the micrographs of samples fabricated with 95, 90, 85, 84, and 83 wt.% 5324 material and 5, 10, 15, 16, and 17 wt.% "10μ" copper particles. The copper powder was screened to remove large lumps prior to addition to the 5324 powder mixture. The density of these samples increased with increasing copper content as expected. The samples also show relatively low porosities. Electron probe microanalysis of all these samples was carried out to determine the composition of the metal phase.

It appeared that the observed copper particle size in the fabricated samples was different from what vendors indicated for the supplied material. This difference could be due to a wide distribution of particles supplied by the vendor and also agglomeration of particles during fabrication. In order to determine the size of the particles actually present in the fabricated sample, we used an optical method utilizing the OPTIMAX System IV chord size distribution program. The unit determines the longest chord that separates two parallel lines or the edges of the particles or grains being measured, regardless of the shape of the grain. Limitations of the measuring system include the fact that the plane of a polished surface may not pass through the center of the grain and the system is unable to detect very small grains.

It was found that agglomeration size and number increased with increased copper content.

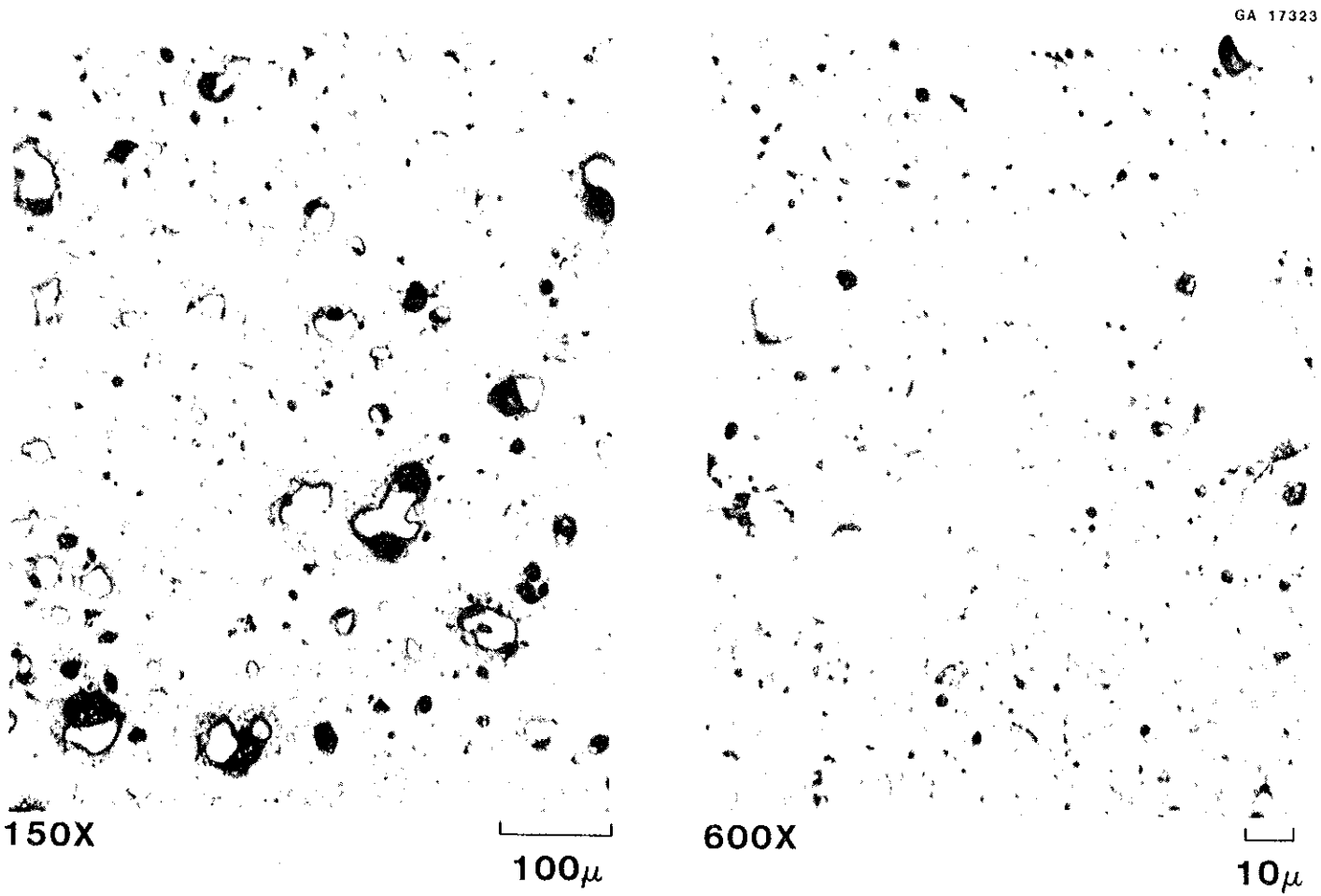

S #578667: 95 Wt. % 5324 + 5 Wt. % Cu
(10μ As Received)
Figure 18

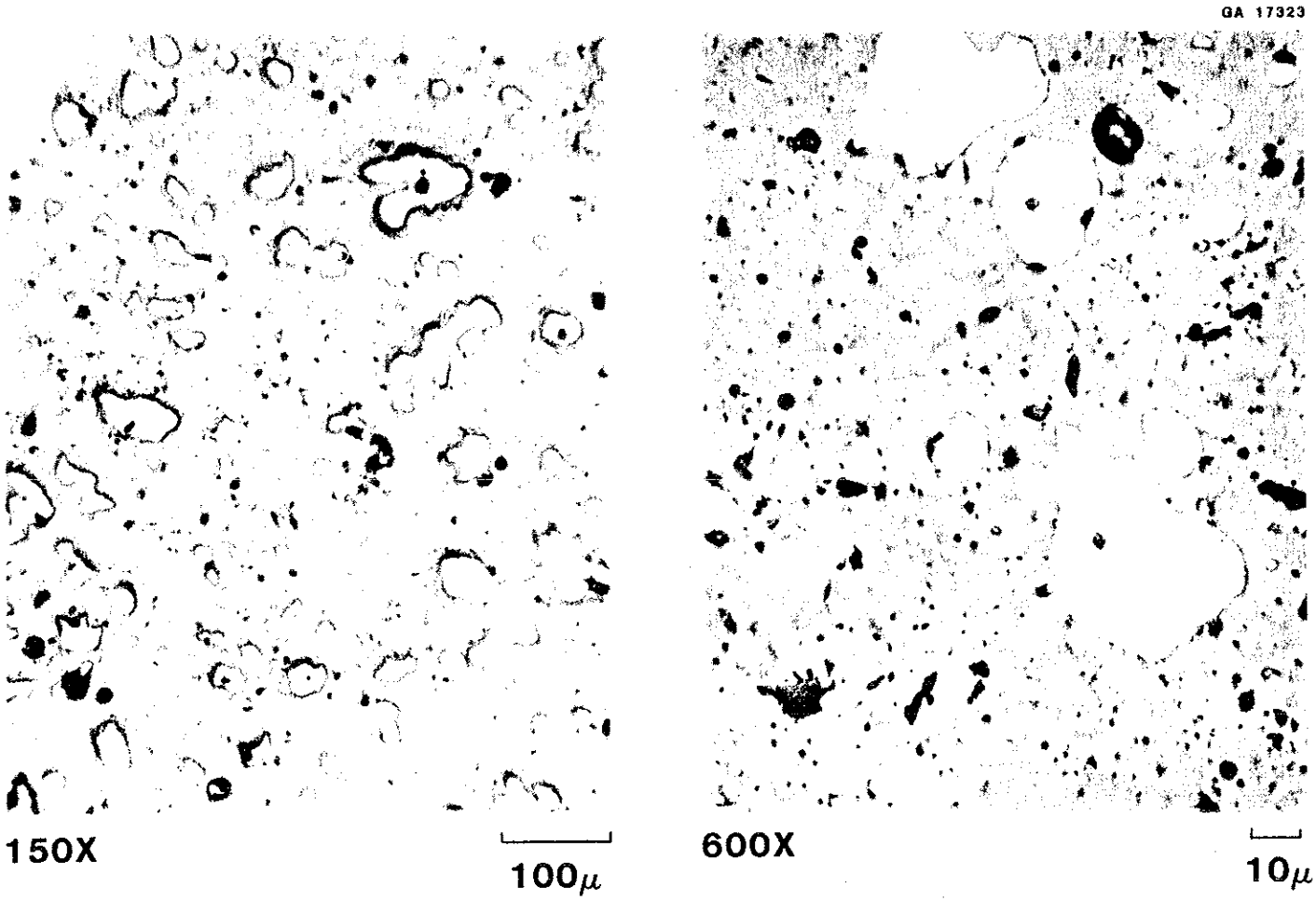

S #578668: 90 Wt. % 5324 + 10 Wt. % Cu
(10μ As Received)
Figure 19

GA 17323

150X

100μm

600X

10μm

S#578669: 85 Wt. % 5324 + 15 Wt. % Cu
(10μm As Received)
Figure 20

GA 17323

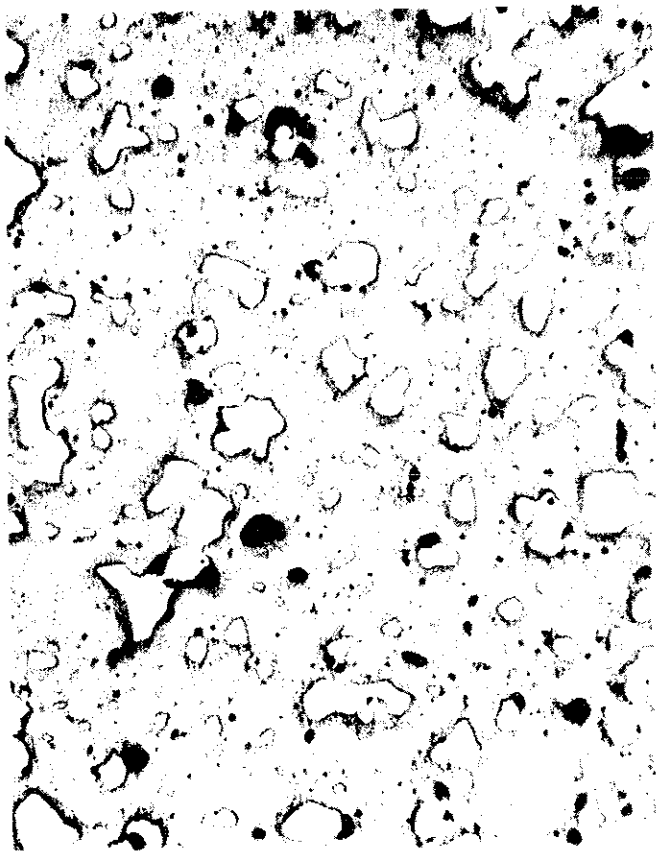

150X

100μ

600X

10μ

S #578674: 84 Wt. % 5324 + 16 Wt. % Cu
(10μ As Received)
Figure 21

GA 17323

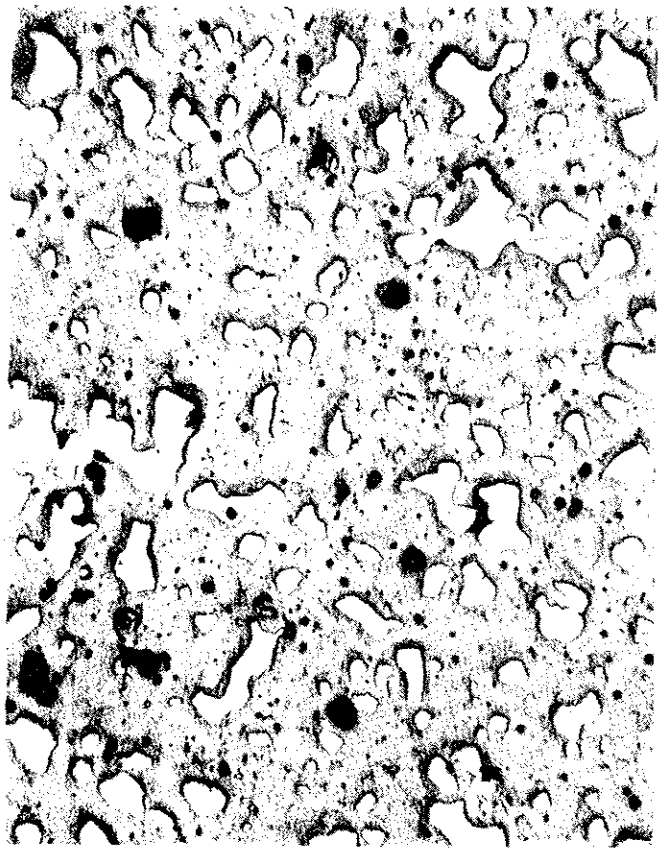

150X

100μ

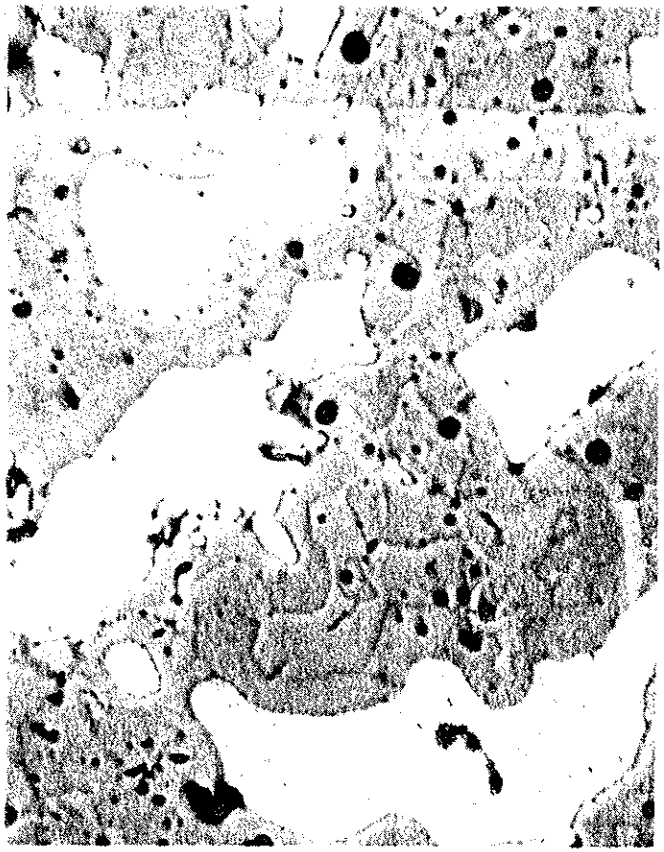

600X

10μ

S #578676: 83 Wt. % 5324 + 17 Wt. % Cu
(10μ As Received)
Figure 22

GA 17323

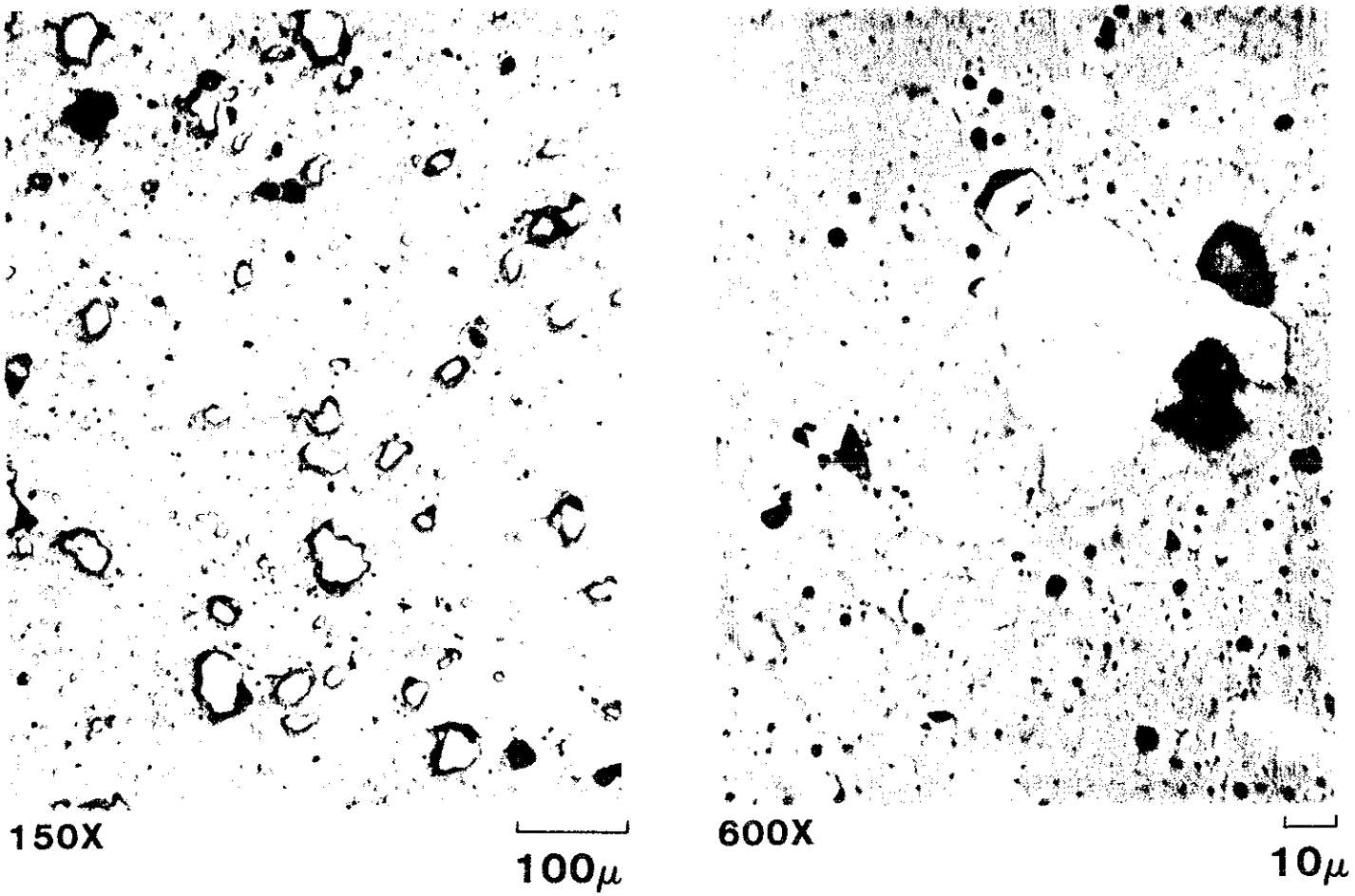

S #578686: 95 Wt. % 5324 + 5 Wt. % Cu
(10μ As Screened)
Figure 23

GA 17323

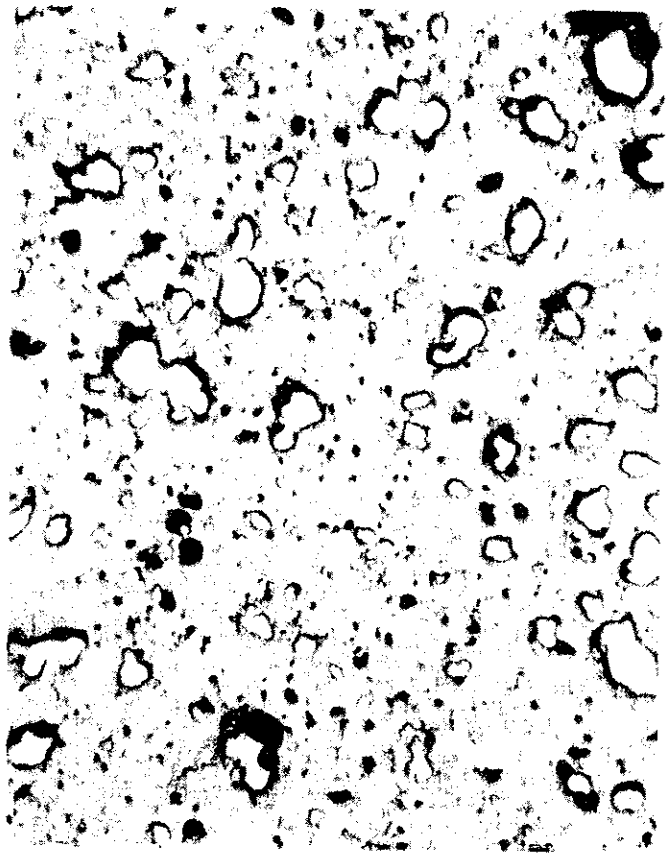

S #578684: 90 Wt. % 5324 + 10 Wt. % Cu
(10μ As Screened)
Figure 24

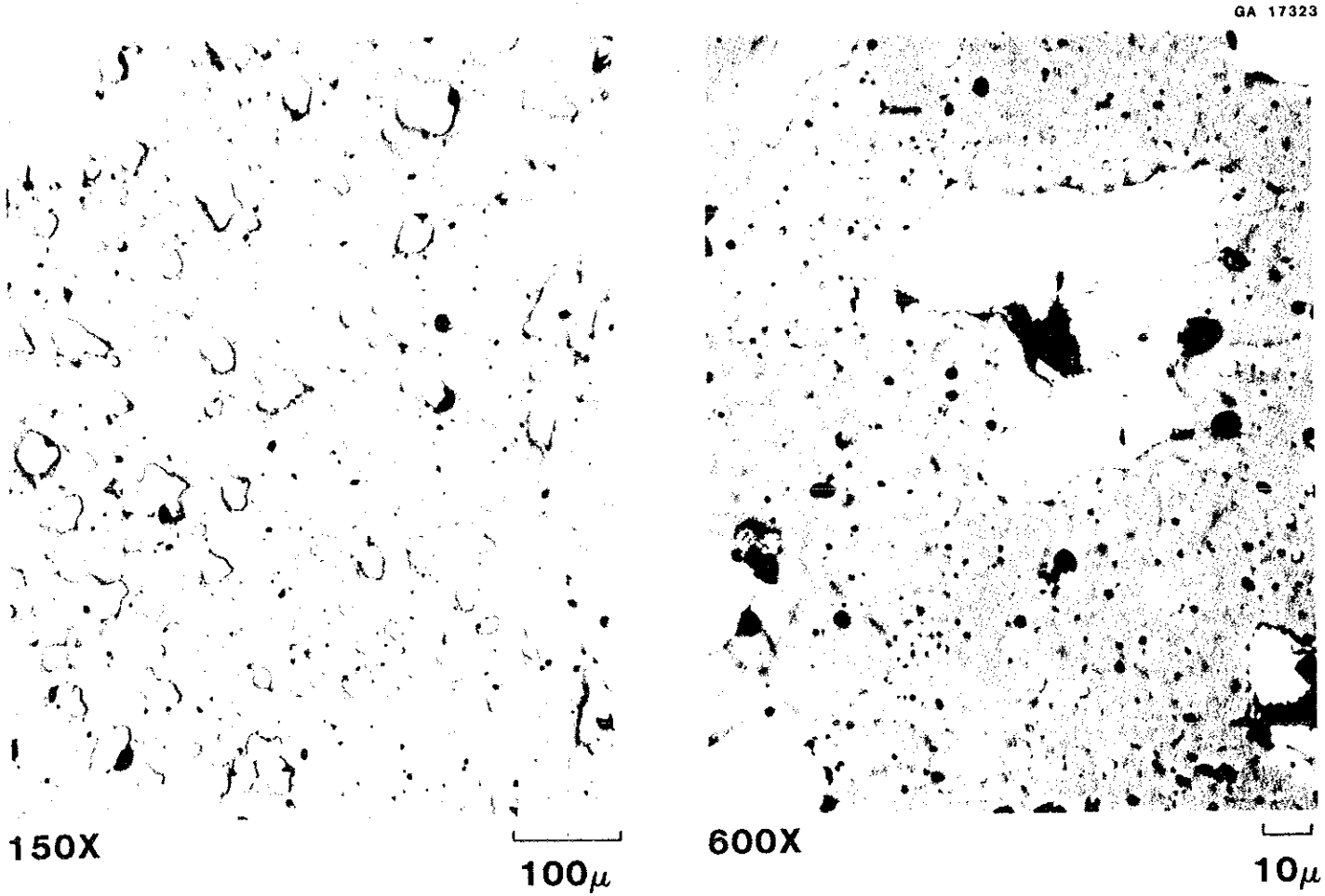

S #578685: 85 Wt. % 5324 + 15 Wt. % Cu
(10μ As Screened)
Figure 25

GA 17323

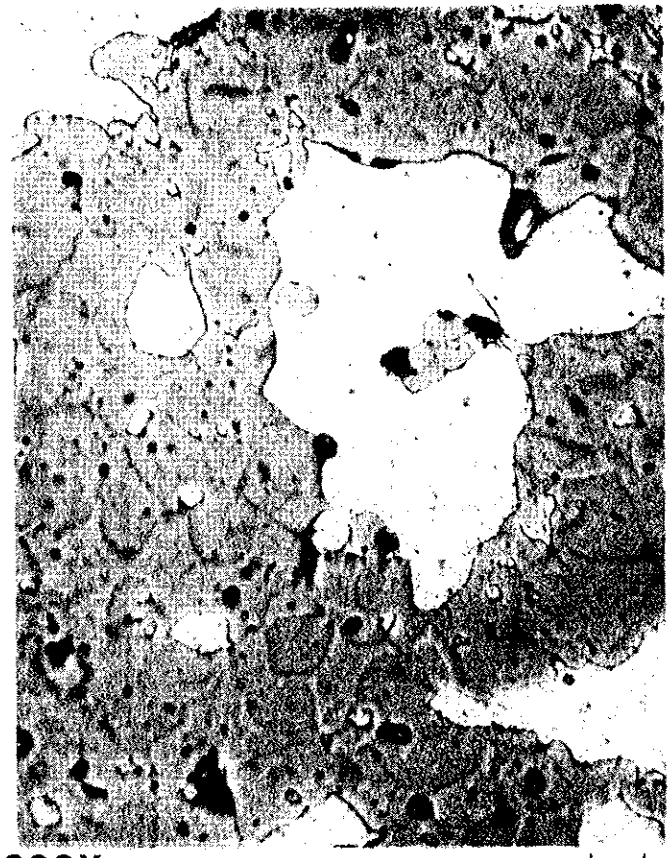

S #578682: 84 Wt. % 5324 + 16 Wt. % Cu
(10μ As Screened)
Figure 26

GA 17323

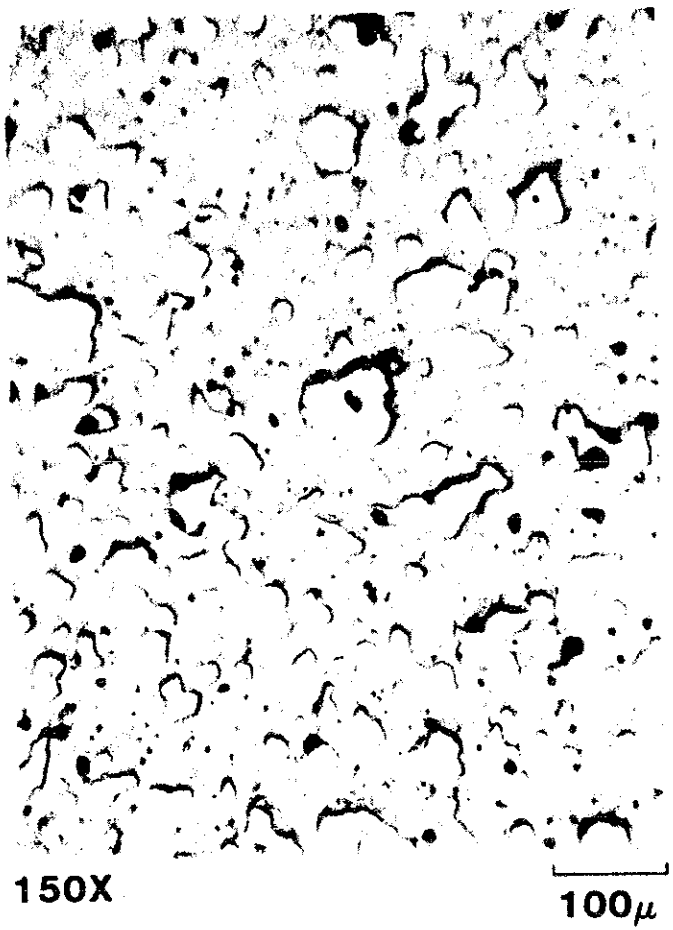

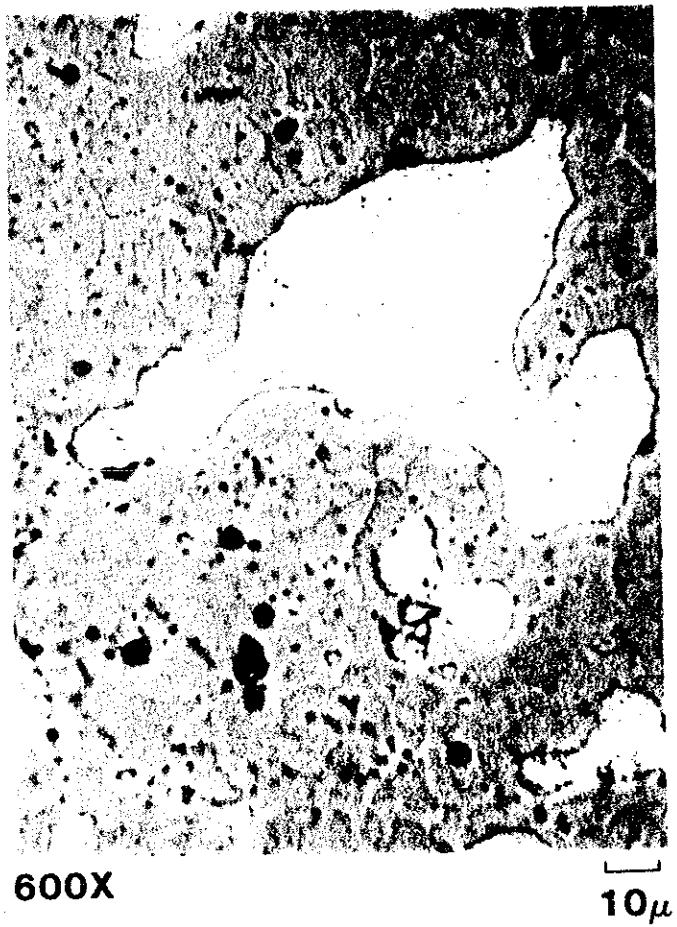

S #578683: 83 Wt. % 5324 + 17 Wt. % Cu
(10μ As Screened)
Figure 27

Figure 28 shows the typical chord size distribution of copper metal grains with 5% copper metal in 5324 with "1μ" as-received copper particles. The average grain size, as determined by OPTIMAX System, turned out to be 9.78 μm. Figure 29 represents 17 wt.% "10μm" as received Cu grains. The fabricated part showed an average grain size of 13.7 μm.

Table 20 shows the summary of complete particle size analysis. B and C represent unscreened material. SCR represents materials that were screened to eliminate large agglomerates. The grain size represents the average size of copper particles. We have also carried out microprobe analyses of these particles. The composition of the metal phase, the metal grain size, and metal percent area as determined by optical analysis is shown in Table 21.

2) Electrical Properties of Improved Cermets

As pointed out earlier, the 6846 type cermet material containing $Ni_xFe_{3-x}O_4$ (spinel), $Ni_yFe_{1-y}O$, and Ni_zFe_{1-z} alloy phases has adequate electrical conductivity. Figure 30 shows the electrical conductivity of 6846 type material fabricated with 20 wt.% Fe, 20 wt.% Fe_3O_4 and 60 wt.% NiO using 94-2 raw material combination (Fe: Quebec Atomet, Fe_3O_4: Pfizer, BK 5000 and NiO: Ceramic Color and Chemical). Electrical conductivity of this material is above 300 $\Omega^{-1}cm^{-1}$ at 1000°C. The electrical conductivity appears to be metallic and conductivity increases with decreasing temperature. On the other hand the 5324 all-oxide type material containing $Ni_xFe_{3-x}O_4$ and $Ni_yFe_{1-y}O$ phases possess rather poor electrical conductivity. Electrical conductivity measurements and analyses of spinel type materials have received considerable attention in the literature (42-45). Figure 3 shows a plot of conductivity, σ vs. $\frac{1}{T}$ for this type of material (51.7 wt.% NiO, 48.3 wt% Fe_2O_3). This material behaves like a semiconductor and conductivity increases with increase in temperature. At 1000°C the electrical conductivity is approximately 0.8 $\Omega^{-1}cm^{-1}$.

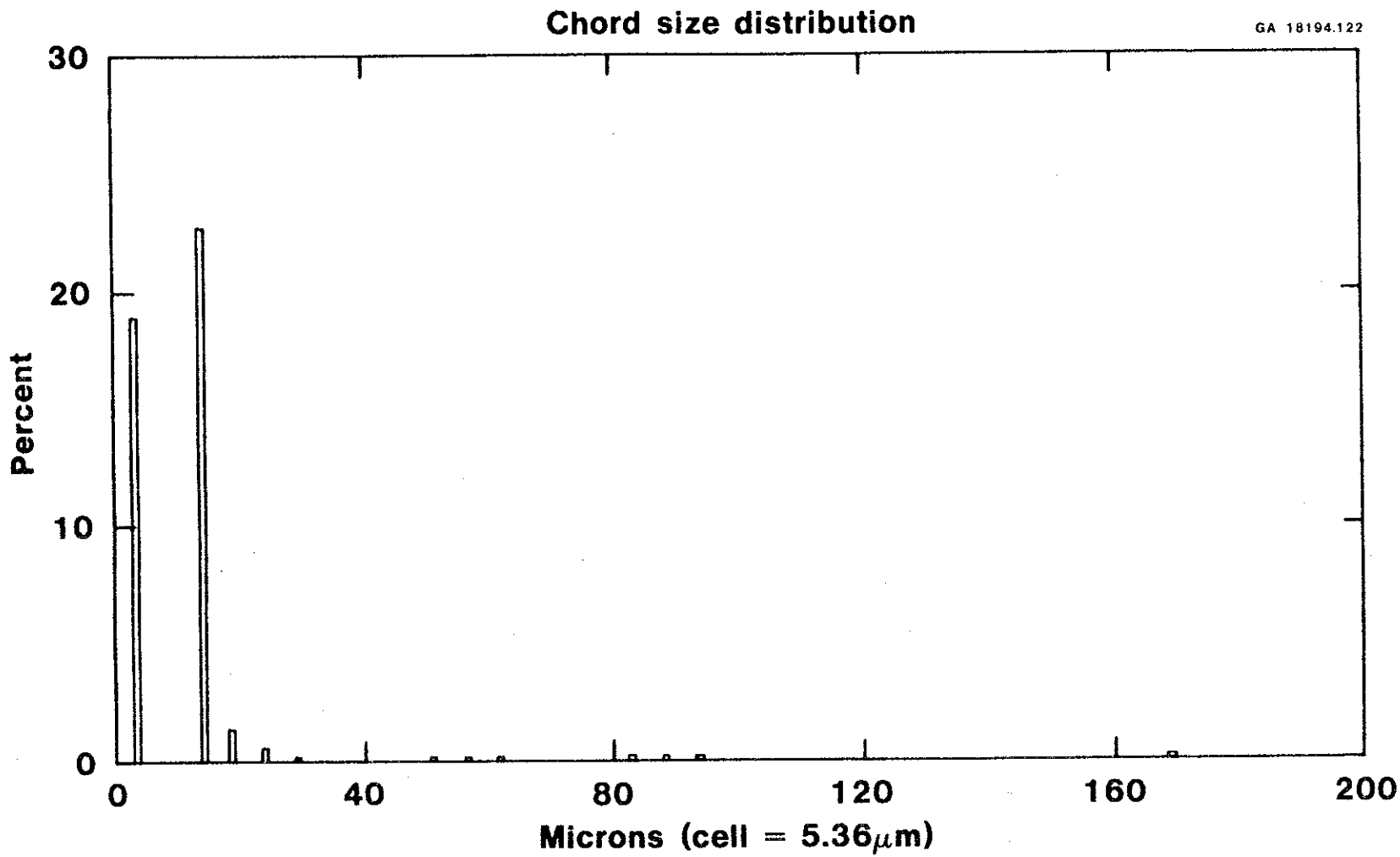

Copper Metal Grains
S #568654 5% 1μm Copper
Average Grain Size 9.78 μm

Figure 28

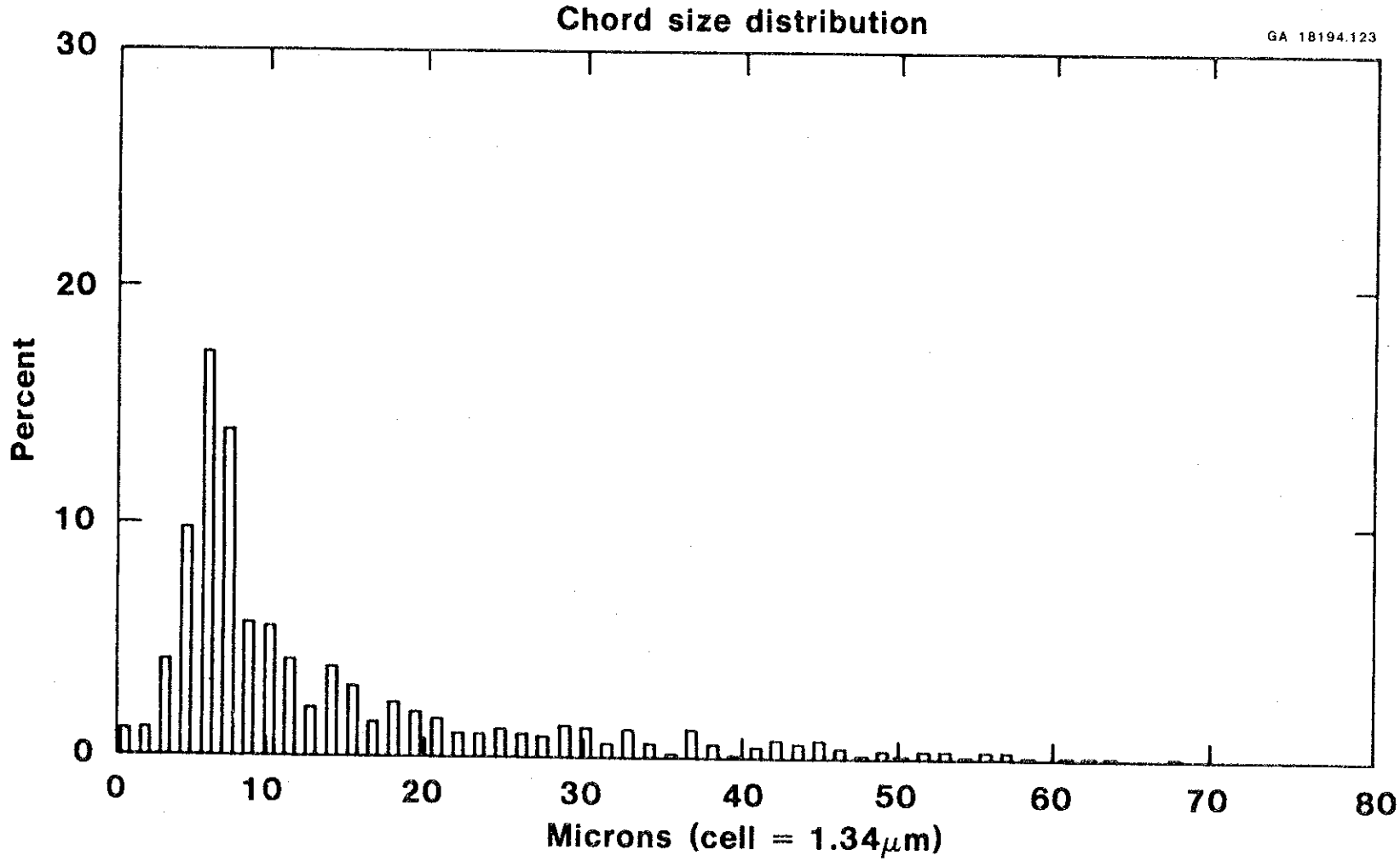

Copper Metal Grains
S #568676 17% Composition 10μm Copper
Average Grain Size 13.71μm
Figure 29

TABLE 20

Metal Particle Size Analyses in Sintered Inert Anodes

Inert Anode No.	% Cu	µm Cu	Comp	Area of Each Field (sq mm)	Void Percent of Area	Plus Minus	No. of Fields Tested	Metal Percent of Area	Plus Minus	No. of Fields Tested	No. of Grains In 1.0 (sq mm)	Oxide Percent of Area	Grain Size	Plus Minus
1 667	5	10	B	0.114	3.07	1.49	20	3.84	0.74	20	642	93.09	7.55	6.56
2 668	10	10	B	0.114	2.41	0.71	20	8.36	2.21	20	536	89.23	10.85	8.80
3 669	15	10	B	0.114	2.09	0.60	20	10.95	2.60	20	427	86.96	11.55	10.11
4 674	16	10	B	0.114	3.05	0.95	20	10.80	1.97	20	364	86.05	13.84	11.97
5 676	17	10	B	0.114	2.63	0.67	20	13.42	1.98	20	407	83.95	13.71	11.99
6 686	5	10	SCR	0.114	1.26	0.44	20	5.31	0.77	20	848	93.43	6.50	5.50
7 684	10	10	SCR	0.114	3.04	1.23	20	6.55	1.42	20	546	90.41	10.07	7.92
8 685	15	10	SCR	0.114	2.09	0.60	20	9.83	1.30	20	398	88.08	14.31	11.65
9 682	16	10	SCR	0.114	2.39	0.70	20	9.83	2.42	20	354	87.78	14.91	12.51
10 683	17	10	SCR	0.114	2.27	0.72	20	10.97	2.63	20	354	86.76	13.71	12.18
11 654	5	1	C	0.114	3.62	1.86	20	4.24	3.60	20	745	92.14	9.78	11.16
12 655	10	1	C	0.114	5.50	3.65	20	6.50	2.25	20	847	88.00	10.39	10.55
13 656	15	1	C	0.114	7.66	3.68	20	7.31	2.72	20	751	85.03	11.56	13.06
14 672	5	1	SCR	0.114	2.13	0.69	20	4.28	0.66	20	1147	93.59	5.79	1.97
15 670	10	1	SCR	0.114	3.64	1.02	20	5.54	1.07	20	1034	90.82	6.74	3.21
16 671	15	1	SCR	0.114	4.51	0.99	20	9.43	1.66	20	974	86.06	8.52	5.39
17 680	16	1	SCR	0.114	7.28	1.18	20	9.26	0.86	20	1117	83.46	8.29	4.75
18 681	17	1	SCR	0.114	5.66	1.34	20	10.28	1.28	20	979	84.06	9.80	6.42

TABLE 21

Analysis of Metal Grains in Cu-5324 Cermet Compositions

% 5324	ANODE COMPOSITION % Cu "10 μ as received"	"10 μ screened"	"1 μ as received"	"1 μ screened"	SAMPLE NO.	COMPOSITION OF METAL PHASE Ni	Cu	Fe (Wt.%)	Metal Grain Size	Metal Area %
95	5				578667	23.4	74.9	1.7	7.55 ± 6.6	3.84 ± 0.74
90	10				578668	21.1	77.5	1.4	10.85 ± 8.8	8.36 ± 2.2
85	15				578669	17.5	81.0	1.5	11.55 ± 10.1	10.95 ± 2.6
84	16				578674	14.3	84.4	1.3	13.84 ± 11.9	10.90 ± 1.97
83	17				578676	17.9	80.5	1.6	13.71 ± 12.0	13.42 ± 1.98
95		5			578686	19.7	78.1	2.2	6.5 ± 5.5	5.3 ± 0.77
90		10			578684	16.0	82.4	1.6	10.1 ± 7.8	6.5 ± 1.4
85		15			578685	15.4	83.1	1.5	14.3 ± 11.7	9.8 ± 1.3
84		16			578682	14.2	84.3	1.5	14.9 ± 12.5	9.8 ± 2.4
83		17			578683	14.5	84.2	1.3	13.7 ± 12.8	10.97 ± 2.6
95			5		578654	15.7	81.8	2.5	9.78 ± 9.2	4.24 ± 3.6
90			10		578655	13.9	83.7	2.4	10.4 ± 10.3	6.5 ± 2.3
85			15		578656	11.3	87.2	1.5	11.6 ± 11.0	7.3 ± 2.7
95				5	578672	22.4	74.3	3.4	5.8 ± 2.0	4.3 ± 0.7
90				10	578670	19.4	77.5	3.1	6.74 ± 3.2	5.5 ± 1.1
85				15	578671	14.7	83.2	2.1	8.5 ± 5.4	9.4 ± 1.7
84				16	578680	17.2	80.3	2.5	8.3 ± 4.8	9.3 ± 0.9
83				17	578681	16.3	81.2	2.5	9.8 ± 6.4	10.3 ± 1.3

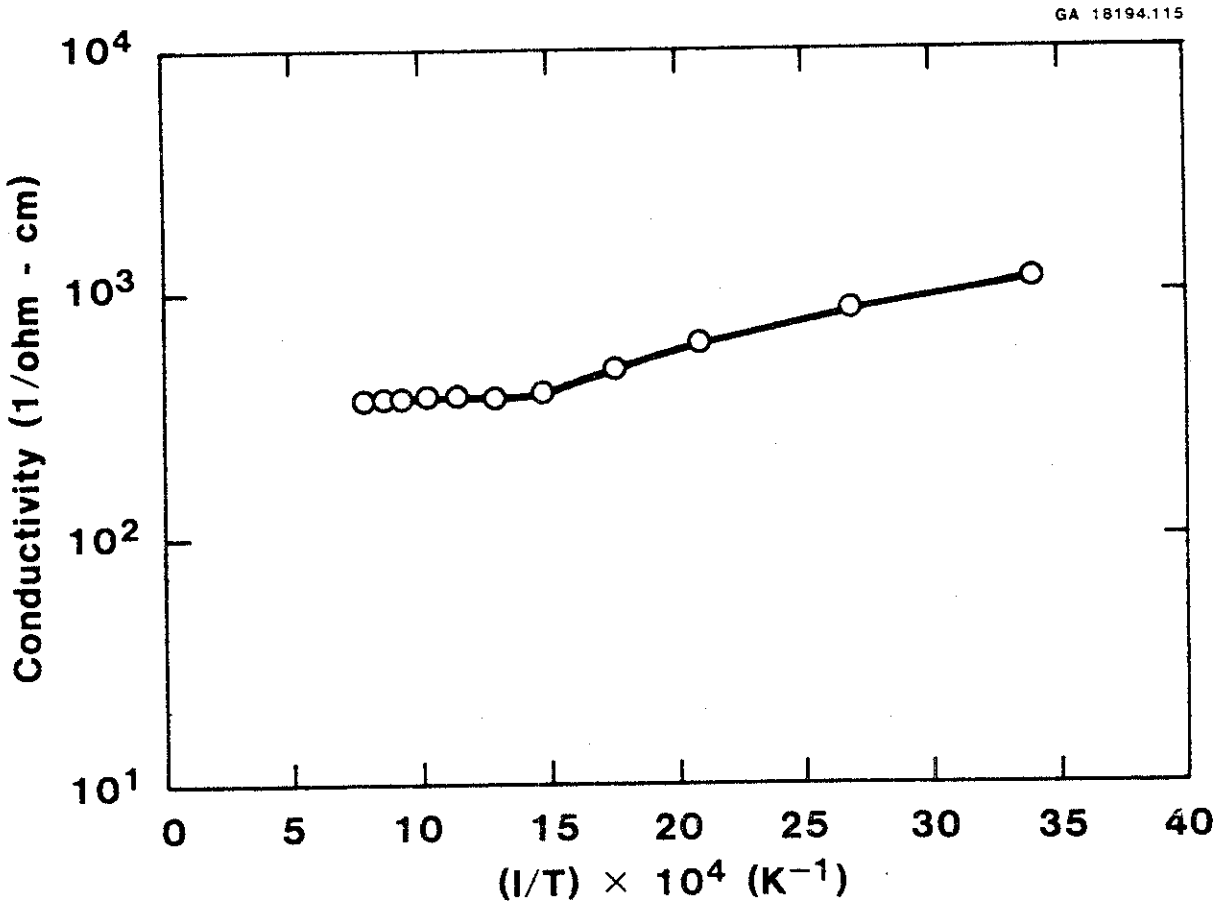

Electrical Conductivity of 6846 Composition Reaction-Sintered Cermet Inert Anode 94-2

Figure 30

The increase in conductivity in 6846 type material is believed to be due to the presence of the metallic type material. Reaction-sintering Fe with NiO leads to the displacement reaction in the 6846 type material and forms an interwoven network of Ni-Fe alloy with the oxide matrix. Nearly a thousandfold increase in electrical conductivity is thus due to the presence of this semi-continuous "metal" phase. The presence of a continuous metal phase also leads to the metallic type conductivity in these materials.

However, these materials were found to develop an oxide layer, during electrolytic production of aluminum, which was porous and not easily controllable. Thus the electrical conductivity gain was being lost over a period of time and also the porous oxide scale was easily dislodged, leading to excessive metal contamination in the aluminum produced. The Ni-Fe alloy phase was also found to show "corrosion currents" in G. P. Tarcy's electrochemical studies, indicating that the metal phase was anodically dissolving (46).

In order to circumvent all these problems, we found that copper alloys were beneficial. Copper metal was found to be stable with 5324 type material in earlier studies (prior to this cooperative agreement). Copper also enhances densification of these materials. A series of samples were made with 5324 composition and their electrical properties and Hall cell performance were determined. Table 22 shows the electrical conductivity values at various temperatures for 5324-Cu cermet compositions. Figure 31 shows the electrical conductivity value at 960°C as a function of wt.% Cu in 5324 material. Figure 32 shows the same data plotted as a function of vol.% Cu in 5324 material. Figure 33 shows a plot of log σ vs. $10^4/T$ with 5324-17 wt.% Cu material. From the tables and figures, the following points can be drawn: (a) the electrical conductivity is found to increase with increasing amounts of copper in 5324 material, (b) electrical conductivity increases with increase in temperature as would be expected of a

TABLE 22

Electrical Conductivity of 5324 Cu-Cermet Anodes

Sample No.	Wt.% 5324	Wt.% Cu	Nominal Particle Size μ	Screened Yes/No	σ ohm^{-1} cm^{-1} at 200°C	400°C	600°C	800°C	960°C	1000°C
578654	95	5	1	No	6.82	10.47	15.81	21.25	25.90	27.00
578655	90	10	1	No	6.93	10.93	16.46	22.64	29.20	30.77
578656	85	15	1	No	7.15	12.00	18.04	24.52	30.80	32.32
578672	95	5	1	Yes	7.20	11.39	17.29	22.94	27.70	28.70
578670	90	10	1	Yes	7.52	11.78	17.76	24.06	29.10	30.11
578671	85	15	1	Yes	8.71	13.41	20.33	27.47	33.80	35.35
578680	84	16	1	Yes	9.55	15.46	23.28	31.05	39.20	41.09
578681	83	17	1	Yes	10.15	16.03	24.34	32.88	41.20	43.17
578667	95	5	10	No	6.02	10.06	15.40	21.06	25.80	27.19
578668	90	10	10	No	7.37	12.38	19.82	26.93	34.60	36.93
578669	85	15	10	No	10.73	18.28	28.15	37.25	47.80	50.72
578674	84	16	10	No	22.18	35.83	51.54	67.88	82.00	85.34
578676	83	17	10	No	24.01	36.80	53.67	68.65	86.30	90.83
578686	95	5	10	Yes	6.45	10.04	15.27	21.08	27.20	28.61
578684	90	10	10	Yes	8.50	13.64	20.70	28.26	35.50	37.08
578685	85	15	10	Yes	12.94	20.96	31.23	42.69	54.60	57.08
578682	84	16	10	Yes	13.17	22.10	33.11	45.66	59.10	62.86
578633	83	17	10	Yes	17.89	28.60	41.61	56.02	70.80	75.21

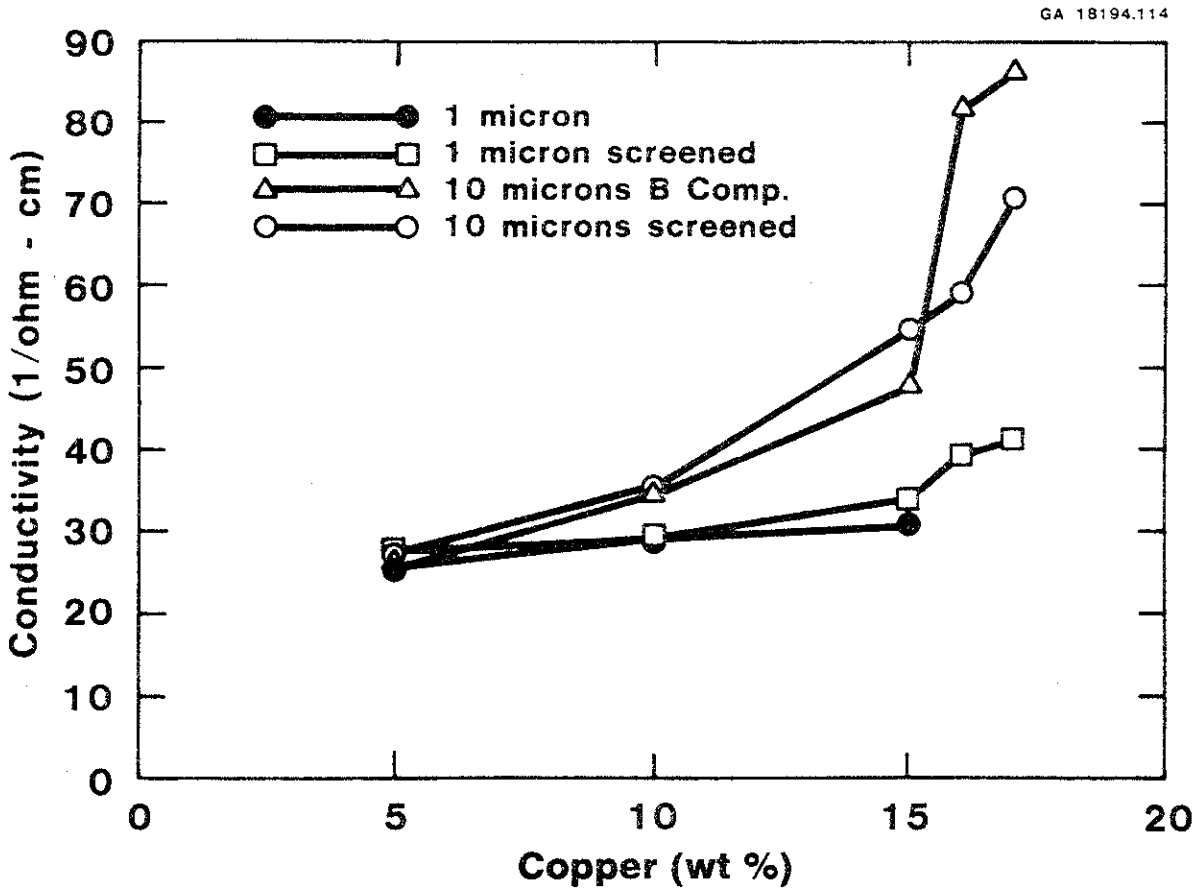

Conductivity of 5324 + Cu Cermet Inert Anodes at 960 Deg. C

Figure 31

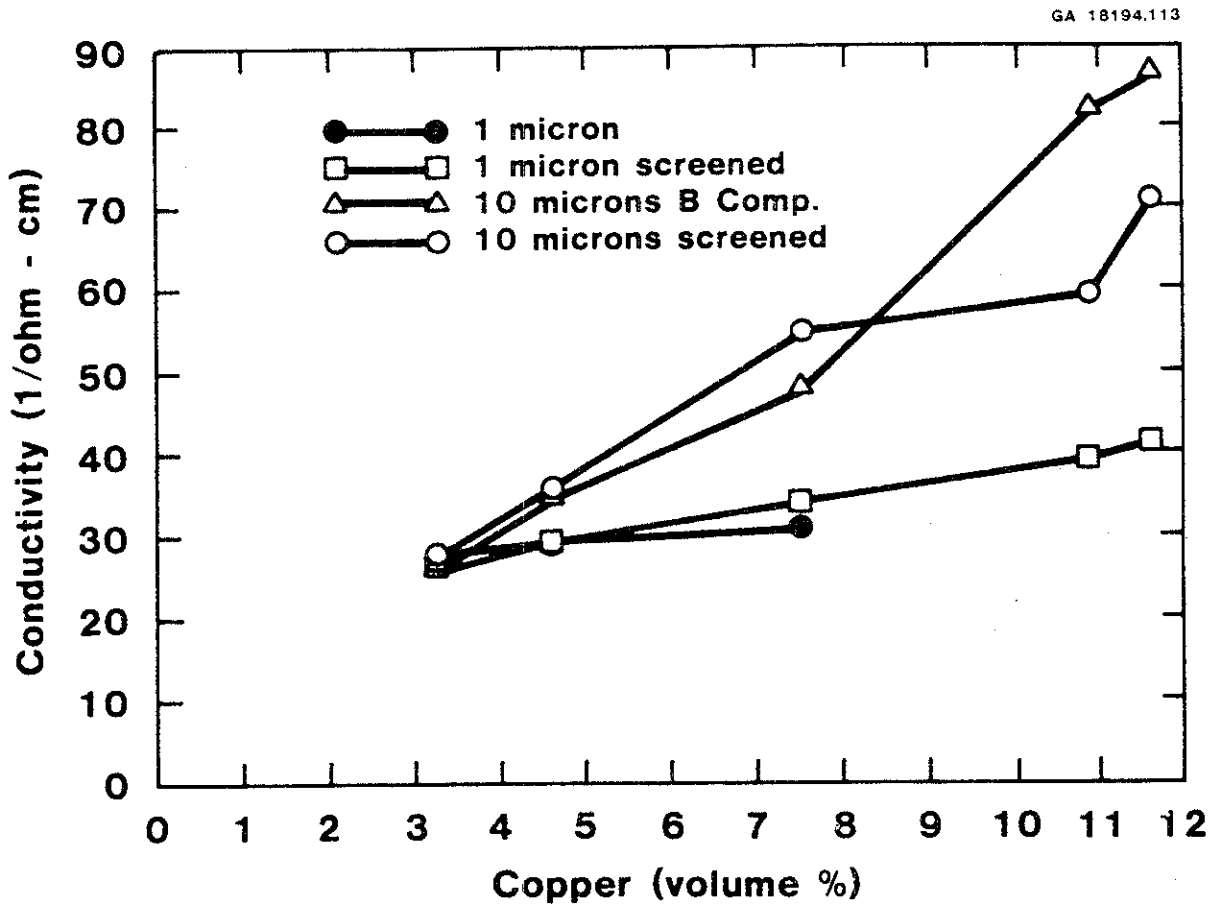

Conductivity of 5324 + Cu Cermet Inert Anodes at 960 Deg. C

Figure 32

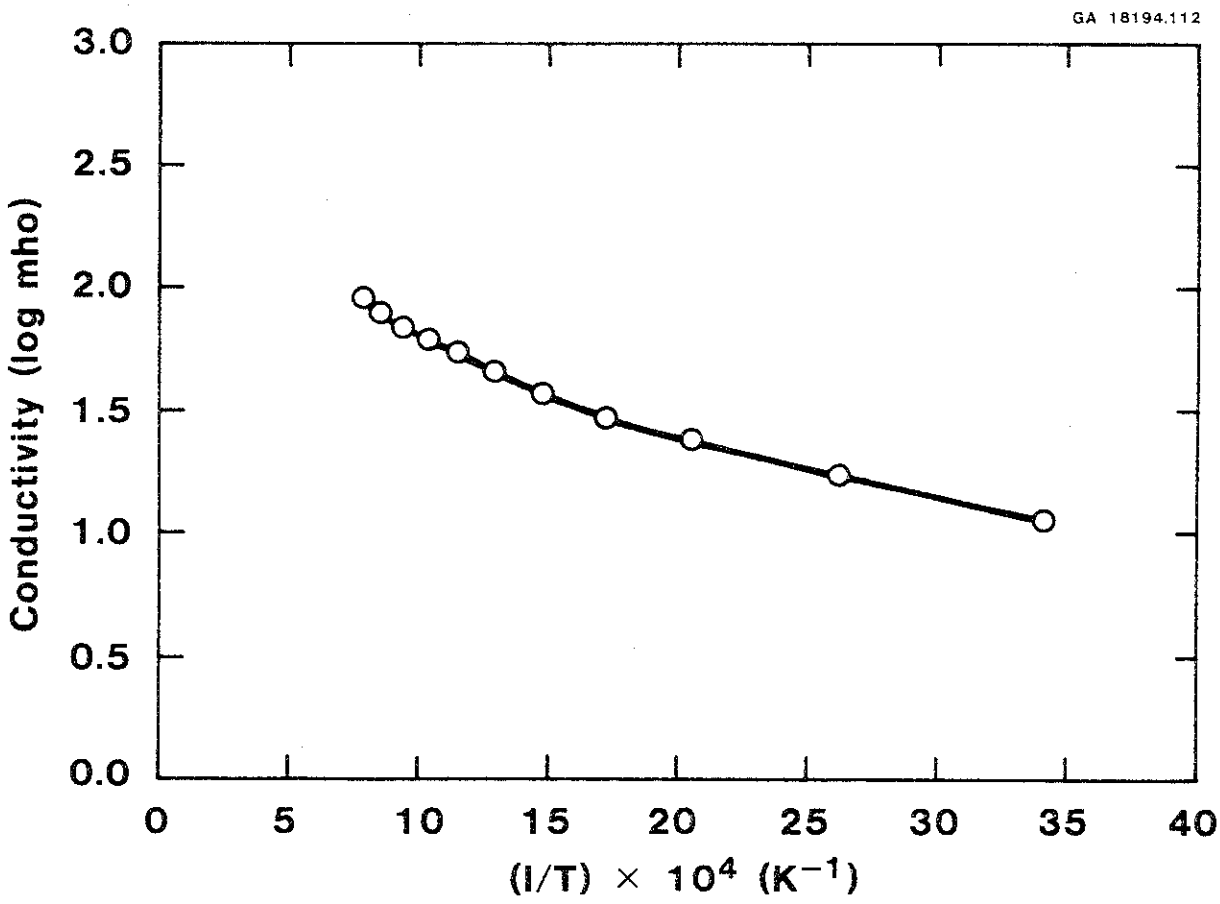

Electrical Conductivity of Inert Anode 19-2: 83 Wt. % 5324 + 17 Wt. % Cu
Figure 33

semiconductor, (c) the log σ vs. 1/T plot in Figure 33 indicates changes in slope around 700°C. At lower temperatures conductivity is probably influenced by grain boundary and dislocation effects. The electrical conductivity of 5324-17 wt.% Cu material is nearly 200 times more than 5324 material alone and it is possible to obtain substantial electrical conductivity increase without reaction sintering.

The electrical conductivity of semiconductors involving inclusions of another phase has been dealt with recently by C. Wagner (47). Maxwell (48) calculated the conductivity of two-phase mixtures in terms of the bulk conductivities of the individual phases. In these calculations, effects due to an electrical double layer at the interface of the coexisting phases have been disregarded. Thus, when metallic or highly conducting particles are introduced in an ideal insulator as matrix, the DC conductivity of the two-phase mixture is zero according to Maxwell. C. Wagner took into account the effects due to occurrence of an electrical double layer at the interface between metal and insulator and thus obtained finite conductivity for these conditions.

Utilizing C. Wagner's derivation, Tare and Wagner (49) derive electrical conductivity, σ, as

$$\sigma = \frac{22\ \varepsilon\ kT\mu}{4\ \pi\ e}\ \frac{f}{r^2} \qquad (16)$$

where ε is the dielectric constant, e and μ are the charge and mobility of the electrons, f is the volume fraction of dispersed particles, and r is the radius of the particles. The equation predicts that the electrical conductivity would be proportional to the volume fraction of dispersoid and inversely proportional to particle size of the dispersoid.

Figure 32 does not clearly represent this situation. However, the particle size and volume fraction represented in Figure 32

were derived from a nominally 10μ and 1μ particle Cu supplied by the vendor. The particles clearly agglomerate during sintering. Further, finer particles tend to have higher oxidation.

From Table 21 and Figure 32 it is seen that the higher the metal percent area (vol.%), the higher the metal grain size even though the starting metal powder was from the same source. It is also seen that the copper alloy particles tended to be enriched with copper in samples containing higher amounts of copper to start with as compared to samples which contained lower amounts of copper. For example, with "1μ as-received" copper particles with 5 wt.% Cu-5324 material, the fabricated samples contained alloy particles with 22 wt.% Ni, 74.3 wt.% Cu and 3.4 wt.% Fe; the metal grain size was 5.8 ± 2.0 μm and the metal area percent was 4.3 ± 0.7%. With the 17 wt.% Cu-5324 material, the fabricated samples contain 16.3 wt.% Ni, 81.2 wt.% Cu, and 2.5 wt.% Fe; the metal grain size was 9.8 ± 6.4 μm and metal area percent was 10.3 ± 1.3%.

Figure 34 shows the electrical conductivity at 960°C vs. the metallic grain size for various amounts of metals as determined by optical method. For smaller metal grains (<11 μm), the electrical conductivity was seen to increase with decreasing grain sizes whereas for larger average size metal grains, the electrical conductivity was found to increase with increasing average grain size. Wagner's equation would predict that small Cu particle sizes would increase conductivity for same volume percent metal. The metallic grain sizes vary widely, as shown in the statistics of Tables 20 and 21 and Figures 28 and 29. A better form of equation in the present context would be to use the modified Wagner equation

$$\sigma = \frac{22}{4} \frac{\varepsilon\, kT\mu}{\pi e} \frac{\Sigma}{j} \frac{f_j}{\gamma_j^2} \qquad (17)$$

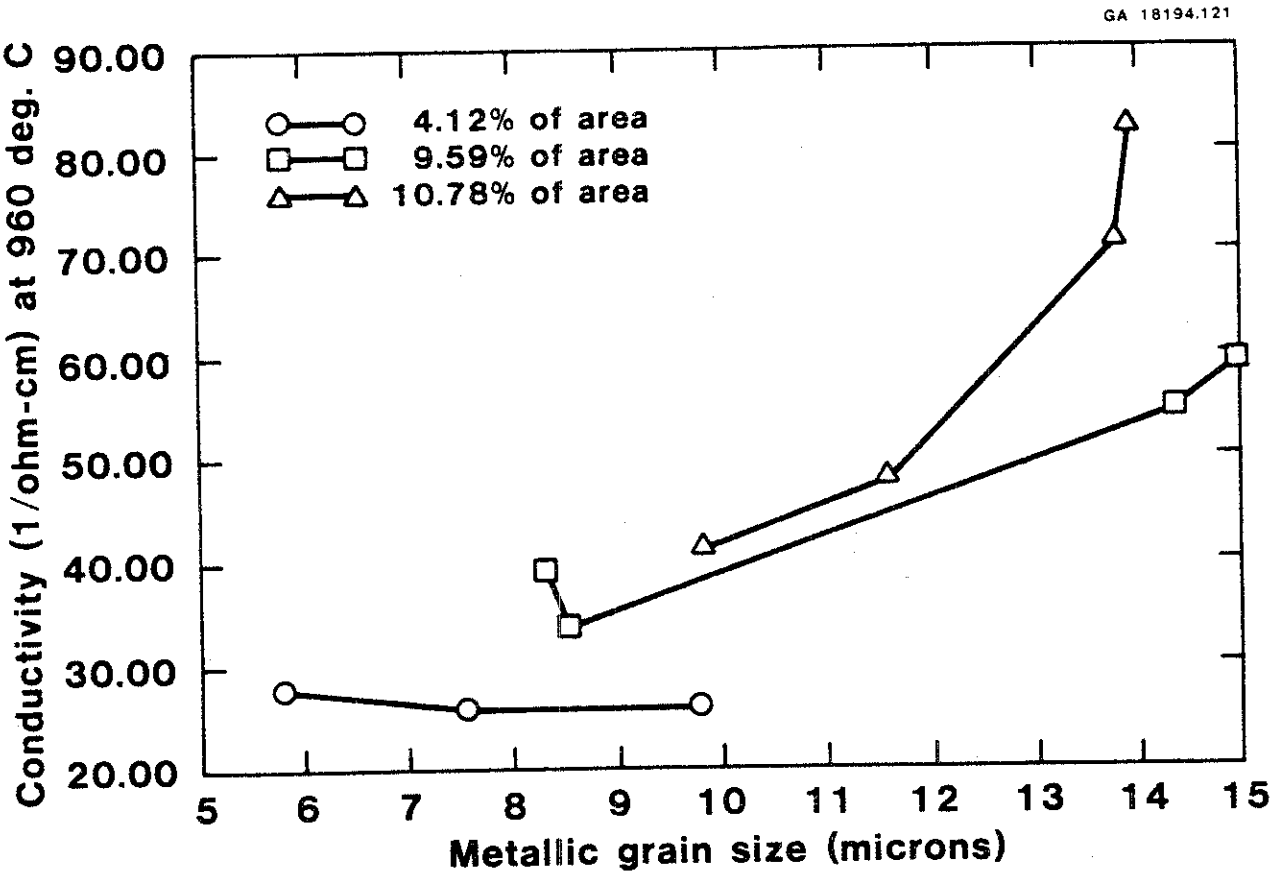

Inert Anodes Fabricated from 5324 Oxide Powder + Copper Powder

Figure 34

where f_j represents the volume or (area) fraction of particles with radius r_j. Such equations give better fit with observed results, but analyses have not been fully completed.

Wagner's equation predicts that for a given volume fraction of metal phase, the conductivity could be substantially increased by decreasing the average grain size. We utilized the services of Dr. S. Diamond of Battelle Columbus Laboratories to use a vibratory milling technique with 5 and 15 wt.% Cu-5324 powder. The vibratory milled powder was then fabricated into parts using conventional technique (pressing and sintering at 1350°C and 1200°C). The anodes with smaller metal grain sizes showed an increased conductivity. Anodes sintered at 1200°C showed higher conductivity and smaller metal grain size because of lowered agglomeration. Figure 35 shows the comparison of samples prepared from vibratory milled vs. unmilled powders.

In summary, adequate electrical conductivity of 5324-Cu sample was obtainable, and there is still room for further improvement.

3) Effect of Electrolyte Composition

The performance of the 6846 anodes was greatly dependent on the electrolyte composition. In order to study the effect of the electrolyte composition on 5324-17% Cu cermet, a set of eight experiments were carried out. The bath ratio was varied between 1-1.2, the CaF_2 was varied between 0-10 wt.%, MgF_2 was varied between 0-5 wt.%, and LiF was varied between 0-5 wt.%.

Table 23 shows the results of these tests. The table lists the electrolyte composition, operating temperatures, current efficiencies, and the analyses of metal (Al) produced using 83 wt.% 5324-17 wt.% Cu anodes. The results show wide variation in performance. However, the electrolyte composition containing 1.0 ratio bath with 5 wt.% MgF_2 and 10 wt.% CaF_2 operating at 948°C performed the best. Further work should be carried out with these compositions.

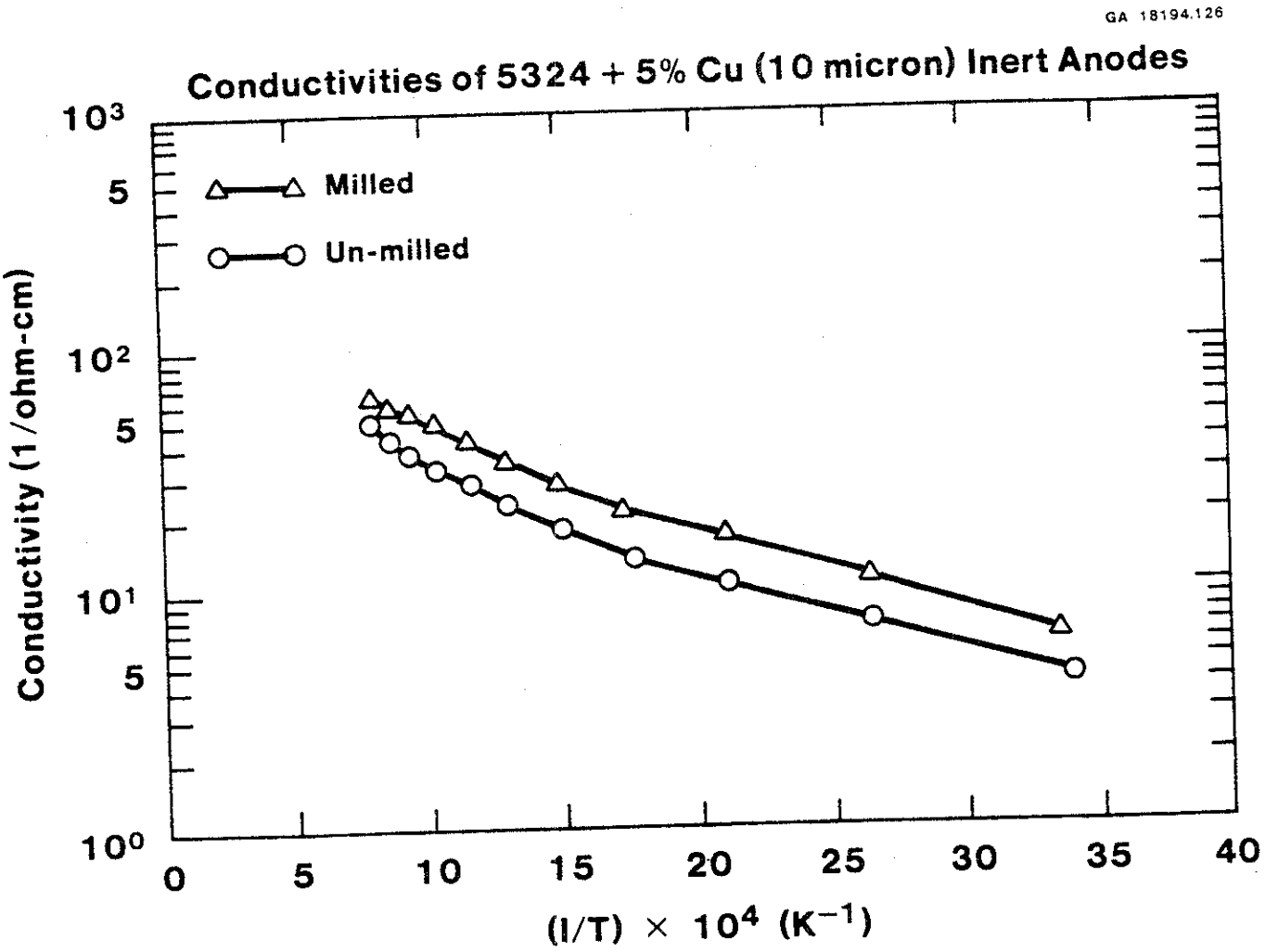

Comparison of Vibratory-Milled vs Un-Milled Powders
Figure 35

TABLE 23

Hall Cell Test Results
Effect of Bath Composition on Anode Performance
83 Wt.% 5324-17 Wt.% Cu (1μ) 30 Hour Test

Anode No.	Ratio NaF/AlF	% Al_2O_3	% MgF_2	% LiF	% CaF_2	Temp °C	Current Eff.%	Metal Contamination Wt.% Fe	Ni	Cu
081585	1.0	5.97				942	86.0	0.3	0.09	0.15
072485	1.0	5.16	5	5		943	58.0	1.58	0.44	0.26
080185	1.0	4.5	5		10	948	71.7	0.13	0.02	0.05
080785	1.0	3.87		5	10	953	62.3	1.46	0.45	0.41
071185	1.2	6.51		5		942	66.8	0.62	0.18	0.18
081285	1.2	3.83	5	5	10	943	56.8	2.35	1.6	1.8
070285	1.2	8.0	5			950	79.2	0.35	0.11	0.16
082085	1.2	5.86			10	971	67.4	0.68	0.2	0.22

4) Effect of Cathode Area on Anode Performance

It has been recognized that the size of the cathode area may become important for anode performance. If the rate of transfer of Fe, Ni, and Cu in the bath to aluminum at the metal-bath interface is rate controlling, reducing the cathode area may lead to an improved anode performance. Normally, we used a 7.5 cm diameter cathode and a 2.5 cm diameter anode. Further improvements in quality of metal produced would be expected with decreased anode areas. In order to test the concept, a cell with the configuration shown in Figure 36 was utilized. One-quarter inch TiB_2 was used as the cathode surface and the aluminum deposited was allowed to drain to the sump area at the bottom. The design was meant to limit the cathode surface. It is not clear whether the purpose was fully served, but no dramatic improvements in anode performance was noted during this test. Further testing in a larger cell would be desirable.

h. Other Compositions

Several experiments were carried out with NiO-Cu (metal), (15 wt.% Cu and 20 wt.% Cu) and Fe_2O_3-Cu (metal) anodes. These anodes were produced by powder metallurgy technique. Further, Ni-Cu-Fe alloy of composition formed in 5324-17 wt.% Cu (i.e., 1.3 Fe, 14.5 Ni, 84.2 Cu Alloy) was also fabricated and evaluated in a Hall cell. A Ni-Fe-Cu-Al alloy was tested.

Table 24 shows the results of bench scale Hall tests with NiO-Cu, Fe_2O_3-Cu, Cu-Ni-Fe, and Cu-Ni-Fe-Al alloys. It has been mentioned earlier that 5324-17 Cu cermet anode develops Cu-rich metal particles near the bottom surface of the anode. Further, aluminum produced using these anodes consistently shows high amounts of iron metal relative to nickel even though the anode contains higher amounts of NiO. Additionally, nickel-metal anodically dissolves out from Cu-Ni-Fe alloy phase in the 5324-Cu cermet anodes. It was, therefore, decided to examine the possibility of using NiO-Cu cermet anodes. Two

GA 18194.125

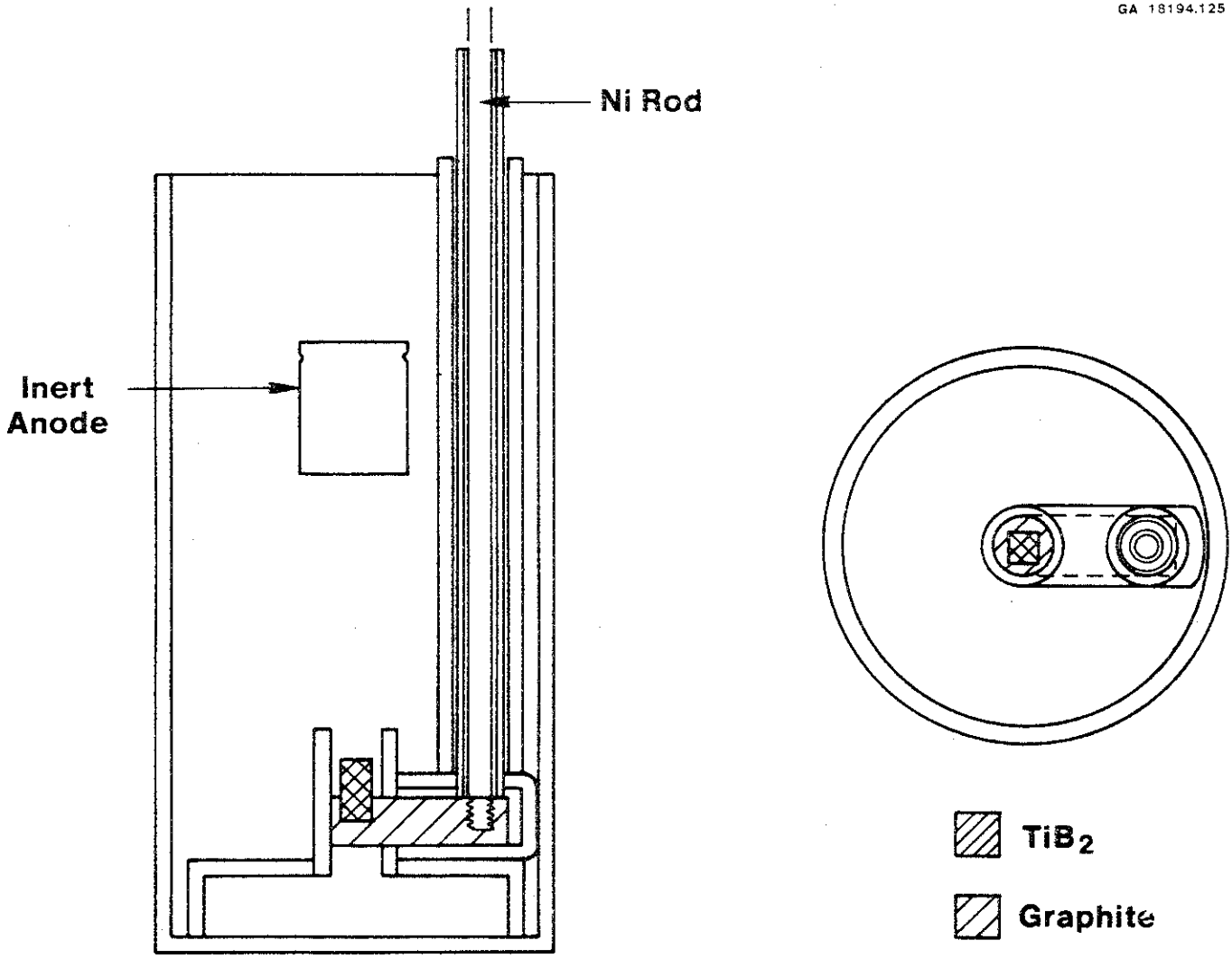

Note: All cell components not identified are alumina.

Reduced Cathode Area Hall Cell
Figure 36

TABLE 24

Bench-Scale Hall Cell Tests With NiO-Cu, Fe_2O_3-Cu and Cu-Fe-Ni Alloy Inert Anodes

1.15 Ratio Bath, 5% CaF_2 at 960°C

Anode No.	Anode Composition wt.%	Density g/cc	Run Time hrs.	Current Eff %	Aluminum Contamination wt.%			Bath Analysis (before/after)			Comments
					Cu	Fe	Ni	Cu	Fe	Ni	
051485	1.3Fe, 14.5Ni, 84.2Cu Alloy	7.28	30	69.8	6.2	0.2	0.31	<.005/ .09	.016/ .009	<.005/ .005	
052285	1.3Fe, 14.5Ni 82.2Cu, 2Al	6.47	30	72.03	4.6	0.2	0.2	<.005/ .044	.012/ .009	<.005/ .005	
041085	76.9Fe_2O_3 23.1Cu	5.3	30	85.0	0.51	0.97		<.005/ .028	.018/ .059	<.005/ .005	
031485	80NiO 20Cu	6.04	26	79.7	0.68		0.21	<.005/ .007	--	<.005/ .033	
032085	85NiO 15Cu	5.99	30	82.8	0.66		0.31	<.005/ .065	.019/ .010	<.005/ .031	

anode compositions containing 15 and 20 wt.% Cu metal in NiO were fabricated. The NiO-Cu anode was porous. Microstructural examination revealed a large number of pores in the anode material.

These two anode compositions were used as anodes with 1:1 ratio bath containing 5 wt.% CaF_2 and ~6.5 wt.% Al_2O_3 at 960°C. The anodes were tested for ~30 hours. Anode 031485 containing 80 wt.% NiO and 20 wt.% Cu led to aluminum containing 0.21 wt.% Ni and 0.68 wt.% Cu, whereas anode 032085 containing 85 wt.% NiO and 15 wt.% Cu produced aluminum containing 0.31 wt.% Ni and 0.66 wt.% Cu. The current efficiency in these two tests were ~79.7% and 82.8% respectively.

These anodes were sectioned after termination of the Hall cell test, polished and examined metallographically. The anodes were found to develop "oxide scales" on the outer surface (~2 mm deep). A schematic cross-section of anode 031485 containing 80 wt.% NiO and 20 wt.% Cu is shown in Figure 37. Areas 1, 2, 3 and 4 represent the areas where the microprobe analysis was carried out. Backscattered electron picture and the corresponding X-ray images for Ni, Cu, Al, O, Na, Ca and F from area 1 showed that the bottom layer (~50-60μ) is composed primarily of NiO with little "Cu." On the very bottom of this layer was found nickel aluminate. The whole layer was very dense compared to the rest of the field.

Metallic particles of Cu were found randomly distributed in the next area. This area also showed a significant amount of bath. Backscattered electron picture and corresponding X-ray images for Ni, Cu, Al, O, Na, Ca and F from area 2 showed "Cu metal," NiO, and small amounts of bath and Al_2O_3 (polishing medium). The area contained substantial amounts of copper metal and oxide.

Area 3 in Figure 37 represents a transition area and shows the backscattered electron picture and corresponding X-ray images. It is seen that copper is present in relatively metallic form near the bottom of the field, i.e., no significant amount of oxygen is associated with copper in this area. This area represents a relatively unaffected

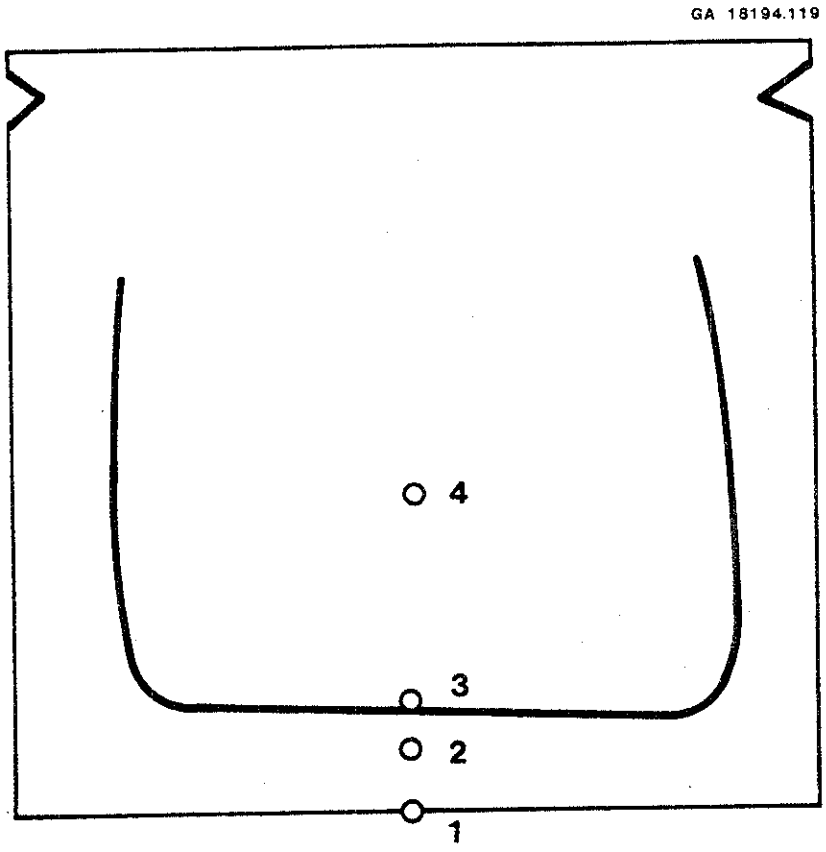

Showing the Positions where Microprobe Analysis was Carried Out Anode 031485: 80 Wt% NiO + 20 Wt% Cu. Area 1 is at Bottom of Scale, Area 2 is in the Middle of the Scale, Area 3 in on the Top, and Area 4 is in the Interior

Figure 37

area. No significant amounts of electrolyte were found in this area either. The top of the picture represents the affected area; copper oxide was found in this area along with NiO.

Area 4 in Figure 37 represents a relatively unaffected area. Figure 38 shows the backscattered electron picture and corresponding X-ray images from this area. This area is relatively dense where "copper metal" is present. However, other areas are porous and it is seen that the electrolyte found its way to this area.

Analysis of the aluminum metal produced using this anode showed 0.21 wt.% Ni and 0.68 wt.% Cu. Anode 032085 containing 85 wt.% NiO and 15 wt.% Cu was also used for 30-hour electrolysis. The metal produced using this anode also contained 0.31 wt.% Ni and 0.66 wt.% Cu. Both these anodes were of low density and substantial electrolyte penetration occurred. In the outer layer (4-5 mm) copper was oxidized and in the bottom 50-60 μm practically no copper was found. Copper was preferentially removed from this area and no sign of passivation of copper was found in these materials.

Table 24 also shows the results with an anode containing 76.9 wt.% Fe_2O_3 23.1 wt.% Cu anode. The anode was produced by compacting Fe_2O_3 and Cu powder. The anode was evaluated in a Hall cell at 960°C for 30 hours with a bath ratio of 960°C and containing 5 wt.% CaF_2. The aluminum produced during this test was contaminated with ~0.97 wt.% Fe and 0.5 wt.% Cu. This result shows that Fe_2O_3 is probably more soluble in the bath and less corrosion resistant than NiO. This fact has been shown to be true in solubility test measurements by D. H. DeYoung(8). Cu metal was found to be passivating in either of these tests, i.e., with NiO or Fe_2O_3. Significant amounts of copper were found to go into the metal if it was exposed to the electrolyte. No metallic copper was found near the surface either.

Table 24 shows the results with a 1.3 Fe, 14.5 Ni, 48.2 Cu alloy. From earlier tests it was found that when 17 wt.% Cu powder is introduced into the 5324 all-oxide powder, pressed and sintered in an

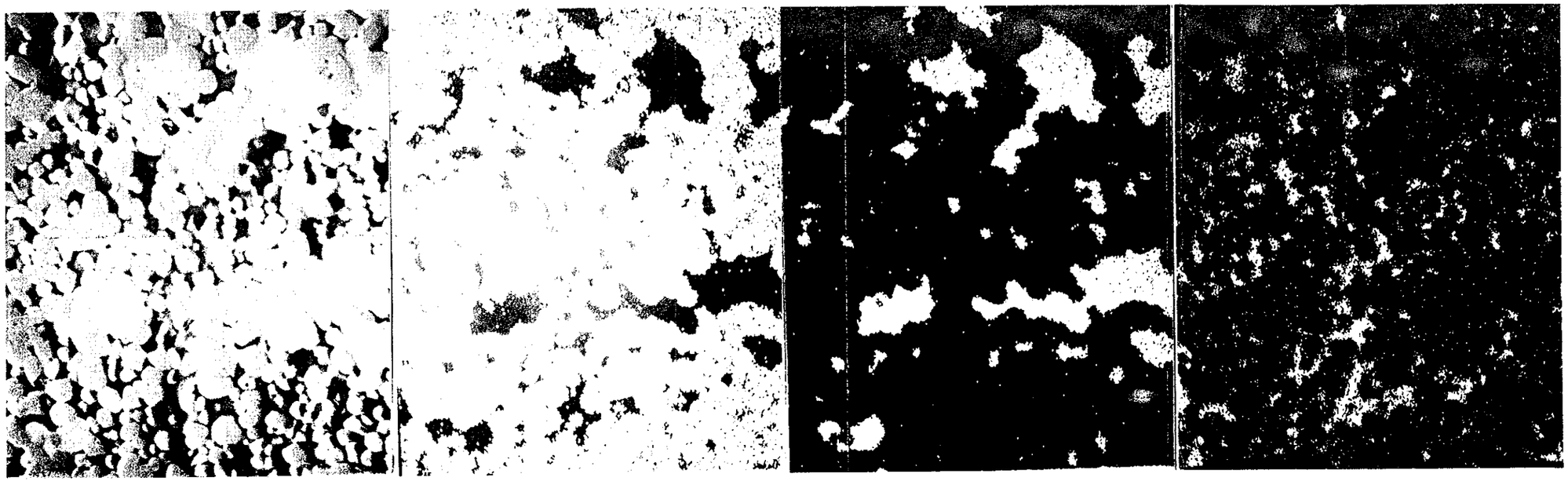

Backscattered electron | Ni | Cu | Al

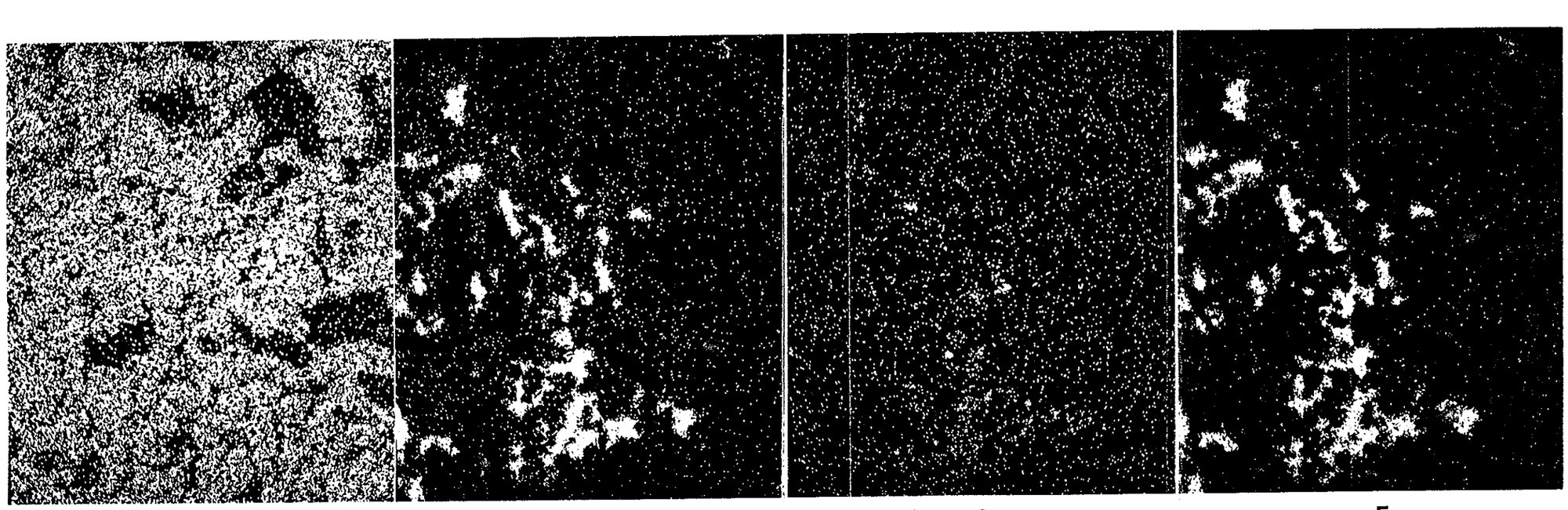

O | Na | Ca | F

Represents Area 4 in Figure 37
500X 20μm ⊢⊣
Figure 38

argon atmosphere at 1350°C for 2 hours, the "metal phase" in the oxide contains an alloy of ~1.3 wt.% Fe, 14.5 wt.% Ni and 84.2 wt.% Cu. It was, therefore, decided to study this alloy composition as an anode material. Anodes were fabricated with this composition by powder metallurgy technique. The alloy anode, 051485, was evaluated in the Hall cell at 960°C for 30 hours in a 1:1 ratio bath. The alloy scaled badly and the metal produced was contaminated with 6.2 wt.% Cu, 0.2 wt.% Fe and 0.31 wt.% Ni. The metallic surface beyond the scale was enriched with Cu at the surface. No sign of passivation of this alloy phase was seen. The passivating film in 17 wt.% Cu-5324 was believed to be copper aluminate and later identified as a mixture of copper aluminate and Cu_2O. It was, therefore, decided to add Al powder to the Cu-Fe-Ni alloy and study the alloyed anodes behavior during electrolysis. The anode contained 1.3 wt.% Fe, 14.5 wt.% Ni and 82.2 wt.% Cu and 2 wt.% Al metal. The anode was fabricated using the powder metallurgy technique. This alloy performed much better compared to the alloy without Al addition. Significantly less scaling was observed; although the metal produced using this anode was again badly contaminated with Cu (4.6 wt.%), Ni (0.2 wt.%) and Fe (0.2 wt.%).

Figure 39 shows a schematic of sectioned and polished anode 051485 (containing 1.3 Fe, 14.5 Ni, 48.2 Cu) after 30 hours Hall cell test. Backscattered electron image and corresponding X-ray pictures were obtained from areas representing (1) near the bottom surface and (2) near the center of the anode. Figure 40 represents area 1. It was seen that the bottom-most layer may indeed contain some Cu-aluminate type phase. The alloy phase was found to be badly corroded and scaled. Practically no sign of any nickel metal was found in this alloy. This is a clean demonstration of preferential loss of nickel from the alloy phase. The metal left behind was almost pure copper. Any nickel present there was in the form of NiO. On the other hand, deeper inside the material (area 2) the alloy phase contained Ni, Fe, Cu and some NiO and Fe-oxide. The voids were filled with Al_2O_3 (polishing material).

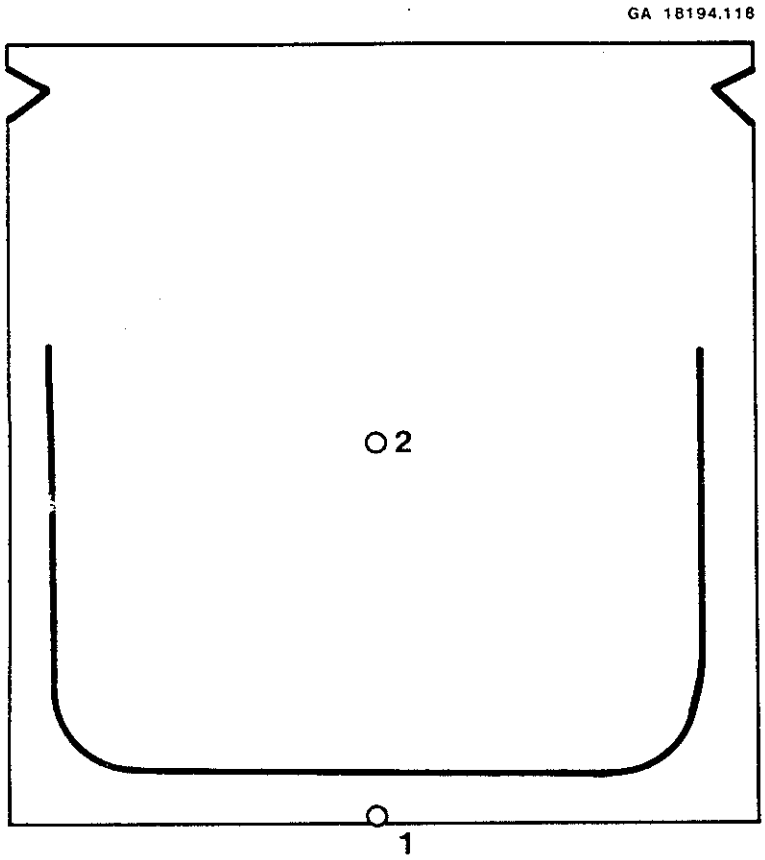

Anode 051485
After Hall Cell Test
1.3 Wt% Fe, 14.5 Wt% Ni, 84.2 Wt% Cu
Figure 39

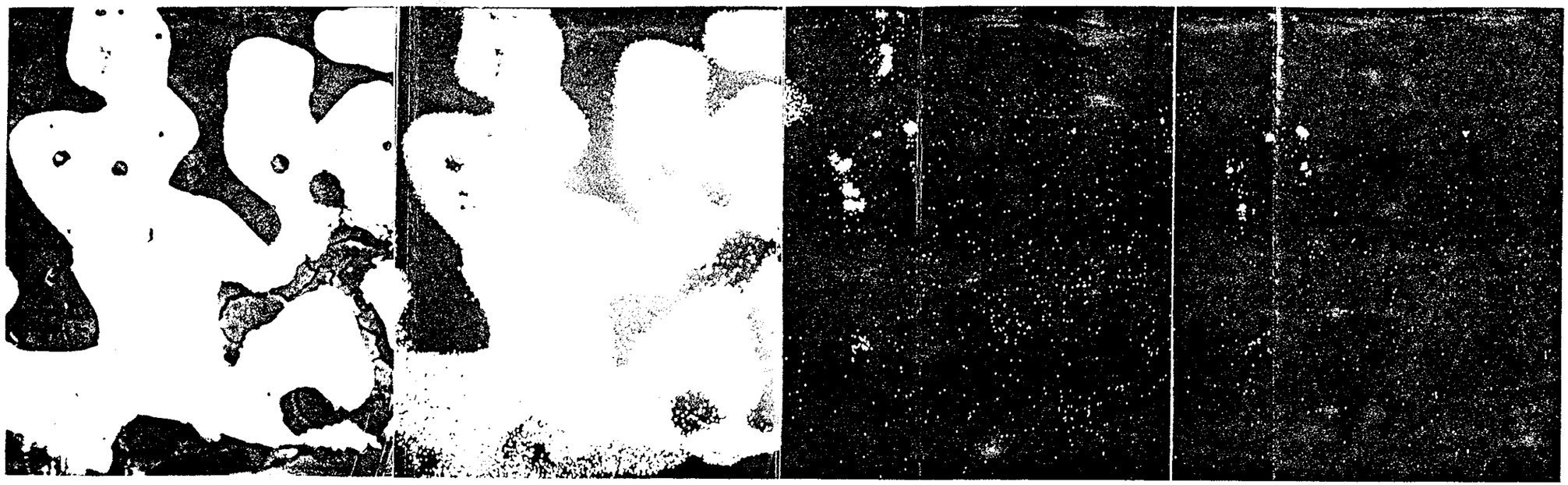

Backscattered electron | Cu | Ni | Fe

O | Na | F | Al

Represents Area 1 in Figure 39
500X 20ΛW ⊢⊣
Figure 40

B. Inert Anode Corrosion Studies

1. Objective

The primary objectives of this part of the program were to determine the dissolution rate of inert anodes in Hall cell electrolyte, and to identify factors which control the dissolution of the anodes. Therefore, the solubilities and dissolution rates of the inert anode constituents were to be determined as a function of bath composition, temperature and other cell conditions.

2. Introduction

A primary criterion of an inert anode material for aluminum electrolysis is that it must be relatively insoluble in the cryolite-based electrolyte. The most promising inert anode materials are oxides which have small but finite solubilities in the electrolyte. Nickel ferrite-based materials have been identified by Ray (14, 15) as reasonably good anode materials. The life of these anodes and the purity of aluminum produced from them are directly related to the rate at which they dissolve in the electrolyte. Metals such as nickel (15) or copper (46) have been added to the nickel ferrite materials to improve the electrical conductivity. Since oxides form on the surface of these metallic constituents during operation, the dissolution of the nickel ferrite will still control the anode life and aluminum purity.

The purpose of this program is to reduce the contamination of metal produced using inert anodes, and to increase the life of the anodes by understanding and controlling the dissolution of the anodes. Cermet materials with two oxide phases ($NiFe_2O_4$ and NiO) and a metal phase (Ni or Cu) have shown the greatest promise. The dissolution of the oxide phases was addressed in this study.

The rate of dissolution of a solid in a liquid is governed by thermodynamic (solubility limits) and kinetic (viscosity, diffusivities, convection, etc.) factors. Therefore the project consisted of two major parts. First, the solubilities of inert anode materials (Fe_2O_3, NiO and $NiFe_2O_4$) in NaF-AlF_3-Al_2O_3-CaF_2 melts have been measured as a function of bath composition and

temperature. This work has been documented in quarterly reports (3-5, 8, 50, 51). The objectives of the solubility measurements were to identify conditions which minimized solubilities and obtain the thermodynamic information needed to interpret kinetic data. Second, the rates of dissolution of inert anodes have been measured as a function of temperature, bath composition, forced convection, polarization of the anode, the presence of dissolved reduced species and the presence of carbon or Al_4C_3. This work has also been covered in quarterly reports (8-13, 50, 51).

As a corollary to this work, some alternate anode materials (other than Fe_2O_3, NiO and $NiFe_2O_4$) were investigated. This work involved fabrication and solubility measurements of these materials. Although this task was not directly relevant to the investigation of corrosion mechanisms, it will be included with other solubility measurements. It has been covered in previous quarterly reports (9-11, 13).

This section of the report is divided into two major sections. Part A will cover the solubility measurements on the inert anode component oxides. Part B will cover the dissolution rate measurements made on inert anode materials.

3. Part A - Solubility Measurements

a. Literature Review

Some data are reported in the literature for the solubilities of Fe_2O_3, NiO, and $NiFe_2O_4$ in Na_3AlF_6 and in Na_3AlF_6-5% Al_2O_3 melts, but there has been no systematic study of the solubilities over temperature and electrolyte composition ranges for which Hall cells can be operated. Additionally, there are significant differences between the results from different investigators. Belyaev et al. (52) measured the solubilities of NiO and Fe_2O_3 in Na_3AlF_6 and Na_3AlF_6-5% Al_2O_3 melts. Rolin and Bernard (53) reported solubilities of Fe_2O_3 and NiO in Na_3AlF_6. Johansen (54) measured a portion of the Na_3AlF_6-Fe_2O_3 phase diagram using the DTA technique. Recently Horinouchi et al. (2) reported measurements of solubilities of NiO, Fe_2O_3, and $NiFe_2O_4$ in Na_3AlF_6-10 wt.% Al_2O_3 melts. With the exception of Johansen's phase diagram, all of these measurements were made at approximately 1000°C.

The scope of this work was to determine solubilities from 1025°C down to the liquidus temperature of the electrolyte, from bath ratios (weight NaF/weight AlF_3) of 0.7 to 1.3, and for electrolytes containing 0.5 to 6.5 wt.% Al_2O_3. Several measurements were also made at bath ratios of 1.5 and 2.8. The effects of CaF_2, MgF_2, LiF, ZrO_2 and SiO_2 additions to certain electrolyte compositions on the solubilities of NiO and Fe_2O_3 were also determined.

b. Experimental Method

Solubility measurements were made using an equilibration technique. Pellets of the oxides were equilibrated with the melt, and samples of the melt were periodically withdrawn and chemically analyzed for the oxide components.

The experimental apparatus is shown in Figure 41. Approximately 250 g of melt was contained in a 125 ml platinum crucible. This crucible was nestled in an alumina crucible, which in turn was supported on bubble alumina in a closed-end alumina tube. To minimize thermal convection

GA 18194.7

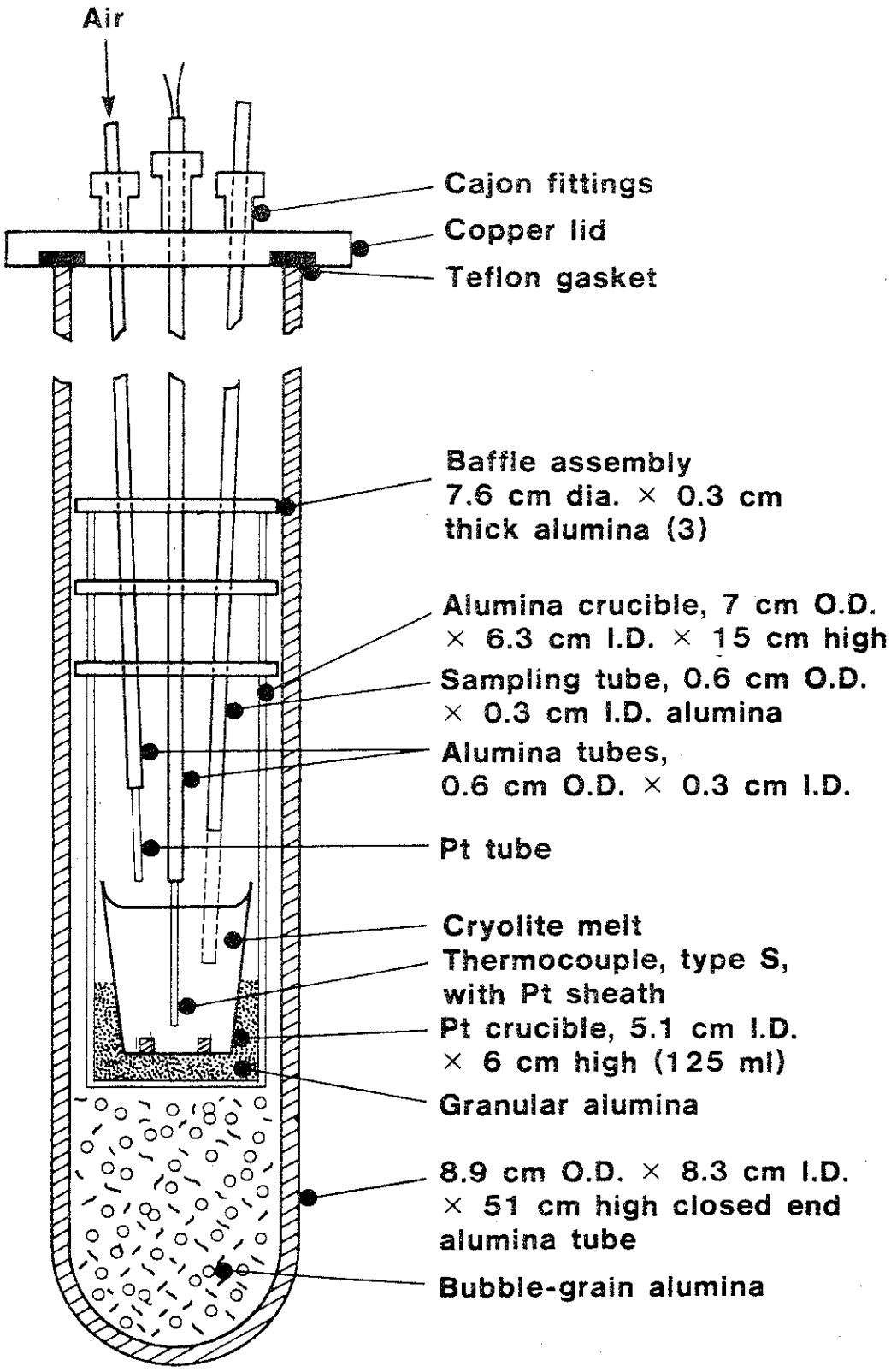

Experimental Apparatus for Solubility Measurements

Figure 41

in the furnace, a baffle constructed of three alumina plates was placed on top of the alumina crucible. The entire assembly was inserted in a Kanthal-wound resistance furnace. The top of the tube was sealed with a water-cooled copper cap using a teflon gasket. Ports in this cap with sealable fittings provided access for a thermocouple, gas inlet and exit tubes, and a sampling tube. The temperature of the melt was monitored using a type S thermocouple, protected from the melt by a platinum sleeve.

Crushed Greenland cryolite, Alcoa-produced AlF_3, reagent grade CaF_2 and calcined $Al(OH)_3$ were used to prepare the melts. The cryolite and the AlF_3 were chemically analyzed prior to use, and melt compositions were based upon these analyses and the charge weights.

Samples of the melt were withdrawn into an alumina tube by a syringe assembly attached to the top of the tube. The samples were crushed, mixed and analyzed for impurities by either the inductively coupled plasma technique (ICP) or by atomic absorption. The precision of the analyses is approximately ± 5% of the total quantity present. Prior to analysis the samples were dissolved in either HCl or HNO_3.

Reagent grade NiO (Fisher N-69) and Fe_2O_3 (Fisher I-116) were used to prepare oxide pellets without further purification. Manufacturer's analyses of these materials are given in Appendix A. The raw materials were mixed, uniaxially pressed into 0.95 cm diameter x 1.59 cm high cylinders at 172 MPa, and sintered in air at 1350°C for 16 h. Samples of the resulting pellets were analyzed by X-ray diffraction to confirm the phase of the material. The densities of the pellets were NiO-5.72 g/cm^3, Fe_2O_3-5.13 g/cm^3, $NiFe_2O_4$-4.64 g/cm^3. For each experiment approximately 2-3 g of oxide were added to the melt. Each pellet was broken into 3 to 5 pieces before adding it to the melt.

Air was circulated over the bath surface during the experiment and periodically bubbled into the melt to provide stirring and to equilibrate the melt with air. The air was dried by passing it through a

column of calcium sulfate (drierite). After bubbling the melt was allowed to settle for at least 25 minutes before sampling.

The duration of an experiment was typically 80-100 h, during which the melt was cycled through 3 or 4 temperatures. After initial experiments in which the equilibration time was determined, two melt samples from the end of each time period at a given temperature were analyzed to determine the solubility. For some experiments, several melt samples were analyzed for bath ratio (weight NaF/weight AlF_3) and Al_2O_3. The bath ratio was determined by pyrotitration and the Al_2O_3 concentration was determined from the weight of insolubles in an aqueous $AlCl_3$ solution.

Figures 42 and 43 show the approach to equilibrium for Fe_2O_3 and NiO, respectively. Steady-state concentrations, which were taken to be the equilibrium solubilities, were reached approximately 8 h after the oxide pellets were dropped into the melt. The melt was allowed to equilibrate for approximately 24 h at each temperature.

To assure that the steady-state, plateau concentrations were true equilibrium solubilities, equilibrium was approached from both directions during several experiments (Figure 44). The initially measured solublity (melt changing from a lower temperature to a higher temperature and dissolving NiO) agrees with the result obtained later (melt changing from a higher temperature to a lower one and precipitating out NiO). In general, the solublity for most experiments was measured at a higher temperature and then at a lower temperature, followed by at least one measurement at an intervening temperature. In this way equilibrium was approached from both directions, and the consistency of the results from a given experiment was evidence for equilibrium. Occasionally results were not consistent; these experiments were repeated.

The bath ratio changed somewhat during the experiments, particularly for those with initially low bath ratios and of long duration. The maximum increase in bath ratio due to vaporization of $NaAlF_4$ was approximately 0.1, though it was usually about 0.05. As will be shown

GA 18194.12

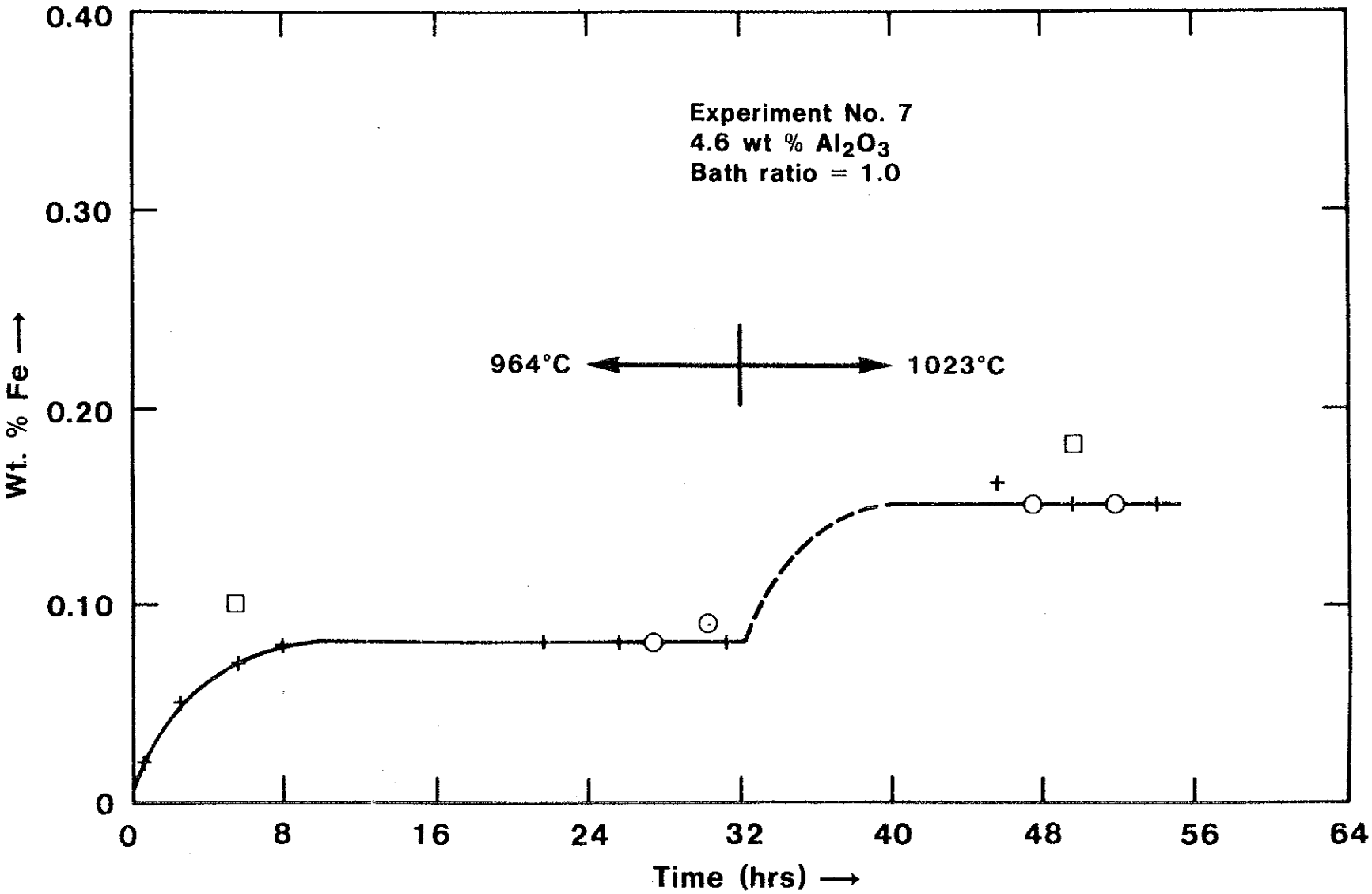

Bath Analyses Illustrating Time Needed for Equilibration of Fe_2O_3 with the Melt

Figure 42

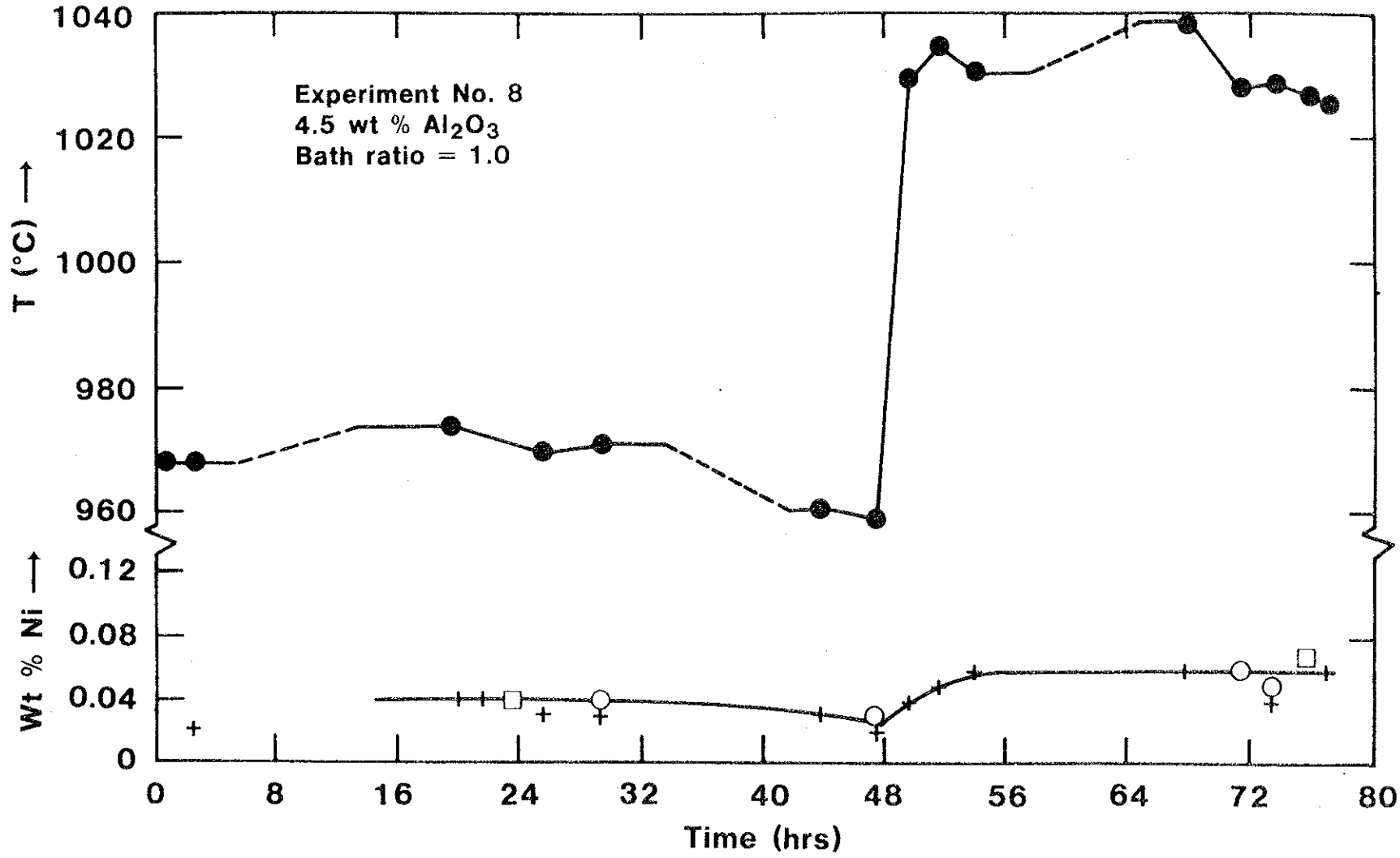

Bath Analyses Illustrating Time Needed for Equilibration of NiO with the Melt

Figure 43

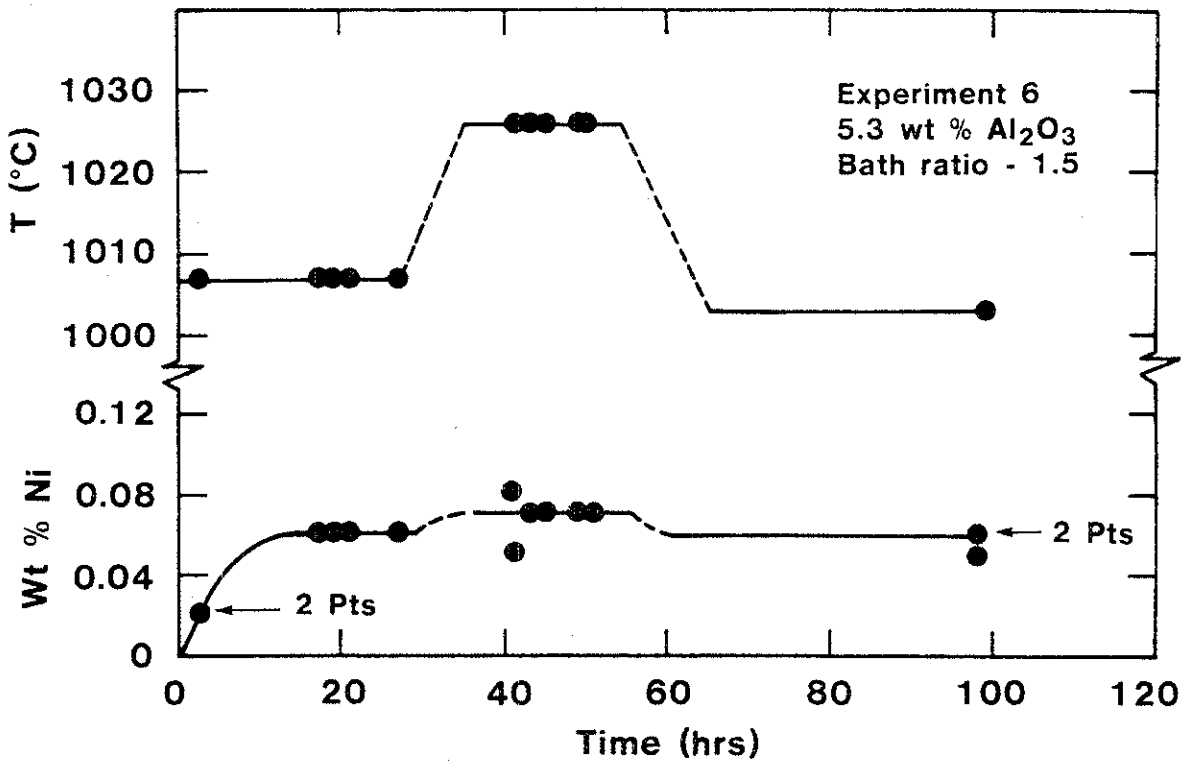

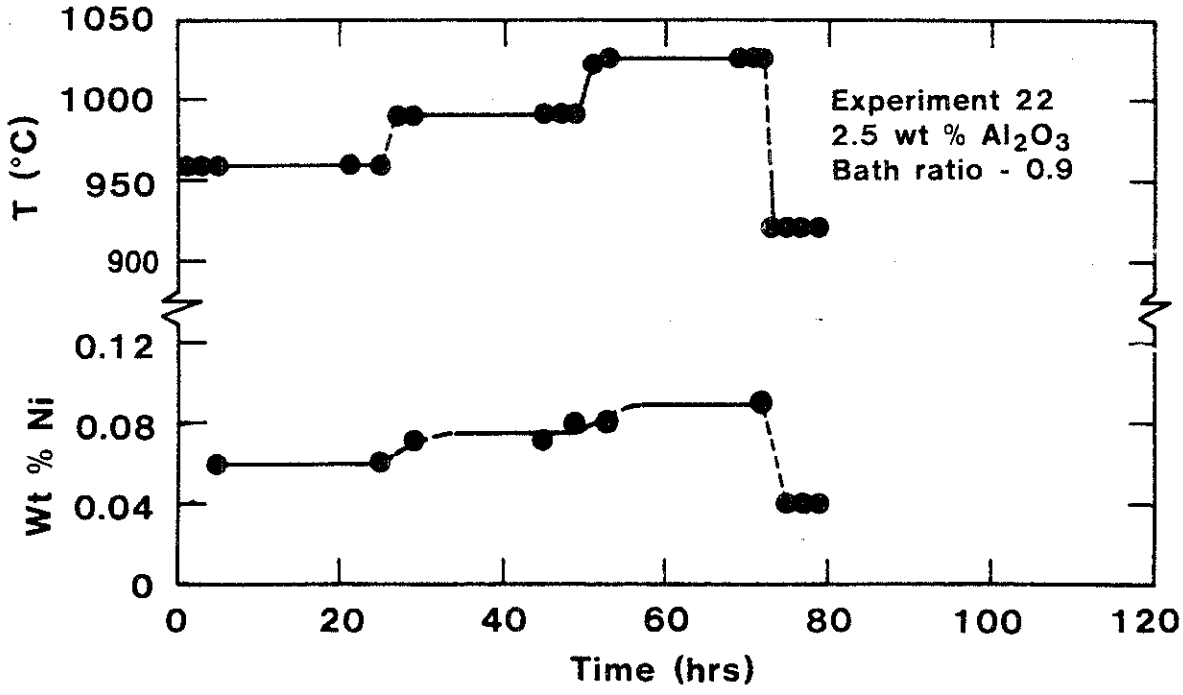

Approach to Solubilities from Lower and Higher Temperatures

Figure 44

later, this change had a small effect on the solubilities. In Figure 45, bath ratio and percent Al_2O_3 are plotted vs. time for several experiments. Nominal starting ratios and Al_2O_3 concentrations are indicated in parentheses for the respective runs. The uncertainties in bath composition are estimated to be ± 0.5% in Al_2O_3 and +0.1, -0 in bath ratio.

c. Results and Discussion

1) Effects of Temperature and Bath Composition

a) Solubilities

Figures 46-48 show the solubilities of Fe_2O_3, NiO and $NiFe_2O_4$, respectively, as a function of temperature. Measurements were made to the liquidus temperature for each bath composition. Lines connecting the data points for each experiment are not meant to indicate that the solubilities vary linearly with temperature; rather, they group the data from each experiment. The solubilities of Fe_2O_3 are approximately twice those for NiO. The solubilities for Fe_2O_3 and NiO from $NiFe_2O_4$ are less than the solubilities of Fe_2O_3 and NiO, respectively; this is expected because of the added thermodynamic stability of the ferrite over the simple oxides. These data are for melts containing no additions of CaF_2, MgF_2, LiF, ZrO_2 or SiO_2, although all melts contained a nominal 1.3 wt.% CaF_2.

The uncertainty in the sample analyses is ± 5% of the amount of soluble oxide present, which corresponds to ± .01 to ± .001% Fe and ± .005% to ± .0005% Ni. Experimental results for identical bath compositions are within these uncertainties. This is illustrated in Figure 46 by results for Fe_2O_3 for a melt composition of 2.5% Al_2O_3, 0.9 bath ratio. Likewise, it is demonstrated in Figure 47 by the NiO results for melt compositions of 2.5% Al_2O_3, 0.9 bath ratio, and 4.5% Al_2O_3, 1.1 bath ratio.

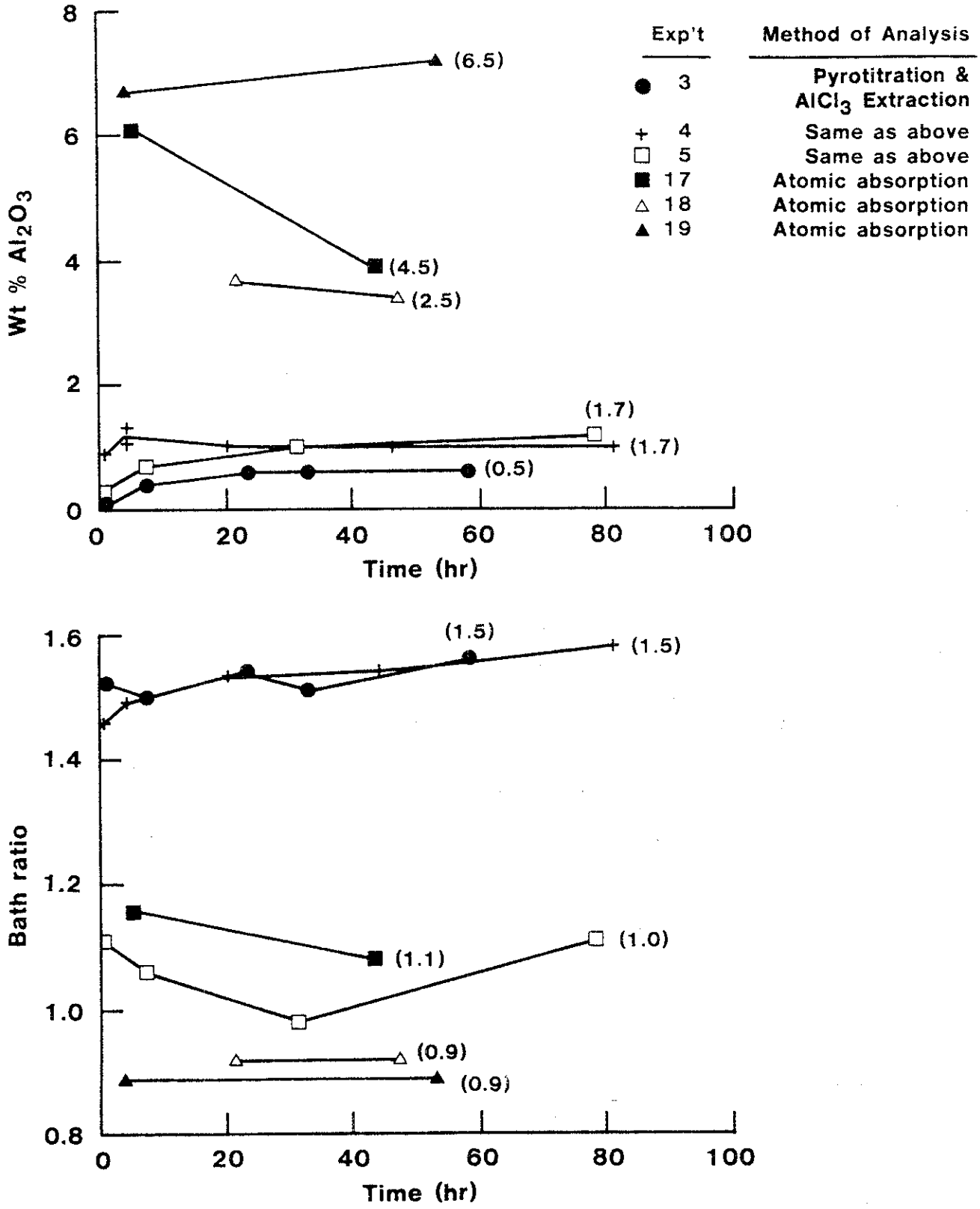

Analysis of Melts from Selected Experiments for Bath Ratio (wt NaF/wt AlF_3) and Al_2O_3. Numbers in Parantheses Indicate Nominal Starting Bath Ratio and Al_2O_3 Concentration

Figure 45

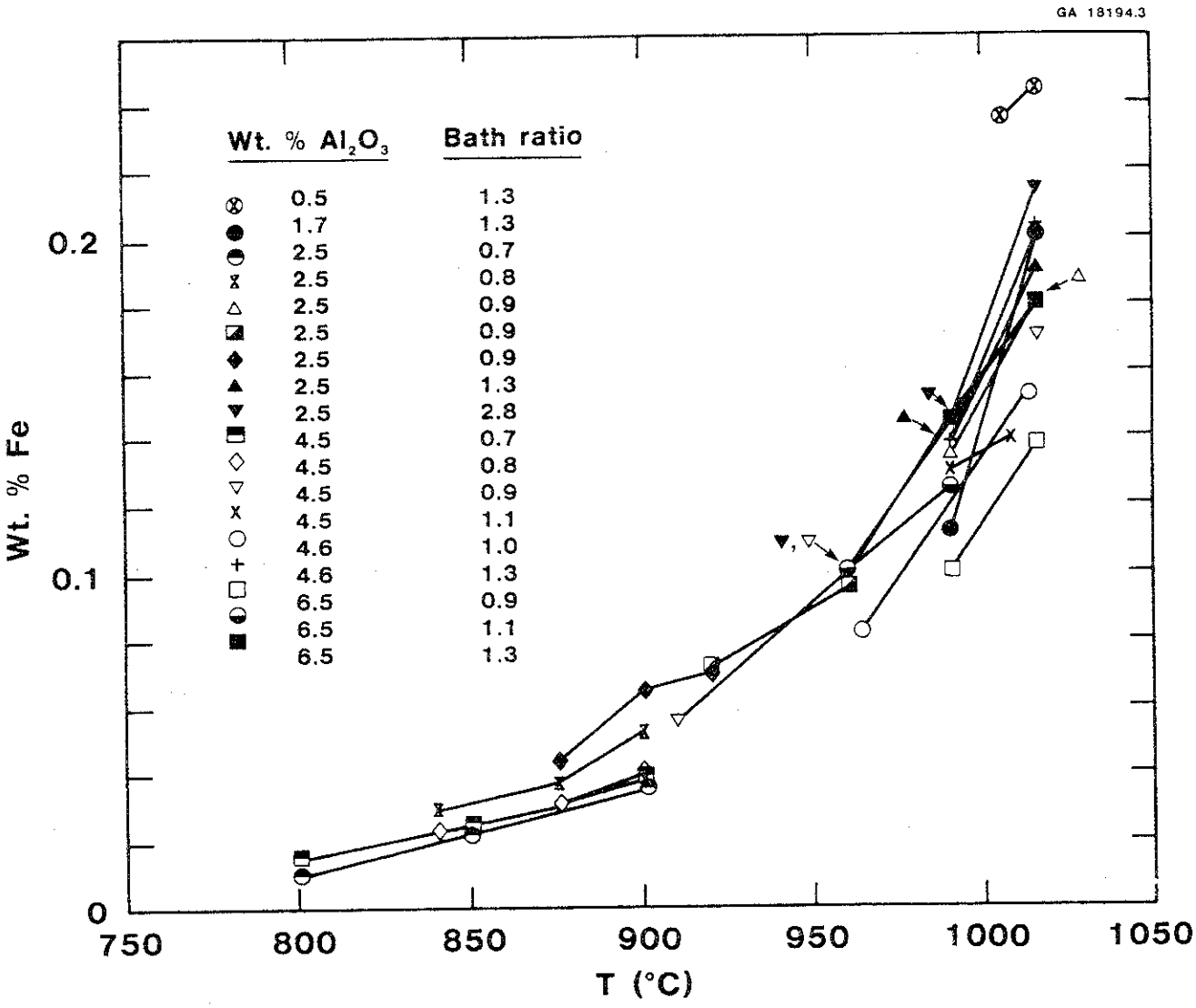

Solubility of Fe_2O_3 in $NaF-AlF_3-CaF_2-Al_2O_3$ Melts
Figure 46

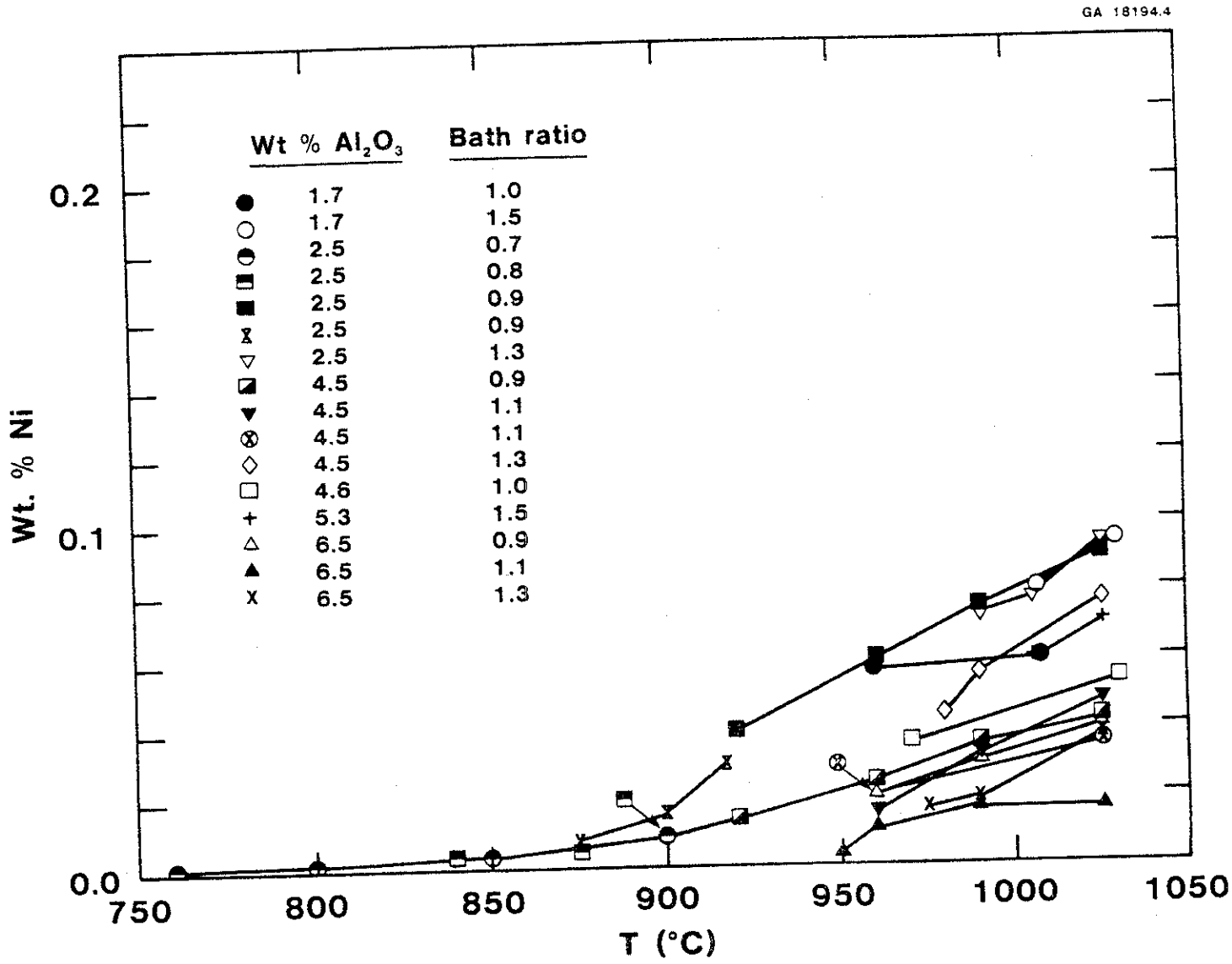

Solubility of NiO in $NaF-AlF_3-CaF_2-Al_2O_3$ Melts
Figure 47

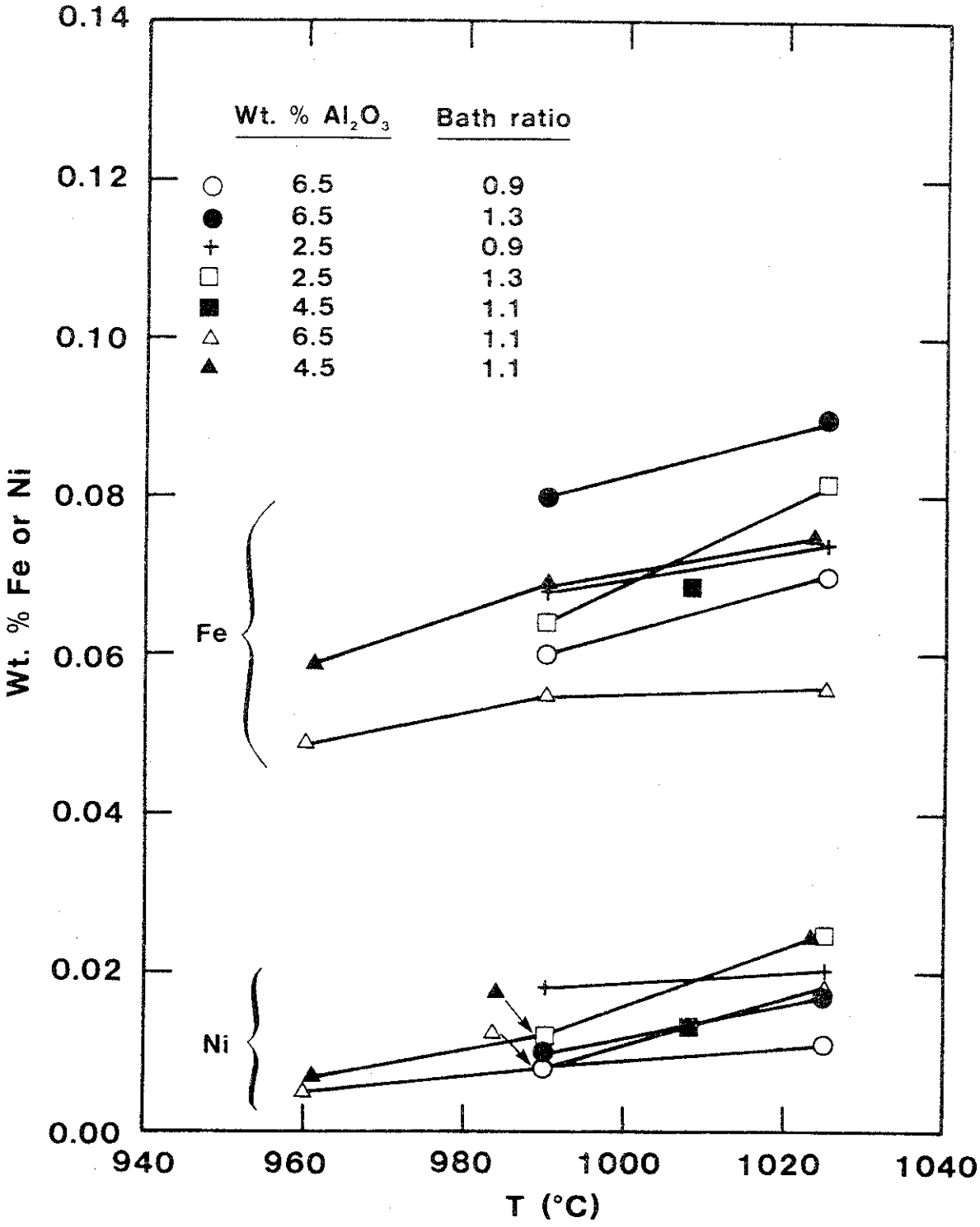

Solubility of $NiFe_2O_4$ in $NaF-AlF_3-CaF_2-Al_2O_3$ Melts
Figure 48

The $NiFe_2O_4$ data indicate that nickel ferrite did not dissolve stoichiometrically. The weight ratio Fe/Ni ranges from appproximately 3 to 8. However, the bath contains a background level of approximately 0.02 wt.% Fe, so that stoichiometric dissolution of $NiFe_2O_4$ into a bath already containing Fe would result in Fe/Ni ratios of those reported.

Figures 49 and 50 show the variation in solubilities with Al_2O_3. These are crossplots of some of the data in Figures 46 and 47; each point shown is an experimentally measured point. The solubilities decrease with Al_2O_3, and the effect is stronger for NiO than for Fe_2O_3. For Fe_2O_3, the solubility is approximately constant for melts with more than 2.5% Al_2O_3. The biggest change occurs at less than 2% Al_2O_3 for both oxides. The behavior seems to follow a solubility-product-type relationship so that as the activity of Al_2O_3 decreases, the solubility of the iron or nickel oxide increases. It does not simply substitute for Al_2O_3 as a source of oxide ion to dissolve in the melt. Because of this effect of Al_2O_3, it appears that neither iron nor nickel oxides are dissolving as metal-oxide anions such as a nickelate ion, NiO_2^{2-}. If they were, it would be expected that Al_2O_3 would increase the solubility of these ions. For example, a possible dissolution reaction would be

$$3NiO + Al_2O_3 + 6NaF = 3\ Na_2NiO_2 + 2AlF_3 \qquad (18)$$

An increase in the activity of Al_2O_3 would drive the reaction to the right and increase the solubility of the NiO. The dissolving species are more likely metal cations, metal fluoride anions, or metal oxy-fluoride anions for which a decrease in the Al_2O_3 activity would increase their solubility. For example, the dissolution of NiO to form a nickel fluoride anion would proceed by the overall reaction,

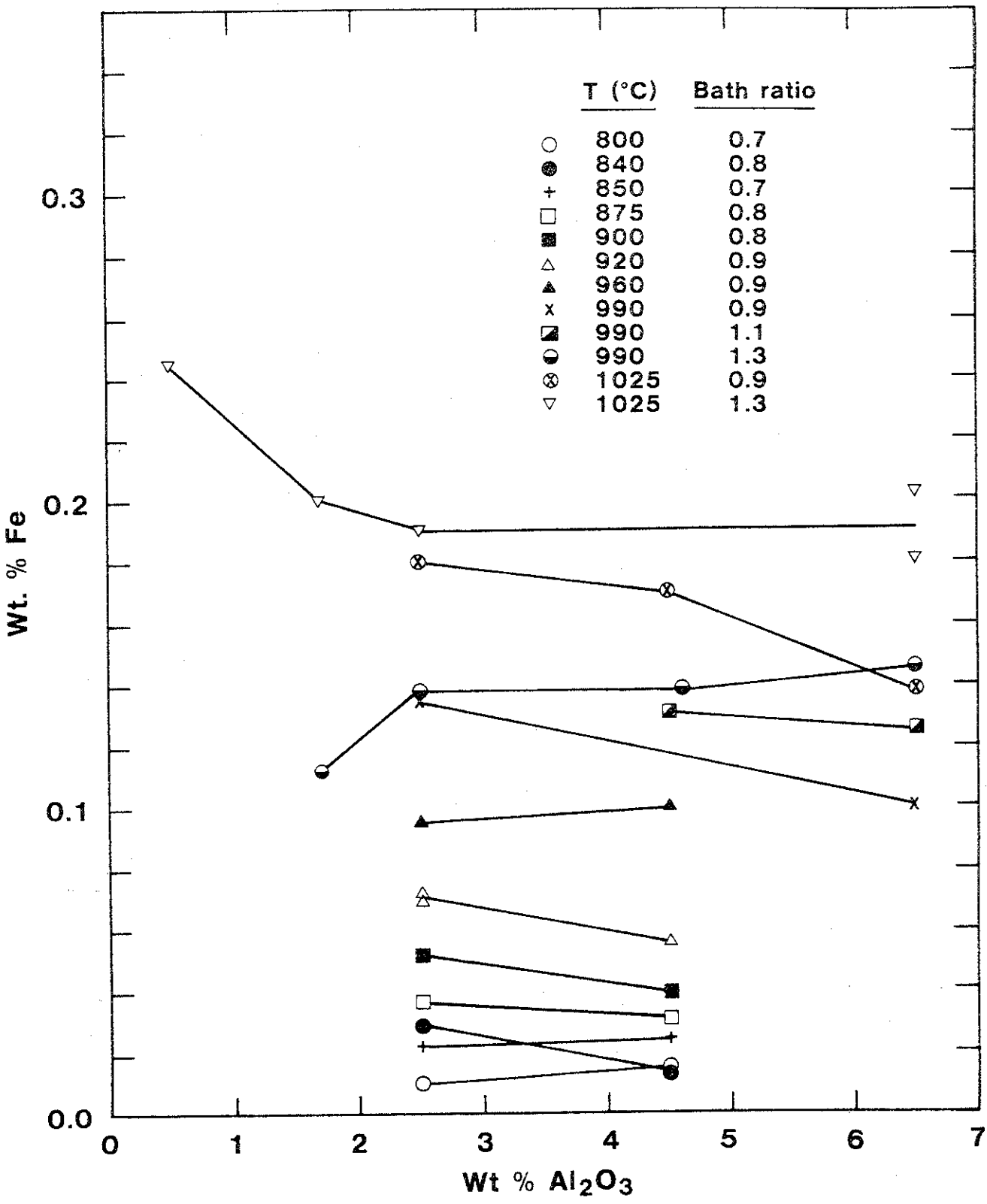

Effect of Al_2O_3 Concentration in the Melt on the Solubility of Fe_2O_3

Figure 49

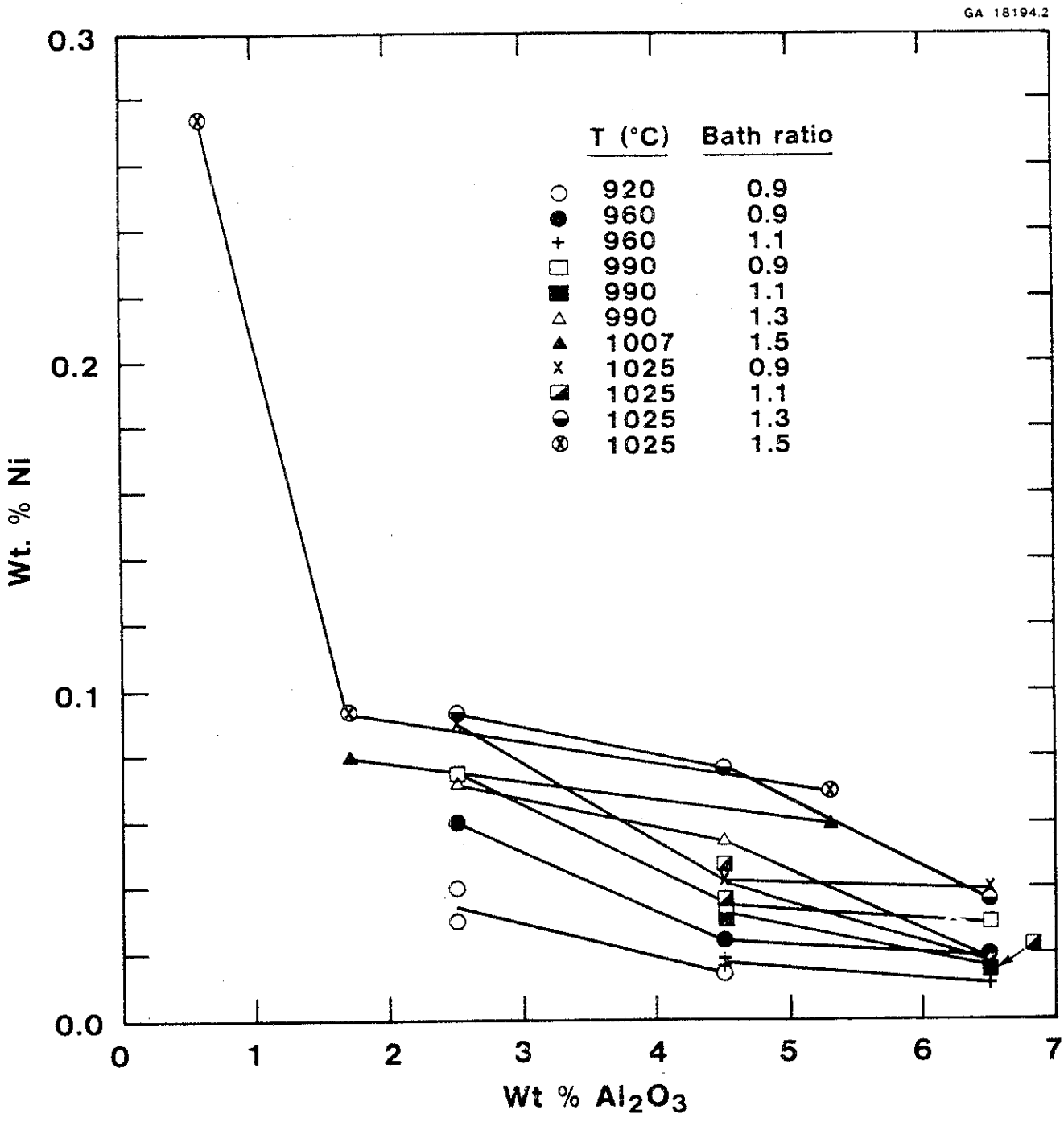

Effect of Al_2O_3 Concentration in the Melt on the Solubility of NiO

Figure 50

$$3NiO + 2AlF_3 + 3NaF = 3NaNiF_3 + Al_2O_3 \quad (19)$$

in which the activity of the dissolved compound would be inversely proportional to the activity of Al_2O_3 to the one-third power.

Figures 51 and 52 show the solubilities plotted as a function of bath ratio. The solubility of Fe_2O_3 decreases moderately with decreasing bath ratio, while there does not appear to be any change in the solubility of NiO within the uncertainty of the measurements. It is difficult to infer any information on the ionic species for Fe and Ni which form on dissolution of the oxides, other than discussed above, because of the limited basicity range over which data was obtained. In the $NaF-AlF_3$ system the activity of AlF_3 changes by one order of magnitude from a bath ratio of 0.9 to 1.3, while the activity of NaF changes by a factor of 3 over the same compositional range (55). Measurements over several orders of magnitude would be needed to infer any further structural information.

b) Enthalpy of Dissolution

The enthalpy of dissolution of the oxides in the melts can be obtained from the solubility data. Since all solubilities which were measured were relatively small, the assumption of Henrian behavior in the solution may be reasonable. The activities of the dissolved species can be represented by

$$a_{NiO} = \gamma_{NiO} X_{NiO} \quad (20)$$

and

$$a_{Fe_2O_3} = \gamma_{Fe_2O_3} X_{Fe_2O_3} \quad (21)$$

At saturation with respect to the solid, a_{NiO} and $a_{Fe_2O_3}=1$, therefore

$$\gamma_{NiO}^{\circ} = 1/X_{NiO}^{sat} \quad (22)$$

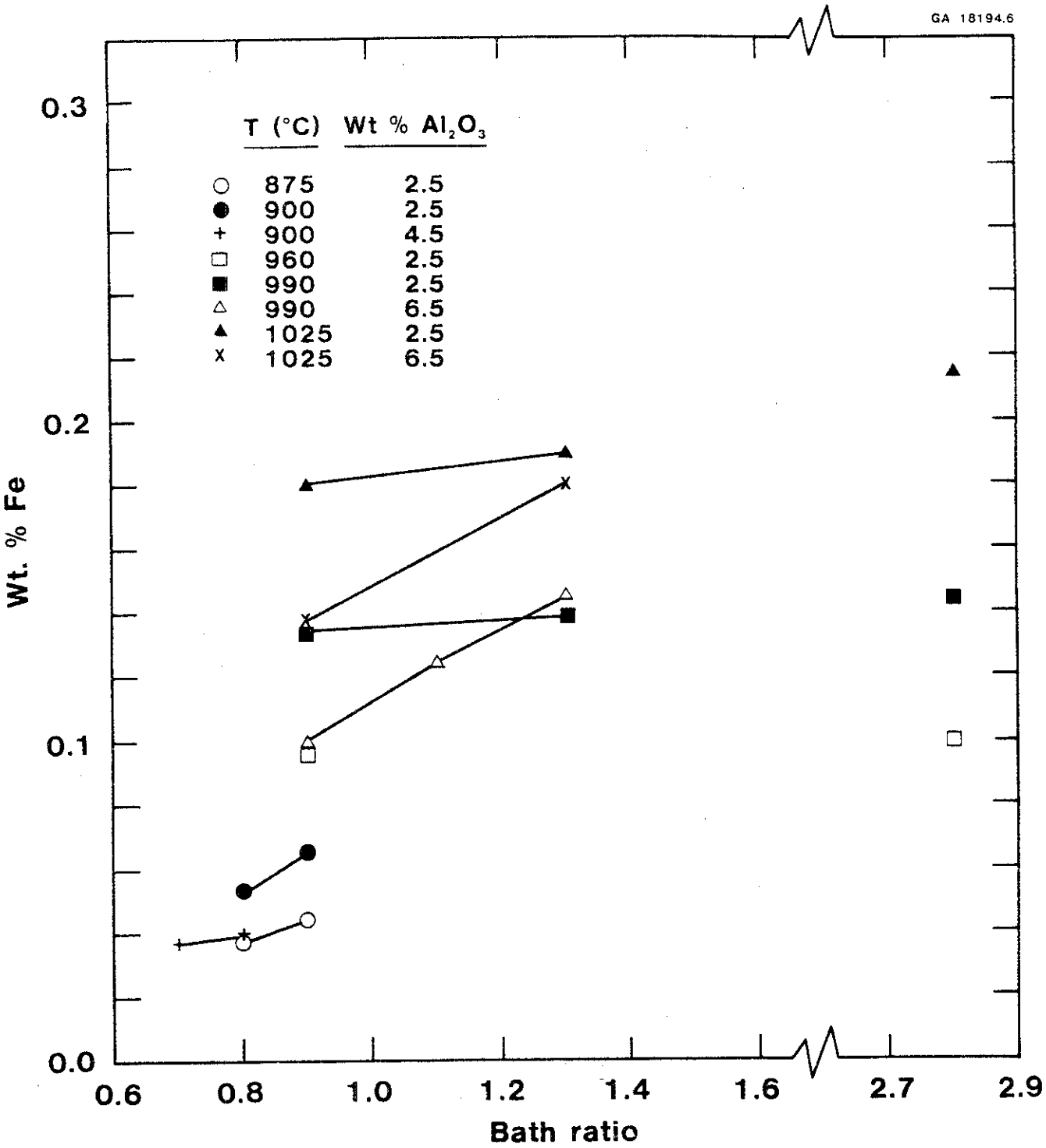

Effect of Bath Ratio (Wt NaF/Wt AlF_3) on the Solubility of Fe_2O_3

Figure 51

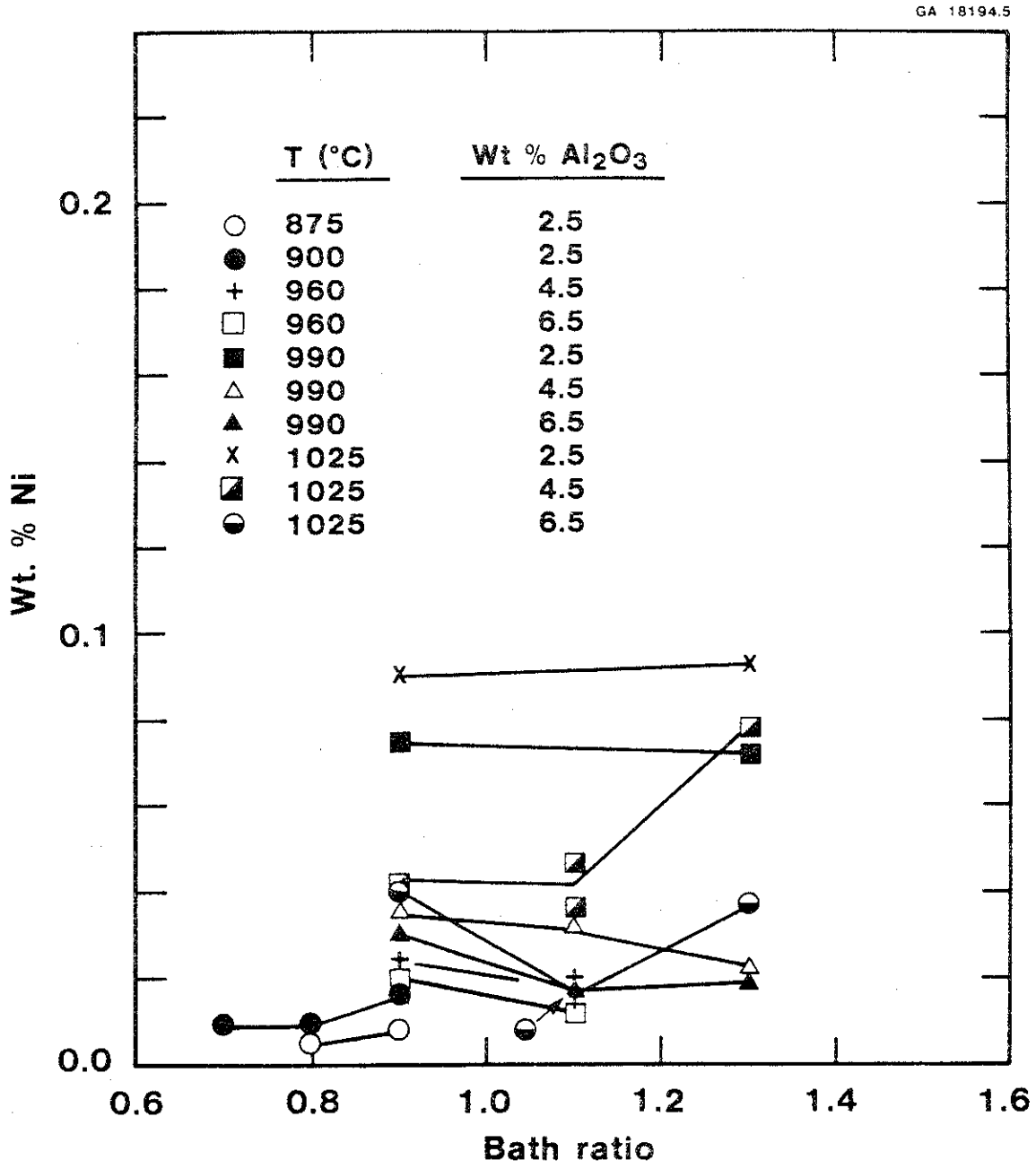

Effect of Bath Ratio (Wt NaF/Wt AlF_3) on the Solubility of NiO

Figure 52

and

$$\gamma_{Fe_2O_3}^{\circ} = 1/X_{Fe_2O_3}^{sat} \quad (23)$$

From the Gibbs-Helmholtz equation,

$$\partial \ (2.303R \log \gamma_i)/ \partial \ (1/T) = \Delta H_i^M \quad (24)$$

Therefore log (X_i^{sat}) or log (wt.% i) should vary linearly with 1/T provided the assumption of Henrian behavior holds and ΔH_i^M is constant with temperature.

Figures 53 and 54 show the data for Fe_2O_3 and NiO plotted in this manner. The correlation for Fe_2O_3 is quite good, even though data for all melt compositions are included. This indicates that the changes with Al_2O_3 concentration and bath ratio are relatively small compared to changes in solubility with temperature. Data for melts with less than 1.5% Al_2O_3 were not included. The correlation for NiO is not as good, but this is expected since the Al_2O_3 concentration in the melt had a larger influence than the Fe_2O_3. Attempts at fitting the data to the proposed model at constant Al_2O_3 concentration gave a better correlation for melts with 2.5% Al_2O_3, but poorer correlation for melts with higher concentrations. This is true because data in melts with higher concentrations of Al_2O_3 were obtained over a limited temperature range. Therefore, the best correlation is obtained by using all compositions. The least-squares equations are

$$\log \text{wt.\% Fe} = 4.71 - 7080/T \quad (25)$$

and

$$\log \text{wt.\% Ni} = 6.27 - 9740/T \quad (26)$$

The partial molar enthalpies of dissolution of the oxides, ΔH_i^M, calculated from the slopes of these equations are +33.1 and +44.6 kcal/mole for Fe_2O_3 and NiO, respectively.

Figure 55 shows the solubility data from $NiFe_2O_4$ plotted as a function of inverse temperature. Least-squares lines were

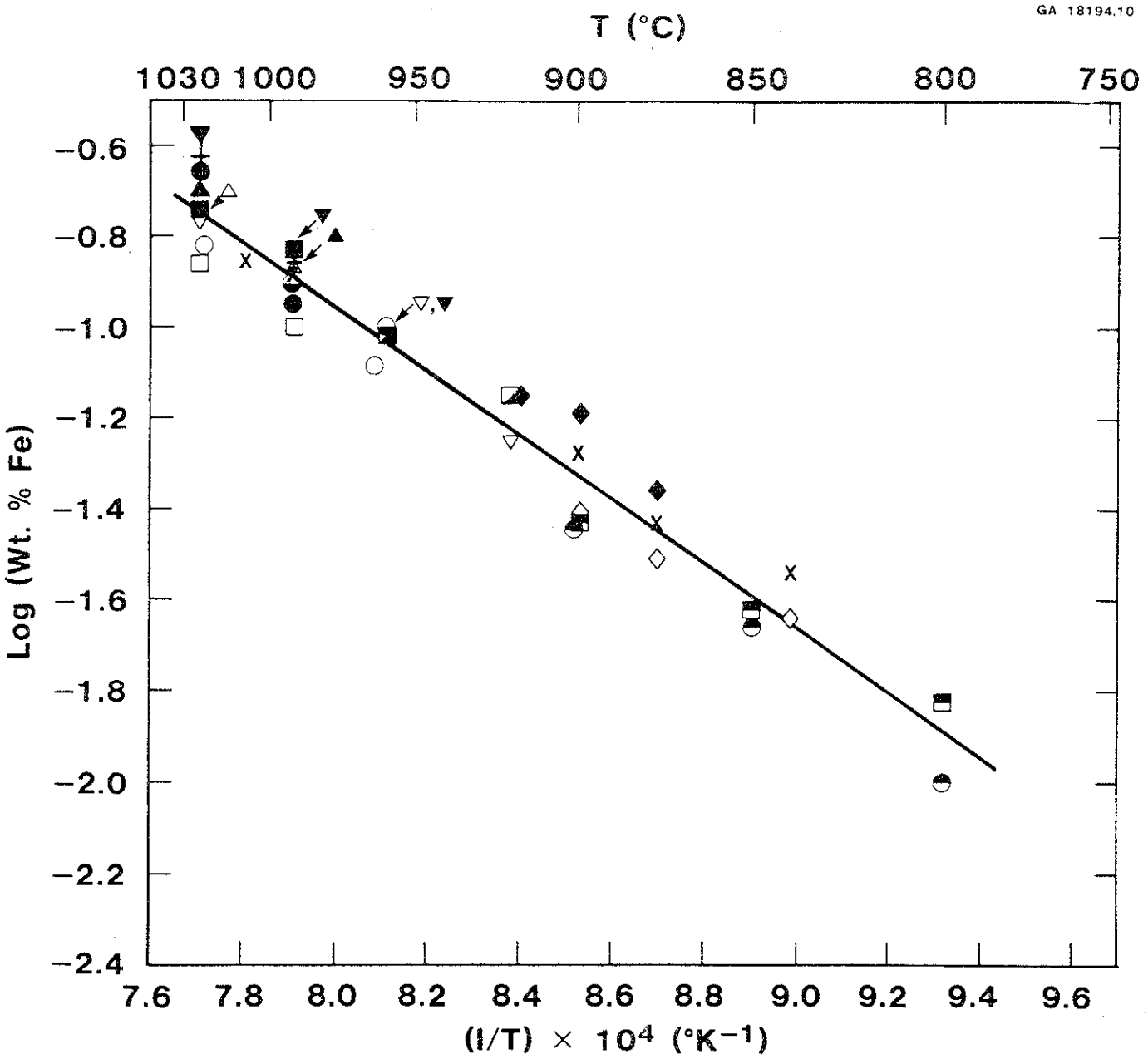

Least-Squares Fit of the Fe_2O_3 Solubility Data. Symbols Represent Compositions Noted in Figure 46.
Figure 53

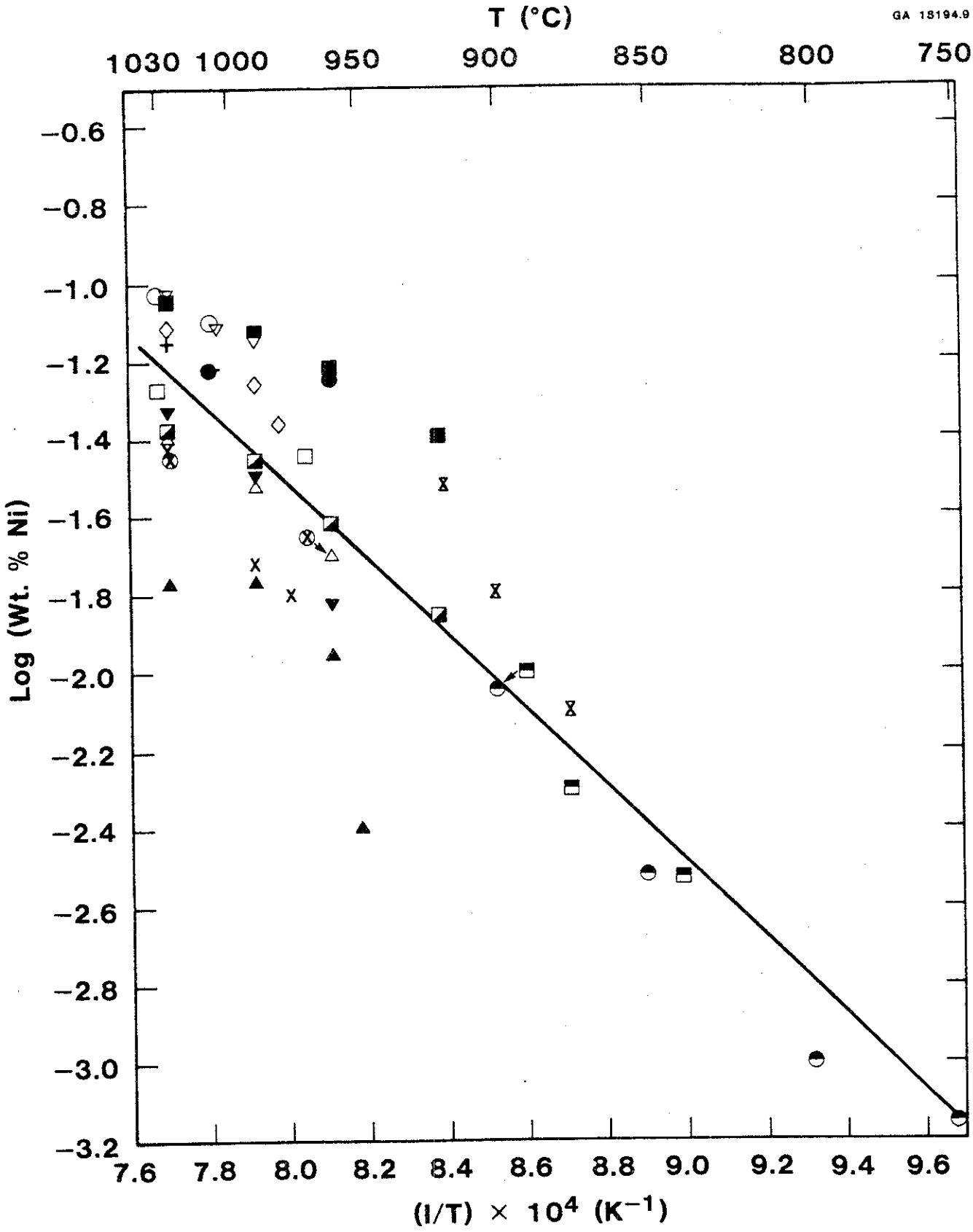

Least-Squares Fit of the NiO Solubility Data. Symbols Represent Compositions Noted in Figure 47.

Figure 54

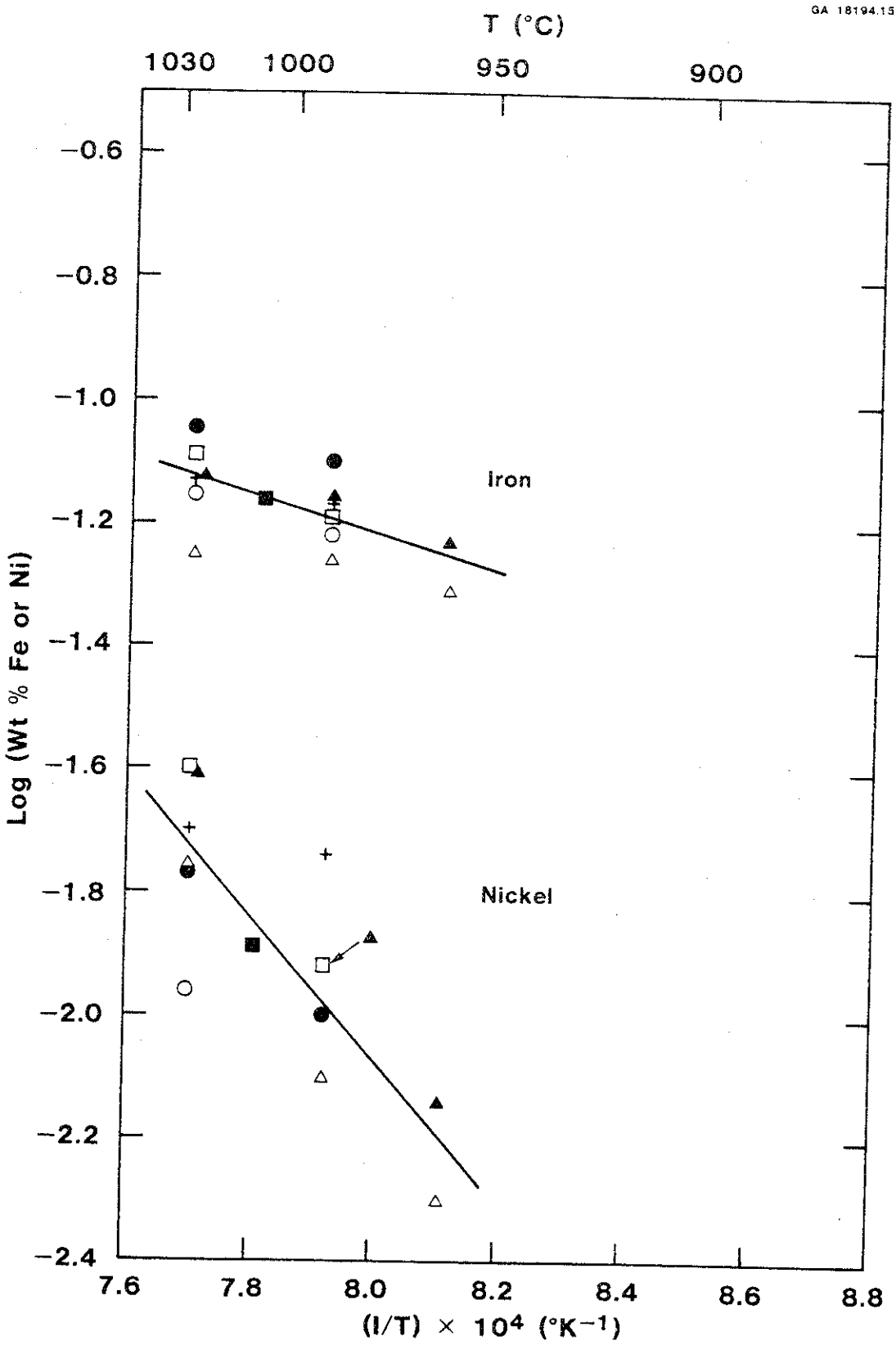

Least-Squares Fit of the Solubility Data for $NiFe_2O_4$. Symbols Represent Compositions Noted in Figure 48.

Figure 55

calculated, although the temperature range for the data was limited and the correlation coefficients were poor. The least-squares lines are

$$\log \text{wt.\% Fe} = 1.26 - 3100/T \quad (27)$$

and

$$\log \text{wt.\% Ni} = 7.25 - 11700/T \quad (28)$$

c) Comparision to Other Thermodynamic Data

To assess whether the measured data agree with other thermodynamic data found in the literature, the standard free energy of formation of $NiFe_2O_4$ was calculated from the above Henrian activity coefficients and the measured solubility of $NiFe_2O_4$. For the formation of stoichiometric $NiFe_2O_4$, ΔG_f° can be calculated from the relationship,

$$\Delta G_f^\circ(NiFe_2O_4) = -2.303\ RT \log[1/(\gamma_{NiO} \cdot X_{NiO} \cdot \gamma_{Fe_2O_3} \cdot X_{Fe_2O_3})] \quad (29)$$

where X_{Fe2O3} and X_{NiO} are the mole fractions of Fe_2O_3 and NiO in the melt which is saturated with $NiFe_2O_4$. Substituting the activity coefficients calculated from Equations 22, 23, 25 and 26, and saturation concentrations from Equations 27, and 28 into this equation gives a free energy of formation of -4920 cal/mole at 1000°C. Kubaschewski (56) reported the free energy of formation from the simple oxides to be

$$\Delta G_f^\circ(NiFe_2O_4) = -4750 - 0.9\ T \text{ cal/mole } (855 < T < 1700^\circ K) \quad (30)$$

with an uncertainty of ± 1000 cal/mole; at 1000°C the free energy of formation is -5900 ± 1000 cal/mole. The results of this study are, therefore, in agreement with this independent thermodynamic data, which was obtained by an emf cell method. There are several measurements of the solubilities of Fe_2O_3, NiO, and $NiFe_2O_4$ in Na_3AlF_6-Al_2O_3 melts reported in th...

literature. Table 25 compares available data for Fe_2O_3 to that from this study. There is an order of magnitude discrepancy for the literature data, and the result of this study lies between them. Actually no measurements were made in pure Na_3AlF_6; the cryolite contained 0.5% Al_2O_3. Considering the rather large effect Al_2O_3 has on the solubilites at low concentrations of Al_2O_3, the agreement between this study and Belayeav (52) and Rolin (53) seems reasonable. The value measured by Johansen (54) seems high, but if the cryolite was extremely pure this value would be plausible. The agreement between this study and Horinouchi (2) for melt containing 10% Al_2O_3 seems reasonable. The major disagreement is between Belyaev and this study for melt with 5% Al_2O_3. In defense of this study, it should be noted that concentrations greater than 0.02 are always found in bath (saturated with Al_2O_3) in Hall cells operated with $NiFe_2O_4$-based inert anodes. This would make the Belyaev data at least an order of magnitude too low.

Table 26 gives a comparision of data for NiO. The agreement for Na_3AlF_6 is reasonable. In melt with 5% Al_2O_3, Belyaev's measured solublity is greater than found in the present study, although the difference is not nearly as great as for Fe_2O_3. Table 27 compares results for $NiFe_2O_4$. The agreement between this study and Horinouchi's measurement is good, and the two sets of data are probably within the combined uncertainties of the measurements. Both sets of data give free energies of formation of $NiFe_2O_4$ that are within the ± 1000 cal/mole uncertainty for the literature data for ΔG_f° ($NiFe_2O_4$).

d) Na_3AlF_6-Fe_2O_3-NiO Phase Diagram

A portion of the Na_3AlF_6-Fe_2O_3-NiO phase diagram can be calculated from the solubility measurements for Fe_2O_3 and NiO and the standard free energy of formation of $NiFe_2O_4$. This

TABLE 25

Solubility of Fe_2O_3 in Na_3AlF_6-Al_2O_3 Melts at 1000°C

	Solvent		
Investigator	0% Al_2O_3	5% Al_2O_3	10% Al_2O_3
Belyaev (52)	0.18	0.003	
Rolin (53)	0.14*		
Johansen (54)	1.07		
Horinouchi (2)			0.14
Present Study	>0.27**	>0.22**	<0.22***

*Value for 1030°C
**Value for bath ratio = 1.3, 0.5 wt.% Al_2O_3
***Value for bath ratio = 1.3, 4.6 wt.% Al_2O_3

TABLE 26

Solubility of NiO in
Na_3AlF_6-Al_2O_3 Melts at 1000°C

	Solvent		
Investigator	0% Al_2O_3	5% Al_2O_3	10% Al_2O_3
Belyaev (52)	0.32	0.18	
Rolin (53)	0.15*		
Horinouchi (2)			0.18
Present Study	0.25**	0.07***	<0.07***

*Value for 1030°C
**Value for melt with 0.6 wt.% Al_2O_3
***Value for melt with 5.3 wt.% Al_2O_3

TABLE 27

Solubility of $NiFe_2O_4$ in Na_3AlF_6-10% Al_2O_3 Melt at 1000°C

Investigator	Fe	Ni
Horinouchi (2)	0.05	0.02
Present Study	0.058*	0.009*

*Value for melt with 6.5 wt.% Al_2O_3 bath ratio 1.1

calculated diagram is actually for the "melt" -Fe_2O_3-NiO system, where "melt" is a Na_3AlF_6-AlF_3-Al_2O_3 composition of approximately 1.1 bath ratio, 4.5 wt.% Al_2O_3. The diagram is, therefore, a pseudo ternary diagram.

The method of calculation is simple and contains one key assumption, which is that Henry's law holds for solutions of Fe_2O_3 and NiO in the cryolite-based melt for the dilute solutions that are involved. From this assumption the activity coefficients for Fe_2O_3 and NiO in the melt are calculated from the measured solubilities for these oxides using Equations 22 and 23. The liquidus isotherms for saturation with respect to $NiFe_2O_4$ (line a, Figure 56) are then calculated using Equations 29 and 30. The liquidus isotherms for saturation with respect to Fe_2O_3 and NiO (lines b and c, Figure 56) are calculated using Equations 20 through 23.

This calculation assumes $NiFe_2O_4$ is stoichiometric. Actually, $NiFe_2O_4$ has a range of stoichiometry, with the phase containing excess Fe_2O_3. This could be incorporated into the calculation by modifying Equation 29 to include an activity for $NiFe_2O_4$ of less than one. Activities of NiO and Fe_2O_3 in the spinel would be needed.

Figure 56 shows the calculated isothermal section for the system at 960°C. The dashed lines represent the effects of the uncertainty in the thermodynamic data for $NiFe_2O_4$ of ± 1000 cal/mole. The solubility measurement for $NiFe_2O_4$ made during this study, taken from Figure 47 or 54, is denoted in the figure. It is emphasized that the phase diagram calculation is independent of this measurement. The denoted point represents the agreement between measurements of this study and the thermodynamic data for $NiFe_2O_4$.

Figure 55 shows why it is desirable to formulate nickel ferrite anodes with a slight excess of NiO. The solubility

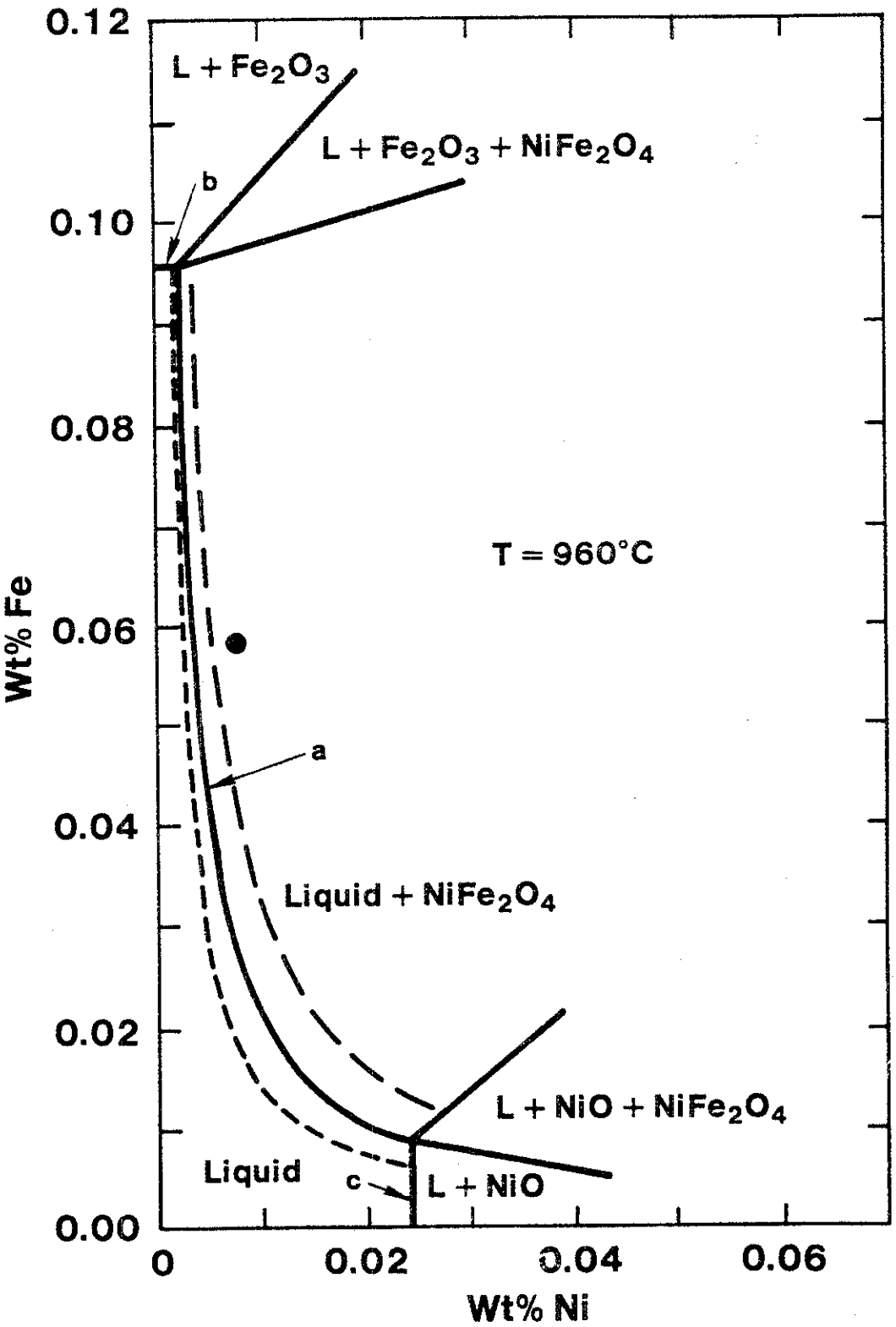

Calculated Isothermal Section for the Fe_2O_3-NiO-(NaF-AlF_3-Al_2O_3) Pseudo Ternary System at 960°C

Figure 56

of nickel ferrite is given by the liquidus surface (line a) which runs from about 0.095% Fe, 0.005% Ni to 0.01% Fe, 0.024% Ni. The composition of bath saturated with a nickel ferrite anode can be any point on this line. The equilibrium bath composition would be determined by the initial bath composition, the stoichiometry of the "$NiFe_2O_4$" that is dissolving, and the relative rates of Fe and Ni dissolving from the ferrite. In a reduction cell there would be an additional factor, the relative rates at which NiO and Fe_2O_3 are reduced at the cathode. By adding NiO to the nickel ferrite inert anode, the stoichiometry is such that the solubility of the nickel ferrite is given by the point of two-fold saturation of the liquid with respect to NiO and $NiFe_2O_4$, approximately 0.01% Fe, 0.024% Ni. This point is the intersection of lines a and c in Figure 56. The overall solubility from "$NiFe_2O_4$", $XFe_2O_3 + X_{NiO}$, would be a minimum near this point of two-fold saturation. To maintain the system close to this point, excess NiO should be added to the anode so that the equilibrium melt composition is given by the intersection of the $NiFe_2O_4$ and NiO liquidus isotherms (lines a and c in Figure 56).

2) Effects of Bath Additives

The purpose of determining the effects of additives to the bath on the solubilities of Fe_2O_3 and NiO was primarily to find additives which would lower the solubilities so that inert anode life and metal purity would be increased. For one of the additives, SiO_2, the effect on solubilities was needed because certain baths used in bench scale cells contained small quantities of it. In general, additives were chosen that were more stable than Al_2O_3 so they would not be reduced at the cathode in a Hall cell. Additives that were tested were CaF_2, MgF_2, LiF, ZrO_2 and SiO_2.

a) Effect of SiO_2 additions: Additions of SiO_2 to the bath were

found to greatly increase the solubility of Fe_2O_3 (Figures 57 and 58. Figure 58 is a crossplot of data from Figure 57 and illustrates that the solubility varies linearly with the concentration of SiO_2 in the bath. This increase with increasing SiO_2 is analogous to the observed effect of SiO_2 on the solubility of Al_2O_3 in cryolite that has been reported in the literature (57). One explanation for the effect of SiO_2 is that it forms a complex ionic species with Fe_2O_3 which is more soluble than the normal ionic species for iron in cryolite-based melts. Another explanation is based on the observed effect of SiO_2 on the solubility of Al_2O_3--silica forms a complex ionic species with Al_2O_3 which reduces the activity of Al_2O_3 and as shown earlier, lowering the activity of Al_2O_3 will increase the solublity of Fe_2O_3.

b) Effect of CaF_2 additions: Calcium fluoride is an additive which is stable in bath in a Hall cell; it is not reduced but remains in bath as a fluoride. Therefore, it was desired to know its effect on the solubilities of Fe_2O_3 and NiO. Additions of 10% were chosen because it was thought that a cell could be run reasonably well with this addition without making major changes in operating practice. Most commercial cells already operate with approximately 5% CaF_2.

Figures 59 and 60 show the solubilities of Fe_2O_3 and NiO in melts with additions of 10 wt.% CaF_2, and compares them to results without the additions. In all cases the solubilities are decreased by the CaF_2. The changes are significant in some cases, ranging to approximately a 50% decrease. The melts which contained 10% CaF_2 had slightly lower concentrations of Al_2O_3 than those without because of dilution by CaF_2. This means that for a constant concentration of Al_2O_3 the decrease in solubility would be even greater than those shown in Figures 59 and 60. One interpretion of these decreases in solubilities is that CaF_2 may increase the activity of Al_2O_3 (it does reduce the solubility) which in turn would decrease the solubilities of Fe_2O_3 and NiO.

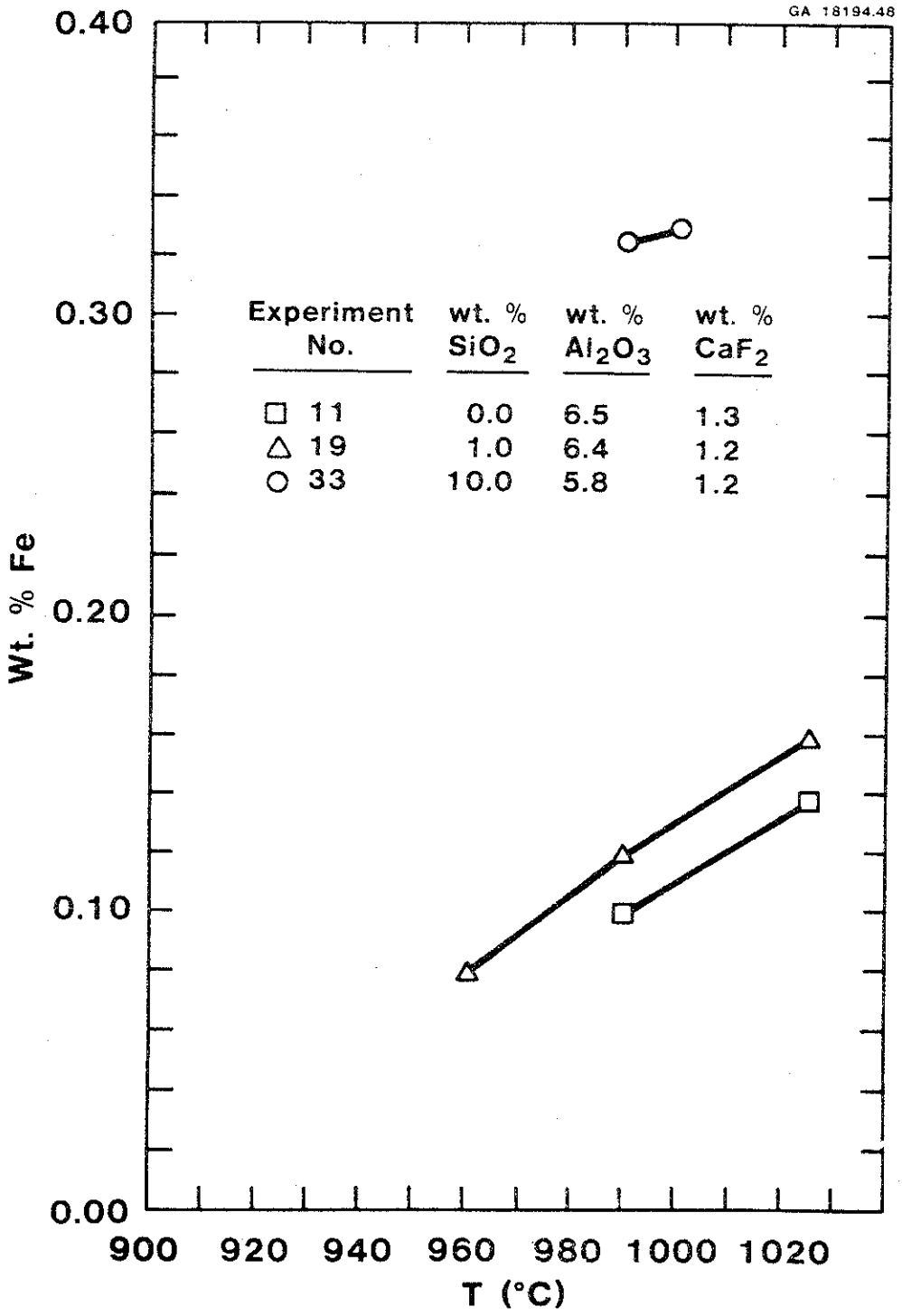

The Effect of SiO_2 on the Solubility of Fe_2O_3 in $NaF-AlF_3-CaF_2-Al_2O_3$ Melts with a Bath Ratio of 0.9

Figure 57

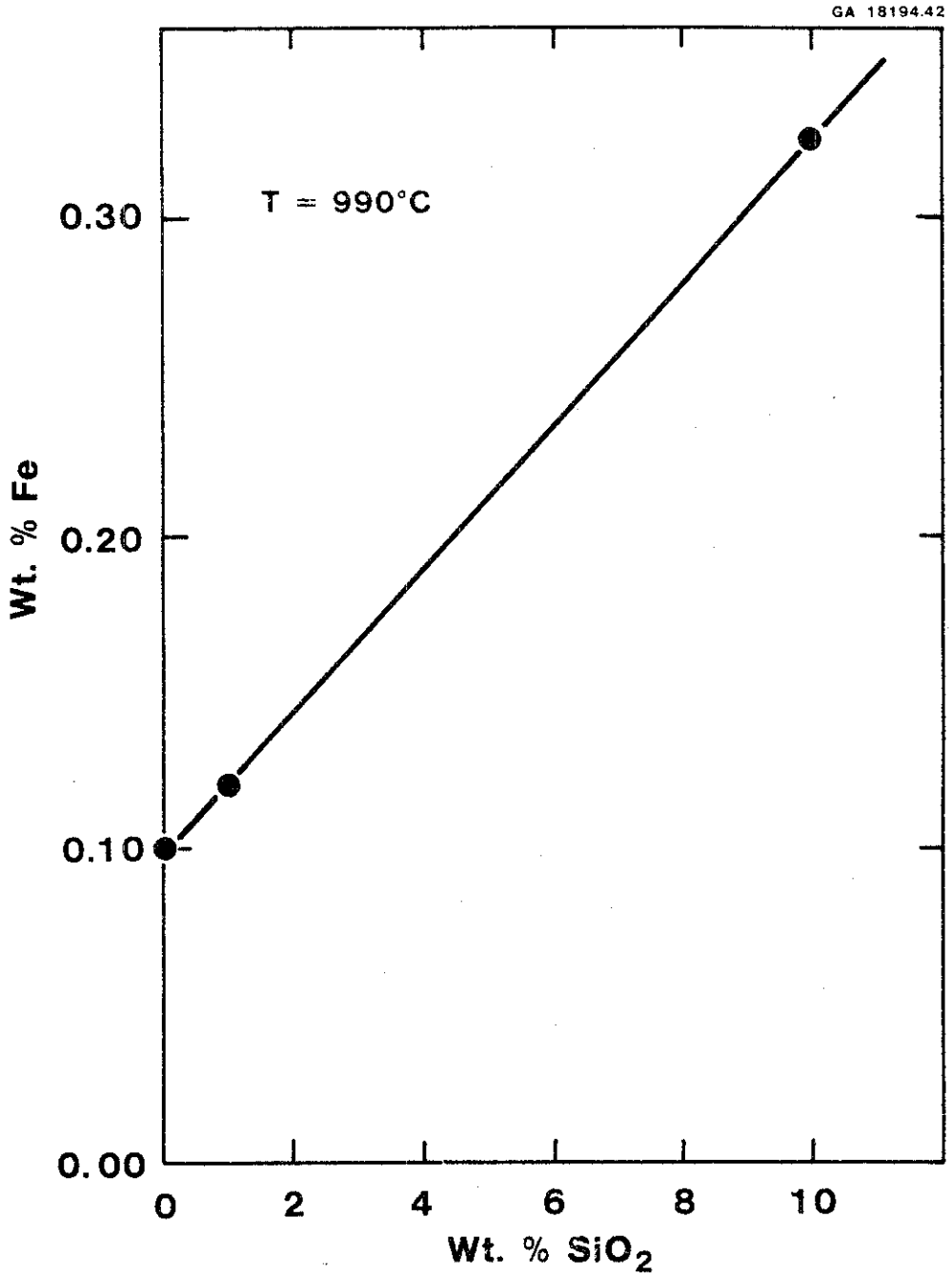

The Effect of SiO_2 on the Solubility of Fe_2O_3 in $NaF-AlF_3-CaF_2-Al_2O_3$ Melts. Melt Composition Given in Figure 57
Figure 58

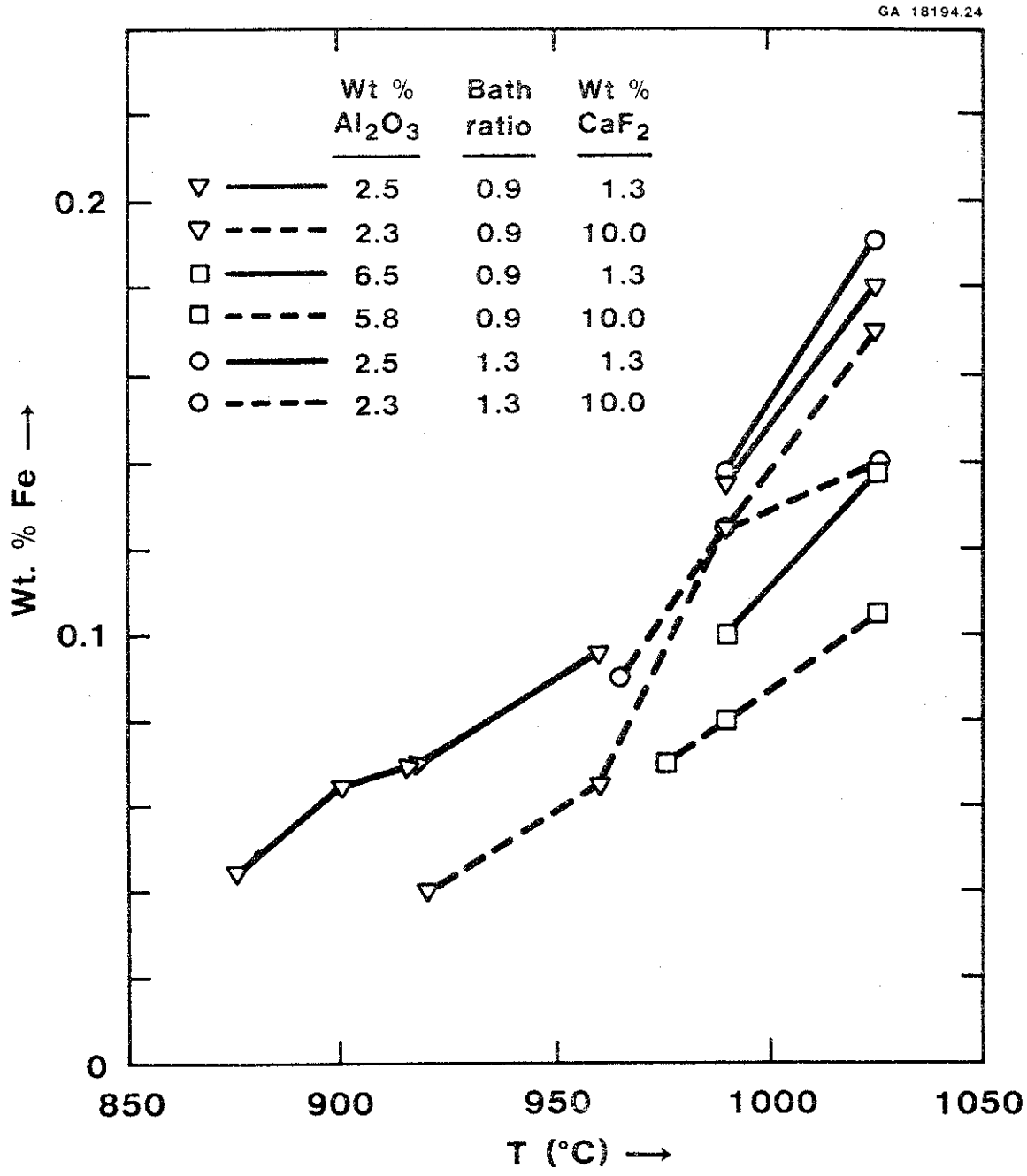

Effect of CaF_2 on the Solubility of Fe_2O_3 in $NaF-AlF_3-CaF_2-Al_2O_3$ Melts.
Figure 59

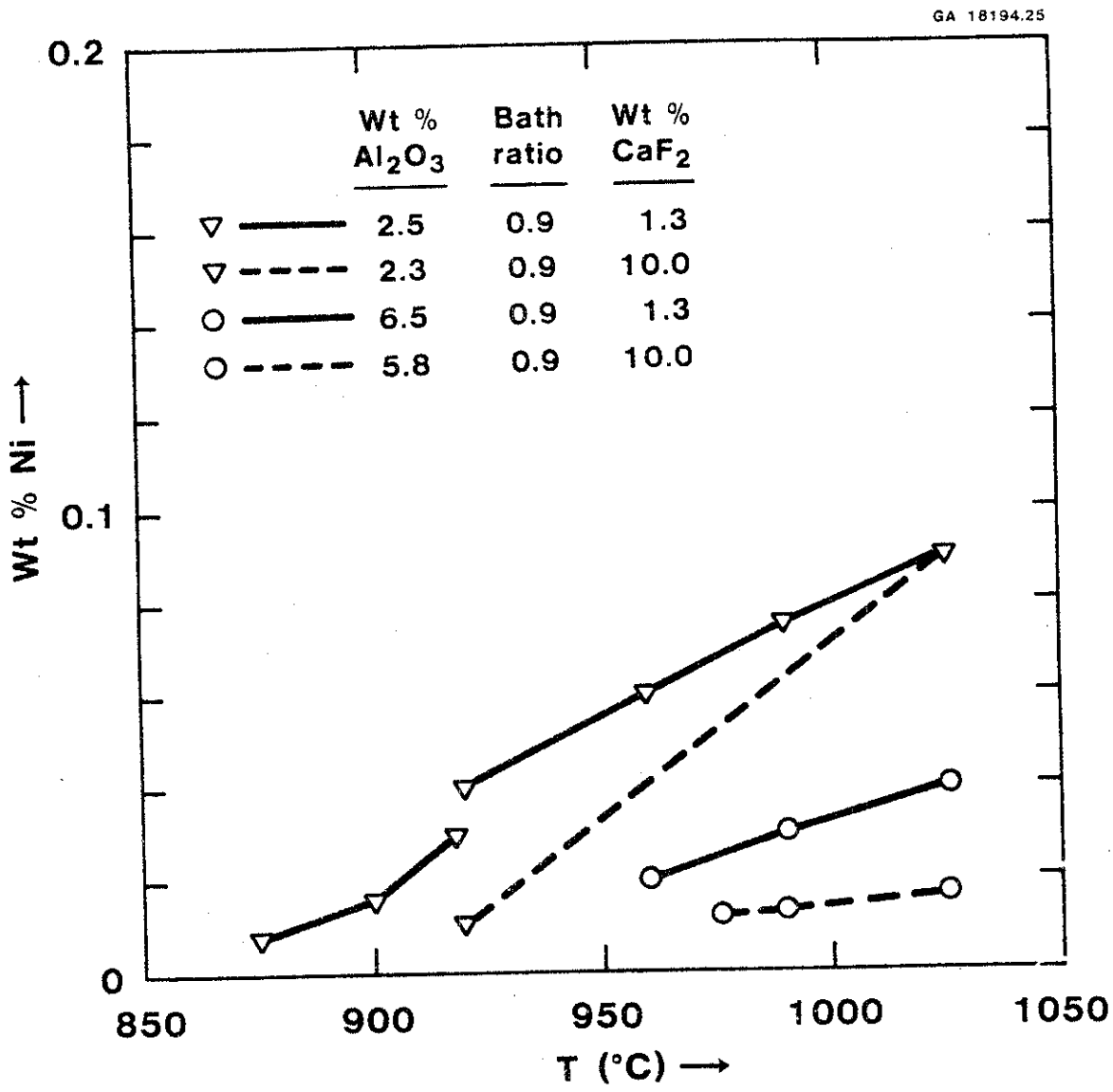

Effect of CaF_2 on the Solubility of NiO in $NaF-AlF_3-CaF_2-Al_2O_3$ Melts.
Figure 60

c) Effect of MgF_2 additions: Magnesium fluoride is another additive which is stable in bath in a Hall cell, so a knowledge of its effect on inert anode solubilities was needed. The level of MgF_2 added was, on a mole basis, equal to the level of CaF_2 added in the tests discussed above.

Figures 61 and 62 show the solubilities of Fe_2O_3 and NiO in baths containing additions of MgF_2, as well as solubilities in analogous melts without MgF_2. Dashed lines represent results for melts with MgF_2, and solid lines represent results for melts without MgF_2. As seen, for almost all melt compositions and temperatures the solubilities of the oxides are decreased by the addition of MgF_2. For some compositions the NiO solubility was decreased by more than 50%.

Selected melt samples were analyzed for Mg, and results are given in Table 28. The data shown there are in good agreement with the charged concentration of Mg (3.1 wt.%), as all analyzed values are within 12% of this charged concentration. It was reported in one of the quarterly reports that analyzed Mg contents were much lower than charged Mg contents, but these subsequent analyses showed the earlier analyses were in error.

One interpretation of these decreases in solubilities is that, similar to CaF_2, MgF_2 might increase the activity of Al_2O_3 (it does reduce the Al_2O_3 solubility) which in turn would decrease the solubilities of Fe_2O_3 and NiO. However, the decrease in Al_2O_3 solubility with increasing MgF_2 is proportionately much less than the decrease in NiO solubility. There may be an intrinsic chemical effect of MgF_2 on the NiO solubility.

d) Effect of LiF additions: Lithium fluoride is another additive that is stable in bath in a Hall cell. Therefore its effect on the solubilities of Fe_2O_3 and NiO were deter-

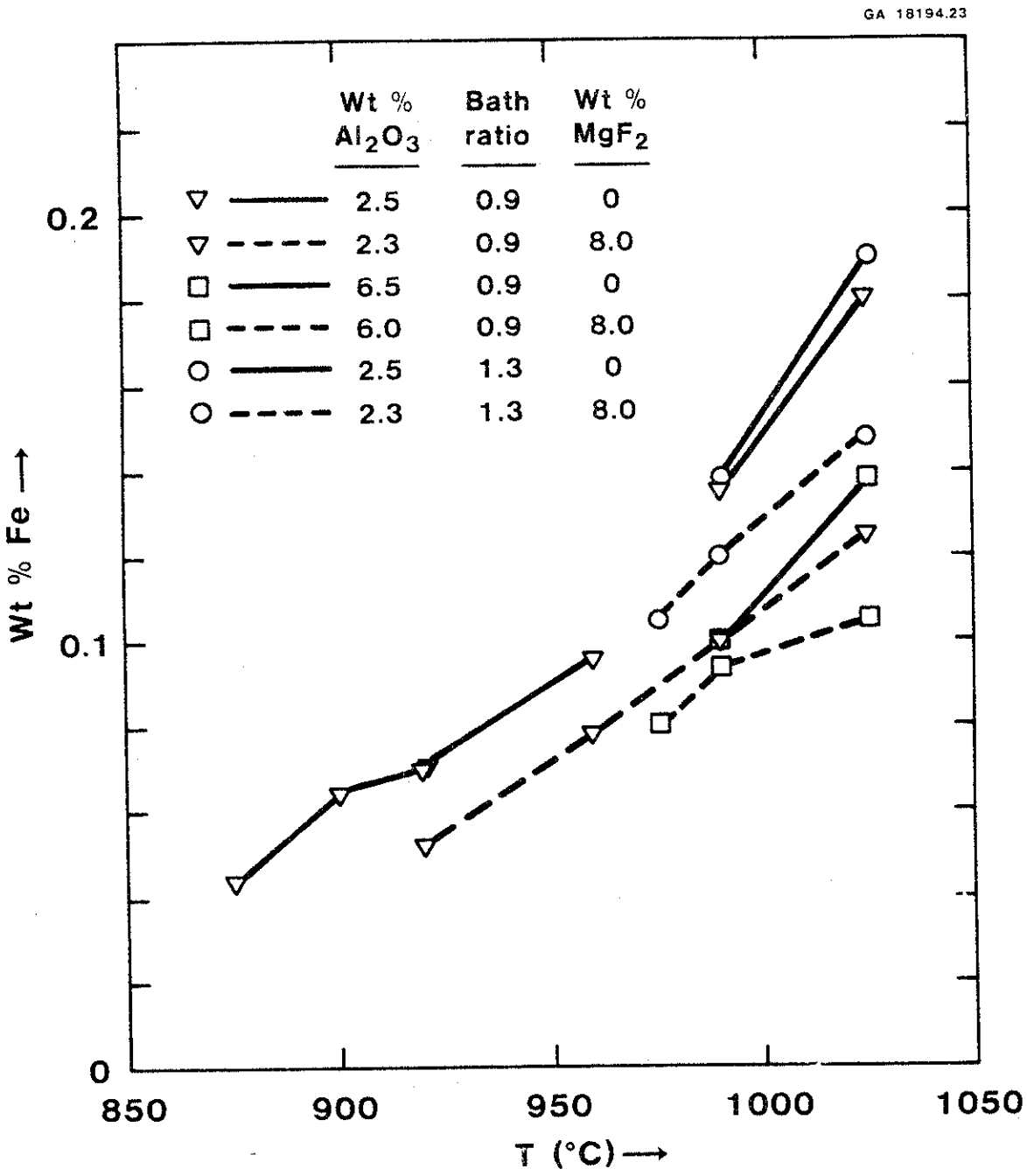

Effect of MgF_2 Additions on the Solubility of Fe_2O_3 in $NaF-AlF_3-CaF_2-Al_2O_3$ Melts. All Melts Contained 1.3 wt% CaF_2

Figure 61

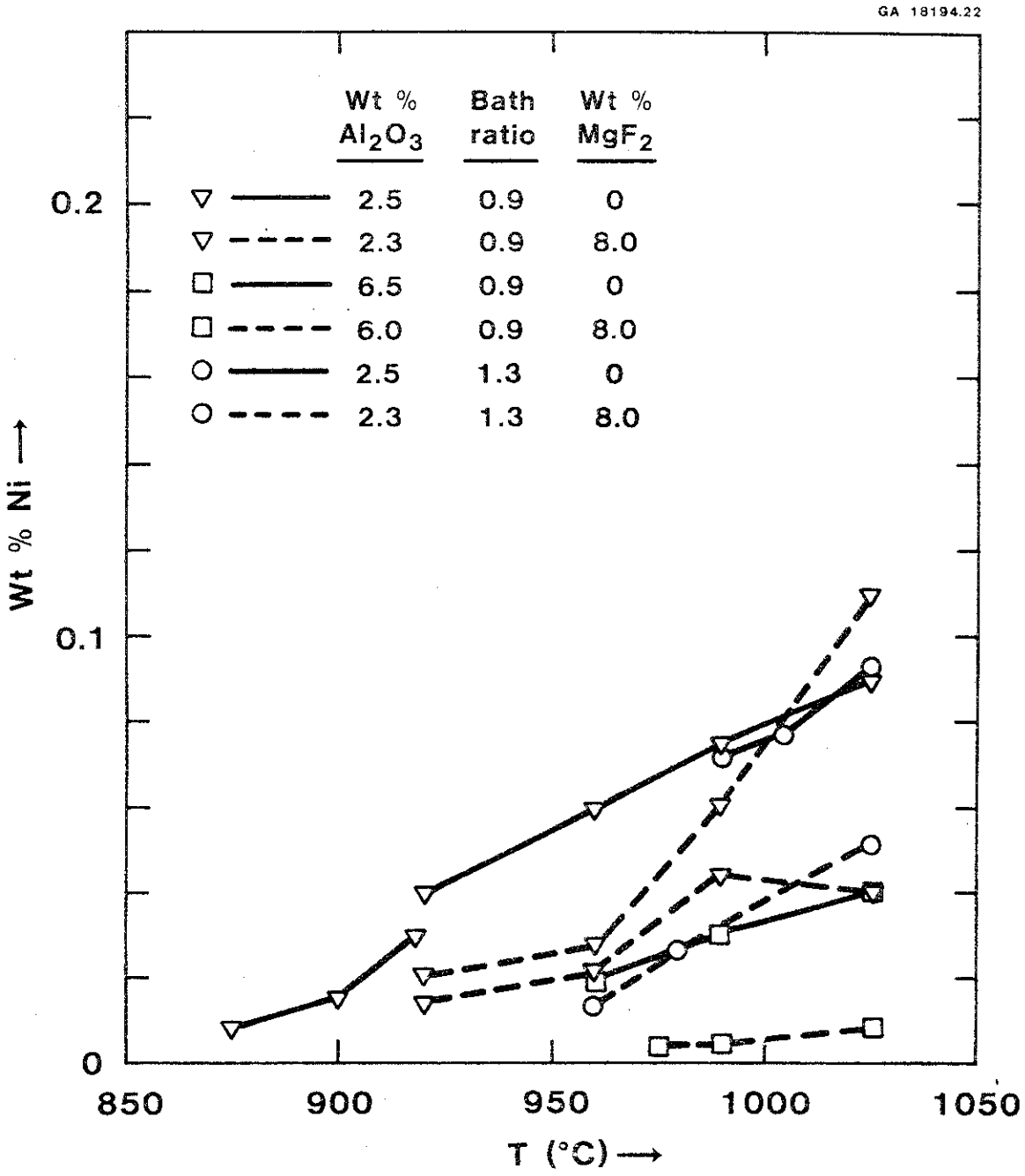

Effect of MgF_2 Additions on the Solubility of NiO in $NaF-AlF_3-CaF_2-Al_2O_3$ Melts. All Melts Contained 1.3 wt% CaF_2

Figure 62

TABLE 28

Analyzed Mg Concentrations in Bath to Which 8.0 Wt.% MgF_2 Was Added (3.1 Wt.% Mg)

Sample Number	Wt.% Mg
55-9	3.22
56-9	3.22
56 (bath remaining after experiment)	2.96
58-9	3.27
59-8	3.10
60-8	2.81
62-8	3.19
72-4	2.76
72-5	2.75
72-8	2.86
72-11	2.83
72-14	2.87
72-17	2.85
72-20	2.86
72-21	2.88
72 - Average	2.83
82-4	2.95
82-7	2.97
82-7	3.00
82-9	3.03
82-12	3.02
82-14	3.10
82-17	3.12
82-19	3.18
82-22	3.21
82 - Average	3.06

mined. The quantitiy of LiF which was added was such that assuming complete dissociation to Li^+ and F^-, the molar concentration of foreign ions added was equal to that which occurred upon the addition of CaF_2 in experiments discussed above, also assuming complete dissociation of CaF_2.

The solubilities of Fe_2O_3 and NiO in melts with a 5 wt.% addition of LiF are given in Figures 63 and 64, and are compared to solubilities in analogous melts without LiF. For most melts there was a decrease in solubility with the LiF addition, though this was not universally true. It is not surprising that LiF would decrease the Fe_2O_3 and NiO solubilities. Like CaF_2 and MgF_2, LiF is known to decrease the solubility of Al_2O_3.

e) Effect of ZrO_2 additions: Additions of ZrO_2 were tested because zirconia is one of the few oxides that will not react with AlF_3 to form the fluoride (ZrF_4) and Al_2O_3, and that has a decomposition potential approximately equal to Al_2O_3. Thus zirconia should exist in the bath as an oxide complex and may not be readily reduced at the cathode. The rationale behind adding ZrO_2 was that it was thought possible to get more oxide dissolved into the bath by adding both ZrO_2 and Al_2O_3 rather than just Al_2O_3. Because Al_2O_3 decreased solubilities of both Fe_2O_3 and NiO, it was postulated other oxides which are not strong compound formers with Al_2O_3 may also reduce these solubilities.

The solubilities obtained with the additions of ZrO_2 are shown in Figures 65 and 66, and are compared to results for corresponding melt compostions without ZrO_2. For each base melt composition, additions of ZrO_2 decreased the NiO solubility. However, the additions caused little change in the solubility of Fe_2O_3.

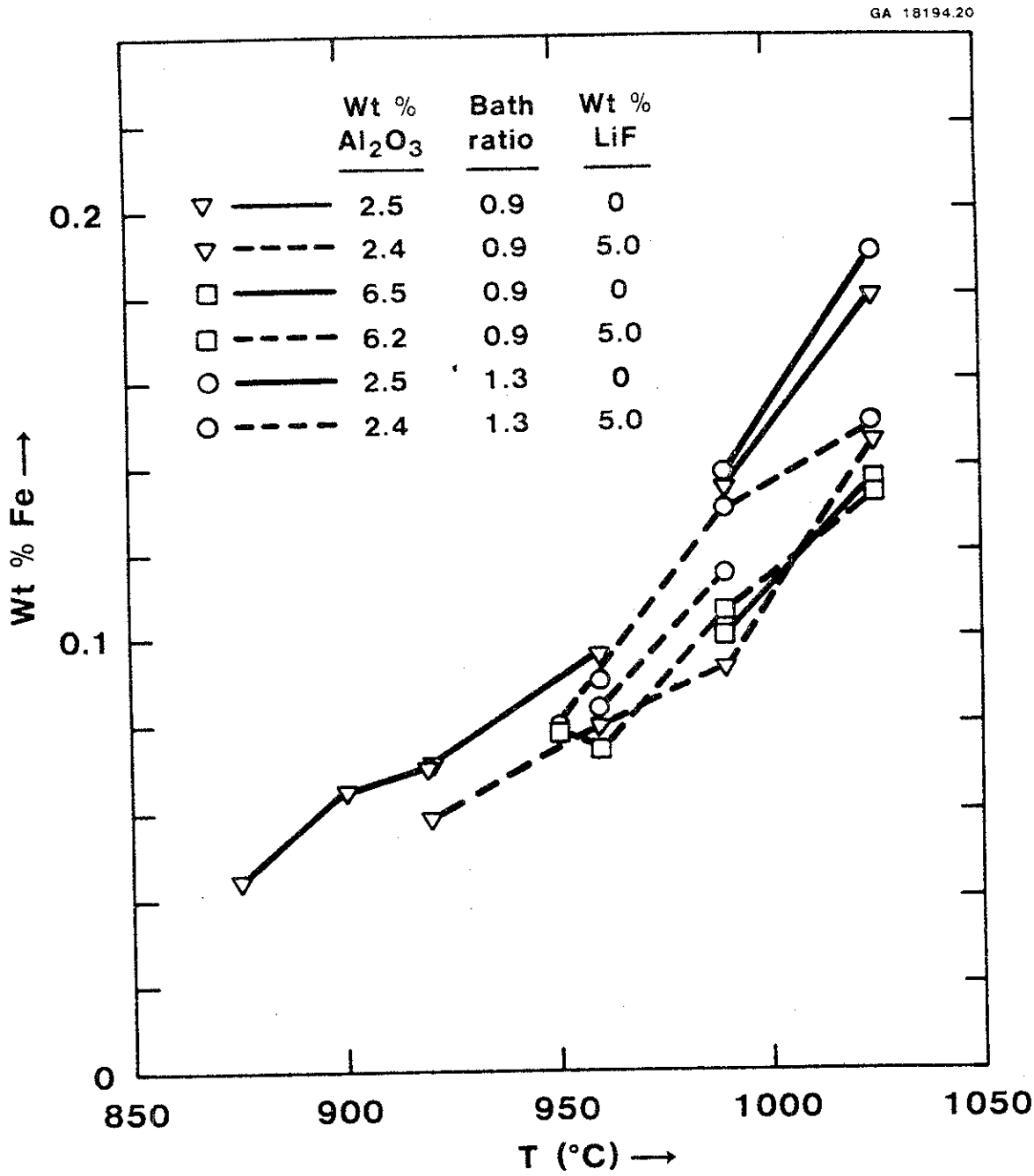

Effect of LiF Additions on the Solubility of Fe_2O_3 in $NaF-AlF_3-CaF_2-Al_2O_3$ Melts. All Melts Contained 1.3 wt% CaF_2.

Figure 63

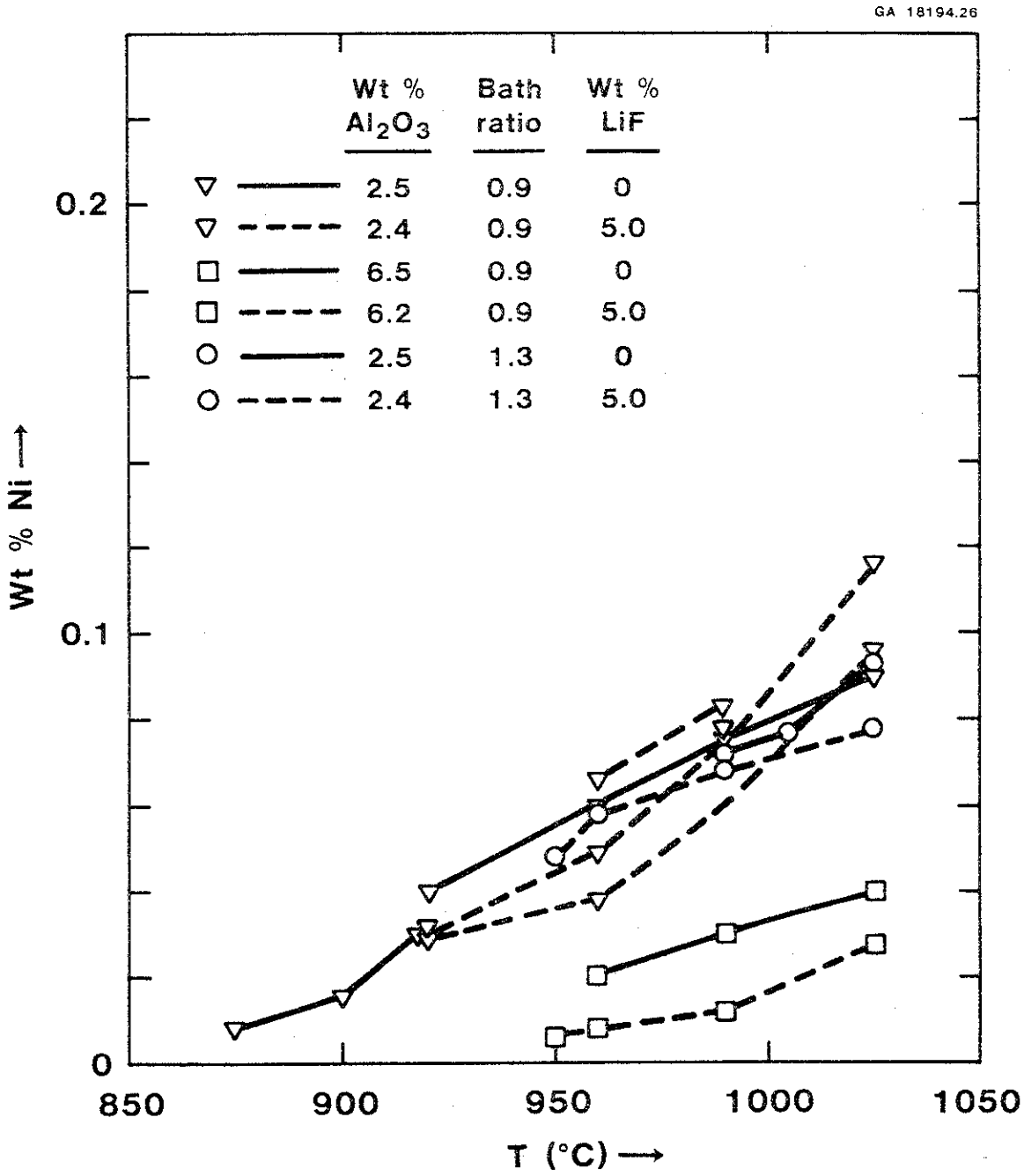

Effect of LiF Additions on the Solubility of NiO in $NaF-AlF_3-CaF_2-Al_2O_3$ Melts. All Melts Contained 1.3 wt% CaF_2.

Figure 64

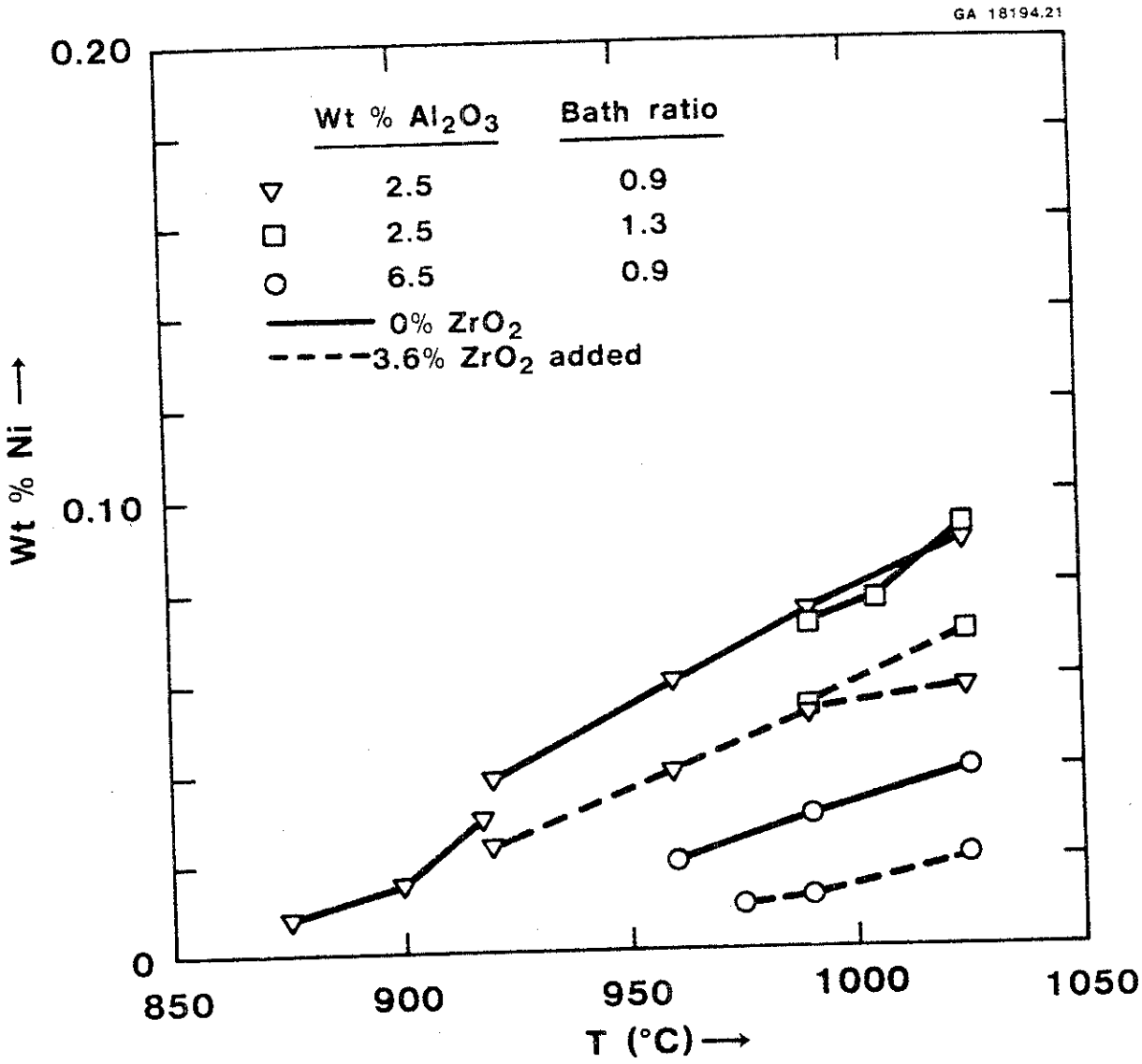

Effect of ZrO_2 Additions to the Melt on the Solubility of NiO in $NaF-AlF_3-CaF_2-Al_2O_3$ Melts. All Melts Contained 1.3 wt% CaF_2.
Figure 65

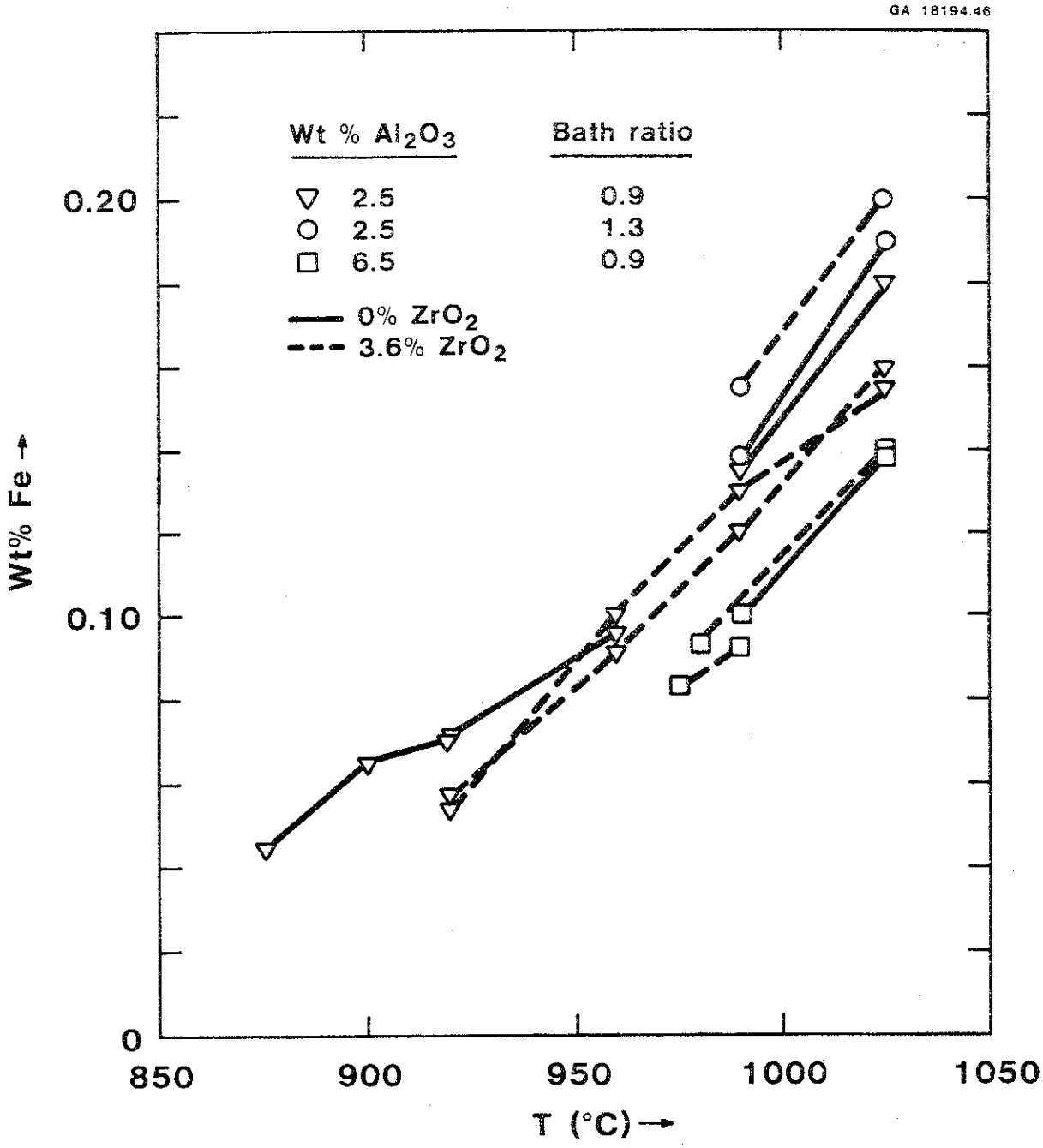

Effect of ZrO_2 Additions to the Melt on the Solubility of Fe_2O_3 in $NaF-AlF_3-CaF_2-Al_2O_3$ Melts. All Melts Contained 1.3 wt% CaF_2.

Figure 66

To properly assess the effects of ZrO_2, a comparision should be made on the basis of total oxide dissolved in the melt Al_2O_3 + ZrO_2. Analyses of melt samples for Zr showed that, at most, only half of the ZrO_2 which was added had dissolved. Figure 67 shows the ZrO_2 solubility. The data fall into two groups which correspond to the concentration of Al_2O_3 in the bath. The solubility of ZrO_2 decreases with increasing Al_2O_3, which is expected from a simple solubility product relationship for the oxides.

Using these measured solubilities for ZrO_2 and the concentrations of Al_2O_3 in the melts, the solubilities of Fe_2O_3 are shown as a function of oxygen content in the melt (Figures 68 and 69). Lines were drawn through the data for Zr-free melts. In general, the points for melts containing ZrO_2 fall within the estimated error of ± 0.01 wt.% Fe from the lines. Therefore, there is no significant additional effect of ZrO_2 other than the decrease expected from additional oxygen added to the melt. At the higher concentration of Al_2O_3 (6.5%) the solubility of ZrO_2 is so low that it makes a negligible contribution to the oxygen solubility. In conclusion, the addition of ZrO_2 to the bath will not significantly lower the solubility of Fe_2O_3 either by an intrinsic chemical effect or by the possibility of increased oxygen solubility.

The solubility of NiO is shown as a function of oxygen content in the melt in Figures 70 and 71. Lines are drawn through the data for Zr-free melts. Some of the data for melts with ZrO_2 fall within the estimated uncertainty of ± 0.005 wt.% Ni from the lines, while some are below the line by more than this uncertainty. At high Al_2O_3 contents and high bath ratios the addition of ZrO_2 decreases the NiO solubility. It is interesting that there is an effect on NiO, an oxide for which Al_2O_3 strongly affects the solubility, while there is no effect on Fe_2O_3, an oxide for which Al_2O_3 does not affect the solubility at concentrations above 2.5 wt.%.

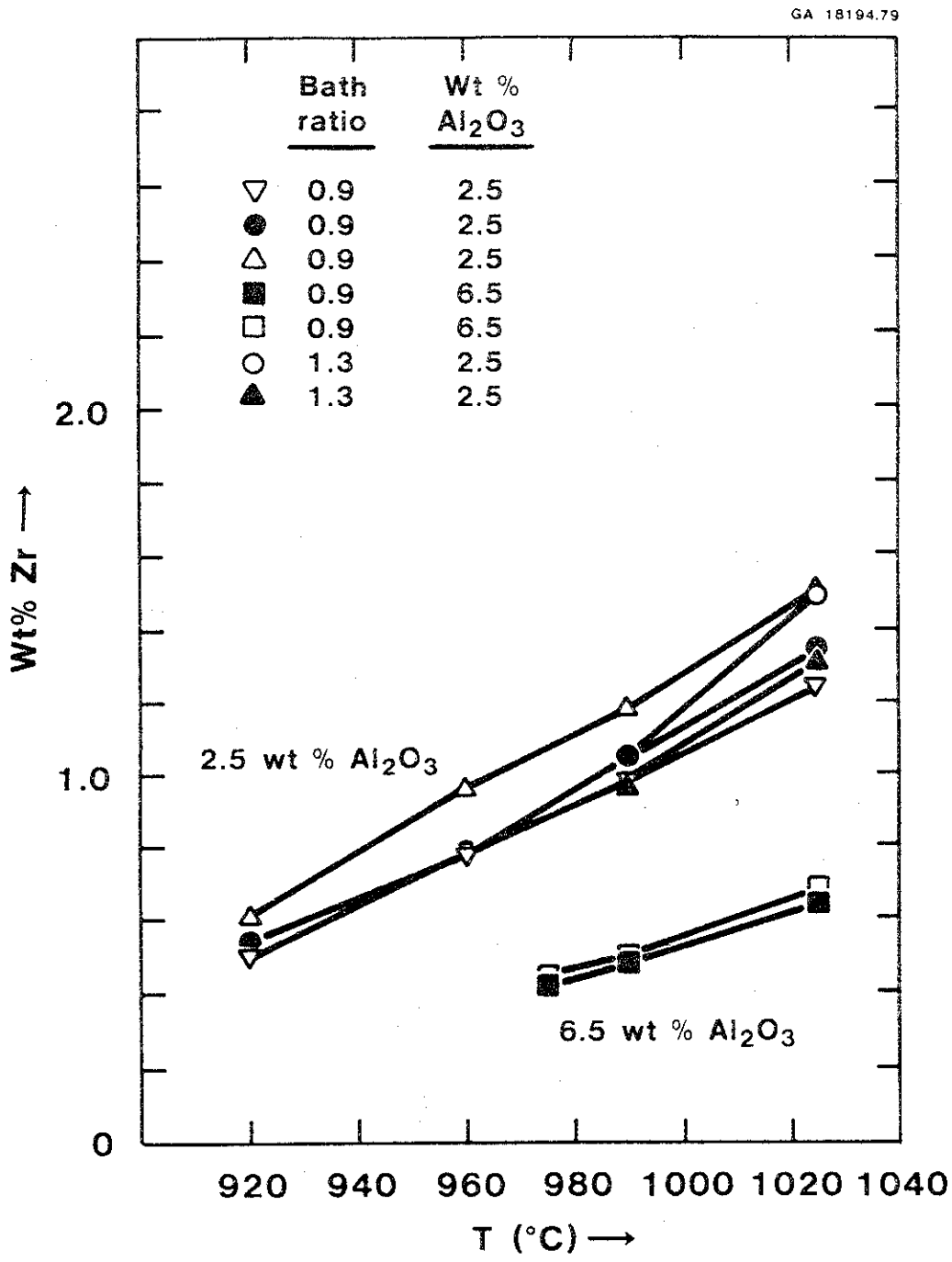

The Solubility of ZrO_2 in $NaF-AlF_3-CaF_2-Al_2O_3$ Melts Containing Small Amounts of NiO or Fe_2O_3. All Melts Contained Approximately 1.3 Wt % CaF_2

Figure 67

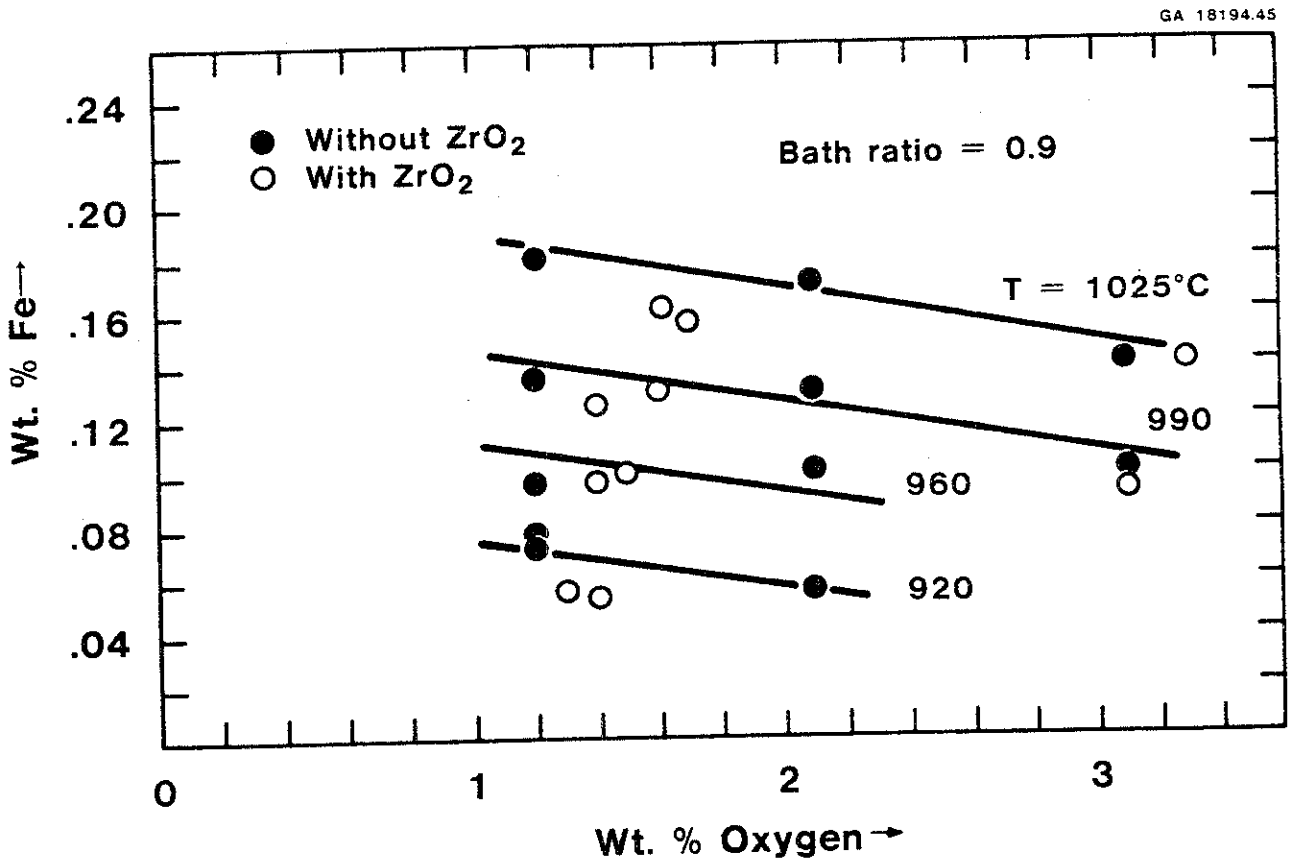

The Solubility of Fe_2O_3 in $NaF-AlF_3-CaF_2-Al_2O_3-ZrO_2$ Melts with Bath Ratios of 0.9.
Figure 68

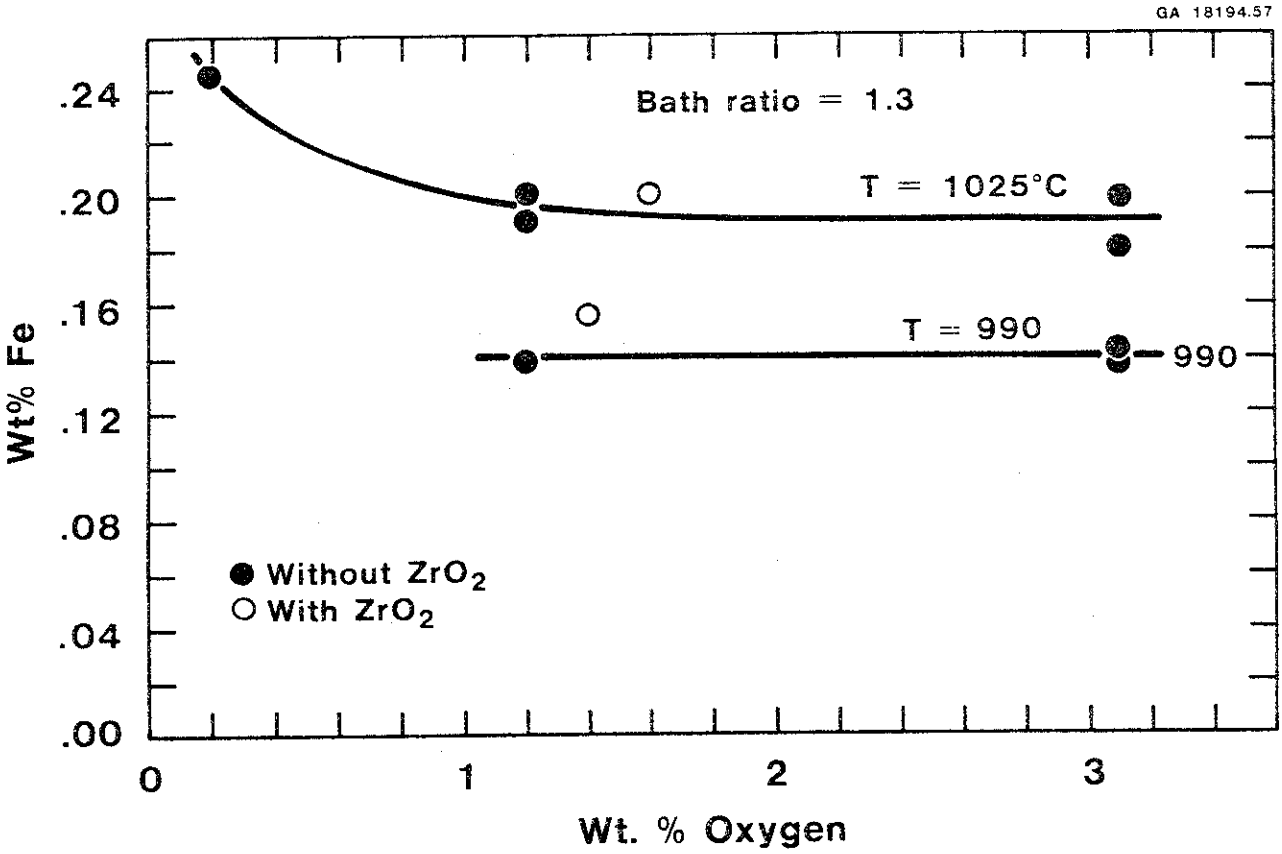

The Solubility of Fe_2O_3 in $NaF-AlF_3-CaF_2-Al_2O_3-ZrO_2$ Melts with Bath Ratios of 1.3.

Figure 69

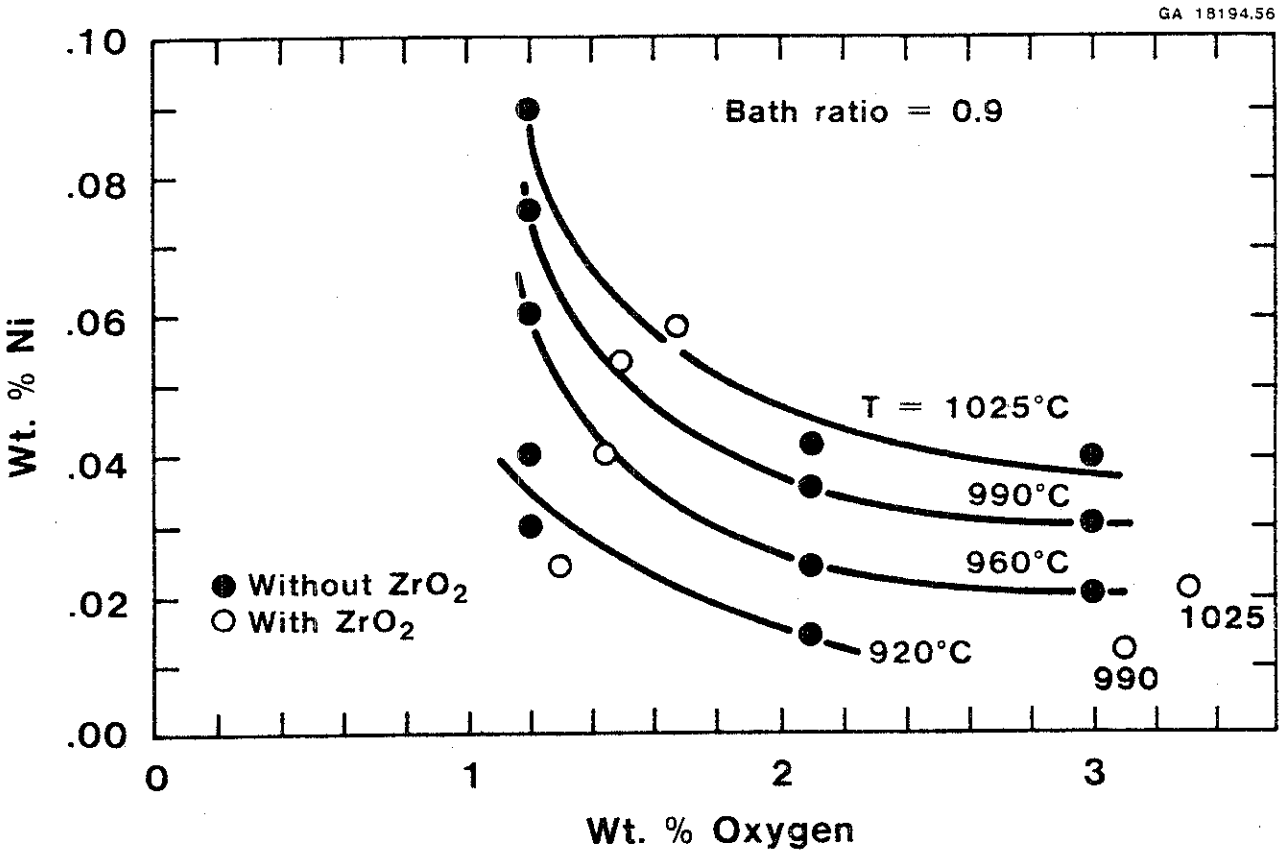

The Solubility of NiO in $NaF-AlF_3-CaF_2-Al_2O_3-ZrO_2$ Melts with Bath Ratios of 0.9.

Figure 70

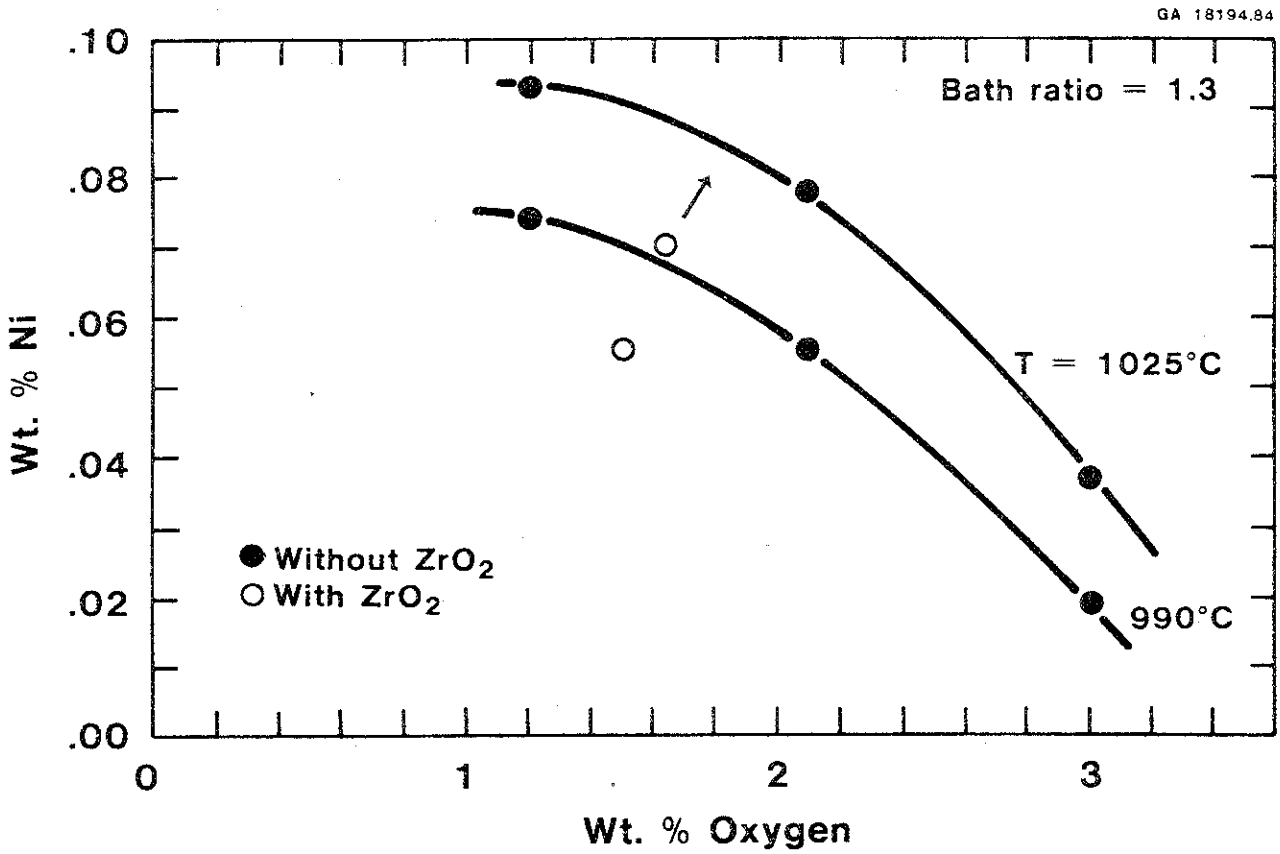

The Solubility of NiO in $NaF-AlF_3-CaF_2-Al_2O_3-ZrO_2$ Melts with Bath Ratios of 1.3.

Figure 71

f) Effects of combined additions of basic fluorides: Very low solubilities of NiO and Fe_2O_3 were measured for baths with low bath ratios (0.7 to 0.9) and at low temperatures (760-920°C). However, bench scale Hall cell tests (4) showed that under these conditions the oxides in the inert anode material react to form fluorides which are very soluble in Hall cell bath. This resulted from the relatively high aluminum fluoride activity at low bath ratios and low temperatures. Therefore, it was reasoned that low-melting baths obtained by additions of basic fluorides might offer low inert anode solubilities and relatively low aluminum fluoride activities so as to prevent fluorination of the inert anode. Therefore solubilities of NiO and Fe_2O_3 were measured in melts containing additions of 4-6% of CaF_2, MgF_2 and LiF.

Table 29 shows the compositions of melts which were tested and the liquidus temperatures of these melts obtained using the "Bath Properties" computer program (58). Compositions were chosen to obtain a liquidus temperature just below 920°C. As shown in Table 29, the molar basicities ranged from 3.13 to 3.92. For comparison, by the definition given in Table 27, the molar basicity of pure cryolite would be 3.00 and the molar basicity of a "standard" bath with a 1.0 bath ratio containing 2.5 wt.% Al_2O_3 and 1.3 wt.% CaF_2 is 2.26. Thus the melts tested were quite basic and should have rather low activities of AlF_3.

The results for the solubility measurements in these high basic fluoride melts are given in Figures 72-77. Previous results for melts of the appropriate compositions are presented for comparison.

The results for Composition HB-1 (bath ratio = 1.1) are shown in Figures 72 and 73. At temperatures below 990°C, solubilities of NiO and Fe_2O_3 in the high basic fluoride bath were moderately lower than in the comparable melts without the

TABLE 29

High Basic Fluoride Melts Used for Solubility Measurements

Composition Number	Bath Ratio	CaF_2 wt.%	MgF_2 wt.%	LiF wt.%	Al_2O_3 wt.%	Liquidus Temperature °C	Molar Basicity
HB-1	1.1	5.0	5.0	4.0	2.5	919	3.13
HB-2	1.2	4.0	4.0	6.0	2.5	917	3.42
HB-3	1.3	5.0	6.0	6.0	2.5	913	3.92

Molar Basicity = $(X_{NaF} + X_{LiF} + X_{MgF_2})/(X_{AlF_3})$

X_i = mole fraction i

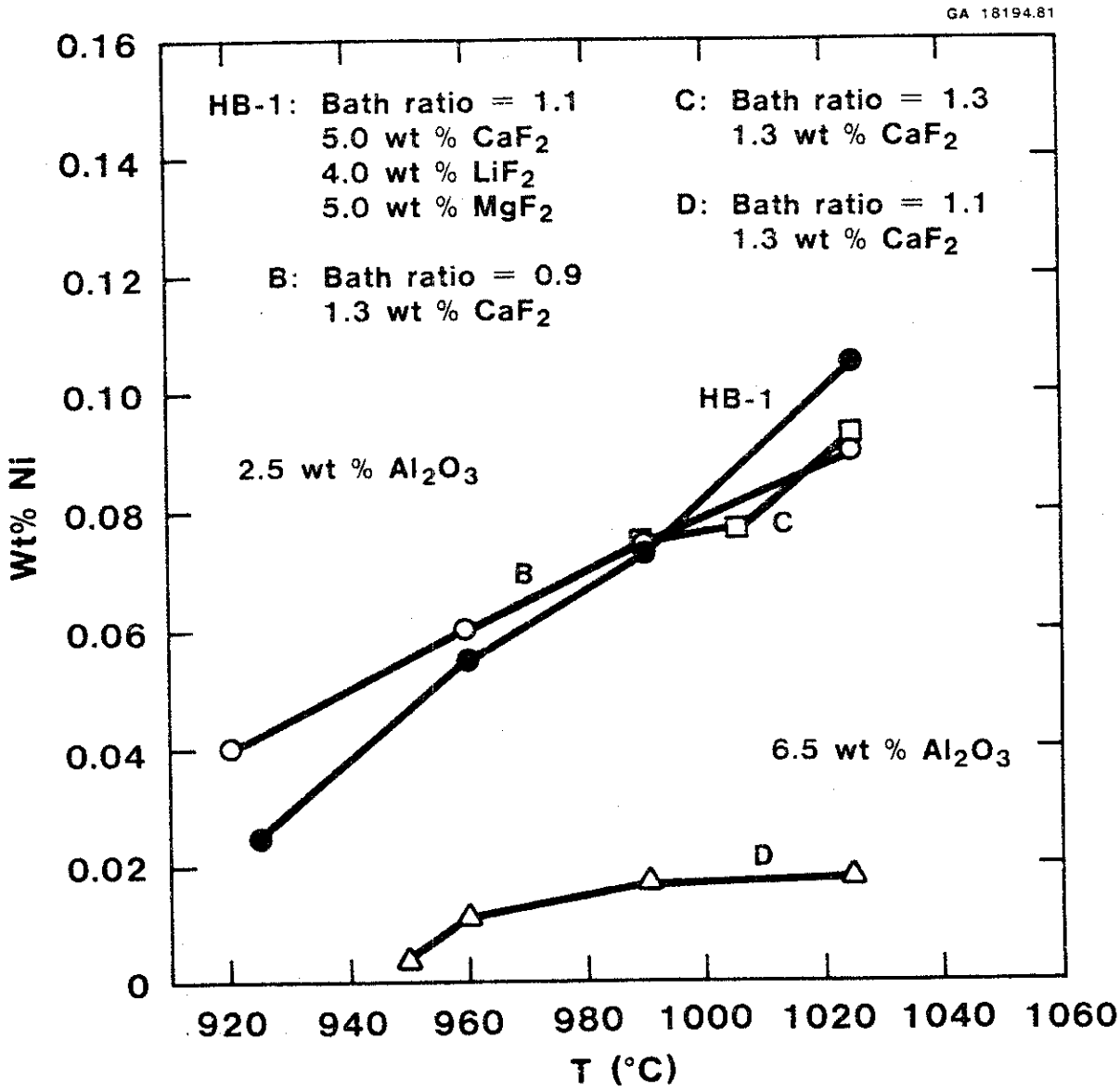

Effect of Combined Additions of CaF_2, MgF_2, and LiF on the Solubility of NiO in NaF-AlF_3-Al_2O_3 Melts.

Figure 72

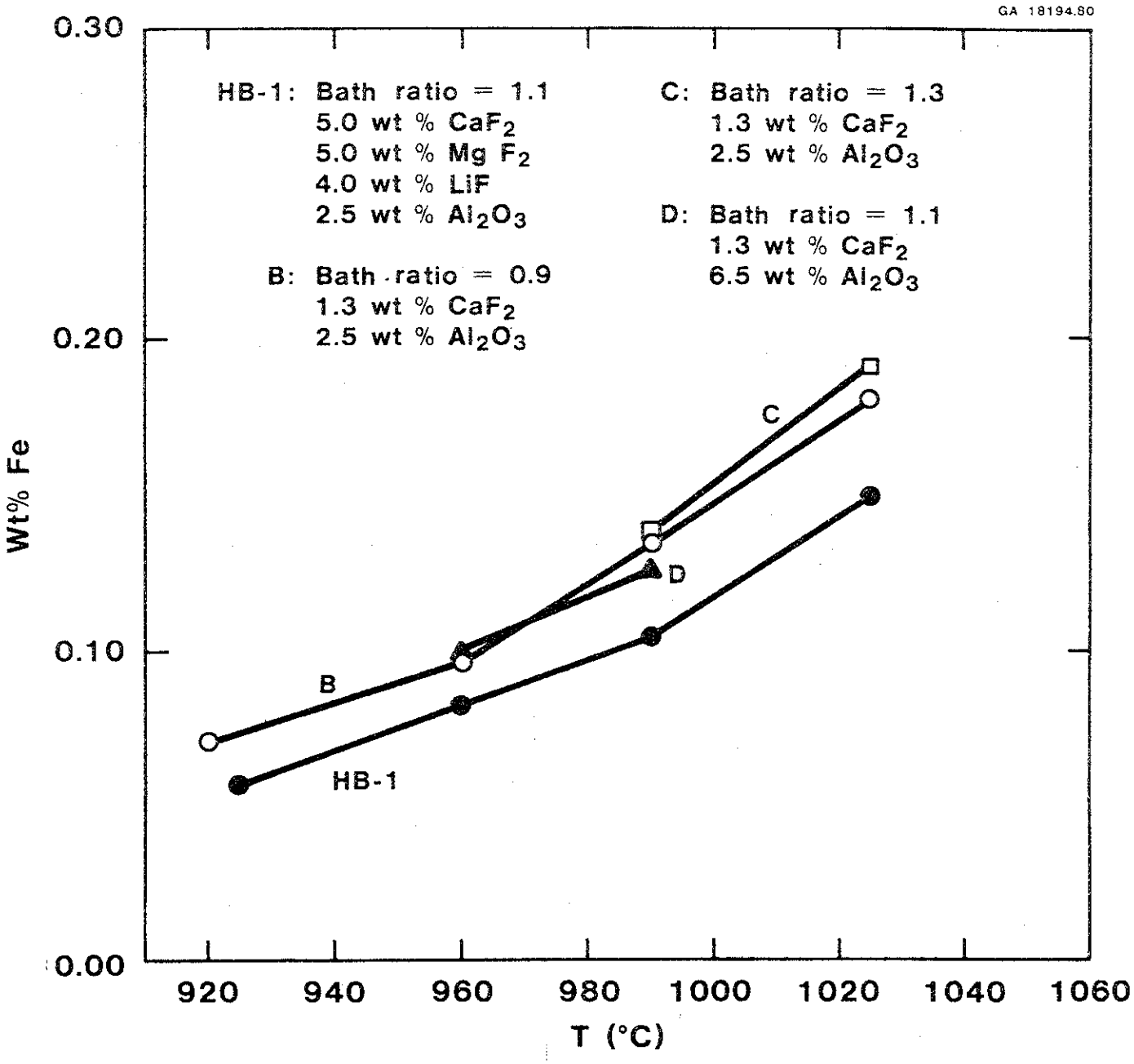

Effect of Combined Additions of CaF_2, MgF_2, and LiF on the Solubility of Fe_2O_3 in $NaF-AlF_3-Al_2O_3$ Melts.
Figure 73

basic fluoride additions. However, it is important to note that for NiO (Figure 72) a much lower solubility is achieved in the high alumina melt. It is concluded that this high basic fluoride melt offers no advantage for inert anode operation.

The results for composition HB-2 are shown in Figures 74 and 75. These plots show that the solubilities are somewhat decreased by the additions of basic fluorides, though as seen in Figure 74 a lower solubility of NiO can be achieved by an addition of Al_2O_3. The solubility of Fe_2O_3 in the "standard" melt was not significantly changed by further additions of Al_2O_3 above 2.5 wt.%. Therefore, it is concluded that additions of the basic fluorides offer some improvement for Fe_2O_3, but no improvement for NiO.

Figures 76 and 77 show the results for bath composition HB-3. The conclusions are identical to those given for composition HB-2. The addition of the basic fluorides did not decrease the solubility of NiO, as can be seen in Figure 76. Also shown is the greatly decreased solubility in the melt containing 6.5 wt.% Al_2O_3. As shown in Figure 77, the basic fluoride additions do decrease the solubility of Fe_2O_3 while the addition of Al_2O_3 has a negligible effect. Thus, the basic fluoride additions offer some improvement for Fe_2O_3, but do not yield an improvement for NiO.

Table 30 gives the analyzed compositions of the high basic fluoride melts. In general, the concentrations of Ca and Mg are slightly lower than the charged concentrations, and the concentrations of Li are equal to, or slightly higher than the charged concentrations. Overall, the discrepancies between analyzed and charged concentrations are not large.

Additions of MgF_2, CaF_2 and LiF generally decreased the solubility of Al_2O_3. It is not unreasonable to expect they would

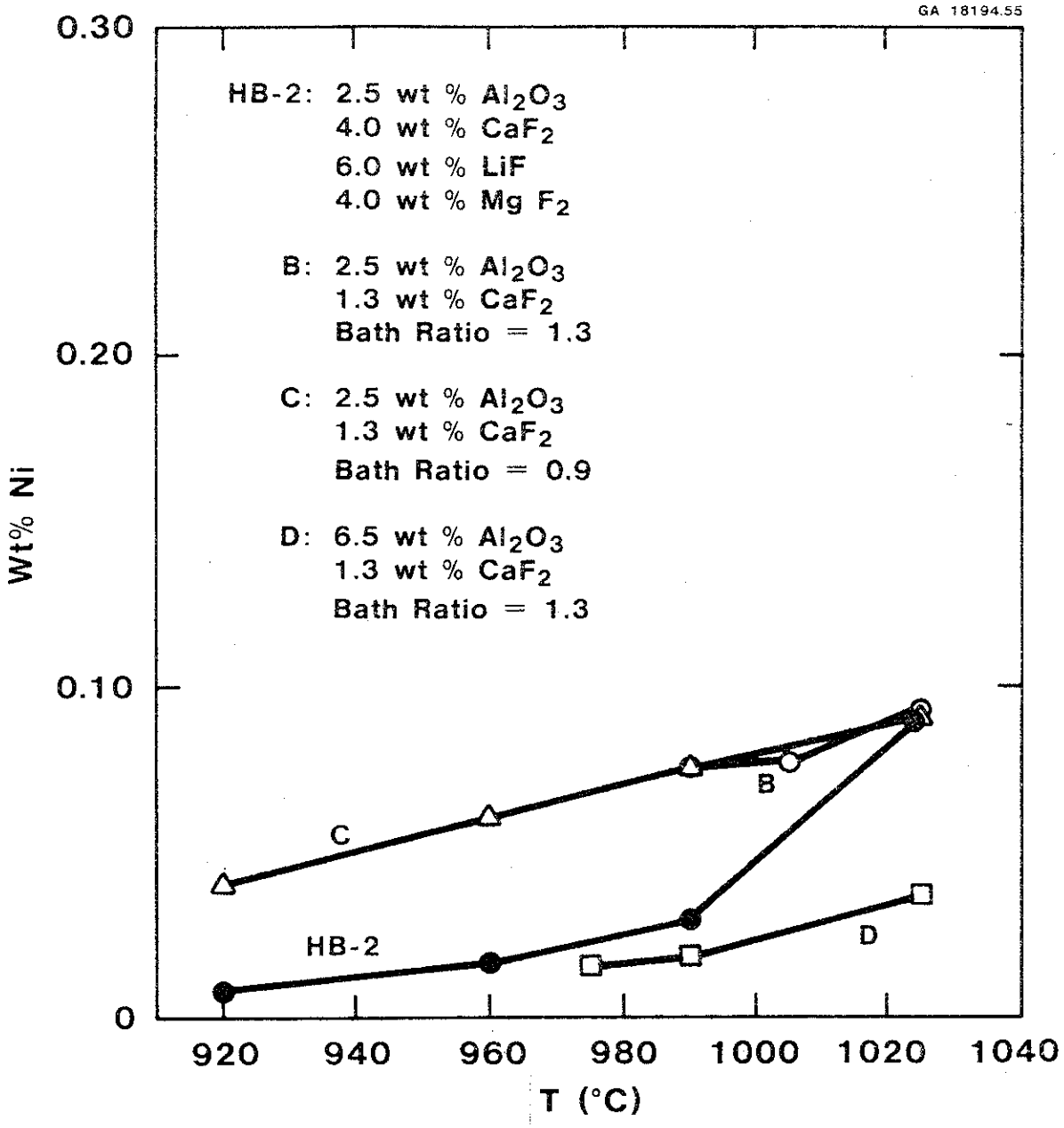

Effect of Combined Additions of CaF_2, MgF_2, and LiF on the Solubility of NiO in $NaF-AlF_3-Al_2O_3$ Melts.

Figure 74

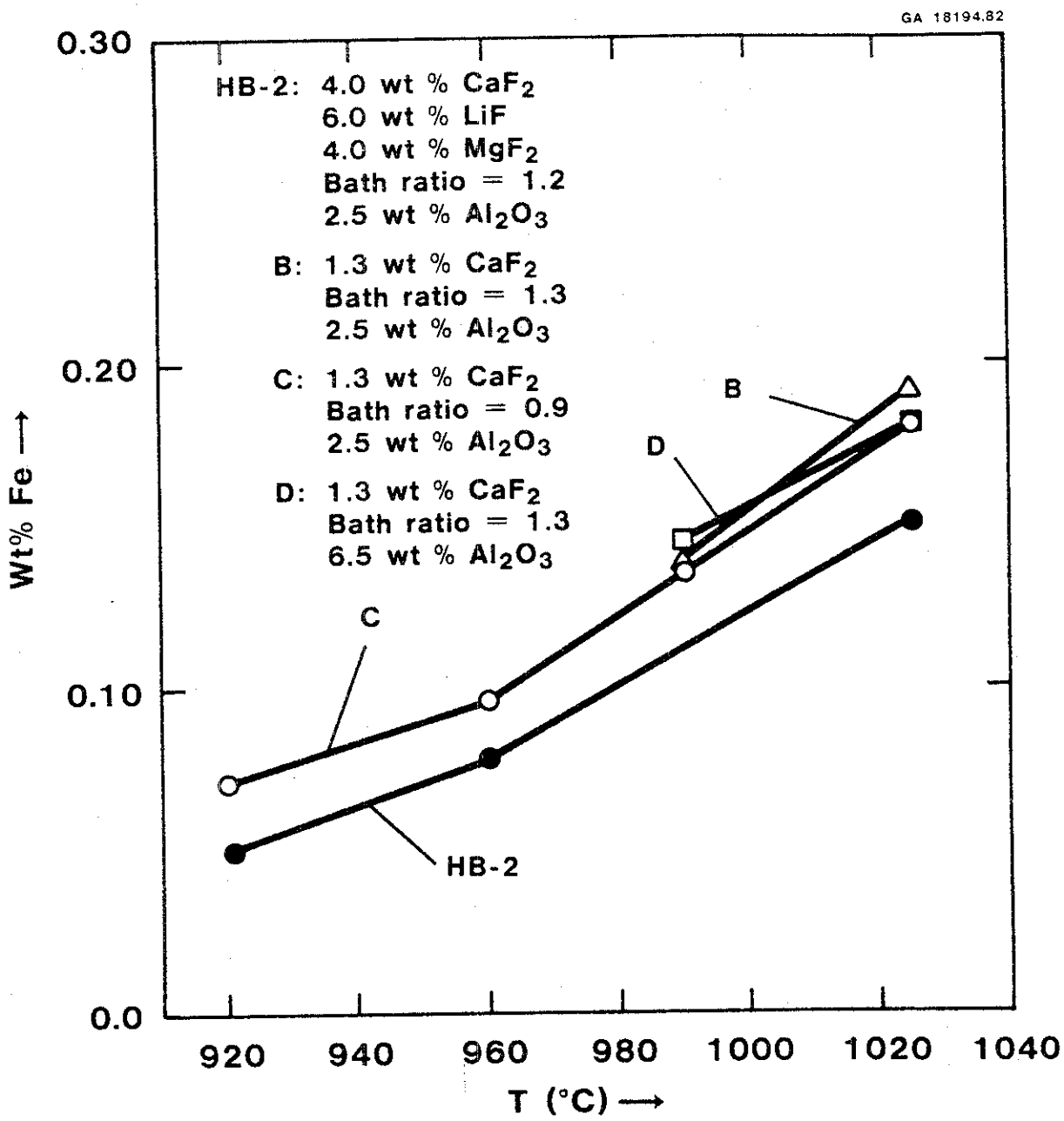

Effect of Combined Additions of CaF_2, MgF_2, and LiF on the Solubility of Fe_2O_3 in NaF-AlF_3-Al_2O_3 Melts
Figure 75

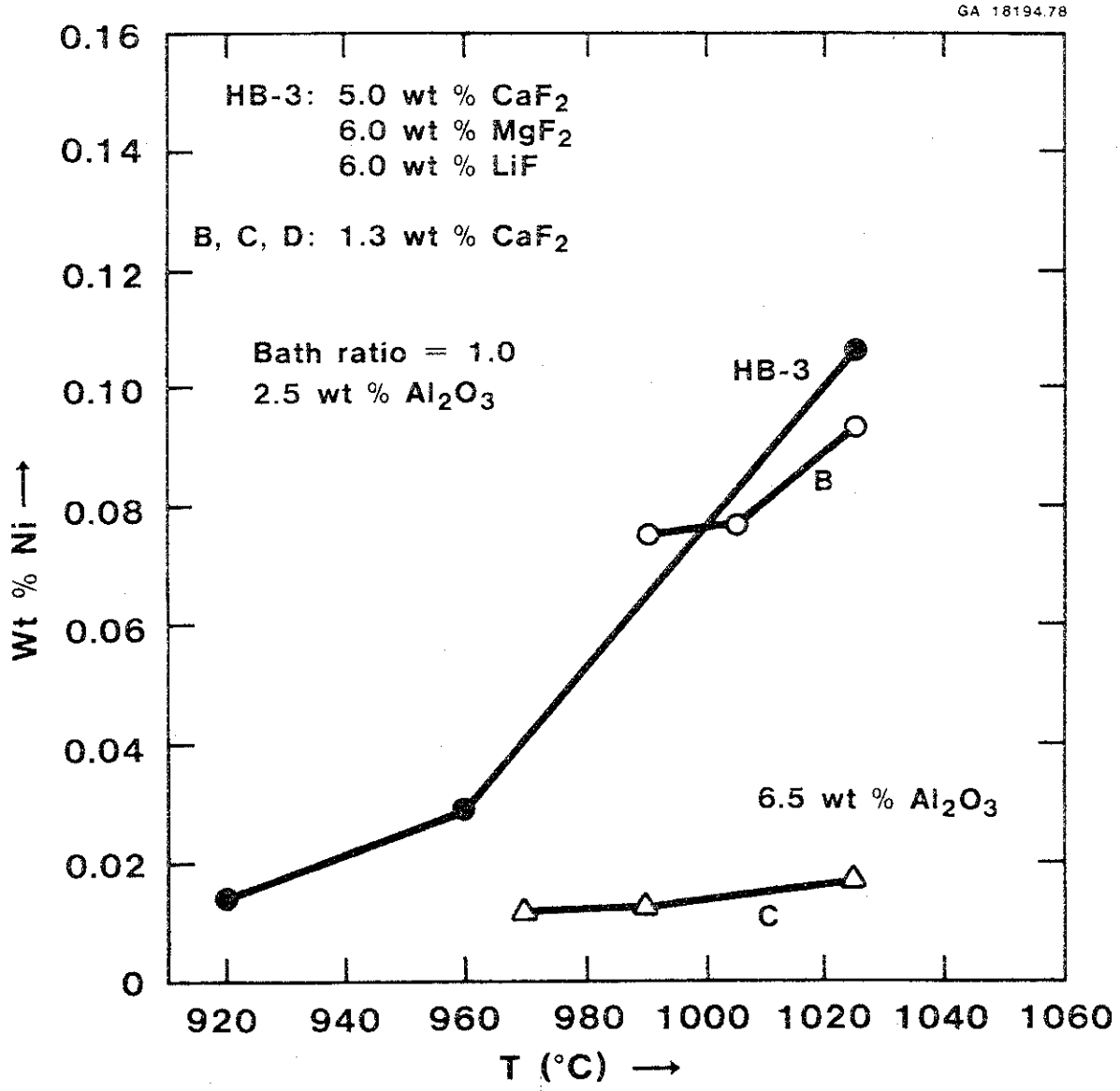

Effect of Combined Additions of CaF_2, MgF_2, and LiF on the Solubility of NiO in NaF-AlF_3-Al_2O_3 Melts

Figure 76

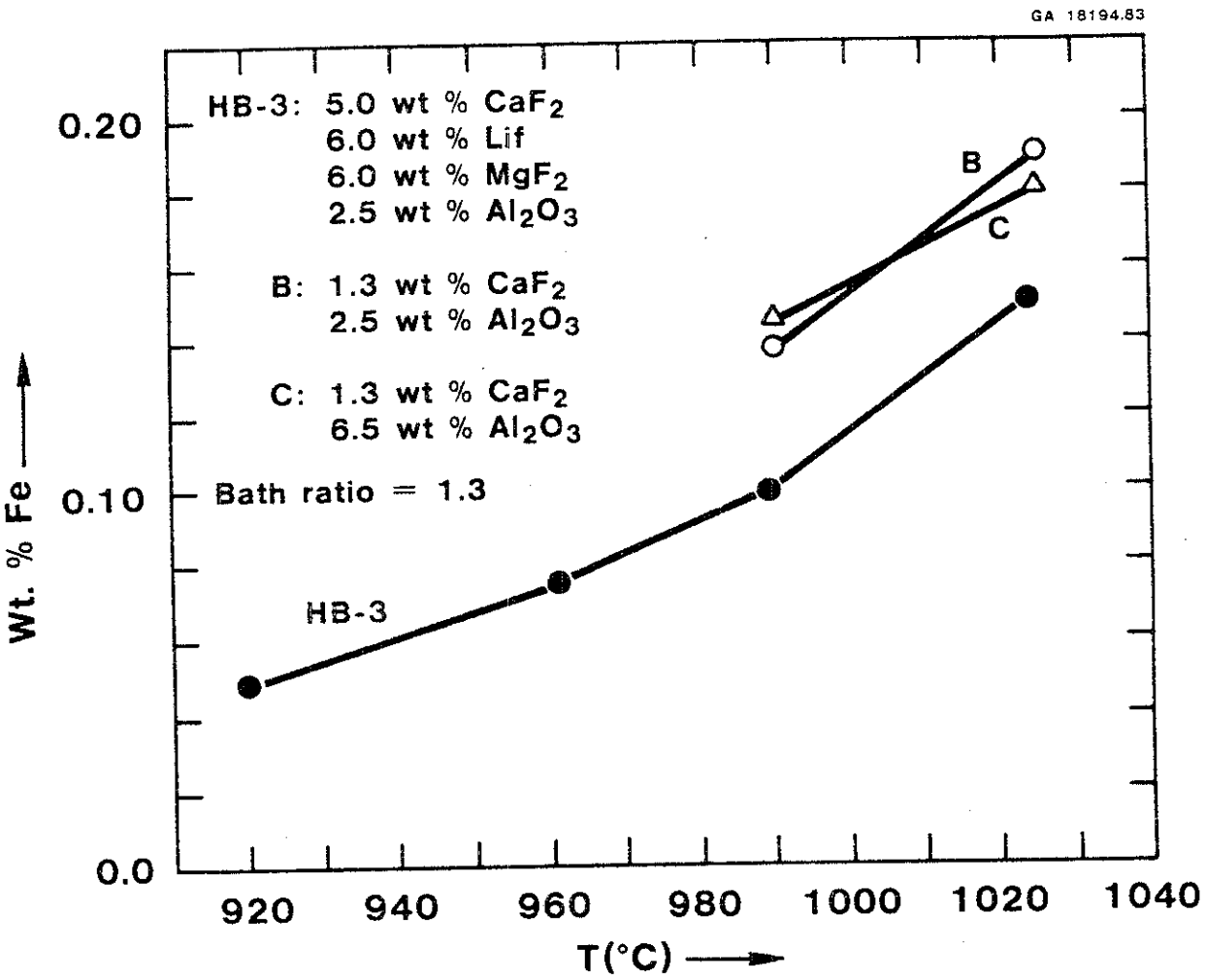

Effect of Combined Additions of CaF_2, MgF_2, and LiF on the Solubility of Fe_2O_3 in NaF-AlF_3-Al_2O_3 Melts
Figure 77

TABLE 30

Sample Analyses for High Basic Fluoride Baths

Sample No.	Composition Number	Analyzed Concentrations wt.%			Charged Concentrations wt.%		
		Ca	Mg	Li	Ca	Mg	Li
74-4	HB-1	2.36	1.64	0.95	2.56	1.95	1.07
5		2.40	1.64	0.96			
9		2.36	1.64	0.96			
10		2.43	1.68	0.98			
16		2.46	1.71	0.98			
17		2.32	1.58	0.94			
22		2.41	1.67	0.99			
23		2.40	1.66	0.99			
75-5	HB-1	2.33	1.63	1.31	2.56	1.95	1.07
6		2.35	1.63	1.33			
9		2.34	1.63	1.35			
12		2.35	1.63	1.30			
15		2.20	1.41	1.37			
18		2.19	1.39	1.13			
20		2.21	1.41	1.11			
21		2.22	1.43	1.07			
76-4	HB-3	2.38	2.14	1.94	2.56	2.34	1.60
5		2.38	2.12	1.65			
11		2.40	2.11	1.70			
13		2.37	2.08	1.39			
16		2.40	2.12	1.69			
17		2.40	2.16	2.00			
77-4	HB-3	2.41	2.14	1.53	2.56	2.34	1.60
7		2.44	2.14	1.54			
10		2.46	2.13	1.55			
13		2.47	2.14	1.52			
17		2.49	2.15	1.53			
20		2.50	2.16	1.52			
23		2.43	2.16	1.55			
24		2.36	2.15	1.52			
78-4	HB-2	2.04	1.54	1.58	2.05	1.56	1.60
7		2.04	1.56	1.54			
10		2.10	1.56	1.56			
13		2.10	1.55	1.56			
16		2.10	1.56	1.57			
19		2.08	1.56	1.56			
79-4	HB-2	2.03	1.50	1.60	2.05	1.56	1.60
7		2.05	1.50	1.59			
10		2.06	1.51	1.60			
13		2.04	1.50	1.61			
16		2.10	1.52	1.62			
19		2.10	1.52	1.61			
21		2.13	1.54	1.63			
22		2.12	1.53	1.63			

decrease the solubilities of other oxides. However, it can be generalized from the above data that for NiO the effect of Al_2O_3 additions in decreasing the solubility is much stronger than the effect of basic fluoride additions. Hence, the gain achieved by basic fluoride additions is more than offset by the decreased alumina solubility. This is not true for Fe_2O_3 where a modest decrease in solubility resulting from the basic fluoride additions is not offset by the decreased alumina solubility.

3) Alternate Anode Materials

As will be shown later in the report, the rate at which the anode materials dissolve is limited by the mass transport of the dissolution products away from the anode-bath interface through the hydrodynamic boundary layer. That is, the rate of dissolution can be described by the equation

$$\text{Rate} = k\,(C_s - C_b) \qquad (31)$$

where k is a constant, C_s is the solubility of the oxide in the electrolyte, and C_b is the bulk concentration of the dissolving species in the electrolyte. One way to reduce the dissolution rate is to reduce C_s, the solubility. The goal of this portion of the program was to reduce C_s by identifying new materials or by doping the nickel ferrite. Accordingly, this part of the program was divided into two segments. The goal was pursued by identifying dopants and potential new oxides, fabricating small pellets of the materials, and measuring their solubilities in Hall cell bath.

a) New Materials

Material Selection: Two systems were chosen for investigation; cobalt-based and chromium-based oxides. These systems were chosen because the solubility of the pure oxides Co_3O_4 and Cr_2O_3 in cryolite are quite low and these materials

form relatively stable double oxides with other species. Table 31 gives solubilities for some oxides which were reported by Grjotheim (1), and shows that solubilities of Co_3O_4 and Cr_2O_3 are quite low. The free energies of formation of some double oxides involving cobalt and chromium oxides are given in Table 32. These data were obtained from Kubaschewski (56). The double oxides given were chosen for further investigation because their free energies of formation from the simple oxides are all more negative than that for $NiFe_2O_4$. Hence, in one sense, they are more stable. The materials chosen for solubility tests are given in Table 33.

Fabrication: Table 33 also gives the mixtures used to fabricate these materials. Tables 34 and 35 give the fabrication procedures for the cobalt and chromium oxides, respectively. Also given are the results of X-ray diffraction analyses of the material after each fabrication sequence, and resulting densities. Table 36 gives the sources of raw materials used in this work. In general, chemically pure oxides were mixed, pressed and sintered in air. A binder (isostearic acid) was necessary for only the pure Co_3O_4 and $CoCr_2O_4$ materials. For the cobalt-based materials, a sintering temperature of 1350°C was required to obtain single-phase materials. For the chromium-based materials, a sintering temperature of 1450°C was required to produce single-phase Cr_2O_3 and $CoCr_2O_4$, while single-phase $NiCr_2O_4$ and Ce_2O_3-Cr_2O_3 were not produced. The synthesis of single-phase $NiCr_2O_4$ was not pursued further because of the limited time available for this part of the project.

X-ray diffraction analyses showed no reaction occurred between CeO_2 and Cr_2O_3 during the high-temperature sinter. There appeared to have been some reaction at 1350°C (major unidentified phase, Table 35), but no reaction occurred at 1450°C. A cerium oxide-chromium oxide double oxide has been reported to be relatively stable (56). The original

TABLE 31

Solubilities for Oxides in Cryolite
5% Al_2O_3 Bath at 960°C
Reported by Grjotheim (1)

Oxide	Solubility, Wt.%
Co_3O_4	0.140
Cr_2O_3	0.050
NiO	0.18
Fe_2O_3	0.003

TABLE 32

Free Energy of Formation of Some Double Oxides

Reaction	ΔG° @ 960°C (cal/mole)
$CoO + Fe_2O_3 = CoFe_2O_4$	- 7,800 ± 1000
$CoO + Cr_2O_3 = CoCr_2O_4$	-11,700 ± 900
$NiO + Cr_2O_3 = NiCr_2O_4$	-10,300
$Ce_2O_3 + Cr_2O_3 = Ce_2O_3 \cdot Cr_2O_3$	-27,400 ± 2000
$NiO + Fe_2O_3 = NiFe_2O_4$	- 5,900 ± 1000

TABLE 33

Formulation of New Material

	Starting Mixture				
Oxide	Co_2O_3	Cr_2O_3	NiO	Fe_2O_3	CeO_2
CoO*	100				
$CoFe_2O_4$	34.2			65.8	
$Co_{0.5}Ni_{0.5}Fe_2O_4$	17.4		15.7	67.0	
$Co_{0.25}Ni_{0.25}Fe_2O_4$	8.8		23.7	67.5	
Cr_2O_3		100			
$CoCr_2O_4$**	35.3	67.7			
$NiCr_2O_4$		67.1	32.9		
$Ce_2O_3 \cdot Cr_2O_3$		30.6			69.4

*Used 1 drop (approximately 0.017 g) isostearic acid/g mixture as a binder.

**Used 2 drops (approximately 0.034 g) isostearic acid/g as a binder.

TABLE 34

X-ray Diffraction Results and Densities for Cobalt-Based Materials

Fabrication Procedure	Sample No.	Oxide	X-ray Diffraction Results	Density g/cm^3
1. Presintered mixed oxides in air at 1125°C for 12 hours, furnace-cooled.	557112	CoO	Major CoO, Major Co_3O_4	
	557113	$CoFe_2O_4$	Entirely $CoFe_2O_4$	
	557114	$Co_{0.5}Ni_{0.5}Fe_2O_4$	Major structure similar to $CoFe_2O_4$ or $NiFe_2O_4$, Major alpha Fe_2O_3	
	557115	$Co_{0.25}Ni_{0.75}Fe_2O_4$	Same as above.	
2. Pressed presintered oxides, sintered in air at 1200°C for 24 hours.	557112	CoO	Major CoO, Minor Co_3O_4	3.83
	557113	$CoFe_2O_4$	Major $CoFe_2O_4$, trace possible Fe_2O_3	3.75
	557114	$Co_{0.5}Ni_{0.5}Fe_2O_4$	Major single phase (Co,Ni) Fe_2O_4 trace possible Fe_2O_3	3.66
	557115	$Co_{0.25}Ni_{0.75}Fe_2O_4$	Same as above.	
3. Pressed presintered oxides, sintered in air at 1200°C for 24 hours, air-quenched.	557112	CoO	Entirely CoO	
4. Pressed presintered oxides, sintered in air at 1350°C for 24 hours, air-quenched.	557112	CoO	Entirely CoO	4.57
	557113	$CoFe_2O_4$	Single phase (looks like cobalt iron oxide; $CoFe_2O_4$)	4.55
	557114	$Co_{0.5}Ni_{0.5}Fe_2O_4$	Single phase (looks like cobalt iron oxide; $CoFe_2O_4$. Slight shift probably caused by Ni)	4.51
	557115	$Co_{0.25}Ni_{0.75}Fe_2O_4$	Same as above.	4.30

TABLE 35

X-ray Diffraction Results and Densities for Chromium-Based Materials

Fabrication Procedure	Sample No.	Oxide	X-ray Diffraction Results	Density g/cm^3
1. Presintered mixed oxides in air at 1125°C for 17 hours, furnace cooled.	557132	$CoCr_2O_4$	Major single phase resembling $CoCr_2O_4$, but shifted.	
	557133	$NiCr_2O_4$	Major $NiCrO_3$ type phase, major $NiCr_2O_4$ type phase.	
	557134	Ce_2O_3-Cr_2O_3	Major CeO_2, Major Cr_2O_3	
	557529	Cr_2O_3	Major Cr_2O_3, Minor nearly identical to Cr_2O_3, but slightly shifted.	
2. Pressed presintered oxides, sintered in air at 1350°C for hours, furnace-cooled.	557132	$CoCr_2O_4$	Major single phase resembling $CoCr_2O_4$, but shifted.	3.06
	557133	$NiCr_2O_4$	Major $NiCr_2O_4$, Trace Cr_2O_3	3.61
	557134	Ce_2O_3-Cr_2O_3	Major CeO_2, Minor Cr_2O_3	3.97
3. Pressed presintered oxides, sintered in air at 1350°C for 24 hours, air-quenched.	557132	$CoCr_2O_4$	Major $CoCr_2O_4$, trace unidentified.	
	557133	$NiCr_2O_4$	Major $NiCr_2O_4$, trace Cr_2O_3, trace inidentified.	
	557134	Ce_2O_3-Cr_2O_3	Major unidentified (possible single phase not indexed), Minor Cr_2O_3	
4. Pressed presintered oxides, sintered in air at 1350°C for 24 hours, air-quench, grind to -325 mesh, press, sinter in air at 1450°C for 24 hours, air quench.	557132	$CoCr_2O_4$	Entirely $CoCr_2O_4$	
	557133	$NiCr_2O_4$	Major $NiCr_2O_4$, trace CrO_2	
	557134	Ce_2O_3-Cr_2O_3	Major CeO_2, major Cr^2O^3	
5. Sinter oxide in air at 1450°C for 24 hours.	578657	Cr_2O_3	Entirely Cr_2O_3	

TABLE 36

Raw Materials Used for Cobalt and Chromium Oxides

Cobalt (III) Ozide, Co_2O_3
Alpha No. 23129

Fe_2O_3
MCB Reagents FX-230
99% Fe_2O_3 minimum

NiO
Fisher N-69
99.6% NiO

Cr_2O_3
Fisher C-334
99.4% Cr_2O_3

CeO_2
Alpha Products 21109
99.9% CeO_2

reference (59) to the thermodynamic data was then obtained, and it was found that $CeCrO_3$ ($Ce_2O_3 \cdot Cr_2O_3$) is not stable in air, so the reaction

$$2\ CeO_2 + Cr_2O_3 \rightarrow 2\ CeCrO_3 + 1/2\ O_2 \qquad (32)$$

will not occur. This is consistent with the present results and means that the double oxide $CeCrO_3$ ($Ce_2O_3 \cdot Cr_2O_3$) is not a feasible inert anode material.

A procedure for fabrication of $CuFe_2O_4$ was developed during this study (11), although time did not permit solubility tests to be made on this material. It was found that pellets of $CuFe_2O_4$ could be produced by sintering reagent grade $CuFe_2O_4$ at 900°C or by pre-sintering CuO and Fe_2O_3 at 1125°C, then sintering at 900°C for a much longer time than the presinter. The low-temperature final sinter is necessary to avoid liquid formation. The phase diagram for the system shows that liquid can form above 1015°C.

Solubility tests: These tests were conducted by procedures described earlier. Tests were made in a cryolite-based melt contained in a platinum crucible in an air atmosphere over the range of temperature of 960 to 1025°C.

Results for cobalt oxide-containing materials are shown in Figures 78, 79 and 80, and are compared with earlier results for Fe_2O_3, NiO, and $NiFe_2O_4$. The results for the cobalt-containing materials presented in these figures are from the same experiments, but are presented separately for clarity. Figures 78, 79 and 80 give iron, cobalt and nickel concentrations in the saturated baths, respectively. Figure 78 shows that the iron solubilities of the cobalt ferrites are significantly less than for Fe_2O_3, but not significantly different from that of nickel ferrite. Therefore, considering iron, the cobalt-containing materials are not significantly

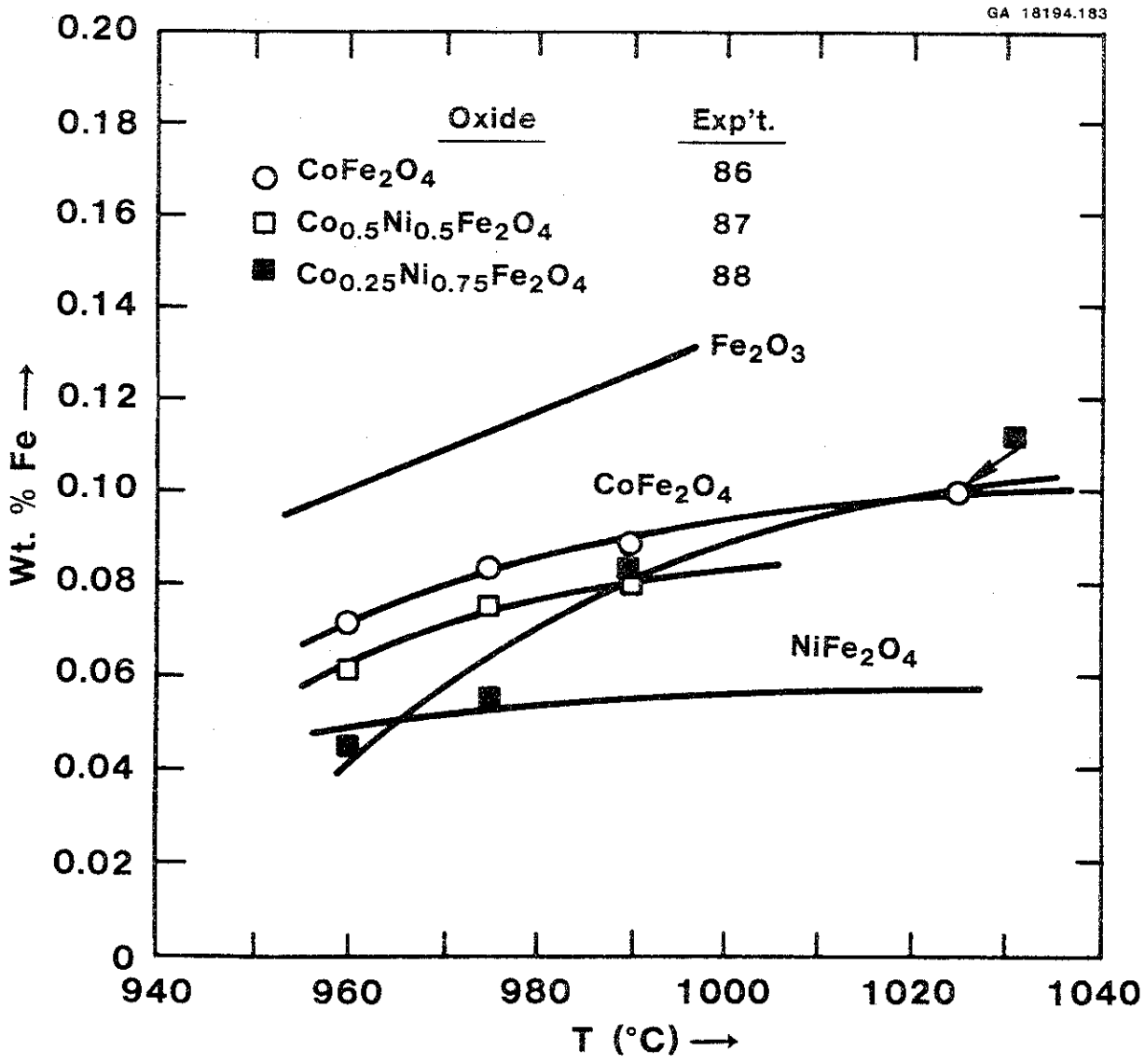

Iron Solubility from Cobalt-Nickel Ferrites in Hall Cell Bath of Composition 6.5% Al_2O_3, 1.3% CaF_2, Bath Ratio 1.1

Figure 78

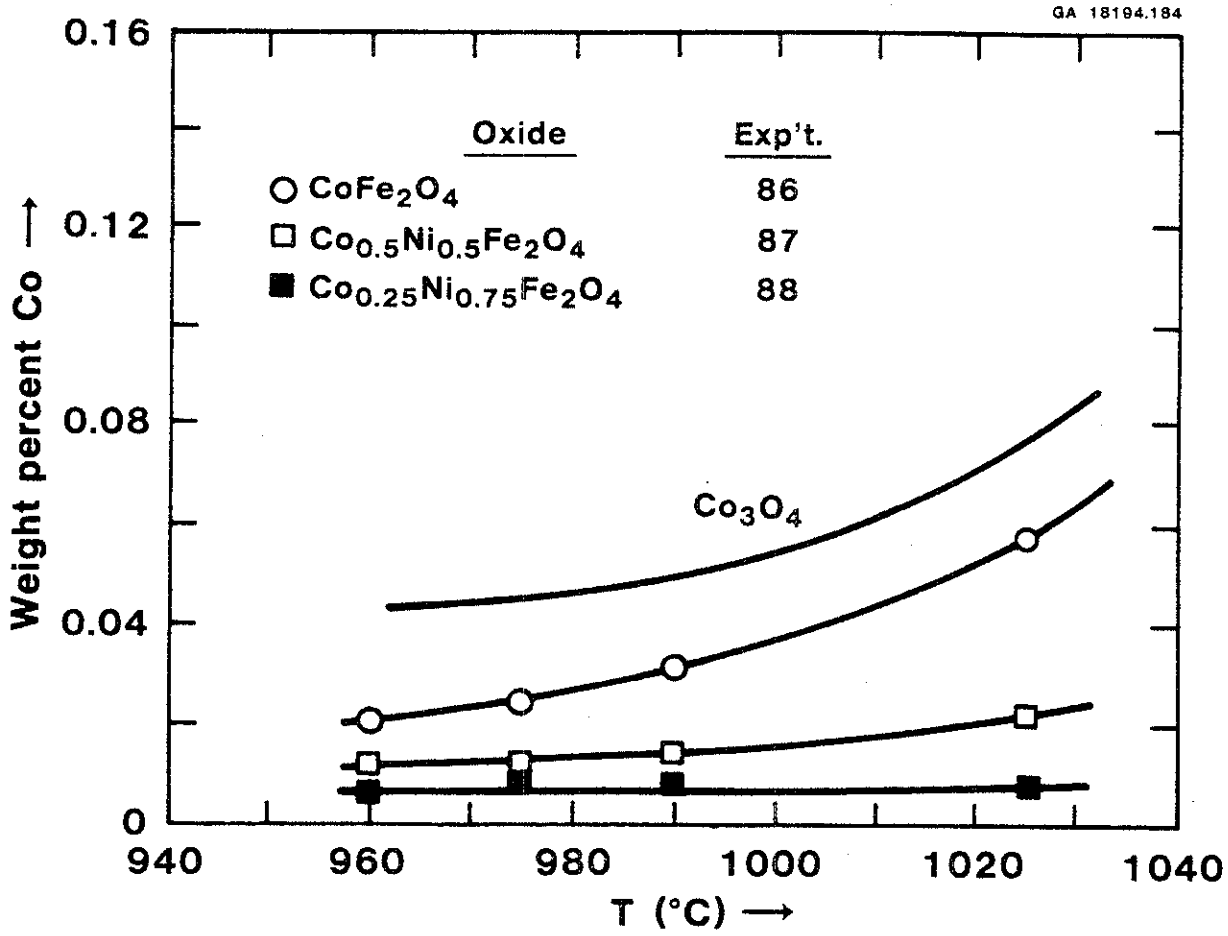

Cobalt Solubility from Cobalt-Nickel Ferrites in Hall Cell Bath of Composition 6.5% Al_2O_3, 1.3% CaF_2, Bath Ratio 1.1

Figure 79

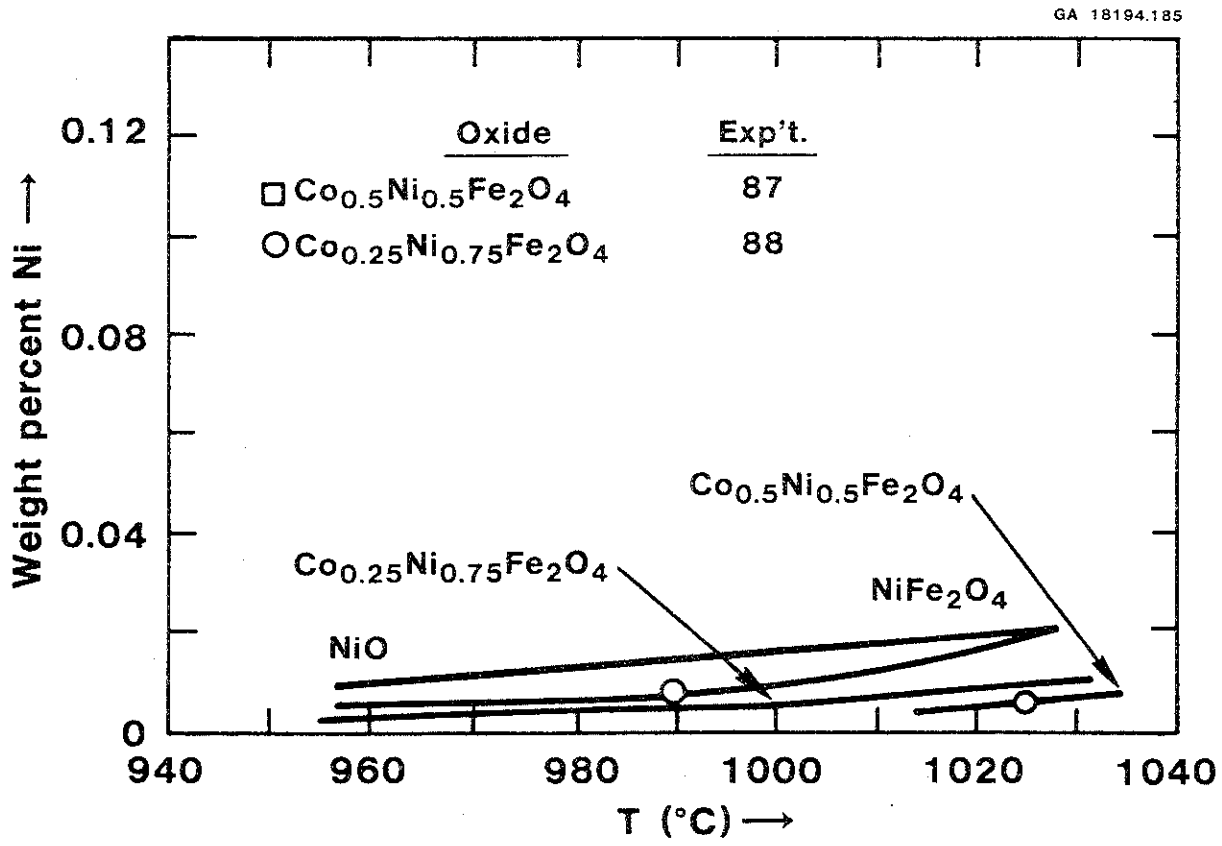

Nickel Solubility from Cobalt-Nickel Ferrites in Hall Cell Bath of Composition 6.5% Al_2O_3, 1.3% CaF_2, Bath Ratio 1.1

Figure 80

different from nickel ferrite. It is expected that cobalt ferrites have lower iron solubility than that for Fe_2O_3 because of the higher thermodynamic stability of the ferrites over the simple oxide.

Figure 79 shows the cobalt solubility for the cobalt-containing materials. As seen, the cobalt solubility decreases in the order

$$Co_3O_4 > CoFe_2O_4 > Co_{0.5}Ni_{0.5}Fe_2O_4 > Co_{0.25}Ni_{0.75}Fe_2O_4 \quad (33)$$

This is consistent with the decreasing concentration or activity of cobalt in the oxide, as is clearly seen in Figure 81. It should be noted that during the solubility test, the CoO pellet reacted to form Co_3O_4 (9).

The nickel solubilities for the cobalt-containing materials are shown in Figure 80. The nickel solubility decreases in the order

$$NiO > NiFe_2O_4 > Co_{0.25}Ni_{0.75}Fe_2O_4 > Co_{0.5}Ni_{0.5}Fe_2O_4. \quad (34)$$

Similarly to cobalt, the nickel solubility decreases with deceasing concentration or activity of nickel in the oxide.

Overall, these results show that from a solubility standpoint the cobalt oxide materials offer no improvement over nickel ferrite. The iron solubility is approximately the same, and replacing nickel with cobalt reduces the nickel solubility but adds at least an equivalent level of cobalt solubility. Cobalt is more expensive than nickel, so there is no gain in using a cobalt ferrite.

The results for solubility tests for $CoCr_2O_4$ and $NiCr_2O_4$ are given in Figures 82 and 83. Figure 84 gives results for Cr_2O_3, and compares them to the other chromium oxides. The

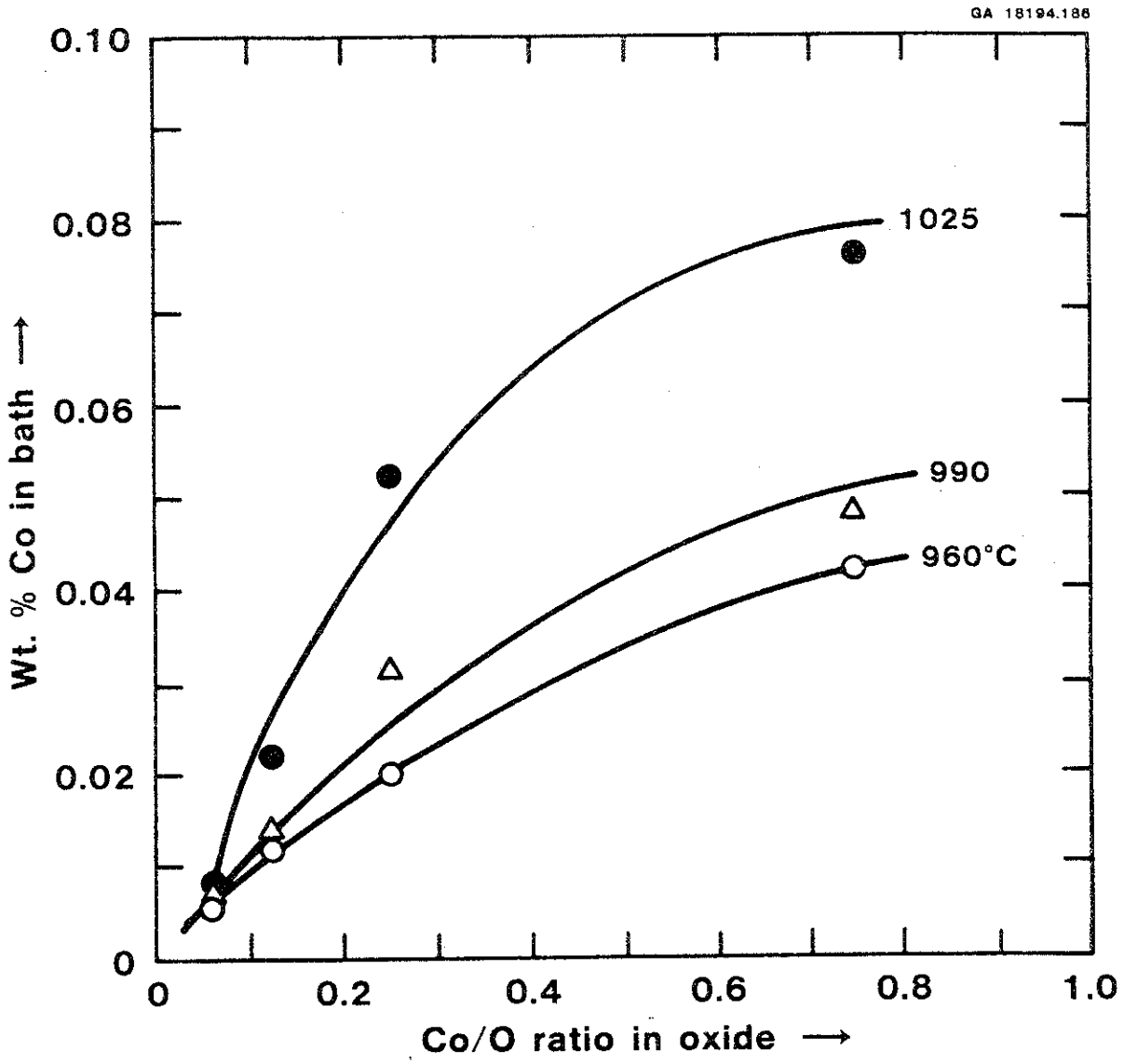

The Solubility of $Co_xNi_{1-x}Fe_2O_4$ in Hall Cell Bath of Composition 6.5% Al_2O_3, 1.3% CaF_2, Bath Ratio 1.1.

Figure 81

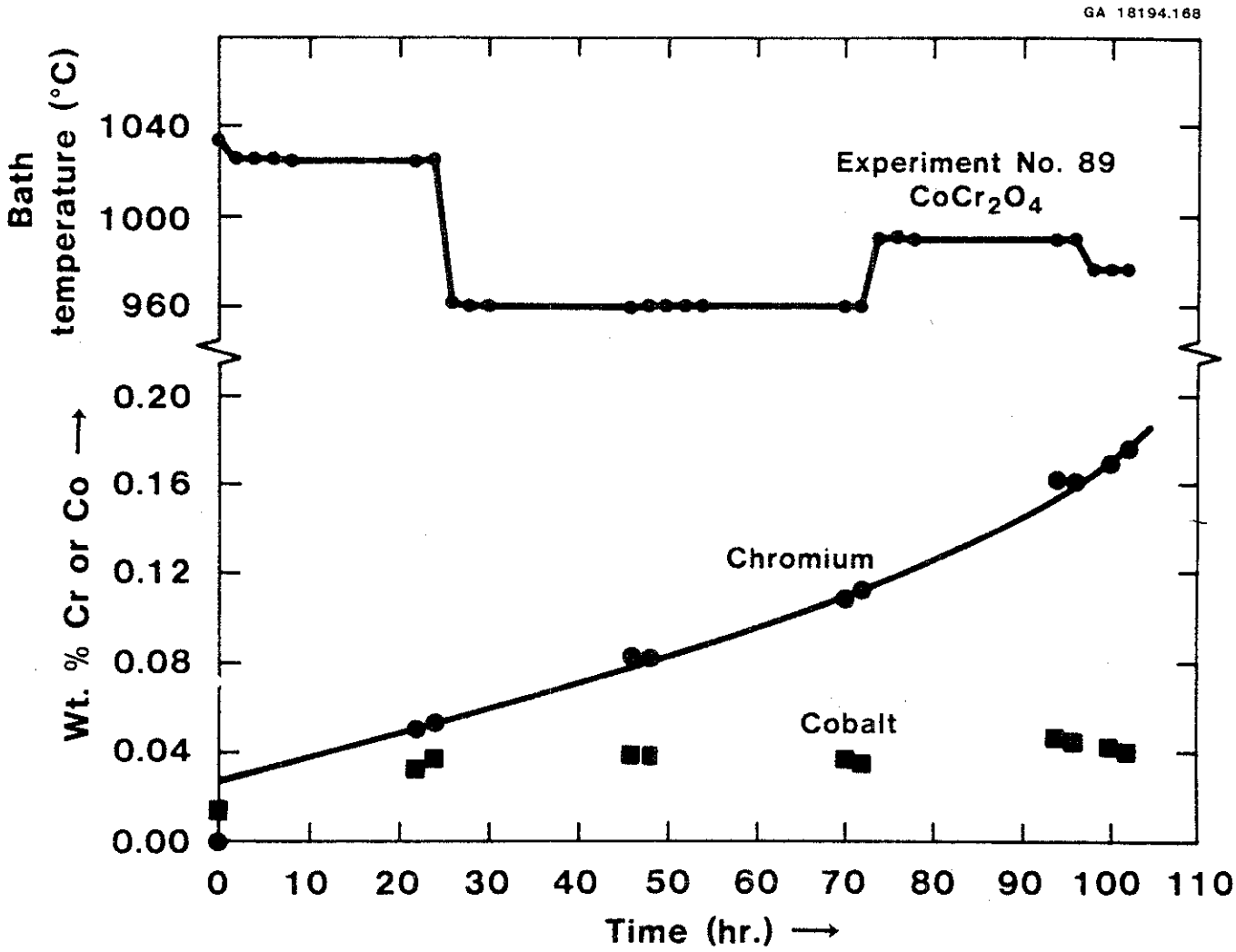

Bath Analyses for Dissolution of $CoCr_2O_4$ during the Solubility Experiment. Initial Bath Composition: 6.5% Al_2O_3, 1.3% CaF_2, Bath Ratio 1.1.

Figure 82

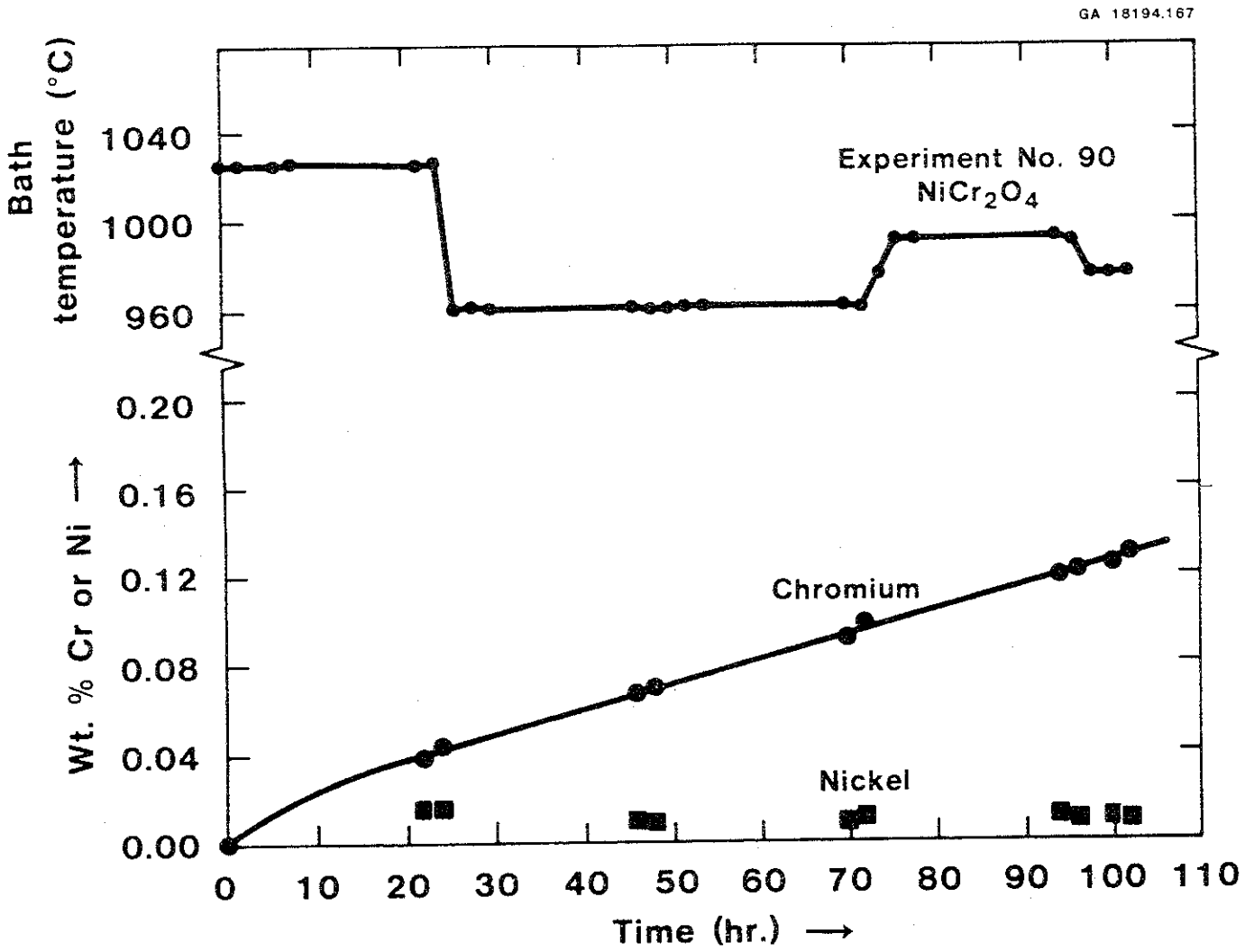

Bath Analyses for Dissolution of $NiCr_2O_4$ during the Solubility Experiment. Initial Bath Composition: 6.5% Al_2O_3, 1.3% CaF_2, Bath Ratio 1.1.

Figure 83

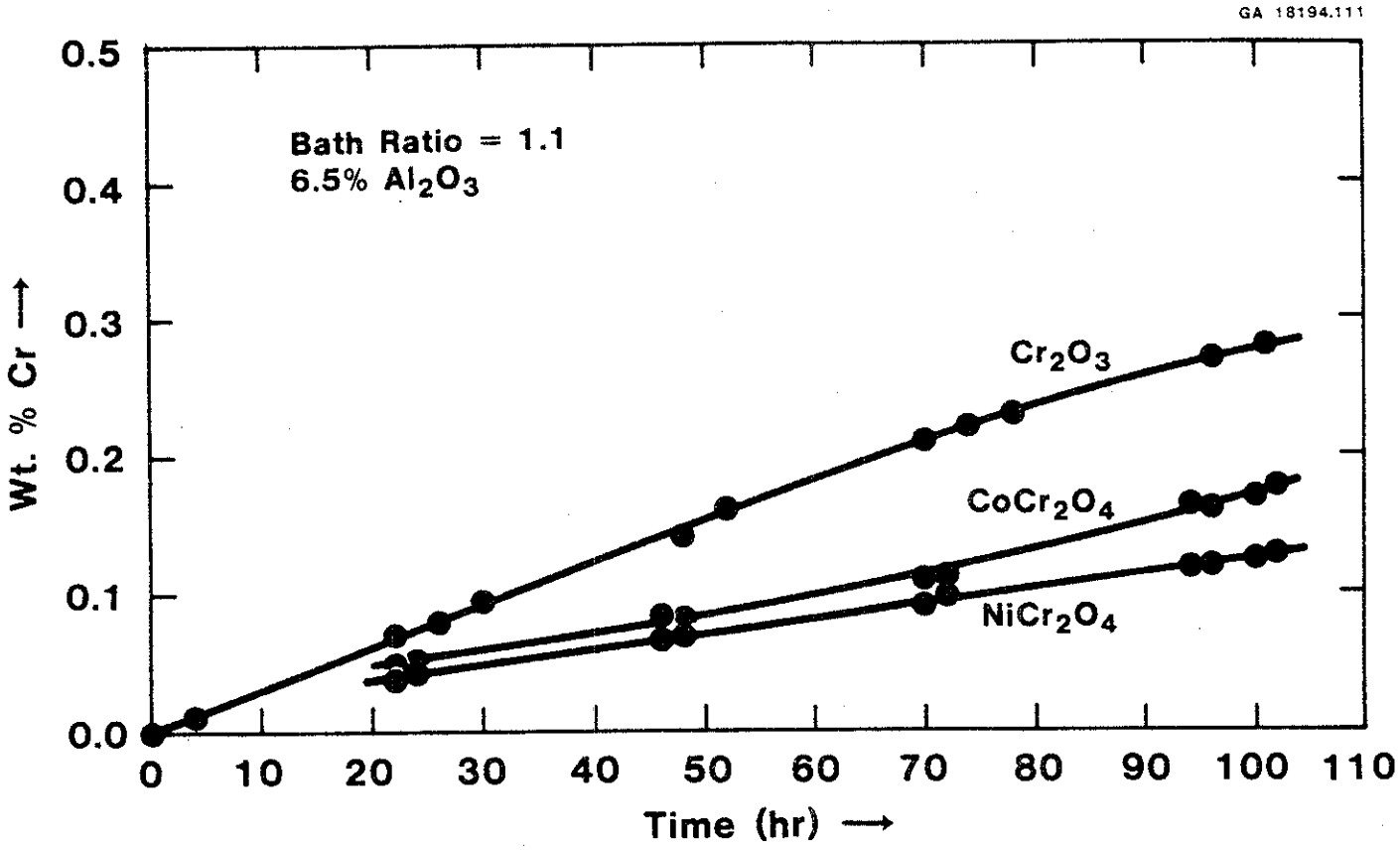

Chromium Concentrations in Bath Resulting from the Dissolution of Several Chromium Oxide Materials

Figure 84

behavior is quite different from that described above. For both materials the chromium concentration in the bath continually increased with time, almost linearly. There appeared to have been no correlation of the rate of increase in chromium concentration with the temperature of the bath. This is in contrast to the concentration plateaus observed for other materials (NiO, Fe_2O_3, $NiFe_2O_4$). It is apparent that the bath did not reach saturation with respect to chromium.

Several conclusions can be drawn from this behavior: (1) the dissolution reactions for these oxides appears to be of zero order for the duration of these experiments. The rate does not depend on the concentration of chromium already dissolved in the bath; (2) the reaction is not mass transfer controlled, but probably chemical reaction controlled. Rotating disk studies for nickel ferrite type anode materials showed their dissolution rate was controlled by mass transfer, and solubility tests of these materials gave curves similar to Figure 42, which are quite different than those in Figure 84. A plateau (saturation solubility) was reached in approximately 10 h. Since the crucible size, quantity of bath, and stirring were the same in the chromium oxide experiments as in the nickel ferrite experiments, the mass transfer should have been similar. Hence, the differing behavior indicates the dissolution of the chromium materials was not controlled by mass transfer but by a chemical reaction at the surface. This needs to be verified by rotating disk experiments.

Obviously, solubilities cannot be obtained from these results because the test duration was not long enough. The solubilities are higher than the highest concentrations observed, 0.176, 0.128 and 0.28% Cr for $CoCr_2O_4$, $NiCr_2O_4$ and Cr_2O_3, respectively. For $CoCr_2O_4$ and $NiCr_2O_4$ these are 2-4 times higher than the solubility of Fe from $NiFe_2O_4$. On this basis

it would appear that these materials would be unsuitable as inert anodes. However, their rate of dissolution is slower than that for $NiFe_2O_4$. For example, at 1025°C the bath in these solubility experiments would become saturated with $NiFe_2O_4$ in less than 24 h, saturation being approximately 0.056% Fe. For $NiCr_2O_4$ the concentration of Cr after 24 h at 1025°C was approximately 0.04%. Another positive point for the chromium materials is that if their dissolution is controlled by a surface chemical reaction, then there should be possibilities for slowing the dissolution by inhibiting the reaction.

One final point should be noted concerning the chromium materials. There was significant intergranular penetration of bath into the oxide pellets. For $CoCr_2O_4$, the oxide pellets disintegrated, while for $NiCr_2O_4$ the pellet was penetrated by bath. Grain boundary penetration is probably a result of impurities or more soluble species which exist at grain boundaries. In theory, this can be avoided by using purer materials and/or improved fabrication techniques. Whether this is practical remains to be determined. The dissolution behavior should be even better if this problem were solved.

b) Doped Nickel Ferrite

The purpose of doping the nickel ferrite is to reduce the activities of Fe_2O_3 and NiO in the spinel, and by doing so, to reduce their solubilities. The dopant should either be an oxide which is more stable than Al_2O_3 or one which has a lower solubility in Hall cell bath than Fe_2O_3 or NiO, so that contamination of the aluminum is not increased by the dopant.

Composition: Several dopants for nickel ferrite were selected - Al, Mg, Li and Zn. Table 37 lists the compositions which were fabricated. It was decided to add 2, 5, 10

TABLE 37

Compositions of Doped Nickel Ferrites

Composition Name	Composition, Wt.%					
	NiO	Fe_2O_3	Al_2O_3	MgO	ZnO	Li_2O_3
A19	31.2	66.8	2.0			
A122	30.2	64.8	5.0			
A143	28.7	61.3	10.0			
A180	25.5	54.5	20.0			
Mg9	31.4	67.0		1.6		
Mg23	30.6	65.4		4.1		
Mg46	29.2	62.5		8.2		
Mg91	26.5	56.7		16.8		
Zn9	30.8	65.9			3.2	
Zn23	29.4	62.8			7.9	
Zn46	27.0	57.7			15.3	
Zn91	22.6	48.4			28.9	
Li9	31.4	67.1				1.5
Li24	30.7	65.6				3.7
Li49	29.5	63.0				7.6
Li102	26.9	57.5				15.6

and 20 wt.% Al_2O_3 to stoichiometric $NiFe_2O_4$. The other compositions were formulated so that the mole ratio $X_i/X_{Ni} + X_{Fe}$ (mole fraction dopant/mole fraction nickel + mole fraction iron) for the Mg, Li and Zn-doped samples is equivalent to the corresponding ratio in the aluminum-doped samples. Table 38 gives the chemical formula for each composition.

Fabrication: The procedure for fabrication of these materials was to mix chemically pure raw materials, press into 1 inch diameter cylinders, pre-sinter the cylinders in air at 1125°C for 24 h, and quench to room temperature. Next the cylinders were crushed and ground to -325 mesh, pressed to the desired size, sintered in air at 1450°C for 24 h, and quenched to room temperature. Table 39 gives the sources of raw materials used. X-ray diffraction patterns were obtained for materials after the pre-sinter and after the final sinter to determine if the materials were single-phased.

Table 40 gives X-ray diffraction results for the pre-sintered materials. Most of the materials had two phases as the reaction for the formation of the ferrite was apparently not completed at this lower temperature. All of the Al, Mg and Li-doped samples sintered at 1450°C were found to be of a single phase having a $NiFe_2O_4$-type structure. Three of the four Zn-doped ferrites were single-phase. The composition containing the largest addition of zinc had two phases, one being the ferrite-type and the other unidentified. The d spacing from the strongest peak (311 plane) was found to shift progressively with the quantity of Al, Mg or Zn added (Figure 85). There was no noticeable shift in lattice parameter with additions of Li.

Solubility Measurements: The experimental procedure was the same as previously described. Because of a time limitation, not all of the compositions that were produced were tested.

TABLE 38

Chemical Formulas for Doped Nickel Ferrites

Composition Name	Formula						
	Ni	Fe	Al	Mg	Zn	Li	O
Al9	0.97	1.93	0.09				4
Al22	0.92	1.83	0.22				4
Al43	0.84	1.68	0.43				4
Al80	0.70	1.40	0.80				4
Mg9	0.98	1.95		0.09			4
Mg23	0.94	1.88		0.23			4
Mg46	0.88	1.77		0.46			4
Mg91	0.77	1.55		0.91			4
Zn9	0.98	1.95			0.09		4
Zn23	0.94	1.88			0.23		4
Zn46	0.88	1.77			0.46		4
Zn91	0.77	1.55			0.91		4
Li9	0.99	1.98				0.09	4
Li24	0.97	1.94				0.24	4
Li49	0.94	1.88				0.49	4
Li102	0.87	1.74				1.02	4

TABLE 39

Raw Materials Used for Doped Nickel Ferrites

Fe_2O_3	Fisher I-116, 99.5% MCB FX-230, 99.0%
NiO	Ceramic Color and Chemical Company, 99.2%
MgO	Fisher M-51, 99.6%
ZnO	Fisher Zn-52, 99.9%
Li_2CO_3	Fisher L-119, 99.4%
Al_2O_3	Alcoa C-331, calcined, 99.7%

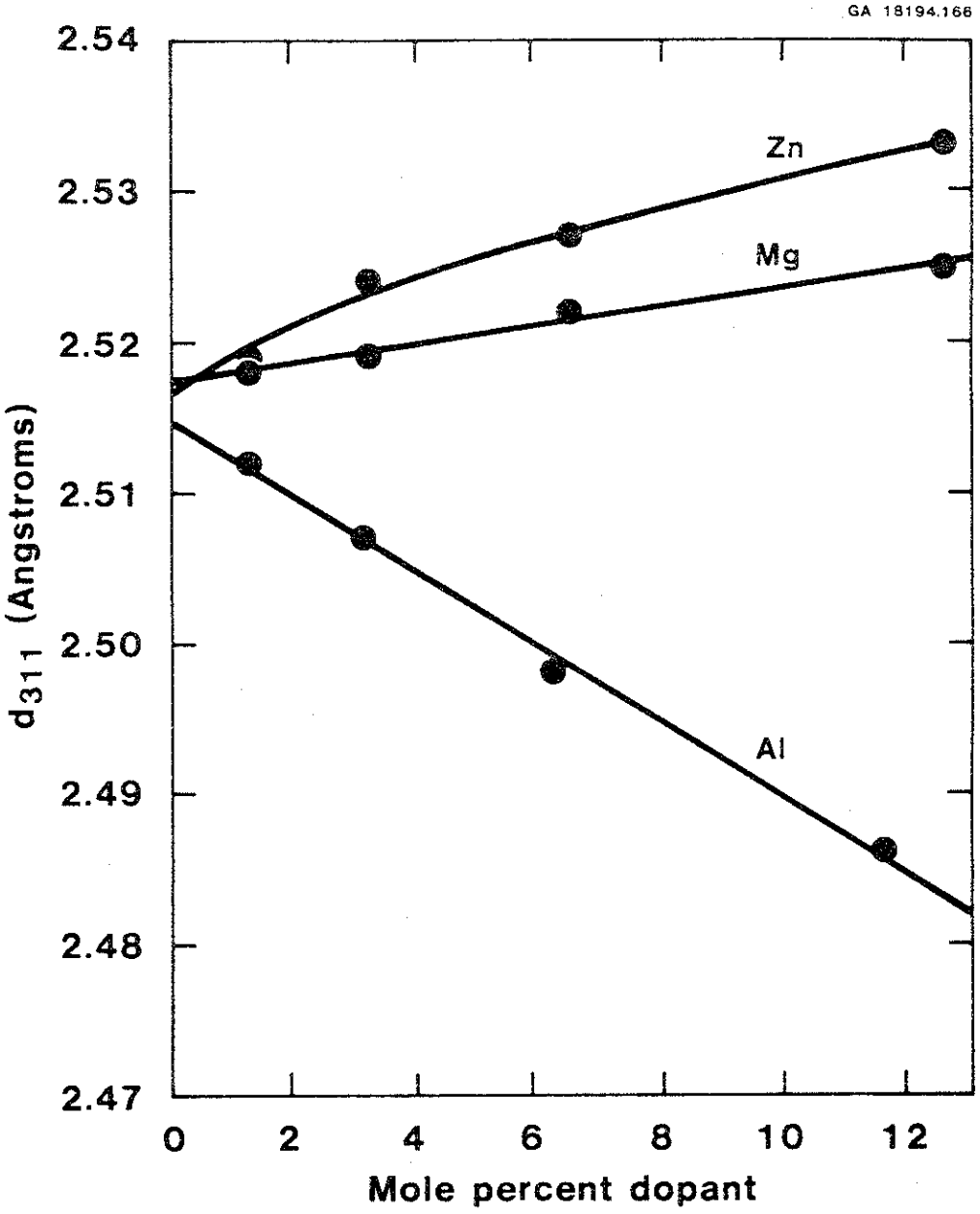

Distance between 311 Planes for Doped $NiFe_2O_4$ Sintered in Air at 1450°C

Figure 85

TABLE 40

X-ray Diffraction of Al, Mg, Zn and Li Doped Nickel Ferrites Which Were Presintered in Air at 1125°C for 24 Hours

Oxide	X-Ray Diffraction Results
Al9	Major $NiFe_2O_4$ type phase*, very small Fe_2O_3
Al22	Major $NiFe_2O_4$ type phase*, minor Fe_2O_3
Al43	Major $NiFe_2O_4$ type phase*, minor Fe_2O_3
Al80	Major $NiFe_2O_4$ type phase*, minor Fe_2O_3, trace alpha alumina
Mg9	Major $NiFe_2O_4$ type phase, trace possible Fe_2O_3
Mg23	Entirely $NiFe_2O_4$ type phase
Mg46	Major $NiFe_2O_4$ type phase, trace possible Fe_2O_3
Mg91	Entirely $NiFe_2O_4$ type phase
Zn9	Major probable (Zn, Ni) Fe_2O_4 phase** Major Fe_2O_3
Zn23	Major probable (Zn, Ni) Fe_2O_4 phase** Major Fe_2O_3
Zn46	Major probable (Zn, Ni) Fe_2O_4 phase** Major Fe_2O_3
Zn91	Major probable (Zn, Ni) Fe_2O_4 phase** Major Fe_2O_3, Minor ZnO
Li9	Major probable (Li, Ni) Fe_2O_4 phase Major Fe_2O_3
Li24	Major probable (Li, Ni) Fe_2O_4 phase Major Fe_2O_3
Li49	Major probable (Li, Ni) Fe_2O_4 phase Trace Fe_2O_3
Li102	Entirely single phase; probable (Li, Ni) Fe_2O_4 phase

*As Al_2O_3 is added, this phase has broader diffraction peaks and the peaks shift.
**The diffraction peaks for (Zn, Ni) Fe_2O_4 progressively shift as the amount of Zn is increased.

Figure 86 shows the results for Al and Mg-doped spinels and compares them to results for pure nickel ferrite. The iron solubility is increased by increasing quantities of Al or Mg added to the spinel, while the nickel solubility is decreased slightly by these additions. Although the quantity of data is sparse, the trends are consistent in both the Al and Mg-doped spinels.

Figure 87 shows results for the Li and Zn doped ferrites and compares them to results for pure nickel ferrite. The concentration of zinc from ZN-9 was too small to be measured, < 0.005%. The iron solubility was increased by additions of Zn to the spinel, while the nickel solubility was essentially unchanged. The effect of Li was similar, except the increase in Fe was greater and the Ni solubility appeared to be slightly decreased. The trends are the same as for the Al and Mg-doped spinels.

The Al, Mg, Zn and Li-doped nickel ferrites can probably be considered to be solid solutions of $Al_2O_3.Fe_2O_3$, $MgFe_2O_4$, $ZnFe_2O_4$ and $Li_{0.5}Fe_{2.5}O_4$ with $NiFe_2O_4$. Apparently the Al, Mg and Li materials have reduced activities of NiO and thereby reduced nickel solubilities. However, the increased iron solubilities for all of the compositions indicates that $Al_2O_3.Fe_2O_3$, $MgFe_2O_4$, $ZnFe_2O_4$ and $Li_{0.5}Fe_{2.5}O_4$ are less stable than $NiFe_2O_4$ and therefore more soluble.

In conclusion, all of the dopants caused an increase in the iron solubility. It appears that for a dopant to be successful, the analogous ferrite formed from the dopant should be less soluble than nickel ferrite. Hence, the nickel ferrite would serve no purpose (from a solubility standpoint), and the concept of doping appears to be infeasible.

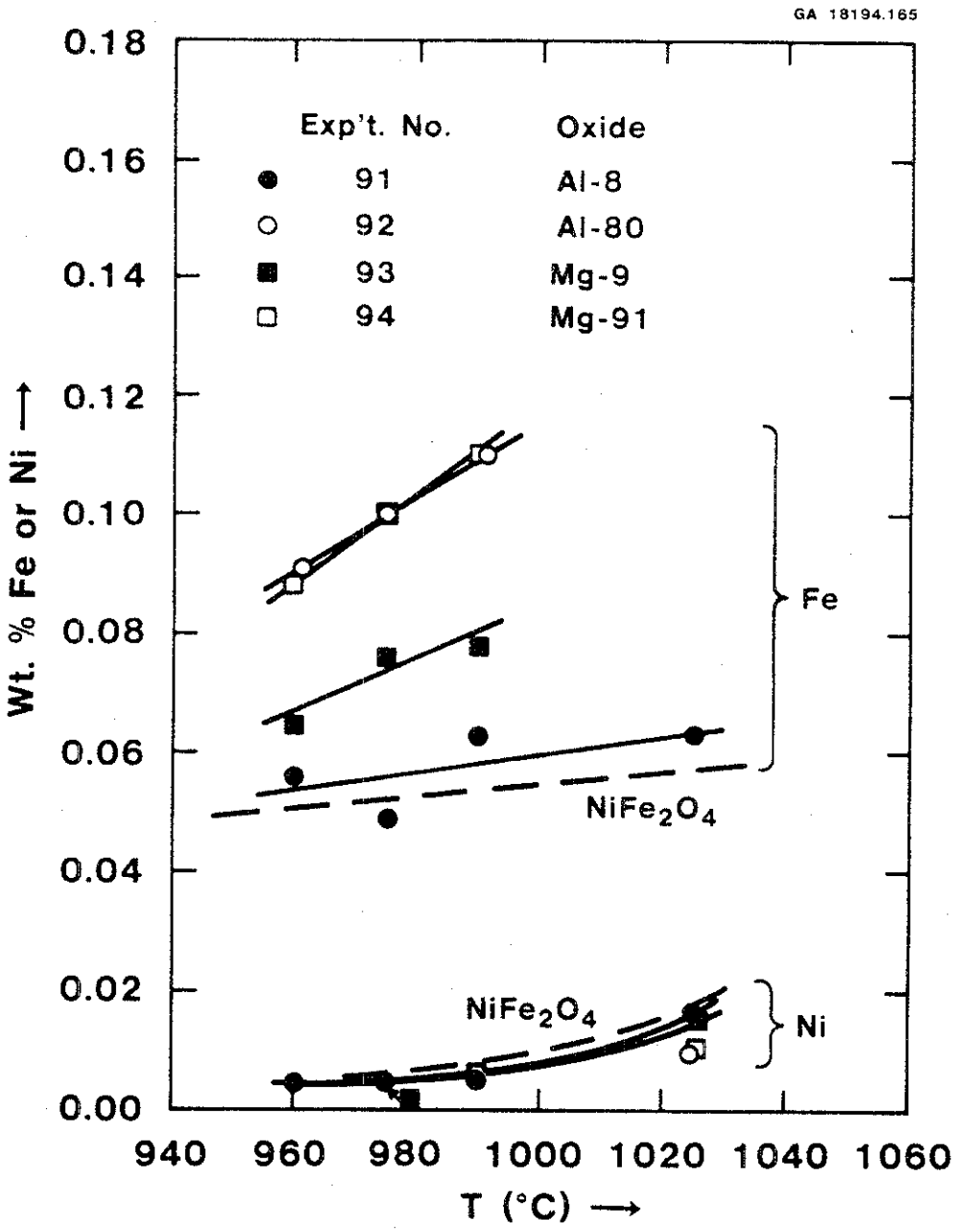

The Solubility of Doped Nickel Ferrites in Hall Cell Bath
Bath Composition: 6.5% Al_2O_3, 1.3% CaF_2, Bath Ratio 1.1
Figure 86

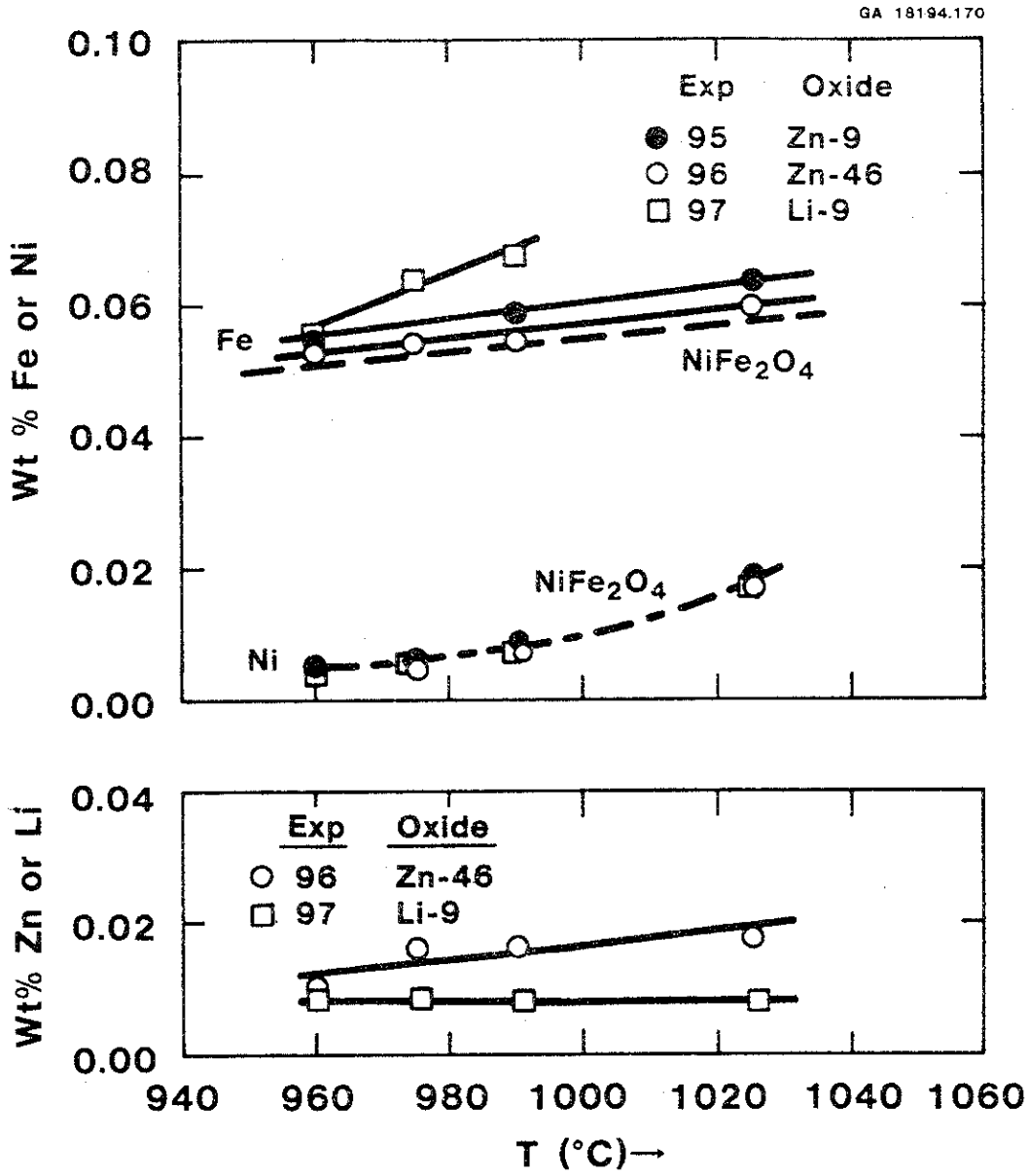

Solubilities of Zn and Li Doped Nickel Ferrite Compared to the Solubility of $NiFe_2O_4$. Bath Composition Bath Ratio 1.1, 6.5% Al_2O_3, 1.3% CaF_2.
Figure 87

c) Suggestions for Further Work

Some suggestions for future work are in order. If work on alternate materials were continued, the program would be modified as outlined in Table 41. Basically, materials to be tested would be selected, synthesized and tested by solubility and dissolution rate tests. If materials passed these tests, they should then be tested for 30 h in the bench scale Hall cell.

The synthesis/fabrication of materials would continue as it has, with characterization of the materials by x-ray diffraction. Tests of the solubility of the material would be shortened by making a measurement at only one temperature. Three or more smaller crucibles of bath should be placed in a furnace at one time to permit at least three materials to be tested simultaneously.

The dissolution rate test would be modified somewhat. The rotating disk technique would be used with electrolysis maintained at 1 A/cm^2. The test would be run for approximately 4 h, and a tungsten counter electrode would be used instead of a molten aluminum pool. The oxide being tested would be fabricated as a platinum cermet, i.e., platinum powder and the oxide powder would be mixed, pressed, and sintered to form the anode. The rate of dissolution would be measured by cross-sectioning the anode after the test and microscopically measuring the distance the oxide phase has receded behind the front of platinum particles. This should enable a faster evaluation of the dissolution rate because it would avoid analysis of many bath samples. However, less information would be obtained. For example, analysis of bath samples gives information on preferential dissolution of one of the components of the material. For a screening test, a faster evaluation would be desirable.

TABLE 41

Proposed Alternate Materials Program

I. Select Materials

II. Fabricate and Characterize Test Samples

III. Measure Solubility of Material in Al_2O_3-Saturated Bath at 960°C

IV. Measure Dissolution Rate of Material (platinum metal phase) with Rotating Electrode under Electrolysis

V. Decision for Scale-up to 30-Hour Hall Cell Test

VI. Modify Material and Repeat Test Sequence

A list of candidate materials which would be tested is given in Table 42. Work on chromium oxides would continue because of the results discussed earlier which indicate their dissolution is chemical-reaction controlled. A number of copper-containing oxides would be evaluated. Copper is an excellent metal component of the cermet inert anode because of its slow rate of anodic dissolution in cryolite. Therefore, oxides which are compatible with copper should be tested. Next, there are several oxides, Y_2O_3 and Nb_2O_3, for which there are no solubility data in cryolite reported in the literature, but which are rather refractory in nature. Finally, there are several mixed oxides which have been reported in the literature to be stable in molten cryolite (2).

4) Implications for Hall Cell Operation

The solubility data that were obtained have several implications regarding Hall cell operation with nickel ferrite-based inert anodes. First, the electrolyte should have as high a concentration of Al_2O_3 as possible to minimize the solubilities of the anode materials. This is not standard operating practice for commercial Hall cells, and therefore may require some developmental effort.

Second, a $NiFe_2O_4$-based anode should be composed of NiO-rich $NiFe_2O_4$. The solubility of Fe from $NiFe_2O_4$ will be a maximum at the Fe_2O_3- $NiFe_2O_4$ phase boundary, and will be equal to the solubility of Fe_2O_3. The solubility of Ni from $NiFe_2O_4$ will be a maximum at the NiO- $NiFe_2O_4$ phase boundary, and will be equal to the solubility of NiO. Since the solubility of NiO is less than the solubility of Fe_2O_3, the overall solubility of $NiFe_2O_4$ ($X_{Fe_2O_3} + X_{NiO}$) will be a minimum near the NiO- $NiFe_2O_4$ phase boundary. A slight excess of NiO added to the anode composition would accomplish this.

TABLE 42

Candidate Materials for Solubility and Dissolution Rate Tests

---

$FeCr_2O_4$

Fe_2O_3-Cr_2O_3 solid solution

$MgCr_2O_4$

Cabot 214 (Ni-20 Cr-4 Al-Y)

$CuFe_2O_4$

$CuAlO_2$

$CuAl_2O_4$

Y_2O_3

Nb_2O_5

$NiMn_2O_4$

$SnZn_{1.8}Ni_{0.2}O_4$

Third, the cell should be operated at as low a temperature as possible to minimize the anode solubility. This is true as long as the oxides are the stable solid phase in equilibrium with cryolite.

Fourth, additions of CaF_2, $MgF_2$and LiF to the bath would, to some extent, reduce the solubilities of inert anode components. Additions should be made only to the extent that Al_2O_3 solubility is not greatly sacrificed.

Fifth, the presence of SiO_2 in the Hall cell bath should be avoided, though amounts of < 0.5 wt.% could be tolerated.

d. Conclusions from Solubility Results

The solubilities of Fe_2O_3, NiO and $NiFe_2O_4$ have been measured in $NaF-AlF_3-CaF_2-Al_2O_3$ melts. The solubilities of these oxides increase with decreasing concentration of Al_2O_3 in the melt. The solubility of Fe_2O_3 decreases with decreasing bath ratio, while the solubility of NiO does not change with bath ratio, within the uncertainty of the measurements. The partial molar enthalpies of dissolution of Fe_2O_3 and NiO in the cryolite-based melt were determined to be 33.1 and 44.6 kcal/mole, respectively. The solubility of $NiFe_2O_4$ is lower than the solubilities of its constituent oxides. The free energy of formation of $NiFe_2O_4$ calculated from the solubilities of the simple oxides and the ferrite is in good agreement with data reported in the literature, which had been determined by an independent technique. This agreement permits the solubility of the ferrite to be predicted for the entire range of melt compostion and temperature for which the solubilities of simple oxides were measured. The results of this study show that a Hall cell using nickel ferrite-based inert anodes should be operated at low temperatures, the electrolyte should contain high concentrations of Al_2O_3, and the anode should be formulated with excess NiO.

The effects of SiO_2, CaF_2, MgF_2, LiF and ZrO_2 additives to the $NaF-AlF_3-Al_2O_3$ melts on the solubilities of Fe_2O_3 and NiO were

determined. The addition of SiO_2 greatly increases the solubility of Fe_2O_3, and therefore should be avoided in Hall cell bath. The additions of CaF_2, MgF_2 and LiF all to some extent decrease the solubility of Fe_2O_3 and NiO. These additions should be beneficial to the operation of an inert anode Hall cell, but only to the extent that the solubility of Al_2O_3 is not significantly decreased. Combined additions of CaF_2, MgF_2 and LiF reduce solubilities of inert anode components, but again are beneficial only to the extent that the Al_2O_3 solubility is not significantly decreased. The additions of ZrO_2 decreased the solubility of NiO, but did not change the solubility of Fe_2O_3. The effect on NiO was explained by additional oxygen added to the melt, not an intrinsic chemical effect of ZrO_2 on NiO.

Several new systems were explored for possible inert anode materials. The solubilities of Co_3O_4, $CoFe_2O_4$, and mixed cobalt-nickel ferrites were measured. The solubility of Co_3O_4 is higher than NiO, and the mixed cobalt-nickel ferrites have solubilities consistent with this. From a solubility standpoint the cobalt materials offer no improvement over nickel ferrite. Several chromium oxide materials were studied. Solubility tests were conducted on Cr_2O_3, $CoCr_2O_4$, and $NiCr_2O_4$. The dissolution of all of these materials appeared to be controlled by a chemical reaction step. Solubilities were not obtained because of the slow dissolution rates of these materials. The tests did show that the solubilities are higher than $NiFe_2O_4$. These chromium oxides warrant further investigation because of their slow dissolution rate.

The solubilities of several doped nickel ferrites were measured. Dopants were added in solid solution to the spinel in attempt to reduce the activities of NiO and Fe_2O_3 in the material. Al, Mg, Zn and Li were selected as dopants. This was not successful because in each case the solubility of Fe from the ferrite was increased. The nickel solubility was slightly decreased by the Al, Mg and Li dopants.

4. Part B - Rate Measurements

a. Literature Review

The most promising inert anode materials are cermets--the metallic phase is needed to achieve a high electrical conductivity. This type of material will degrade by both electrochemical corrosion and chemical dissolution. The electrochemical corrosion has been investigated by Tarcy (7,46), and it was found that the Ni alloy phase in the Ni cermet materials undergoes anodic dissolution. Thus, in operation the metallic front recedes into the anode. This is a type of internal oxidation. This problem was solved by using copper as the metallic phase instead of nickel. However, the anode still dissolves in Hall cell bath as the oxide phases in nickel ferrite-based anodes have finite solubilities in cryolite melts, as shown in Part A of the corrosion studies section of this report. The intent of this work was to study the dissolution of the oxide phases in the anode material. The work was aimed at the chemical corrosion rather than the electrochemical corrosion.

A different experimental method was needed to study chemical corrosion than electrochemical corrosion. In electrochemical corrosion, a flow of electrons is associated with the corrosion reactions, thus electronic instrumentation can be used to study the corrosion process and measure corrosion rates. In chemical corrosion, the ions dissolving in the molten salt are already in their oxidized states, therefore there is no flow of electrons associated with the corrosion process. To measure chemical corrosion rates, either the sample can be measured or weighed before and after the corrosion, or the concentrations of the dissolving material in the electrolyte can be measured.

There are numerous studies of high temperature dissolution of solids in liquids reported in the literature, each for a particular system. No references were reported for the dissolution kinetics of NiO, Fe_2O_3, or $NiFe_2O_4$ in cryolite-based melts. It appeared that the only studies of dissolution of solids in cryolite melts were of the dissolution of Al_2O_3 (60-62), which are obviously of great importance to Hall cell

operation. There is also some data on the dissolution of MgO and SiO_2 (61), which showed that their dissolution was controlled by mass transport. Gerlach (60) found that the dissolution of solid (sintered) alumina in cryolite-based melts was controlled by mass transport.

Examples of other high temperature solid-liquid systems in which the dissolution was studied are Al_2O_3 in molten $CaO-Al_2O_3-SiO_2$ (63); mullite, anorthite, and silica in $CaO-Al_2O_3-SiO_2$ (64); lime in $CaO-FeO-SiO_2$ (65); Fe in molten Fe-C alloys (66); Al_2O_3 in Na_2O-SiO_2 (67); $Al_2O_3-Cr_2O_3$ solid solutions in $CaO-Al_2O_3-MgO-SiO_2$ melts (68); Al_2O_3 and Cr_2O_3 in molten Na_2SO_4 (69). In most of these studies, mass transport is the rate limiting step for dissolution. At high temperatures chemical kinetics are sufficiently fast that most processes are limited by mass transport or heat transfer, and the above mentioned studies reflect this trend. One exception is Al_2O_3 and Cr_2O_3 in molten Na_2SO_4 (69); their dissolution was not controlled by mass transport or heat transfer. Further information on high temperature dissolution of solids in liquids for specific systems can be found in an extensive review by Weirauch (70).

Since most studies of high temperature dissolution of solids in liquids have shown that mass transport is the rate limiting step, it is important to control the mass transport in any experimental study. Rotating disks or rotating cylinders provide a means to do this. The equations for fluid flow in a rotating disk system have been solved by Cochran (71) and Levich (72,73). The boundary layer thickness at the disk surface depends on the angular velocity of the disk and can be calculated. An important attribute of this system is that the boundary layer is constant across the disk surface. The fluid flow equations for rotating cylinders have not been solved, but a dimensionless correlation for mass transport in such systems has been worked out by Tobias (74). A thorough discussion of the rotating disk system has been given by Bard and Faulkner (75). Because the hydrodynamic equations for a rotating disk have been solved and because it would be experimentally easier to build a rotating inert anode disk than a cylinder, this technique was chosen for the inert anode dissolution rate measurements.

b. Scope of Work

The rates of dissolution of inert anodes were measured with a rotating disk apparatus. The variables which were investigated were the rotational speed of the anode, melt composition, temperature, electrochemical polarization of the anode, presence of molten aluminum in the system, and additions of carbon and Al_4C_3 to the melt.

The purpose of varying the rotational speed of the anode was to determine the effect of mass transport on the rate of dissolution. This was done for relatively uncomplicated conditions in an air atmosphere with no aluminum metal present in the system.

The next variable investigated was the polarization of the anode (potential and current density). To perform these tests it was necessary to first develop a stable, reliable reference electrode for the system. The tests were performed without molten aluminum being present to avoid possible complications from the presence of dissolved Al in the melt.

Next the molten aluminum was added to the system. In these tests it was necessary to polarize the anode to keep it from being chemically reduced by dissolved Al in the melt.

Finally, the effects of carbon/Al_4C_3 additions to the bath were determined. This information was needed because in a pilot or commercial cell it would be difficult to avoid carbon from the sidelining or from carbon anodes used for cell start-up. From results in bench-scale cells, it was suspected that carbon or Al_4C_3 from graphite containers was increasing the corrosion of the anode. Possibly the carbon or carbide would migrate to the anode. It was hypothesized that these reductants could, on a local scale, reduce a tiny area of the anode surface which would subsequently spall off upon oxidation. Another possibility was that the reductants could decrease the diffusion boundary layer at the anode by taking dissolved Fe and Ni oxides out of solution by reducing them. Both of these phenomena would increase the

dissolution rate. The experimental procedures for all of these tests were slightly different, and these differences will be noted in the next section of the report.

Most of the dissolution tests were performed on Ni cermet anodes, composition 6846. This composition consisted of 20 wt.% Fe - 20 wt.% Fe_3O_4 - 60 wt.% NiO, and contained $NiFe_2O_4$, NiO and Ni phases. The dissolution tests were started before the development of the copper cermet anodes. Some tests were performed using the all-oxide material (composition 5324), for both polarized and unpolarized anodes. This composition consisted of 51.7 wt.% NiO - 48.3 wt.% Fe_2O_3, and contained $NiFe_2O_4$ and NiO phases. Finally, several tests were performed on the copper cermet material, composition 5324 + 17 wt.% Cu.

c. Experimental Methods

1) General

The rotating disk system used to measure the rates of dissolution of unpolarized inert anodes under air atmospheres is schematically shown in Figure 88. For these tests at oxidizing conditions, the molten $NaF-AlF_3-CaF_2-Al_2O_3$ melts were contained in platinum crucibles. The platinum crucible was placed in an alumina crucible, which in turn was placed on bubble alumina at the bottom of a closed-end alumina tube. This entire assembly was placed in a Kanthal-wound resistance furnace. A Marinite XL lid was used to cover the large alumina tube. Holes drilled in the lid provided access for a thermocouple, gas inlet tube, sampling tube and anode connecting rod.

The temperature of the melt was read with a platinum shielded type S thermocouple. Melt samples were periodically taken throughout the run by withdrawing a portion of melt into an alumina tube. Dried air was passed over the surface of the melt during each experiment.

The anode was rotated using a Pine Instrument electrochemical

GA 18194.19

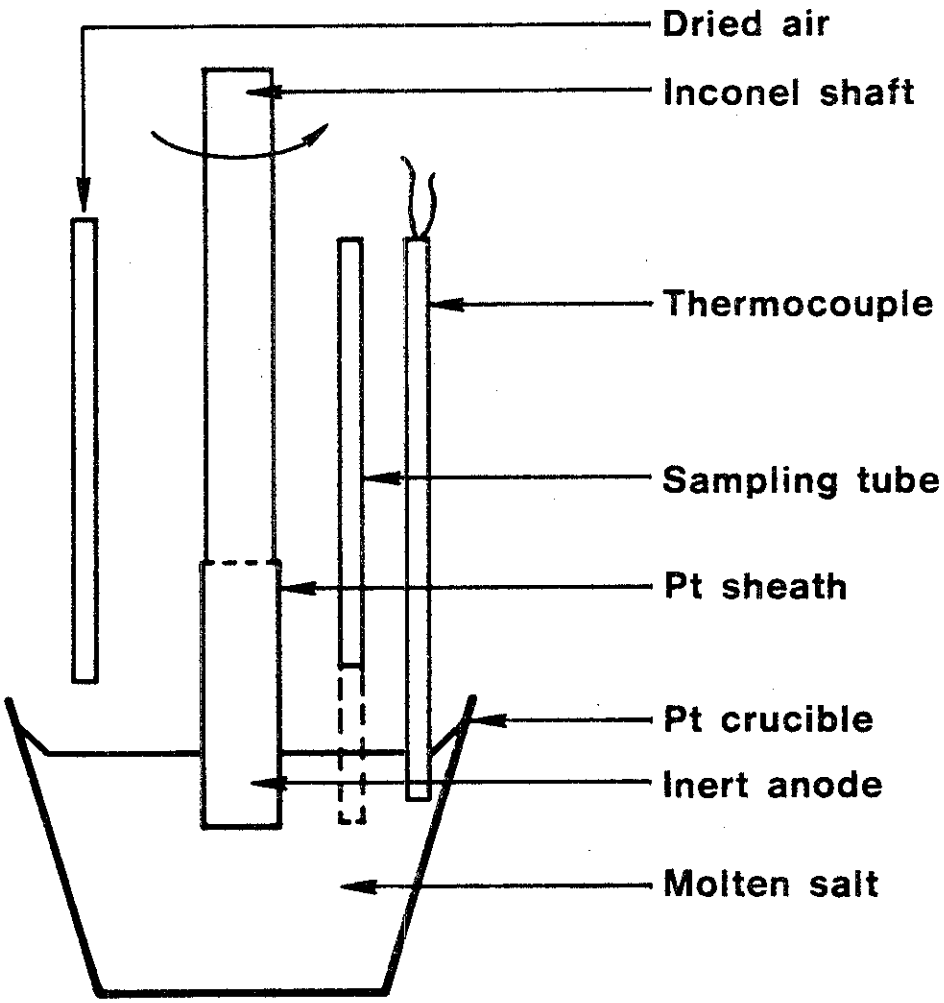

Schematic Diagram of Rotating Disk Apparatus used for Dissolution Rate Measurements made Under Oxidizing Conditions
Figure 88

rotator. The anodes were welded to an Inconel 601 shaft, and this shaft was connected to the rotator by a drill press type chuck. The top end of the anode consisted of Ni that was incorporated during anode fabrication. This nickel end was machined to form a centered pin protruding from the top of the anode so the anode could be keyed to a centered hole drilled into the Inconel shaft. The anode was then spot welded to the shaft. More extensive welding produced cracking in the anode assembly, presumably because of nonuniform thermal expansion. The anode assembly is shown in Figure 89.

2) Sample Fabrication

Anode fabrication procedures were similar to those used for other inert anodes in this project. For the Ni cermet anodes (designated 6846) the raw materials were Fe powder, Fe_3O_4, and NiO. For the all-oxide anodes (designated 5324) the raw materials were Fe_2O_3 and NiO. For copper cermets, Cu powder was added to 5324 powder. Table 43 gives compositions of the anodes as well as sources of the raw materials. Weyand (3, 11) has extensively characterized the raw materials and has developed the fabrication procedures for these three types of anodes. For all of the anode compositions, the raw materials were blended and most were screened (-100 mesh).

The blended mixtures were pressed in a 1.3 cm diameter cylindrical die to 172 MPa. Prior to pressing, a layer of Ni powder was poured on top of the anode powder. This Ni powder consisted of 60% Puratronic grade (Alpha No. 400026, 99.999%, -120 +425 mesh) and 40% plasma spray grade (Atlantic Equipment Engineers, 99.9%). It was found that the particle size of the powder was critical to achieve a good bond between the Ni and the inert anode, and to match the shrinkage of the Ni powder to the shrinkage of the anode that occurs upon sintering. This mixture of Ni powders was found to be optimum. More of the finer powder gives too much shrinkage, and more of the coarse powder (plasma spray grade) makes bonding impossible.

GA 18194.90

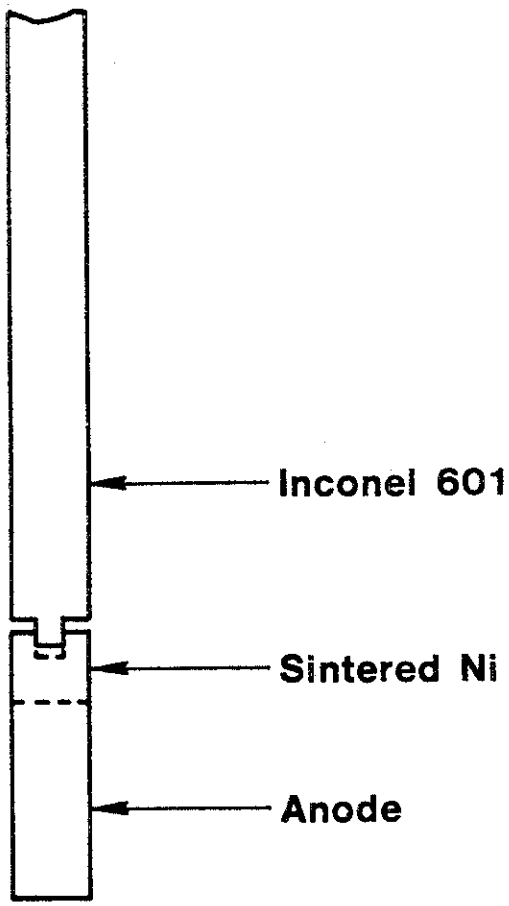

Anode Assembly Used for Dissolution Rate Measurements
Figure 89

TABLE 43

Materials Used for Chemical Corrosion Measurements

MATERIAL	DESIGNATION	RAW MATERIALS	GRADE	SOURCE	MICROSTRUCTURE (Volume %)	DENSITY g/cm^3
All-oxide	5324	51.7 wt.% NiO 48.2 wt.% Fe_2O_3		Stackpole	82% $NiFe_2O_4$ 18% NiO	5.5
Ni Cermet	6846-94-2	20 wt.% Fe_3O_4 60 wt.% NiO	BK-5000 N-139	Pfizer Ceramic Color & Chemical	75%$NiFe_2O_4$ 1%NiO	5.82
		20 wt.% Fe	Atomet 95	Quebec	24%Ni	
Cu Cermet	5324 + 17% Cu	83 wt.% 5324 powder		Stackpole	77%$NiFe_2O_4$	5.98
		17 wt.% Cu		Alfa	10%NiO 13%Cu	

The raw material for the all-oxide material, composition 5324: 51.7 wt.% NiO-48.3 Fe_2O_3, was prepared by calcination and spray drying. To bond the Ni layer to this material (5324), a graded layer needed to be incorporated. A layer of 50% Ni powder - 50% 5324 powder was placed on top of the 5324 powder in the die, and a layer of Ni powder was placed on top of the mixed powders. After sintering, this top Ni layer could be welded to an Inconel rod. To bond the Ni layer to the Cu cermet, a layer of 50% of (83% 5324 powder-17% Cu powder) and 50% Ni powder was needed between the anode and the Ni layer. The compacts were sintered at 1350°C for 2 h in an argon atmosphere. A heat-up rate of 100°C/h was used and the anodes were furnace-cooled (50-100°C/h).

For experiments conducted under oxidizing conditions (air atmosphere, no Al present), the sides of the anodes were masked with platinum foil so that only the bottom surface of the anode was exposed to the melt. To bond this foil to the anode, the side of an anode was painted with a Pt ink (Englehard No. 6082). This was baked at 850°C for 0.5 h to drive off the organic solvent. A Pt foil (0.001 inch thick) was wrapped around the anode and a snug fitting alumina tube was slid over the foil. This assembly was fired at 1000°C for 2 h to achieve good bonding between the foil and the anode. Since the thermal expansion of the alumina is less than the anode material, the alumina sleeve provided pressure between the foil and the anode during firing.

For experiments conducted with polarized anodes, it was necessary to shield the side of the anode with an electrical insulating material. For runs where the melt was saturated with Al_2O_3, alumina tubes were used as the shield. BN sleeves were used for runs at lower Al_2O_3 concentrations. In all tests, the Inconel connecting rod was shielded with a BN sleeve to prevent oxide scales formed on the Inconel from falling into the melt and adding Fe and Ni. The bottom surfaces of anodes were polished and reoxidized for 2 h in air at 1000°C prior to each experiment.

3) Experiments under Oxidizing Conditions

The experimental procedure was rather simple for tests on unpolarized anodes. Bath was melted in a platinum crucible. When thermal equilibrium was reached, the anode was lowered into the melt and rotation begun. Bath samples were periodically withdrawn and analyzed for Fe and Ni, thereby tracking the dissolution. Samples were analyzed by either atomic absorption or by the inductively coupled plasma technique. Weights of bath samples were recorded, as was the weight of bath remaining after the test. As will be discussed later in the report, this weight data was needed to determine dissolution rate constants from the sample analyses.

4) Experiments with Polarized Anodes, No Aluminum Present

The cell for these experiments is shown in Figure 90. Either an alumina or a boron nitride crucible was used to contain the melt, depending on whether the melt was saturated with Al_2O_3. Since the anode was polarized in these tests, some Fe and Ni dissolving from the anode was reduced at the counter electrode (cathode). The dissolving impurities can both accumulate in the melt and be plated onto the cathode. To track the dissolution of the anode, solid copper cathodes were used and were replaced every one-half hour and analyzed for impurities. The cathode and the plated material were completely dissolved in acid before analysis to include all Fe and Ni accumulating there. In addition, melt samples were periodically taken and analyzed.

A reference electrode was needed to conduct these experiments. A floating aluminum electrode was used (Figure 91). The development of this electrode was covered in a quarterly report (8). At the beginning of each test, before the anode was immersed in the melt, the reference electrode was immersed and checked by polarizing a Pt anode (0.08 cm dia.) relative to it and recording the potential for oxygen evolution. This was repeated until a constant value was obtained (approximately 1 h). During the actual experiment

GA 18194.16

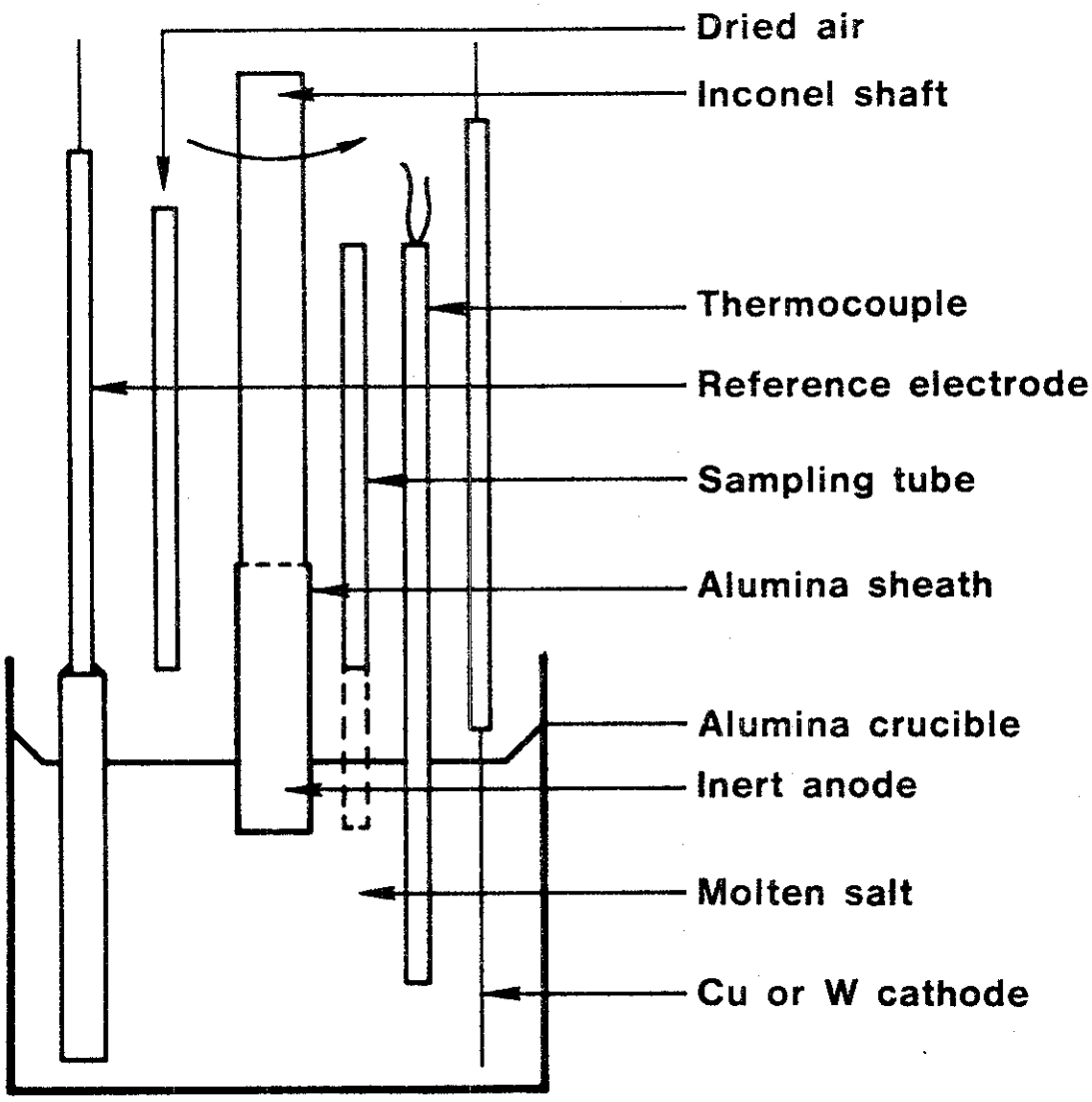

Schematic Diagram of Cell Used for Dissolution Measurements of Polarized Anodes Without Aluminum Metal Pads
Figure 90

GA 18194.187

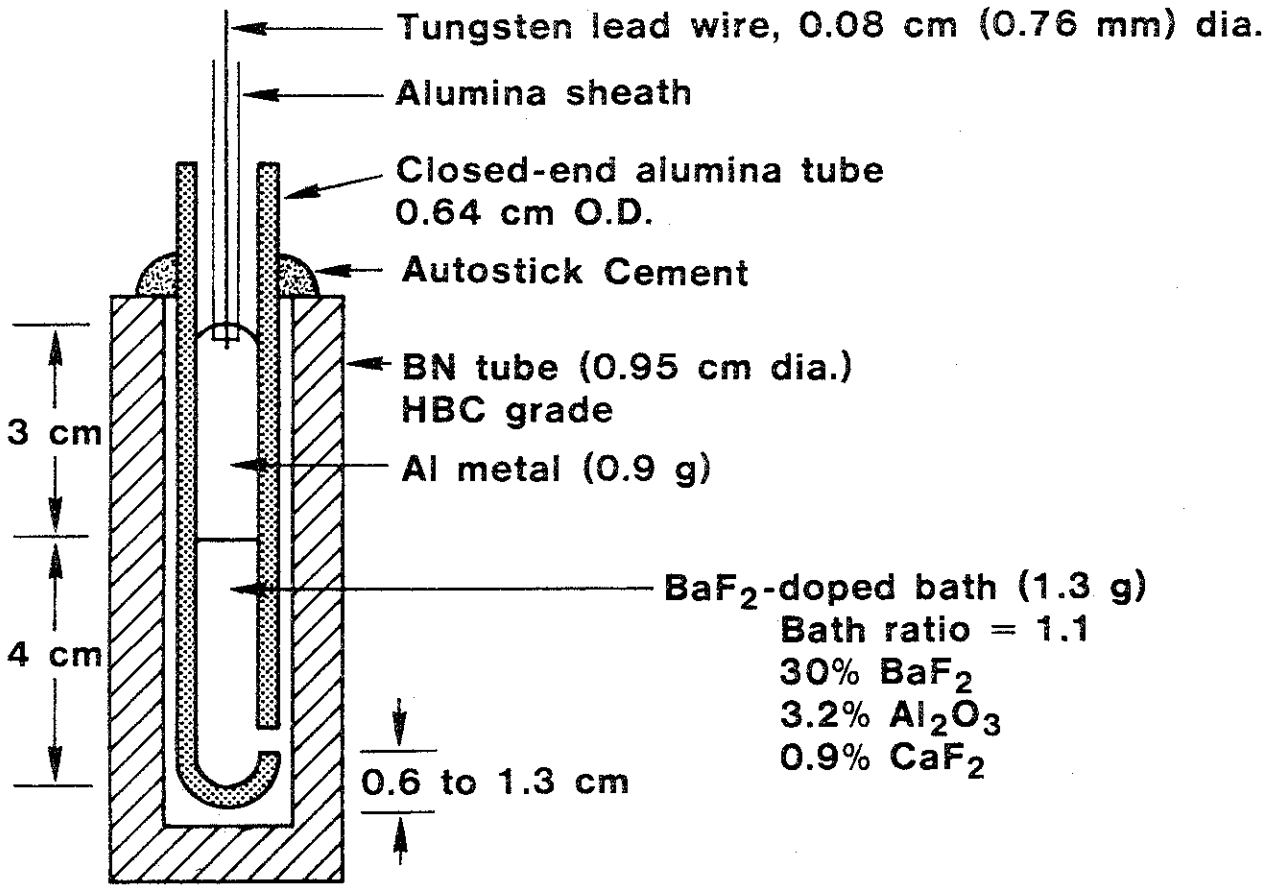

Floating Metal Reference Electrode

Figure 91

all potentials were referenced to this value for oxygen evolution on platinum. After the experiment the platinum wire was inserted into the melt and the reference electrode was rechecked. The electrode was stable to within +0, -40 mv over an 8 h period.

5) Experiments with Aluminum Metal Pads

These experiments were performed to determine the effect of dissolved reduced species (which result from contact of bath with a metal pad) on the rate of inert anode dissolution. By necessity, these experiments also include the effect of current through the anode (and, of course, gas generation). Without current the dissolved reduced species will reduce the surface of the anode (50). To determine the effect of dissolved reduced species, the results of these experiments with metal pads present were compared to experiments with copper cathodes.

The cell used for the experiments with metal pads is shown in Figure 92. The initial metal depth was 3.2 cm and the bath depth 6.4 cm. When the system had reached thermal equilibrium, an inert anode was lowered into the bath, the current was immediately turned on, and rotation of the anode at 300 rpm was begun. Samples of bath and metal were taken every one-half hour. Metal samples were taken using evacuated pyrex "pin" sampling tubes which were inserted in a brass holder. When the pyrex tube was immersed in metal, the thin bubble near the tip of the tube softened, was broken open by the pressure of the metal, and the tube then filled with metal. The metal samples were analyzed for Fe and Ni by atomic absorption. The potential of the anode was monitored with a floating aluminum reference electrode.

During each experiment a layer of sludge accumulated on top of the metal pad. This was found to consist of bath and Al_2O_3, and was relatively rich in iron and nickel. This material did not settle out or form during solidification because Fe and Ni concentrations

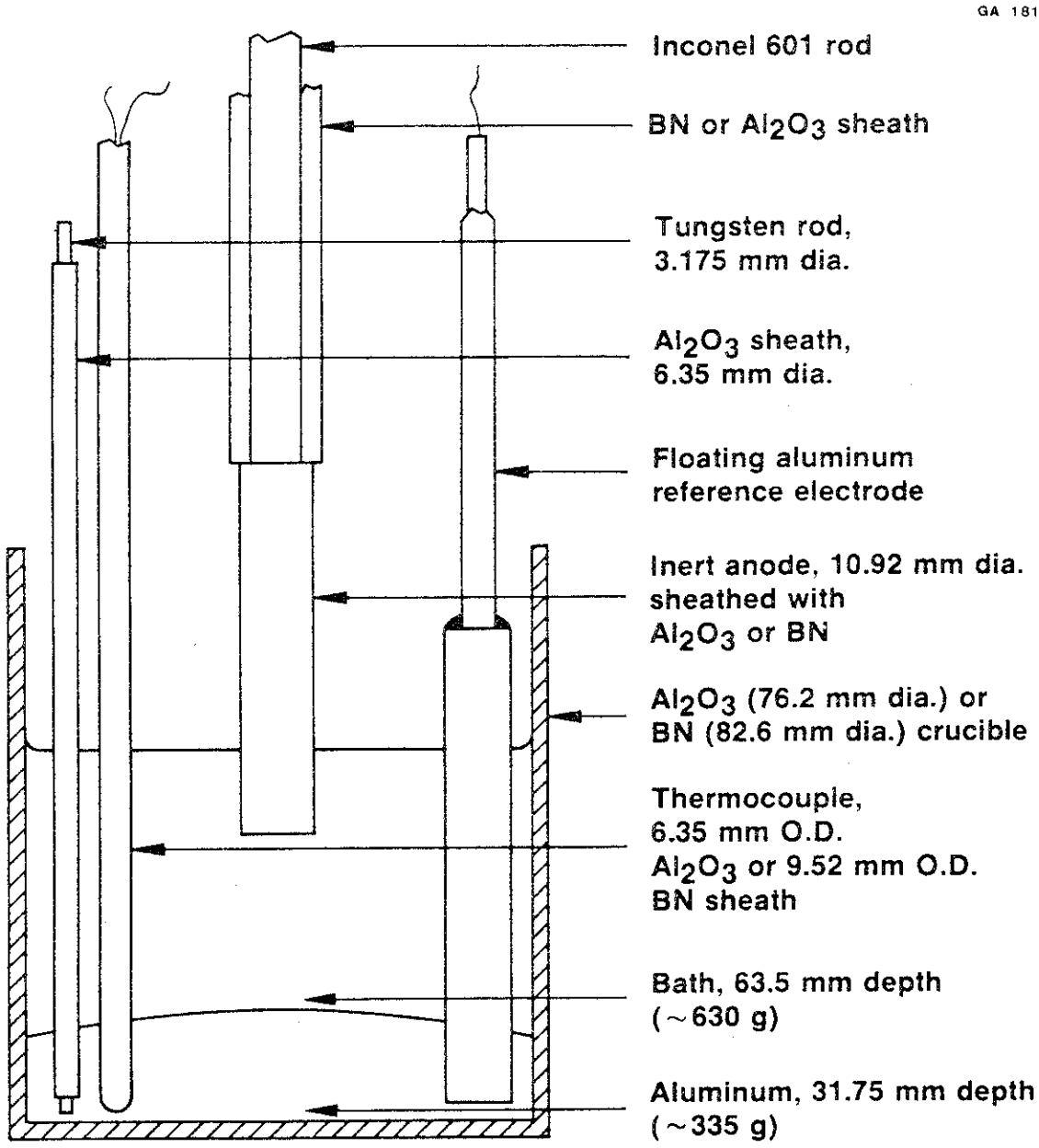

Cell Used for Measurements of Dissolution Rates of Inert Anodes With a Metal Pad in the System

Figure 92

in the bulk of this bath which remained above this sludge were consistent with final bath samples taken during the experiment. The formation of the sludge will be discussed later in the report. Results from analyses of bath and metal samples taken during the experiment, and analysis of the sludge recovered, were then used to calculate dissolution rate constants.

Many of these experiments were conducted in Al_2O_3 crucibles. After these experiments the bath could not be separated from the crucible. Therefore, after each experiment the crucible was broken and the skim was separated from the remaining bath. Then the skim and remaining bath, including portions of the alumina crucible, were crushed and analyzed for Fe, Ni, and free Al_2O_3. From the original and final concentrations of Al_2O_3 in the bath, the quantity of alumina crucible included in the sample can be calculated and subtracted out to get the actual quantities of skim and bath.

6) Experiments to Test Effect of Carbon/Al_4C_3

To determine if carbon or Al_4C_3 adversely affected anode dissolution, experiments were conducted with carbon or Al_4C_3 fed into the cell. One test was run with a cathodically polarized rod suspended in the bath to form Al_4C_3 in situ. All experiments were conducted with a molten aluminum cathode because it was thought that a sink was needed for any reduced Fe and Ni which could be formed by the carbon/Al_4C_3.

The cell used was identical to that used in other experiments with molten aluminum cathodes (Figure 92). The experimental procedure was identical to that used previously, except that pellets consisting of a mixture of bath and either carbon or aluminum carbide were fed into the cell.

Every 15 minutes a pellet of bath + carbon or aluminum carbide was dropped into the cell. For carbon additions the composition of

the pellets were 12.5% carbon - balance bath, with each pellet containing approximately 0.31 g carbon (ENID coke, -100 +200 mesh). For carbide additions the composition was 25% Al_4C_3 - balance bath, with each pellet containing approximately 0.31 g Al_4C_3 (Alfa Products No. 11118, -100 mesh). This corresponds to an accumulation of 1% carbide in the bath over the duration of the test, which is the approximate solubility of carbide in the bath (76). After the experiment the skim which accumulated on the surface of the metal pad was recovered and also analyzed for Fe and Ni.

In an attempt to generate aluminum carbide in situ during an experiment, one run was made with a cathodically polarized graphite rod suspended in the bath. This rod was electrically connected in parallel with the aluminum cathode, so that part of the current would flow through the rod.

A variable resistance was added in series to the graphite rod to control the relative amounts of current flowing through the aluminum cathode and this rod. The resistence was adjusted so that the current through the rod was 100 ma and the cathode current was 900 ma. Since there is a possibility that Fe and Ni would plate onto the graphite rod, the rod was replaced every one-half hour. The material adhering to the ends of these rods was dissolved off and analyzed so that the rate of deposition of these impurities could be established. Except for the graphite rods, the experiment was conducted by the same procedure used for other experiments.

7) Effect of Sampling Depth on Concentrations in Bath

The question of whether the bath is well mixed during a dissolution experiment arose during this study. As a result, bath samples were sequentially taken at differing depths during one experiment. Bath samples were taken from 1.3 to 7.6 cm below the surface at five-minute intervals to avoid cooling of the bath by

the alumina sampling tubes. Normally just the bath withdrawn into the sampling tube is crushed and analyzed. In this instance the bath which froze on the outside of the tube was also analyzed. Figure 93 shows there was no change in sample analysis with depth, so the bath was well mixed and segregation of the impurities was not a problem.

d. Results and Discussion

1) Experiments Under Oxidizing Conditions

a) Analysis of Data

Figures 94-96 show the bath analyses for typical dissolution tests conducted under oxidizing conditions. The concentrations gradually approach a steady-state plateau, which is the solubility of the material in the melt. The concentrations given in Figures 94-96 were tested according to various rate equations and were found to fit a first order equation.

The rate constants were calculated from the integrated form of the rate equation rather than the differential form, because the differential form uses only the initial data. The derivation of this equation will be given here. The rate equation for mass transport controlled dissolution is:

$$R = k\ (C_s - C_b)\ A \qquad (35)$$

where R is the dissolution rate (g/s), k is the rate constant (cm/s), C_s and C_b are the solubility and the instantaneous concentration of the dissolving species in the bulk of the melt (g/cm^3), and A is the projected area of the anode (cm^2). This rate is related to the change in concentration in the bath by:

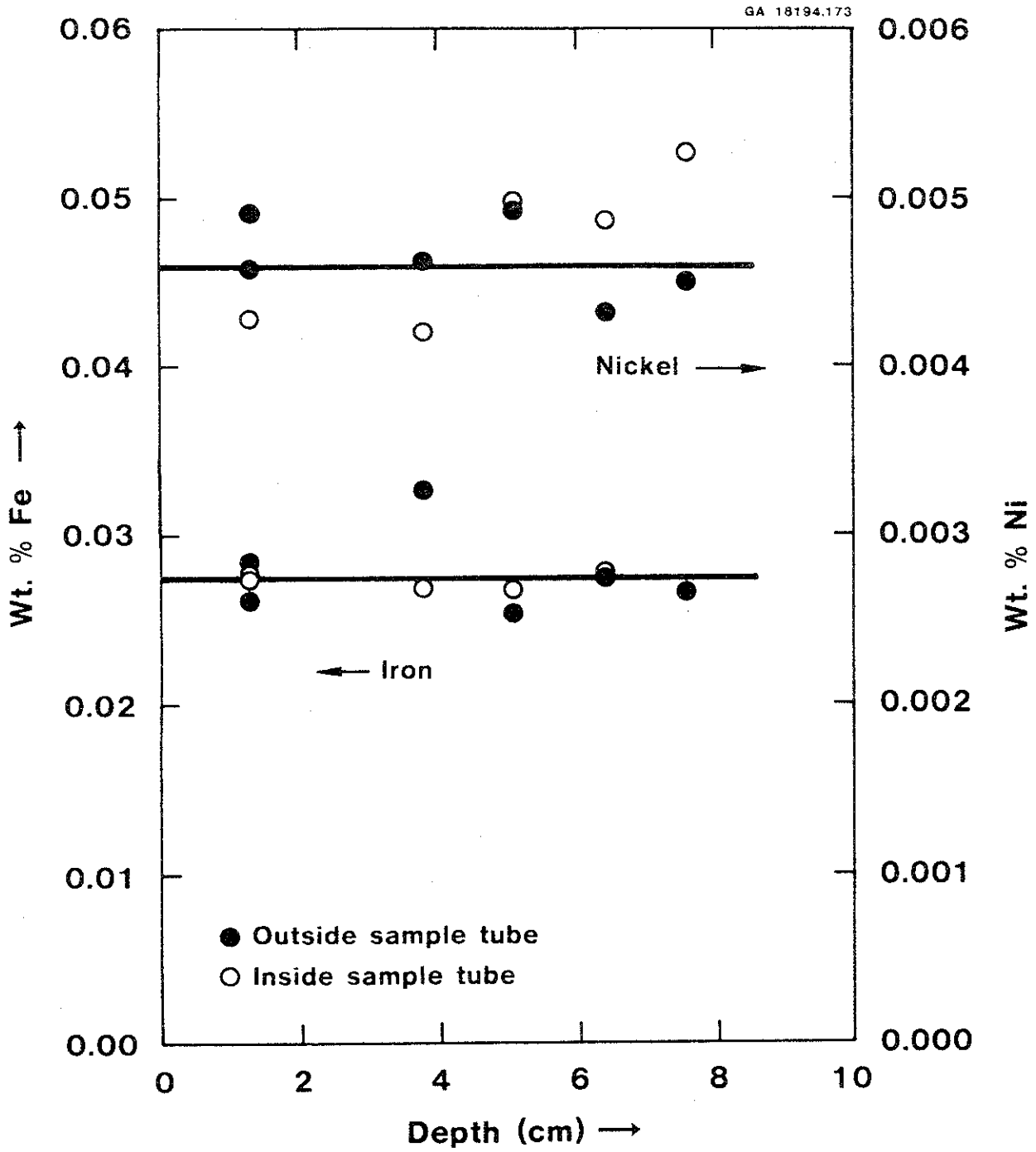

Variation of Bath Analysis with Depth during Experiment R80.

Figure 93

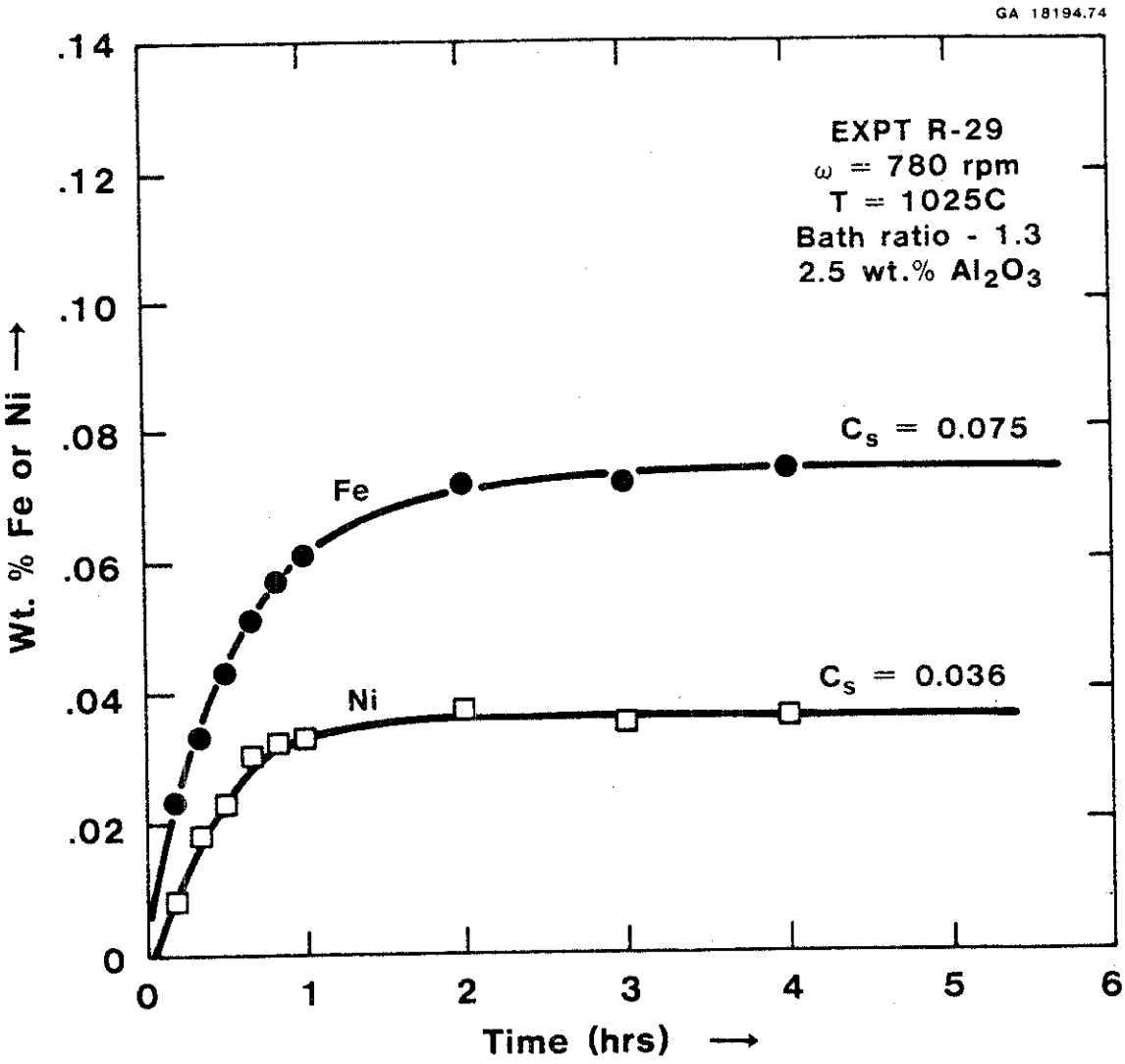

The Dissolution of Ni Cermet (6846) Inert Anode Material from a Rotating Disk at 780 rpm. Melt Contained 1.3 wt. % CaF_2

Figure 94

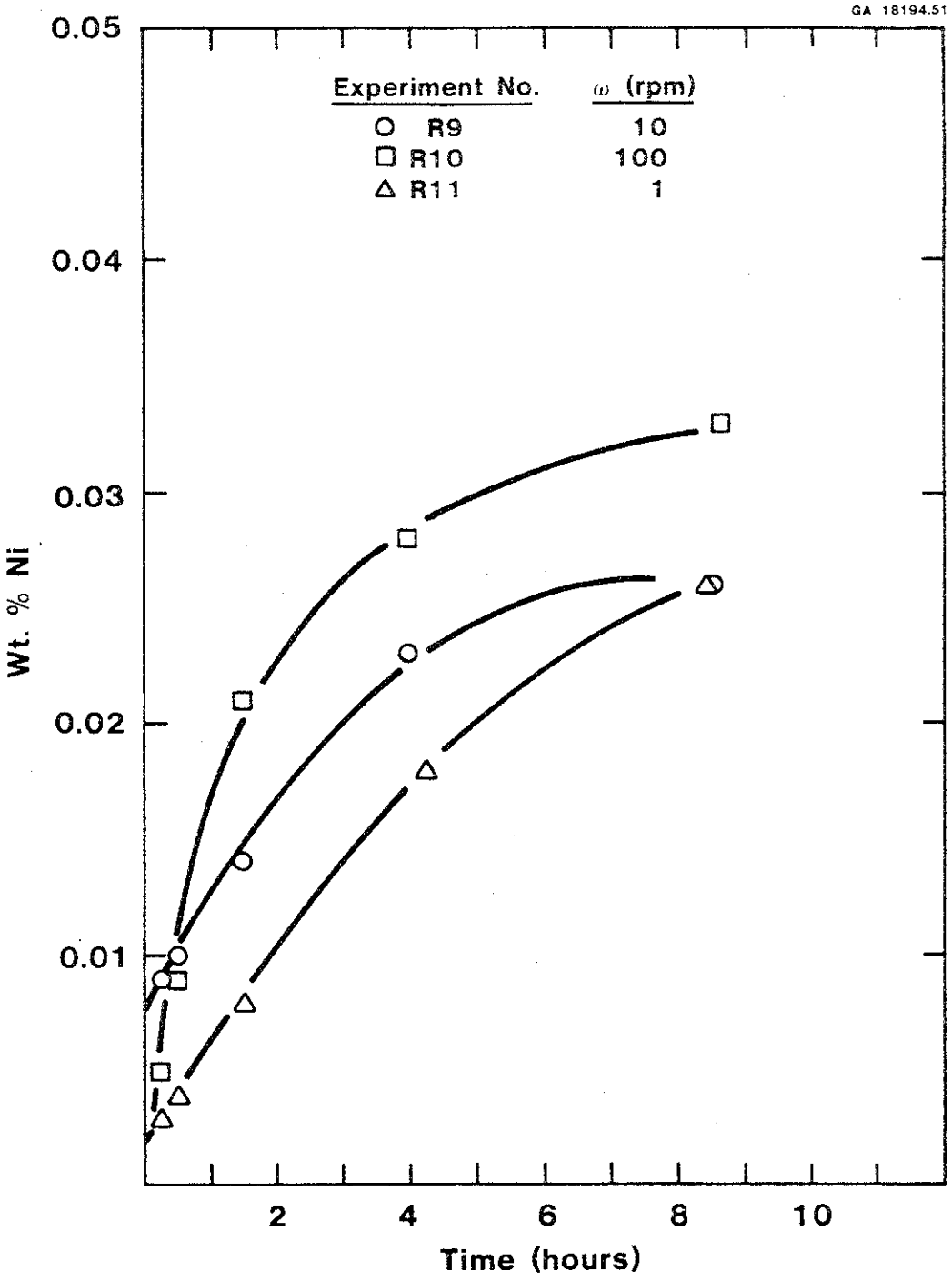

The Nickel Dissolution from Ni Cermet (6846) Inert Anodes in an $NaF-AlF_3-CaF_2-Al_2O_3$ Melt Bath Ratio 1.3, 2.5 wt. % Al_2O_3, 1.3 wt. % CaF_2) at 1025°C
Figure 95

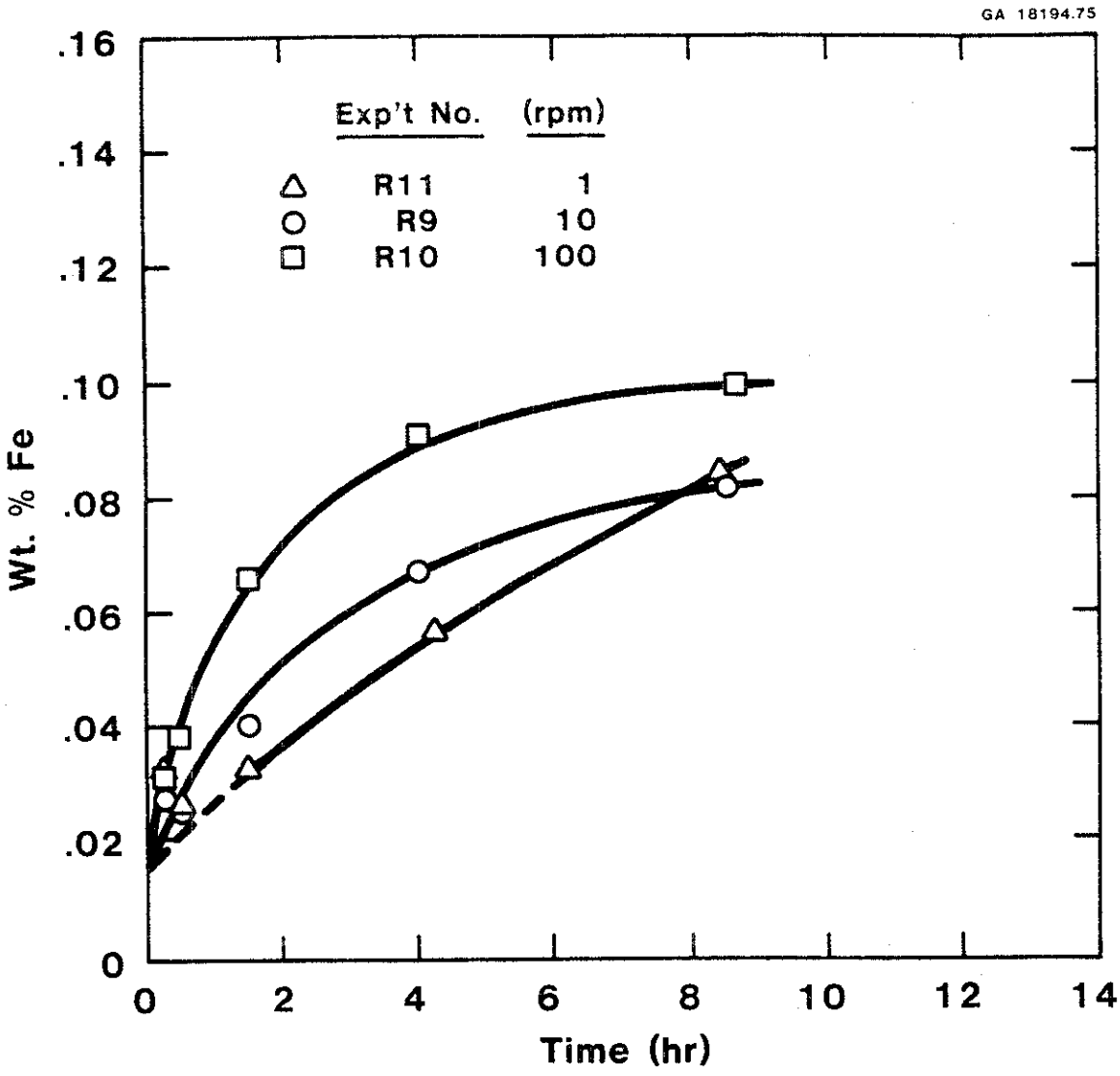

The Iron Dissolution from Ni Cermet (6846) Inert Anodes in an $NaF-AlF_3-CaF_2-Al_2O_3$ Melt Bath Ratio 1.3, 2.5 wt. % Al_2O_3, 1.3 wt. % CaF_2) at 1025°C
Figure 96

$$R = \frac{dC_b}{dt}\left(\frac{W_b}{\rho_{bath}}\right) \tag{36}$$

where t is time, W_b is the mass of the bath into which the anode is dissolving, and ρ_{bath} is the density of the bath. Combining Equations 35 and 36, the differential rate equation is obtained:

$$\frac{dC_b}{C_s - C_b} = -\left[\frac{k\pi r^2 \rho_{bath}}{W_b}\right] dt \tag{37}$$

where r is the radius of the anode. Integrating this equation from $C_b = C_b^o$ (initial concentration of the dissolving species in the bath) at t = 0 to $C_b = C_b$ at time t yields,

$$\ln (C_s - C_b) = -(k\pi r^2 \rho_{bath}) \int_o^t \left(\frac{1}{W_b}\right) dt + \ln (C_s - C_b^o) \tag{38}$$

The mass of bath, W_b is not constant but varies with time because of bath removed by sampling and some vaporization. Since W_b varies noncontinuously with time, the integral must be evaluated numerically or graphically. Based on Equation (38), a plot of

$\ln (C_s - C_b)$ vs $\int_o^t \left(\frac{1}{W_b}\right) dt$ should yield a straight line

with a slope of $-(k\pi r^2 \rho_{bath})$, and an intercept of $\ln (C_s - C_b^o)$. The concentration terms can also be expressed in weight percentages. The rate constant k is then calculated from the slope.

Figures 97 and 98 show plots for these data based on the integrated rate equation. The integral

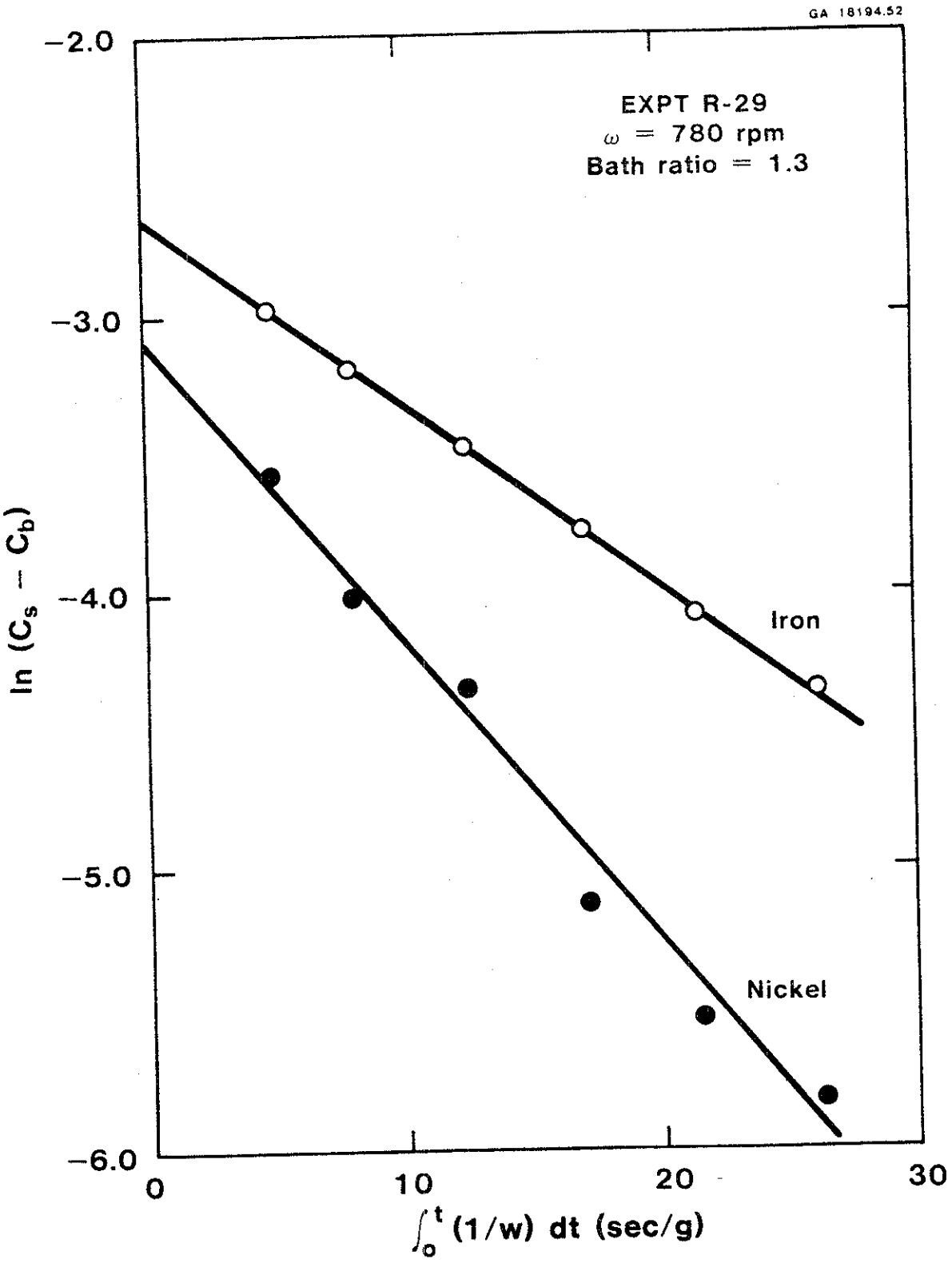

Dissolution Data for Experiment No. R29 Plotted According to the Integrated Rate Equation for Mass Transport-Controlled Dissolution.

Figure 97

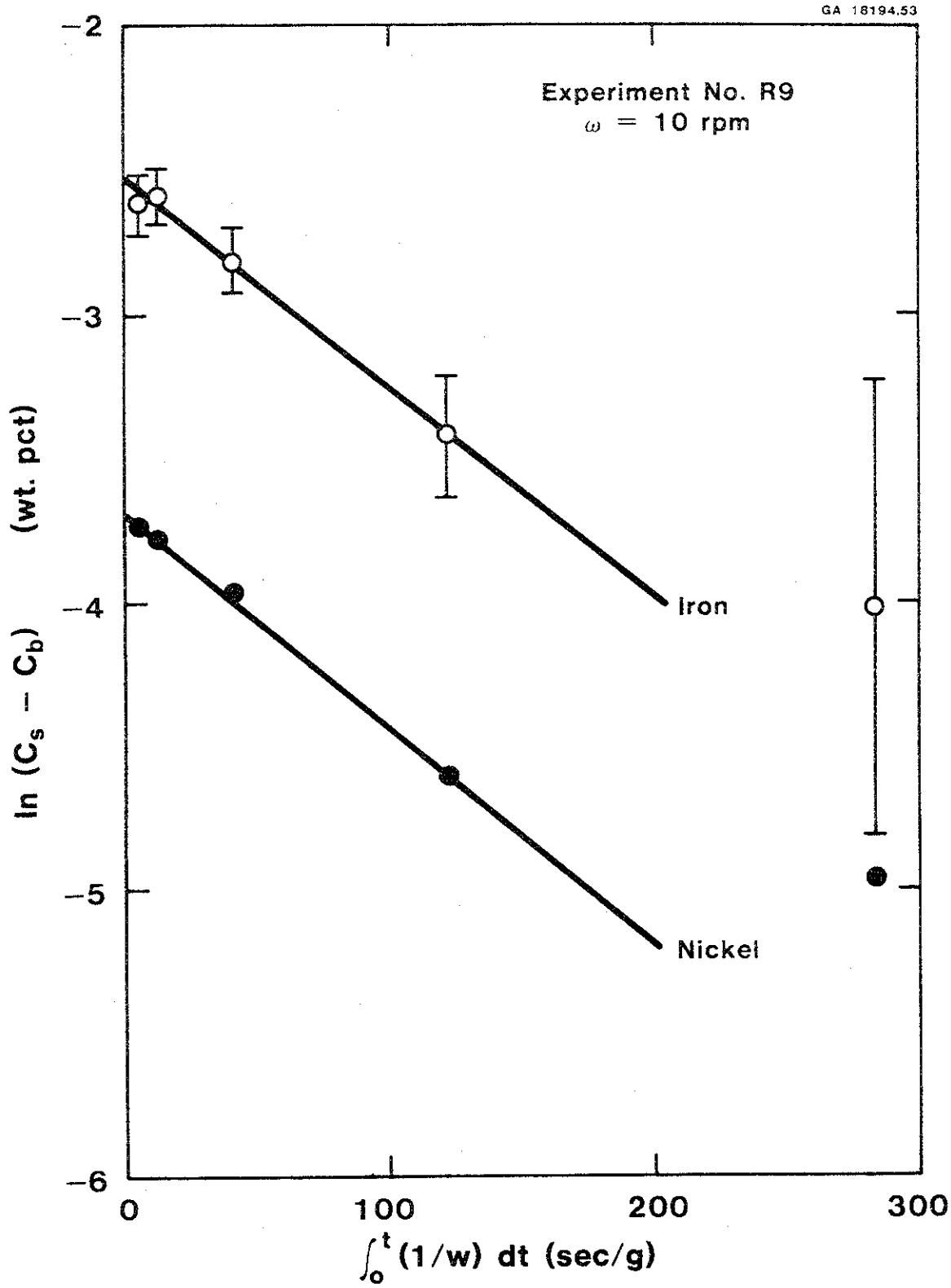

Inert Anode Dissolution Data Plotted According to the Integrated Form of the Rate Equation for Mass Transport-Controlled Dissolution.

Figure 98

$\int_0^t \left(\frac{1}{W}\right) dt$ was evaluated numerically, with changes in the mass of bath because of sampling and vaporization were taken into account. Data for times greater than 4.5 h were not used to obtain least-squares fits for the data, because at long times C_b approaches C_s and the error in $\ln (C_s - C_b)$ due to random error in the sample analyses becomes very large. The error bars for the iron curve in Figure 97 were calculated for a random error of ± 0.005 wt.% Fe for the sample analyses.

The rate constants for dissolution, k, were calculated from the slopes of the least-squares lines such as shown in Figure 97, using Equation (38). The numerical analyses, plotting of the data, and least squares fitting of the data were performed using a BASIC computer program.

b) Results

The dissolution rate constants obtained from experiments for unpolarized anodes under oxidizing conditions are given in Tables 44 and 45. These results are for Ni cermet anodes, and include results from tests conducted to determine the effects of rotational speed of the anode, anode age, temperature and bath composition.

Effect of rotational speed: The rate constants are shown as a function of the square-root of the rotational speed, $\omega^{1/2}$ (Figure 99). The data plotted was taken from Table 44 and the "A" experiments given in Table 45. The least-squares lines drawn through the data are:

$$k_{Fe} = -1.14 \times 10^{-3} + (0.99 \times 10^{-3})\ \omega^{-1/2}, \quad (39)$$

$$k_{Ni} = -0.74 \times 10^{-3} + (1.23 \times 10^{-3})\ \omega^{-1/2} \quad (40)$$

TABLE 44

Dissolution Rate Constants for 6846 Ni-Cermet
Inert Anodes in Bath Under an Air Atmosphere

Experiment No.	T(°C)	Bath Composition		Rotational Speed	Rate Constant, k x 10^3 (cm/s)	
		Bath Ratio	Al_2O_3 (wt.%)	ω (rpm)	Fe	Ni
R9	1025	1.3	2.5	10	2.6	5.8
R10	1025	1.3	2.5	100	9.1	7.1
R11	1025	1.3	2.5	1	2.8	3.4
R22	1025	1.3	2.5	300	12.8	17.8
R27	1025	1.3	2.5	780	32.8	31.0
R29	1025	1.3	2.5	780	25.6	41.3
R30	1025	1.3	2.5	300	11.8	17.2
R32	1025	1.1	2.5	300	13.4	18.9
R33	1025	1.1	4.5	300	11.0	17.4
R34	960	1.1	4.5	300	4.4	5.1
R40	960	1.1	4.5	300	2.5	7.4
R41	960	1.1	6.5	300	3.7	2.7

TABLE 45

Effect of Test Time on the Dissolution Rate Constants
for 6846 Ni-Cermet Inert Anodes in Bath
Under an Air Atmosphere

Experiment No.	T(°C)	Bath Ratio	Al_2O_3 (wt.%)	Initial Bath Wt. (g)	Duration of Test (h)	Rate Constant, k x 10^3, (cm/s) Fe	Ni
R43A	1025	1.3	2.5	150	6	17.7	24.4
R43B	1025	1.3	2.5	150	6	14.3	34.5
R45A	1025	1.3	2.5	300	12	11.8	17.1
R45B	1025	1.3	2.5	150	6	16.7	22.7
R47A	960	1.1	4.5	150	12	3.9	6.7
R47B	960	1.1	4.5	150	12	3.0	5.8
R48A	960	1.1	4.5	300	24	5.0	6.2
R48B	960	1.1	4.5	150	12	4.9	3.4

where ω is in units of rpm. The fit was good, with correlation coefficients greater than 0.93.

The linear relationship between k and $\omega^{1/2}$ is evidence that mass transport is the rate limiting step for dissolution of the anode. The non-zero intercept may be due to natural convection in the system, or possibly increased agitation in the bath due to wobble in the anode.

Assuming the Levich equation holds for this system (in the absence of natural convection and wobble, it does), the diffusion coefficients for iron and nickel can be calculated from the slopes of lines in Figure 99. The Levich equation in dimensionless numbers is:

$$Sh = 0.6201\ Re^{1/2}\ Sc^{1/3} \qquad (41)$$

or

$$\frac{kr}{D} = 0.6201\ \left(\frac{\nu}{D}\right)^{1/3}\ \left(\frac{\omega r^2}{\nu}\right)^{1/2}$$

where Sh, Re, and Sc are the Sherwood, Reynolds, and Schmidt numbers. Rearranging gives $k = 0.6201\ D^{2/3}\ \nu^{-1/6}\ \omega^{1/2}$. Taking the kinematic viscosity to be 1.3×10^{-2} cm^2/s, the rate constant predicted by the Levich equation is:

$$k = 1.279\ D^{2/3}\ \omega^{1/2}, \qquad (42)$$

and the diffusion coefficient could be calculated from the slope of a plot of k vs. $\omega^{1/2}$ where ω is in radians/s. The diffusion coefficients for iron and nickel calculated from the slopes of lines in Figure 98 are 1.2×10^{-4} and 1.6×10^{-4} cm^2/s. The order of magnitude of these values is in agreement with diffusion coefficients for other species in cryolite-based melts, which are in the range of 10^{-4} to 10^{-5} cm^2/s (77). It should be noted that the diffusion coefficients calculated from Equations 41 and 42 are for the

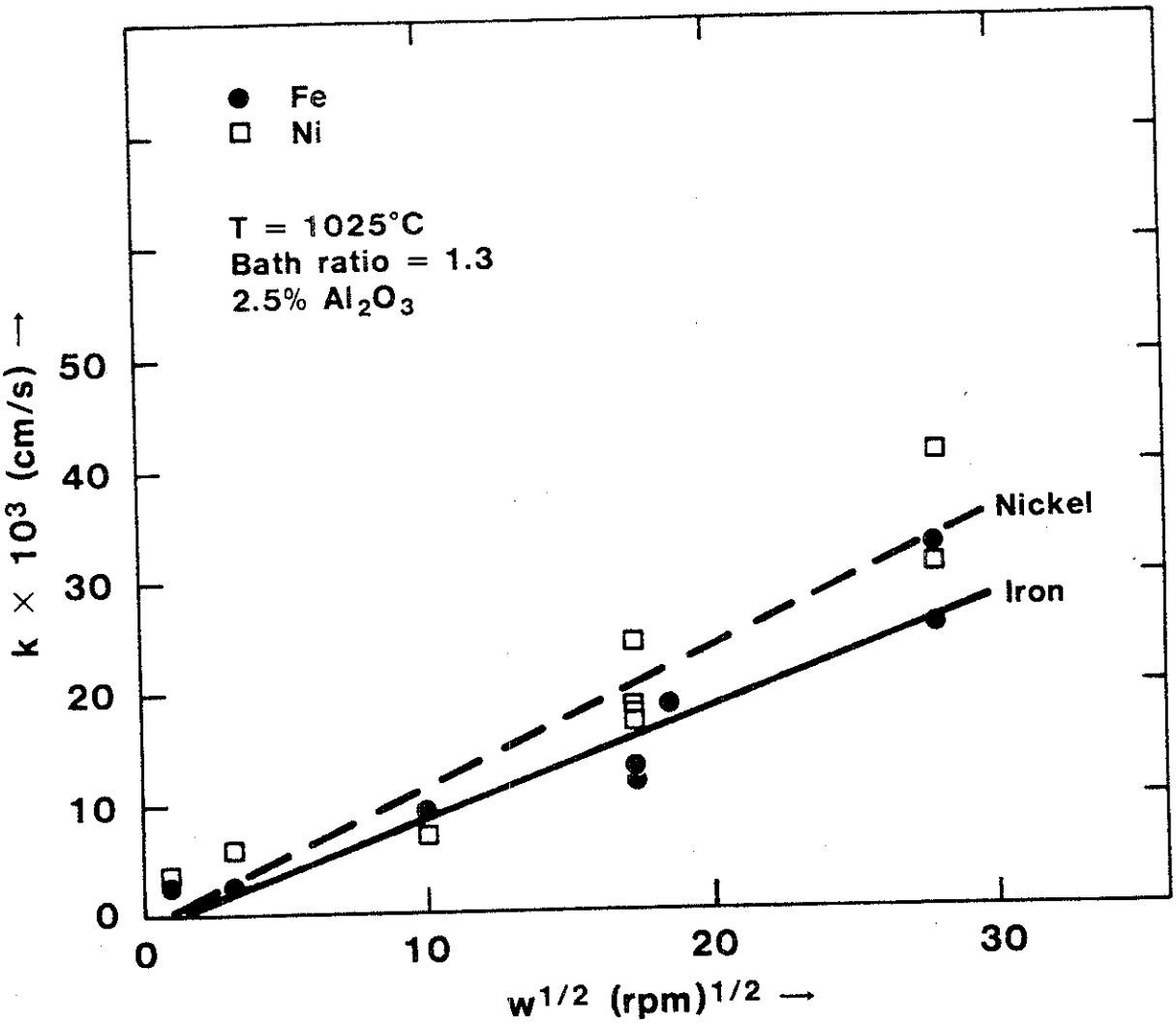

Dissolution Rate Constants for Ni Cermet (6846) Anode Material in Bath under Air Atmosphere.
Figure 99

iron and nickel species which exist in the bath, which are unknown at the present time.

In summary, the rate constant for dissolution varies linearly with $\omega^{1/2}$; this means that mass transport is the rate limiting step for dissolution of the anode in bath under oxidizing conditions. Diffusion coefficients calculated from the experimental data are consistent with published values for other species in cryolite-based melts.

Effect of temperature and bath composition: Experiments were conducted at both 1025 and 960°C, and at several different concentrations of alumina. Basically, tests were made at either 1025°C, 1.3 bath ratio, 2.5 wt.% Al_2O_3 or 960°C, 1.1 bath ratio, 4.5 wt.% Al_2O_3 (or 6.5 wt.% Al_2O_3). The first combination of conditions was intended to be a worst case, and the second was intended to be a best case which represented our standard operating conditions. The worst case conditions gave much more dissolution; therefore the rates were easier to measure. This was a logical choice for the first measurements.

Figure 100 shows the rate constants obtained for differing conditions. The data for 1025°C, 1.3 bath ratio, 2.5 wt.% Al_2O_3 were taken from Figure 99. The lines are least squares fits to these data. As seen, the rate constants decrease with decreasing temperature/bath ratio, and at a constant temperature they decrease slightly with increasing Al_2O_3 concentration in the melt. The decrease with decreasing temperature is expected, though the magnitude of decrease is larger than expected. The decrease with increasing Al_2O_3 content was not necessarily expected; even though the solubility is decreased with increasing Al_2O_3 content, this solubility change does not affect the rate constant (it does, of course, affect the dissolution rate). Apparently increasing concentrations of Al_2O_3 decrease the diffusion

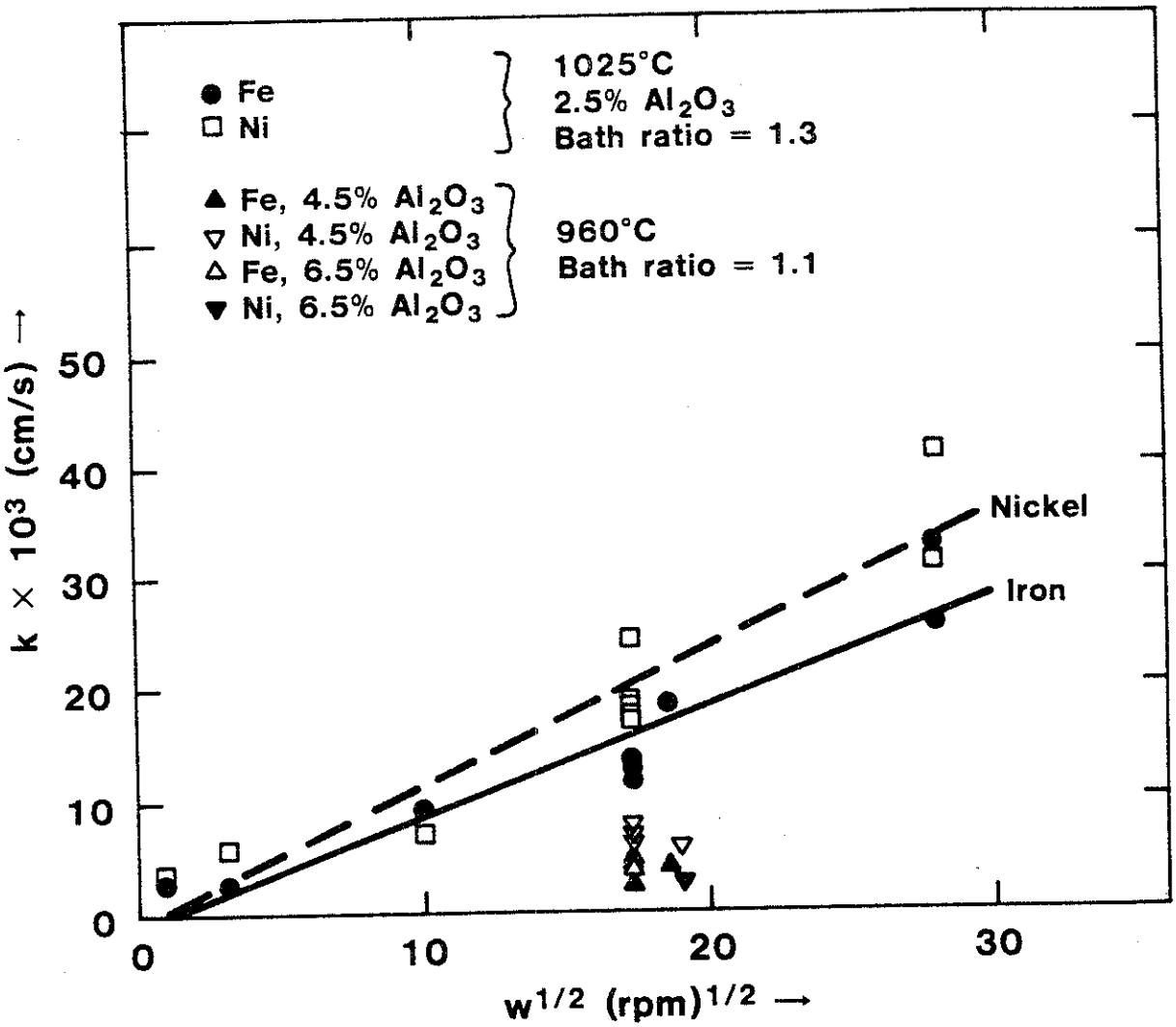

Effect of Bath Composition/Temperature on Dissolution Rate Constants for Ni-Cermet (6846) Inert Anode Material

Figure 100

coefficients for the dissolved Fe and Ni species.

In Experiment R32, the bath ratio was 1.1 compared to the ratio of 1.3 used for previous dissolution tests. The results from this experiment are compared with previous results in Figure 101. There appears to be no significant change in rate constant with bath ratio.

The Levich equation can be used to theoretically estimate the change in rate constant expected for a change in bath ratio. One form of this equation is

$$k = 0.6201\ D^{2/3}\ \omega^{1/2}\ \nu^{-1/6} \qquad (43)$$

where D is the diffusion coefficient for the dissolving species, ω is the rotational frequency (radians/s), and ν is the kinematic viscosity. Assuming that D does not change significantly with bath ratio, the change in k can be estimated by the Levich equation. Using viscosity data from Reference (78), the change in k for a change in bath ratio from 1.3 to 1.1 was +2.2 percent. As seen in Figure 99, the precision of the data was not high enough to detect a change this small.

Effect of anode age: Experiment Nos. R43 to R48 were conducted to determine whether the dissolution rate constants change with age. Each experiment consisted of two runs using the same anode.

At the conclusion of the first experiment for each anode, the anode was raised 3 cm above the bath surface and allowed to furnace cool. The anode was then removed and placed in a glove box until the next run. The calculated rate constants from these experiments are given in Table 45.

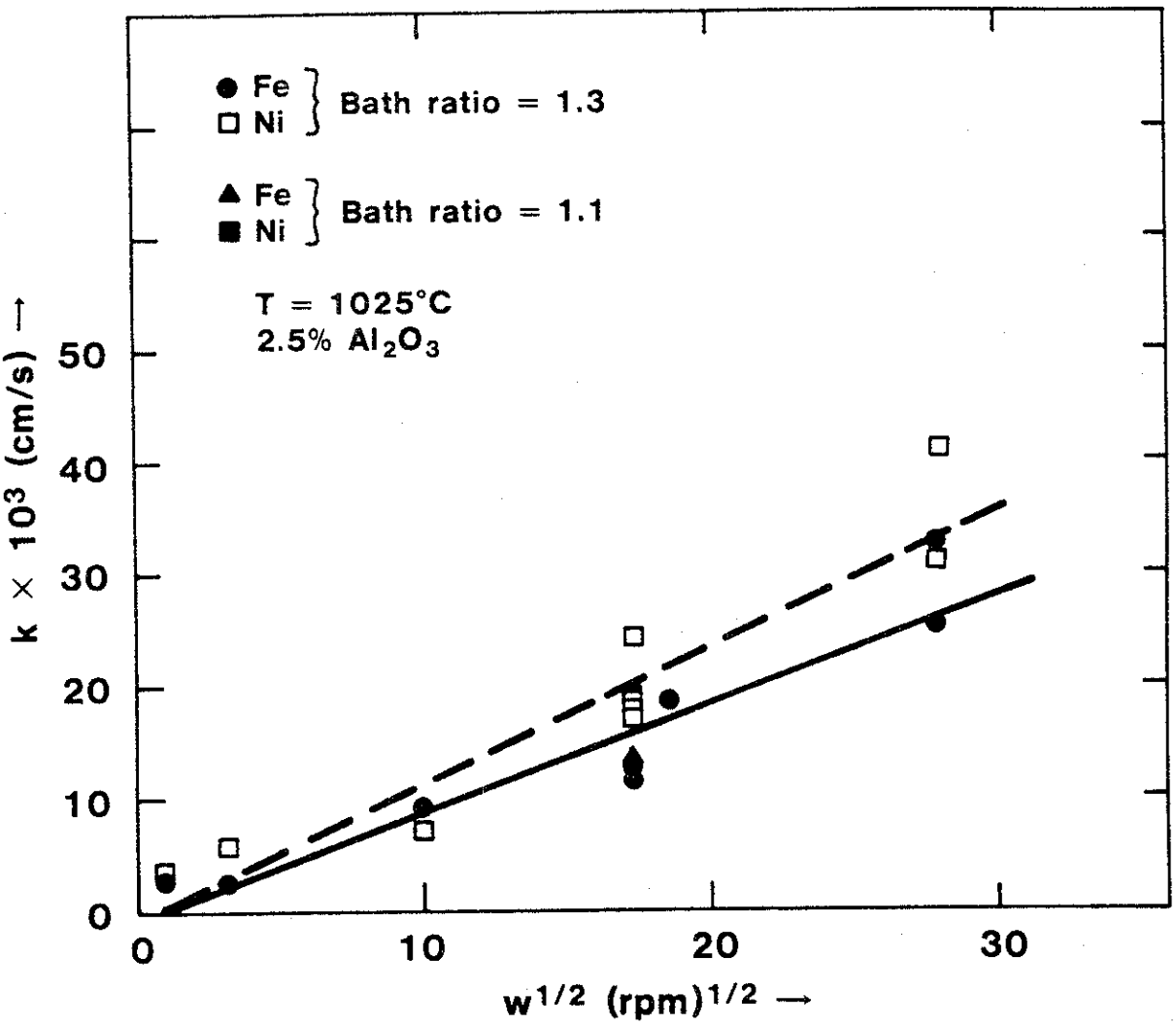

The Effect of Bath Ratio on the Dissolution Rate Constants for Ni-Cermet (6846) Inert Anode Material
Figure 101

Segments A and B for each experiment were run using the same anode, but with fresh bath each time. Thus, for segment A the anode is new, while for segment B the anode was previously aged for the duration of segment A. The data taken at 1025°C (Experiments R43 and R45) do not show any trend for changes in dissolution rate with anode age. Experiment No. R43 was made using 150 g of bath for bath segments, while Experiment No. R45 was made with 300 g of bath for the A segment and 150 g of bath for the B segment. Thus, rate constants were obtained at 3 ages for the anode. For iron, the rate constant decreased from A to B in R43 and increased from A to B in R45. For nickel, the measured rate constants increased from A to B in both experiments, but the increase is greater in R43 (for short-time aging) than in R45 (for long-time aging). No trend with aging can be discerned. The data for iron fall within the reproducibility of the measurements as determined from previous work ($\pm$ 5 x 10^{-3} cm/s), while the data for nickel fall outside of this reproducibility. This will be discussed later.

The data obtained at 960°C do show a slight decrease with anode age, but the values all fall within the previously determined reproducibility for k at this temperature of $\pm$ 1.5 x 10^{-3} cm/s. Also, the magnitude of the decrease with age is not consistent with age ($\Delta k = -0.9 \times 10^{-3}$ for 12 h age, and -0.1×10^{-3} for a 24 h age). Therefore, no trend is apparent within the uncertainty of the measurements.

The data do show a large change in rate constant with temperature. Table 46, which gives averages for this set of data, illustrates this. This factor of 3 or 4 increase in rate constant with temperature (and also decreased Al_2O_3) when combined with a factor of 2 increase in solubility with temperature, gives a factor of 6 to 8 increase in dissolution rate with temperature.

TABLE 46

Mean Rate Constants for Dissolution of 6846 Ni-Cermet Materials in Bath Under Oxidizing Conditions, Experiments R43-R48

Bath Ratio	Wt.% Al_2O_3	T(°C)	k (cm/sec)		Standard Deviation	
			Fe	Ni	Fe	Ni
1.3	2.5	1025	15.1×10^{-3}	24.7×10^{-3}	2.6×10^{-3}	7.2×10^{-3}
1.1	4.5	960	4.2×10^{-3}	5.5×10^{-3}	0.9×10^{-3}	1.5×10^{-3}

An interesting observation is that at 960°C, the average rate constants for iron and nickel are approximately equal, while at 1025°C the rate constant for nickel is significantly higher. Also, the standard deviation for nickel is higher than that for iron. This was not noted in earlier work, though more data was obtained in this series of tests than previously obtained for the same conditions. One explanation for the higher standard deviation for nickel is that the concentrations of nickel in the bath are approximately one-half those for iron, therefore the relative precisions of the chemical analyses are lower. As yet there is no explanation as to why the rate constant for nickel is higher than iron at 1025°C. Possibly it is the result of anodic dissolution of the Ni metal phase (through local cell action) which could result in an enchanced solubility for Ni within the boundary layer. For example, nickel metal could anodically dissolve by the electrochemical reaction:

$$Ni \rightarrow Ni^{2+} + 2e^{-}. \qquad (44)$$

Somewhere at the anode-bath interface a corresponding cathode reaction such as

$$\frac{1}{2} O_2 + 2AlF_4^{-} + 2e^{-} \rightarrow 2F^{-} + (Al_2OF_6)^{2-} \qquad (45)$$

would occur. The net result is that nickel is dissolving as NiO, which has a higher solubility than $NiFe_2O_4$. After an initial period the metal phase close to the surface is consumed, so for the remainder of the test the material dissolving is essentially all nickel ferrite. The steady-state concentrations of iron and nickel in the bath would be similar to the case where only nickel ferrite were dissolving, but the measured rate constant for nickel would be higher than if only nickel ferrite were dissolving.

2) Experiments with Polarized Anodes, Copper Cathodes

a) Analysis of Data

Figure 102 shows the bath analyses for a typical run. For each experiment there was an accumulation of impurities in the bath. Although some impurities are being plated onto the cathode, the rate at which the anode is dissolving is apparently faster than this rate. It should be noted that the area of the cathode is relatively small in these experiments. The average rates of accumulation of impurities in the bath and at the cathode are listed in Table 47. The rate of accumulation at the cathode ranges from approximately 3 to 51% of the total dissolution rate for iron (with all but one value being less than 30%), and from 3 to 30% of the total rate for nickel.

To calculate rate constants, a modified first order rate equation was derived which included the copper cathodes as well as the bath as sinks for impurities. A simple mass balance for impurities can be written,

$$\begin{array}{rcl} \text{Rate of anode dissolution} & = & \text{Rate of accumulation in bath} \\ & + & \text{Rate of accumulation in cathode} \end{array} \qquad (46)$$

For first order dissolution the rate is described by

$$\text{Rate} = k\,(C_s - C_b)\,A\,(\rho_{bath}/100). \qquad (47)$$

where k is the dissolution rate constant, C_s and C_b are the solubility and bulk concentrations of the dissolving species, respectively, A is the geometric area of the dissolving solid, and ρ_{bath} is the density of the bath. The rate of accumulation of the impurity in the bath can be written as

$$R_{bath} = (W_{bath}/100)\,(dC_b/dt) \qquad (48)$$

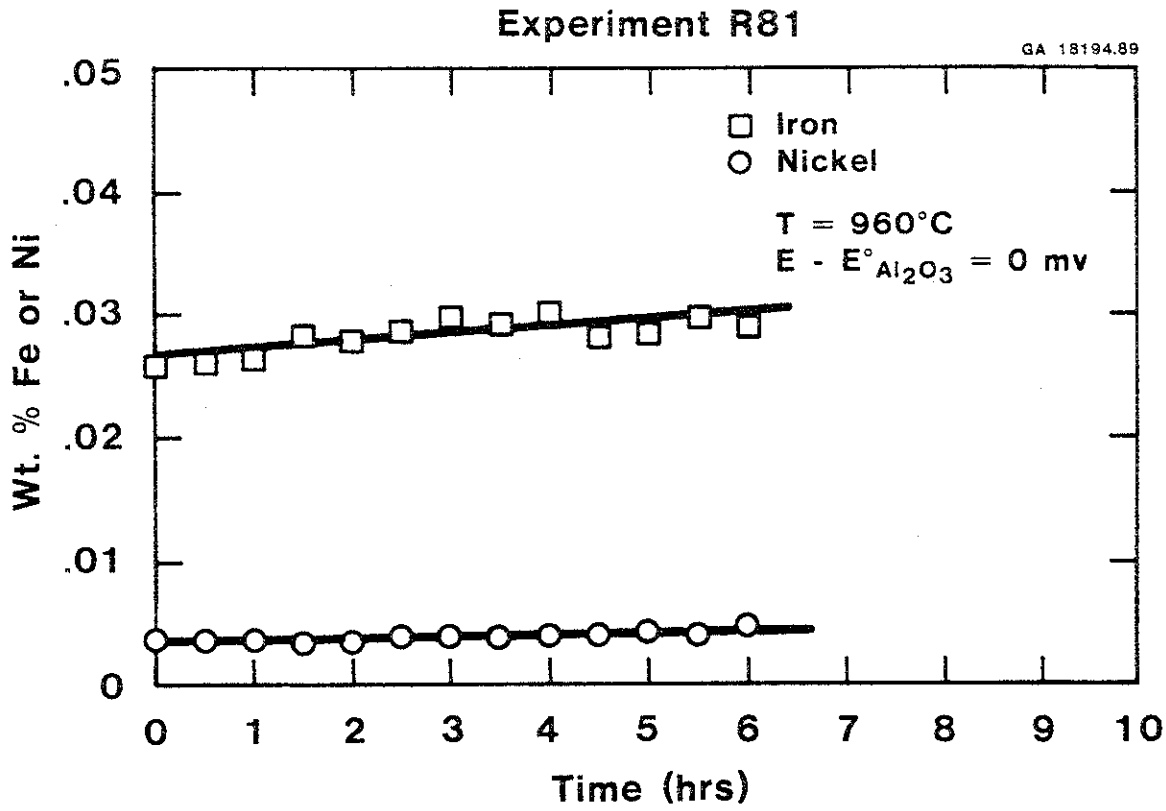

Bath Analysis for Experiment R81, Ni Cermet Anode (6846) Dissolving in Bath of Composition 6.5% Al_2O_3, 1.3% CaF_2, 1.1 Bath Ratio. Solid Copper Cathodes were used in the Cell.
Figure 102

TABLE 47

Average Accumulation Rates of Inert Anode Constituents in Bath and Copper Cathodes

Experiment No.	Iron Accumulation Rate x 10^7 (g/s)		Nickel Accumulation Rate x 10^7 (g/s)	
	Bath	Copper Cathodes	Bath	Copper cathodes
R56	83	4.9	25	7.0
R58	73	18	29	15
R60	87	3.4	24	14
R61	25	13	4.2	1.8
R62	78	1.7	51	18
R63	55	24	39	2.7
R79B	24	0.78	7.4	2.0
R80	19	1.3	4.4	1.7
R81	11	1.9	1.8	1.3
R91	22	1.6	5.1	2.0
R92	21	15	5.9	1.1
R96	14	1.6	4.5	1.7
R97	31	8.0	4.7	1.2
R100	22	10	7.9	1.1
R101	25	26	11	3.0
R102	55	8.3	21	2.1
R103	94	2.9	25	0.75
R104	52	2.2	26	5.0
R106	58	2.1	29	6.1

where W_{bath} is the weight of bath into which the anode is dissolving.

Substituting Equations (47) and (48) into (46) gives

$$k\ (C_s - C_b)\ A\ (\rho_{bath}/100) = (W_{bath}/100)\ (dC_b/dt) + Rc \qquad (49)$$

where R_c is the rate of reduction of impurities at the solid cathodes. R_c can be written as

$$Rc = dW_i/dt \qquad (50)$$

where W_i is the weight of impurity plated onto the cathode. Substituting Equation 50 into 49, rearranging, and integrating from time zero to time gives

$$(100) \int (1/W_{bath})[1/(C_s - C_b)]dW_i - \ln (C_s - C_b)$$

$$= kA\rho_{bath} \int (1/W_{bath})dt \qquad (51)$$

Both integrals in this equation need to be integrated numerically because of the discrete nature of the data. This was done with a BASIC computer program. If the dissolution process is first order, a plot of the left hand side of Equation (51) (referred to as the Y Function) vs. $\int (1/W_{bath})dt$ will be linear.

An example of the data plotted in this manner is given in Figure 103. As seen, they show that the dissolution is a first order process. Least squares analyses were performed for the data shown in Figure 103. From Equation (51) and the least squares slope, the disslution rate constant was calculated. This data analysis process was repeated for all of the experiments conducted with copper (or in one case tungsten) cathodes.

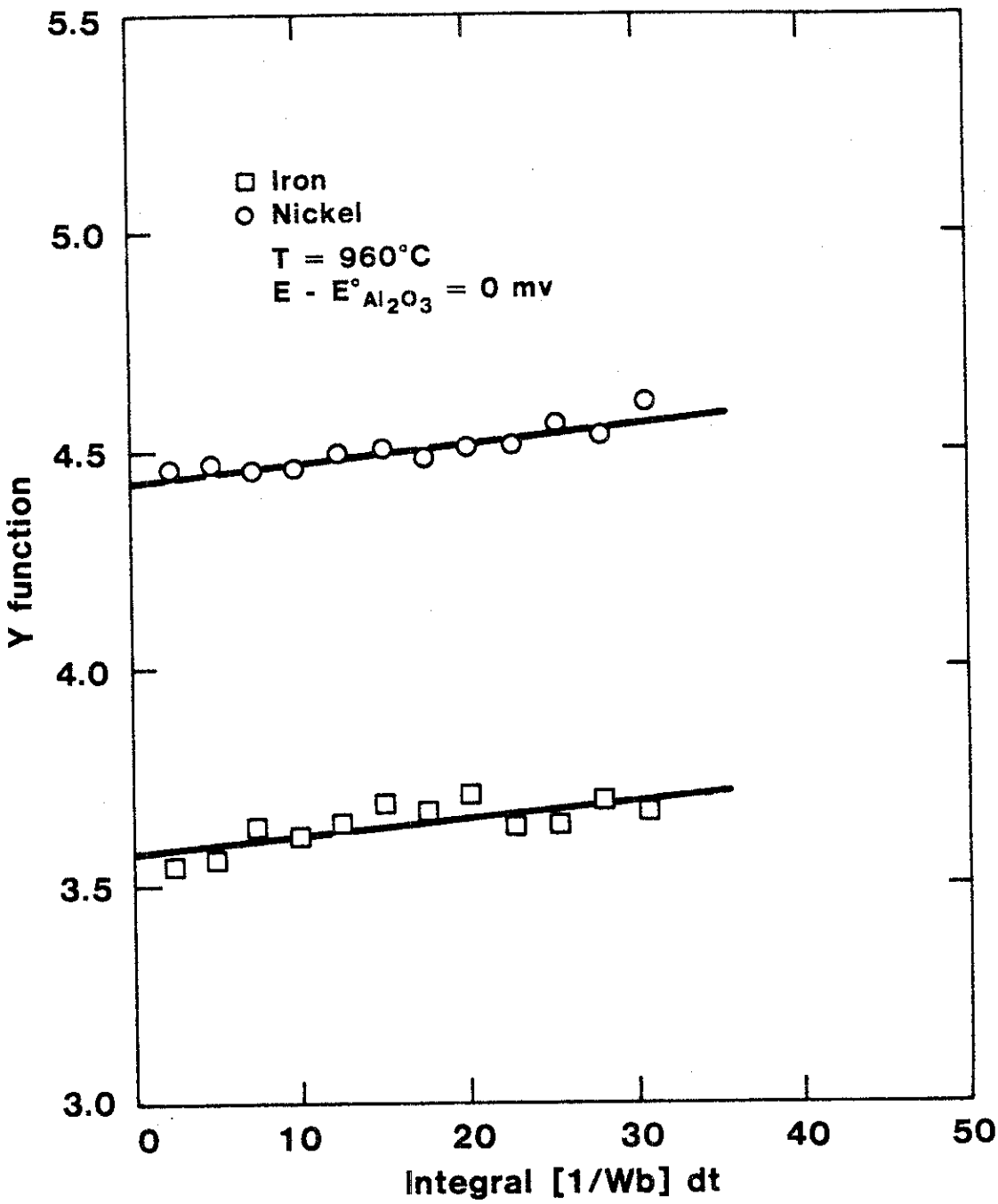

Dissolution Data from Experiment R81 Plotted According to the Integrated, first Order Rate Equation. Bath Composition was 6.5% Al_2O_3, 1.3% CaF_2, 1.1 Bath Ratio, and Solid Copper Cathodes were Used.

Figure 103

b) Results

The conditions for experiments conducted with copper cathodes are given in Table 48, as are the dissolution rate constants that were calculated from the slopes of the least squares lines discussed above. Experiments were conducted at either constant potential (0, 125, or 250 mv below the decomposition potential for Al_2O_3) or at constant current (525 or 1050 ma/cm^2).

The dissolution rate constants are shown as a function of current density in Figures 104 and 105. Figure 104 gives the rate constants for Fe and Ni in a bath with 6.5% Al_2O_3. Data points for low current densities (<200 ma/cm^2) were from constant potential experiments. In these tests the currents varied, so average currents were used in Figures 104 and 105. The data at the low current end of the plot show that the reproducibility is about $\pm$ 1 x 10^{-3} cm/s. The data show a maximum at approximately 500 ma/cm^2. This could be due to a shielding effect of the evolving gas at higher current densities, though no maximum was found for experiments in which an aluminum pool was used as the cathode, as will be discussed later in this report. Initially, the rate constants should increase with current because of the increased stirring caused by oxygen evolution.

Figure 105 shows results for a bath with 4.5% Al_2O_3. In this case no maximum was observed. A comparison of Figures 104 and 105 shows that the dissolution rate constants increase with decreasing Al_2O_3 content in the bath.

Figures 106-107 show the dissolution rate constants from constant potential experiments plotted as a function of the potential of the anode. As seen, the dissolution rate constants are not affected by the anode potential per se. This is evidence that the effect of current on the

TABLE 48

Dissolution Rate Constants From Experiments with Copper Cathodes

Experiment No.	Temp. °C	Bath Ratio	Wt.% Al_2O_3	Constant Potential $E-E^{\circ}_{Al_2O_3}$ (mv)	Constant Current I (ma)	i (ma/cm²)	k x 10^3 (cm/s) Fe	Ni
R56	1025	1.3	2.5	0		97.5	5.7	8.0
R58	1025	1.3	2.5	0		91.3	6.4	5.1
R60	1025	1.3	2.5	0		160.1	6.0	5.5
R61	960	1.1	4.5	0		135.7	4.3	2.4
R62	1025	1.3	2.5	-250		98.2	6.4	13.1
R63	960	1.1	4.5		500	525	16.7	12.1
R79B	960	1.1	6.5	-250		36.1	2.7	4.2
R80	960	1.1	6.5	-125		46.2	3.8	2.7
R81	960	1.1	6.5	0		65.0	2.1	2.3
R91	960	1.1	6.5	-250		38.7	3.7	3.2
R92	960	1.1	6.5		500	525	7.7	4.8
R96	960	1.1	6.5	-125		62.3	2.4	1.8
R97	960	1.1	6.5		1000	1050	8.2	4.3
R100	960	1.1	6.5		1000	1050	6.2	4.5
R101	960	1.1	6.5		500	525	10.1	6.7
R102	960	1.1	4.5		500	525	8.2	10.9
R103	960	1.1	4.5		1000	1050	17.8	11.2
R104	960	1.1	4.5	-250		58.3	8.0	8.4
R106	960	1.1	4.5	-125		58.9	10.1	11.2

Anode rotation speed in all experiments was 300 rpm.

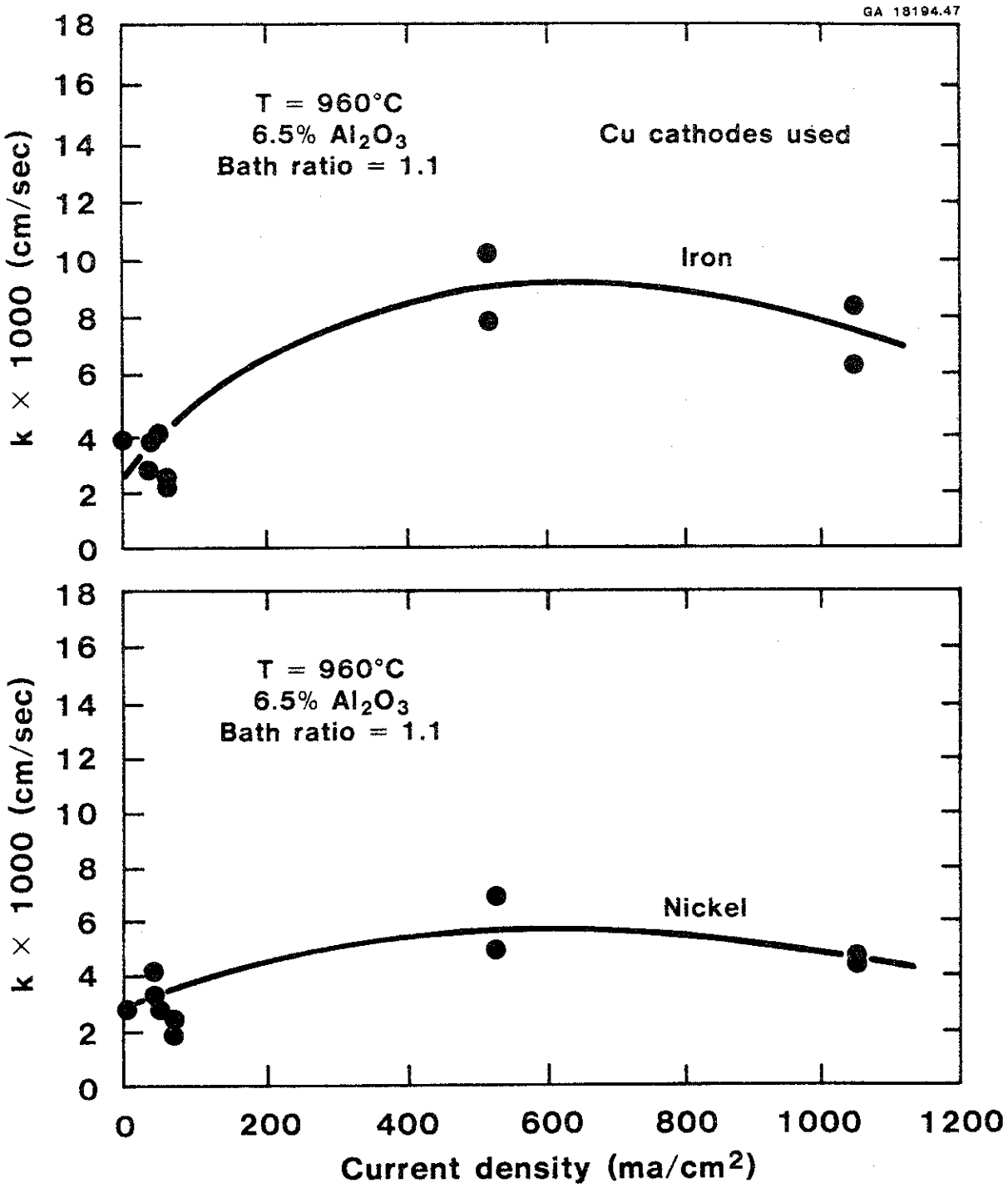

Effect of Current Density on Dissolution Rate Constants Determined from Tests in which Solid Copper Cathodes were Used. Bath Contained 6.5% Al_2O_3 (Saturated)

Figure 104

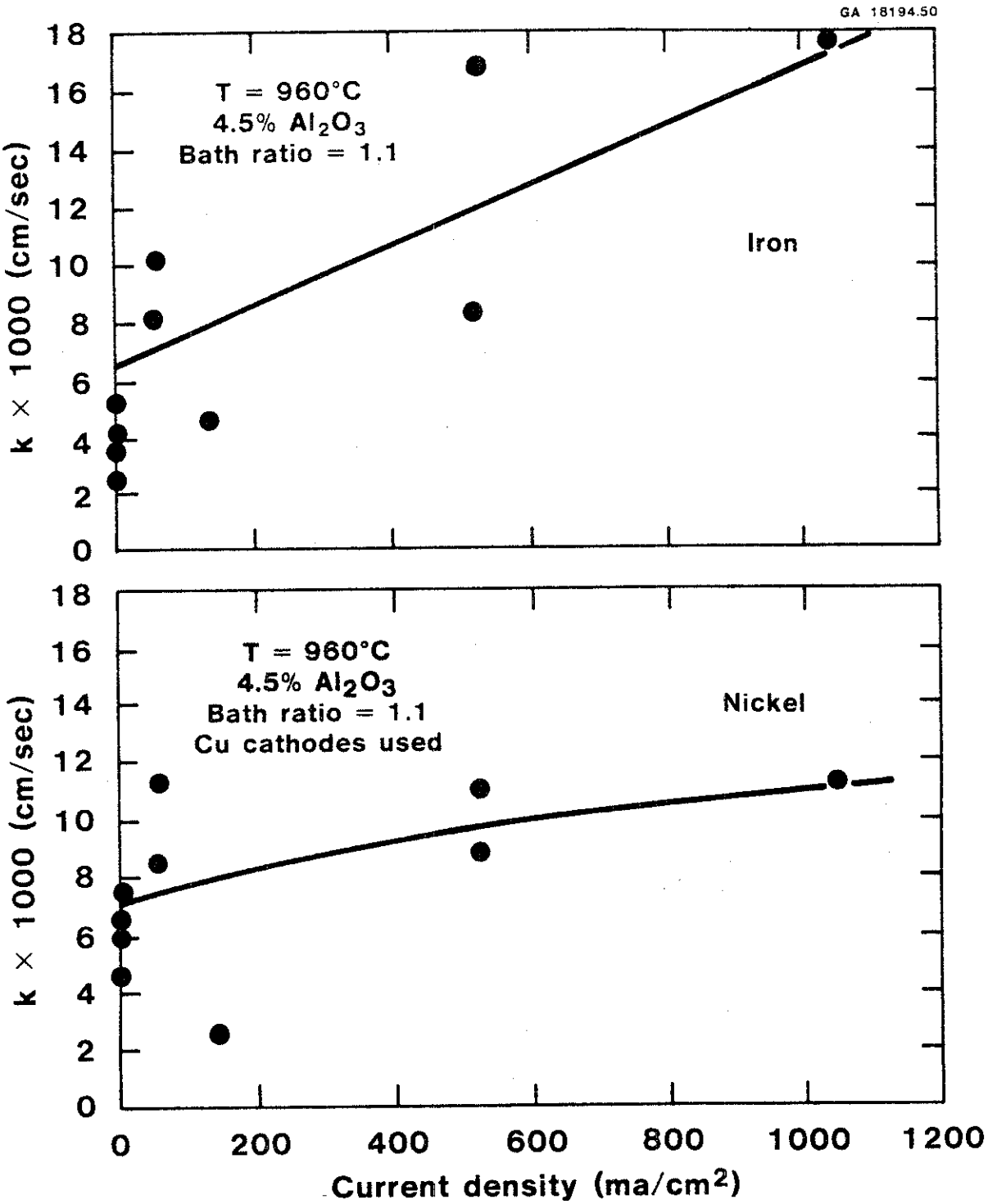

Effect of Current Density on Dissolution Rate Constants Determined from Tests in which Solid Copper Cathodes were Used. Bath Contained 4.5% Al_2O_3

Figure 105

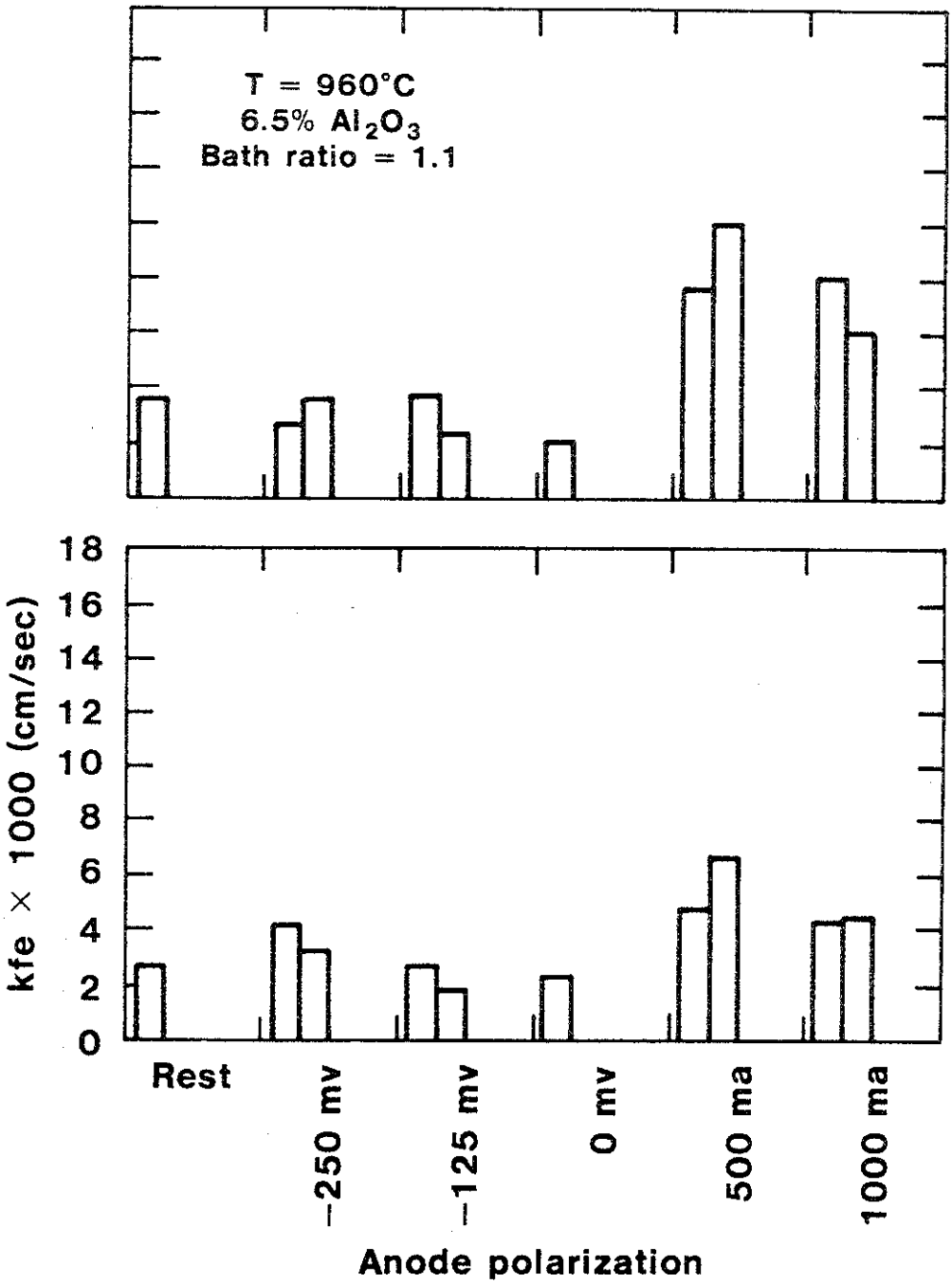

Dissolution Rate Constants from Experiments with Copper Cathodes. Bath Saturated with Al_2O_3.
Figure 106

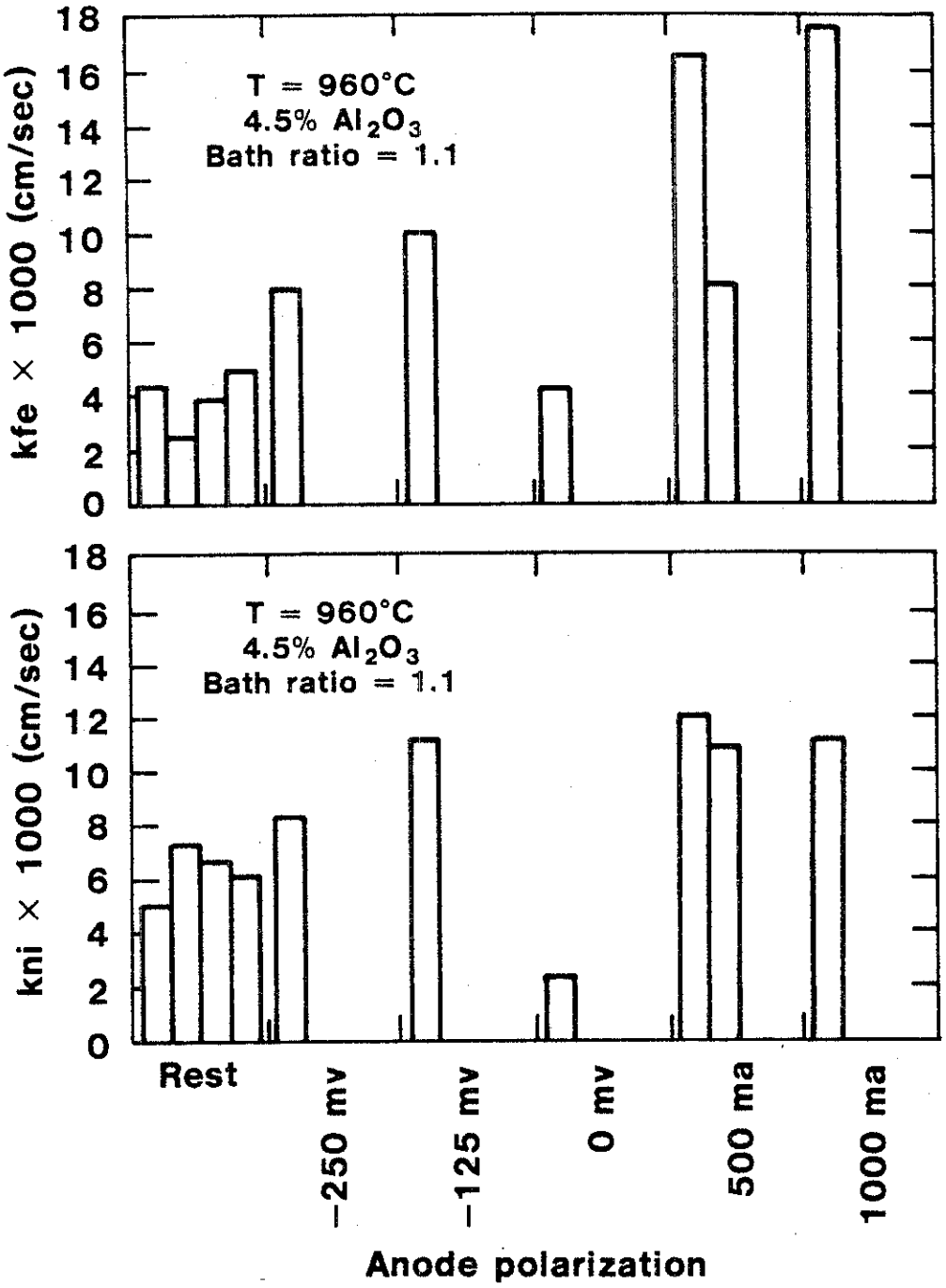

Dissolution Rate Constants from Experiments with Copper Cathodes. Bath not Saturated with Al_2O_3
Figure 107

dissolution rate constants is due to the evolution of gas at the anode. It should be noted that these data were included in Figures 104 and 105.

3) Experiments With Aluminum Metal Pads

a) Analysis of Data

The bath analyses from one of the experiments with a metal pad are shown in Figure 108. The concentrations of Fe and Ni in the bath increase in some tests and decrease in others. This does not appear to correlate with any of the controlled differences in the experiments, but in any case, the changes in concentrations are small. Perhaps the integrity of the skim which forms on the metal pad determines whether the bath increases or decreases in the impurities. This skim will be discussed below.

Analyses of the metal from one of these experiments are given in Figure 109. In all cases, the concentrations of Fe and Ni in the metal increase with time. For most experiments the metal is fairly pure at the end of the run, but it should be noted that the calculated quantity (assuming 100% current efficiency) of metal produced during the test (~ 2 g) is insignificant compared to the quantity of metal initially present (~ 300 g).

After each test, a dark gray bath layer was found covering the metal pad. Evidence of the existence of this during the experiments was that occasionally a very dark bath sample was obtained, apparently when the sample tube got into this skim layer. Figure 110 shows this dark bath layer. This skim was a matrix of bath with embedded alumina crystals. Close to the bath-metal interface small metallic spheres were embedded in the matrix; from a microprobe analysis these appeared to be alumina. There was no detectable build-up of Fe and Ni in

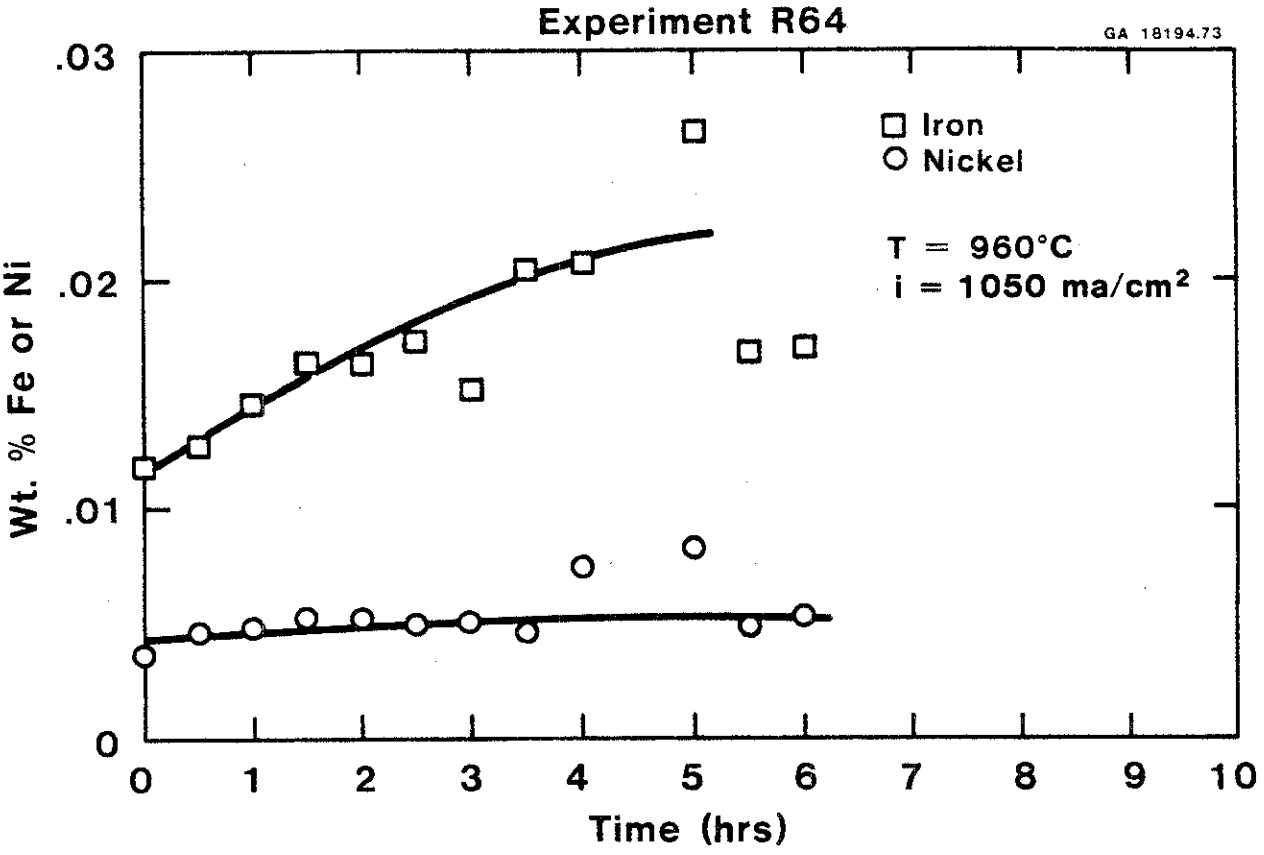

Bath Analysis for Experiment R64, Ni Cermet Anode (6846) Dissolving in Bath of Composition 6.5% Al_2O_3 1.3% CaF_2, 1.1 Bath Ratio. Metal Pad was Present in the Cell.
Figure 108

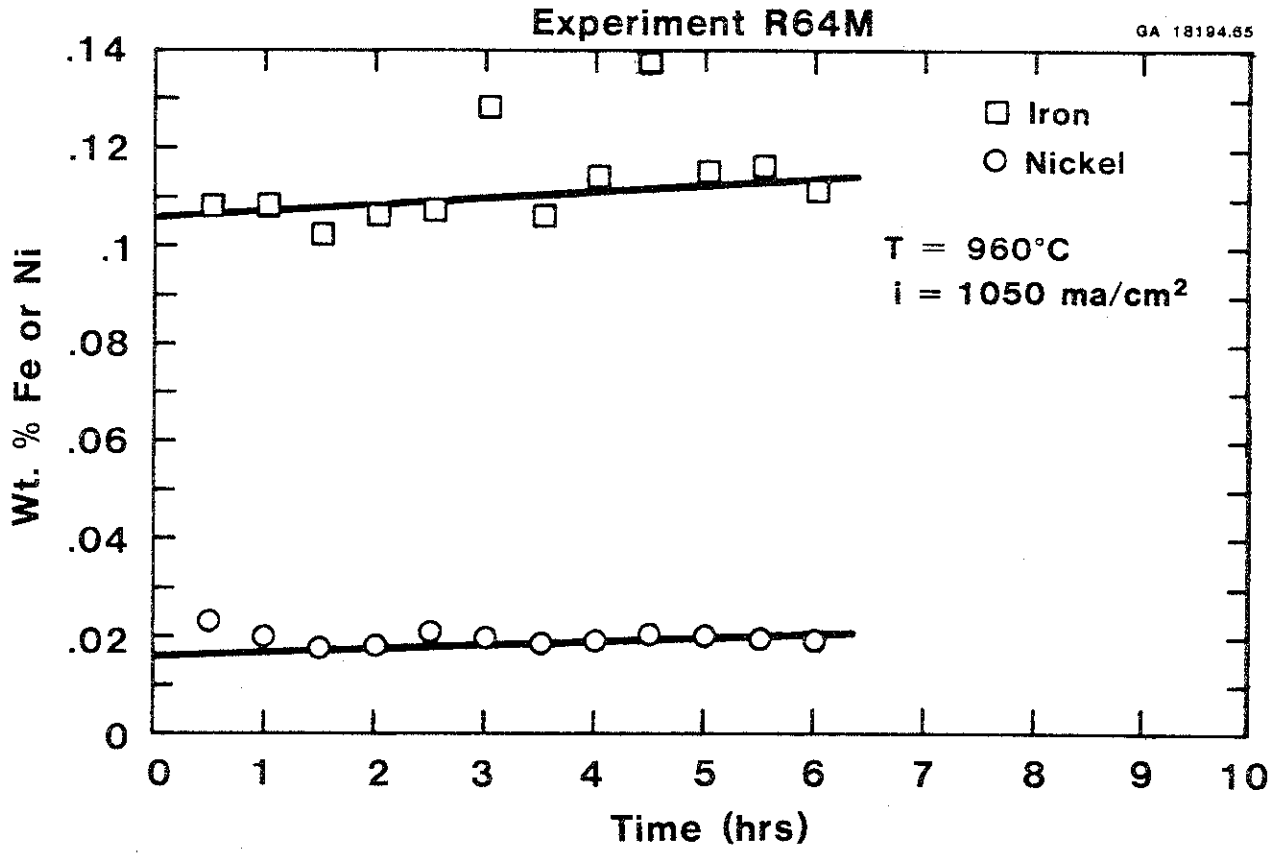

Metal Pad Analysis for Experiment R64

Figure 109

GA-16852.56

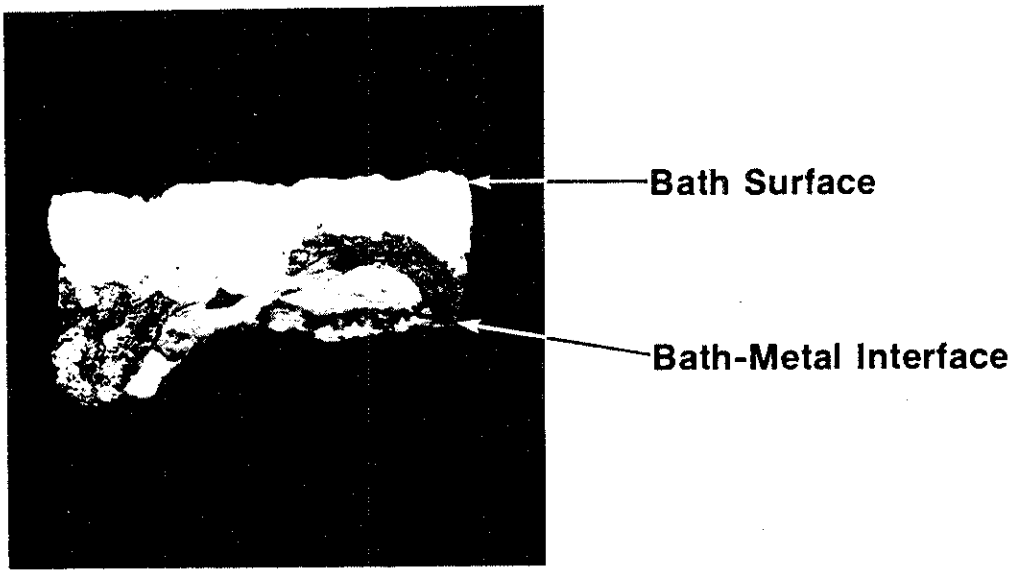

Cross Section of Bath From Experiment R55 Illustrating the Layer of Gray Skim

Figure 110

these spheres. Micrographs and electronmicroprobe analyses of this material were presented in a quarterly report (10).

For each experiment the dark layer was separated from the normal white bath, and the two portions were analyzed for Fe and Ni. Table 49 gives the results. The concentrations of Fe and Ni in the bulk (white) bath are quite low, being about that for normal synthetic bath, while the concentrations in the skim are significant. The concentrations in this layer are as great or greater than the concentrations in the metal pad; however, the total weight of metal present was more than the weight of skim.

The distribution of Fe and Ni between the skim, metal pad, and bath are shown in Figures 111 and 112. The quantities which accumulate in each are roughly equivalent, or at least the same order of magnitude. This demonstrates that the rate at which the impurities report to the metal is less than the rate of anode dissolution, but not much less the anode dissolution rate. Therefore, the dissolution of the anode is under mixed control. This would be true to a greater extent in a conventional Hall cell where the ratio of cathode area to anode area is much smaller than in the cell used in this study. This data shows that the accumulation of impurities in each of the skim, metal and bath must be accounted for when calculating the dissolution rate constants.

To calculate rate constants, a modified first order rate equation was derived which included the metal and skim as well as the bath as sinks for impurities. A simple mass balance for impurities can be written,

$$\begin{array}{lcl} \text{Rate of anode dissolution} & = & \text{Rate of accumulation in bath} \\ & + & \text{Rate of accumulation in metal} \\ & + & \text{Rate of accumulation in skim} \end{array} \qquad (52)$$

TABLE 49

Analysis of Skim From Experiments with Metal Pads

Experiment No.	Wt.% Fe	Wt.% Ni	Skim Weight (g)
R64	0.0441	0.0250	242
R67	0.03734	0.00904	131
R68	0.04306	0.01222	161
R70	0.04258	0.01110	101
R71	0.04938	0.01543	174
R73	0.05524	0.00723	95
R74	0.02866	0.00361	169
R76	0.03255	0.00411	246

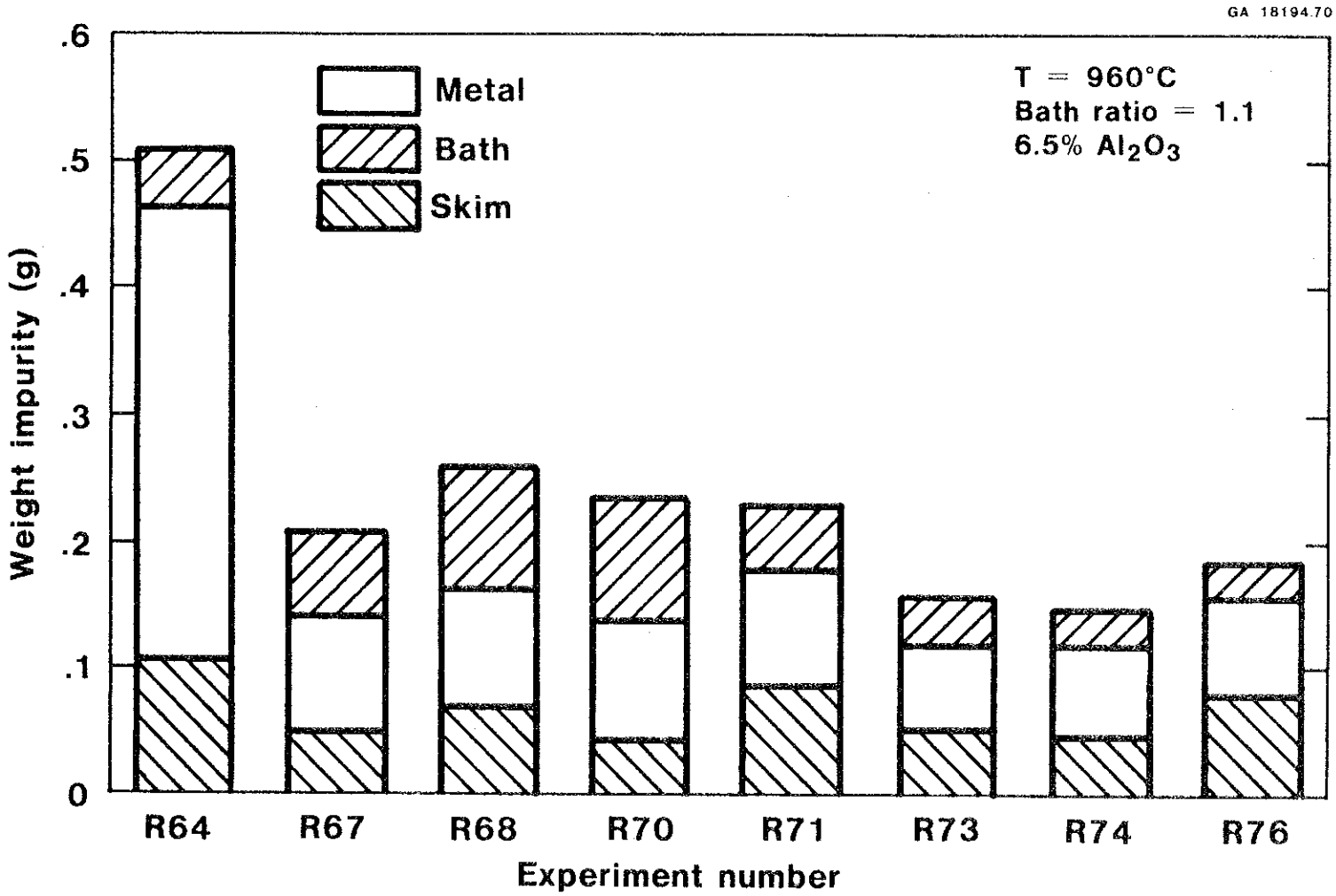

Iron Distribution for Dissolution Experiments with Metal Pads Present in the Cell

Figure 111

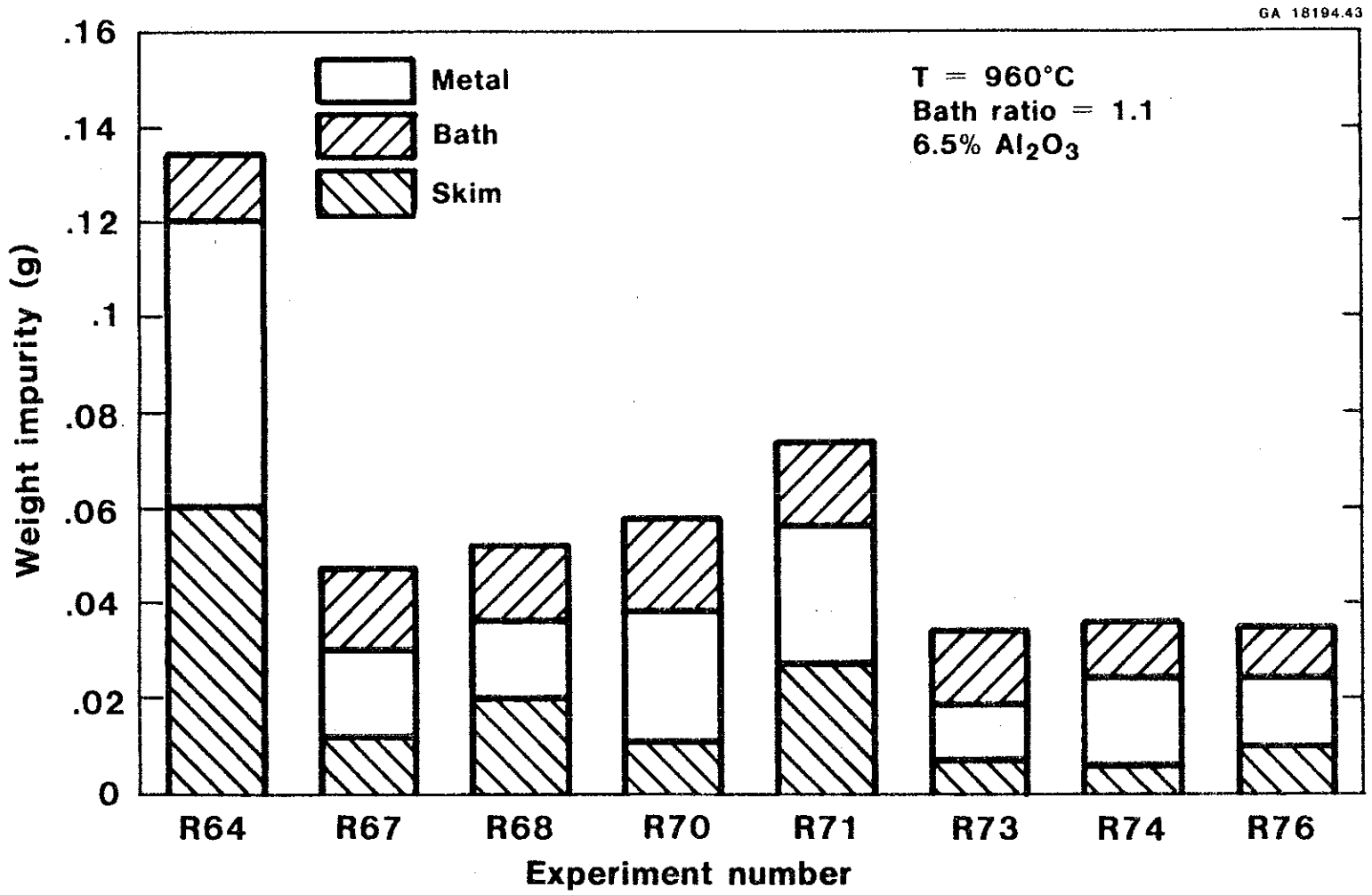

Nickel Distribution for Dissolution Experiments with Metal Pads Present in the Cell

Figure 112

For first order dissolution the rate is described by

$$\text{Rate} = k\,(C_s - C_b)\,A\,(\rho_{bath}/100) \tag{47}$$

where k is the dissolution rate constant, C_s and C_b are the solubility and bulk concentrations of the dissolving species, respectively, A is the geometric area of the dissolving solid, and ρ_{bath} is the density of the bath. The rate of accumulation of the impurity in the bath can be written as

$$R_{bath} = (W_{bath}/100)\,(dC_b/dt) \tag{48}$$

where W_{bath} is the weight of bath into which the anode is dissolving.

Substituting Equations (47) and (48) into (52) gives

$$k\,(C_s - C_b)\,A\,(\rho_{bath}/100) = (W_{bath}/100)(dC_b/dt) + R_m + R_s \tag{53}$$

where R_m and R_s are the rates of accumulation in the metal pad and skim, respectively. Rearranging and integrating the equation gives

$$(R_m + R_s)(100) \int (1/W_{bath})[1/(C_s - C_b)]dt - \ln (C_s - C_b)$$

$$= kA\rho_{bath} \int (1/W_{bath})dt \tag{54}$$

This assumes that R_m and R_s are constant. If the dissolution process is first order, then plotting the left hand side of this equation vs. $\int (1/W_b)dt$ should give a straight line.

To fit the data to Equation (54), R_m and R_s must be determined. The rate of accumulation R_m of impurities in the metal pad was determined by plotting the quantity of impurity dissolved in the metal pad vs. time and performing a least-

squares analysis on the data. Figure 109 shows the metal analyses for Experiment R64, which were obtained by atomic absorption analyses of samples taken during the run. Figure 113 shows the corresponding plot of the quantity of impurities dissolved in the metal. This differs from Figure 109 in that it includes the impurities removed as a result of sampling the metal. As seen, the data are reasonably linear with time, so R_m is constant. For most experiments the data were reasonably linear with time. Data points which appeared to be anomalously above or below other points were not included in the least-squares analyses.

Several assumptions were made regarding the rate of accumulation of impurities in the skim: (1) that the rate of formation of the skim was constant, and (2) that the rate of incorporation of impurities in the skim was constant. With these assumptions, R_s was calculated for each experiment. The data were then plotted according to Equation (54). The definite integrals were evaluated by numerical integrations. Least-squares analyses of the data were performed, and from the slopes of the lines the rate constants for dissolution were calculated. All of these operations - calculation of R_m and R_s, numerical integrations, least-squares analyses, plotting of the data - were done with a BASIC program.

Figure 114 shows the data for a typical experiment plotted according to the integrated rate Equation (54). The data are linear with time, indicating that the dissolution process is first order. It also shows the assumption that the rate of accumulation of impurities in skim is constant is reasonable. As was done for the metal analyses, data points which appeared to be anomalously different from the rest of the data were not included for the least-squares analyses. The dissolution rate constants were calculated from the least-squares slopes of the lines shown in Figure 114 and Equation 54.

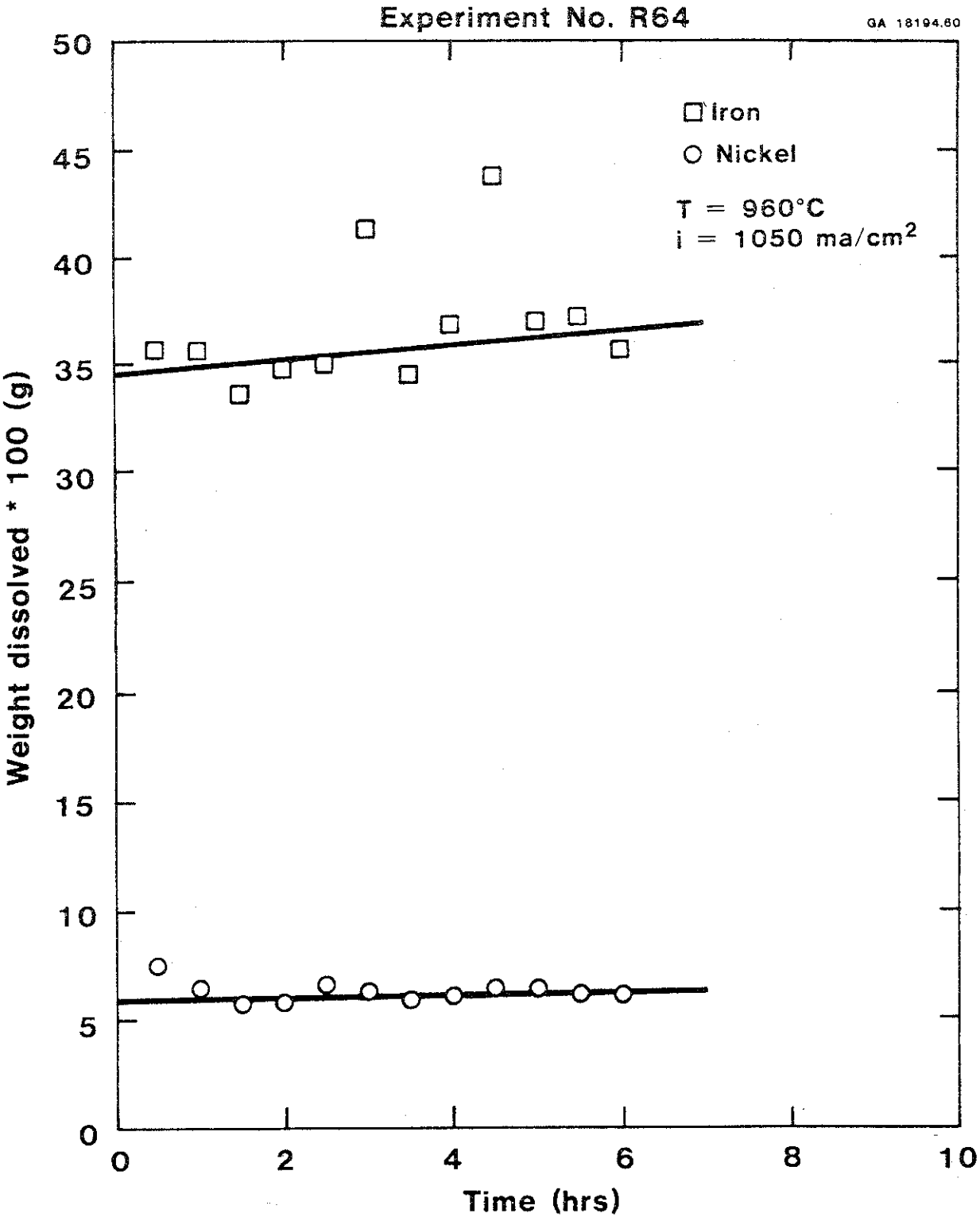

Total Weight of Impurities Dissolved in the Aluminum Metal Pad in Experiment R64

Figure 113

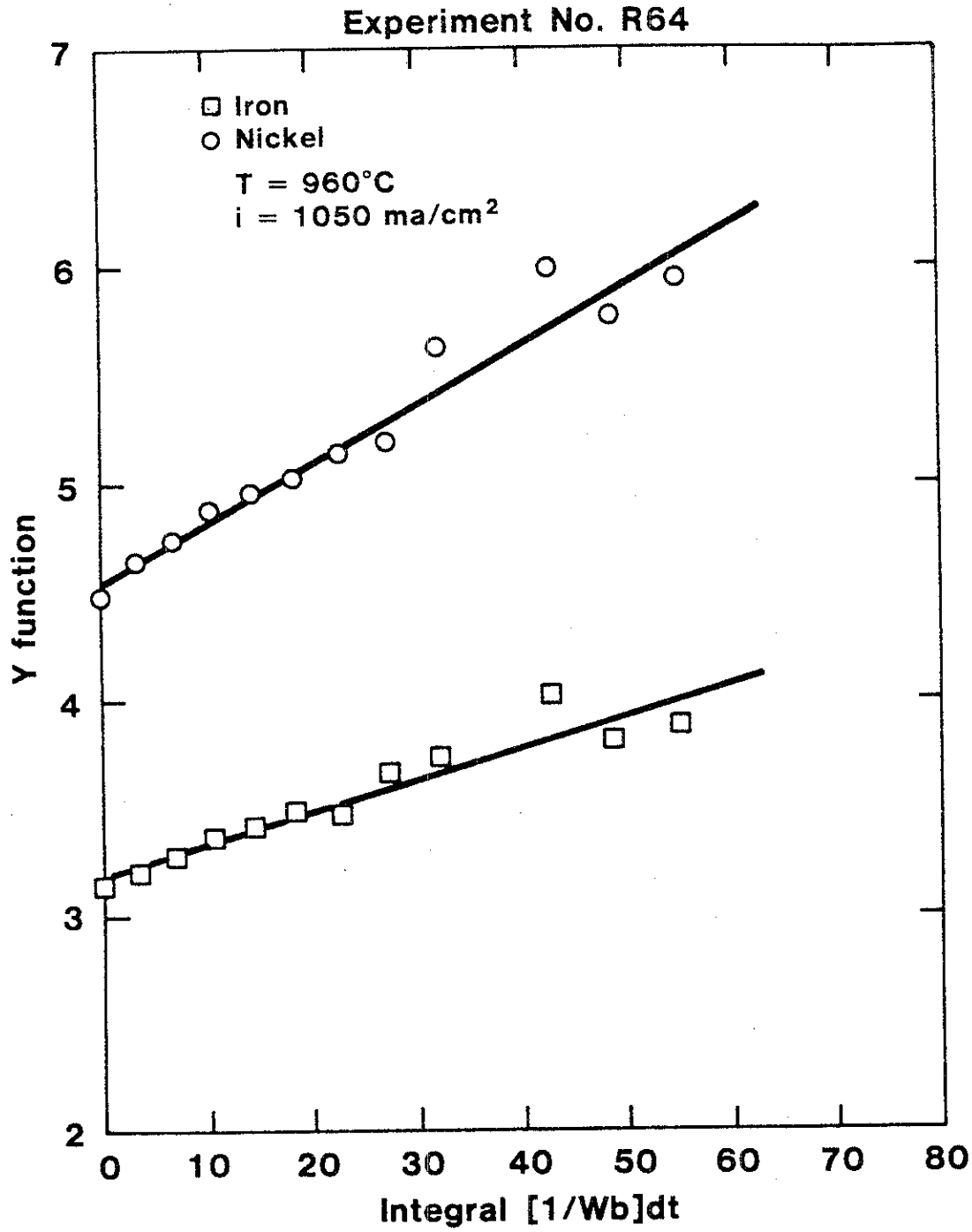

Dissolution Data from Experiment R64 Plotted According to the Integrated, First Order Rate Equation. Bath Composition was 6.5% Al_2O_3, 1.3% CaF_2, 1.1 Bath Ratio, and an Aluminum Metal Pad was Present in the Cell

Figure 114

b) Results

The dissolution rate constants calculated from the slopes of data plotted according to first order rate equations are given in Table 50. Experiments were conducted with the anode maintained at either constant potential (0, 125, or 250 mv below the decomposition potential for Al_2O_3) or at constant current (525 or 1050 ma/cm^2). Figures 115 and 116 show the dissolution rate constants plotted as a function of anode current for melts containing 6.5 wt.% Al_2O_3. In tests with the anode maintained at a constant potential the current decreased throughout the test (apparently as the internal oxidation of nickel progressed), so average currents obtained by the total charge which passed through the anode were used.

The data from these tests with metal pads present show that there is no large change in rate constant caused by the presence of the aluminum pad. The points at zero current in Figures 115 and 116 are data obtained with no metal present. These data were from previously discussed results for tests without aluminum present and under oxidizing conditions (Tables 44 and 45). The data at low, but not zero current (~ 50 ma) were from experiments in which metal pads were present.

An unpolarized anode will be reduced by dissolved aluminum in bath which always exists when molten aluminum is present in the system. Polarizing the electrode anodically will oxidize the dissolved aluminum as it reaches the anode surface and prevent reduction of the material. None of the anodes from this series of tests were reduced, so an anodic polarization of 250 mV below the decomposition potential for Al_2O_3 is sufficient to protect the anode from reduction. This potential corresponded to a current density of approximately 35 ma/cm^2.

TABLE 50

Dissolution Rate Constants from Experiments with Aluminum Metal Pads

Experiment No.	Constant Potential $E-E^{\circ}_{Al_2O_3}$ (mv)	Constant Current I (ma)	i (ma/cm^2)	k x 10^3 (cm/s) Fe	Ni
R64		1000	1050	7.6	14.2
R67		1000	1050	6.3	8.0
R68		500	525	8.7	6.6
R70		1000	1050	7.1	8.1
R71		500	525	5.6	11.6
R73	-250		36.3	3.4	2.2
R74	-125		35.6	1.6	0.5
R76	0		44.6	2.2	0.5

Bath composition for all experiments was: 1.1 bath ratio, 6.5 wt.% Al_2O_3, 1.3 wt.% CaF_2.

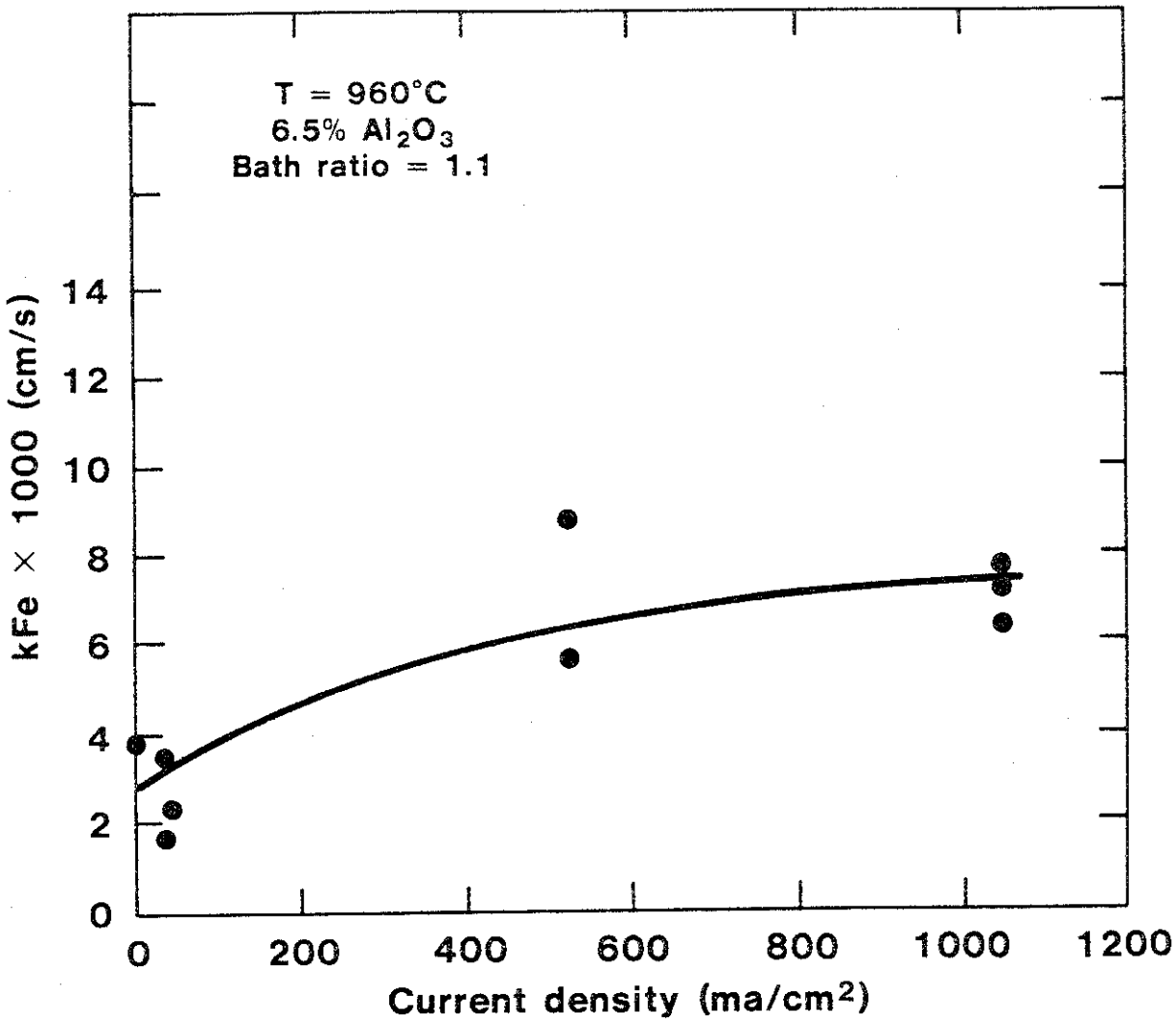

Dissolution Rate Constant for Iron for Ni Cermet (6846) Inert Anodes at 960°C in Bath of Composition 6.5% Al_2O_3, 1.3 Wt % CaF_2, 1.1 Bath Ratio. An Aluminum Metal Pad was Present in the Cell.

Figure 115

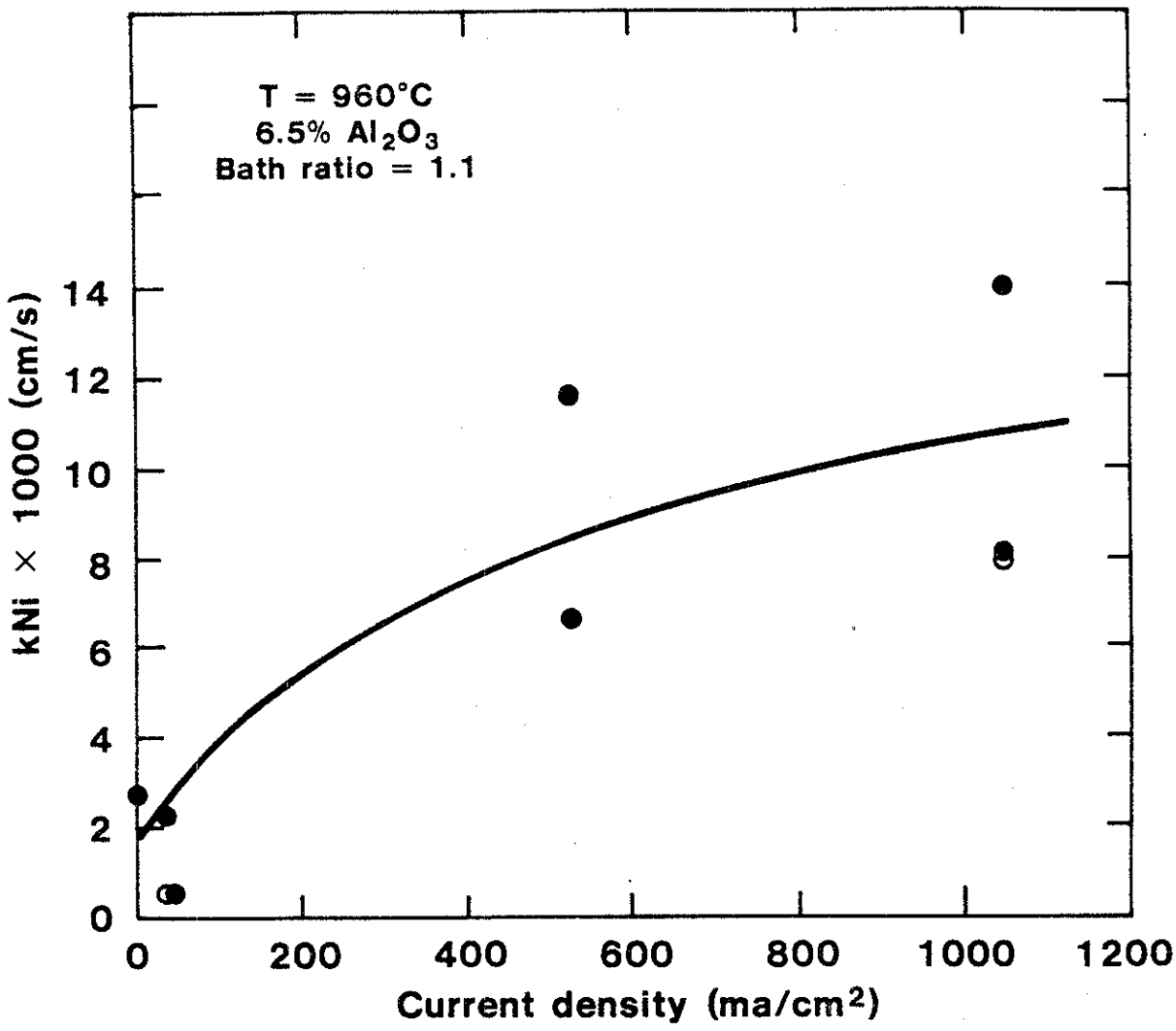

Dissolution Rate Constant for Nickel for Ni Cermet (6846) Inert Anodes at 960°C in Bath of Composition 6.5% Wt % Al_2O_3, 1.3 Wt % CaF_2, 1.1 Bath Ratio. An Aluminum Metal Pad was Present in the Cell.

Figure 116

The increase in rate constant with increasing current can be explained by increased mass transfer at the anode surface caused by gas evolution at the anode surface. As was true for experiments with copper cathodes, the potential of the anode per se did not influence the dissolution rate constants. Figure 117 shows the rate constants as a function of anode potential for constant potential experiments.

Figures 115 and 116 show that the rate constants increase with current density although the increase is not linear. There have been other measurements of gas evolving electrodes reported in the literature, though none for cryolite-based systems. These studies have been summarized by Selman and Tobias (79). Most of these studies were for vertical or upward facing horizontal electrodes in aqueous systems. The closest configuration to the present system would be vertical electrodes. In most of the studies it was found that the mass transfer coefficient, k, was proportional to the volume rate of gas generated, raised to a power between 0.17 to 0.87, i.e.,

$$k \propto (Q/A)^P , \quad 0.17 \leq P \leq 0.87 \tag{55}$$

where Q is the volume rate of gas generated and A is the geometric area of the electrode. Since the volume rate of gas generated is proportional to the current, k should depend on current density raised to the P power. The data were fit to a relationship of the type

$$k = k_o + B(i)^P \tag{56}$$

where k_o, B and P are constants. For iron the best fit values for k_o, B, and P were 2.3×10^{-3}, 1×10^{-4}, and 0.51, respectively. For nickel the values for k_o, B, and P were 5.2×10^{-4}, 2.5×10^{-4}, and 0.53 respectively. These values were obtained by nonlinear regression. Therefore the data

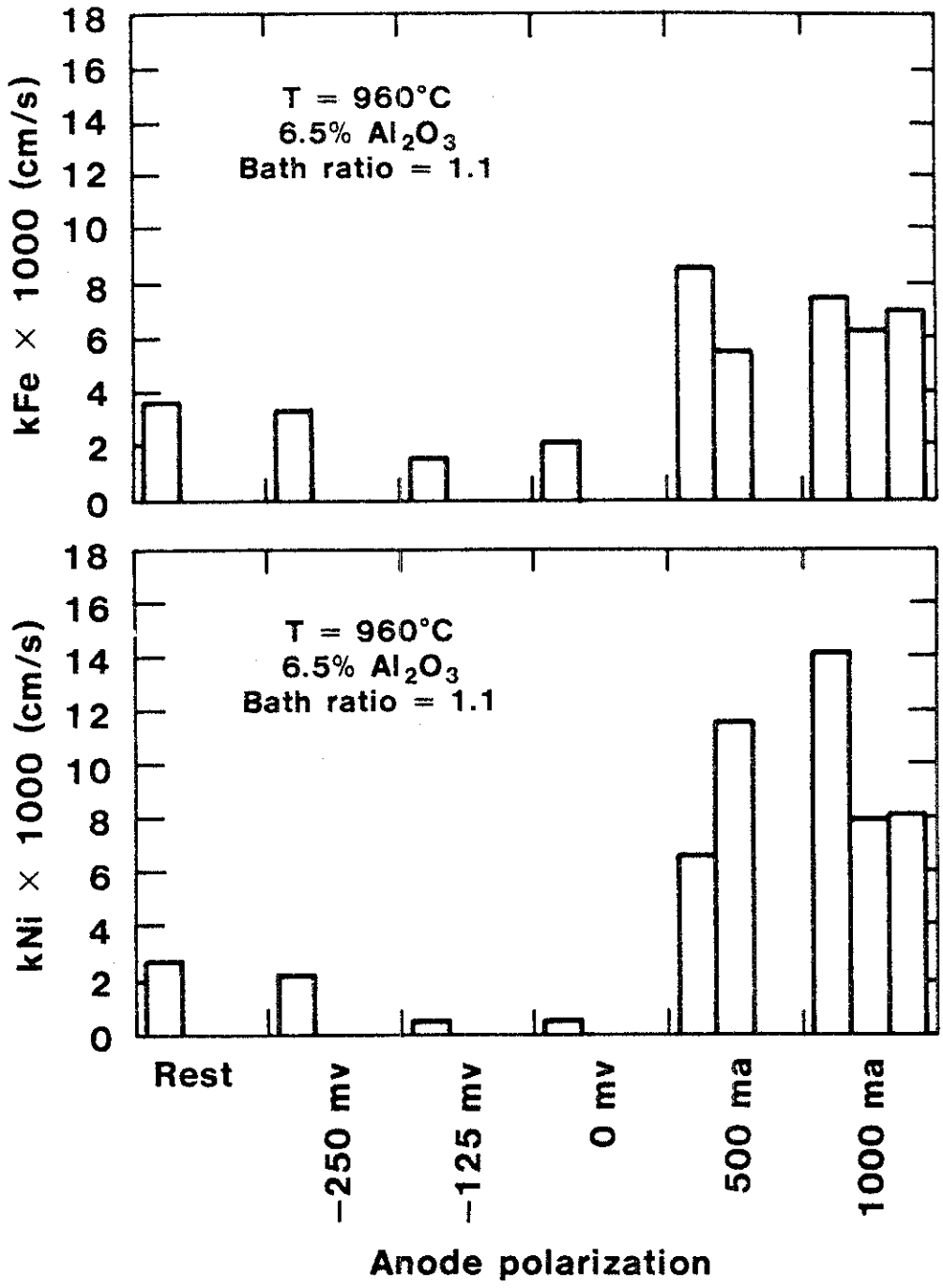

Rate Constants for Dissolution of Ni Cermet (6846) Inert Anodes at 960°C in Bath of Composition 6.5 Wt % Al_2O_3, 1.3 Wt % CaF_2, 1.1 Bath Ratio. An Aluminum Metal Pad was Present in the Cell.
Figure 117

from this study qualitatively fit in with other work on gas evolving electrodes.

The results can be compared to earlier reported tests in which copper cathodes were used. Figure 118 shows the comparison for rate constants for iron. It is apparent from this figure that the presence of an aluminum metal pad had no influence on the rate constant for iron. Figure 119 also compares Ni rate constants obtained with and without the molten aluminum cathode. At low current densities there is no influence of the aluminum cathode, while at higher current densities the Al cathode appears to have increased the dissolution rate constant. It is not obvious why the aluminum should increase the nickel rate constant and not the iron rate constant. Perhaps the reduction of nickel oxide dissolved in the bath by dissolved Al (or some other dissolved reduced species) is faster than the reduction of dissolved iron oxide. It should be noted that at the higher current density, where the difference was observed, the reproducibility of the data is the poorest.

Two rate experiments, R66 and R72, were conducted in a high alumina (14 wt.%) - high temperature (1025°C) bath. Dissolution rate constants from these experiments are given in Table 51. These rate constants are compared to those for our "standard" bath in Figures 120 and 121. There does not appear to be significant differences, although the scatter is fairly large. It should be noted that scatter in the results seems to increase with current density. Within the uncertainty of the data, there is no change in rate constant between the two bath compositions.

The actual dissolution rate of an anode is proportional to the product of the rate constant and the equilibrium solubility, i.e.,

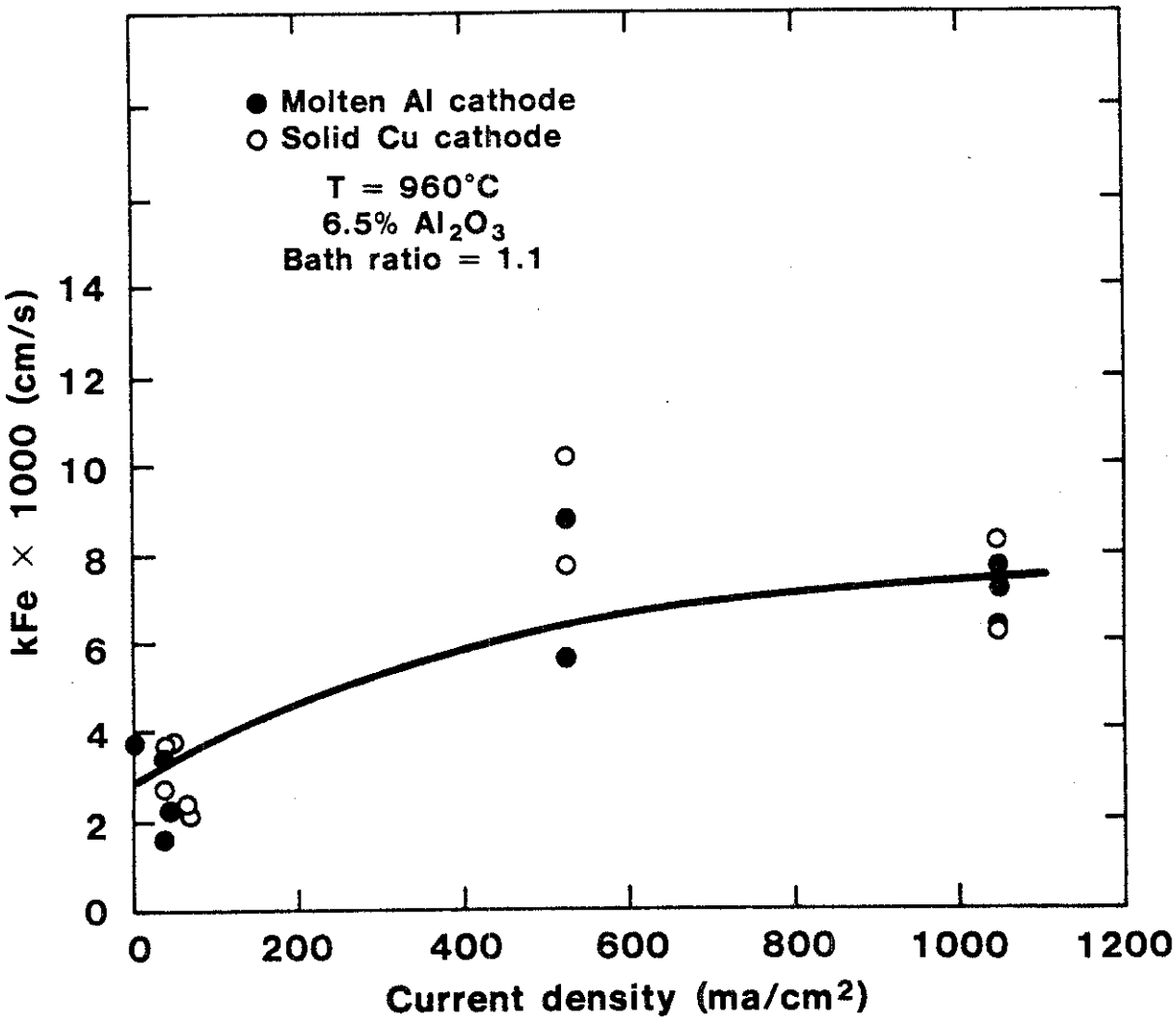

Comparison of Iron Dissolution Rate Constants for Ni Cermet (6846) Material Determined from Tests With and Without an Aluminum Metal Pad.
Figure 118

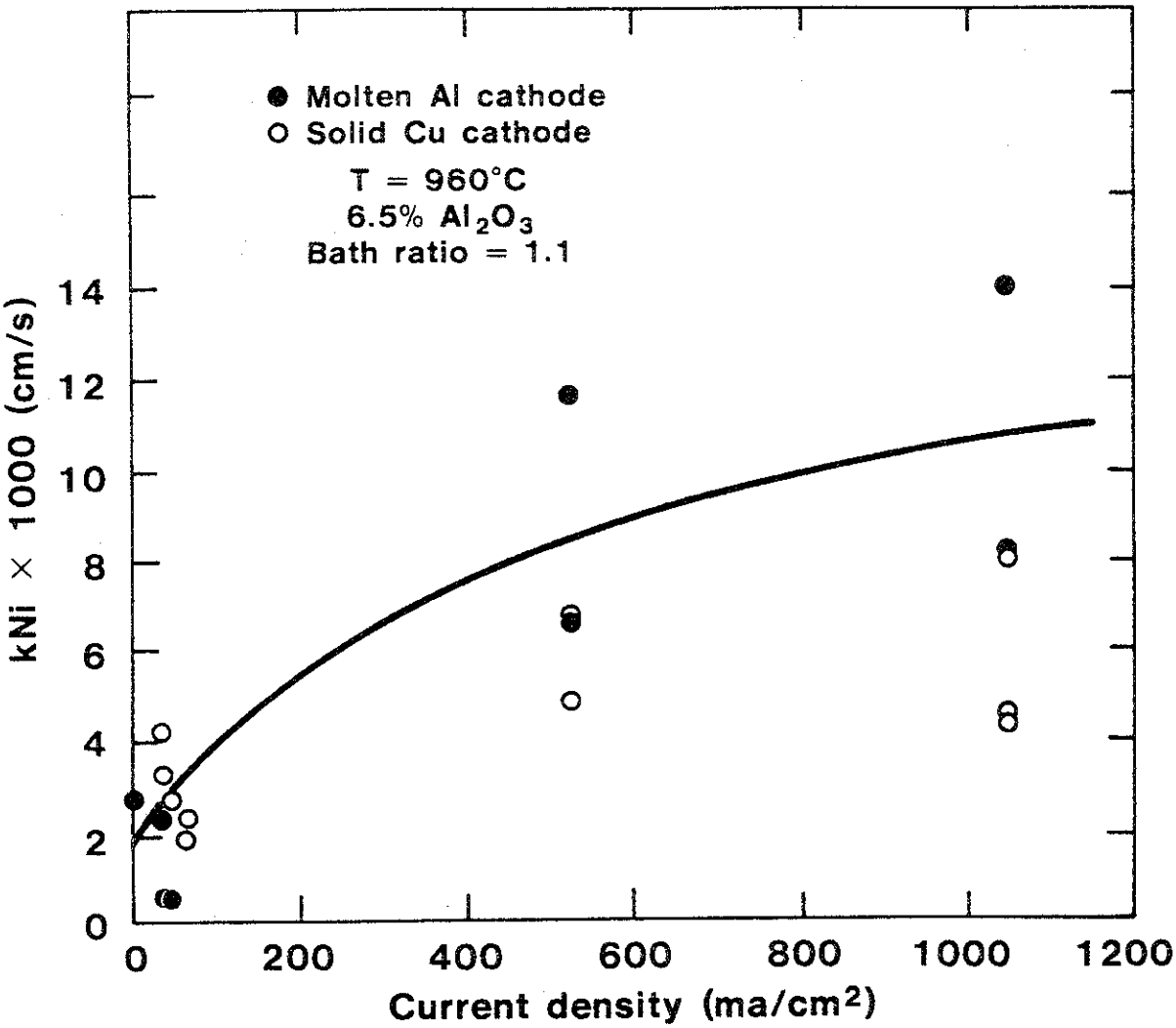

Comparison of Nickel Dissolution Rate Constants for Ni Cermet (6846) Material Determined from Tests With and Without an Aluminum Metal Pad
Figure 119

TABLE 51

Dissolution Rate Constants from High Alumina-High Temperature Experiments

Experiment No.	I(ma)	i (ma/cm^2)	k x 10^3 (cm/s) Fe	Ni
R66	1000	1050	3.2	8.8
R72	500	525	6.7	10.6

Temperature: 1025°C

Bath Composition: 14% Al_2O_3, bath ratio 1.3, 1.3% CaF_2

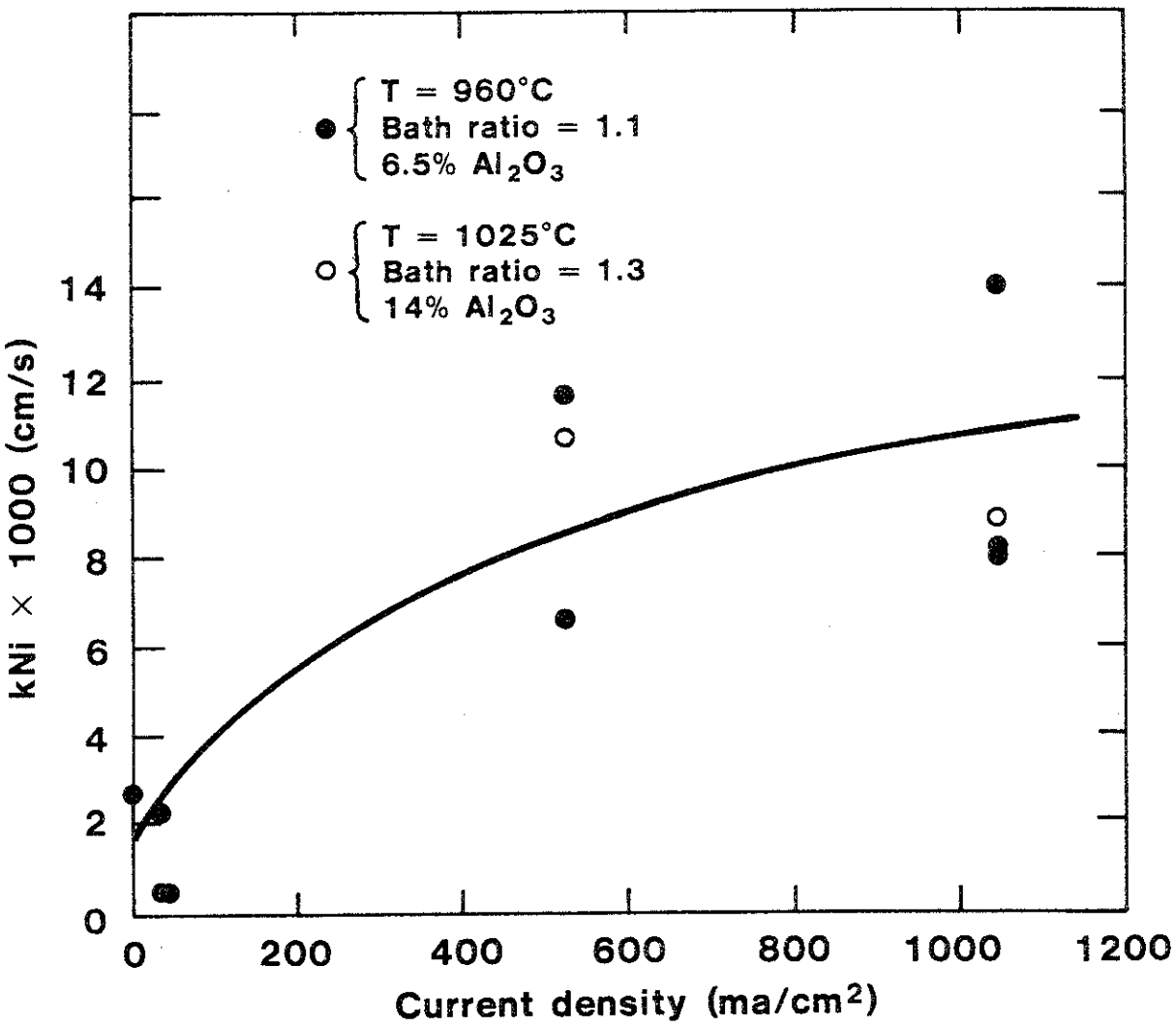

Dissolution Rate Constants for Nickel in the High Temperature-High Alumina Bath Compared to Those for the "Standard" Bath. Ni Cermet (6846) Material.
Figure 121

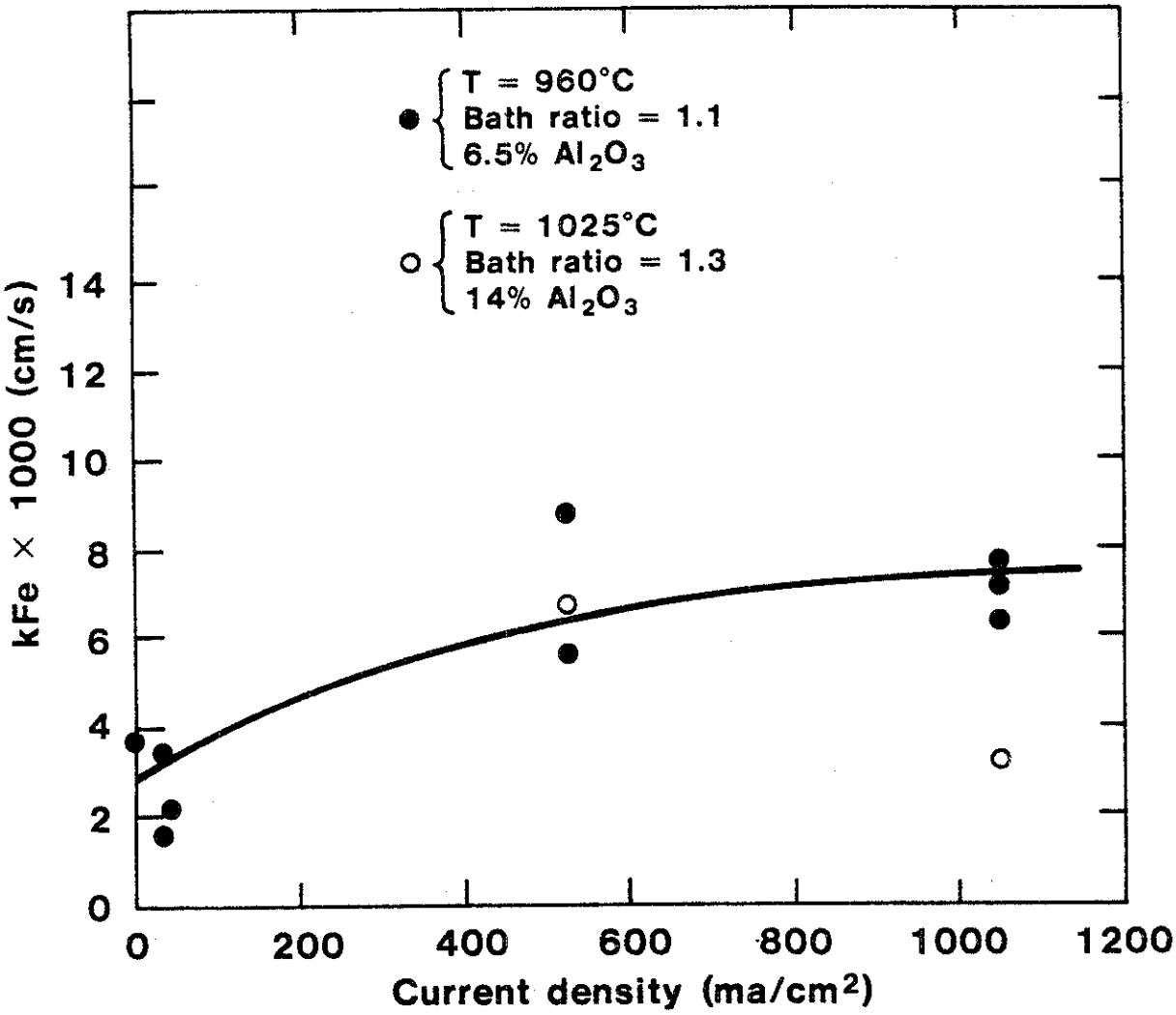

Dissolution Rate Constants for Iron in the High Temperature-High Alumina Bath Compared to Those for the "Standard" Bath. Ni Cermet (6846) Material.
Figure 120

$$\text{Rate} = k (C_s - C_b) A \quad (57)$$

where C_s and C_b are the equilibrium solubility and the bulk concentration of the dissolving species, and A is the geometric area of the anode. While rate constants for the two baths were similar, the solubilities were not. The solubility for this composition was given in Part A of this report. Figure 122 compares the product kC_s for the two bath compositions. As seen, this product is lower for the high alumina-high temperature bath, particularly for iron. This means that the dissolution rate of the anode would be lower in this bath. Based on these results, it was recommended that this bath composition/temperature combination be tested in a pilot Hall cell.

4) Effect of Carbon/Al_4C_3 on Dissolution Rate

a. Analysis of Data

The data were analyzed exactly the same way as other tests with aluminum metal pads. The data were plotted according to Equation 54, and dissolution rate constants were calculated from the slopes of these lines. This program was modified from the one used for other experiments in that it accounted for additions of bath which were periodically made while adding the carbon or aluminum carbide.

The procedure for analysis of the data was slightly modified to treat the run with the cathodically polarized graphite rod. The quantities of iron and nickel which were plated onto the graphite rods were determined by analysis and are cumulatively shown in Figure 123. The least-squares slopes of these lines represent R_c, the rate of accumulation of impurities at the carbon rod. The analyses were corrected for the Fe and Ni found in a blank rod. The integrated form of the first order rate equation was modified to include this

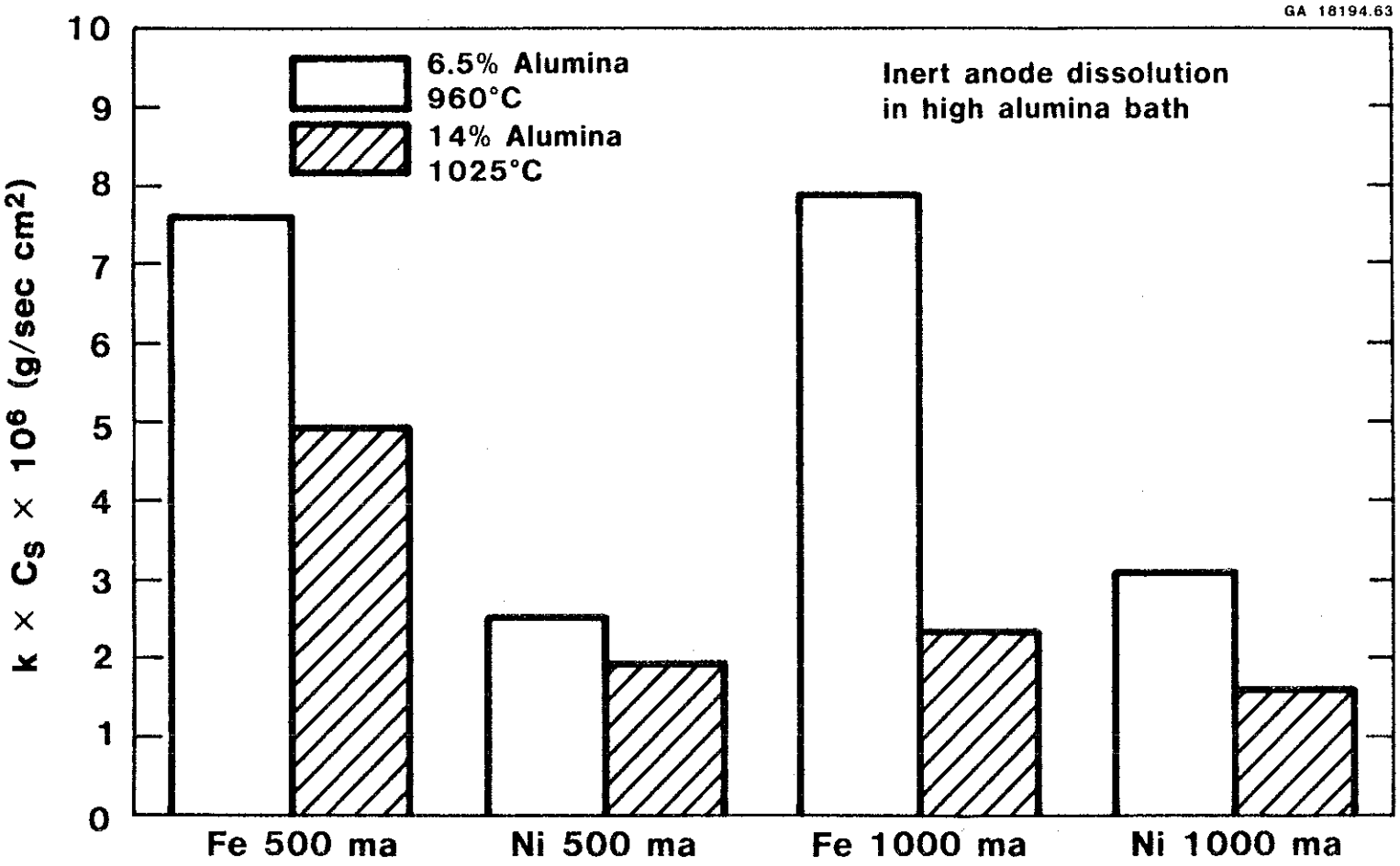

A Comparison of k × C_S, which is Proportional to the Total Dissolution Rate, for the High Temperature-High Alumina Bath to that for the "Standard" Bath.

Figure 122

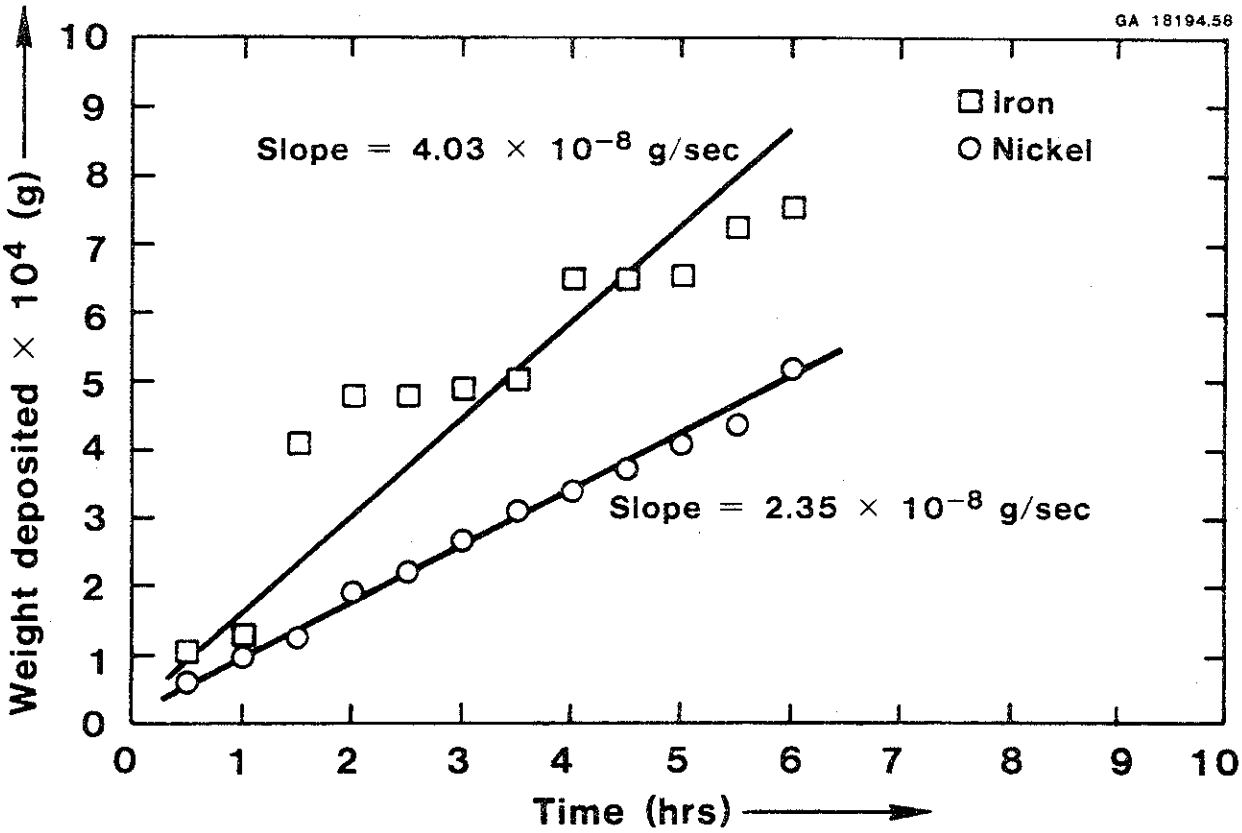

Quantities of Iron and Nickel Plated onto the Cathodically Polarized Graphite Rods in Experiment R88

Figure 123

sink for Fe and Ni. Since R_c is approximately constant, the modified equation is

$$(R_m + R_s + R_c)(100) \int_o^t (1/W_{bath})[1/(C_s - C_b)]dt -$$

$$\ln (C_s - C_b) = kA \rho_{bath} \int_o^t (1/W_{bath})\, dt \qquad (58)$$

where the variables have their usual meanings.

b) Results

Figure 124 shows the distribution of Fe and Ni between the bath, metal, and skim for these experiments. In general, the Fe and Ni follow the same pattern for a given experiment, although the accumulations of Fe are higher than Ni. One trend which can be observed is that the accumulations in metal in experiments with Al_4C_3 additions (R87, R90, R93) is lower than for experiments with carbon additions. This could be the result of increased reduction of the dissolved iron and nickel oxides in the bath by the carbide instead of the reduction occurring at the metal pad surface.

In one experiment (R87) there was a negative accumulation of impurities in the bath. This is because the rate at which Fe and Ni are being incorporated into the skim is greater than the rate at which they are dissolving from the anode. In several experiments (R87 and R90) there was a small negative accumulation of impurities in the metal pad. There is no explanation for this, except the values are small and could be within experimental error of zero.

Data plotted according to Equation (54) or (58) were again linear, indicating the dissolution is first order. The dissolution rate constants calculated from the slopes of these lines are given in Table 52.

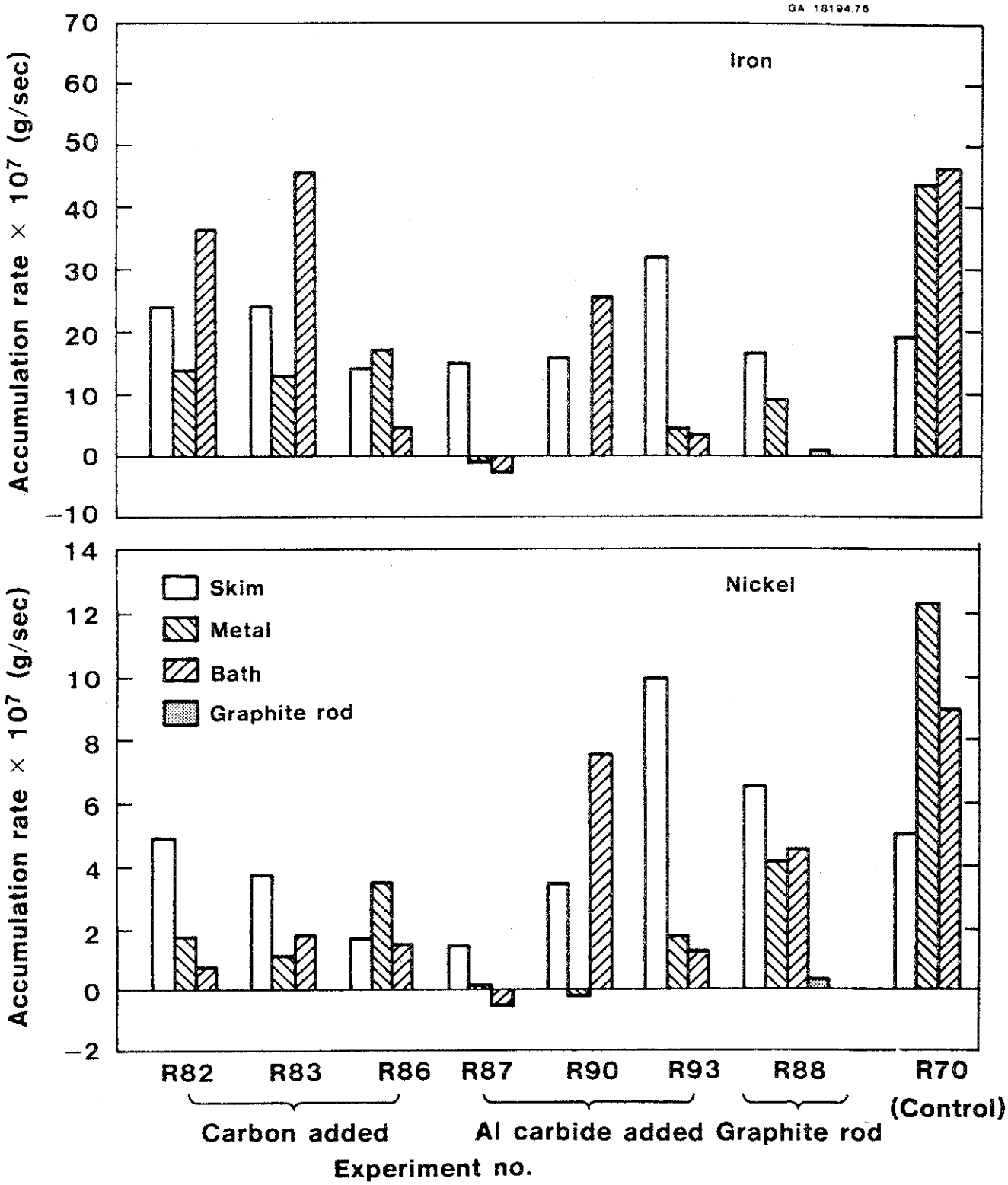

Distribution of Impurities Dissolving from Anode in Experiments Designed to Determine the Effects of Carbon and Al_4C_3 on the Anode Dissolution

Figure 124

TABLE 52

Dissolution Rate Constants from Experiments with Carbon or Aluminum Carbide Additions

Experiment No.	Al_2O_3	Additive	I(ma)	i (ma/cm^2)	k x 10^3 (cm/s) Fe	Ni
R82	6.5	C	1000	1050	12.2	3.2
R83	6.5	C	500	525	7.8	3.1
R86	6.0	C	1000	1050	5.4	3.2
R87	5.5	Al_4C_3	500	525	1.2	0.1
R90	5.0	Al_4C_3	1000	1050	4.8	4.7
R93	5.0	Al_4C_3	1000	1050	4.1	5.3
R88*	6.0	--	1000	1050	3.4	8.0

T = 960°C, Bath ratio = 1.1

*Polarized graphite rod suspended in bath

During the first experiment in which Al_4C_3 was added (R84, which was not analyzed because the sheath around the anode was lost during the run), voltage spiking began. This could be eliminated by increasing the rotational speed of the anode. It was suspected that the carbide was oxidizing by the reaction

$$Al_4C_3 + O_2 \rightarrow 2\ Al_2O_3 + 3\ CO \qquad (59)$$

to form alumina which was producing a mucky bath. Because of the effect of increasing rotational speeds, it is believed an alumina-rich layer was forming on the anode or cathode. In subsequent experiments it was found that this spiking could be postponed or eliminated by beginning the run with a slightly lower alumina content. All experiments were conducted in alumina crucibles, so the bath was always saturated regardless of the initial content.

The rate constants obtained from these experiments are plotted as a function of current density through the anode (Figures 125 and 126). They are compared to results obtained from other experiments with metal pads which were given in the previous section.

At least one trend is apparent - all rate constants for experiments with Al_4C_3 additions lie below the control data. This can be explained by the oxidation of the carbide to form alumina, e.g., Equation 59, and thereby forming a "mucky" bath, which decreases the dissolution rate of the anode. It is interesting to note that the results for the run with the cathodically polarized graphite rod were similar to the results for runs in which aluminum carbide was added, although no additional alumina would be formed in this run. The addition of carbon had a mixed effect. No effect on the rate constant could be discerned for iron (Figure 125). The

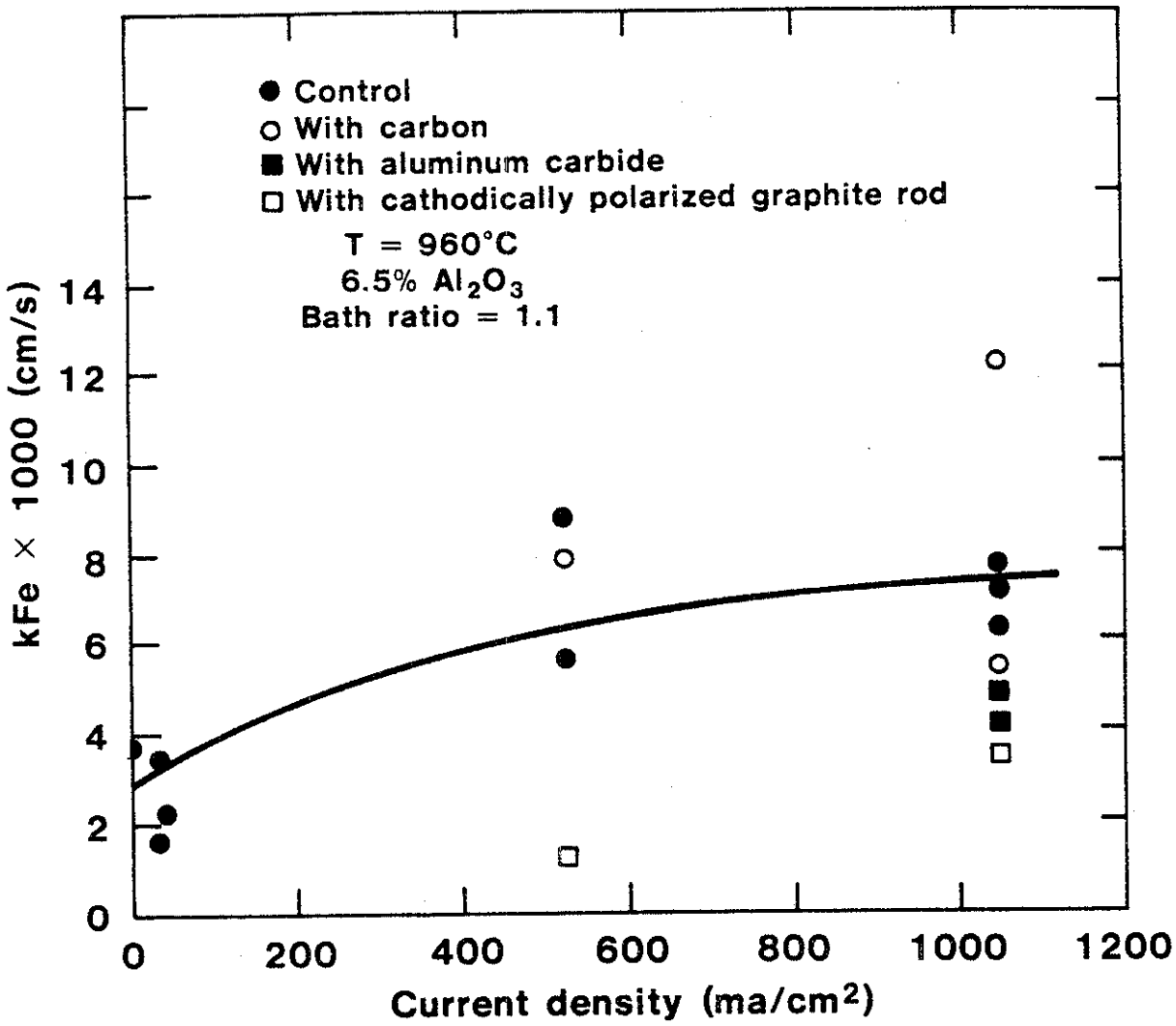

The Effect of Carbon and Aluminum Carbide Additions to the Bath, and the Effect of Suspending a Cathodically Polarized Graphite Rod in the Bath on the Dissolution Rate Constant for Iron. Rotation Speed for the Anode was 300 RPM. Ni Cermet (6846) Material.

Figure 125

carbon decreased the dissolution rate for nickel (Figure 126). There is no satisfactory explanation for this.

Contrary to what was suspected, it is apparent that neither carbon nor aluminum carbide additions were detrimental to the dissolution performance of the inert anodes. This indicates that carbon dust in a cell from preceeding carbon anodes would have no effect on the inert anodes, and the carbon from exposed sidewalls would not be detrimental. The experiment with the cathodically polarized graphite rod showed no increase in rate. The additions of aluminum carbide decreased the dissolution rate of the anode, although this effect is probably due to the way Al_4C_3 was added in these experiments, not the Al_4C_3 per se. These results indicate that any detrimental effects on anodes in bench-scale cells which appear to be caused by an exposed carbon sidewall are more likely due to either aluminum forming on the wall and being swept into contact with the anode, or by poor ratio control caused by intercalation of sodium at this sidewall.

5) Results for Differing Anode Compositions

a) All-Oxide Material (5324)

Several tests were made using the 5324 material consisting of 51.7% NiO-48.3% Fe_2O_3. The phases present in this material are $NiFe_2O_4$ and NiO. The purpose of these tests were to determine how well the oxide material alone, without any metallic phase, would perform.

Unpolarized anodes: The dissolution rate constants are given in Table 53. These rate constants are compared with results obtained from Ni-cermet anodes (6846) (Figure 127). The rate constants at 960°C are within the uncertainties of the measurements of the unpolarized Ni-cermet material (6846). The rate constants at 1025°C are also similar to those

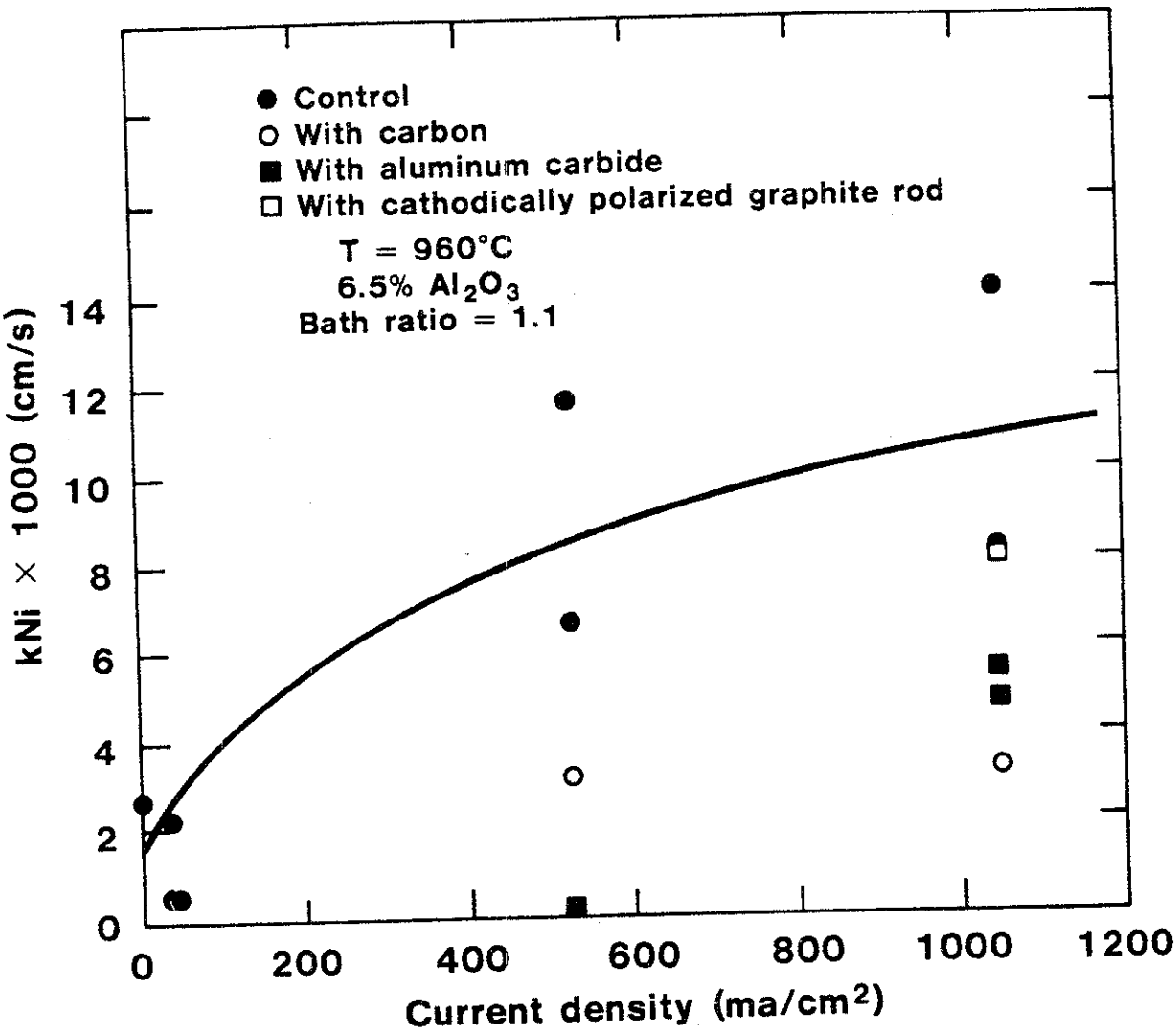

The Effect of Carbon and Aluminum Carbide Additions to the Bath, and the Effect of Suspending a Cathodically Polarized Graphite Rod in the Bath on the Dissolution Rate Constant for Nickel. Rotation Speed for the Anode was 300 RPM. Ni Cermet (6846) Material.

Figure 126

TABLE 53

Dissolution Rate Constants for 51.3% NiO
48.7% Fe_2O_3 Anode Material (5324)

Experiment No.	Temp. °C	Bath Ratio	wt.% Al_2O_3	k x 10^3 (cm/s) Fe	Ni
R94	960	1.1	6.5	1.6	3.1
R95	1025	1.3	2.5	10.2	13.6
R114	960	1.1	6.5	4.1	6.2

i = 1050 ma/cm^2, Cu cathodes used

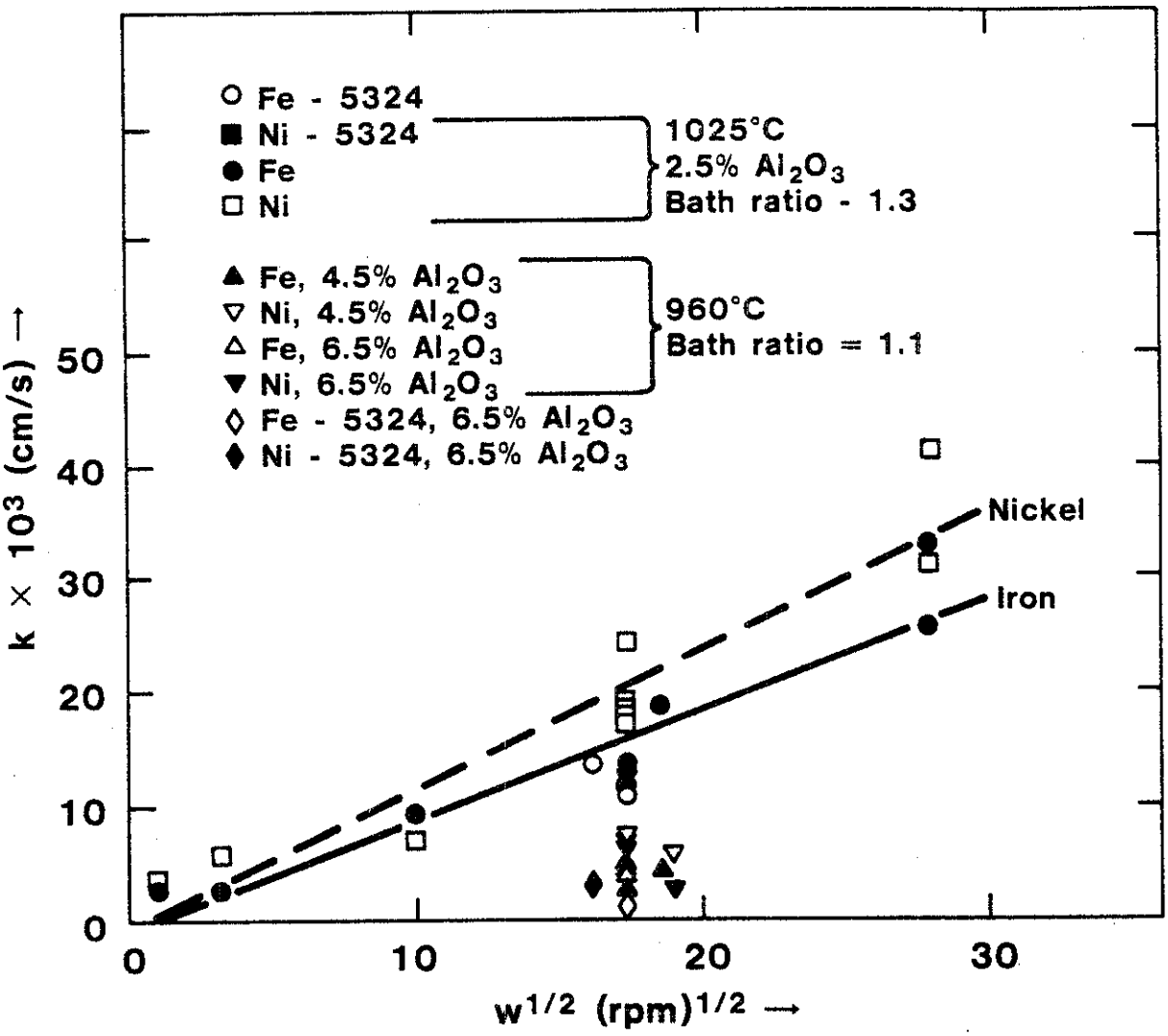

Comparison of the Dissolution Rate Constants for the All Oxide (5324) Material and the Ni Cermet (6846) Material. Anodes were Unpolarized.

Figure 127

measured for the Ni-cermet material. There is no significant difference between the two materials.

Polarized anodes: Because of the higher electrical resistivity of the all-oxide materials compared to the cermets, the internal temperature of an anode during the start of one of the experiments was measured. A hole was drilled through the Inconel connecting rod and into the anode so that a thermocouple could be placed 0.63 cm above the bottom surface of the anode. The passage of current through the anode produced a 3°C increase in temperature. This would have an insignificant effect on the anode dissolution.

Figure 128 compares results for the all-oxide material to results for Ni cermets and for an anode run at a constant current density of 1050 ma/cm^2. There does not appear to be a significant difference between the two materials.

This information fits in with the mass-transport-controlled mechanism that was proposed as a result of earlier data. The Ni-cermet material has an oxide layer on its surface, as all of the anodes used were preoxidized. An oxide layer that consists primarily of $NiFe_2O_4$ forms on the surface of the anodes during service. Thus, the surface presented to the bath is similar for both materials. Since mass transport through the fluid boundary layer at the anode surface controls the dissolution rate, the rates should be the same for both materials. The Ni-cermet material develops internal porosity, but there is no reason this should influence mass transport through the boundary layer.

This model predicts that both the cermet and all oxide materials ($NiFe_2O_4$-based) for polarized anodes should have the same rates of dissolution, even though the metallic portion of the cermet may be anodically dissolving. Nickel ions must diffuse through this fluid boundary layer, whether they come

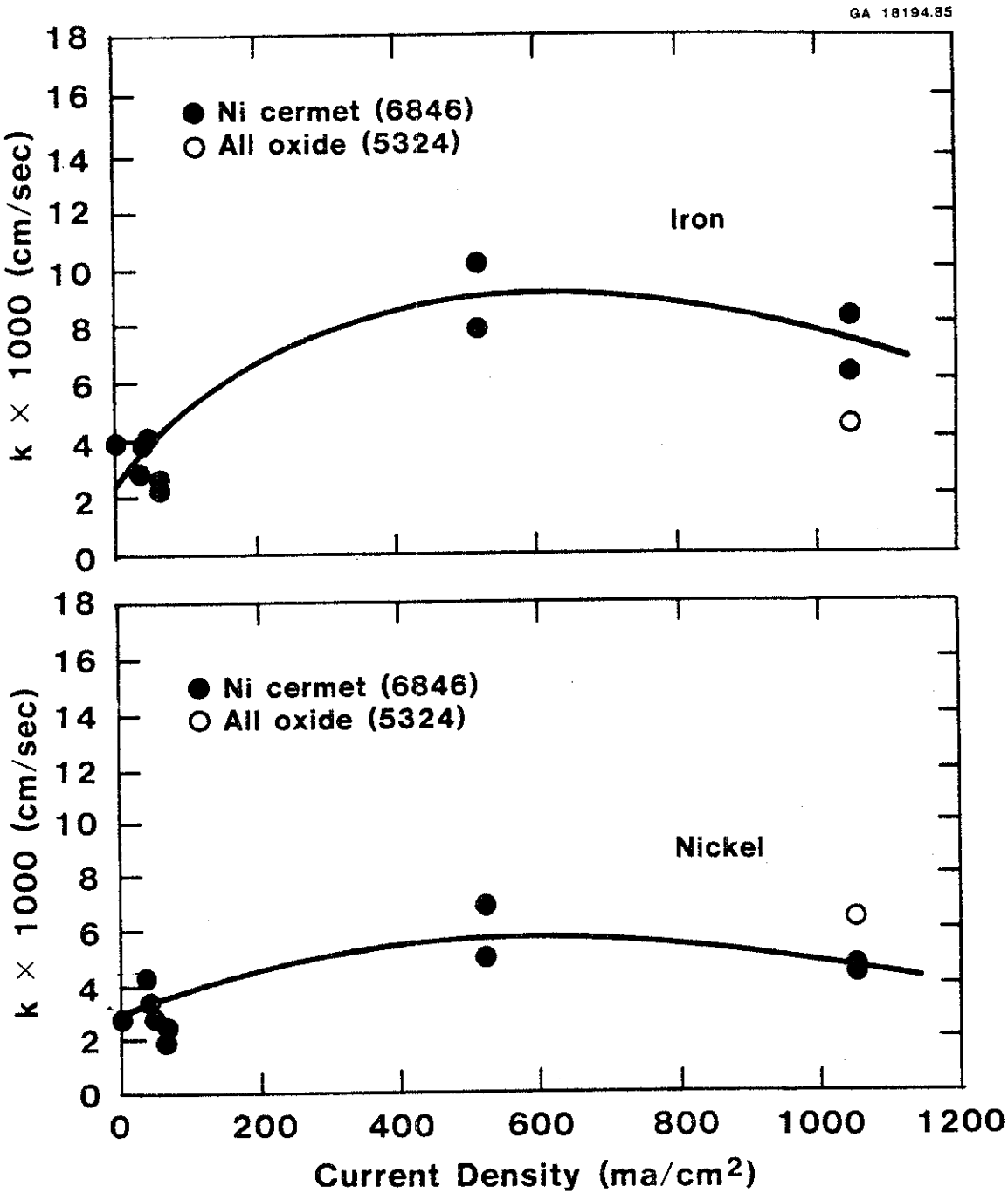

Comparison of Dissolution Rate Constants for the All Oxide (5324) Material and the Ni Cermet (6846) Material. Anodes were Polarized, and Solid Copper Cathodes were Employed.

Figure 128

from anodically dissolved metal or chemically dissolved oxide. Results for polarized oxide materials are consistent with this model.

b) Cu Cermet (5324 + 17% Cu)

Several tests were performed on the Cu-cermet material. Tests were performed for anodes polarized using solid copper cathodes. Anodes were maintained at either a constant potential (at the decomposition potential for Al_2O_3) or a constant current (1050 ma/cm^2). The data were analyzed the same way as other experiments performed using copper cathodes. The dissolution rate constants are given in Table 54. Rate constants could not be calculated for copper because of the lack of knowledge of the passive copper oxide phase that forms on the copper metal and its solubility.

The dissolution rate constants for the Cu-cermet anodes are compared to those for Ni-cermet anodes (Figure 129). There does not seem to be significant differences between the two materials, although the reproducibility for results with the Cu-cermets are poor. As discussed for the all-oxide (5324) material, these results are consistent with a mass transport controlled mechanism for dissolution.

c) Single Crystal $NiFe_2O_4$

One test was performed with a single crystal of $NiFe_2O_4$ that was obtained from Prof. Donald Sadoway, MIT. This crystal was grown in the laboratory of Dr. John Haggerty at MIT. An X-ray pattern obtained at MIT confirmed that this material was a single crystal. Polishing a cross-section of the sample revealed cracks. Cracks were probably difficult to avoid for samples of this diameter (7 mm) in the laser-heated crystal growth apparatus.

TABLE 54

Dissolution Rate Constants for Cu-Cermet
(5324 + 17% Cu) Material

Experiment	$E-E^{\circ}_{Al_2O_3}$ (mV)	I(ma)	i (ma/cm²)	k x 10^3 (cm/sec) Fe	Ni
R117	0		30	1.0	0.8
R118		1000	1050	5.0	5.9
R119	0		30	1.5	6.0
R120		1000	1050	2.2	8.8

Melt composition: Bath ratio 1.1, 6.5% Al_2O_3
Temperature: 960°C

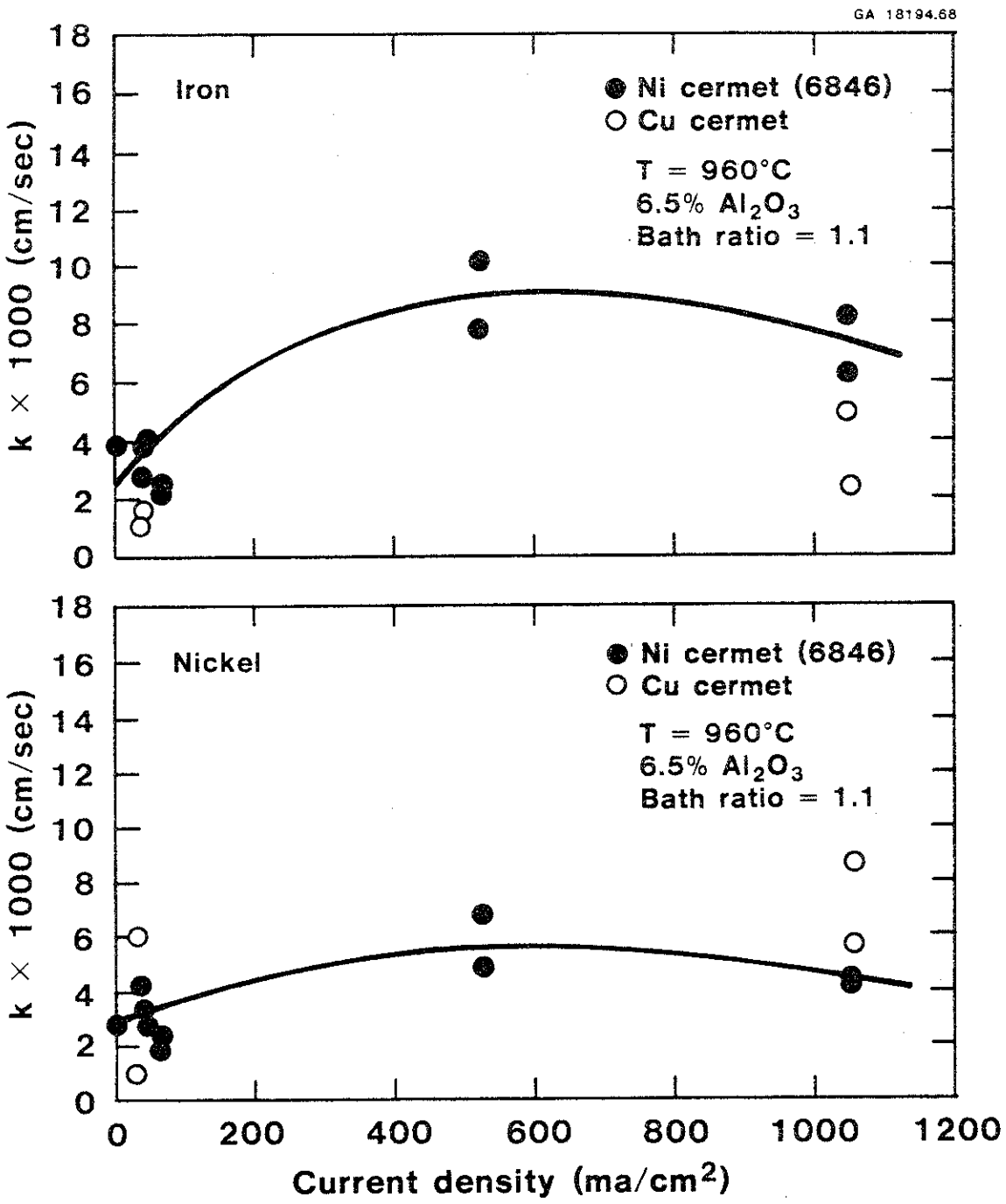

Comparison of the Dissolution Rate Constants for the Cu Cermet (5324 + 17% Cu) Material and the Ni Cermet (6846) Material. Anodes were Polarized, and Solid Copper Cathodes were Employed

Figure 129

The dissolution rate of the crystal was measured the same way as other materials, with one exception. Electrical contact to the sample was made by Pt wire wound in a circumferential notch cut in the top end of the sample. The sample with Pt lead wire was inserted into a 7 mm inside diameter alumina tube. The bottom surface of the sample was metallographically polished. Figure 130 gives a photograph of the sample.

The fit between the sample and the alumina tube was not tight; bath certainly penetrated and wet the side of the crystal. This resulted in a bigger area of the crystal dissolving than just the bottom surface. The measured rate constants would then be higher than the actual values. The effective area of the crystal is probably not more than twice the bottom area. Hence, the measured dissolution rate constants would be at most a factor of two high.

The current density (based on bottom surface area) was held at 1050 ma/cm^2. Copper cathodes were used in this test.

Figure 131 shows the measured rate constants for the single crystal and compares them to ratio constants measured for the Ni-cermet (6846) materials. These data fit the mass-transport-controlled mechanism for dissolution, though they do not prove it. If dissolution was controlled by a chemical reaction, grain boundaries and crystallographic orientation of the crystal could have a big influence on the dissolution. Grain boundaries and crystallographic orientation would not influence a mass-transport-controlled process.

The rate constants for dissolution of the single crystal should be the same as for polycrystalline materials. The increased rate constants seen for the single crystal appears to be the result of the higher but undefined surface area.

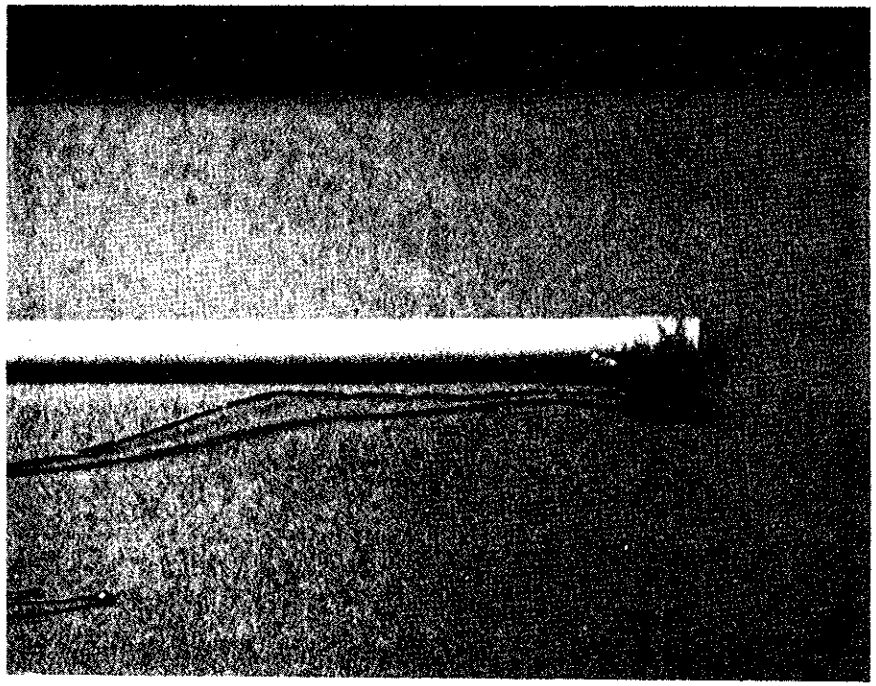

Single Crystal $NiFe_2O_4$ with Pt Connection.
Larger Diameter Crystal was used in Test
Figure 130

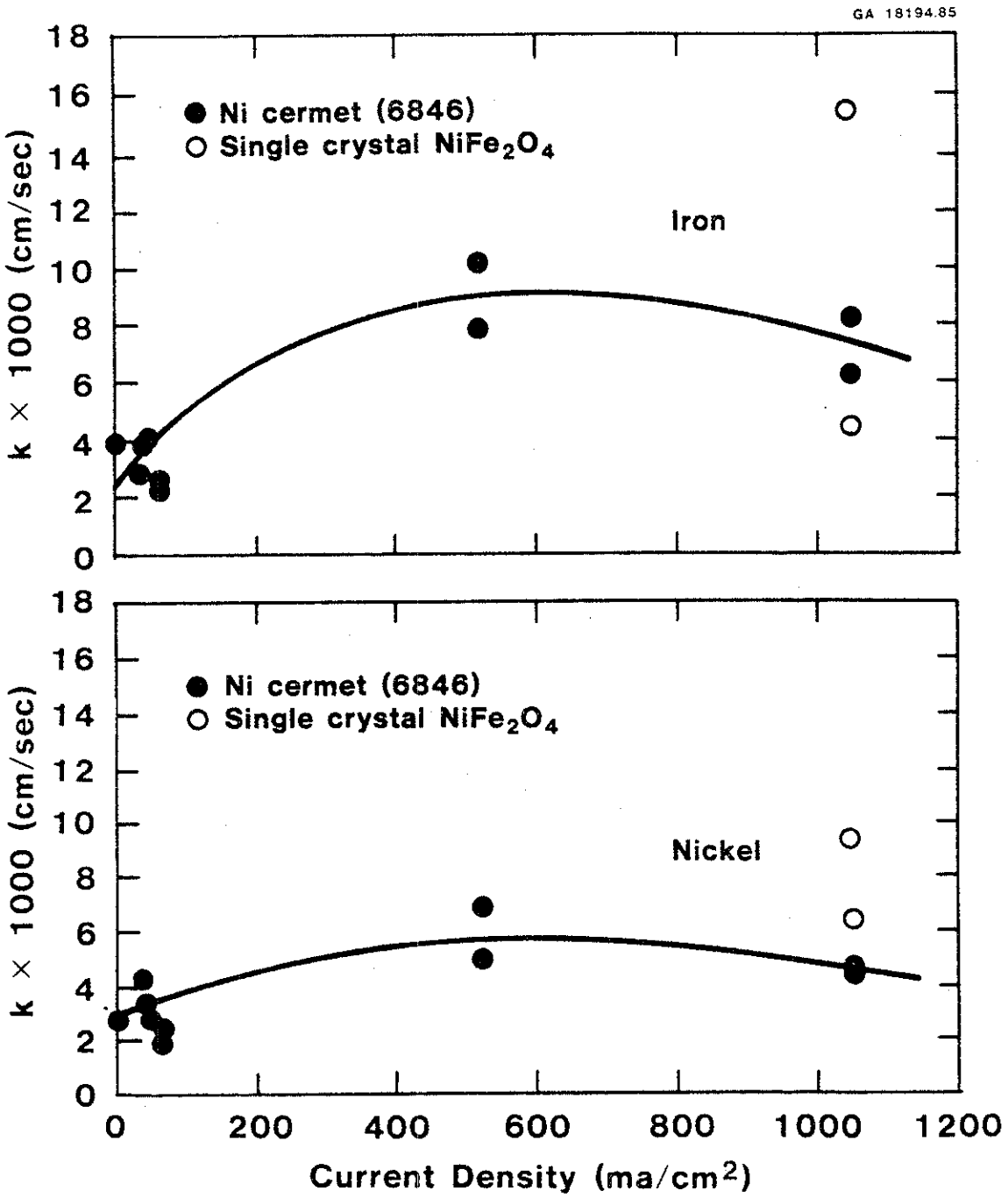

Comparison of the Dissolution Rate Constants for Single Crystal $NiFe_2O_4$ to the Polycrystalline, Ni Cermet (6846) Material. Anodes were Polarized, and Solid Copper Cathodes were Used.

Figure 131

e. Conclusions From Rate Measurements

A rotating disk system was employed to measure the rates of dissolution of inert anodes. The dissolution rates for anodes in cryolite-based melts in an air atmosphere with no aluminum present (oxidizing conditions) was found to increase with rotational speed of the anode. The dissolution proceeded by first-order kinetics, and the rate constant was proportional to the square-root of the rotational speed. This indicates that mass transport is the rate limiting step for dissolution. The rate of dissolution did not change with anode age, as shown by measurements over a 36-hour period.

A series of experiments was conducted to determine the effects of polarization, current (gas evolution), dissolved reduced species (the presence of a metal pad) and additions of carbon/Al_4C_3 to the melt on the rate of dissolution. The dissolution rate constants increased with current through the anode, presumably because of increased stirring caused by oxygen evolution. At the higher Al_2O_3 levels in the bath (6.5%), the dissolution rate constant shows a maximum at 500 ma/cm^2. Possibly at higher current densities, shielding by gas bubbles becomes important and decreases the rate constant. A comparison of test results using copper cathodes with no aluminum present to those with a molten aluminum cathode, shows that the metal pad did not increase the rate constant for iron. At current densities of 1 A/cm^2 the metal pad increased the rate constant for Ni. No increase was found at low current densities. Continuous additions of carbon or Al_4C_3 to the bath did not increase the dissolution rates of the anodes.

C. Electrochemical Studies

1. Objective

The primary objective of this phase of the project was to develop an understanding of the electrochemical dissolution mechanisms active in the corrosion of inert anodes and develop a material or method to control the electrochemical dissolution. In addition, the voltage characterization of the 2500-A Hall cell was to be determined.

2. Introduction

The amount of corrosion that occurs on or in inert anodes during their use is a major problem because it leads to metal contamination and anode destruction. Corrosion can occur by chemical and electrochemical dissolution mechanisms. It has been observed in work previously reported (7) that electrochemical corrosion is occurring with anodic current at potentials less than that required for Al_2O_3 decomposition. This type of current is referred to as background current and experiments have shown that it is caused by active anodic dissolution of the Ni metal phase in the inert anode. These determinations were gathered by chronoamperometry and cyclic voltametry electrochemical techniques. The potential of a working electrode is suddenly pulsed from one potential to another during chronoamperometry experiments to monitor the current-time response and differentiate between electrochemical mechanisms. The potential of a working electrode is scanned while monitoring the current during cyclic voltometry experiments. The important variables for characterization of the electrochemical spectrum of the inert anode in the anodic region include: scan rate, potential, current, and concentration of electrolyte species.

Approaches to reduction or elimination of the anodic dissolution process have included: freezing bath inside the pores of the anode by addition of dopants to the anode, noble metal additions, reduced amount of metal, discontinous metal phase, and use of passivating metal phases. A description of the anodic dissolution mechanism and the development of a

cermet containing a passivating alloy to replace the nickel metal is included in this section of the report.

A primary goal of the inert anode program was to demonstrate energy savings at a reduced anode-to-cathode distance (ACD). This goal was not tested directly because the heat balance of the 2500-A cell would not allow operation at a lower ACD. An indirect method of determining the voltage characteristics of the cell were applied. This technique involved the development and use of a reference electrode and a mechanical manipulator to accurately position the reference electrode in the cell.

3. Experimental Procedures

The electrochemical study of the inert anode focused on three different areas. The first and most comprehensive was a study of the electrochemical corrosion of the metal phase of the inert anode. This study led to the development of an improved metal phase for the inert anode. The second area of investigation was a study of the performance of the improved cermet anode during long term electrolysis. The third area was a comparison of the voltage characteristics of a 2500-A cell operated with carbon anodes or with inert anodes. Each of these areas had its own experimental procedures which are described below.

a. Electrochemical Characterization

Two different cell designs were used to test the stability of various alloy phases in cermet inert anodes. One cell was used for corrosion studies and rapid screening of candidate materials. The second cell was used for longer term, more rigorous evaluation of the most promising material.

The cell shown in Figure 132 was used for the electrochemical corrosion studies and for screening various metals, alloys and cermets as inert anodes for aluminum smelting. The cell was a conventional three-electrode design (80). The use of an annealed molybdenum counter electrode was necessary to prevent interference of the

GA 18194.33

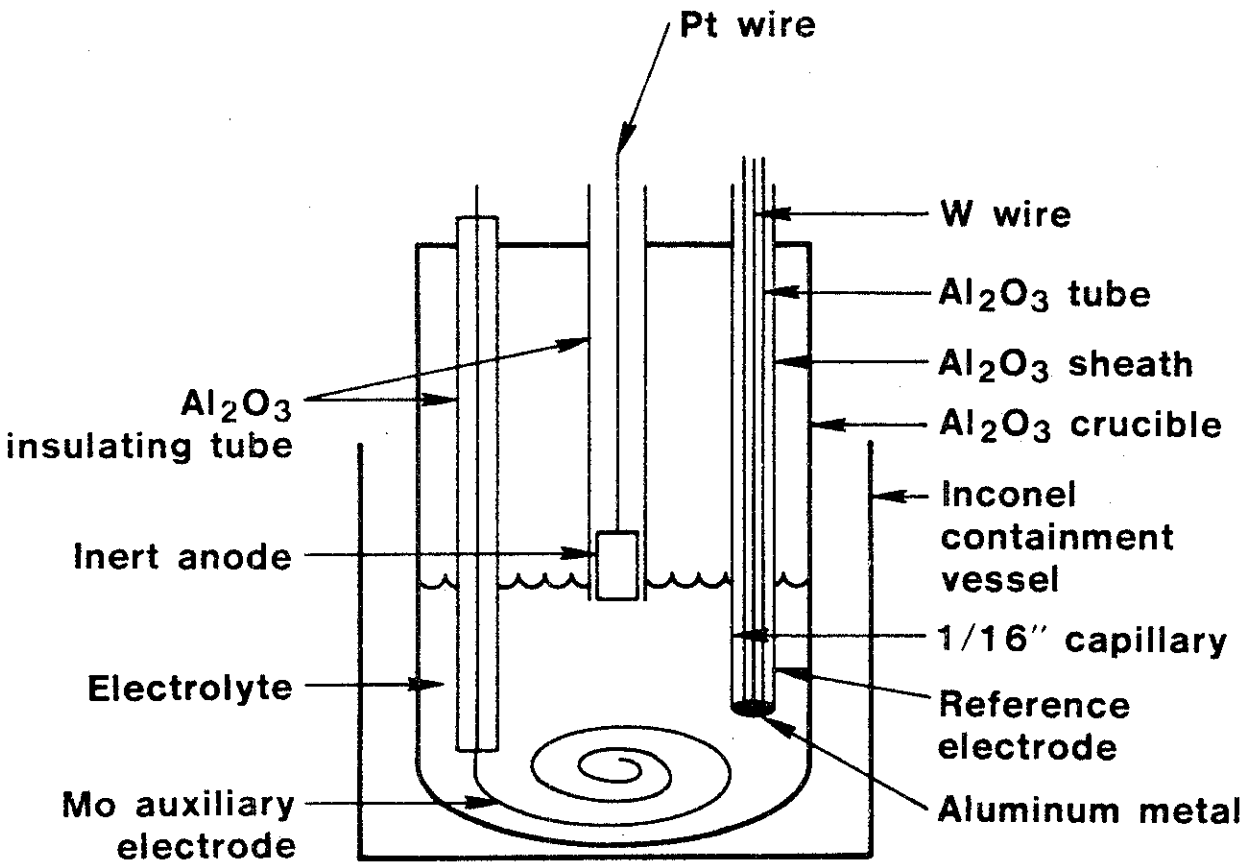

Cell Design for Electrochemical Corrosion Study and Material Screening
Figure 132

corrosion current measurements caused by electrochemical reoxidation of dissolved aluminum at potentials that are negative relative to the O_2 discharge potential. The reference electrode was of traditional design (40). In order to define the electrode area, the working electrode was shielded with an alumina tube and immersed a minimum amount [<1 mm] into the electrolyte. A three-hour galvanostatic [1 amp/cm^2] polarization of the cermets or a half-hour galvanostatic [1 amp/cm^2] polarization of the metals was followed by a linear sweep voltammogram at 1 mv/sec. The open circuit potential [o.c.p.] was defined as the potential at which there was no current. The corrosion current was defined as the amount of anodic current that occurred on the anode at a potential that was just cathodic of the thermodynamic oxygen evolution potential. After electrolysis, the anode was cross-sectioned and examined by electron microprobe analysis. The suitability of the material as an inert anode was judged by three criteria; low corrosion current, large positive open circuit potentials, and microstructural integrity of the anode's metal phase.

The most promising anode material was galvanostatically polarized [1 amp/cm^2] ($\approx$95 amperes) for 100, 165 and 264 hours in three separate experiments. Extended time testing of the material was performed in a cell similar to the cross-section view shown in Figure 133. In the extended testing, it was necessary to simulate a conventional Hall cell. This required the use of carbon cathode bottom, insulating side walls (simulated with alumina liners), liquid aluminum metal cathodes, alumina feeding and metal tapping. The condition of the metal phase in the anode after electrolysis was evaluated by cross-sectioning the anode and examining the integrity of the metal phase near the surface of the anode.

The instrumentation used in these studies is all commercially available. The voltammetry and 3-h galvanostatic polarizations were performed with an EG&G Model 173 or Tacusell Model PIT 20-6X potentistat. The potential, or current, was controlled with an EG&G Model 175 programmer. The ohmic losses were measured with an Electrosynthesis

GA 18194.30

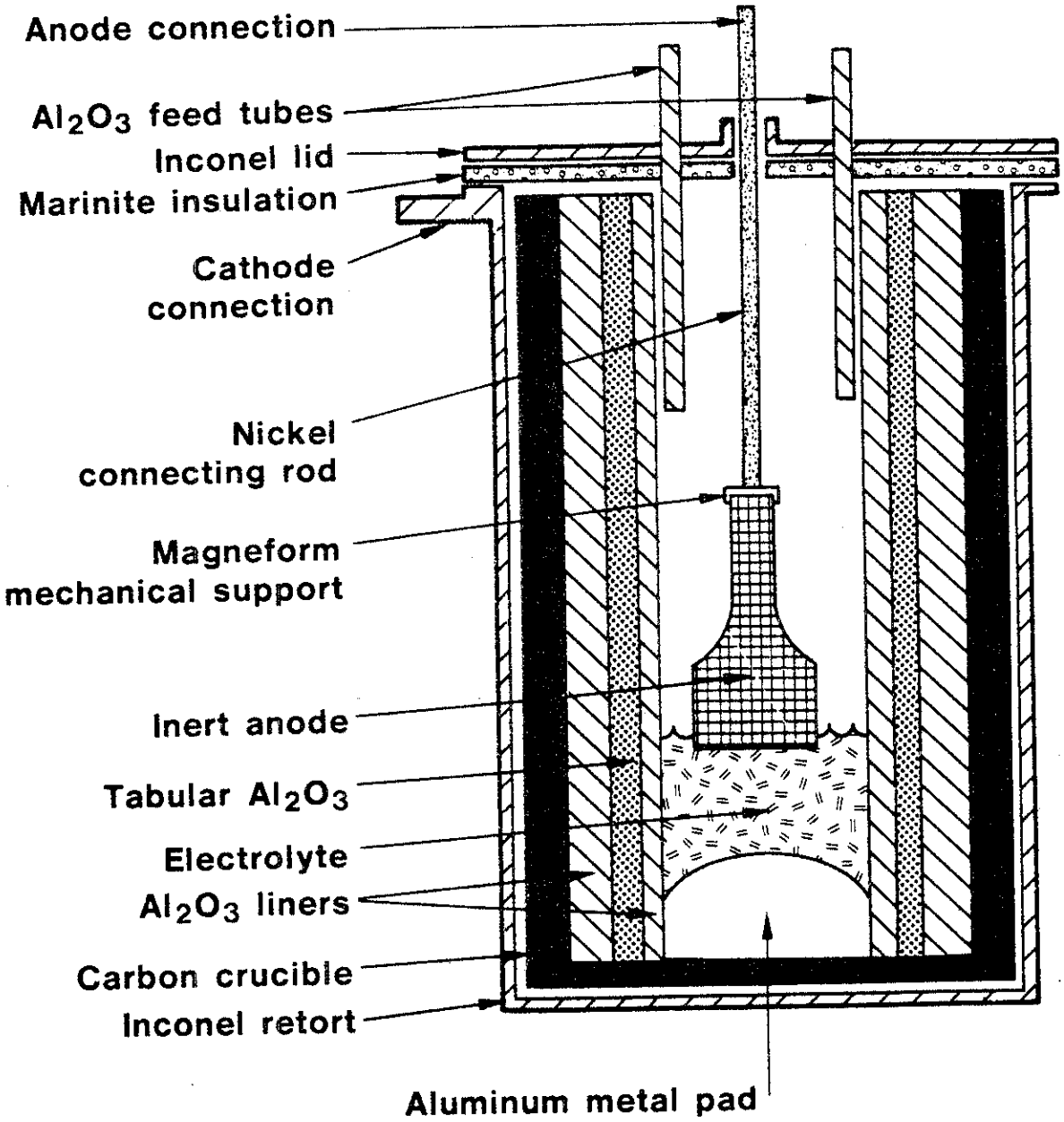

Cell Design for Long Term Testing of Inert Anodes

Figure 133

Co. Model 800 IR measurement system. During the long term electrolysis experiments the anode was galvanostatically polarized with a Sorenson DCR 20-125 DC power supply.

The electrolyte composition was checked by analysis both before and after the experiment. Unless otherwise noted, all experiments in the short term electrolysis cell (Figure 132) were carried out in a 1.15 NaF/AlF_3 wt. ratio, 5 wt.% CaF_2, saturated Al_2O_3 melt at 980°C.

All experiments in the long term electrolysis cell (Figure 133) had the same electrolyte composition targets, but operated at 960°C. Except for Al_2O_3 which was held at saturation by feeding at a rate consistent with 100% current efficiency, the target electrolyte composition (1.15 ratio) varied considerably during the long term electrolysis. No effect on the anode's corrosion rate or stability was observed for the variations in melt composition.

The cermet materials were fabricated by either reaction sintering or by conventional sintering. In the reaction sintering technique the starting materials react during the sintering process to produce new phases (e.g., $5\ NiO + Fe_2O_3 + 2Fe \rightarrow 2NiFe_2O_4 + 3Ni$). In the conventional sintering technique, the starting materials are simply pressed into the desired finished shape and sintered. In both cases the experimental fabrication procedures were the same. The starting materials were uniaxially or isostatically pressed at 20000 psi and then sintered for 2 h at 1350°C in an argon atmosphere.

The finished anode compositions are described below. The reaction-sintered nickel metal cermet was a composite material containing nickel metal (actually 95% Ni, 5% Fe) as intertwined stringers through the ceramic matrix. The chemical composition was approximately 30% Ni, 56% $NiFe_2O_4$, and 14% NiO. The copper-rich copper-nickel alloy cermet was a composite material having isolated metal particles in the ceramic base. Its chemical composition was 20% copper-nickel alloy (80% Cu, 20% Ni), 64% $NiFe_2O_4$, and 16% NiO. The platinum metal cermet also had isolated metal particles; the chemical composition was

20% Pt, 64% $NiFe_2O_4$, and 16% NiO. An isolated nickel metal cermet was also produced. The chemical composition was 20% Ni, 64% $NiFe_2O_4$, and 16% NiO. A reaction-sintered interwoven copper-nickel alloy phase cermet was also made. The chemical composition was approximately 30% interwoven copper-nickel alloy (90% Ni, 10% Cu), 56% $NiFe_2O_4$, and 14% NiO.

b. Long Term Testing

The 60-A cell galvanostatic polarization experiments were performed in a cell design as shown in Figure 133. In run 1, only one alumina side liner was used; while in runs 2 and 3 the crucible side walls were isolated from the anode by placing two Al_2O_3 cylinder liners between the crucible walls and the anode comparent. Tabular Al_2O_3 was placed between the liners to act as both a baffle to fluid bath flow and as a reserve of Al_2O_3 to impede the dissolution rate of the outermost liner. The single Al_2O_3 liner in run 1 was worn through. This led to a hole in the inert anode probably due to direct electrical shorting of the anode with the side walls of the crucible. The outermost liner was intact after the conclusion of runs 2 and 3, while the innermost liner in both runs had some holes through it. The anodes in runs 2 and 3 displayed no holes. We believe the use of the double liners effectively solved the electrical shorting problem.

The cathode was a carbon crucible. The crucible was electrically connected to the Inconel retort containment vessel by placing between the carbon crucible and the retort a small amount of cryolite in runs 1 and 2, and graphite powder in run 3. The crucible froze to the Inconel retort in Experiments 1 and 2. The graphite powder made it easier to dismantle the cell after the experiment.

In run 1, alumina was fed through a single-point feeder while in runs 2 and 3 alumina was fed to the cell through two feed tubes which were 180° from each other. This was done to maximize the uniform distribution of the Al_2O_3 feed in the cell. It was noted that the Al_2O_3 inner liner lasted longer with dual point feeding than with single point feeding.

Current was supplied and controlled with a Sorenson DCR 20-125 DC power supply. The ohmic voltage component of the cell was monitored with a Scribner Associates Model 810 IR measurement system. Temperature was monitored with an Omega Model 4002 KC thermocouple monitor used in conjunction with a type K thermocouple. The data was logged and recorded with an Apple II Plus personal computer interfaced with an Isaac A-D converter. The data logging program was written by Dr. D. H. DeYoung for use with the 2500-A cell testing of 6846 material. The modifications of the program that were necessary for the 7.6 cm anode testing described in this report were also implemented by DeYoung.

The Al_2O_3 refractories were obtained from McDanel Refractory Co. The carbon crucible was machined in-house with existing materials. The inert anodes were 5324-Cu (83/17) composition which were manufactured and machined in-house using previously described materials and techniques described in the fabrication section of this report. The electrical connection to the anode was made by brazing a Cu/Ni (85% Cu, 15% Ni) alloy between the nickel current carrier and the inert anode.

The current was controlled by manual observation and adjustment of the Sorenson power supply to a set point of 1 A/cm^2 based on the bottom immersed area of the anode. The anode immersion depth was measured with a molybdenum dip stick and controlled by raising the anode with a machine screw jack type of height adjustment when the depth was too great [> 1.9 cm], or by raising the electrolyte level when the immersion depth was too low [< 0.6 cm]. Since we anticipated that the 5324-Cu (893/17) composition would not internally oxidize, we controlled the anode-to-cathode distance by maintaining a constant voltage across the cell. The cryolite ratio was controlled by frequent sampling and chemical analysis (via pyrotitration) with adjustment of the ratio after the analysis back to the target of 1.15 wt. ratio NaF/AlF_3. The Al_2O_3 concentration was kept concentrated by feeding at 95-100% current efficiency.

Electrolyte samples were taken throughout the run for analysis of impurities. Aluminum metal samples were taken throughout the run for chemical analysis [via atomic absorption (AA) or induction coupled plasma (ICP)] of the contamination levels in the metal in runs 2 and 3. Both types of samples were taken by siphoning the liquid into an alumina or quartz sampling tube and then allowing the sample to freeze.

The anode dimensions were measured before and after the run to determine the dimensional changes that occurred. The aluminum was recovered after the cell cooled to room temperature so that the overall coulombic efficiency could be determined. The anode was sectioned and polished in order to determine the extent of internal oxidation of the metallic phase in the anode and the integrity of the electrical connection.

c. Voltage Characteristics of the 2500-Ampere Cell

1) Materials

a) Cell Design

Figure 134 is a schematic diagram of the 2500-A Hall cell used in these studies. Current was monitored on each anode with individual current shunts (not shown). The current load was adjusted to an equal share for each anode by individually adjusting the anode-cathode distance (ACD). Then electrolyte was operated with a saturated Al_2O_3 content in order to minimize inert anode corrosion. This was assured by frequent chemical analysis of the electrolyte. The heat balance characteristics dictated the total current load an overall ACD at which the cell operated. This cell had rather large heat losses compared to a commercial scale cell (150,000 A). The high heat loss required operation at large anode-cathode distances. Whenever the ACD was greatly reduced, the electrolyte would begin to freeze because of an

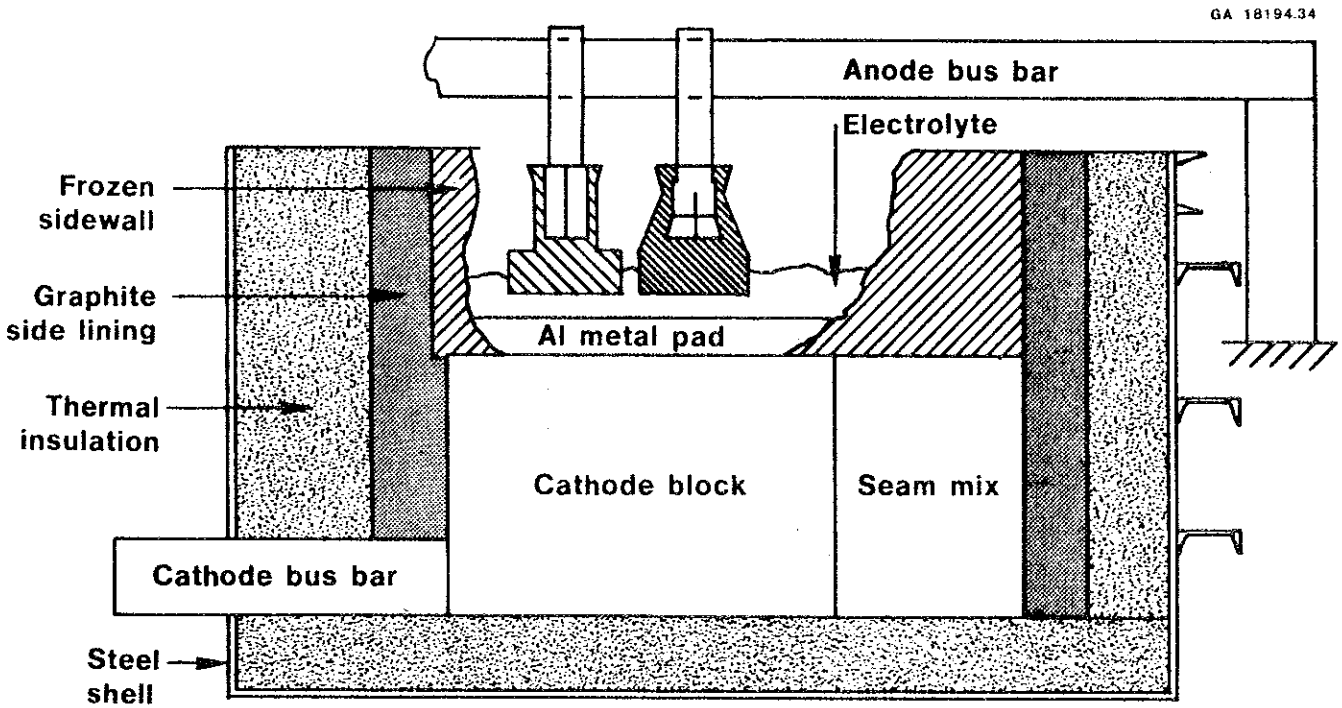

Schematic of the 2500-Ampere Hall Cell
Figure 134

inability to provide enough resistive heating. Likewise, at larger ACD the electrolyte would begin to overheat. In order to obtain the voltage characteristics of the cell, a reference electrode of our own design was used.

b) Reference Electrode Design

The design of the reference electrode is shown in Figure 135. The aluminum pool provides a means of keeping a large pool of aluminum in contact with the electrolyte. This is desirable because any small amount of alloying will not greatly affect the aluminum activity at the electrolyte metal interface.

The small capillary tube assures that the tungsten wire will not come in contact with the electrolyte and set up a mixed potential. Quartz was found to last one-half hour in the electrolyte. The reference electrode was fragile but inexpensive and easy to construct. Several reference electrodes were available for each experiment.

The ohmic drop through the anode material was measured by shorting a platinum probe to the bottom of the anode. The design of the probe is shown in Figure 136. The quartz tube insulates the platinum wire from the electrolyte.

c) Reference Electrode Manipulator

The reference electrode manipulator is an electromechanical device that was used to maneuver the quartz tube reference electrode through the bath in the 2500-A cell. The design features two 40:1 ratio rack and pinion manual drives and one screw-nut driver to effect movement in an XYZ coordinate system. The principal direction (vertical) of motion is monitored by a 12" Sony Magnescale Digital Positioner system.

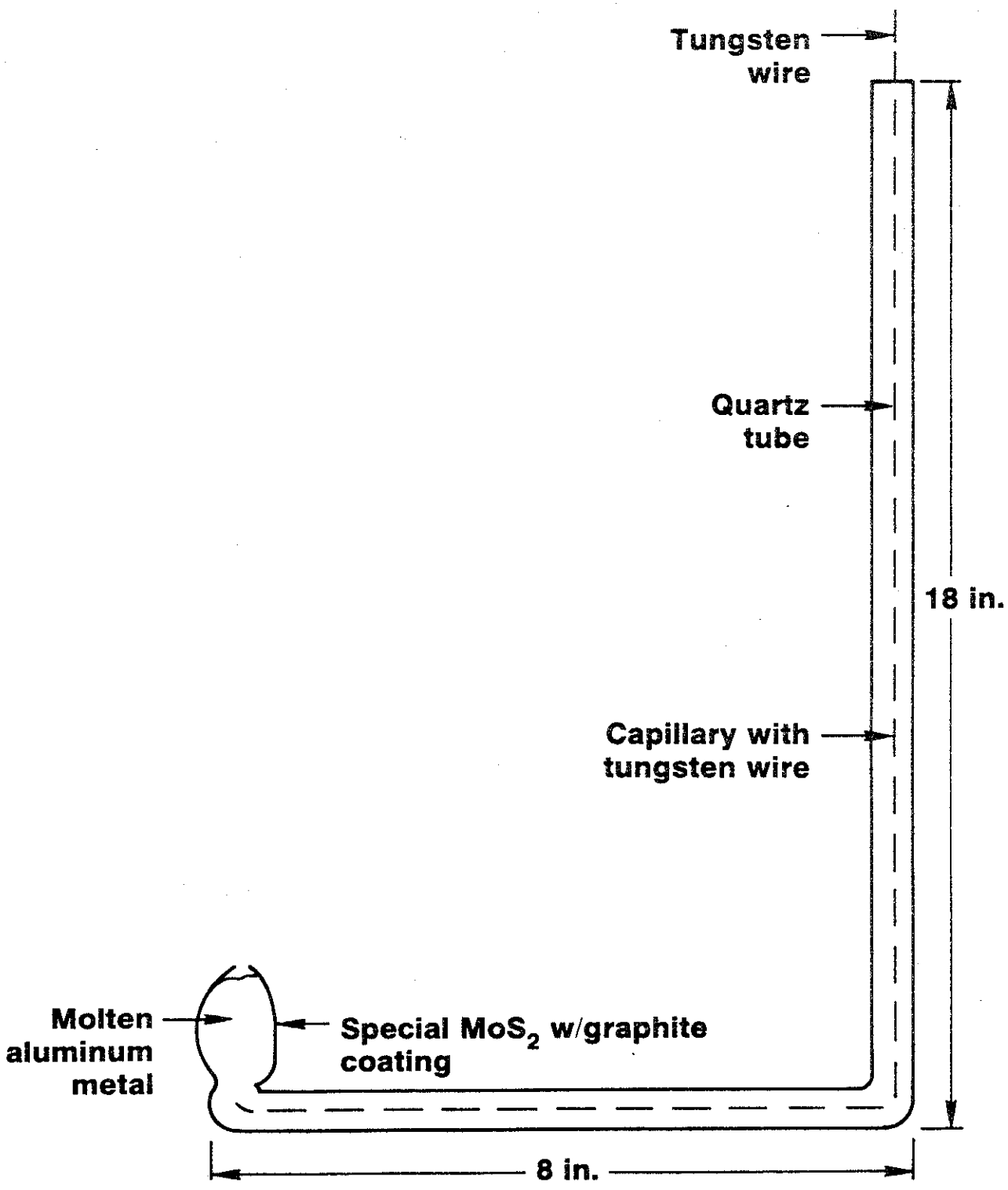

Design of Reference Electrode used for Voltage Characterization of 2500-Ampere Inert Anode Cell

Figure 135

GA 18194.175

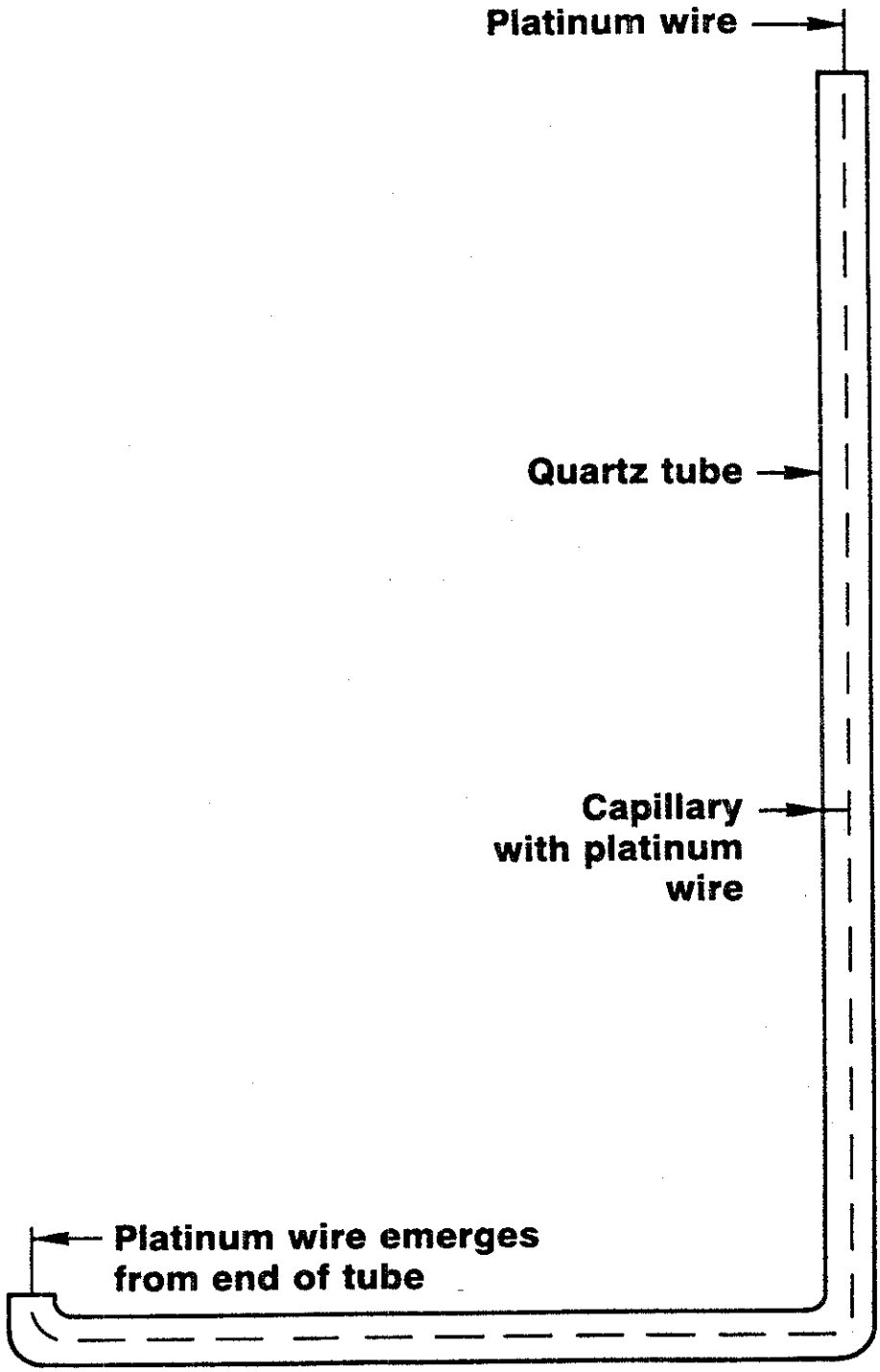

Design of Anode Voltage Drop Probe
Figure 136

In Figure 137, the probe manipulator is shown mounted on the 2500-A cell bus bar. The Sony Magnescale Digital Positioner outputs a stable "BCD signal" that is then fed into a digital-to-analog converter (DAC) to produce a 0-10 VDC analog signal. This signal is then plotted with the potential difference between the reference electrode and the anode on a Houston Instruments XY recorder.

The reference electrode was attached to the mechanical manipulator and lowered to just above the electrolyte for approximately 5 minutes of preheating. After the preheat period, the electrode was lowered into the bath below the anode and positioned so that the opening on the aluminum reservoir was approximately in the middle. The reference electrode was then raised until it just touched the anode's surface. The aluminum is protected from reacting because it is recessed in the quartz containment tube. This was visually detected by a small compression of a spring that is used on the manipulator. The mechanical readout and XY recorder were zeroed. The reference electrode was lowered toward the cathode while simultaneously recording the voltage difference of the anode vs. reference electrode on the Y axis and the distance traveled by the reference electrode on the X axis of the recorder. After the electrode reached the bottom of the cell (usually limited by ledge formation) the travel direction was reversed and the plot redrawn. This assured that the data was reproducible and independent of the direction of travel.

The cell current was changed and the above process repeated. This provided volt/amp data for calculation of the ohmic components in the electrolyte.

After the interelectrode space scans were completed, the reference electrode was disconnected from the manipulator and the electrode was lowered into the metal pad. The

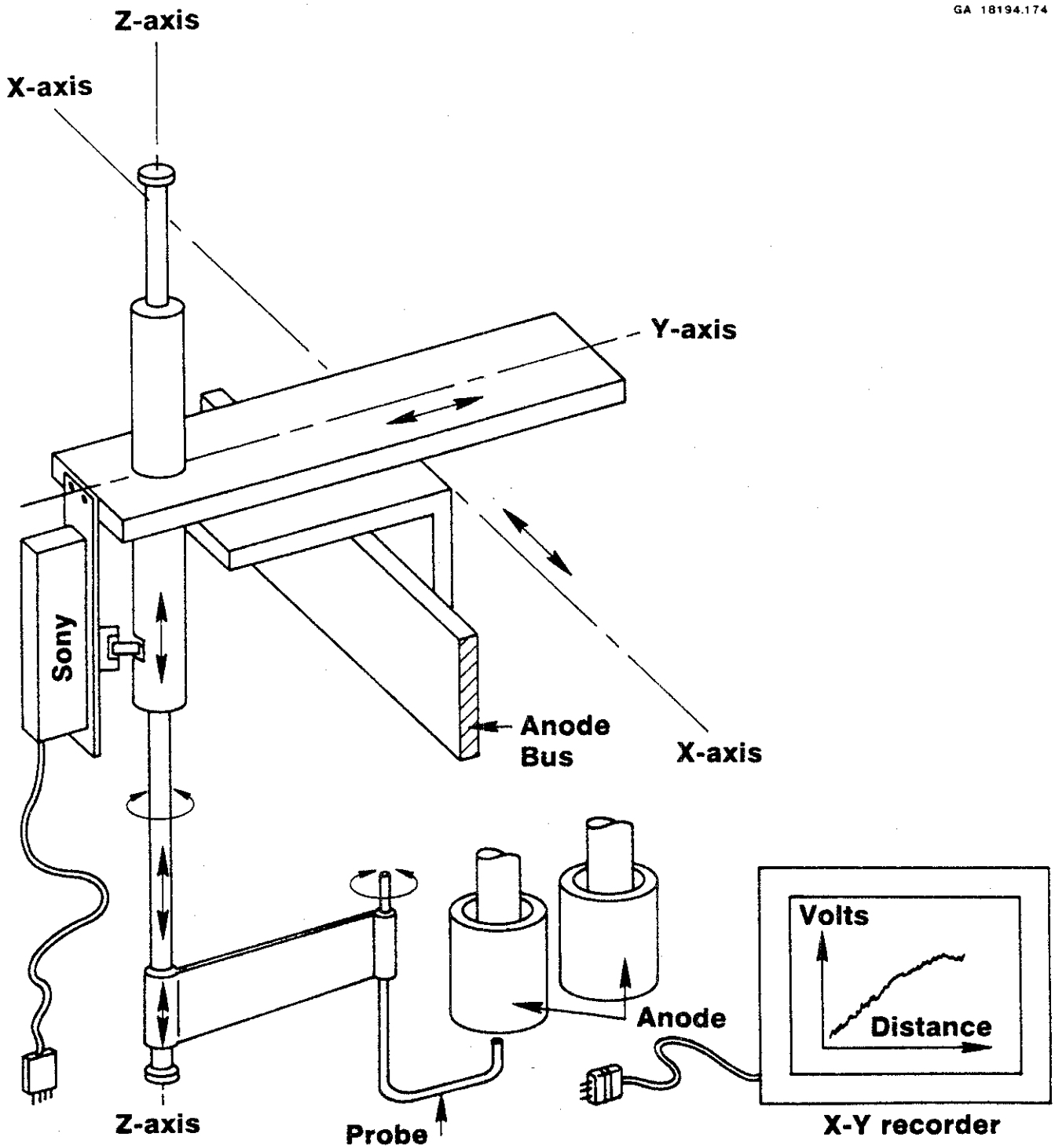

Schematic Representation of the Probe Manipulator
Figure 137

current was changed and cathode and muck voltage drop data collected. The reference electrode was then removed and inspected to make sure aluminum metal was still in the metal reservoir, and that the tungsten wire was not in contact with electrolyte.

The cermet and connection voltage drop was then measured by contacting the cermet with the platinum anode voltage drop probe and varying the current.

4. Corrosion and Passivation of Cermet Inert Anodes

The primary aim of the inert anode project was to develop a suitable inert anode. A suitable material had to be both corrosion resistant and highly electrically conductive. Cermets [a mixture of ceramic oxides and metal] seemed to fit both criteria. This section discusses the electrochemical corrosion and the development of a passive metal phase for the cermet anode.

a. Electrochemical Corrosion Study

During the development of Alcoa's inert anode, the most promising early candidate material was a reaction-sintered $NiFe_2O_4$/NiO-Ni metal cermet material (15). The $NiFe_2O_4$ and NiO imparted a high degree of dimensional stability to the anode because of the low solubilities of these oxide phases in cryolite-base electrolytes (40,51). The nickel metal in the anode provided high electrical conductivity and good mechanical strength.

Preferential corrosion of the alloy phase in this material was a problem. Figure 138 shows a photograph of a cross-sectioned anode after 96 h of electrolysis. The darker region is the zone in which the metal has been leached from the material. This region had poor electrical conductivity [0.5 $ohm^{-1}cm^{-1}$] compared to the starting material [300 $ohm^{-1}cm^{-1}$] and lower mechanical strength. Microscopic examination of this region after the electrolysis period revealed two

GA 18194.40

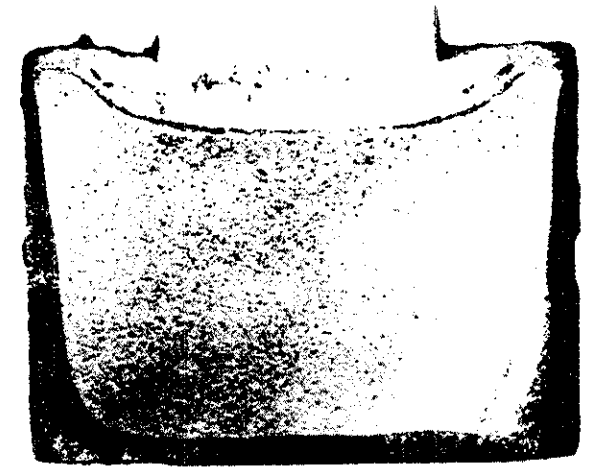

96 hrs. of electrolysis

Cross-Section of a $NiFe_2O_4$/NiO-Ni Metal Inert Anode

Figure 138

important differences from the unaffected region. First, the metal phase was completely missing. Second, the anode was much more porous and the pores were filled with frozen electrolyte.

The cause for this preferential corrosion has been identified as anodic dissolution of the nickel metal in the anode. The equations which describe the anodic dissolution process are:

$$Ni = Ni^{+2}_{(abs)} + 2e \tag{60}$$

$$Ni^{+2}_{(abs)} \xrightarrow[\text{rate determining step}]{\text{mass transport in pores}} Ni^{+2}_{(soln)} \tag{61}$$

$$Ni^{+2} + NiFe_2O_4 \text{ ---> } 4NiO + 2Fe^{+3} \tag{62}$$

or

$$Ni^{+2} + Al_2O_3 \text{ ---> } 3NiO + 2Al^{+3} \tag{63}$$

or

$$Ni^{+2} + 2e \text{ ---> } Ni \text{ [reduced into aluminum metal]} \tag{64}$$

or

$$Ni^{+2} \text{ ---> lost in bath fumes} \tag{65}$$

The primary anode reaction with inert anodes in aluminum smelting is oxygen evolution.

$$Al_2O_3 \text{ ------> } 2Al + 3/2\ O_2 \qquad E^0_{980C} = 2.195 \text{ volts} \tag{8}$$

The anodic dissolution process manifests itself as an anodic corrosion current at potentials negative to the oxygen evolution potential. Figure 139 shows voltammograms obtained at a $NiFe_2O_4$/NiO-Ni alloy cermet working electrode, and at a platinum metal working electrode.

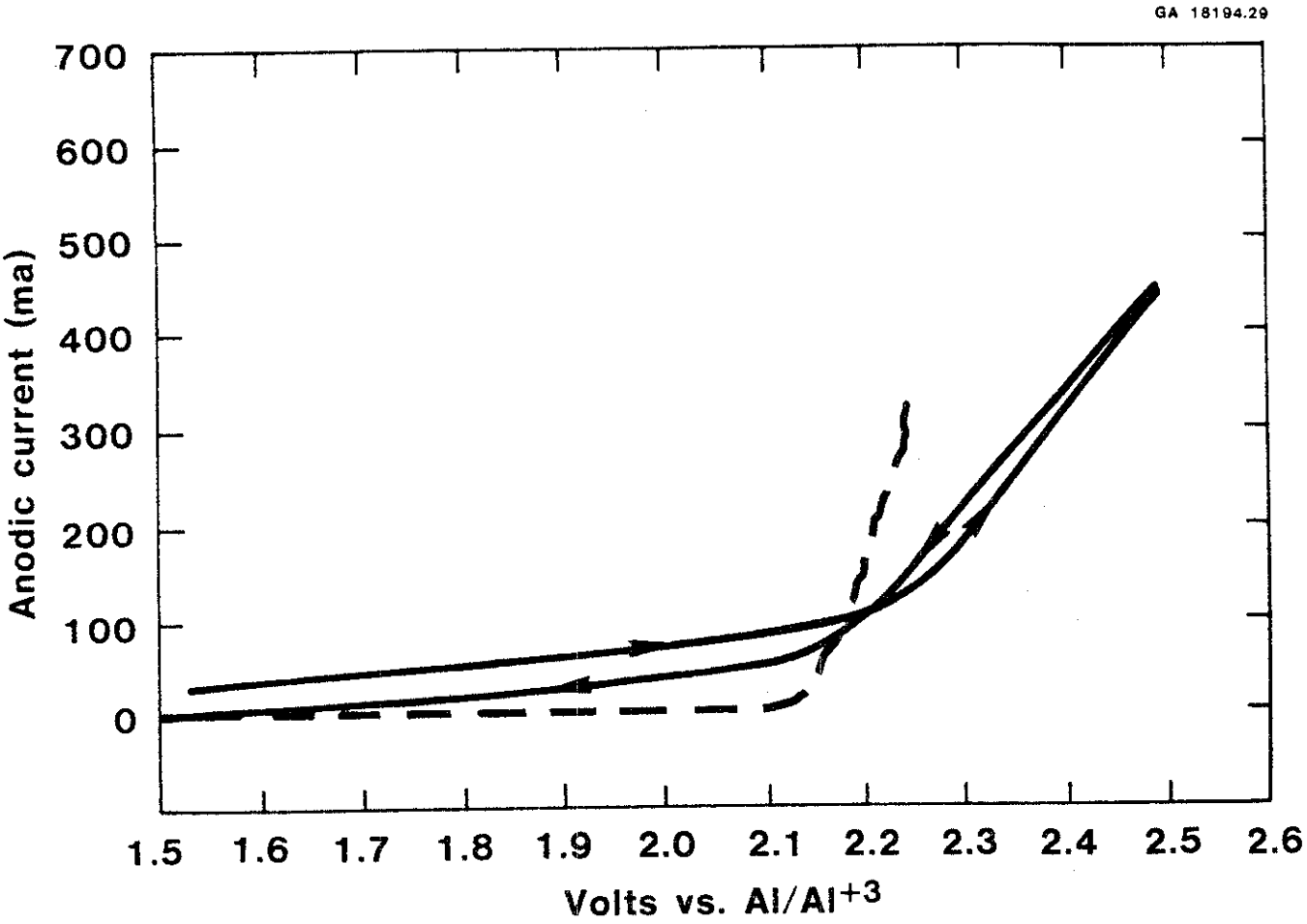

Linear Sweep Voltammograms of $NiFe_2O_4$/NiO-Ni Cermet (———) and Pt (– – –) Working Electrodes (Not I*R Corrected) Scan Rate = 1 ma/sec; NaF/AlF_3 = 1.15; 5% CaF_2; Sat. Al_2O_3; 980°C

Figure 139

An anodic current negative to the thermodynamic oxygen evolution potential is observed on the cermet anode, while it is absent on the platinum anode. In order to minimize the effect of uncontrolled variables [e.g., electrolyte impurities], both electrodes were of identical geometric size and the experiment was performed on both materials with the same electrolyte in the same cell on the same day. Since no current below O_2 evolution was observed on the platinum anode, the current observed on the cermet anode was not the result of electrolyte impurities [e.g., dissolved Al or Na metal, OH*, etc.].

The remote possibility that the corrosion current was caused by an underpotential evolution of oxygen via discharge of OH was eliminated when no oxygen could be detected in the cell offgas during polarization of the anode in the corrosion current region [2.0 V vs. Al]. This corrosion current is specific to the nickel metal alloy phase of the cermet. Figure 140 shows the linear sweep voltammograms obtained using a $NiFe_2O_4$/NiO-Ni cermet anode and a $NiFe_2O_4$/NiO ceramic anode. (No anodic current was observed with the all ceramic anode, composition 5324, at potentials below O_2 evolution.) On the ceramic electrode, the only Faradaic process observed is oxygen evolution, while the cermet electrode exhibits two Faradaic processes. Oxygen evolution is observed at potentials positive to 2.2 V. Anodic dissolution of the metal phase is observed at potentials negative to 2.2 V. Since the corrosion current was eliminated by removing the nickel metal from the anode, it is clear that this corrosion current is caused by the nickel metal.

A linear sweep voltammogram of the cermet anode is plotted in a Tafel format in Figure 141. A limiting current (negligible increase in current with increasing potential) was observed for the corrosion current, indicating that the process was mass transport controlled.

*P. G. Russell at Fourth International Symposium on Molten Salts, Fall Meeting Electrochemical Society, reported anodic currents on cermet anodes at potentials less than 2.2 V vs. Al. He attributed these currents to OH^- dissolved in the melt. A more likely explanation is corrosion of the metal phase in the cermet anode.

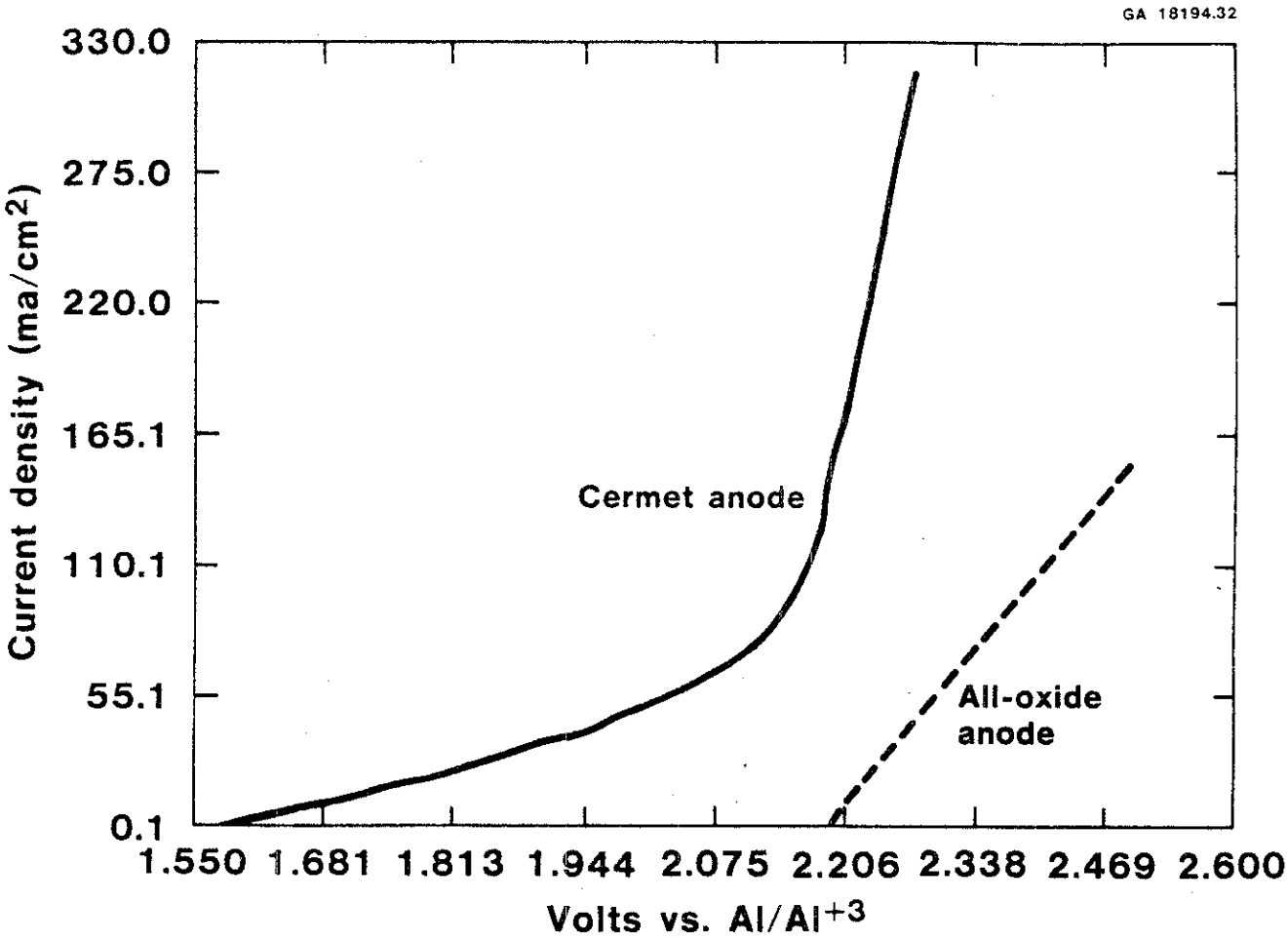

Linear Sweep Voltammograms of $NiFe_2O_4$/NiO-Ni Cermet and $NiFe_2O_4$/NiO Ceramic Anodes (Not I*R Corrected) Scan Rate = 1 mv/sec; NaF/AlF_3 = 1.15; 5% CaF_2; Sat. Al_2O_3; 980°C

Figure 140

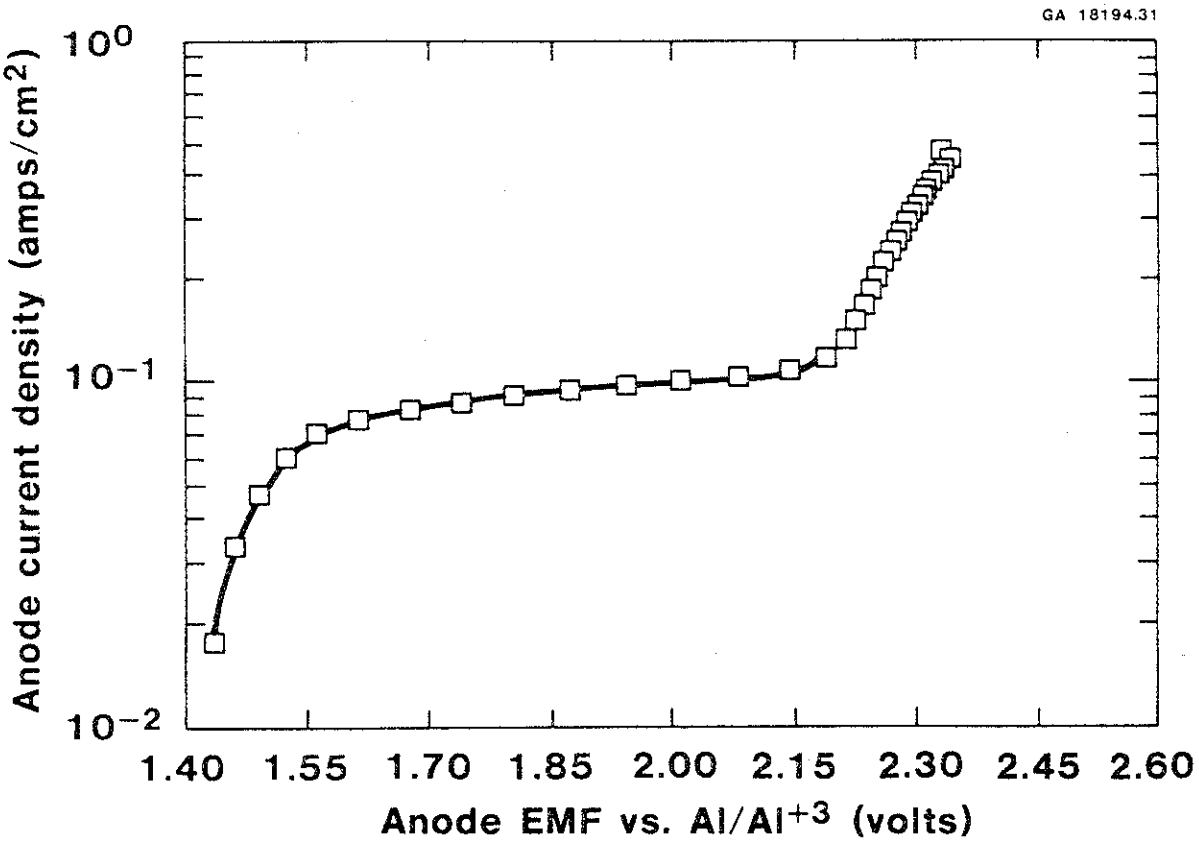

Voltammogram Plotted in a Tafel Format for $NiFe_2O_4$/NiO-Ni Cermet, NaF/AlF_3 = 1.15; 5% CaF_2; Sat. Al_2O_3; 980°C

Figure 141

The limiting corrosion current decreased slowly with time until a steady state was achieved. The steady state limiting corrosion current density varied from one anode to another, but was on the average 26 ma/cm^2. The limiting corrosion current density was also found to be independent of bulk electrolyte mixing, indicating that mass transport control was occurring in the pores of the anode.

b. Porous Electrode Discussion

A rigorous mathematical model for this cermet electrode seemed unlikely. Compared to a smooth electrode, any porous electrode is inherently complicated by unequal electrochemical access. This porous electrode was further complicated by a changing pore structure. This dynamic pore structure was the result of several processes. The primary electrochemical process occurring in the pores [anodic dissolution of Ni metal] was the primary pore generating mechanism in the anode. In addition, the pore structure was also changing by dissolution of the oxide phases inside the pores. Further changes in the pore structure were generated by secondary reaction [e.g., $3Ni^{+2} + NiFe_2O_4 \rightarrow 4NiO + 2Fe^{+3}$]. The oxygen evolution reaction also led to apparent changes in the pore structure via gas bubble plugging of the pores.

Besides being a nonstatic porous electrode, the cermet anode is further complicated by two Faradaic reactions, oxygen evolution and anodic dissolution of nickel metal. The oxygen evolution reaction occurs primarily on the oxide phases of the cermet and obtains its reactants chiefly from the electrolyte, while the corrosion reaction is limited to the metal phase and gets its reactants from the anode. The exact microstructure of the anode varies from anode to anode, making it complicated to determine even the initial geometric accessibility of these phases to the electrolyte.

Although the changing pore structure and multiple Faradaic reactions are the most significant complications, other difficulties also exist. The electrical conductivity of the oxide and metal phases are dif-

ferent by at least three orders of magnitude. This electrode system consists of five phases: three solid electrode phases, a liquid electrolyte phase (that may vary from pore to pore) and a gaseous product phase. The properties of these phases are not clearly defined [e.g., the solubility of O_2 in cryolite is not well known].

Chizmadzhev and Chirkov (81) have discussed, in some depth, porous electrodes more simple than this cermet electrode. It is beyond the scope of this report to completely review their discussion, but noting a few highlights of their paper is worthwhile.

The simple porous electrode has a fixed electrode geometry and only one Faradaic process is occurring. The ohmic drop in the matrix is fixed and negligible compared to the electrolyte. The Faradaic process is not coupled to any other chemical reactions and occurs so fast that the rate is mass transport controlled. Only two phases exist; the electrode matrix and the electrolyte into which the reactants and products of the Faradaic process are infinitely soluble.

Since convection in the porous electrode matrix is negligible, the flux of the component of interest is the sum of two components, diffusion and migration. The driving force for the process is the potential drop across the porous layer in a migration controlled case, and a concentration gradient in the diffusion controlled case. The overall flux will be influenced by the connected porosity of the matrix and the tortuosity of the pores.

It was likely that the anodic dissolution process in the cermet electrode was influenced more strongly by the intrinsic characteristics of porous electrodes than by the parameters described earlier. Simple porous electrode theory was therefore used to guide further development of the material. Examination of the theory suggested the following steps could be taken to limit the anodic dissolution process.

Decrease porosity - This is difficult because the anodic dissolution

process generates the pores. Freezing of electrolyte inside the pores by incorporating CaF_2 in the anode was tried. This failed because the CaF_2 slowly dissolved into the electrolyte but never reached a high enough concentration inside the pores to raise the liquidus temperature.

Increase tortuosity - This could be accomplished by incorporating a discontinuous metal phase inside of the anode or by using more winding "metal worms" in the cermet.

Increase polarization for anodic dissolution - The thermodynamic polarization difference for Ni oxidation and oxygen evolution is the driving force for the anodic dissolution process. The potential drop across the porous layer is driven by the thermodynamic difference in polarization required for anodic dissolution of nickel [1.5 V vs. Al] and discharge of oxygen [2.2 V vs. Al]. This difference can be decreased by using more noble and/or passivating metals.

Decrease temperature - Use of lower liquidus temperature electrolytes would decrease the anode temperature. Lowering of temperatures usually decreases the reaction rate of a chemical reaction.

Decrease active metal phase area - Use of a smaller percentage of metal would decrease the active area for anodic dissolution in the anode. Unfortunately, the electrical conductivity of the cermet also would decrease.

c. Development of an Improved Cermet

All of the above approaches were tried to some degree, but the greatest success was achieved by using an alternate metal phase.

An experimental screening of various pure metals and commercially available alloys was performed to find a metal or alloy that had a higher polarization requirement for anodic dissolution in the cryolite electrolyte than nickel. The metals were examined by performing a

slow [1 mv/sec] linear sweep voltammogram, followed by a galvanostatic polarization at 1 amp/cm^2 for one-half hour. Corrosion currents and open circuit potentials obtained from the linear sweep voltammogram along with optical microscopic examination of the metal anodes were used to determine the corrosion resistance of the candidates being tested.

Table 55 summarizes the results of the metal and alloy screening program. None of the metals or alloys tested, except for platinum, were sufficiently corrosion resistant to serve as an inert anode alone. However, copper and copper/nickel alloys were promising candidates for a metal phase in a $NiFe_2O_4$/NiO cermet. Copper is thermodynamically compatible with the preferred oxide phases [$NiFe_2O_4$/NiO]. Copper was also found to be dramatically more corrosion resistant than nickel in the metal screening program. Figure 142 shows linear sweep voltammograms obtained on both nickel and copper anodes. The noise and absence of a break in the voltammogram for oxygen evolution when using a nickel electrode are good indications of an active corrosion process.

Examination of the nickel electrode after removal from the electrolyte revealed a high degree of pitting corrosion and no adherent protecting film. On the other hand, copper displayed a limiting current behavior for oxygen evolution. Since oxygen evolution is not thermodynamically preferred on a virgin metal surface, a passivating film between the copper metal and electrolyte must have been formed. Upon removal of the copper electrode a thick adherent black film was found on the surface of the copper. Debye-Scherer X-ray diffraction identified the film as 60-70% $CuAlO_2$ and 30-40% Cu_2O. The limiting current was the result of slow passage of ions through this passivating layer.

Copper alloys and platinum metal cermets in a $NiFe_2O_4$/NiO ceramic base were fabricated for comparison testing with the nickel metal cermet. The cermets were galvanostatically polarized for three hours at 1 amp/cm^2, after which slow linear sweep [1 mv/sec] voltammograms were obtained. Figure 143 shows the microprobe elemental dot map

TABLE 55

Electrochemical Corrosion Results
of Metal and Alloys

Metal Alloy	i_{corr} mā/cm²	O.C.P. vs. Al	Comments
NICKEL	>1000	1.48	Massive pitting corrosion; no adherent oxide layer.
PLATINUM	<10	1.9	No observable corrosion.
COPPER	123	1.87	Thick adherent oxide film.
IRON	140	1.34	Thick film, spalling and pitting.
TANTALUM	400	0.9	Massive corrosion.
Ni:Nb (40-600	>1000	0.9	Massive corrosion.
MONEL 400	100	1.42	Microscopic pitting; preferential attack of Ni.
INCONEL 600	168	1.58	Thin oxide layer with some spalling and internal voids.
INCONEL X750	136	1.6	Very thin film; internal voids; very little spalling.
STAINLESS STEEL 316 (low carbon)	500	1.1	Massive corrosion; spalling and pitting
HASTALLOY-C	80	1.3	Good oxide layer; no pitting.
CABOT 214	190	1.6	Dense adherent oxide film; no spalling; internal voids.

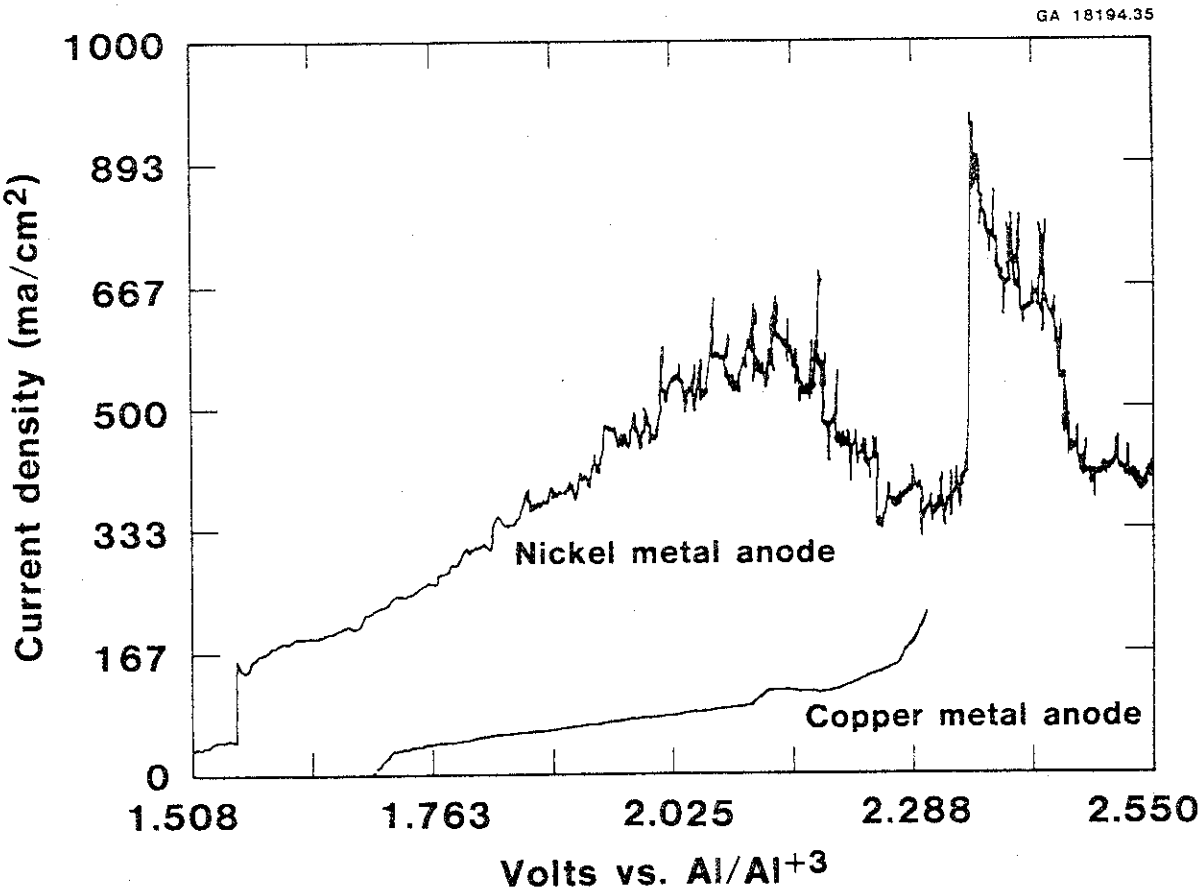

Voltammograms of Cu and Ni Metal Anodes
1 mv/sec; NaF/AlF_3 = 1.15; 5% CaF_2;
Sat. Al_2O_3 980°C

Figure 142

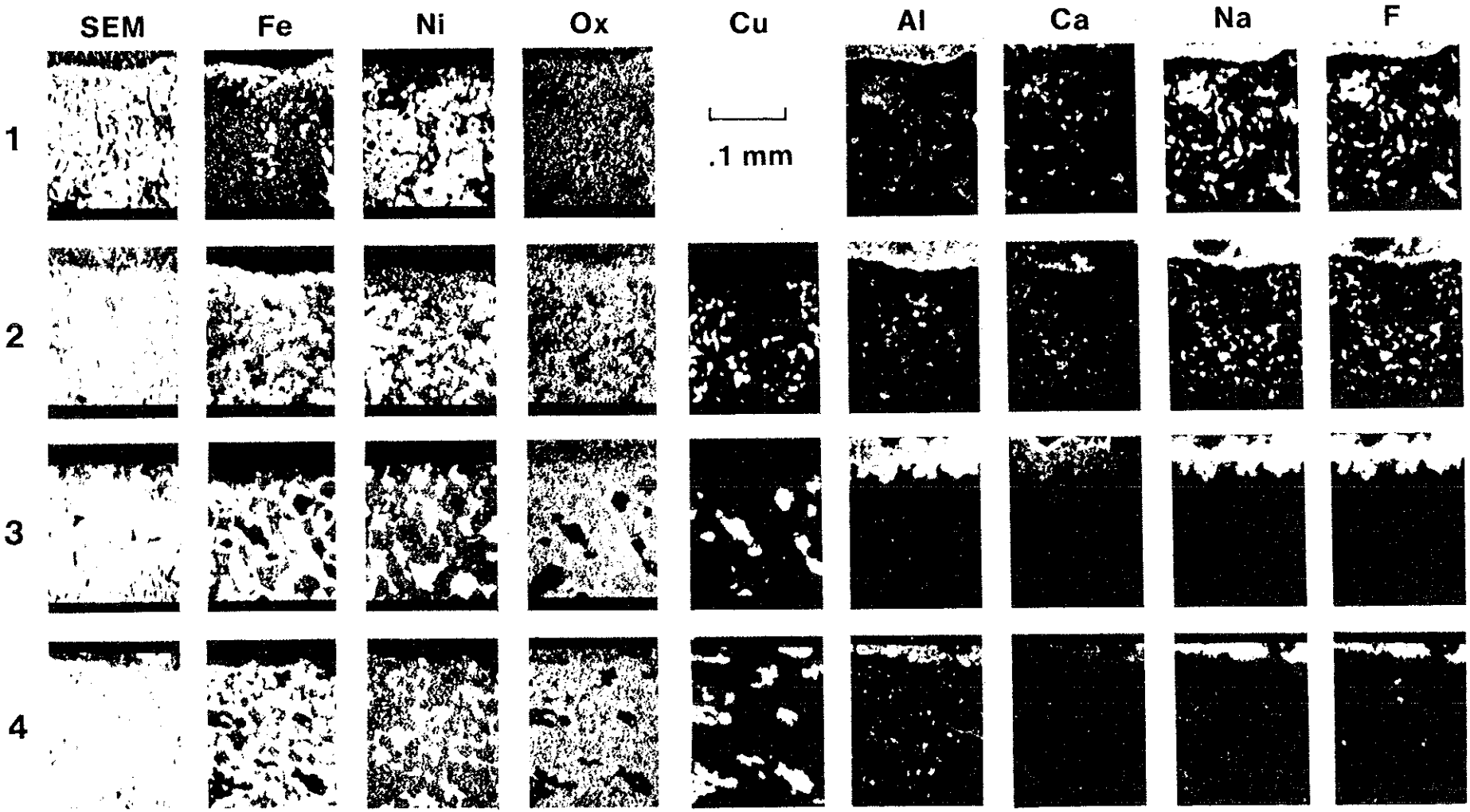

Microprobe Comparison of Various Metal Phases in $NiFe_2O_4$/NiO-Ni Cermets (1 = $NiFe_2O_4$/NiO-Ni Cermet, 2 = $NiFe_2O_4$/NiO-Cu/Ni Alloy Cermet, 3 = $NiFe_2O_4$/NiO-Cu/Ni Alloy Cermet, 4 = $NiFe_2O_4$/NiO/Pt Cermet)

Figure 143

analysis of a cross-section of an area near the surface of the cermets after the electrolysis.

The results of the anodic dissolution process in the nickel metal cermet are evident in the microprobe elemental dot maps. The internal penetration of electrolyte into the anodes matrix is clearly shown by examining the Al, Na, F, and Ca elemental maps. The absence of any metal phase can be seen in the backscattered electron photograph [labeled SEM].

The platinum metal cermet [20% Pt] [Figure 143] displayed no internal penetration of electrolyte or loss of metal. The platinum cermet was unique in one other sense; grains of platinum were observed protruding from the electrode surface. Since the surface of all the cermets were polished to a mirror finish prior to electrolysis, the protruding grains of platinum were not the result of initial surface roughness. The chemically soluble oxide phases were selectively dissolving from the anode surface, leaving behind the platinum grains. The platinum was lost from the anode matrix via grain fallout after the oxide phases surrounding the particle have dissolved. The high cost and low availability of the noble metals [e.g., Pt] preclude their use in commercial inert anodes.

Figure 143 also shows typical microprobe results of some copper alloy cermets. The cermet containing 30% alloy of a composition 90% nickel, 10% copper continued to show some internal penetration of electrolyte, but the amount was significantly decreased. A higher wt.% copper alloy cermet is also shown in Figure 143. Analysis of this cermet containing 20 wt.% alloy of composition 80% Cu, 20% Ni indicated no internal penetration of electrolyte. The micrographs also show metal was clearly present very close to the anode surface, but the nickel metal was selectively oxidized out of the copper alloy leaving behind essentially pure copper. The depth of this selective oxidation zone is less than 1 mm and was not observed to increase on extended electrolysis tests [up to 264 h]. In comparison, the nickel cermet typically internally oxidizes totally to a depth of approximately 0.5 mm in 3 hours.

Electrochemical results support the microprobe results. The comparison voltammetric results [displayed in a Tafel format] obtained on the $NiFe_2O_4$/NiO-Ni alloy cermet and the $NiFe_2O_4$/NiO-Cu alloy cermet are shown in Figure 144. After 3 hours of electrolysis, a corrosion current of approximately 30 ma/cm^2 due to anodic dissolution was found on the Ni alloy cermet, while the copper alloy cermet [80% Cu, 20% Ni] showed no corrosion current down to the detection limits of the experiment [0.2 ma/cm^2].

d. Parameters Affecting the Passivation

Clearly, the elimination of the anodic dissolution process has been accomplished by switching from the nickel metal phase to a copper-nickel alloy phase in the $NiFe_2O_4$/NiO anode. The passivation is dependent on the following three variables.

First, the anode matrix must be a cermet. The passivating oxide that forms has a tendency to spall off the surface of metal anodes during long term electrolysis. The oxide phases of the cermet act as a mechanical barrier to spalling of the passivating layer.

Second, the alloy phase must be a copper-rich copper-nickel alloy. Copper-nickel alloys of various compositions were incorporated into the $NiFe_2O_4$/NiO ceramic base and tested using the above described experimental procedures. The anodes were found to be free of internal electrolyte penetration when the alloy was in the range of 40-95 wt.% Cu with the balance being essentially Ni (see Figure 143 for two examples). It is interesting to note that pure Cu does not work. The Ni must act to cathodically protect the Cu metal in the cermet. Nickel is thermodynamically preferred to oxidize [1.5 V vs. Al] with respect to copper [1.8 V vs. Al]. This preference leads to Ni being selectively oxidized from the metal phase. In the copper alloy cermet all of the metal is not oxidized. The majority of metal [copper] is left unaltered, thus preventing electrolyte from entering the anode matrix. The manner in which the nickel oxidizes is also different in the copper alloy cermet. The nickel forms NiO inside the anode matrix

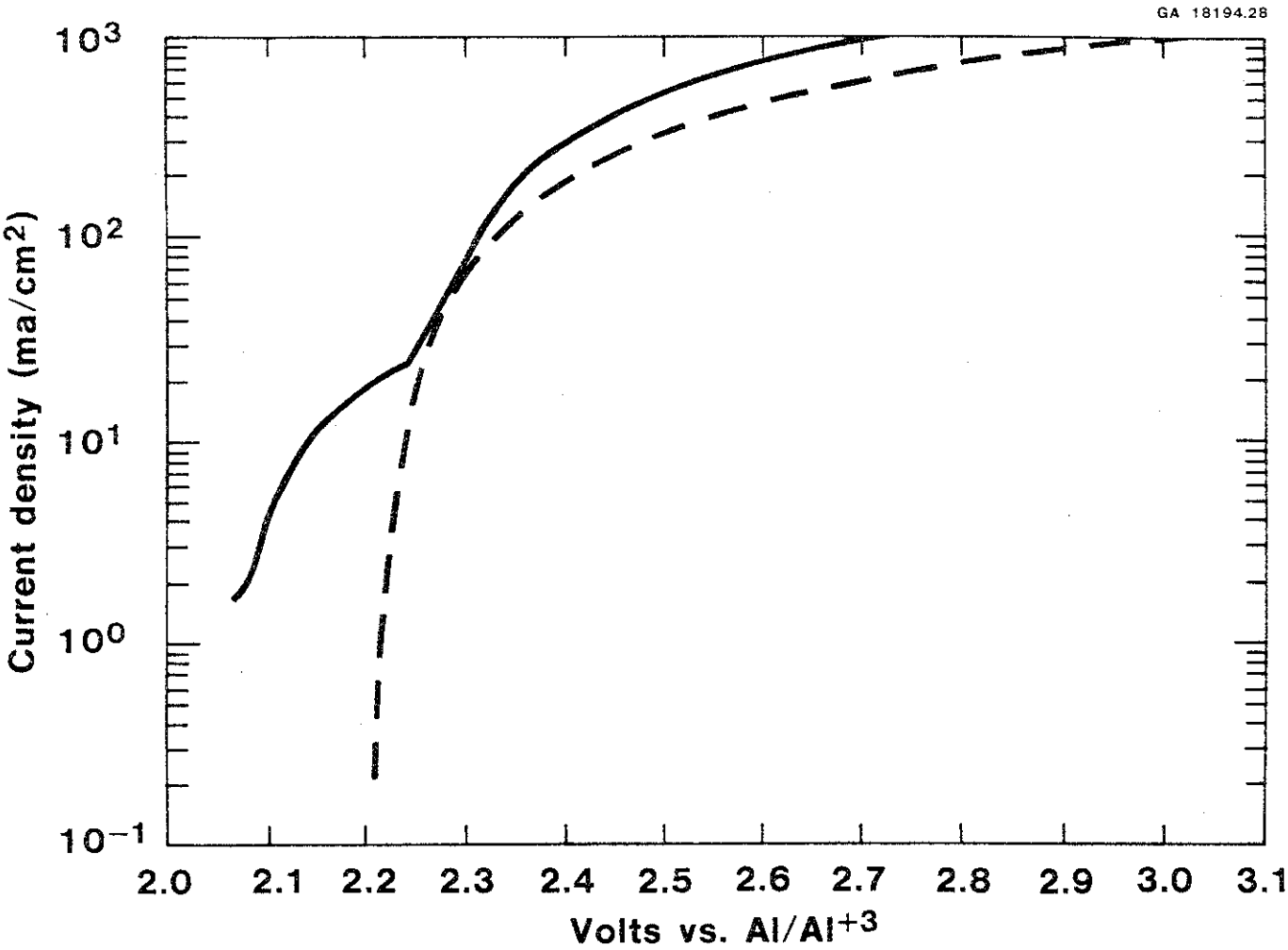

Comparison of Voltammetric Results for $NiFe_2O_4$/NiO-Ni Cermet and $NiFe_2O_4$/NiO-Cu/Ni Alloy Cermet (—— $NiFe_2O_4$/NiO-Ni Cermet; — — $NiFe_2O_4$/NiO-Cu/Ni Alloy Cermet) (Results are Displayed in a Tafel Format and not I*R Corrected) 1 mv/sec; NaF/AlF_3 >1.15; 5% CaF_2; Sat. Al_2O_3; 980°C

Figure 144

instead of anodically dissolving into the electrolyte. The internal formation of NiO helps to plug pores, thus further blocking internal electrolyte penetration. Mass transport of the nickel cations in the copper alloy cermet is through a solid, whereas in the nickel alloy cermet mass transport was through the liquid electrolyte. Mass transport through a solid is generally much slower than through a liquid. As the nickel oxidation process continues, the diffusion path through the solid becomes longer, thus the process slows [probably parabolically] until the rate becomes equal to the chemical dissolution of the oxide phases in the anode.

The third requirement for the passivation is a high concentration [activity] of Al_2O_3 in the electrolyte. Figure 145 shows the microprobe results of an 80% Cu, 20% Ni alloy cermet after three hours of electrolysis in a decreased Al_2O_3 concentration electrolyte [Al_2O_3 = 63% of saturation]. Internal penetration of electrolyte into the anode matrix was observed in the microprobe results. It is encouraging that the degree of penetration was still less than the Ni metal cermet used in a saturated Al_2O_3 electrolyte [compare Figure 144 to Figure 145].

The dependence of the passivation of the cermet anode on Al_2O_3 concentration agrees with other results. As described earlier, Debye-Scherer X-ray diffraction identified the film on a copper metal anode as approximately 60-70% $CuAlO_2$ and 30-40% CuO_2. Decreased Al_2O_3 in the electrolyte would decrease the ability to form the $CuAlO_2$ phase.

The copper alloy cermet anode was also found to be much more oxidation resistant when used in the saturated Al_2O_3 electrolytes than when used in air or oxygen at the electrolysis temperatures. One copper alloy cermet was anodically polarized at 1 amp/cm^2 in a 1.15 NaF/AlF_3, 5% CaF_2, 7.5% Al_2O_3 electrolyte at 980°C for 30 hours. Another copper alloy cermet anode was placed in a furnace with an oxygen atmosphere at 980°C for 30 hours. On completion of the 30 hrs., both anodes were removed and examined for signs of internal metal oxidation. The electrolyzed anode had no signs of internal oxidation, whereas the cermet

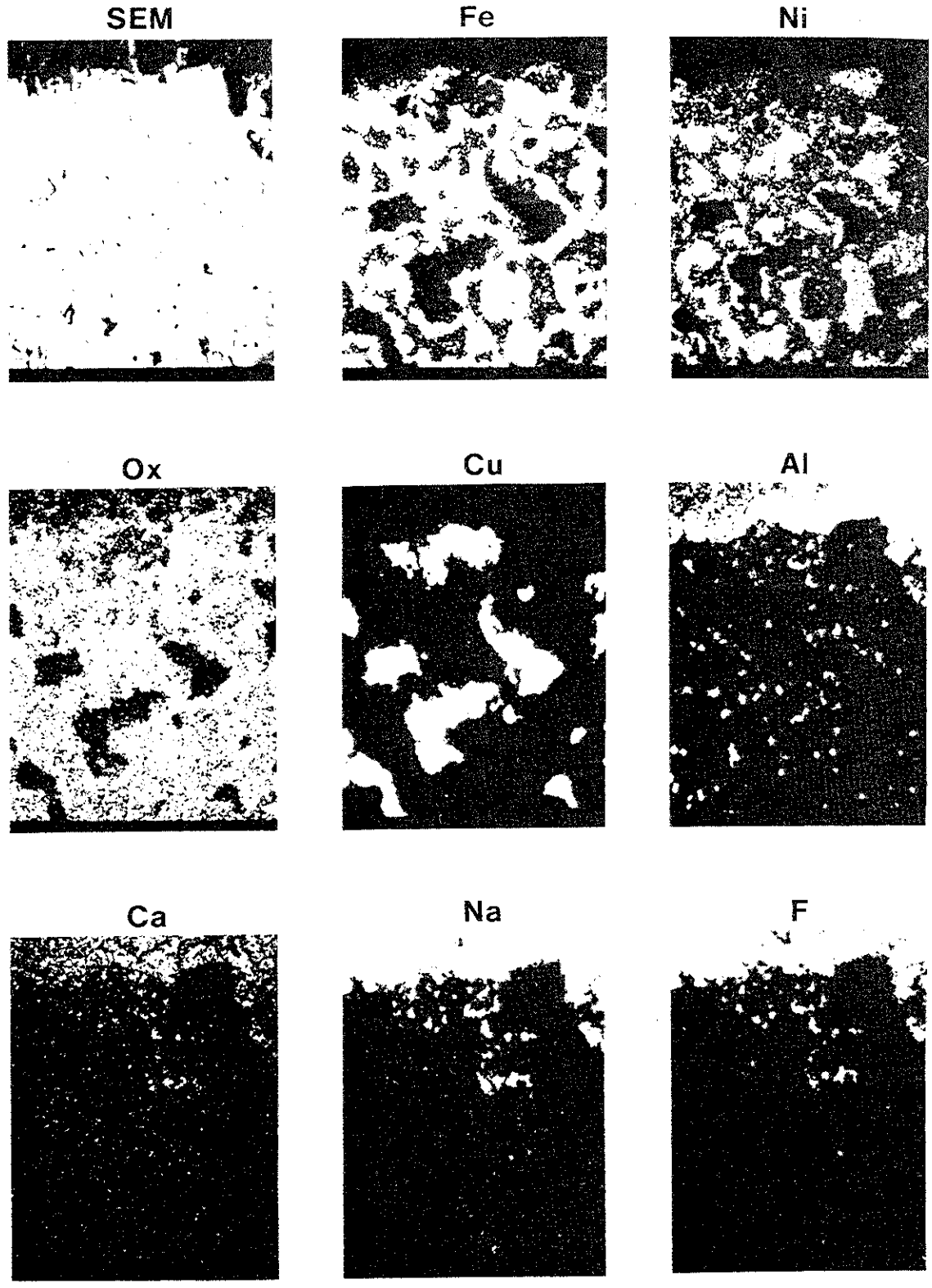

Internal Penetration of Electrolyte into $NiFe_2O_4$/NiO-Cu/Ni Alloy Cermet with Operation in a Decreased Al_2O_3 Concentration (63% Saturation)

Figure 145

that was placed in the oxygen atmosphere had oxidized internally to a depth of approximately 2 mm. Since no dimensional loss of the electrolyzed anode was measurable, the anode was not internally oxidizing and then chemically dissolving at the same rate. (The dimensional loss of a copper cermet that was electrolyzed for almost 11 days was less than 1 mm.) The fact that the copper alloy cermet does not oxidize internally when in the electrolyte can be explained by the passivating influence of the $CuAlO_2$ phase; the formation of which is dependent on Al_2O_3 being present in the electrolyte. Al_2O_3 cannot participate in a passivating film during an O_2 atmosphere oxidation of the material.

e. Parameters not Influencing the Passivation

The passivation was found to be independent of electrolysis time (up to 11 days), current density, percentage of the alloy in cermet, microstructural size of the alloy grains, and dissolved metal in the electrolyte. Figure 146 shows photographs of cross-sectioned anodes after 100 h, 165 h and 264 h of electrolysis. No zone of internal oxidation is visible in any of the anodes. A nickel alloy cermet internally oxidizes to a depth of 1 cm in 100 h (Figure 138), 1.5 cm in 165 h and 4.0 cm in 264 h. The internal depth to which the alloy phase became enriched in copper was also shown to have been limited to less than 0.1 mm in all of the above anodes tested. These extended-time electrolysis tests of the copper alloy cermet show that the passivation is independent of time.

The effect of current density was tested by performing galvanostatic polarizations at three times the normal commercial current density [3 amps/cm^2] for 3 h. Linear sweep voltammograms were then performed on the anode. After the electrolysis period the anode was cross-sectioned and examined by microprobe analysis as described previously. No corrosion currents were observed during the voltammetric scan, and no internal penetration of electrolyte was observed with the microprobe analysis. Current densities higher than 3 amps/cm^2 were not tested.

GA 18194.39

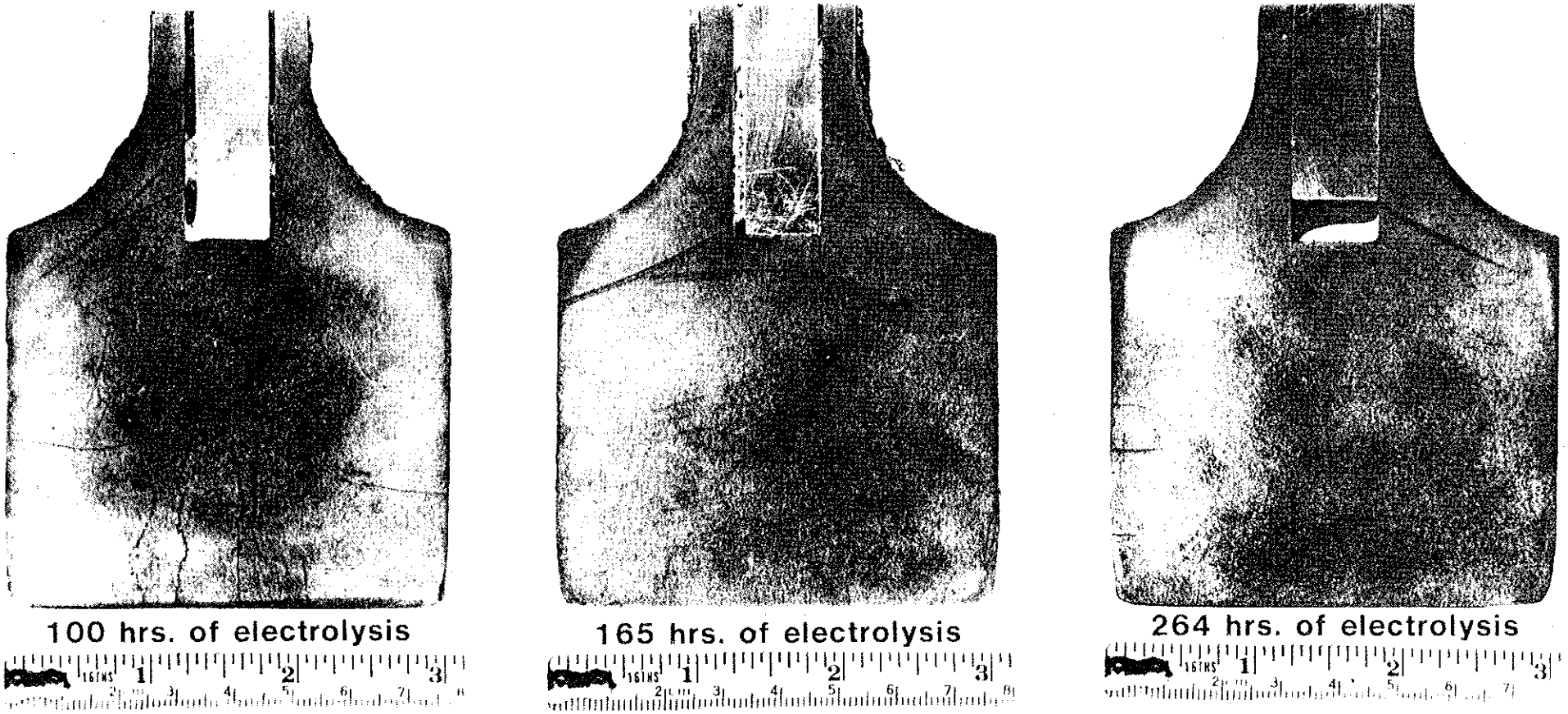

Cross-Sections of $NiFe_2O_4$/NiO-Cu/Ni Alloy Cermets

Figure 146

The passivation was independent of the wt.% of the alloy in the cermet. Cermets containing 5%, 10%, 15%, 17% and 20% metal were fabricated and tested as was previously described. None of these compositions showed any corrosion current or internal penetration of electrolyte into the anodes matrix structure. Cermets containing higher percentages of metal did not produce anodes of sufficient quality to test. The high percentages of metal coupled with the high sintering temperatures caused the anodes to either melt, bleed out the metal phase, or exhibit laminar cracks during the fabrication process. Recent experiments have shown that the metal content can be increased by lowering the sintering temperature and/or increasing the nickel content of the copper alloy. Corrosion testing of these increased-metal-content cermets was not done.

The Ni cermet had a high conductivity [300 $ohm^{-1}cm^{-1}$] due to the reaction sintering process producing continuous metal worms that wind throughout the cermet. On the other hand, the copper cermet had an acceptable, but lower conductivity [90 $ohm^{-1}cm^{-1}$] because the metal phase was distributed as individual particles in the ceramic phase. A nickel cermet was fabricated with individual nickel particles similar to the copper cermet. The individual nickel particle cermet was tested with a three-hour galvanostatic polarization and subsequent microprobe analysis. The microprobe analysis (Figure 147) indicated internal penetration of electrolyte and loss of metal. This proved that the passivation of the metal phase was due to the use of copper alloys, not isolation of the metal grains. Since a continuous metal phase in the cermet gave such high conductivity, there was interest in trying to obtain a continuous metal phase in the copper alloy cermet. A concern existed that a more accessible continuous copper phase might also be prone to anodic dissolution. A copper alloy cermet was fabricated using wires [30 μm x 100 μm x 3000-5000 μm] as the metal phase. The purpose was to simulate a continuous metal phase exposed to the electrolyte in the copper alloy cermet. The copper wire cermet electrode was tested in a similar manner to the previous cermets. No corrosion current was observed on the cermet. Figure 147 shows the microprobe results. No significant internal penetration of elec-

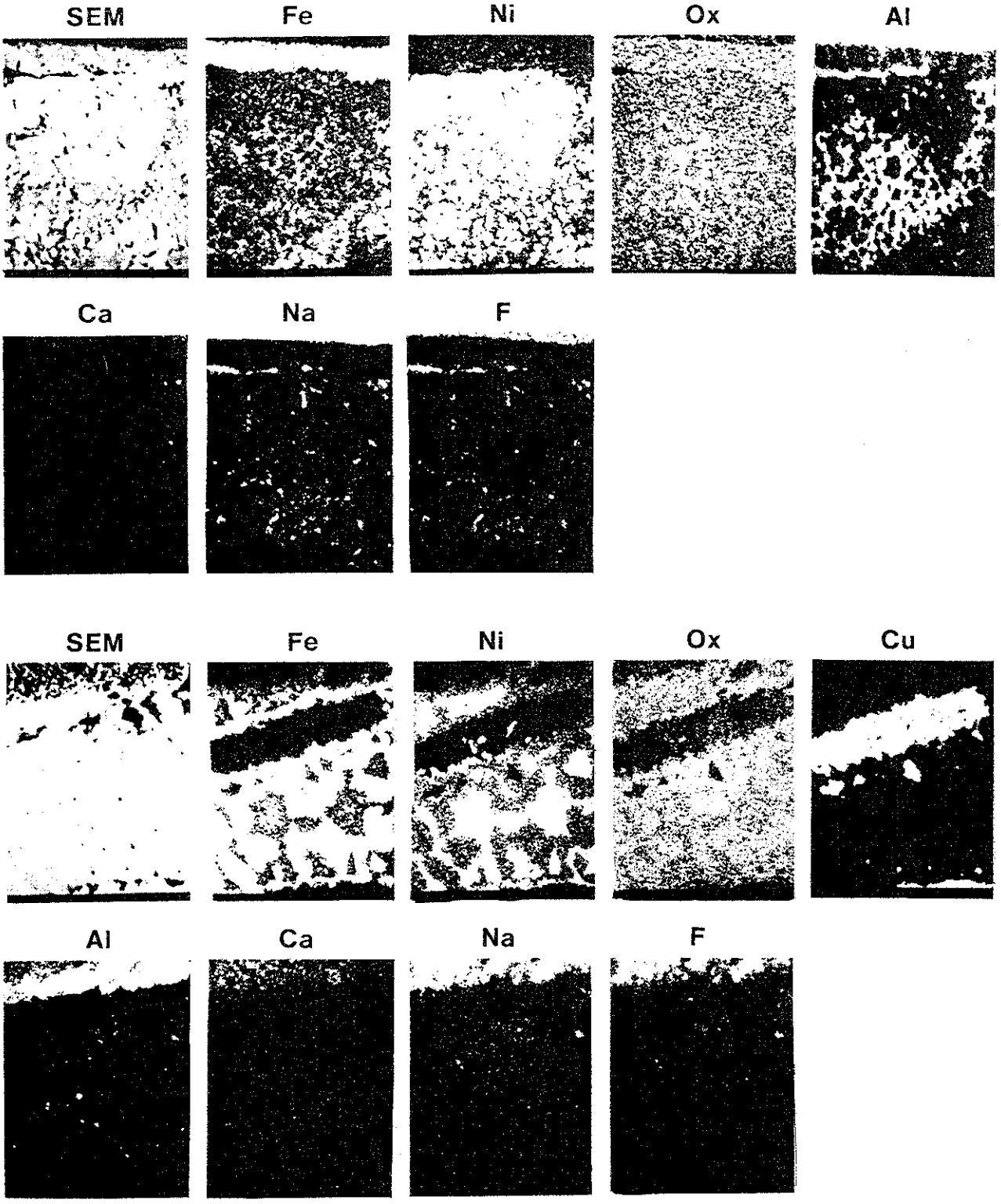

Importance of Metal Phase Composition and Geometry on the Internal Penetration of Electrolyte (1 = $NiFe_2O_4$/NiO-Ni Cermet with Isolated Metal Grains, 2 = $NiFe_2O_4$/NiO-Cu/Ni Alloy Cermet with Alloys Wire)

Figure 147

trolyte was observed along the copper wire, even though the wire was more electrochemically accessible than the reaction sintered nickel metal cermet [nickel metal worms had a diameter of approximately 10 μm]. This result indicates that the use of the copper alloy, not the microstructural arrangement of the alloy was the important passivation parameter in the copper cermet anode. A continuous wormy copper metal phase has not yet been achieved, but a very conductive, corrosion resistant anode may be possible if a method could be found to produce such an anode. Two possible methods to achieve this objective would be: (1) coat ceramic particles with Cu alloy, and (2) use several different fine Cu wire sizes mixed with fine Cu.

Dissolved aluminum metal does not have an effect on the passivation. The anodes shown in Figure 146 were electrolyzed in a cell (Figure 133) that had an aluminum cathode. Experiments were also performed in the three-hour electrolysis cell (Figure 132) with an aluminum cathode. In this cell the cathode area to anode area ratio is much greater than in commercial cells. In commercial cells the ratio of cathode area to anode area is in the range of 1.6-1.2, while in the three-hour experimental cell the ratio was approximately 200. This large excess of cathode area insured a dissolved metal content in the electrolyte even though oxidizing componentsd [NiO, Fe_2O_3. and Cu_2O] were dissolving into the electrolyte from the anode.

f. Conclusions

This study has demonstrated that a practical and stable metal phase in an oxygen-producing anode used for aluminum smelting is achievable. Nickel was an unacceptable metal phase in a cermet anode because of the tendency to anodically dissolve. A stable metal phase was developed by using a copper-rich copper-nickel alloy in a $NiFe_2O_4$/NiO ceramic base. Since this metal phase did not use expensive and rare noble metals it shows practical commercial promise. The stability of the metal phase has been shown to be dependent on three factors: (1) use of a cermet to provide a mechanical barrier to spalling, (2) use of copper-rich copper-nickel alloys to cathodically protect the

copper metal during the initial phases of electrolysis, and (3) high Al_2O_3 concentration [activity] in the electrolyte to assure the formation of a passivating $CuAl_2$ phase.

This study has also shown an experimental approach for screening metal and/or alloys [either independently or incorporated into cermets] that should be generally applicable to other candidate materials being considered as inert anodes for aluminum smelting. The experimental approach uses slow-scan linear-sweep voltammetry, galvanostatic polarizations and microprobe elemental dot map analysis to examine the resistance of metal and alloys to anodic dissolution in cryolite-base melts. The important experimentally determined variables are the corrosion current and the open circuit potential as determined from the voltammetry and the degree of electrolyte penetration after a period of galvanostatic polarization. The degree of internal electrolyte penetration is determined with microprobe elemental dot map analysis.

5. Long Term Testing of the Improved Cermet (5324-Cu)

a. Introduction

Prior to the development of 5324-Cu, all of the inert anode materials that were scaled-up and tested failed. Although the primary failure mechanism was anodic dissolution of the metal phase, poor aluminum metal quality and rapid anode material loss were also significant problems. Another major problem was failure of the anode connection. This was most often due to anodic dissolution of the metal phase. Occasionally a connection failure not related to the anodic dissolution would also occur.

Performance targets were set for each stage of testing of new inert anode materials that had to be met before the next stage of testing was attempted. The following targets were set for the 60-A cell program: (1) internal oxidation rate of less than 8.74 cm/yr (3.44 in/yr), (2) anode dissolution rate less than 6.58 cm/yr (2.59 in/yr),

(3) aluminum metal purity >99.5% based on inert anode constituents, and (4) connection integrity that showed no signs of being affected by the electrolysis process. Time-weighted average results for run 2 (165 h) and run 3 (264 h) are tabulated below. All of the performance targets set for the 60-A cell testing program have been met or exceeded.

Performance Time-Weighted Average Parameter of Both Tests

Internal Oxidation	-	None detected		
Metal Purity	-	%Fe	0.19	0.04
		%Cu	0.10	0.02
		%Ni	0.18	0.04
		%Al	99.53	
Dissolution Rate	-	1.8 ± .25 cm/yr (0.7 ± 0.1 in/yr)		
Connection Integrity	-	Excellent		

This section describes the long-term testing of the improved cermet material.

b. Results and Discussion

The purpose of the 7.5-cm diameter anode 60-A cell test of 5324-Cu [83/17] was to examine four major acceptance criteria which are critical to the success of the inert anode. First, the rate of internal metal loss zone must be less than 8.74 cm/yr. The anodic dissolution of the metal phase in 6846 inert anode material caused the failure of that material. The 5324-Cu [83/17] material has been shown to be resistant to anodic dissolution in shorter-term tests (10-12). The 100-h [run 1], 165-h [run 2] and 264-h [run 3] tests examined the resistance of the anode to anodic dissolution for longer periods of time.

Second, the purity of the aluminum produced must be commercially acceptable. Unfortunately no tolerances are firmly established for copper or nickel concentrations in the aluminum. An aluminum purity of >99.5%, based on the inert anode contaminants, was chosen as the technical goal. Thirty-hour tests performed by Siba Ray (50) have consistently achieved these results, but longer-term tests prior to the tests described in this report failed to achieve these results (8).

Third, the rate of anode material dissolution for the 7.5-cm anode [60-A cell] must be less than 6.58 cm/yr in order to justify the test in a larger cell. This rate would result in a 6 month life in a larger cell. The anode dissolution rate model proposed by Dave DeYoung (40,51) was further confirmed by these experiments.

Fourth, the electrical connection must maintain its integrity for the duration of the test. Connection integrity was a severe problem with the nickel metal phase material. The problem was mostly due to the anodic dissolution of the metal phase, but occasionally one of the diffusion welded connections would fail prior to any evidence of electrochemical attack of the connection. The new brazed connection was evaluated in these tests.

1) Internal Oxidation of Metal Phase

No internal oxidation or internal anodic dissolution zone was observed in any of 5324-Cu[83/17] inert anodes. Figure 148 displays cross-sections of the anodes from the three tests and an anode which was not electrolyzed. Figure 149 shows the extent of internal oxidation of 6846 material with time. We can use the best-fit line in Figure 149 to predict the extent of internal oxidation that would have occurred with a 6846 inert anode material that was run for the same times as the 5324-Cu[83/17]. The results of that exercise are presented in the table below.

ELECTROLYZED FOR DIFFERENT PERIODS OF TIME

Electrolysis Time (Hrs.)	6846 Oxidized Zone (Cm)	5324-Cu[83/17] Oxidized Zone (Cm)
0.00	0.00	0.00
100	1.0	<0.01
165	1.5	<0.01
264	4.0	<0.01

These figures and table demonstrate that no progressive internal oxidation of the metal phase is occurring in the 5324-Cu[83/17]

GA 18194.38

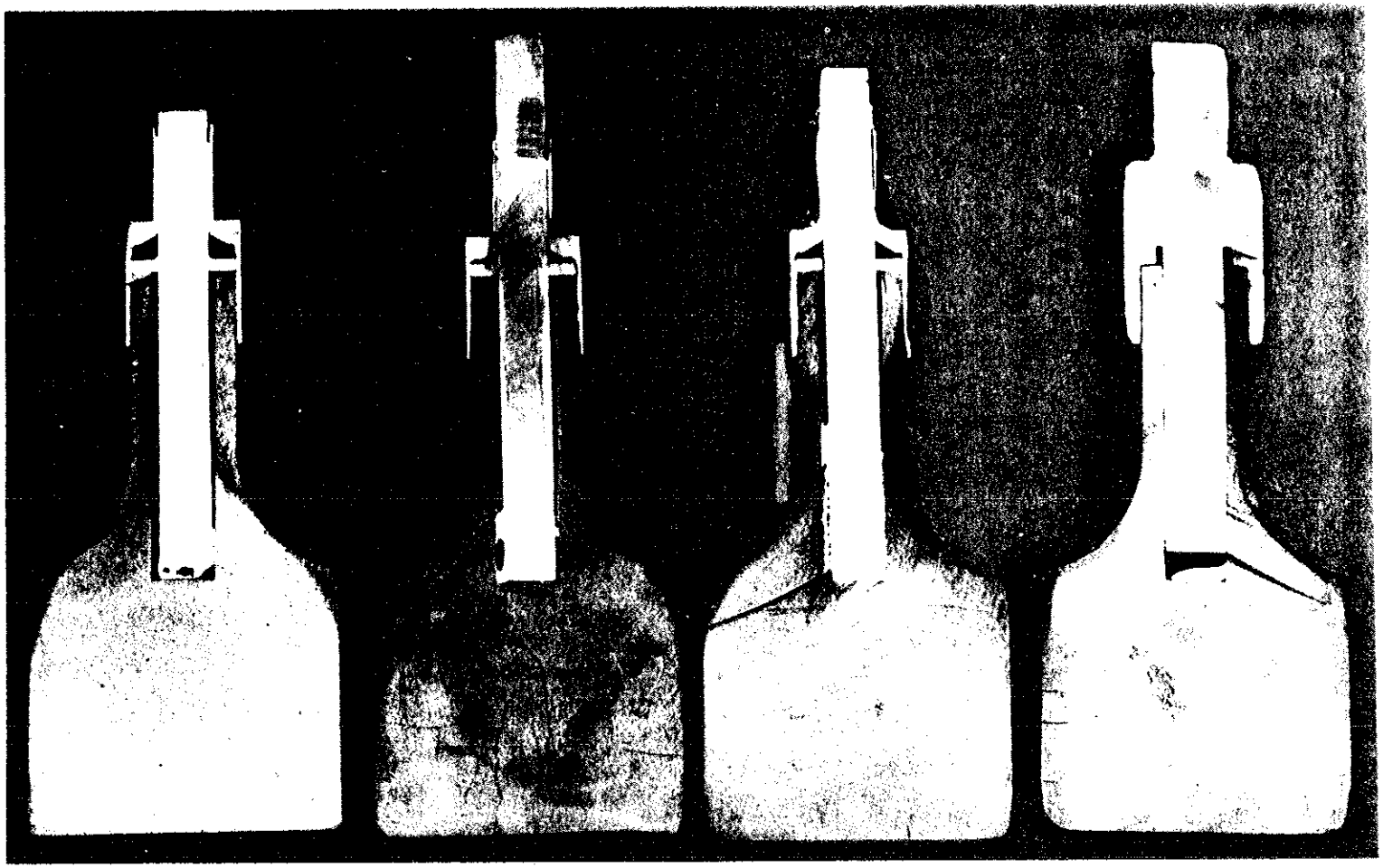

0.0 hrs 0 days	100 hrs 4 days Anode 19-1	165 hrs 7 days Anode 19-3	264 hrs 11 days Anode 19-4

Cross Sections of 5324-Cu (83/17) Material Electrolyzed for Indicated Times

Figure 148

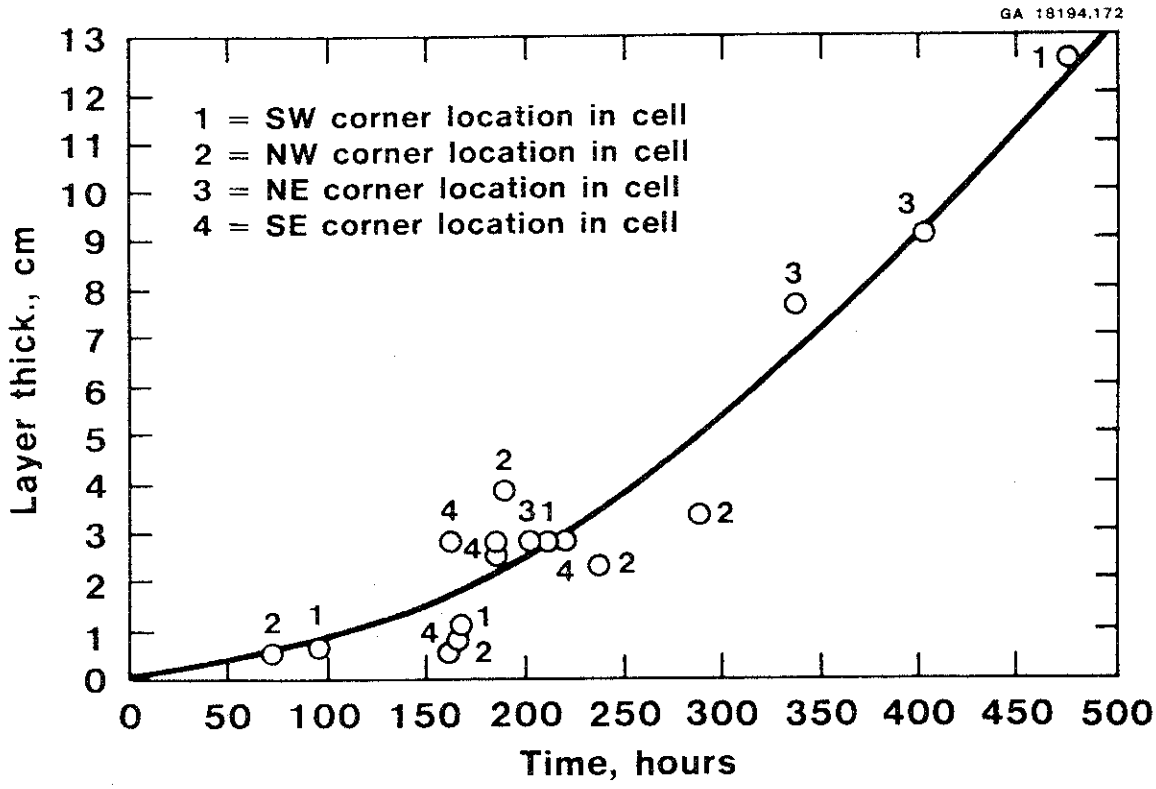

Thickness of Oxidized Zone on 6846 Inert Anodes after 2500 Ampere Hall Cell Testing
Figure 149

material and further support earlier work which showed that the life of the 5324-Cu[83/17] inert anode would not be limited by anodic dissolution of the metal phase. The goal of an internal oxidation rate of less than 8.74 cm/yr has been greatly surpassed.

2) Aluminum Metal Purity

Extended testing of the nickel metal cermet produced very poor quality aluminum metal, with iron contamination in the 1-4% range and nickel contamination in the 0.5-2% range. On the other hand, thirty-hour tests of the nickel metal cermet have consistently produced acceptable metal purity. This apparent contradiction was puzzling, therefore, one purpose of the 60-A cell tests with the improved cermet was to determine achievable metal purity during longer-term electrolysis testing.

Greatly improved (but still unacceptable) metal purity was found at the conclusion of the first long-term test with a 5324-Cu anode. The aluminum metal purity after the 100-h electrolysis period was:

Fe = 0.45%
Cu = 0.20%
Ni = 0.21%

The poor metal quality was due to excessive loss of anode material at a localized area on the anode. This localized loss of anode material manifests itself as a hole on the side of the anode and has been called the anode eater effect in earlier reports. This anode eater effect first became obvious during the operation of the nickel cermet anode in the 2500-A cell. The cause of the effect is thought to be due to shorting of the anode with exposed aluminum metal produced at exposed side walls. Upon examining the cell after the conclusion of the 100-h test, the Al_2O_3 side liner was found to have a hole, thus exposing the bare carbon crucible. The hole in the Al_2O_3 liner was coincident with the hole in the anode, thus supporting the proposition that the

anode eater was caused by shorting at exposed carbon side walls. In runs 2 and 3, two Al_2O_3 liners were used to minimize the chance that carbon side walls would be exposed.

Acceptable metal purity levels were found in runs 2 and 3. Figures 150 and 151 display the impurity concentration in the aluminum produced vs. electrolysis time. The average values and their standard deviations are also reported in the figures. The aluminum metal purity is dependent on both the rate of anode dissolution and the rate of aluminum metal production. The rate of anode dissolution has been discussed theoretically in the previous section, and the specific rate for these tests will be discussed in the next section. The rate of aluminum production is dependent on the current density, electrode area, and coulombic efficiency. It is well known that coulombic efficiency is much lower for new [<30 day old] cells than for the average aluminum cell (82). This low efficiency is caused by intercalation of sodium into the carbon cell lining. Since both tests 2 and 3 were run in new cells and Al contacted the carbon crucible, low coulombic efficiencies were expected. The coulombic efficiencies were 85% in test run 2 and 79% in run 3. Coulombic efficiencies at Alcoa's domestic smelters are generally 93%. Since actual efficiencies are higher than the low values imposed by the experimental conditions [intercalation of sodium in new carbon crucibles] the metal purity results listed in the Table 56 are corrected to 93% efficiency.

The results show that the 5324-Cu[83/17] inert anode material is capable of producing acceptable aluminum metal. This was the first time that aluminum purity of this level had been achieved any test with anodes greater than 2.5 cm diameter and test times longer than 30 hours. It is discouraging that quality is just barely acceptable. Higher current densities will produce aluminum at greater rates, and thus should produce more pure aluminum by diluting the contaminants.

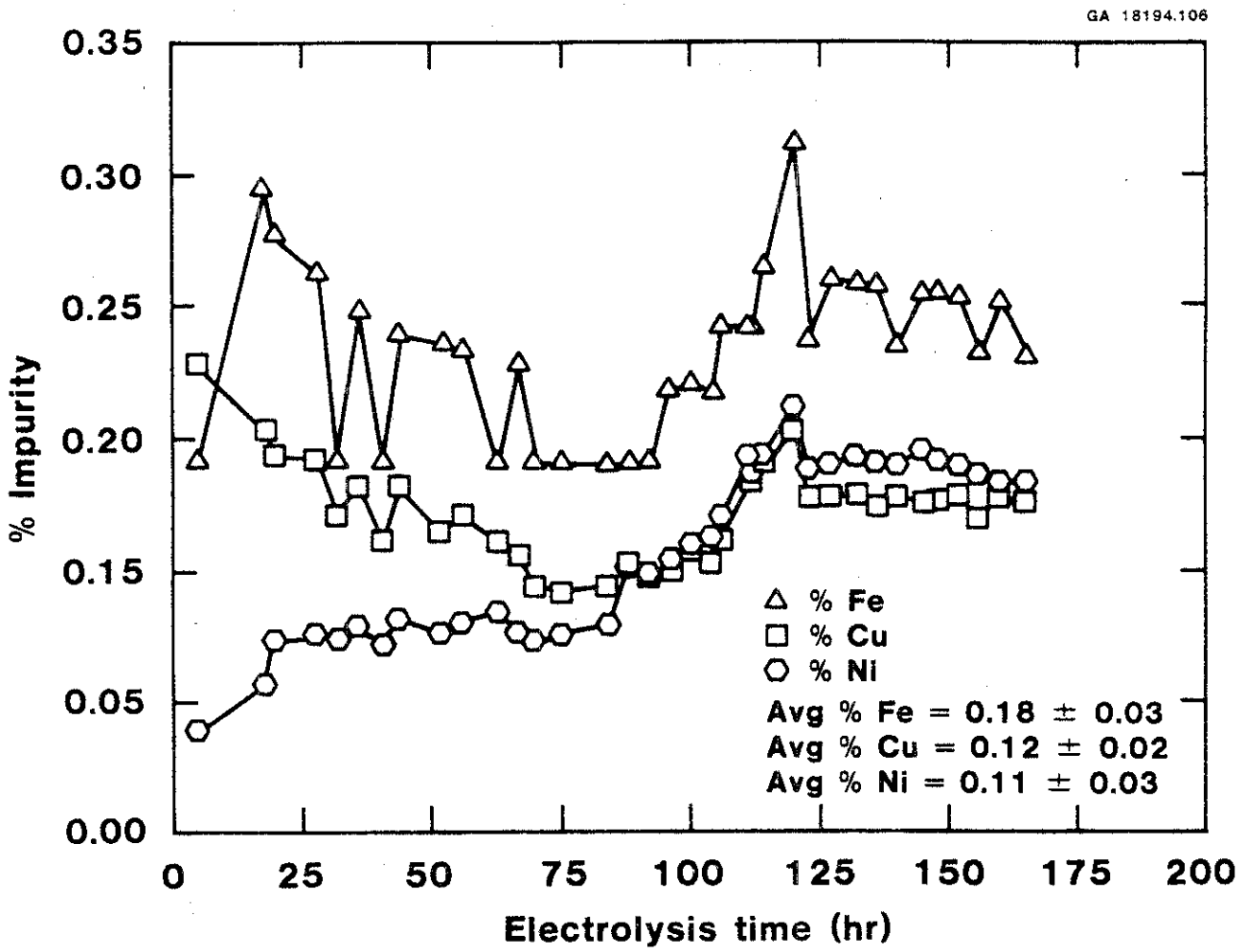

Aluminum Metal Contamination Versus Electrolysis Time for Test 2—165 h.

Figure 150

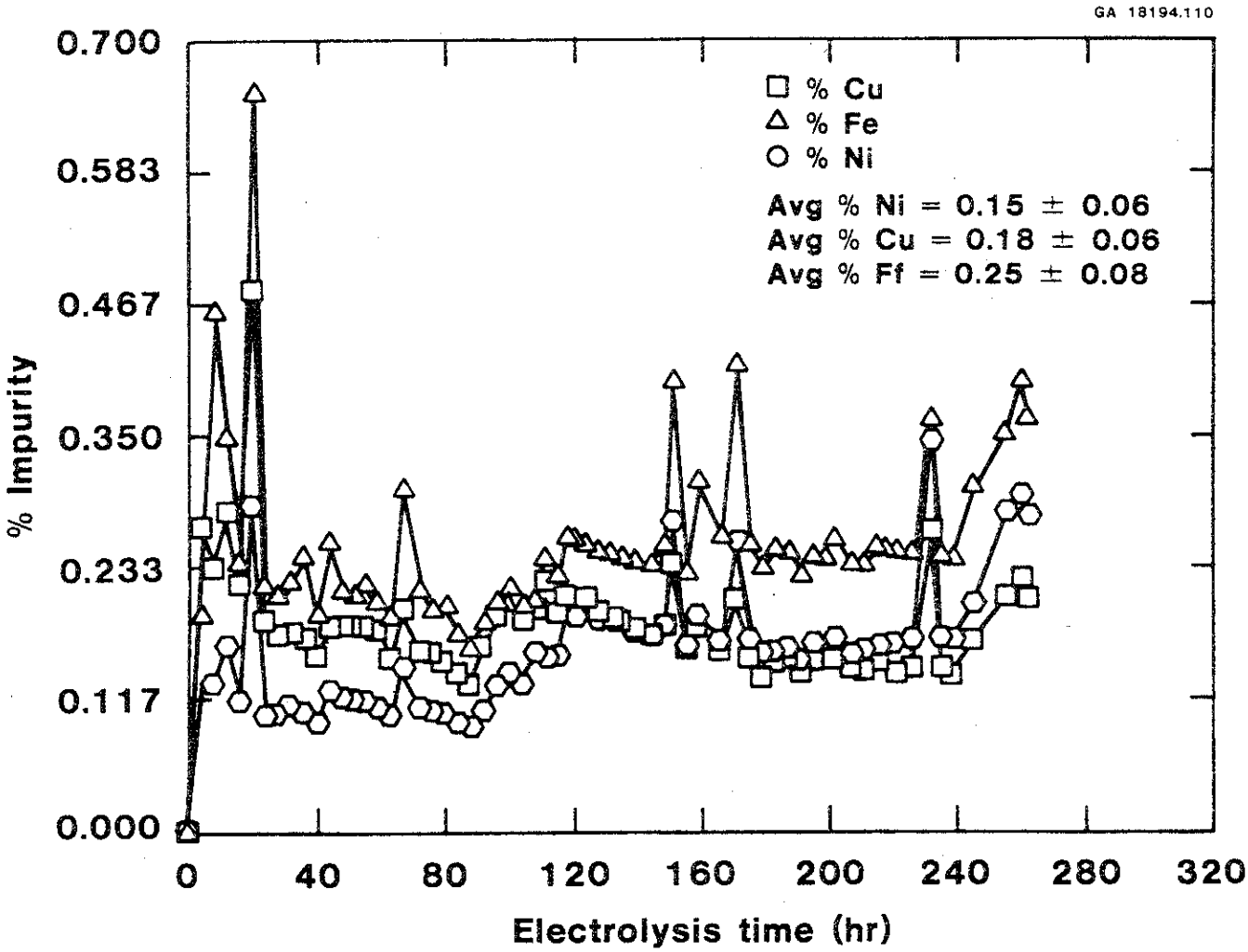

Aluminum Metal Contamination Versus Electrolysis Time for Test 3—264 h

Figure 151

TABLE 56

Metal Purity Results for Long Term Tested
Cu-NiO-$NiFe_2O_4$ Inert Anodes

Conditions	%Fe	%Cu	%Ni	%Al
Run 2, 165 hours 85% C.E.	0.18%	0.12%	0.11%	99.59%
Run 2, 165 hours 93% C.E. (Adj.)	0.16%	0.11%	0.09%	99.64%
Run 3, 264 hours 79% C.E.	0.25%	0.18%	0.15%	99.42%
Run 3, 264 hours 93% C.E. (Adj.)	0.21%	0.15%	0.13%	99.51%

Electrical shorting of the anode with the aluminum metal leads to greatly increased metal contamination. During a short, aluminum can reduce the oxides via the following reaction:

$$8Al + 3NiFe_2O_4 \text{ ---> } 4Al_2O_3 + 3Ni + 6Fe \quad (66)$$

The metallic iron and nickel could then readily dissolve in the liquid aluminum which is in contact with the anode. If the contact between the liquid aluminum and the anode is broken before all of the reduced metal can dissolve, then the metallic nickel and iron will anodically dissolve in the electrolyte via the following reactions:

$$Ni \text{ --->} Ni^{+2} + 2e- \quad (67)$$

or

$$Fe \text{ --->} Fe^{+3} + 3e- \quad (68)$$

The dissolved metals will eventually be reduced at the cathode and further contaminate the aluminum. In either case shorting would lead to increased aluminum contamination.

Shorting was observed with the aid of a digital oscilloscope near the end of run 3. The aluminum metal analysis shows increasing contamination near the end of the run (see Figure 151) due to the shorting. Shorting is also suspected to have occurred at approximately 110 h in run 2 because the cell voltage was erratic. [We did not monitor the cell with an oscilloscope during run 2.] Figure 150 also shows increasing contamination during the suspected shorting period; however, the metal purity began to increase once the shorting was eliminated, which indicates no permanent anode damage occurred.

The ratio of the contaminants in the aluminum metal should match the ratio of the metals in the anode material. The ratio of the metals in the anode can be calculated from the starting composition [17% Cu, 66.4% $NiFe_2O_4$, and 16.6% NiO] to be:

$$\%Cu/\%Ni = 0.574$$
$$\%Fe/\%Cu = 1.859$$
$$\%Fe/\%Ni = 1.067$$

The % Fe contamination did not display any dependence on time, while both nickel and copper displayed a consistent time-related phenomena. In both test runs [see Figures 150 and 151] the % Cu in the aluminum decreased with time, while the % Ni increased with time. Figures 152 and 153 show plots of the copper/nickel ratio vs. time for test runs 2 and 3, respectively. In both runs the ratio starts at about 2-3, and decreases to about 1 to 1.5 cm after approximately 100 h. Figure 153 indicates that the ratio may continue to decrease for some time and can reasonably be expected to approach the 0.574 ratio in the starting material. The reasons for the changing Cu/Ni ratio are not completely understood, but it will be worthwhile to note several observations and ideas concerning the change. First, the changing Cu/Ni ratio that was observed during the first days of electrolysis is not an experimental artifact. Further experimentation will need to be done to confirm that the phenomenon is real, but it seems unlikely that two experiments could be performed in which the ratios matched each other so closely with respect to time. Second, the changing ratios are probably an indication of a changing microstructure in the anode. [The other obvious possibility is that some of the anode constituents are being preferentially lost in the fumes.] The composition of the alloy phase near the surface of the anode changes to a more copper-rich phase during electrolysis. The nickel diffuses out of the metal towards the oxygen at the surface of the anode, yielding NiO at the surface of the metal particle. This nickel oxide is now between the electrolyte and the copper metal and must dissolve before the copper can be attacked. The amount of nickel in the aluminum, therefore, increases with time due to an increasing concentration of NiO on the surface, while the amount of copper decreases with time due to decreasing accessibility to the electrolyte. This process would continue until the diffusion distances became so great [but still<<mm] that the process became

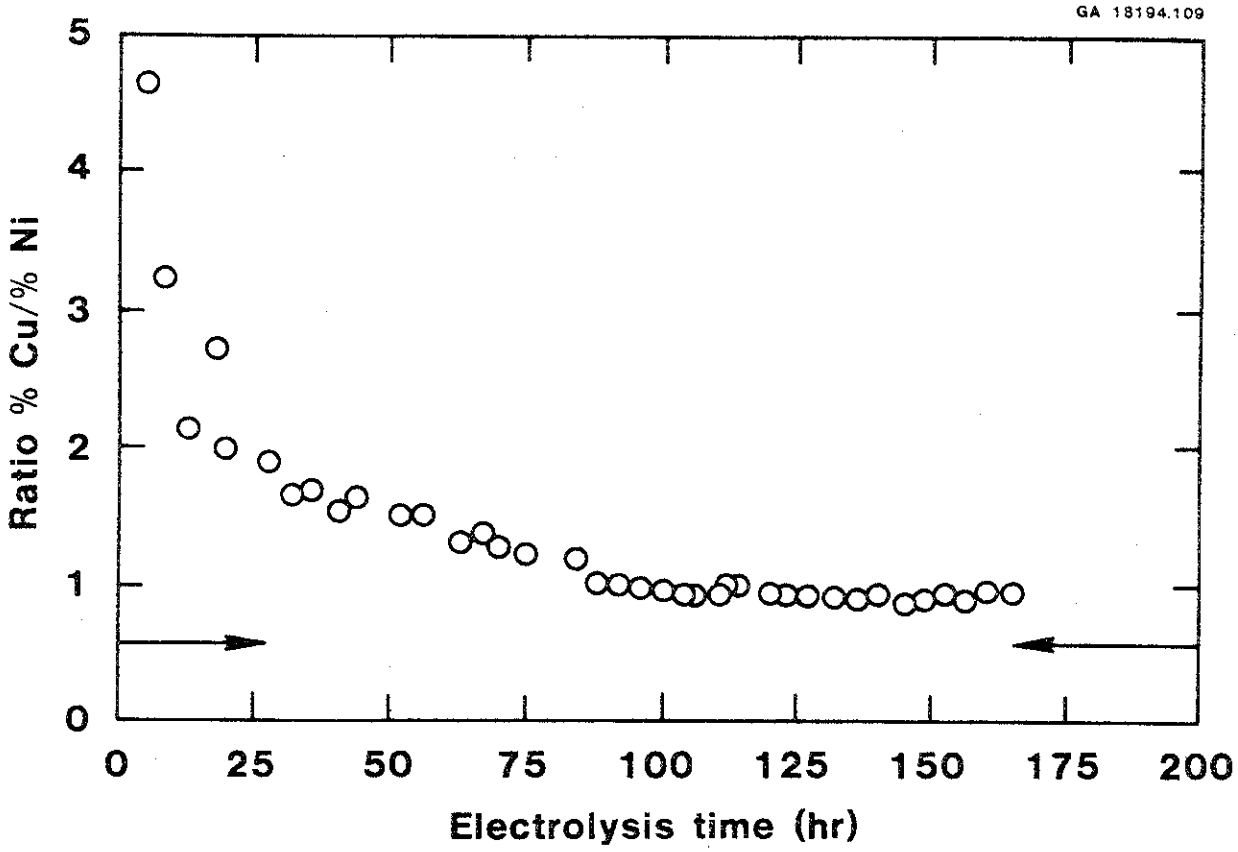

Ratio % Cu/% Ni in Aluminum versus Electrolysis Time, Cu/Ni Ratio in Anode Marked with Arrows, Test 2—165 h

Figure 152

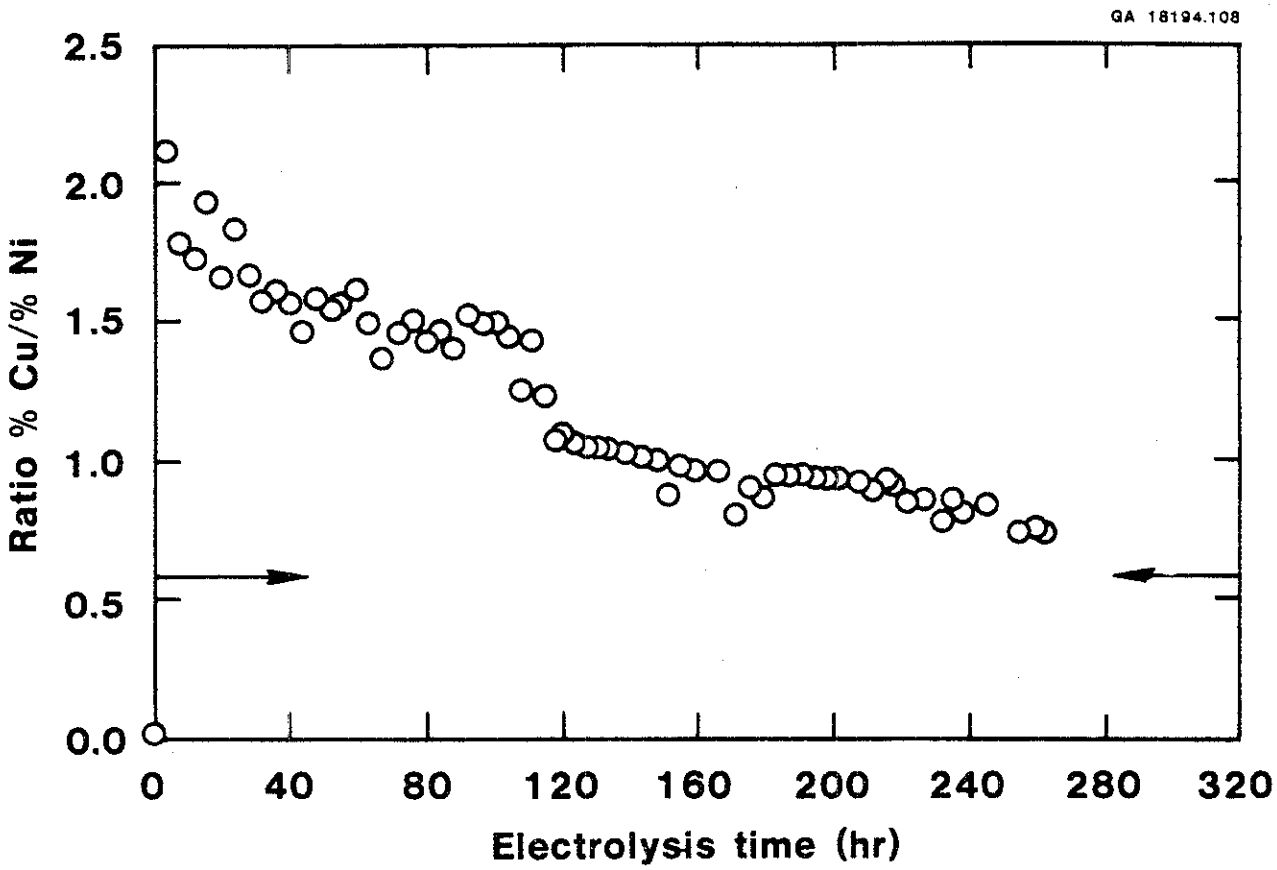

Ratio % Cu/% Ni in Aluminum versus Electrolysis Time, Cu/Ni Ratio in Anode Marked with Arrows, Test 3 - 264 h

Figure 153

hindered by slow mass transport through the solid phase. This process could take a great deal of time to reach this steady state because at the same time that the above described process is occurring the anode surface is dissolving, thus decreasing the diffusion paths and increasing accessibility of the copper to the electrolyte. As the process approaches steady state the overall effect would be that the ratio of the contaminants in the aluminum would approach the ratio of the metals in the anode. Figures 152 and 153 indicate that the ratios in the aluminum are approaching the ratios in the anode. Figures 154 and 155 show the Fe/Cu ratios for runs 2 and 3, while Figures 156 and 157 show the Fe/Ni ratios for runs 2 and 3. Examination of Figures 150 to 157 indicate that in all cases the ratio of the metals in the aluminum tend towards the ratio in the anode which is consistent with the explanation given above. However, further experimentation is necessary to verify this hypothesis.

Using the above experimental and theoretical information, an estimate of expected aluminum metal purity at steady state can be made. If we assume that the iron contamination level continues to be independent of time and is accurately reflected by the methodology in which these tests were performed, then the best estimate of the iron contamination is the weighted average of both test runs [corrected to 93% coulombic efficiency]. If we further assume that at steady state the contamination ratios in the aluminum become equal to the metal content ratios in the anode, then the contamination levels can be calculated to be:

Steady state %Fe = 0.191	0.04
Steady state %Cu = 0.103	0.02
Steady state %Ni = 0.179	0.04
Steady state %Al = 99.53	0.1

These values represent only borderline acceptable aluminum metal purity.

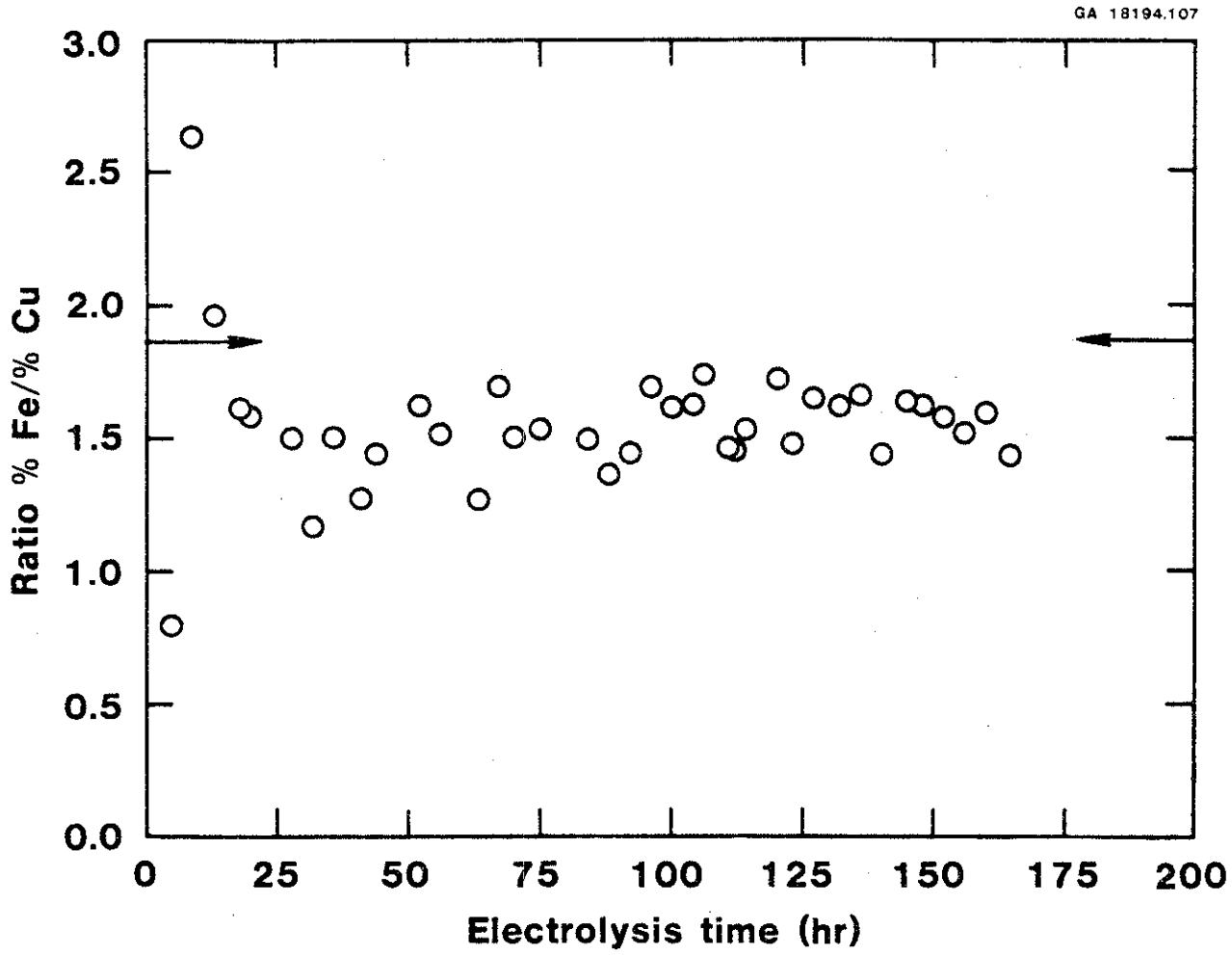

Ratio % Fe/% Cu in Aluminum versus Electrolysis Time, Fe/Cu Ratio in the Anode Marked with Arrows, Test 2 - 165 h

Figure 154

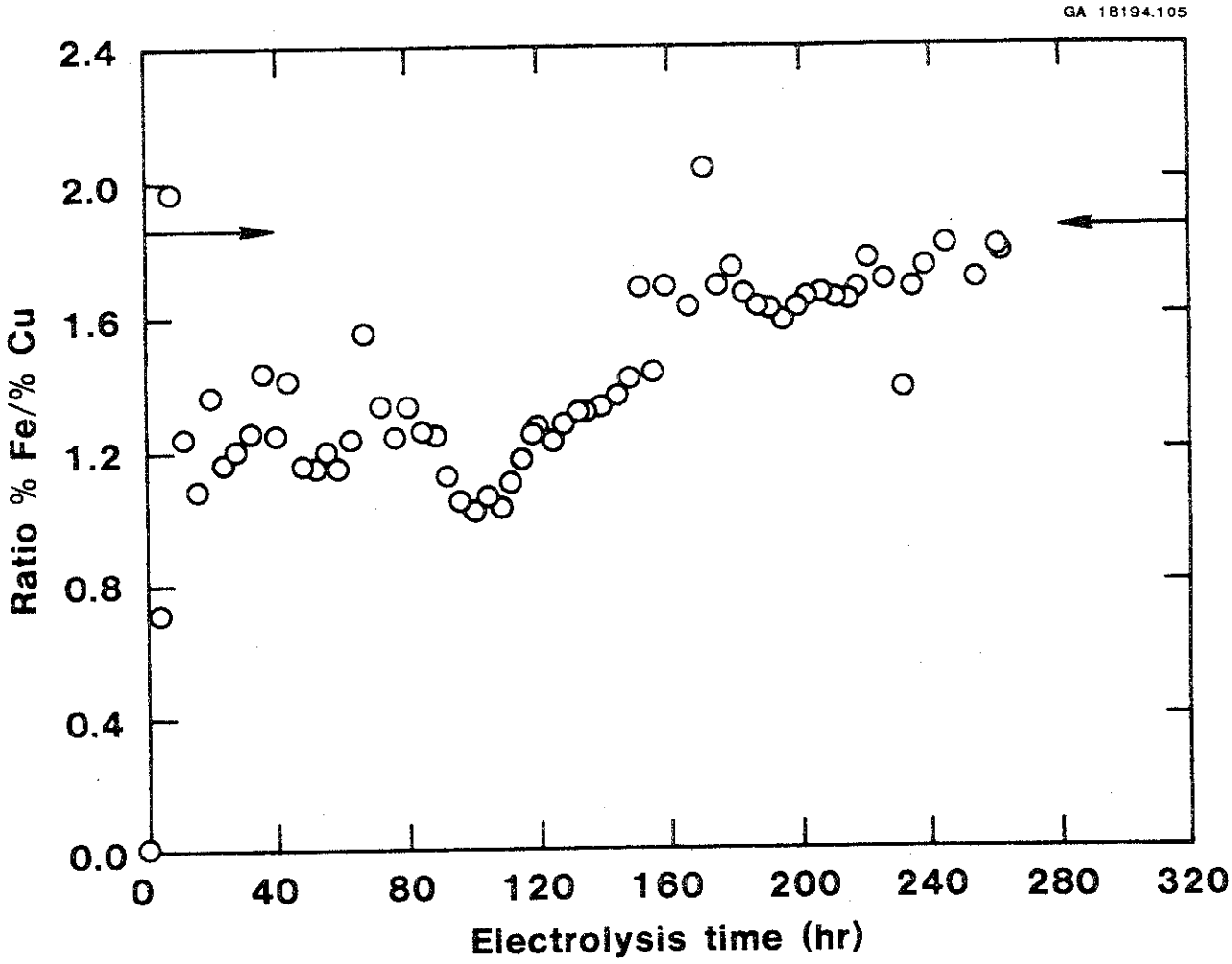

Ratio % Fe/% Cu in Aluminum versus Electrolysis Time, Fe/Cu Ratio in the Anode Marked with Arrows, Test 3 - 264 h

Figure 155

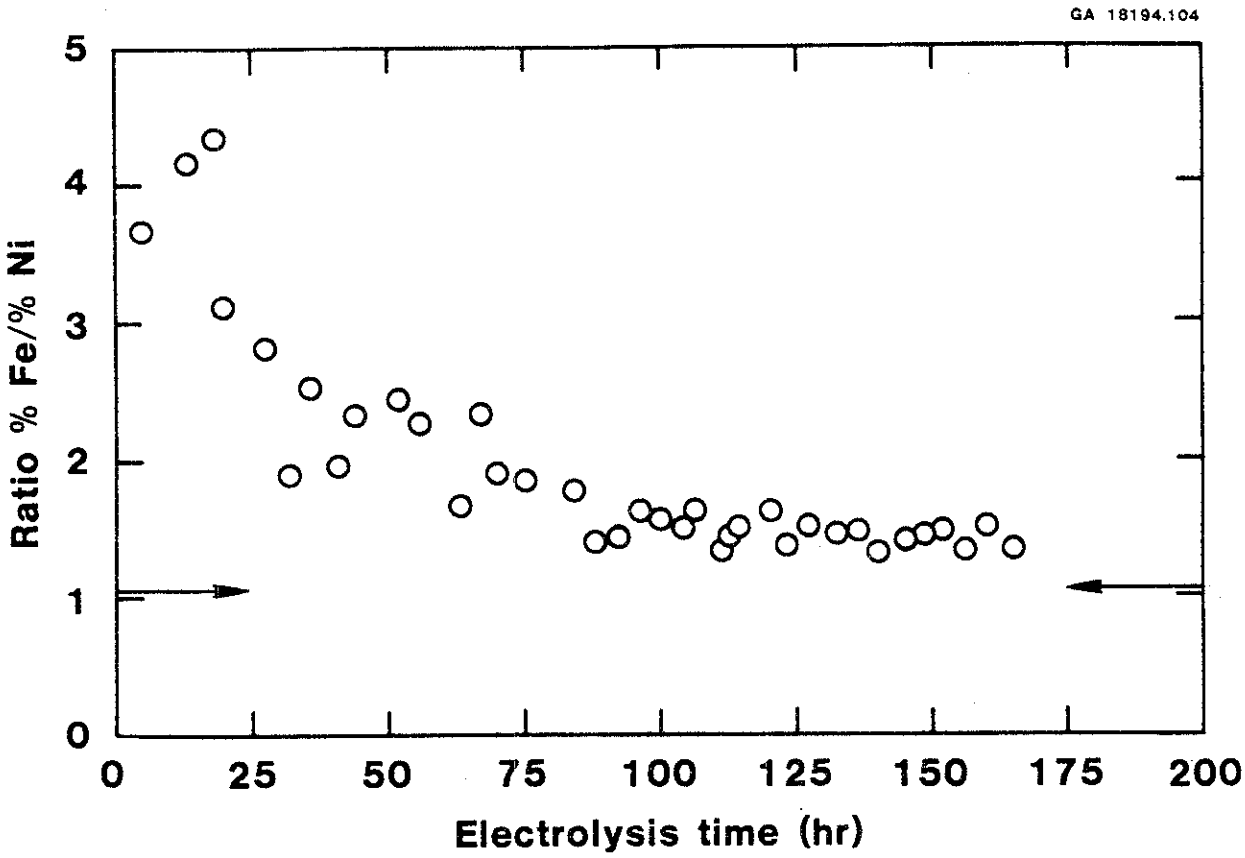

Ratio % Fe/% Ni in Aluminum versus Electrolysis Time, Fe/Ni Ratio in the Anode Marked with Arrows, Test 2 -165 h

Figure 156

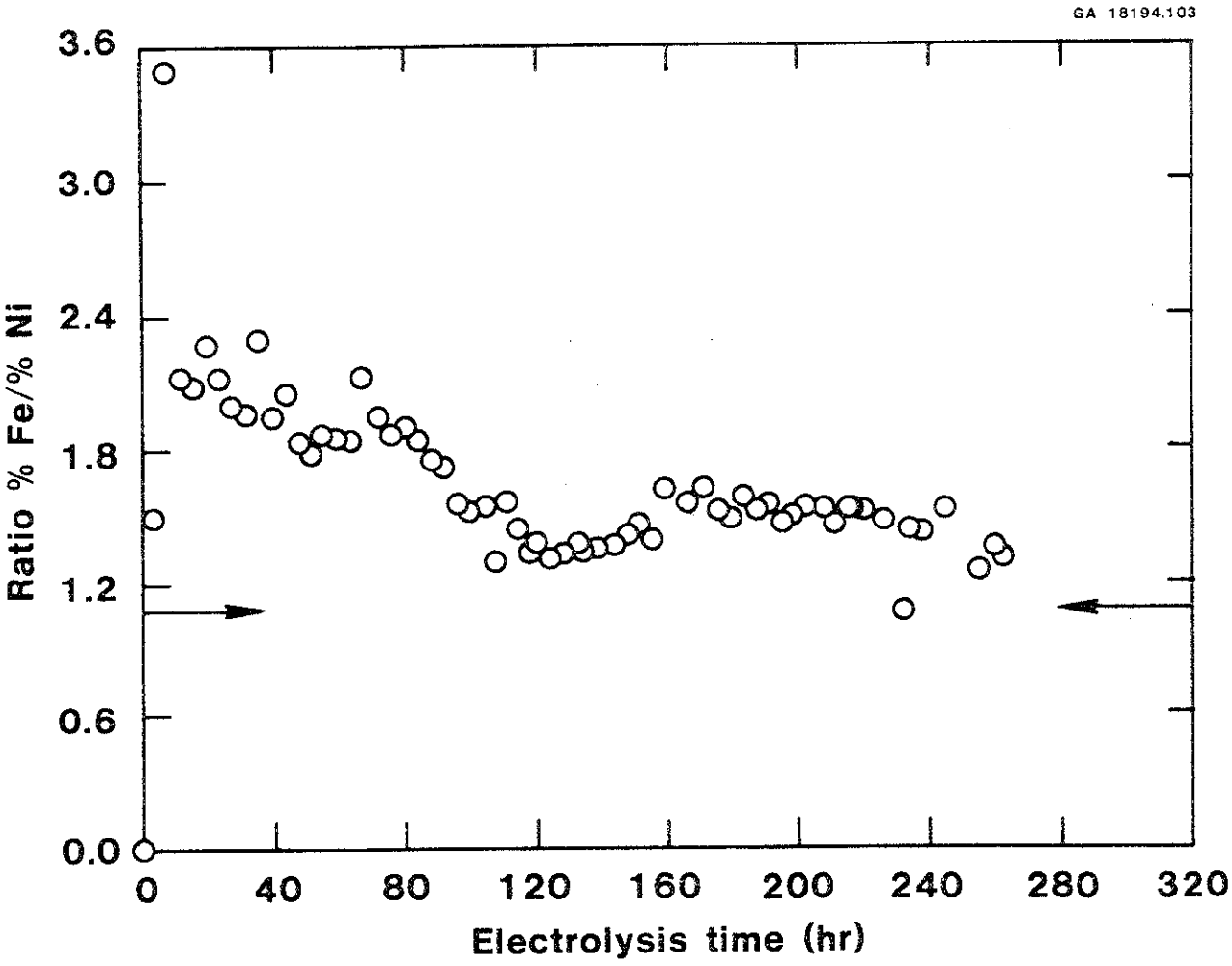

Ratio % Fe/% Ni in Aluminum versus Electrolysis Time, Fe/Ni Ratio in the Anode Marked with Arrows, Test 3 -264 h

Figure 157

3) Anode Dissolution Rates

Since the internal oxidation process has been eliminated, the rate of dissolution of the anode will now determine its life. It is important that the mechanism of dissolution and the overall rate are carefully defined for this life limiting process. DeYoung has studied the anode dissolution process using 6846 as the anode material and proposed that the rate is mass transport controlled (8). DeYoung (83) also used the dissolution studies, along with several model systems to bracket the dissolution rate between 1.3 cm/yr and 25 cm/yr. Weyand (9) used the accumulated data of all the 2500-A cell runs with 6846 material to bracket the dissolution rate between 12.2 cm and 48.8 cm/yr. Keller (84) has proposed that the dissolution process can be controlled by the "plating rate" of the anode constituents at the cathode surface. The cathode plating rate is almost certainly mass transport controlled and can, therefore, be affected by the active cathode area. The high rates of dissolution found in the 2500-A with 6846 material were not expected. These high rates could be the result of a changing dissolution mechanism at longer times or of poor operational control of the 2500-A cell. Regardless of the cause, the high rate of material loss from 6846 material tested in the 2500-A cell was discouraging.

The purpose of the anode dissolution rate study of 5324-Cu material with the 60-A cell was threefold. First, an estimate of achievable dissolution rates of the anode based upon long electrolysis times was needed. Second, an examination of the mechanism of dissolution proposed by DeYoung was needed for 5324-Cu material at long electrolysis times. Third, the role of the cathodic process in controlling the overall rate needs to be determined. The anode dissolution rate was measured by three different techniques. The first technique was a direct measurement of anode change. A direct measurement of mass lost after electrolysis was impractical because of the inability to remove frozen electrolyte and condensed bath fumes from the

electrode; therefore, anode dimension change was used as the direct measurement of anode dissolution rate. The dimension change was determined by measuring the anode diameter and anode height before and after electrolysis. The rate was then calculated by dividing the distance lost by the electrolysis time and converting to a yearly rate in cm per year. The dimension loss from the anode in each of the three experiments is tabulated in the table below:

RUN/[TIME]	SIDE LOSS	RATE SIDE	BOTTOM LOSS	RATE BOTTOM
1/[100 h]	0.075 cm	6.6 cm/yr	0.02 cm	1.78 cm/yr
2/[165 h]	0.027 cm	1.45 cm/yr	0.072 cm	3.8 cm/yr
3/[264 h]	0.111 cm	3.73 cm/yr	0.078 cm	2.62 cm/yr

This direct measurement is in the range predicted by DeYoung (83) and less than the direct measurement of anode loss found by Weyand (9) for 6846. The better performance of the 5324-Cu material in these tests compared to the 6846 material in the 2500-A cell tests is thought to be the result of better operating conditions in this test. The direct measurement of anode loss does suffer from several disadvantages. First, the accuracy of the measurement is dependent on the resolution of the calipers. At best, the calipers were capable of a 0.1 mm resolution, which translates into approximately an error in the range of 1 to 5 percent. Second, the precision of the measurement was considerably less than the best-case accuracy. This is mostly due to frozen electrolyte on the anode. We attempted to remove the electrolyte from the anode surface without removing any anode material. This was a tedious and difficult operation in which we were only moderately successful. The precision of the measurements indicates that the results reported above could be in error by as much as 1.3 cm/yr. Third, microstructural changes in the anode material [e.g., oxidation of the metal phase, grain fall-out, anodic dissolution, internal porosity increases, etc.] are not realistically detected by a macrodimension change. Some of these changes [e.g., swelling due to internal oxidation of the

metal] could lead to overly encouraging results while other changes [e.g., internal anodic dissolution] may not be reflected at all by the dimension changes in the anode. Although there was no indication of serious microstructural changes in run 1 and other earlier work (10,3), we nevertheless backed up our direct measurement of anode dissolution rate with several indirect methods in runs 2 and 3.

The second method of determining the anode dissolution rate was by chemical analysis of the aluminum after the electrolysis period. In this method the anode dissolution rate was calculated from the following equation:

$$RCi = \frac{\%Ci*WtAl*344.8882}{S*rho*A*t} \qquad (69)$$

where: RCi = calculated anode wear rate in cm per year for the Ci component

%Ci = analyzed % contamination of the Ci component in the aluminum after the electrolysis period

WtAl = total mass of aluminum in grams after the electrolysis period [initial charge of aluminum + aluminum produced]

Si = gravimetric ratio of the Ci component in the anode SFe = 0.316; SCu = 0.17; SNi = 0.297

rho = density of the inert anode 6.0 g/cm^3

A = surface area of anode in the electrolyte in cm^2

t = electrolysis time in hours

and 344.8882 is a conversion factor.

The rates determined by this method, as tabulated below, are in relatively good agreement with each other and with rate determination by dimension loss.

RCi	Run 2	Run 3
RFe	1.42 cm/yr	2.67 cm/yr
RCu	1.85 cm/yr	2.79 cm/yr
RNi	1.14 cm/yr	2.18 cm/yr

The difference between the rates determined by this method and the rate by the dimension change measurement could easily be accounted for by a 1.3 cm/yr error in the dimension change measurement. The other possibility is that some of the anode constituents are being lost in the fume, however, previously obtained data on the 2500-A cell with 6846 material do not support the fume loss explanation (85).

It appears that the rate was faster in the 264 h test (run 3) than the 165 h test (run 2). Although this could be an indication that the anode dissolution rate was increasing with time, the apparent rate increase is more likely the result of shorting which occurred at the end of run 3. The misconception of an increasing rate with time points out a shortcoming of both the dimension change measurement technique and the chemical analysis of the final bulk aluminum produced. The shortcoming of both of these techniques is that each relies on a single data point to arrive at the dissolution rate. The single point is taken at the end of the electrolysis period and is, therefore, overly influenced by events which occurred at the conclusion of the test. Both tests ended prematurely due to uncommon occurrences for a commercial Hall cell. [Run 2 ended because the operator accidentally left the feed valve open, which resulted in feeding a day's worth of alumina in 5 minutes. This caused the electrolyte to freeze and the test was aborted. Run 3 was aborted due to shorting of the anode with the cathode. The shorting was caused by muck raising the liquid level in the cell so high that further raising of the anode was impractical.]

In the third method of determining the anode dissolution rate, samples of metal were taken throughout the electrolysis period. The total mass of Fe, Ni and Cu in the aluminum metal at any time could then be determined by using the equation below:

$$Mi_t = [\%Ci_t/100*]*[1Al+(Q_t*FWAL*eff/F*n)]-Ci_0*1Al/100 \quad (70)$$

Where Mi_t = total mass of the ith component in the aluminum at time t

$\%Ci_t$ = percent concentration of the ith component in the aluminum at time t

1Al = initial mass of aluminum added to the cell before the start of electrolysis

Q_t = coulombs at time t

FWAL = atomic weight of aluminum

eff = fraction coulombic efficiency for the process

F = Faradays constant

n = number of electrons

Ci_0 = the percent concentration of the ith component at zero time

A plot of Mi_t vs. t could then be used to examine the rate of dissolution of the various components. Figure 158, 159 and 160 are the iron, nickel and copper plots for run 2, and Figures 161, 162 and 163 are for run 3. The rate was determined by a least-squares regression analysis. The regression line shown in these plots was obtained by ignoring obvious outliers that could have occurred as the result of bad sampling/analysis or because of rare cell operating events [e.g., shorting].

The rate can now be calculated for the dimension of cm per year by using the following equation:

$$Ri = \frac{ri*8760}{Si*rho*A} \quad (71)$$

where ri = the rate of the ith component in grams/hour and all of the other symbols have their previously defined values. The rates from such an exercise are tabulated below:

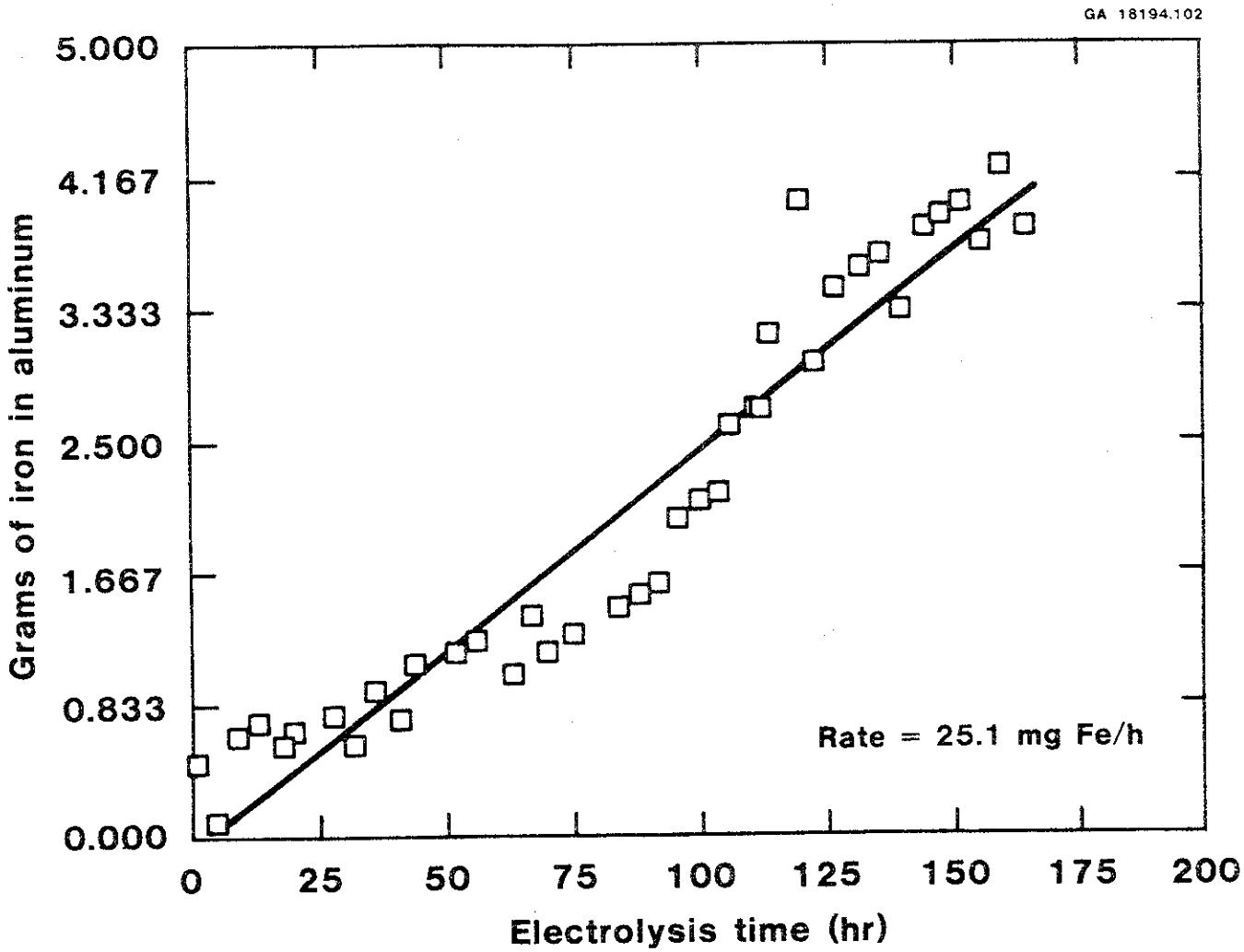

Total Weight of Fe in Aluminum versus Time, Test 2 - 165 h

Figure 158

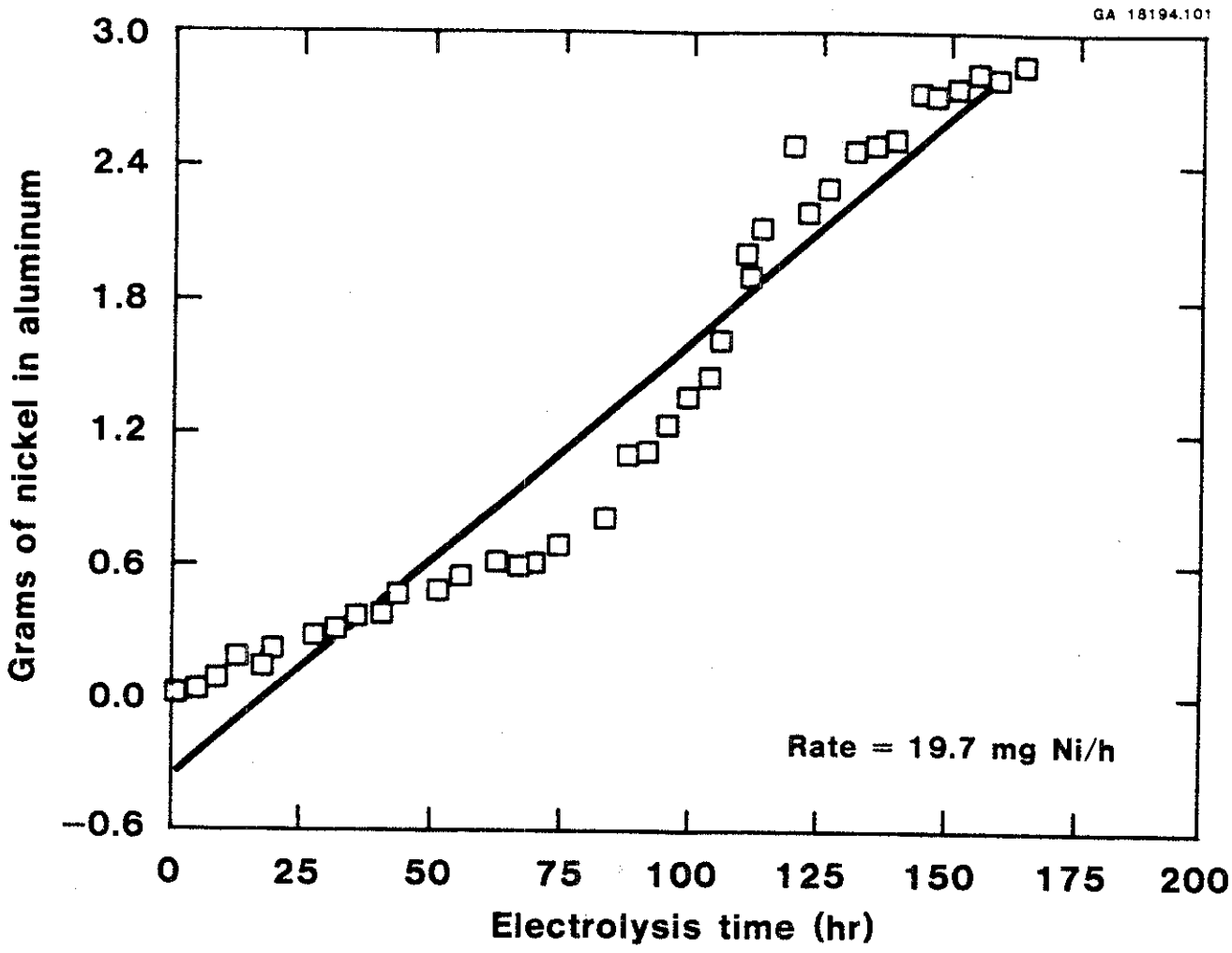

Total Weight of Ni in Aluminum versus Time, Test 2 - 165 h

Figure 159

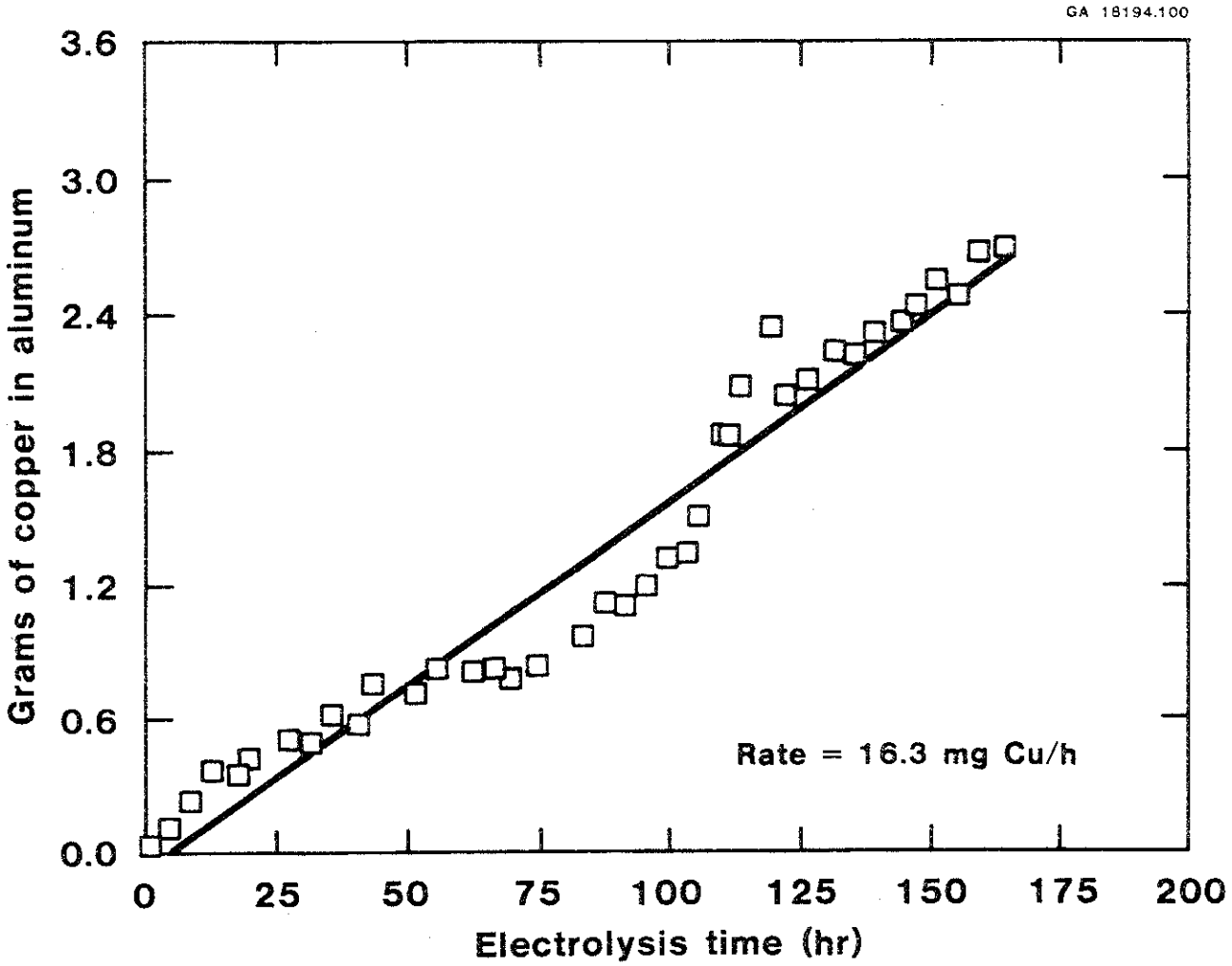

Total Weight of Cu in Aluminum versus Time, Test 2 - 165 h

Figure 160

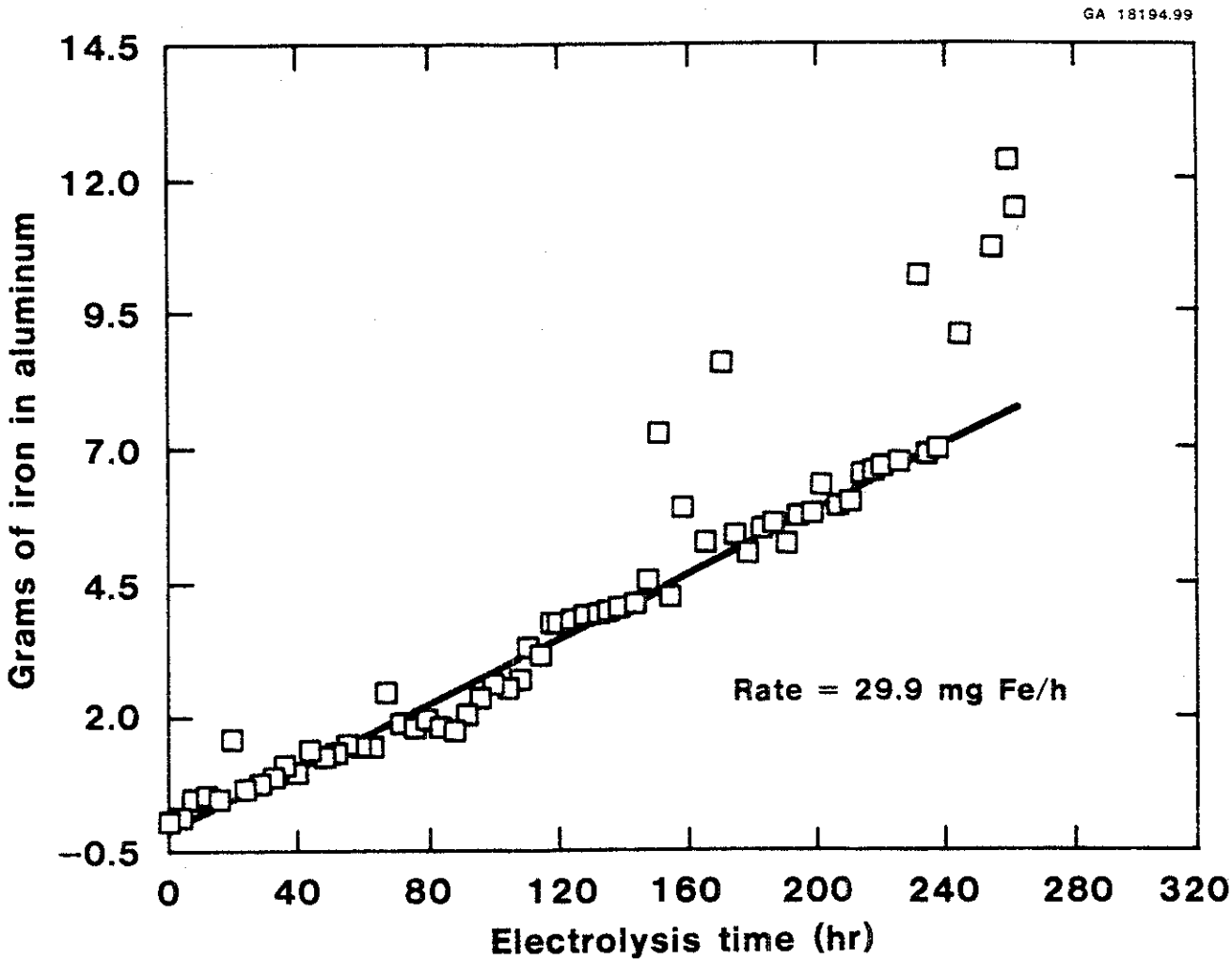

Total Weight of Fe in Aluminum versus Time, Test 3 - 264 h

Figure 161

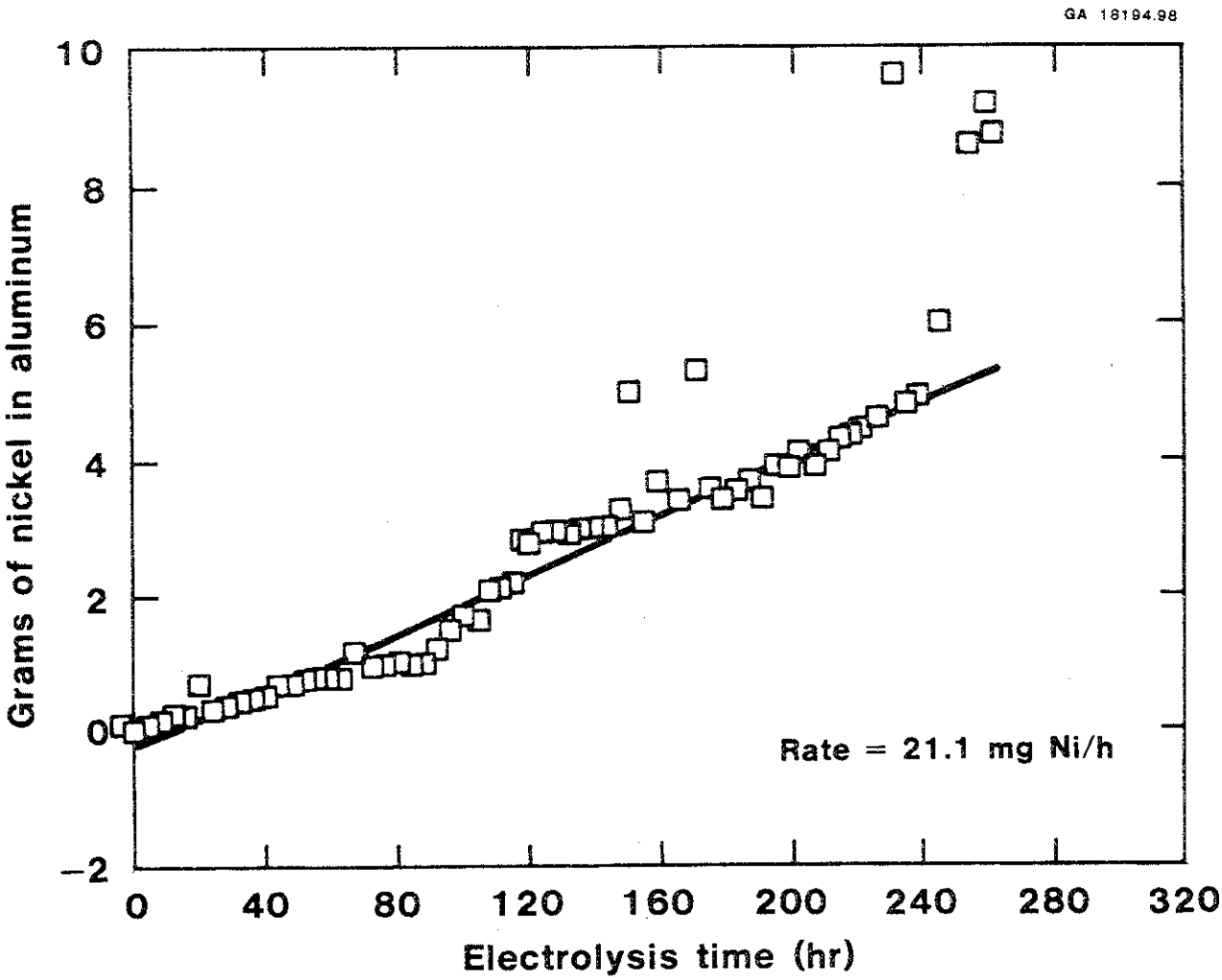

Total Weight of Ni in Aluminum versus Time, Test 3 - 264 h

Figure 162

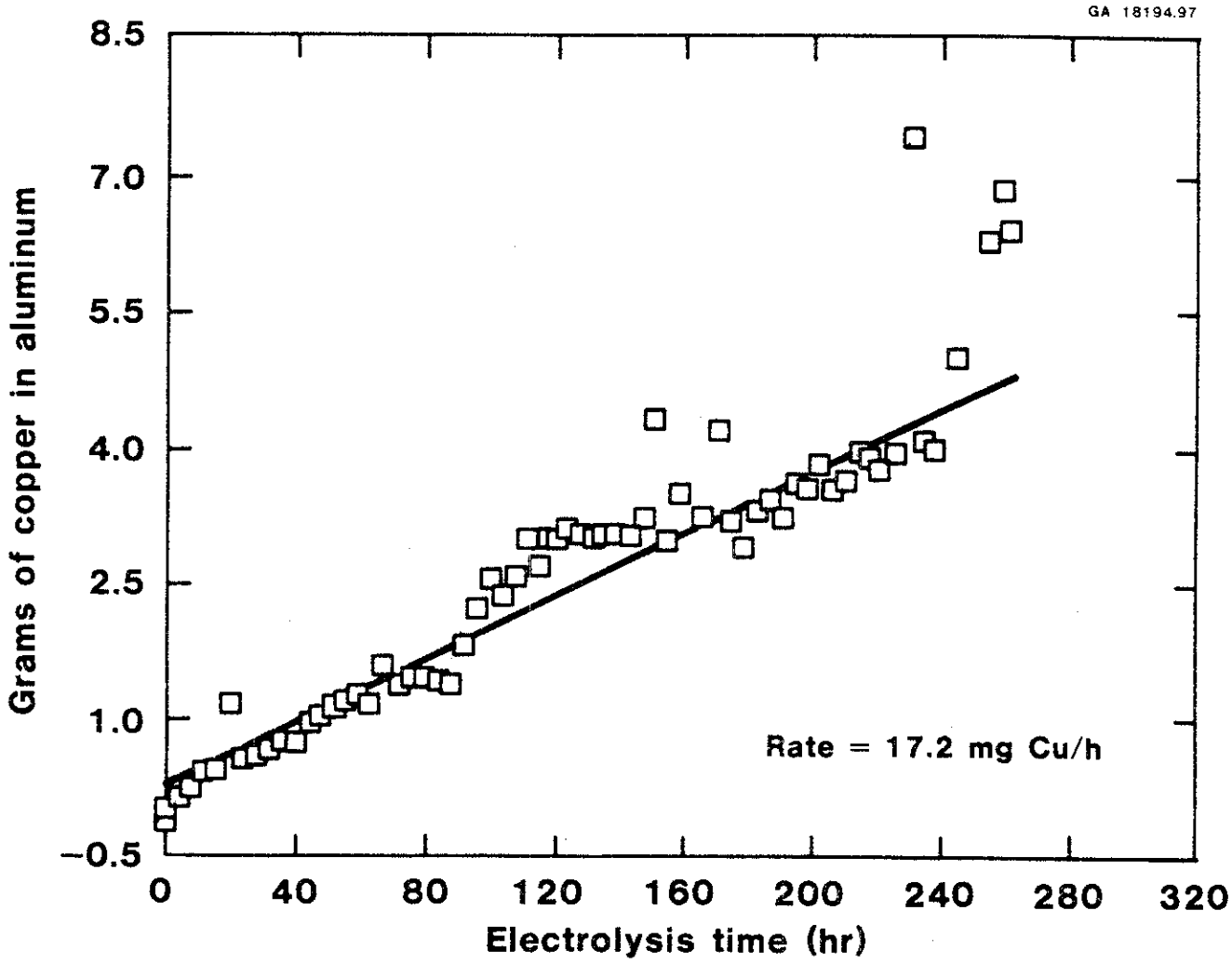

Total Weight of Cu in Aluminum versus Time, Test 3 - 264 h

Figure 163

Ri	Run 2	Run 3
RFe	1.55 cm/yr	1.83 cm/yr
RNi	1.30 cm/yr	1.96 cm/yr
RCu	1.85 cm/yr	1.83 cm/yr

It is encouraging that these rates are also in fair agreement with the rates determined by the other procedures. Probably more significant is that within the precision of the method (0.25 cm/yr), no significant increase in rate with increasing time is observed. The apparent increase in rate with time found by the second measurement technique was probably the result of shorting near the end of the test.

A best-guess estimate of the dissolution rate can be determined for each of the techniques by using a time-weighted average of all the measurements. This method of analysis gives more weight to the longer run, but equal weight to each of the individual determinations [i.e., the rate determination from iron, nickel, and copper are all given equal weights, but the 264-h test is given proportionally more weight than the 165-h test]. The best-guess determination of the rates is tabulated below:

RATE DETERMINATION

Technique	Time-Weighted Average	Standard Deviation
Dimension Change	2.97 cm/yr	1.27 cm/yr
Contamination after Electrolysis	2.01 cm/yr	0.51 cm/yr
Metal Samples during Electrolysis	1.75 cm/yr	0.25 cm/yr

This analysis leads us to conclude that a dissolution rate of between 1.5 and 4.3 cm/yr should be achievable with 5324-Cu [83/17] material. The most confidence is in the rates that were found by the metal samples taken throughout the electrolysis period, therefore, the most likely dissolution rate for 5324-Cu

[83/17], used in a manner consistent with this testing procedure is 1.5 TO 2 cm/yr. A mass transport control anode dissolution mechanism was proposed and experimentally supported with rotating disk experiments by DeYoung (10). The linear nature of the data shown in Figures 159-161 and 162-164 support DeYoungs mechanism. This support is significant in that it shows that the controlling mechanism does not change at longer times [i.e., another process is clearly not incubating while the process proposed and supported by DeYoung is occurring at shorter operating times]. Keller (84) has proposed that the dissolution rate of the anode is ultimately controlled by the plating rate of the anode constituents at the cathode. Under such a mechanistic control the concentration of the anode constituents would build up in the electrolyte until they approached saturation. The anode dissolution rate would then become very slow and be dependent on the rate at which these constituents were plated into the cathodic aluminum metal. Since the cathodic reduction of the Al+3 species to Al is mass transport controlled it is reasonable to assume that all other reductions of metallic species to their zero valence state in this system are also mass transport controlled. The cathodic rate could then be lowered by decreasing the cathodic surface area. One important dimensionless quantity that should be matched, in order to realistically examine anode dissolution rates under cathodic plating rate control, is the ratio of anode area/cathode area. In commercial Hall cells, this ratio is approximately 0.6-0.89 while in these experiments the ratio was 0.3. This difference in electrode area ratio implies that the cathodic plating rate, and thus the anode dissolution rate, may be greater in these experiments than they would be in a commercial cell. On the other hand, mass transport at the cathode in a commercial cell may be higher due to magnetic mixing of the bath and metal pad. Although this effect may more than offset the electrode geometry effect, a fairly quiet metal pad can be obtained with careful cell design or with stable packed bed cathodes. In a commercial cell with a stable cathode surface, anode dissolution rates might be lower than in these experiments.

As was previously stated, the concentration of the anode constituents in the electrolyte should be saturated under strict cathodic control. Figures 164 and 165 show plots of the anode constituents in the electrolyte vs. time for runs 2 and 3, respectively. DeYoung has determined the saturation concentration of iron and nickel at 960°C at 960°C, saturated Al_2O_3, 1.15 ratio to be 0.049% and 0.011%, respectively (49). [The saturation concentration of copper has not been determined.] Both iron and nickel were at saturation concentration in run 3, while iron was at saturation concentration in run 2, nickel was at 60% saturation. These results imply that the process was either at cathodic plating rate control or very close to this type of control. Optimum anode-cathode areas and distances will almost certainly result in greatly reduced anode wear rates for this material.

In conclusion, anode wear rates much less than the goal of 6.58 cm per year have been demonstrated in these tests. A projected wear rate of less than 1.27 cm/yr will almost certainly be achievable if (1) the cell geometry is kept constant with today's commercial cells, (2) the cathode metal surface is kept quiet, and (3) the electrolyte chemistry is kept consistent with the tests described in this report. Further testing of this material in cells which have commercially sized anode area/cathode area ratios is greatly encouraged.

a) Anode Connection Integrity

The brazed connection to the inert anode showed no signs of degradation in run 1 or 3. The apparent poor quality of the connection shown in Figures 146 and 148 was not the result of electrolysis, but was the manner in which the connections were made. [Figure 148 also shows an anode as fabricated with no electrolysis time]. Further work on the connection is recommended.

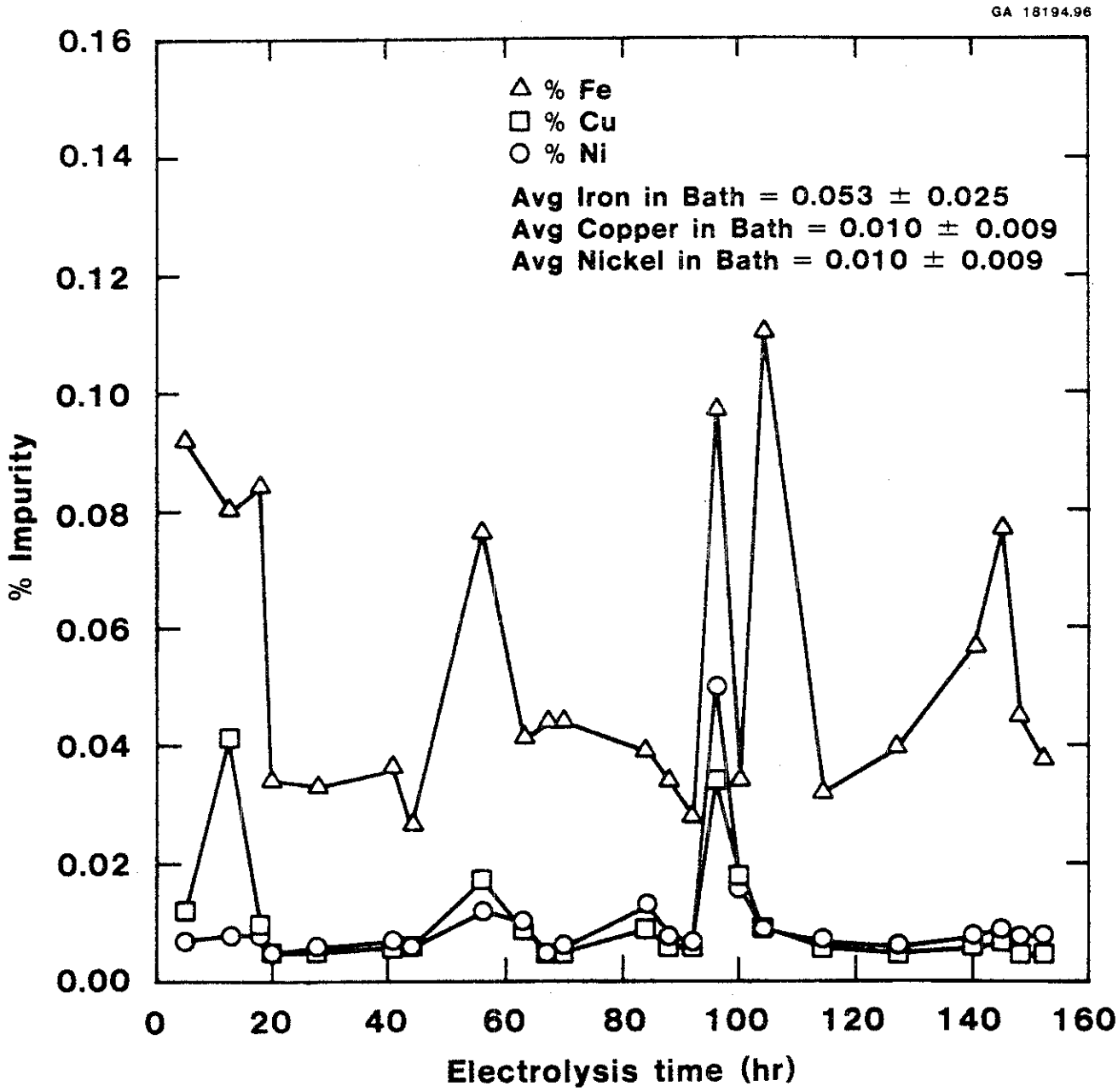

Electrolyte Contamination versus Time, Test 2 - 165 h

Figure 164

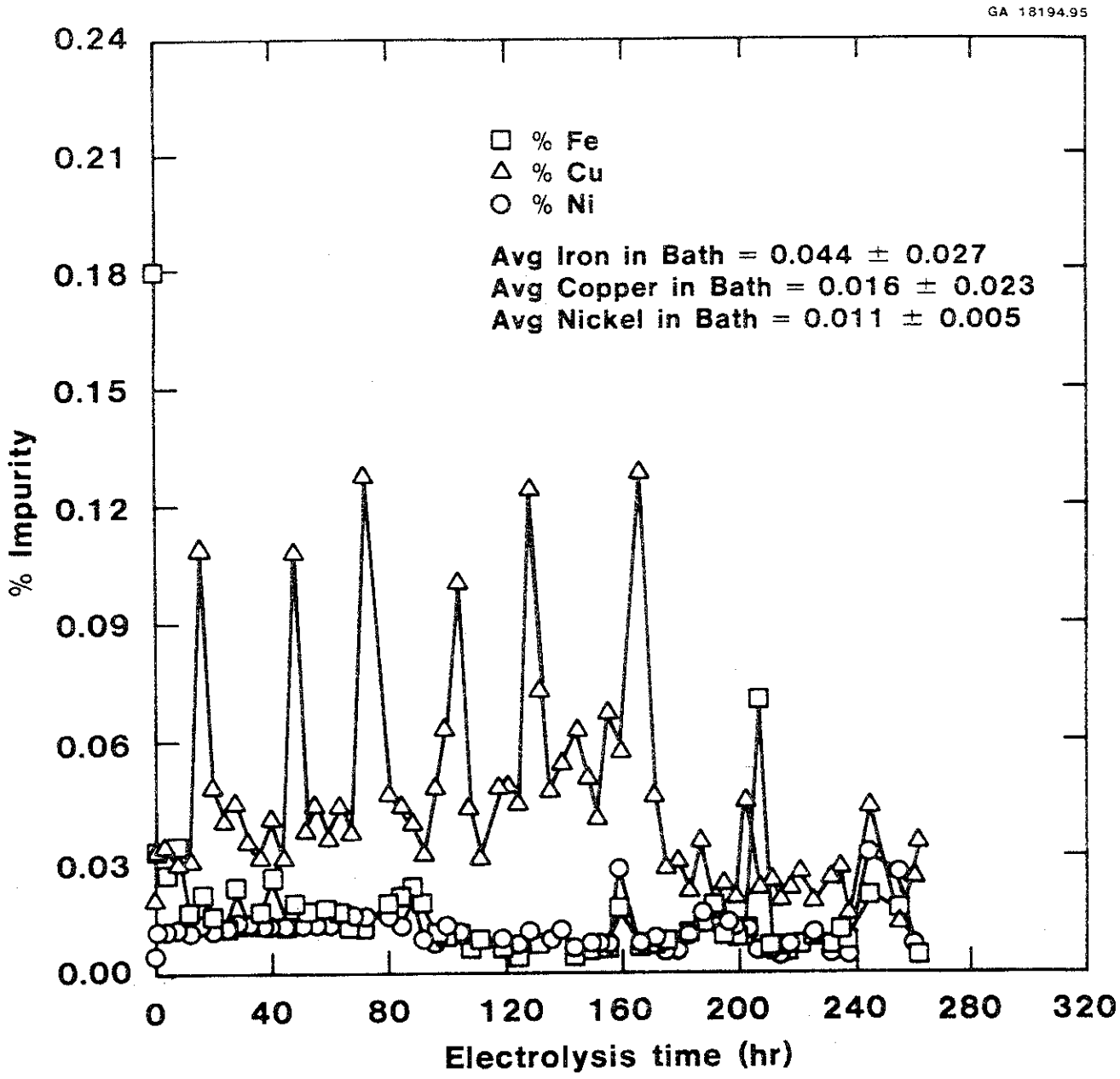

Electrolyte Contamination versus Time, Test 3 - 264 h

Figure 165

5. Voltage Characteristics of the 2500-Ampere Cell

a. Introduction

One goal of the inert anode program was to evaluate the voltage characteristics of inert anode cells operated at reduced inter-electrode distances. This could not be tested directly due to the thermal imbalance of the 2500-A cell at small anode-cathode distances. An indirect method of determining the voltage characteristic of a cell was first described by Haupin (17). A modification has been developed for the voltage characterization of the 2500-A cell. The procedure uses a reference electrode and a mechanical manipulator to accurately position the reference electrode in the cell. The reference electrode is scanned between anode and cathode to determine the voltage components of the cell. The following percent cell voltage breakdown was found with inert anodes:

Decomposition voltage and overvoltage - 23%

Cermet anode and diffusion welded connection voltage drop (ohmic) - 0.3%

Electrolyte voltage drop (ohmic) - 53%

Bubble voltage drop (ohmic) - 7%

Cathode block and Al_2O_3 sludge voltage drop (ohmic) - 16%

Externals - 9.7%

The voltage drop through the inert anode matrix was much smaller than through a carbon matrix. The increased voltage to produce O_2 with inert anodes instead of CO_2 with carbon anodes was, therefore, compensated by lower ohmic losses in the anode materials.

On the other hand, a much larger bubble film ohmic loss was found for inert anodes compared to carbon anodes. The inert anodes also gave a very noisy voltage signal throughout the whole interelectrode space. It is proposed that this noisy signal is due to an emulsion of bubbles in the interelectrode space. The noise would come from bubbles on the sensing tip of the reference electrode probe. This emulsion leads to high resistance in the electrolyte. A large voltage drop was also found at the cathode. This voltage drop is probably due to sludge formation at the cathode.

In summary, the 2500-A cell with similar designs for both the inert anodes and carbon anodes operated at higher voltages with inert anodes than with carbon anodes. The higher voltages are proposed to be caused by increased ohmic losses in the electrolyte due to an emulsion of fine oxygen bubbles.

b. Results and Discussion

Voltage characteristics of the 2500-ampere cell have been broken into the following categories:

1. Anode EMF and overvoltage
2. Anode connection and cermet voltage drop
3. Electrolyte voltage drop
4. Bubble layer voltage drop
5. Cathode block and muck voltage drop
6. Externals

Data for these categories are shown in Table 57. Some additional data on the anode connection and cermet voltage drop are shown in Table 58. These categories are discussed separately below. Wherever appropriate, a comparison to carbon is also made.

1) Anode EMF and Overvoltage

The thermodynamic EMF of the 2500-A inert anode cell can be calculated. The cell was operated with saturated Al_2O_3, therefore, the activity of Al_2O_3 is fixed at unity. The average temperature was 960°C. Since $\Delta G^\circ = nFE^\circ$, it follows that the thermodynamic decomposition potential is 2.21 V.

Overvoltage can be expressed as a Tafel equation:

$$\eta = a + b \log i \qquad (72)$$

TABLE 57

Voltage Characteristics of an Inert Anode Hall Cell
ACD = Bubble Layer + Electrolyte Layer = 6.98 cm

Cell Current (amps)	3400	3200	3000	2800	2600	2400
Anode Current	870	810	748	704	646	596
Pot Temperature	970	967	966	968		
Cell Volts	10.9	10.4	9.8	9.3		
Anode + Connection	0.035	0.034	0.033	0.028	0.025	0.019
E + η	2.3	2.3	2.3	2.3		
Electrolyte Drop	5.83 (0.9 V/cm)	5.63 (0.87 V/cm)	5.37 (0.83 V/cm)	4.79 (0.74 V/cm)		
Bubble Film IR	1.0	0.7	0.6	0.5		
Cathode and Sludge	2.0	1.61	1.51	1.40		
Externals	0.3	0.3	0.3	0.2		
Sum of individual cell voltage component measurements	11.4	9.9	10.1	9.2		
% Error	+4%	-5%	+3%	-1%		

TABLE 58

Relative Comparison of the Effect of Metal Phase Oxidation on the Anode and Connection Voltage Drop (6846 Material)

New Anode		Oxidized Anode	
Amps	Volts	Amps	Volts
870	0.035	890	2.91
810	0.034	828	2.73
748	0.033	772	2.54
704	0.028	664	2.35
646	0.025	614	2.12
596	0.019	0.3	0.167

where η = overvoltage

a = constant

b = constant

i = current density

The Tafel parameters for the nickel metal cermet and the copper alloy cermet were determined in the laboratory. The experiments were done in the cell used for the corrosion study (Figure 132). Tafel behavior was displayed to a current density of 1 A/cm^2. The average Tafel parameters for the nickel metals cermet are:

$a = 0.1009 \pm 0.005$

$b = 0.083 \pm 0.011$

The copper metal cermet had similar parameters.

Excellent agreement was found between the bench-scale results and the measured value (Table 57) on the 2500-A cell. The thermodynamic calculations and Tafel parameters leads to an anode EMF plus overvoltage of 2.33 V vs. Al. A value of 2.3 V was measured in the 2500-A cell.

The carbon electrode system is well studied (83). The thermodynamic voltage is 1.236 V. The Tafel factors are of the order: a = 0.6; b = 0.3. This leads to an anode EMF plus overvoltage of 1.836 V. The inert anode is, therefore, worse than carbon by 0.49 V when considering the polarization effects on the chemical reactions.

2) Anode Connection and Cermet Voltage Drop

The ohmic drop through the nickel metal cermet inert anode connection and material was less than the carbon (graphite) anode. Table 58 shows the ohmic loss in a new inert anode 6846 material with a diffusion weld connection. The 20-mv measured loss agrees well with the expected voltage drop for a cermet anode of this design. The known cermet conductivity is 200

$ohm^{-1}cm^{-1}$, the current density was approximately 2 A/cm^2 with an anode thickness of approximately 2 cm.

The metal phase of the nickel metal cermet anode is slowly lost as the anode is used (10). The low ohmic losses are not maintained as the inert anode is oxidized. Voltage drop data was taken on an inert anode after 14 days of operation. The connection was still intact, but the oxidation (metal loss) had progressed to within several millimeters of the connection. The voltage drop data indicated a 2.55 V drop at a 750 A anode load. Assuming that all of this voltage drop is in the now oxidized cermet, the conductivity is calculated as 14 $ohm^{-1}cm^{-1}$ which is 14 times worse than the starting material.

The voltage drop was also measured on a new carbon anode in the 2500-A cell. The voltage drop through the 25 cm thick carbon anode operating at approximately the same current as the inert anode was 0.415 V.

It has been demonstrated in these experiments that it is possible to design a cermet type inert anode with such favorable material ohmic losses that essentially all of the voltage given up to thermodynamics and kinetics by the production of oxygen instead of CO_2 can be made up. The keys to this appear to be, in decreasing order of importance: high conductivity of a cermet type material; low voltage drop through the connection; short electrical path for current flow. It is imperative from an energy savings point of view that the metal phase of the cermet does not preferentially corrode.

3) Electrolyte Voltage Drop

The resistance of the electrolyte in the 2500-A cell was higher when the cell was operated with inert anodes. The most probable cause for this higher resistance is an emulsion of the fine oxygen bubbles suspended in the interelectrode space.

Figures 166 and 167 show typical interelectrode space voltage profiles for the inert anode at two different current densities. Figure 168 shows a typical interelectrode space voltage profile for the carbon anode. The bath ratio, temperature, and Al_2O_3 content were essentially identical for the inert anode and carbon anode experiments. Several characteristics of these scans are immediately apparent. The voltage initially rises very quickly with short distances from the inert anode. This phenomenon is not observed on a carbon anode. It is believed that this sharp initial rise is due to a dense bubble layer close to the inert anode surface.

The inert anode also exhibits a much noisier signal through the interelectrode space than the carbon anode. The noise level is larger close to the electrode surface than it is farther away. The slope of the voltage-distance plot is also much steeper for the inert anode system than for the carbon anode system. The noise level in the inert anode cell was also larger at higher current densities than at low current densities (Figures 166 and 167). One explanation for noisier signal and steeper slope in the inert anode cell is an emulsion of bubbles in the interelectrode space. The bubble density for such a model is expected to be higher close to the anode surface than farther away. This would lead to an increased measured noise level close to the anode surface. A suspension of bubbles throughout the electrolyte would also lead to noise throughout the interelectrode space and a steeper slope due to an increased apparent resistivity of the electrolyte. The increased noise level at higher current densities is consistent with the explanation; higher current densities lead to higher bubble production rates.

The overall consequence of this emulsion of bubbles in the electrolyte is an increased apparent resistivity of the electrolyte (observed as a steeper slope of the voltage-distance plot). The resistivity increases due to an increased void

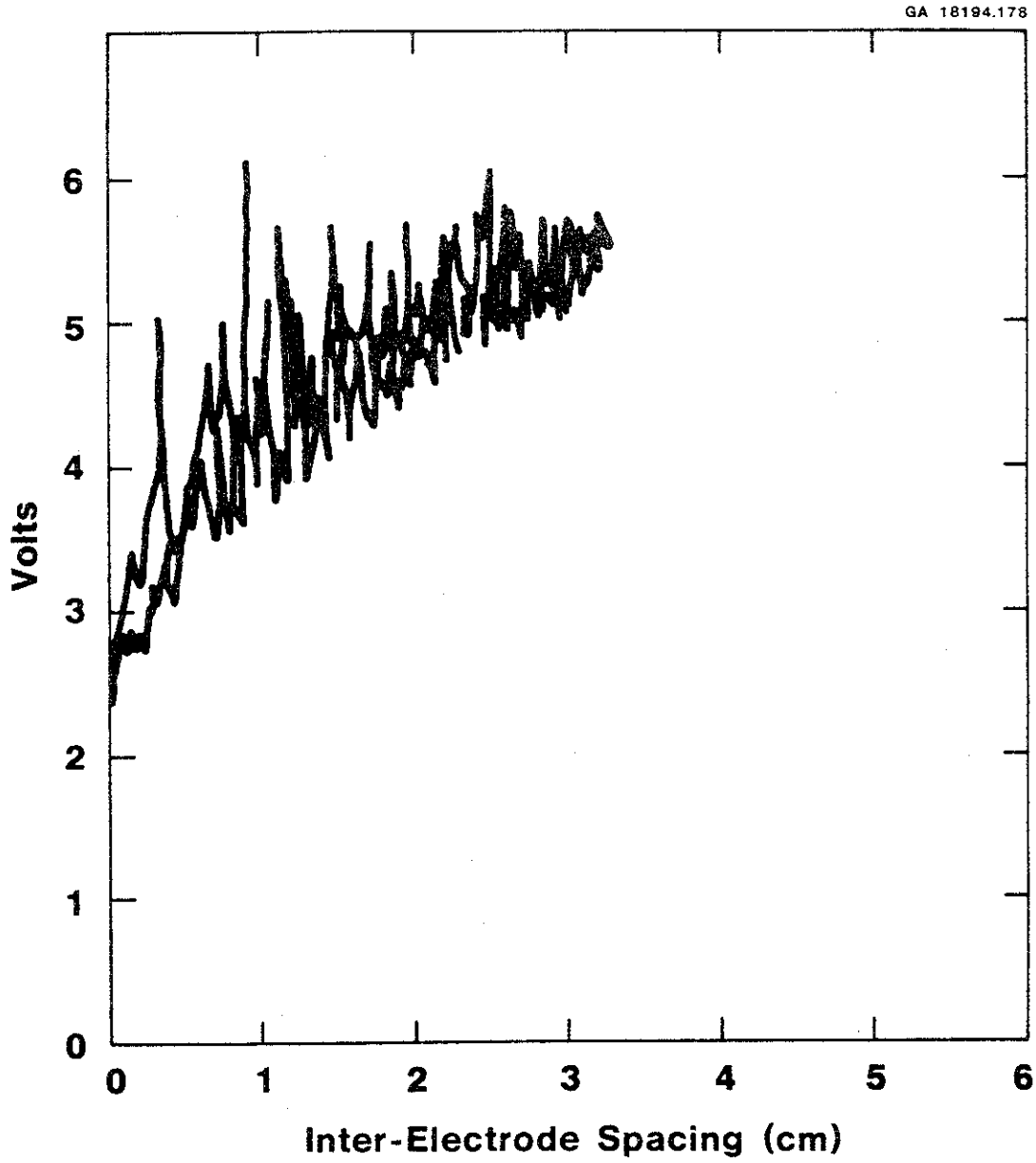

Inert Anode Inner Electrode Space Voltage Scan (Cell Current 2800 A, Anode Current 704 A, Temp. 968°C)

Figure 166

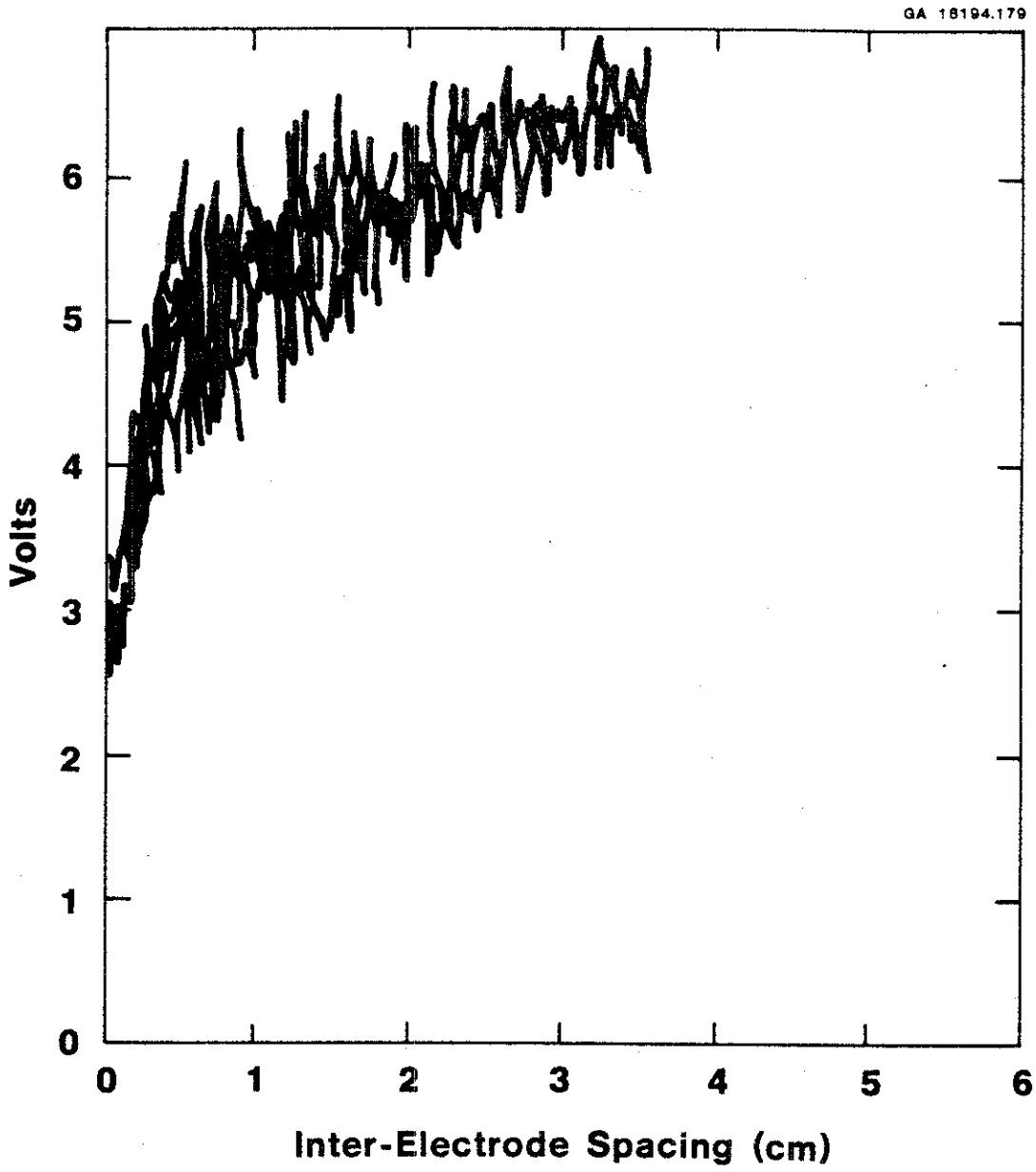

Inert Anode Inner Electrode Space Voltage Scan (Cell Current 3400 A, Anode Current 870 A, Temp. 970°C)

Figure 167

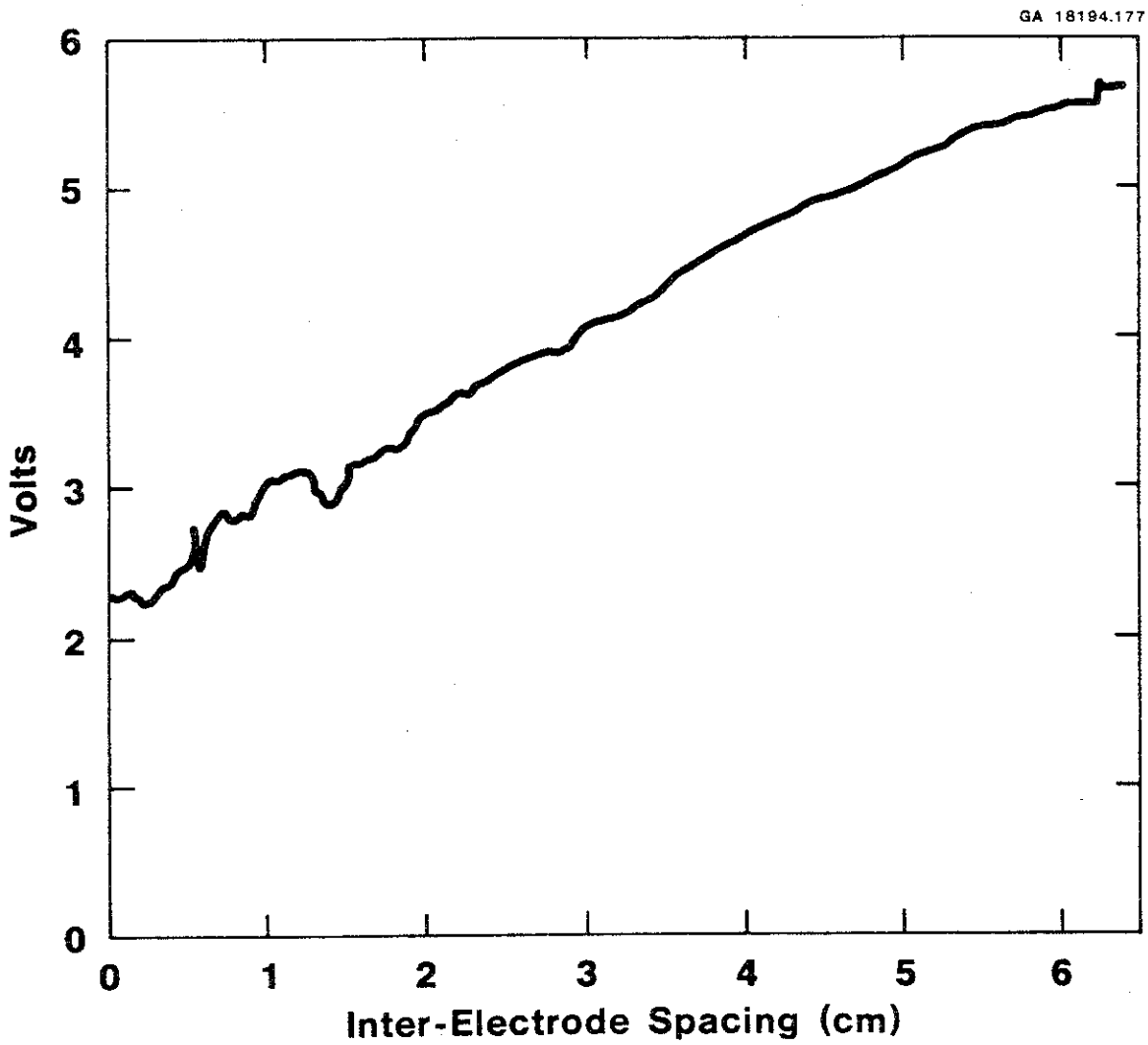

Graphite Anode Inner Electrode Space Voltage Scan (Cell Current 2700 A)

Figure 168

fraction or volume fraction in the interelectrode space that is not available to conduct current.

The increase in resistivity caused by the void fraction could be calculated using a simple Bruggeman model. This model predicts the resistivity in electrolyte with uniformly distributed bubbles and is represented by the following equation:

$$\rho/\rho^{\circ} = [1 - V]^{-3/2} \tag{73}$$

where: ρ = apparent resistivity of the electrolyte
ρ° = resistivity of the bubble-free electrolyte
V = void fraction caused by bubbles

The electrolyte resistivity was measured for both the carbon and inert anode system. If we assume a bubble-free bulk electrolyte is represented by the carbon system, the void fraction can then be calculated for the inert anode case. The slopes of the volt-distance curves in the interelectrode space for carbon and the inert anodes are functions of the actual electrolyte resistivity and current density, which are defined by the following equation:

$$\text{Slope} = \frac{E_{IR}}{L} = \frac{I\rho}{A} \text{ in volts/cm} \tag{74}$$

where: Slope = Slope of the volt-distance curve (Figures 166-168)
E_{IR} = ohmic voltage drop in electrolyte
L = distance traveled in the electrolyte
I = current
ρ = resistivity of the electrolyte
A = area

It follows that the increase in the void fraction for the inert anode system compared to the graphite system can be approximated if it is assumed all other factors are constant for both systems. This is only a moderately good assumption. The measurements were done within days of each other in the same cell with anodes of

the same geometric design and in baths with the same composition. Ledging variations are possible. Since ledge was not quantified, we could only speculate about the impact of this factor.

The increase in void fraction is estimated below by combining the two previous equations:

$$\frac{\text{Slope (inert anodes)} = E_{IR}/L = I\rho/A}{\text{Slope (carbon anode)} - E_{IR}/L = I\rho/A} = (L-V)^{-3/2} \qquad (75)$$

The slope for the inert anode cell was measured at 2800-A, 3000-A and 3400-A. The carbon anode was measured at 2700-A. In order to make the currents equivalent to the slopes for two systems, the inert anode case was determined by linear interpolation to 2700-A. This interpolation gave a slope of 0.73 V/cm. The graphite anode measured slope was 0.54 V/cm. Therefore:

$$\frac{0.75 \text{ V/cm}}{0.54 \text{ V/cm}} = 1.39 = (I - V)^{-3/2} \qquad (76)$$

$V = 0.18$ (or 18% bubble void fraction in the electrolyte)

As expected with a large void fraction, the slopes indicate a 35 percent increase in the resistivity for the inert anode case compared to the carbon graphite case.

Although these initial values indicate that the inert anode will be far worse from an energy savings point of view, this may not be the case for an advanced cell design with an optimized anode design. A consuming carbon anode offers no hope for optimized gas removal as does the nonconsuming inert anode. Small electrolyte changes may change the bubble ohmic losses considerably.

4) Bubble Layer Ohmic Losses

The initial portion of the voltage-distance curve shows an extremely steep rise. This steep rise is due to a very dense layer of bubbles close to the anode surface. The voltage difference between the value determined by extrapolation of the

voltage-distance curve to zero distance and the measured value at zero distance, was taken as the gas film IR. The values for carbon are essentially in agreement with measurements of W. E. Haupin (17). The bubble film layer on the inert anode had an ohmic loss 2-4 times greater than that for carbon. The gas film IR on carbon was measured at 0.25 V, while on the inert anode this ranged from 0.5-1.0 V and increased with current density.

Although gas film values found for the inert anode are much larger than for carbon, the inert anode holds promise for slotting and other advanced designs to remove the bubbles while there is little or no hope for improvement in the gas film IR on carbon.

5) Cathode Drop and Muck

Large ohmic losses were found between the metal pad and cathode bus work in the inert anode cell. It is proposed that these large voltage losses are due to formation of an Al_2O_3 muck that insulates the current path between the molten Al metal and the carbon cathode block. Historically, this muck has been inevitable at high Al_2O_3 concentrations. The inert anode, however, must operate at saturated Al_2O_3 to minimize dissolution of the oxides.

Since no voltage drop data were taken for the carbon anode operating with normal Al_2O_3 concentration, comparisons can only be made between the inert anode actual data and commercial values. Approximately 0.420 V are expected in a commercial cell as compared to 1.5 V measured for the inert anode cell. The extra voltage loss due to muck might be 1.0 V.

The 2500-A cell inherently operates with higher ohmic losses in the cathode block than a commercial cell. A thick cathode was required for thermal insulation in the 2500-A cell.

6) Externals

External ohmic losses were taken as the difference in measured voltage between the point on the bus work where the above measurements were made, and the point where total cell volts were measured by cell operating instruments. These externals contain most of the bus work, the shunt, two clamp connections, and the anode rod. The external ohmic losses should be equivalent for both the inert anode and carbon systems.

c. Conclusions

The voltage components of the 2500-A inert anode cell run have been measured and compared to carbon. The measurements demonstrate it is possible to make a cermet anode and connection of such favorable ohmic characteristic that nearly all of the voltage losses given up to carbon in decomposition voltage (thermodynamic and kinetic) are regained through more favorable ohmic losses in the anode. A very high bubble ohmic loss existed for the inert anodes in this test cell. It may be possible to minimize this bubble ohmic loss by optimized cell/anode design and electrolyte composition additives. A high voltage loss was also measured at the cathode. This high ohmic loss might be caused by mucking that occurs with high Al_2O_3 additions to the cell, or it might be due to the inherent design of the 2500-A pilot cell.

A comparison summary of the inert anode and carbon systems is provided in Table 59.

TABLE 59

Comparison of Inert Anode and Carbon Anode Systems
(2700 Amps and 7 cm (2.75") ACD)

	Inert Anode		Graphite	
	Volts	% of Total	Volts	% of Total
E° + n	2.3	25%	1.8	24%
Anode + Connection	0.03	0.3%	0.4	5.4%
Bubble Film	0.5	5.5%	0.2	2.7%
Electrolyte	4.73	52%	3.50	47%
Voltage Drop	(0.73 V/cm)		(0.54 V/cm)	
Cathode + Muck	1.35	15%	1.35	18%
Externals	0.2	2.2%	0.2	2.7%
	9.1 Volts		7.45 Volts	
Cell Volts	(9.02 Actual)		(7.69 Actual)	
% Error	+ 1%		- 3%	

D. Properties of Fabricated Inert Anodes

1. Objective

The objective of this portion of the research program was to determine the physical, electrical, chemical, thermal and mechanical properties of fabricated inert anodes and relate these properties to performance in the Hall electrolytic cell.

2. Introduction

An understanding of the properties of the inert anode electrodes and other components of the Hall cell is vitally important to the design, fabrication, placement, operation, and evaluation of inert anodes, inert anode connections, and other components of the Hall cell. Properties of interest include the following:

a. Mechanical Properties
   1) Flexural Strength
   2) Tensile Strength
   3) Compressive Strength
   4) Weibull Modulus
   5) Young's Modulus
   6) Shear Modulus
   7) Poisson's Ratio
   8) Fracture Toughness
   9) Fatigue
   10) Creep
   11) Hardness

b. Thermal Properties
   1) Expansion Curves
   2) Thermal Conductivity
   3) Specific Heat

c. Physical Properties
   1) Density
   2) Porosity

d. Chemical Properties
   1) Chemical Composition
   2) X-ray Phase Composition

e. Microstructural Properties
   1) Metal Phase - Size, Amount and Size Distribution
   2) Pore Phase - Size, Amount, and Size Distribution
   3) Oxide Phase - Grain Size and Amount
   4) Fracture Surfaces

f. Electrical Properties
   1) Electrical Conductivity

Other properties investigated and reported extensively in the preceding sections of this report include the chemical dissolution and electrochemical corrosion behavior of inert anodes. Many of the properties listed above were determined and reported in previous quarterly reports (6,8-13). Thermal expansion data were reported in the Twelfth Quarterly Report (6); physical property, microstructural, nondestructive evaluation (NDE), and X-ray phase data were contained in the Fourth annual report (10); and mechanical property data were listed in the Fourteenth (8) and Fifteenth (9) quartertly reports for the nickel cermet (6846) and oxide (5324) compositions. The Seventeenth (11) and Nineteenth (13) quarterly reports listed the mechanical and microstructural properties for the copper cermet (5324 + Cu). Mechanical properties were used to design inert anode shapes. Finite element methods, based on measured properties, were used to calculate expected stress and temperature levels in inert anode assemblies during heatup, transfer, and operation in a 2500-ampere Hall cell (9).

The measured properties of as fabricated inert anodes evaluated during this contract are summarized in Table 60. This property listing is representative of typical inert anode materials of the type and composition

TABLE 60

Properties of As-Fabricated Inert Anodes

Material	Nickel Ferrite-NiO	Ni-Nickel Ferrite	Ni-Nickel Ferrite	Ni-Nickel Ferrite	Ni-Nickel Ferrite	Ni-Nickel Ferrite	Cu-Nickel Ferrite
Composition	51.7w/o 48.3w/o NiO + Fe_2O_3	20w/o 60w/o 20w/o Fe + NiO + Fe_3O_4	20w/o 60w/o 20w/o Fe + NiO + Fe_3O_4	20w/0 60w/o 20w/o Fe + NiO + Fe_3O_4			
Designation	5324	6846	6846	Al-66	5324 + 30% INCO Ni	5324 + 30% 123 Ni	5324 + 17% Cu
Fab. Process	Cal-Sinter	Reaction-Sinter	Cal-Sinter	Cal-Sinter	Cal + Ni Sinter	Cal + Ni Sinter	Cal + Cu Sinter
Property							
Physical							
Theoretical Density, g/cm^3	5.72	6.35	6.35	6.35	6.55	6.55	6.28
Bulk Density, g/cm^3	5.69	5.89	6.12	6.11	6.55	6.52	6.09
Porosity - Open, %	0.16	1.94	0.3	0.2	0.11	0.09	0.06
Mechanical							
Strength - MOR 3pt, MPa							
Strength - MOR 4pt. MPa	165.6	105.8	112.8	126.8	192.4	182.9	104.2
Weibull Modulus, m	13.1	8.0	16.4	4.9	7.8	20.9	12.4
Fracture Toughness, MPa $m^{1/2}$	1.92	4.84	3.75	3.64	5.43	5.15	-.-
Young's Modulus, GPa	155	146	-	175	-	-	145
Shear Modulus, GPa	63	56					55.8
Poisson's Ratio		.29					0.3
Thermal							
Expansion Coef.							
20-500°C, cm/cm/°C x 10^{-6}	11.2	12.7					12.6
20-1000°C, cm/cm/°C x 10^{-6}	11.9	14.2					14.4
Conductivity, 1000°C, W/cm.K	.026	.05					
Specific Heat, cal/gK	.19	.185					
Electrical							
Conductivity							
1000°C, $(ohm-cm)^{-1}$	0.9	380	100	~			89
20°C, $(ohm-cm)^{-1}$	0.011(600°C)	1050					11
Microstructural							
wt.% metal	3	28	30	31	40	39	20
% porosity	3.4	5.3	4	1.6	1.5	1.5	1.2
Chemical							
X-ray Phases	$NiFe_2O_4$,NiO	Ni,$NiFe_2O_4$,NiO	Ni,$NiFe_2O_4$,NiO	Ni,$NiFe_2O_4$,NiO	Ni,$NiFe_2O_4$,NiO	Ni,$NiFe_2O_4$,NiO	Cu,Ni,$NiFe_2O_4$,NiO

listed in Table 60. Properties are dependent upon many factors including raw materials, composition, manufacturing process methods, density, microstructure, test methods, and test conditions. Test conditions that have a significant impact on inert anode properties include time and temperature of the exposure environment. Certainly, not all of the properties have been measured for all possible exposure conditions.

The following text presents brief results on some of the properties measured during the course of the contract.

3. Mechanical Properties

a. Strength

The strength of inert anode materials was determined by testing rectangular prism bars in either three- or four-point flexure. Flexure tests or modulus of rupture tests (MOR) were performed because direct tensile tests are difficult to do on brittle elastic materials and flexure test methods are commonly used by the ceramic community. The strength formulas used for flexure testing are:

$$\text{3pt:} \qquad S = \frac{3\ PL}{2\ bd^2} \tag{77}$$

$$\text{4pt:} \qquad S = \frac{3\ PL}{4\ bd^2} \tag{78}$$

where: P = breaking load
L = outer support span
b = specimen width
d = specimen thickness

The four-point procedure used on 3 x 4 x 45 mm bars was the proposed MIL-STD-1942A "Flexural Strength of High Performance Ceramics at Ambient Temperature" (86). The crosshead speed during loading was 0.5 mm/min. Three-point testing was conducted on 5-6 x 6-11 x 68-70 mm bars using a crosshead speed of 1.0 mm/min.

1) Effect of materials, surface preparation, and temperature.

Three-point test results are shown in Figure 169 for the 6846 Ni-nickel ferrite cermet materials at room and elevated temperatures. The results indicate strength values are dependent upon combination of raw materials, density, surface preparation, and temperature. The 6846 composition, 20% Fe - 60% NiO - 20% Fe_3O_4, was fabricated by reaction sintering several different combinations of raw materials together (see next section on fabrication for explanation of raw material combinations). As fabricated 6846 composition 94-2, 94-12, and 103-7 raw material combination bars were tested at room temperature and the results showed that 94-2 and 94-12 combinations have the same strength while the 103-7 combination has a higher strength. Figure 169 illustrates the positive effect of surface grinding the bars. In all cases, strengths are improved because of surface grinding. Figure 169 compares the strength versus temperature for cermet bars that were fabricated with densities ranging from 5.5 to 6.0 g/cc. As expected, the higher density bars (lower porosity) exhibit higher strengths. In addition, there was a 20 to 40 percent decrease in strength between room temperature and 1000°C for these 6846 composition reaction-sintered bars.

Figure 170 illustrates the three-point flexural strength of 5324 NiO-$NiFe_2O_4$ bars vs. temperature for two sets of bars with different densities and the room temperature strengths for several other sets of bars. The bars labeled J22 were about 4.3 g/cm^3 and the J33 bars were 5.15 g/cm^3 or 75 and 90 percent of theoretical density, respectively. The strengths of the all-oxide 5324 material improved as the density was increased for these materials in later years (80 vs. 81 & 82). Loss in strength does not occur for this material until the testing temperature exceeds 1000°C.

2) Effect of porosity on cermet inert anode strength.

Four-point flexure strength vs. porosity content is plotted in

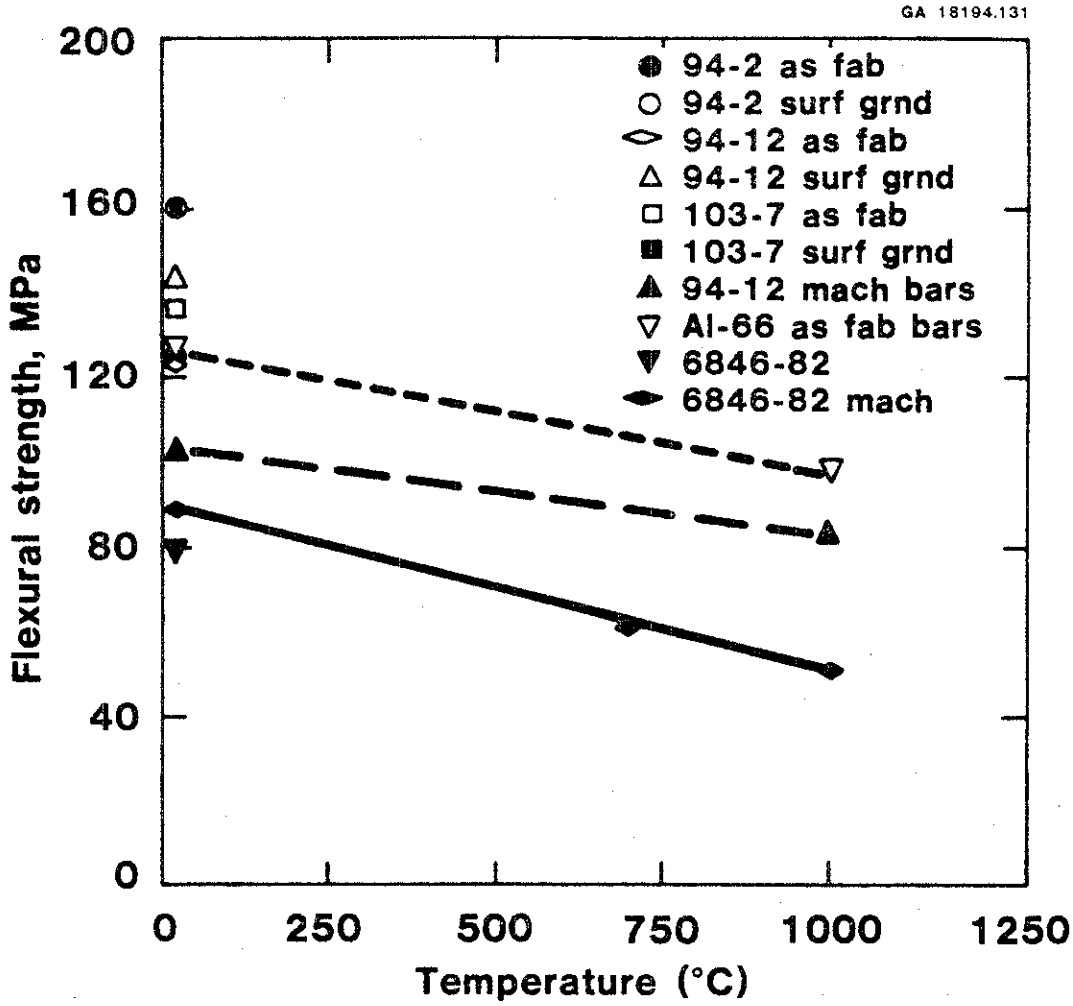

Three-Point MOR Strength of 6846 Cermet Bars Versus Raw Materials Used, Temperature, and Surface Finish
Figure 169

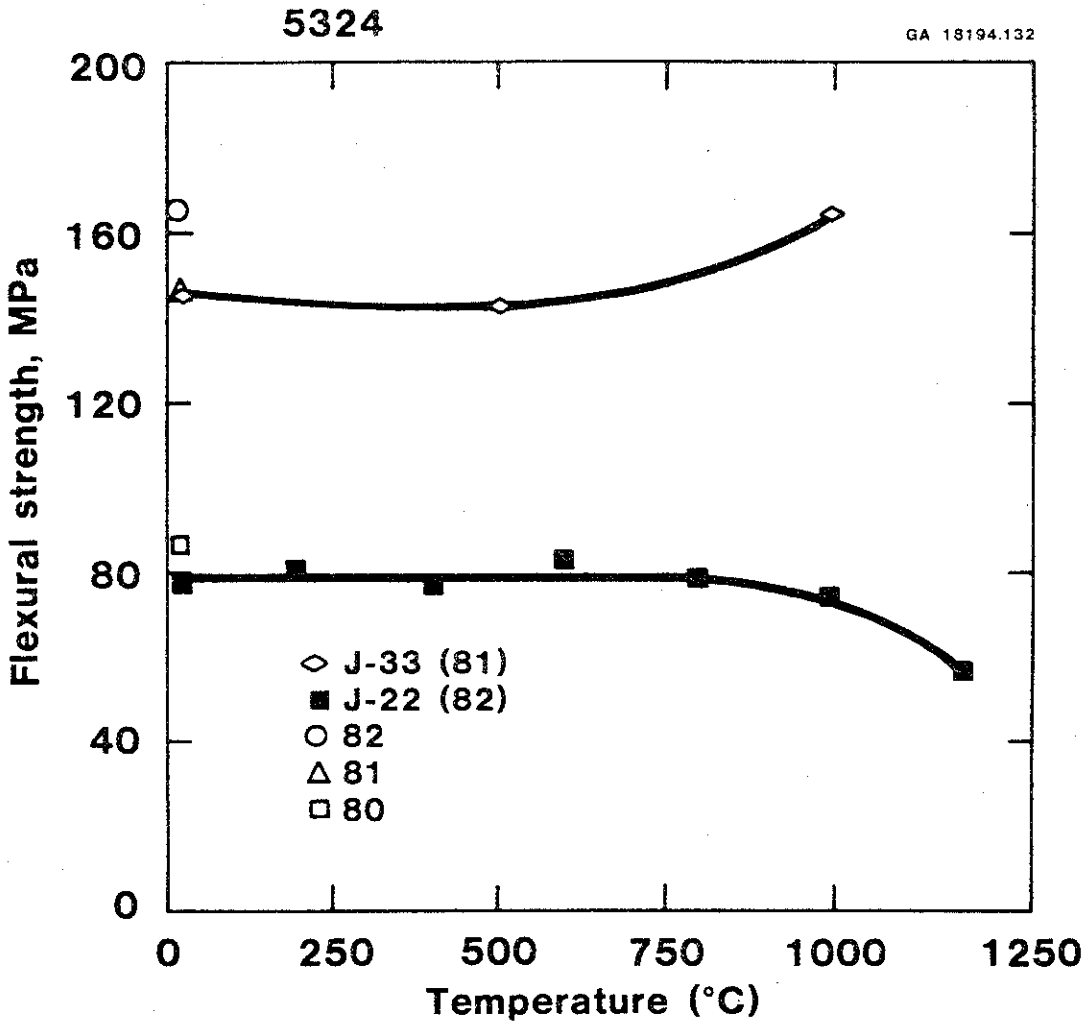

Three-Point MOR Strength of 5324 Oxide Inert Anode Bars
Figure 170

Figure 171 for the 6846 Ni-$NiFe_2O_4$ and Cu-$NiFe_2O_4$ cermet inert anode compositions. The Ni-cermet has a zero porosity strength of about 200 MPa and a strength value of 104 MPa was measured for the Cu-cermet with 1.5 percent porosity. More data are needed for the Cu-cermet material to extrapolate a zero porosity strength value. It should be noted that liquid phase sintering occurs with the Cu-cermet and the interfacial reactions may not lead to as strong a bond as occurs in the Ni-cermet system where solid state diffusion reactions occur.

3) Effect of Hall cell exposure time on inert anode strength.

Desired anode life in the Hall cell is to be measured in terms of years, or at least half years, rather than days. Because of this time requirement for operation in the Hall cell, the strength stability of the inert anode must be characterized and proven. In order to characterize the strength of inert anodes after exposure to the Hall cell environment, several test bars were removed from the upper sidewall and the bottom areas of the tested anodes that had been in the 2500-A cell for 12 and 21 days. The MOR three-point data are presented in Figure 172. As can be seen, the strength of these materials decreased due to exposure time in the cell. The upper sidewall microstructures of the anodes did not change significantly because exposure was limited to vapor species from the bath and not the bath itself. Upper sidewall strength was decreased to approximately 80 percent of the original value after 21 days. More alarming, however, is the fact that the strength of the exposed bottom portion of the anode decreased to about 13 percent of its original value after 21 days. This great reduction in strength is due to the dramatic change in the microstructure which includes an increase in porosity and removal of the nickel alloy metal from the microstructure by electrochemical dissolution in the bath. Therefore, mechanically these Ni-cermet anodes would not hold up for significant lengths of time in the Hall cell environment. The strength of Cu-cermet inert anodes was not tested after Hall cell electrolysis exposure. However, the

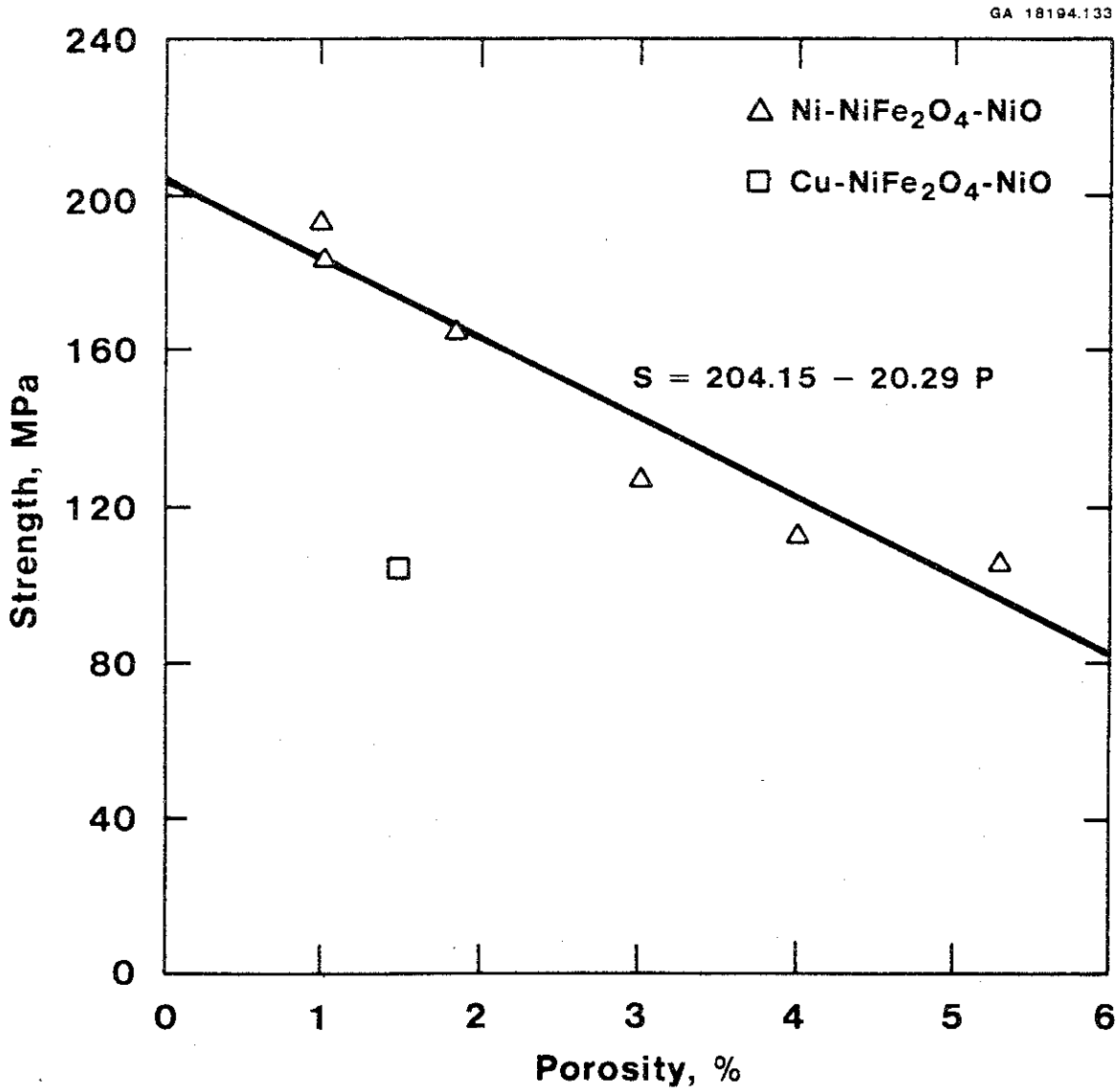

Four-Point MOR Strength of Cermet Inert Anode Versus Porosity

Figure 171

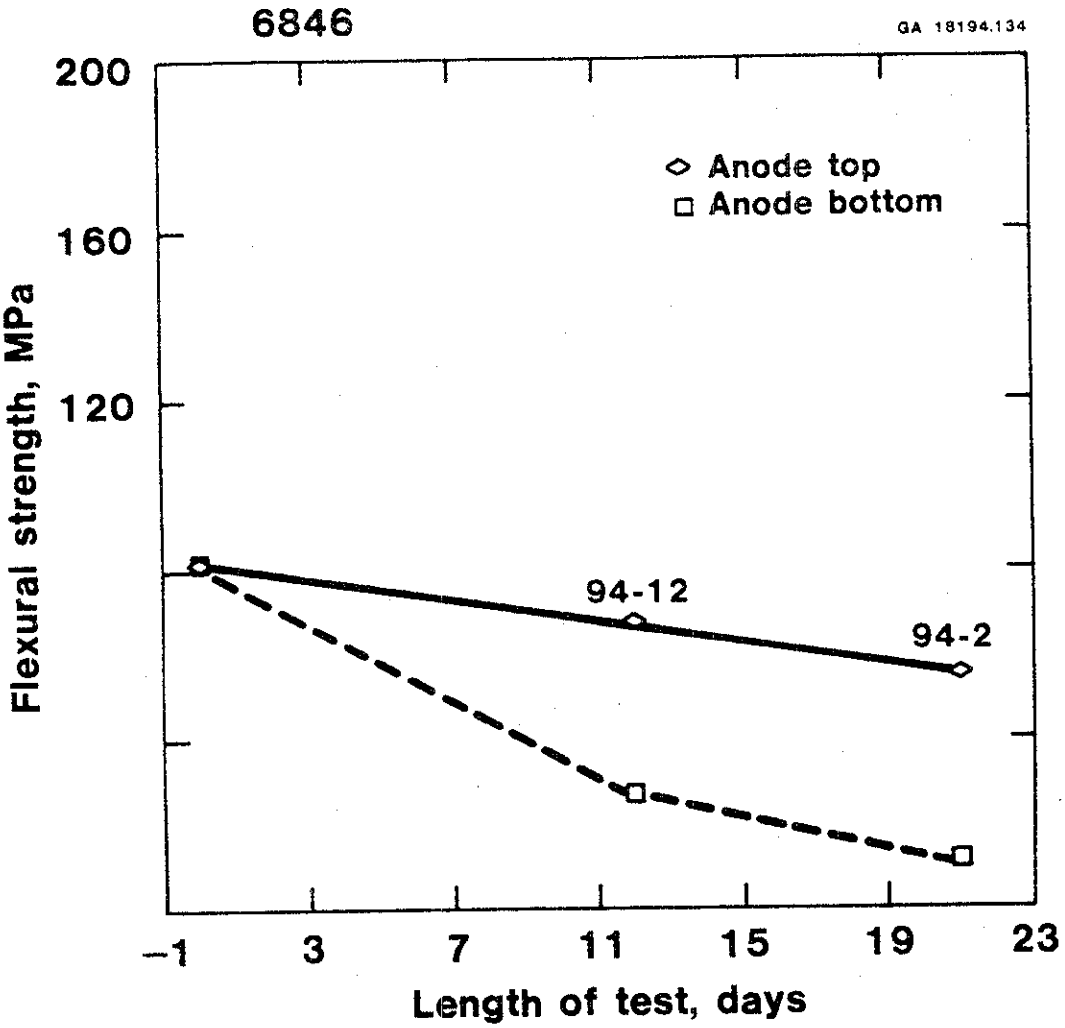

Three-Point MOR Strength of Inert Anode 6846 Cermet Versus Exposure Time and Location in Hall Cell

Figure 172

strength is not expected to change dramatically since the microstructure has not been altered to a great extent by this exposure.

b. Weibull Modulus

In order to evaluate the strengths of inert anode bars and the influence of flaw types and distributions on the strengths, a two-parameter Weibull distribution function was fitted to each of the seven data sets considered. This function is expressed as:

$$F = 1 - \exp - \left[- V_E \left(\frac{\sigma_f}{\sigma_o}\right)^m\right] \quad (79)$$

Where F is the probability of failure, σ_f is the observed maximum stress at fracture, σ_o is a scaling parameter, m is the Weibull modulus, and V_E is the volume of a tensile specimen which, subject to the stress σ_f, would have the same probability of failure as the bar. The probability of failure is expressed as:

$$F = \frac{n}{N+1} \quad (80)$$

Where N is the total number of data points and n is the order of ranking of the n^{th} data point within the weakest to strongest range.

Equation 79 can then be manipulated to the logarithmic form:

$$\ln \ln \left(\frac{1}{1-F}\right) = m \ln \sigma_f + [\ln V_E - m \ln \sigma_o] \quad (81)$$

The Weibull modulus, m, is then obtained from the slope of the line generated from a plot of $\ln \sigma_f$ vs. $\ln \ln \left(\frac{1}{1-F}\right)$.

Figure 173 is a Weibull plot of the breaking strengths for 6846 composition, 94-12 raw material combination, inert anode bars. Forty-four bars were broken at room temperature and 41 at 1000°C. The three-point strength population means were 102.7 and 83 MPa for the room and

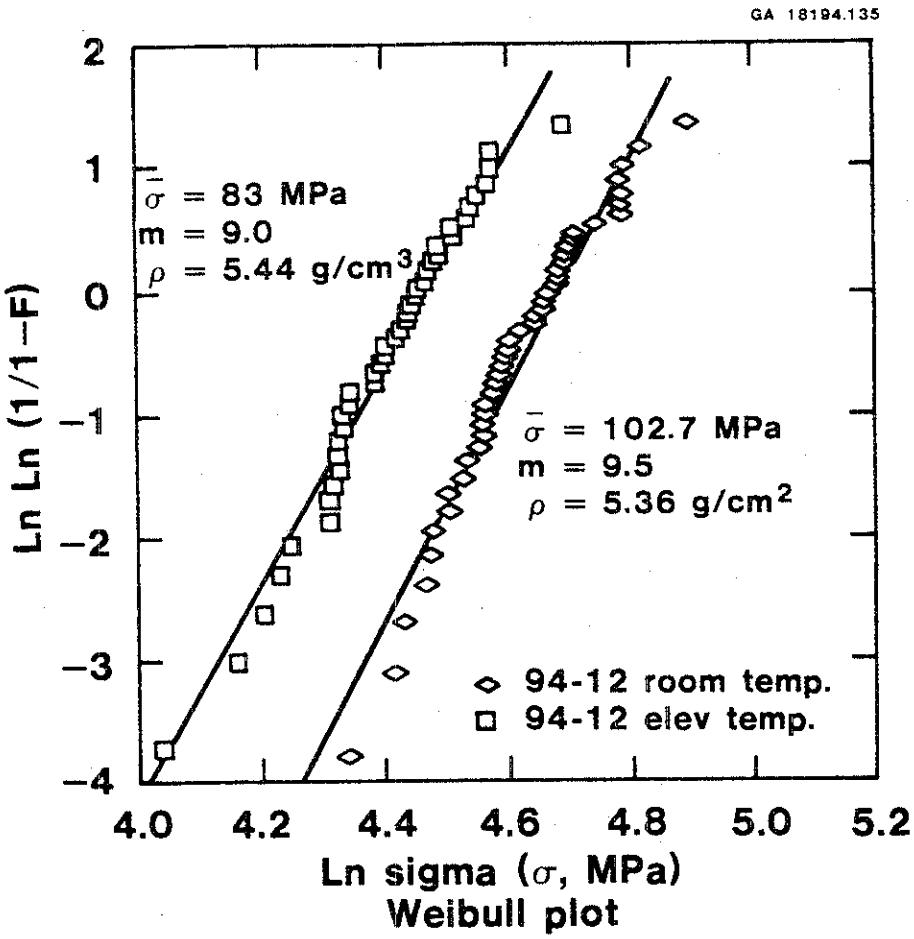

Modulus of Rupture Data (3-pt.) for 94-12 6846 Cermet Inert Anode Bars at 20 and 1000°C

Figure 173

elevated temperatures, respectively. The Weibull modulus values were 9 and 9.5. Four-point strength values can be calculated using the method of Davies (87) and the formula:

$$\frac{\bar{\sigma}_3 pt}{\bar{\sigma}_4 pt} = \left(\frac{m+2}{2}\right)^{1/m} \quad (82)$$

where $\bar{\sigma}$ equals the mean fracture strength and m equals the Weibull modulus. The four-point flexure room temperature strength equals 85.6 MPa and the elevated temperature strength equals 69.2 MPa by this calculation method. The elevated temperature strength is about 20 percent lower than the room temperature strength. These lower strength values would be expected for these low-density cermet anodes (~5.4 g/cm^3).

Additional Weibull plots of Ni and Cu-cermet strengths are shown in Figures 174 and 175. The calcined-sintered 6846 cermet has a higher strength and less data scatter, m = 16.4, than the reaction-sintered 6846 cermet (Figure 174), m = 8.0. The latter appears to have two flaw population types that cause failure, as indicated by the knee in the data plot. The strengths of cermets fabricated by the addition of Ni or Cu metal powder to 5324 oxide powder are shown in Figure 175. The highest strength Ni-nickel ferrite cermet was obtained by using the finer grade Ni powder 123 added to the 5324 oxide. Again, the Cu-cermet is much lower in strength than Ni cermet as is shown in Figure 175. Weibull m values varied from 7.8 to 20.9 for inert anode test bars fabricated by adding Ni or Cu metal powder to the 5324 oxide powder (see next section on fabrication).

c. Fracture Toughness

Fracture toughness was determined by use of two methods. The first method, microindentation-fracture (88) was used on the all-oxide 5324 composition and early samples of the 6846 cermet composition. These early samples were low density (~85 percent of theoretical density).

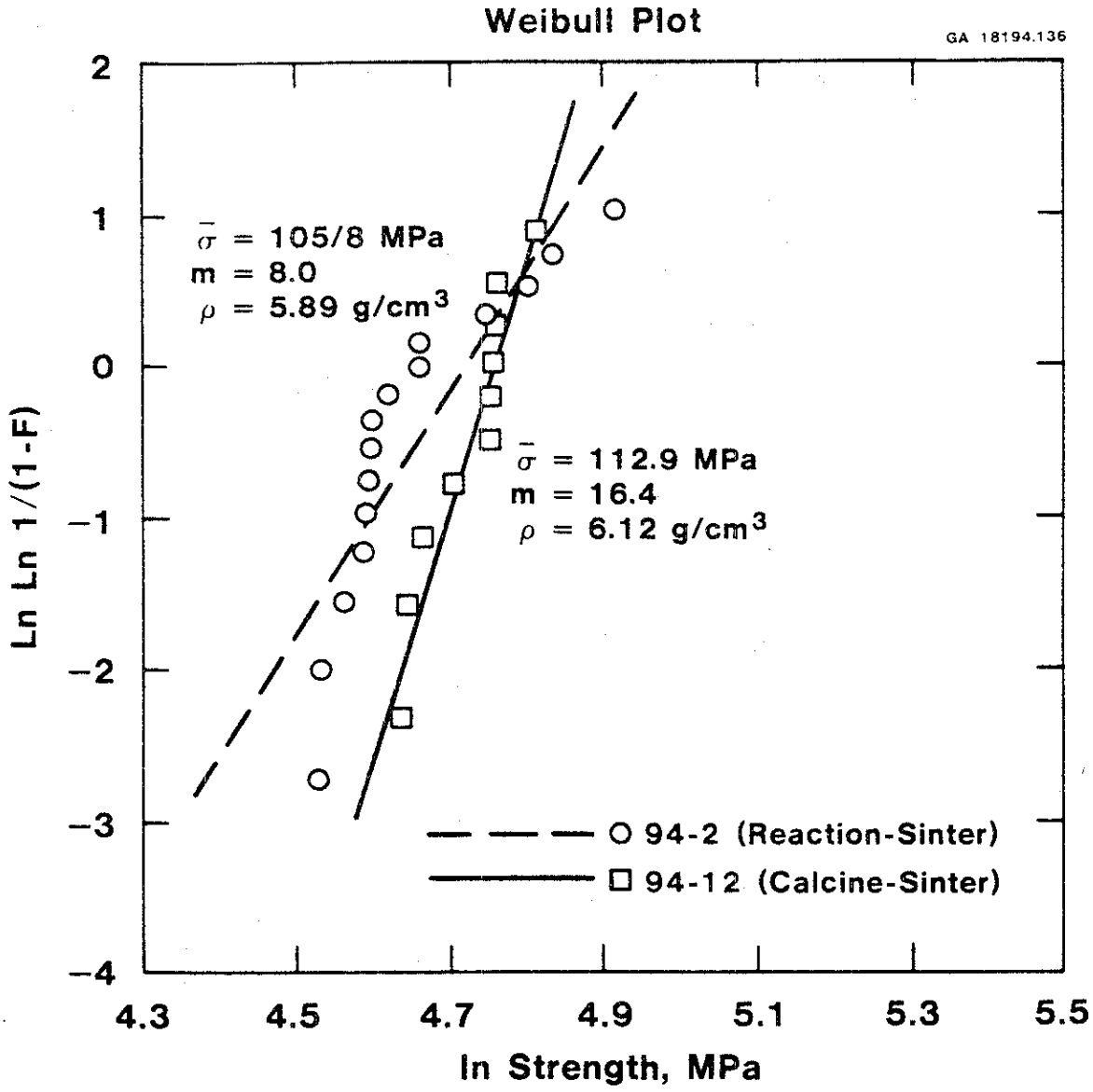

Inert Anode Strength, MOR-4 PT, for Reaction-Sinter and Calcine-Sinter Processed Material

Figure 174

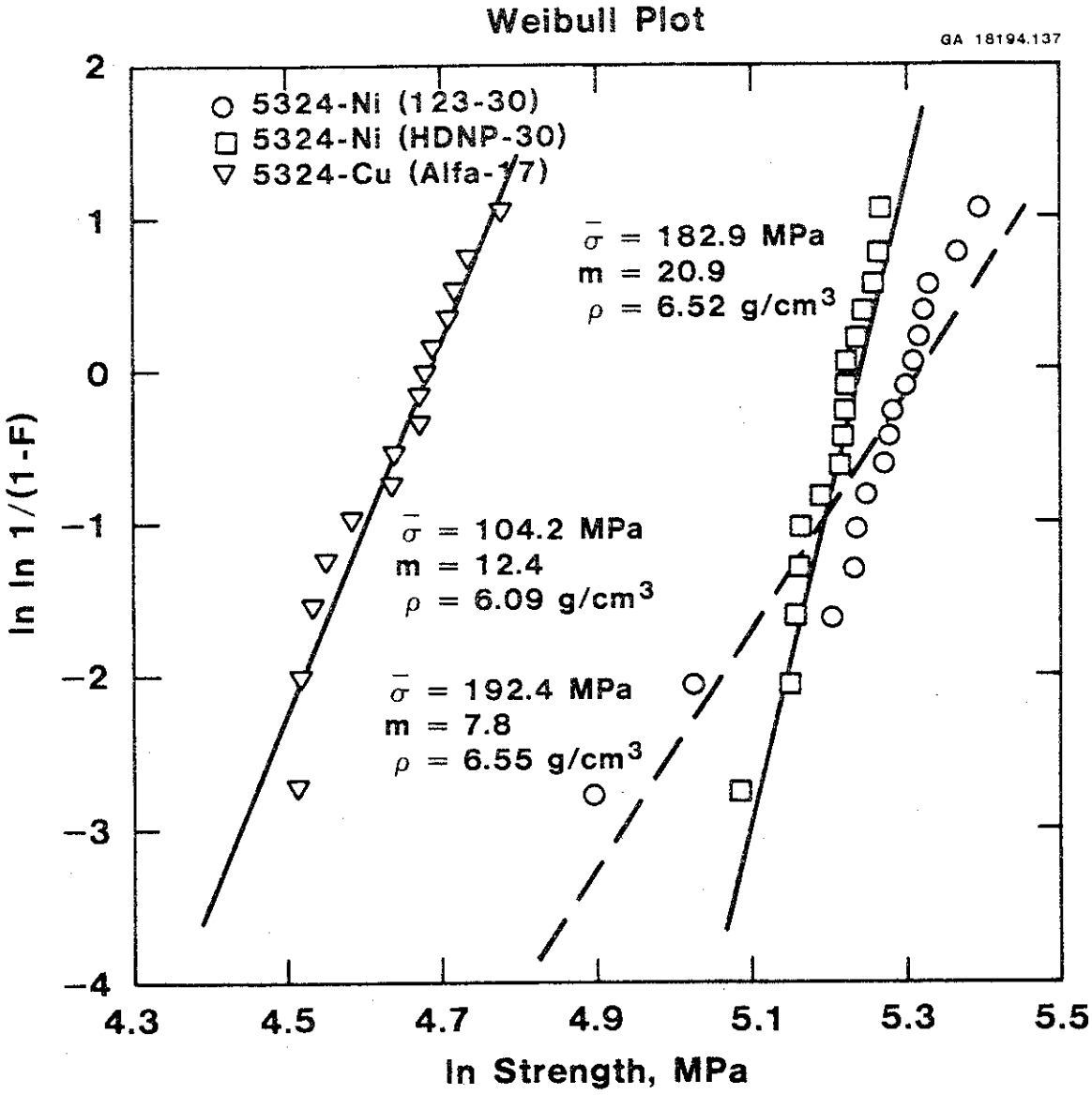

Inert Anode Strength, MOR-4PT, for Metal Added to 5324 Oxide Processed Materials

Figure 175

The test results, by this method, gave low values for fracture toughness as shown in Figure 176. Fracture toughness increases with temperature for the 5324 oxide inert anode. It was expected that the cermet would have a higher fracture toughness than the 5324 oxide. Therefore, a second method of determining fracture toughness, K_{Ic}, was completed using the short-rod technique. The specimen configuration consists of a short rod 12.5 mm in diameter which is 2/3 of its length, with longitudinal slots that form a V-shaped region. A load is applied within the slot, causing a crack to initiate at the point of the V. Increasing load advances the crack until the crack reaches a critical length, where the load reaches a maximum. The maximum load is used to calculate K_{Ic} from the equation (89):

$$K_{Ic} = \frac{AF_c}{B^{3/2}(1-\nu^2)^{1/2}} \qquad (83)$$

where A is a dimensionless constant (20.8 ± 1.0), F_c is the maximum load applied to the specimen, B is the specimen diameter, and ν is the Poisson's ratio.

The fracture toughness of the Ni-cermet inert anode increases with increasing metal content as is shown in Figure 177. This result is expected because the metallic particles or stringers are ductile and the crack can circumvent the ductile particles leaving a continuous metallic stringer between the crack faces, resulting in a toughening effect because these metallic stringers would tend to resist crack opening (90). According to Evans et al. (90), increased yield stress, ductility, and particle diameter of the metallic phase will lead to increased fracture toughness.

d. Young's Modulus

Figure 178 illustrates Young's moduli of 6846 cermet and 5324 oxide inert anode bars vs. temperature. Again, Young's modulus is dependent upon density and the condition of the microstructure of the bars tested. The reduced and partially reduced microstructures of 6846 show

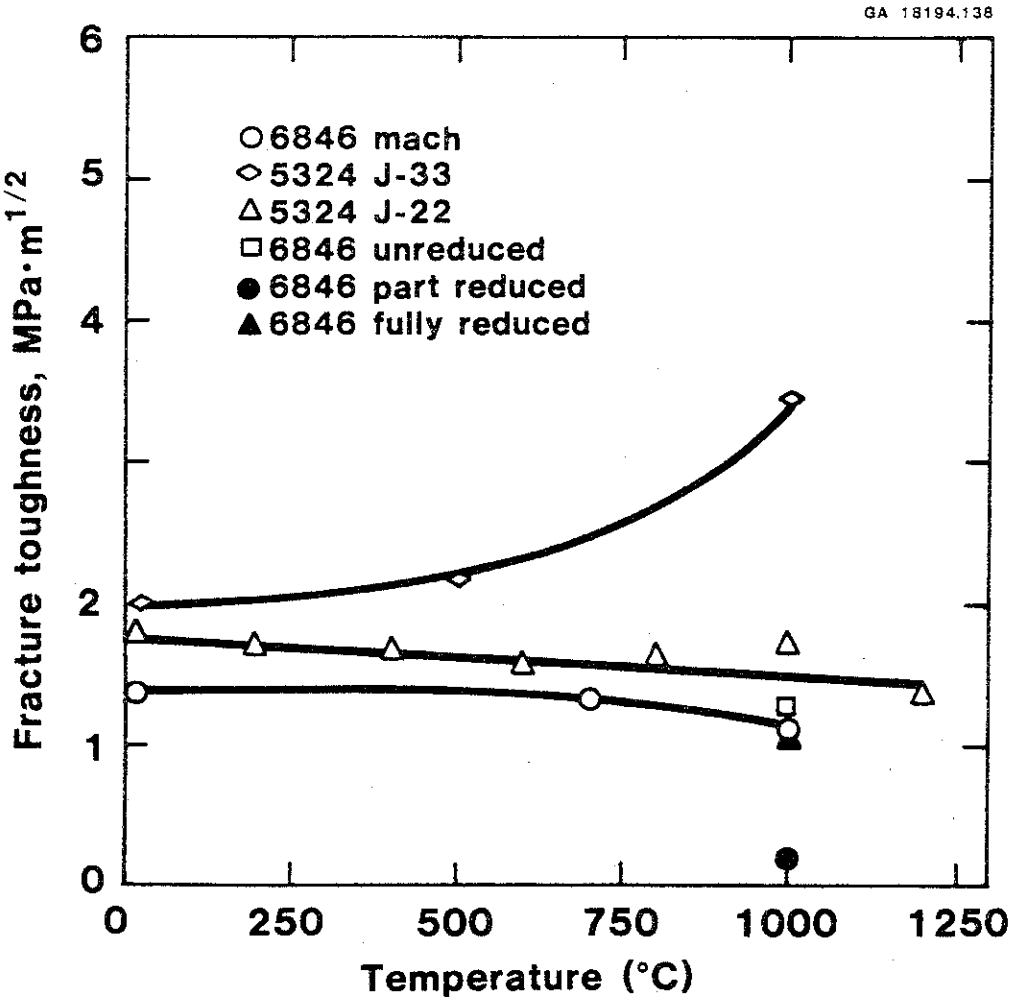

Fracture Toughness of 5324 and 6846 Cermet Bars Versus Temperature

Figure 176

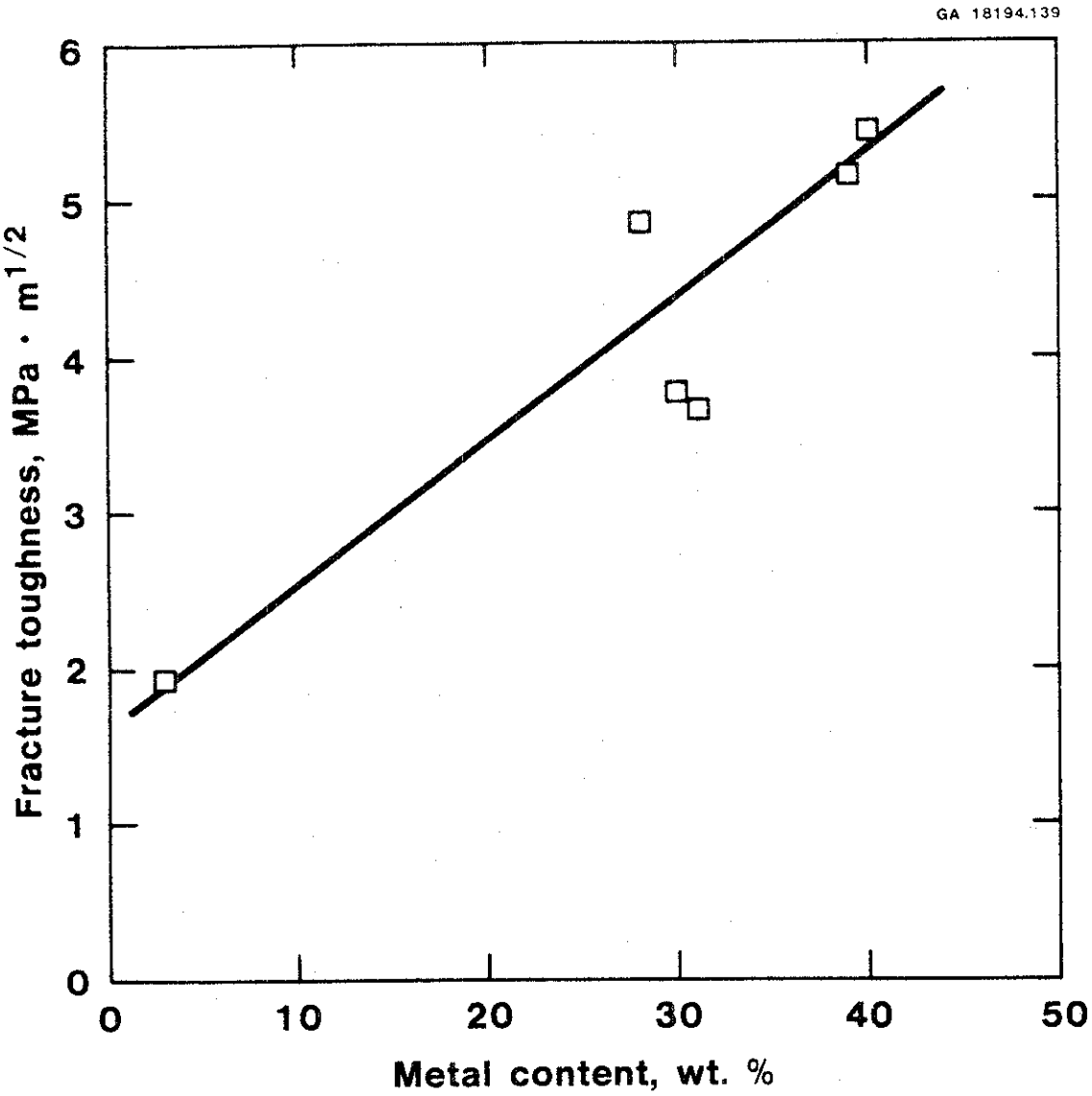

Fracture Toughness of Inert Anode Material Versus Metallic Phase Content

Figure 177

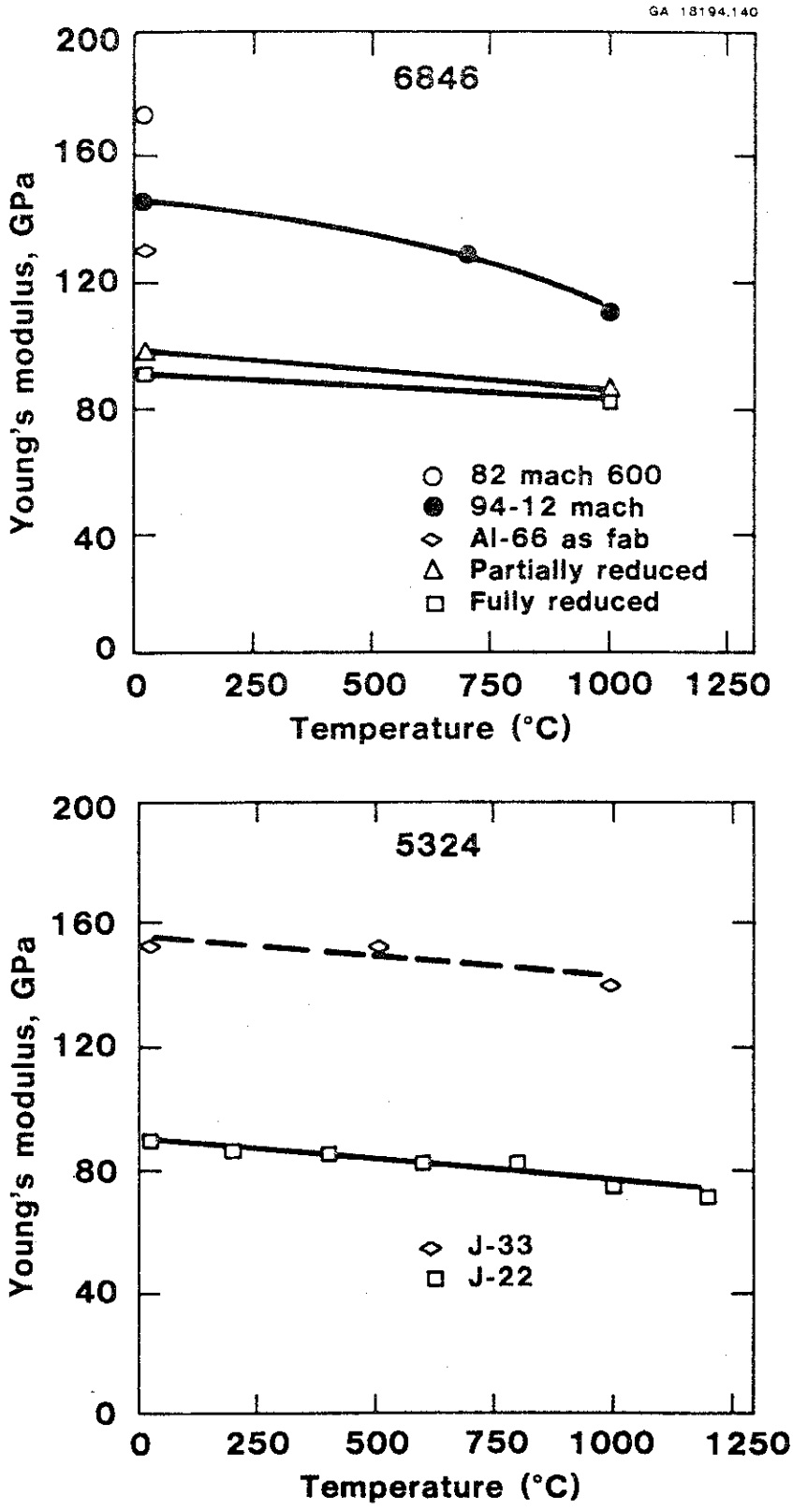

Youngs Moduli of 6846 Cermet and 5324 Oxide Inert Anode Bars Versus Temperature

Figure 178

significantly lower Young's modulus than those for the machined 94-12 6846 composition material because of porosity produced during reduction. The Young's modulus for the 5324 oxide material varies from ~90 to 150 GPa for the 75 and 90 percent theoretically dense materials, respectively. As with strength, elastic properties decrease with temperature for these materials.

e. Other Mechanical Properties

Tensile strength, compressive strength, fatigue, creep, and hardness properties were not determined for inert anode materials during the course of this contract.

4. Thermal Properties

a. Thermal Expansion

Thermal expansion data are needed for all components of the inert anode assemblies to be used in Hall cells. These data are necessary for the design of inert anode shapes, compatibility with the metallic conductor leads for connections, and thermal cycles to be used for heat up, transfer and operation in the Hall cell.

A dilatometer[a] was used to measure thermal expansion of inert anode and inert anode connection materials up to 1100°C. Thermal expansion results were presented in earlier reports for the 5324 oxide inert anode (3), connection components (3), and 6846 cermet inert anodes (6). Additional data have been obtained for the NiO-$NiFe_2O_4$ 5324 plus 17 percent copper composition.

Expansion data for the 5324, 6846, and 5324-17 Cu compositions are listed in Table 61 and plotted as percent expansion vs. temperature in Figure 179. These data show the expansions of the Ni and Cu cermet

---

[a] Netzsch Brothers, Inc., Lionville, PA -- Model 402 E/3/XY

Table 61

Thermal Expansion - Inert Anode Compositions

Temperature °C	% exp. 5324	% exp. 5324	% exp. 5324-Cu
20	0.000	0.00	0.000
100	0.069	0.04	0.085
200	0.173	0.15	0.194
300	0.295	0.28	0.326
400	0.414	0.43	0.464
500	0.538	0.61	0.604
600	0.677	0.78	0.762
700	0.798	0.94	0.903
800	0.917	1.06	1.032
900	1.036	1.18	1.174
1000	1.165	1.39	1.338
1100	1.287	1.79	1.553
Coefficient of Expansion α, 10^{-6} cm/cm°C			
RT-500°C	11.21	12.71	12.58
RT-1000°C	11.89	14.18	13.65
RT-1100°C	11.92	16.57	14.38

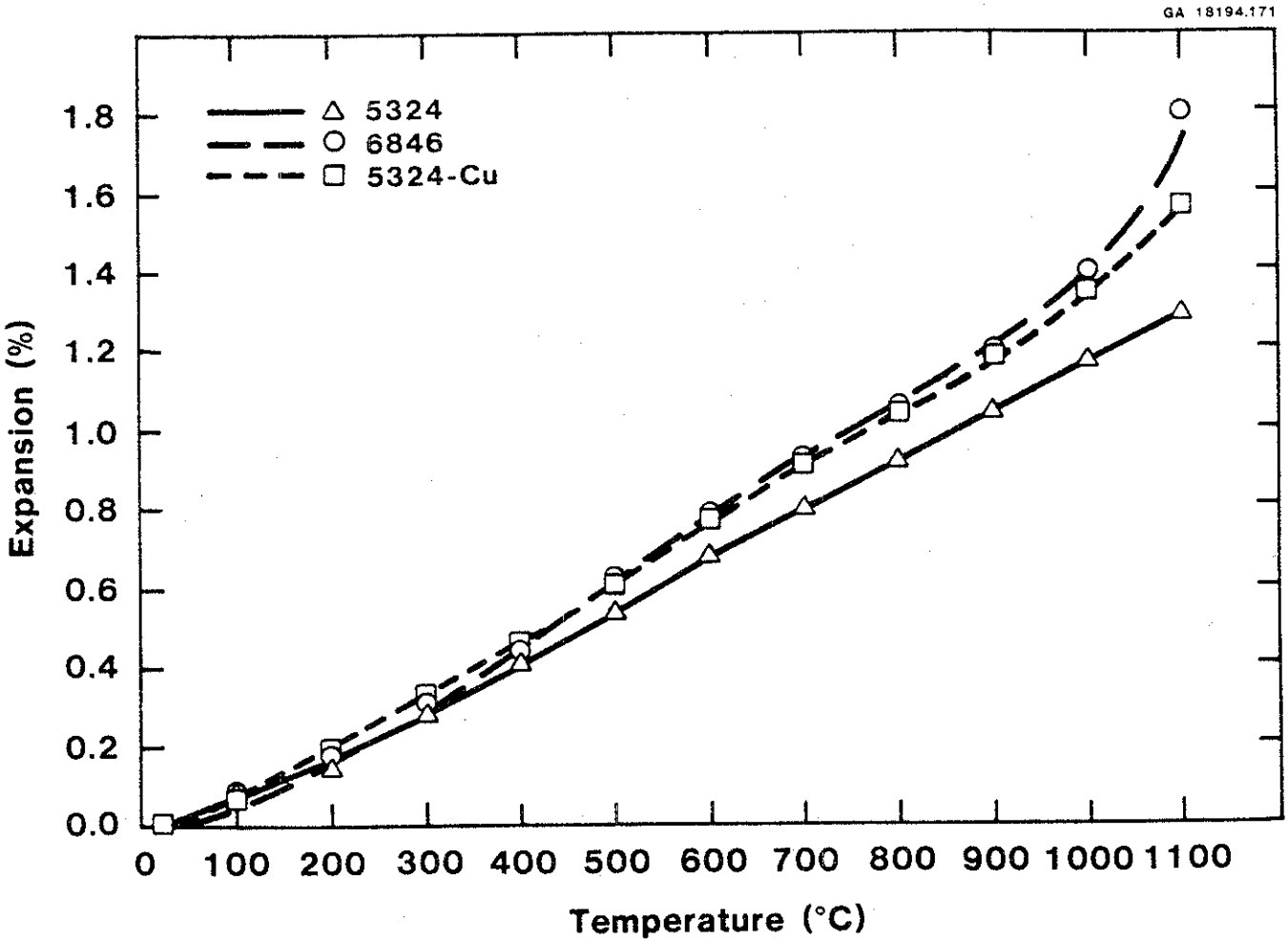

Thermal Expansion - Inert Anode Compositions
Figure 179

materials to be greater than the oxide composition because of the metallic content. Expansion coefficients between room temperature and 1000°C were 11.9, 14.2 and 13.6 cm/cm/°C, respectively, for 5324, 6846, and 5324-17 Cu. Note the sharp upturn in expansion for the cermet materials above 1000°C. Previous studies (6) have shown that the thermal history, metallic content, and microstructural features of the cermet inert anode materials will affect thermal expansion results of cermet materials.

Inspection of the thermal expansion curves indicates a decrease in slope at or near the Curie temperature for these ferrite materials. These temperatures are 580°C for the 5324 composition and about 680°C for the Ni and Cu cermet materials. The 5324 oxide Curie temperature results are similar to those reported by Buessem and Dorf (91) for nickel ferrite.

b. Thermal Conductivity

The thermal conductivity of inert anode materials is needed information for design of anodes and anode connections. This information is useful for the calculation of stresses developed in parts during heat-up, operation, cool down, and unexpected temperature excursions. Since thermal diffusivity is easier to determine, experimentally, than thermal conductivity, thermal diffusivity was determined for the calculation of thermal conductivity values. Thermal diffusivity measurements were made on small (11 mm diameter) disks, 2.8 mm thick. The disks were surface ground flat and parallel. The oxide (5324) and Ni-cermet (6846) compositions were characterized.

Thermal diffusivity was measured by the laser-pulse technique. The time-temperature response on one face of a disk specimen, to a short-duration heat pulse on the opposite face is used to derive the diffusivity value. These measurements are performed at a number of temperatures up to 1000°C to establish a temperature-diffusivity curve. The measurements were conducted in a helium-backfilled evacuation chamber held at a nominal one atmosphere of pressure. Accuracy is

estimated to be ±3 percent. Thermal diffusivity data are shown in Figure 180.

Specific heat values are needed for each of the inert anode materials in order to complete the calculation of thermal conductivity values. The specific heat can be approximated by using the specific heat values for the compounds present in the sintered anodes and calculation of specific heat by the law of mixtures. The specific heat values for Ni, NiO, and $NiFe_2O_4$ were obtained from the literature (92-94).

The specific heat of a material rises to a maximum at its Curie temperature. The Curie temperatures for Ni, NiO, and $NiFe_2O_4$ are 358, 250, and 580°C, respectively.

Thermal conductivity can be calculated from the thermal diffusivity and specific heat values. The relationship between thermal conductivity and thermal diffusivity is given as:

$$\lambda = \alpha \rho Cp \qquad (84)$$

where: λ = thermal conductivity
α = thermal diffusivity
ρ = density
Cp = specific heat

Calculated thermal conductivity results based on the measured thermal diffusivity results are shown in Figure 181. Note that the thermal conductivity results for 6846 are higher than for 5324 at higher temperatures, as would be expected because of its Ni-Fe alloy phase content. These results are comparable to similar materials reported in the literature for NiO, Fe_3O_4 and a Ni-$ZnFe_2O_4$ ferrite (92-94).

5. Other Properties

The electrical properties have been reviewed in the development and sections of this report; the physical and microstructural properties will be reviewed in the fabrication section.

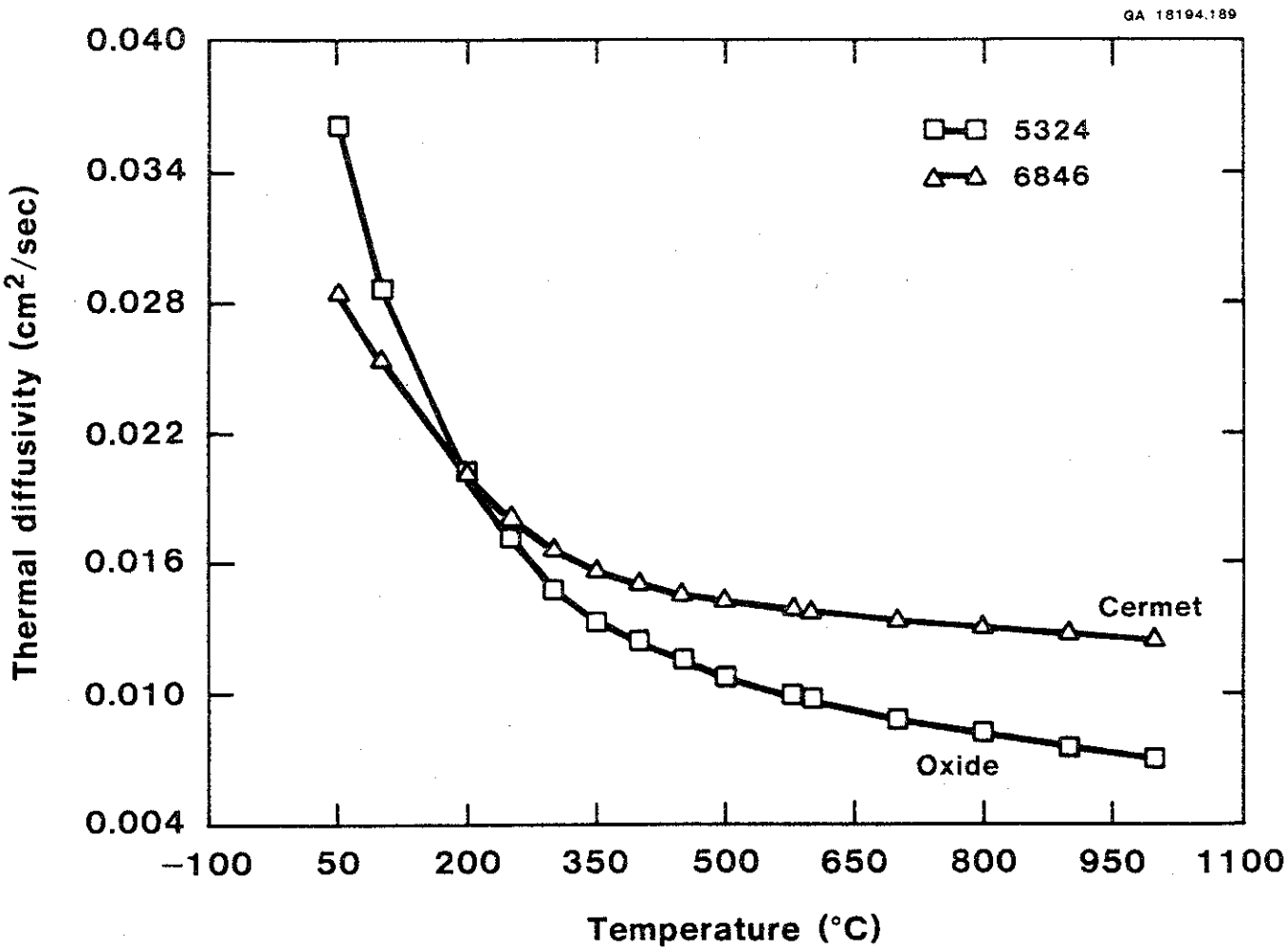

Measured Thermal Diffusivity of Oxide and Cermet Inert Anodes

Figure 180

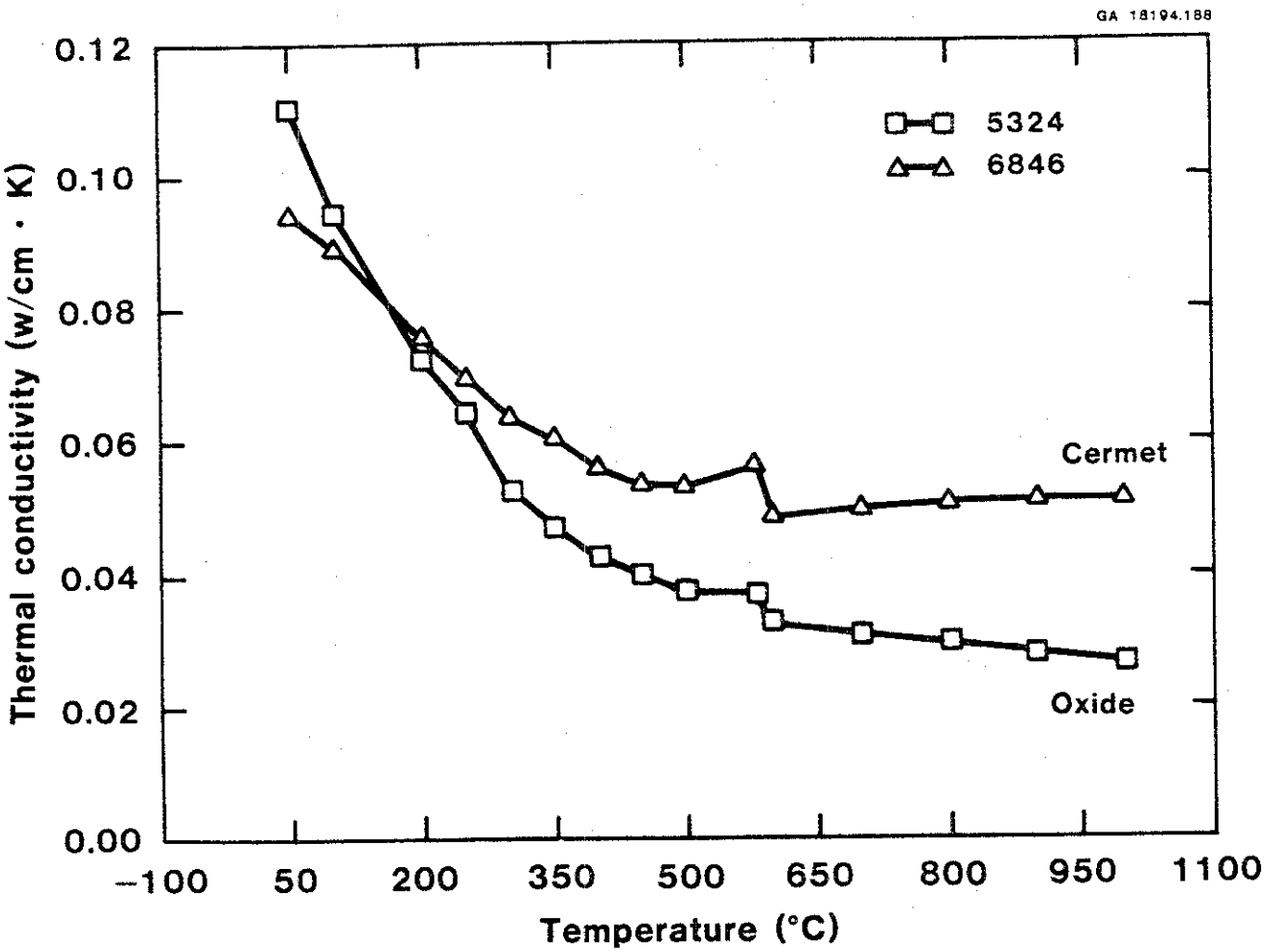

Calculated Thermal Conductivity of Oxide and Cermet Inert Anodes

Figure 181

IV. PHASE II - ANODE FABRICATION STUDIES

1. Objective

The successful fabrication of commercial sized inert anodes for application in 2500- to 20,000-ampere Hall electrolysis cells was the primary objective of this phase of the cooperative agreement. The materials and methods of manufacturing were to be readily available and economically feasible. The manufactured inert anodes were to be usable by "retrofit" into existing Hall cell designs.

2. Introduction

The sizes of carbon anode solid electrodes presently in use in commercial sized Hall cells range from 38 cm wide by 51 cm long by 38 cm high to 66 cm wide by 124.5 cm long by 51 cm high. The fabrication of inert anodes to these same sizes from dense ceramic or cermet materials was envisioned to be a very difficult task because the manufacturing of similar sized solid electrodes has not been reported in the literature. However, review of the literature indicates that large shapes have been manufactured from oxide ceramics. Technical, fine grained, hollow cylinders 50 cm diameter by 46 cm length with a 2.5 cm thick wall have been made from a 95 percent alumina body by isostatic pressing and pressureless sintering. In addition, solid cylinders 23 cm diameter by 180 cm length have also been fabricated by a similar process. Larger shapes, 61 cm diameter by 244 cm long, have been manufactured from an insulator body containing clay and coarser grained alumina and silica by extrusion, careful humidity drying, and pressureless sintering (95).

Large ceramic shapes produced by several refractory companies are often fine grained mixtures of alumina, zirconia and silica. It has been reported that large refractory wall blocks up to 500 cm long have been produced by a slip casting method (96). Another manufacturer produces large alumina blocks up to 34 by 46 by 249 cm by isostatic pressing (97). In addition, large SnO_2 electrodes for glass tank melting have been manufactured by isostatic pressing and sintering (98).

Alcoa investigated manufacturing methods for the production of inert anodes from various oxide compositions before the cooperative agreement was initiated (99). A specific composition investigated was designated as 5324 and consists of 70 mole percent NiO and 30 mole percent Fe_2O_3 (48.3 wt.% Fe_2O_3, 51.7 wt.% NiO). The binary phase equilibria diagram (100) showing this composition is illustrated in Figure 182. The dependent variables studied during this investigation included the sintered anode physical properties of density, apparent porosity, and water absorption. The independent variables covered raw material powder characteristics including crystallite size, size distribution, surface area, and agglomerate size; green pressing parameters; and sintering conditions awhich included time and temperature settings. The investigation led to the recommended manufacturing conditions set forth in the process flow diagram illustrated in Figure 183.

Therefore, based on experience reported in the literature and on previous Alcoa investigations, the manufacturing methods used to fabricate inert anodes for testing in the 60- and 2500-ampere Hall cells were selected from conventional methods commonly practiced by the ceramics industry.

The fabrication studies conducted under the cooperative agreement included raw material selection, powder preparation methods, cold and hot pressing conditions, pressureless sintering conditions, pressure sintering parameters, sintered physical and thermal properties, microstructure, and post-Hall-cell-test evaluations.

Initial evaluations were of the oxide composition 5324. However, the high electrical conductivity level of the oxide composition at operating conditions existing in the electrolysis cell resulted in large voltage drops through the anode. These voltage drops could not be avoided because of the thickness of anode necessary for the corrosion losses anticipated during anode operation. A cermet anode material (15), composition 6846, was developed with electrical conductivity levels similar to anode carbon and the majority of the cooperative agreement fabrication parameters were developed on the 6846 cermet composition.

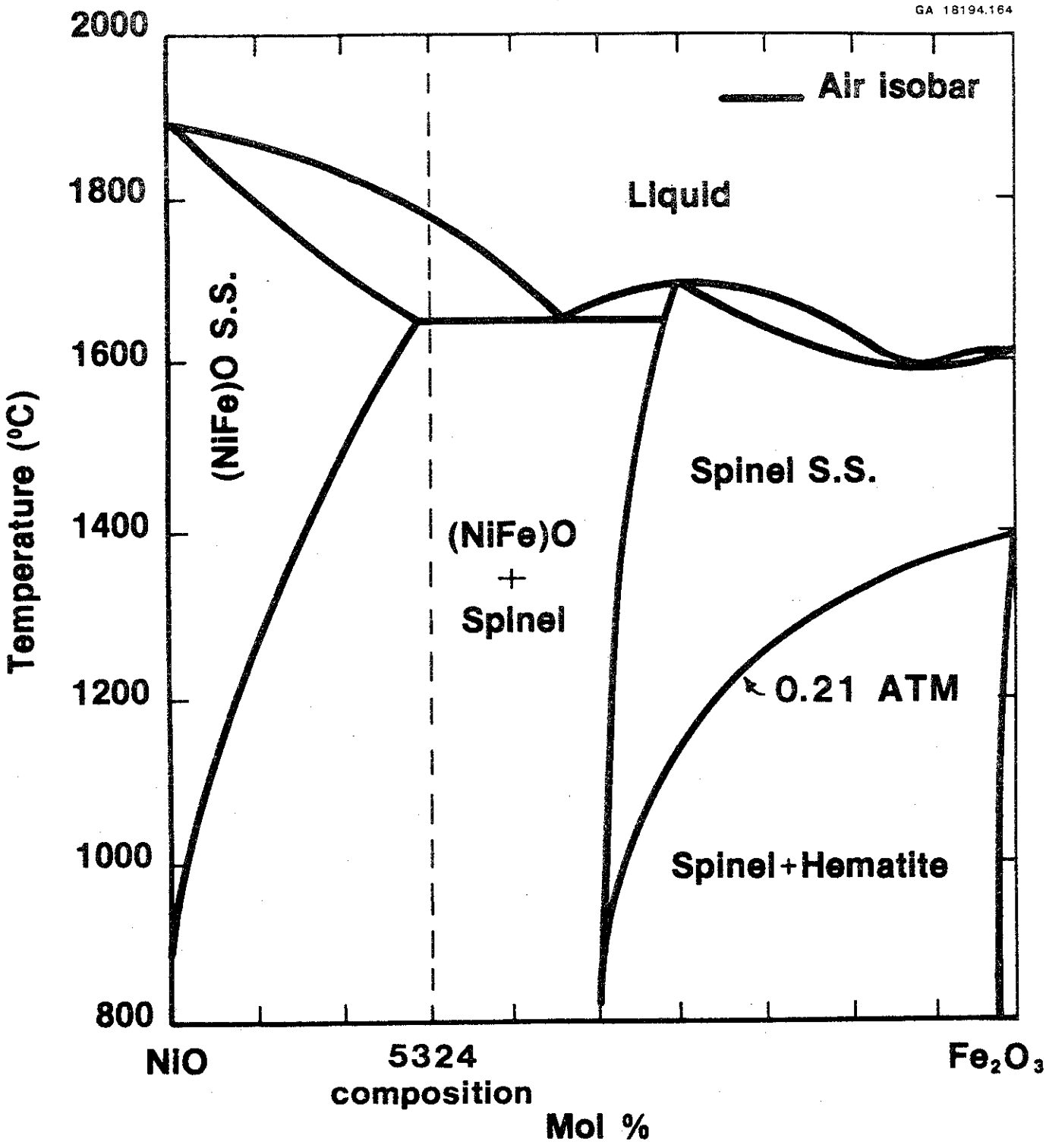

NiO-Fe_2O_3 Phase Diagram (Ref. 100)
Figure 182

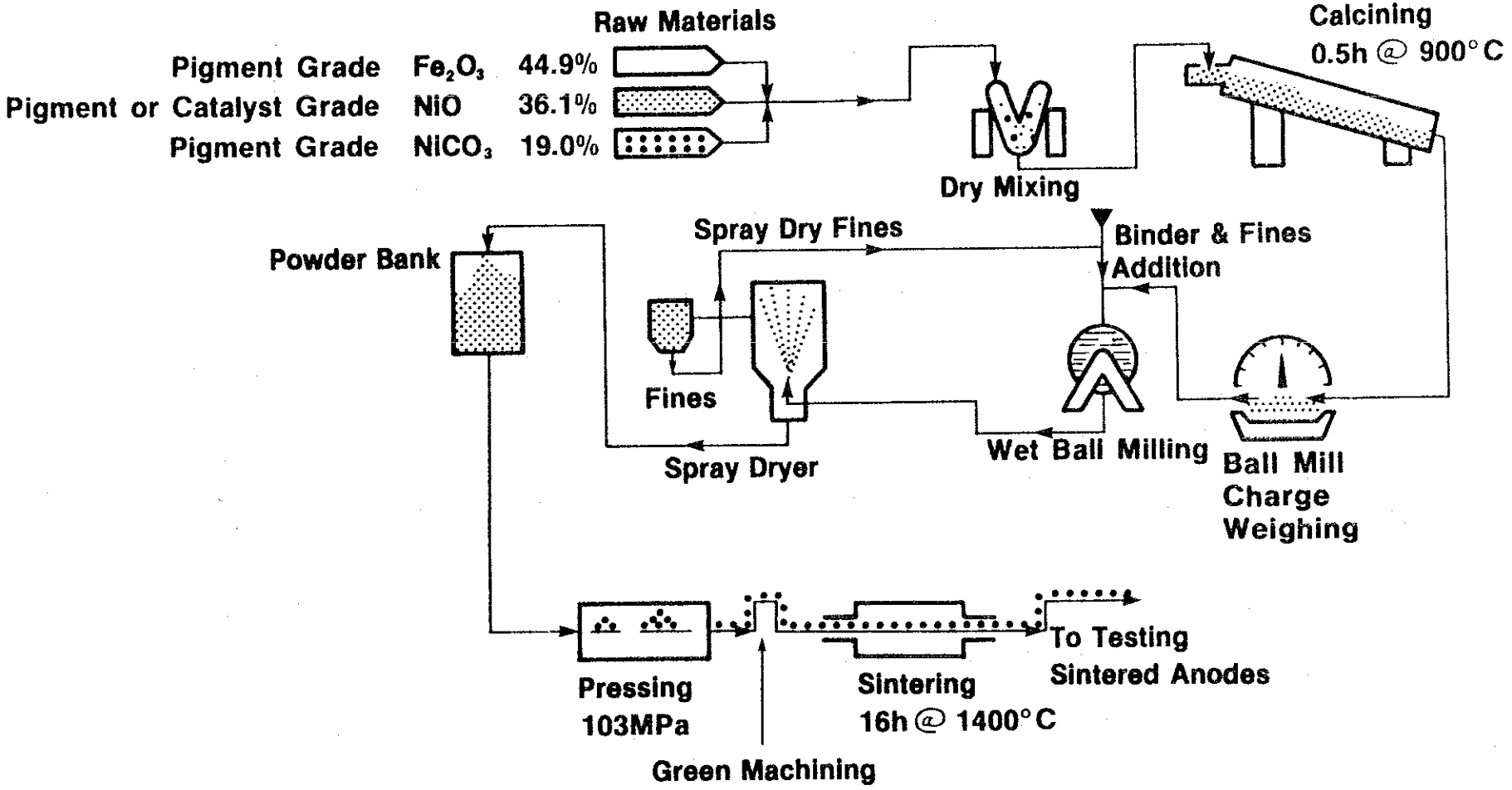

Oxide Inert Anode Fabrication Process
Figure 183

3. Experimental Procedures

a. Compositions and Materials

The initial compositions formulated for the production of inert anodes consisted of the following amounts of raw materials in weight percent:

Formulation	Designation
48.3% Fe_2O_3, 51.7% NiO	5324
20.0% Fe, 60.0% NiO, 20.0% Fe_3O_4	6846
17.0% Cu, 42.9% NiO, 40.1% Fe_2O_3	5324 + 17% Cu

The 5324 and 6846 composition locations are shown in Figure 184 within the Ni-O-Fe phase equilibrium diagram at 1000°C in air (37). The phase relations for the inert anode compositions vary slightly from the diagram shown in Figure 184 because the fabrication temperatures (1300-1400°C) and atmosphere (10^{-4} pO_2) vary from the conditions used to construct the equilibria shown in Figure 184.

In addition to the raw materials listed in the formulations above, Ni and $NiCO_3$ were major ingredients studied in the fabrication of test anodes. Commercially available and economically feasible raw materials were obtained from various processes and vendors who supply the ferrite, pigment, powder metallurgy, and ceramic part manufacturing industries. As-received raw materials were evaluated for particle size distribution, surface area, chemical purity, availability, and cost. In addition, raw materials were evaluated in the final fabricated anode for their effect on sintered bulk density, porosity, microstructure, phase development and performance in 60- and 2500-ampere electrolytic Hall cell tests.

b. Powder Preparation

Powder preparation processes investigated during the experimental

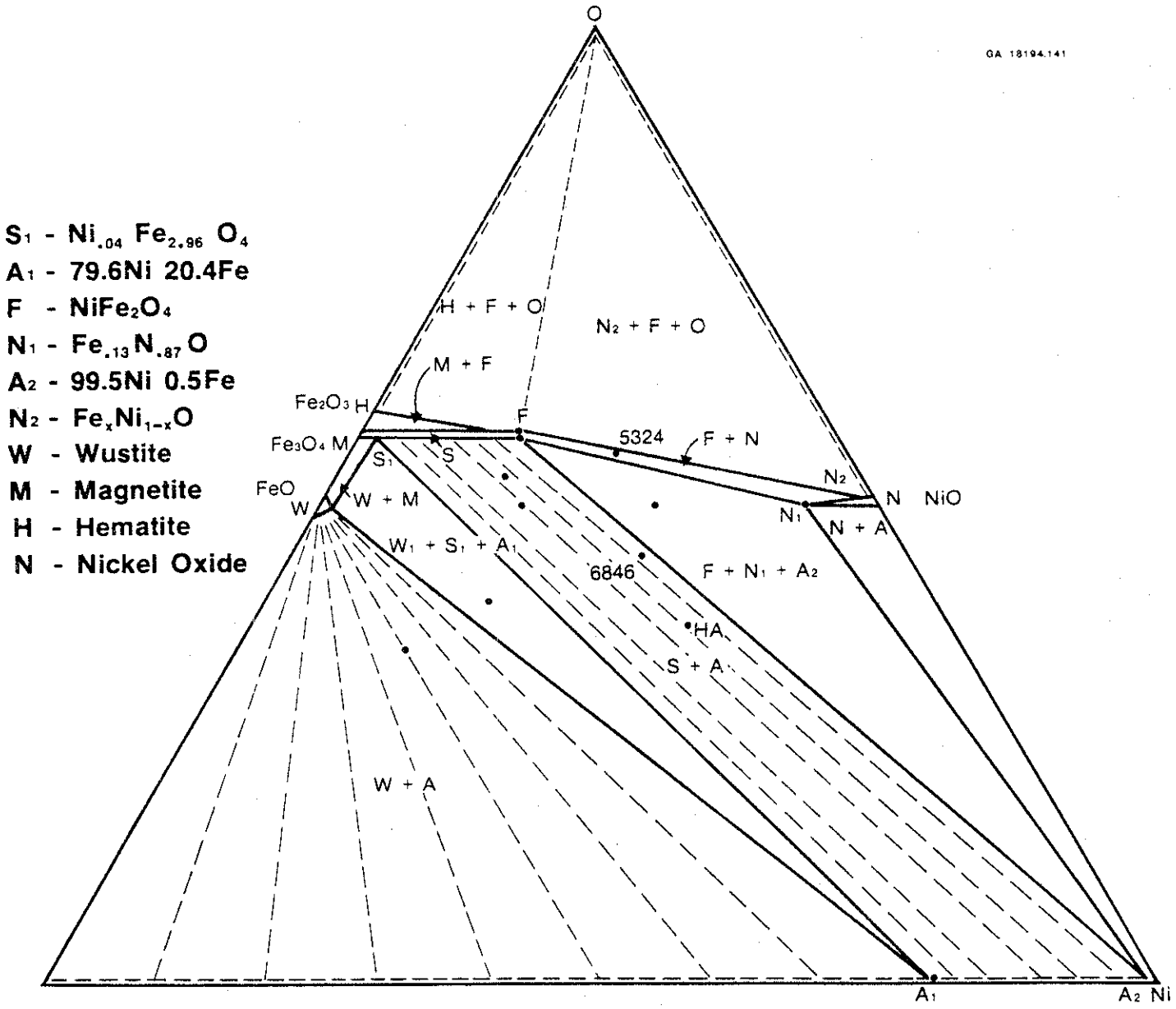

Ni-O-Fe System at 1000°C. (Ref. 37)
Figure 184

program included blending, grinding, calcining, and agglomeration. Raw materials were dry batched and blended in 'V' shaped blenders[a] with an intensifier bar for intimate mixing.

As-received raw materials and mixed calcined powders were ground, if necessary, to make the powders more reactive to produce dense sintered inert anodes for testing. Powder grinding was completed by use of ball mills[b] and fluid energy mills[c].

Batch calcinations were conducted at temperatures ranging from 800 to 1100°C to react the raw materials and create the NiO, $NiFe_2O_4$, and Ni alloy phases present in the final sintered body.

Agglomeration studies were conducted to produce free flowing powder for cold compaction into shapes by uniaxial or isostatic pressing. These pressed shapes were then machined in the green state before sintering. Therefore, the agglomerated powder was prepared with a binder added to give green strength to the cold compact for machining and handling. Agglomeration was conducted by pan pelletizing[d] and by spray drying[e]. Both open and closed system spray dryers were used to produce free flowing pressable powder. Closed system spray drying was necessitated by the readily oxidizable iron metal present in the 6846 cermet compositional mixtures. The spray drying conditions used in the open and closed systems are listed in Table 62. The open spray dryer was used for preparation of 5324 and calcined (reacted) 6846 powders. The closed system was used to spray dry the as-mixed 6846 cermet composition. Spray dried powders were evaluated for flowability, poured and tapped bulk densities, and agglomerated particle size distributions. An example of a closed system spray dryer system used to prepare cermet powders is illustrated in Figure 185.

---

a V Blenders, Patterson-Kelly Co., East Stroudsburg, PA
b Ball Mills, Norton Co., Akron, OH
c Micronizer Fluid Energy Mill, Sturtevant Mill Co., Boston, MA
d Lab Pelletizer, Eirich Machines, Inc., New York, NY
e NA C-1 and Na S-12.5 Spray Dryers, Niro Atomizer Inc., Columbia, MD

TABLE 62

Spray Drying Conditions To Produce
6846 Compositions Inert Anode Powder for Pressing

Model No.	NA C-1	NA C-1	NA S-12.5
System	Closed	Closed	Open
Material	Fe + NiO + Fe_3O_4	Fe + NiO + Fe_3O_4	Ni + $NiFe_2O_4$ + NiO
Feed			
Carrier	Isopropyl Alcohol	Isopropyl Alcohol	Water
% Solids	72.4	71 - 73.7	61.3 - 64
Rate, kg/h	136	145 - 150	80 - 87
Binder, wt. % Solids	1	1	1.5
Binder	Polyvinyl Butyral	Polyvinyl Butyral	Polyvinyl Alcohol
Atomization			
Nozzle	SO 1.2	SF 1.1-SF 1.2	SC 1.0
Nozzle Pressure, psig (MPa)	150 (1.03)	120-150 (.83-1.03)	20-250 (1.52-1.72)
Drying Conditions			
Process Gas Rate, kg/h	990	1080	1350
Inlet Gas Temperaure, °C	112	120 - 127	200
Outlet Gas Temperature, °C	79	77 - 85	100
Condensor Outlet Gas Temperature, °C	30	27 - 29	-

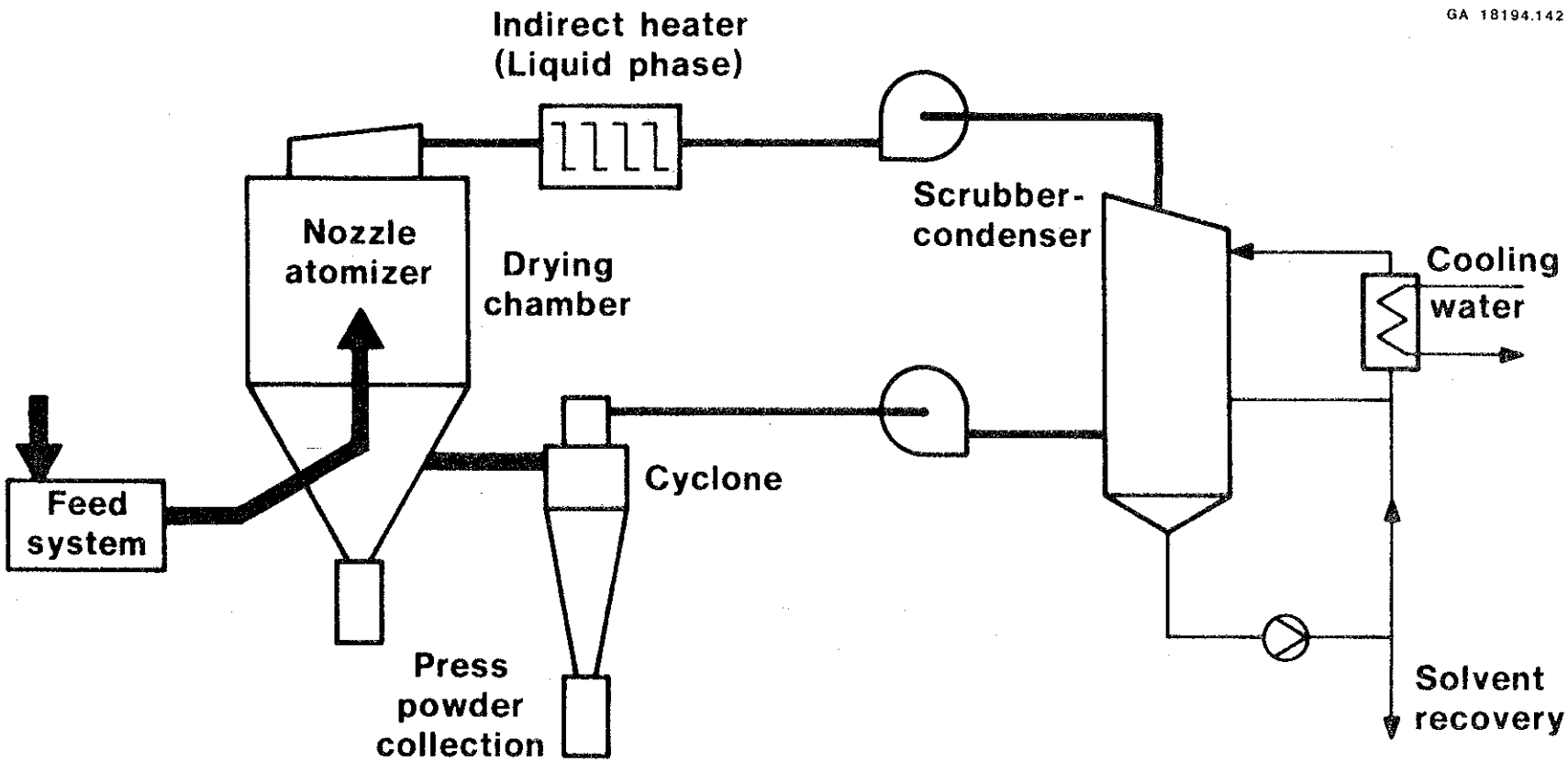

Closed System Spray Dryer Schematic

Figure 185

c. Consolidation Studies

Binders were selected on the basis of compatibility with the liquid carrier for spray drying, green strength development in the pressed compact, defect-free compacts after pressing, compact green densities, ease of removal during processing, and final compact sintered densities.

Inert anode shapes were formed by isostatically pressing and green machining. Consolidation pressures of 100 to 200 MPa were used with holding times of 15 seconds at pressure.

Thermal processing of the green anodes was conducted in controlled atmosphere furnaces using microprocessor controls on time and temperature. The sintered density of inert anodes versus the partial pressure of oxygen was studied. Argon and nitrogen gases and argon-oxygen, CO-CO_2, and CO_2-forming gas mixtures were used to obtain different partial pressures of oxygen. Sintering temperatures of 1250 to 1400°C were investigated. Holding times of two hours for small samples and four to eight hours on the larger anodes were used.

Other processing methods that were briefly investigated included hot pressing (HP) and hot isostatic pressing (HIP) at process temperatures of 900 to 1000°C.

d. Process Flow Diagram Investigations

The experimental program outlined above was designed to determine the optimum process flow paths for the production of dense inert anodes with the desired microstructural, electrical, and mechanical properties for use in Hall electrolytic cells. The process flow sequences and methods investigated, plus additional possible process flow methods not investigated, are shown in Figure 186. As illustrated in Figure 186, there are many process flow paths that can be followed in the production of inert anodes. Not all have been fully explored in this experimental program. Final fabricated inert

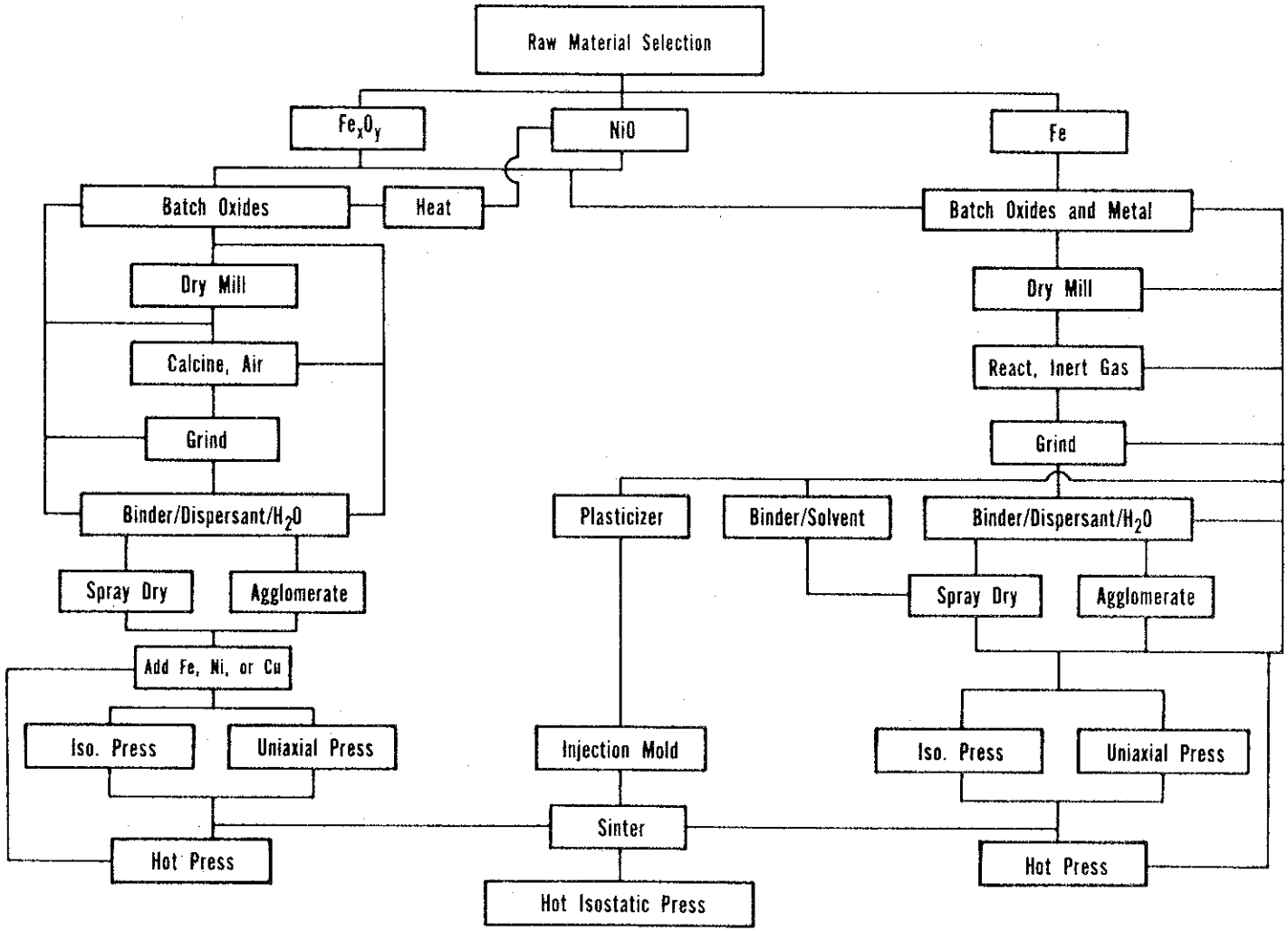

Possible Process Flow Paths for Production of Inert Anodes

Figure 186

anode properties are dependent on the process flow methods used, the conditions existing at each process flow step, and the sequence of process flow steps used. The results obtained using several different process flow methods and sequences will be explained later.

e. Property Evaluations

Final sintered density, porosity, microstructure, and thermal expansion characteristics were determined prior to Hall cell testing. Density and porosity were determined by ASTM Archimedes method C-373. Microstructures were obtained from polished sections using optical and scanning electron microscopes, microprobe for elemental X-ray dot maps and an image analyzer[a] for microstructural feature characterization. Inert anode compact thermal expansion and sintering shrinkage information was determined for design of inert anode structures and for connection development. Shrinkage data are important for determination of sintering cycles and temperatures. Other properties such as strength and elastic properties were presented in Phase I of this report.

4. Results and Discussion

Fabricated inert anodes studied and tested represented the products of the following reactions:

1. $Fe_2O_3 + NiO \rightarrow Ni_xFe_{3-x}O_4 + Ni_yFe_{1-y}O$ [5324] (85)

2. $Fe + Fe_3O_4 + NiO \rightarrow Ni_xFe_{3-x}O_4 + Ni_yFe_{1-y}O + Ni_zFe_{1-z}$ [6846] (86)

3a. $Fe_2O_3 + NiO \rightarrow Ni_xFe_{3-x}O_4 + Ni_yFe_{1-y}O$ [5324] (85)

3b. $Ni + Ni_xFe_{3-x}O_4 + Ni_yFe_{1-y}O \rightarrow Ni_xFe_{3-x}O_4 + Ni_yFe_{1-y}O + Ni_zFe_{1-z}$ [5324 + Ni] (87)

---

[a] Image Analyzer - Optomax, Inc.

4a. $Fe_2O_3 + NiO \rightarrow Ni_xFe_{3-x}O_4 + Ni_yFe_{1-y}O$ [5324] (85)

4b. $Cu + Ni_xFe_{3-x}O_4 + Ni_yFe_{1-y}O \rightarrow Ni_xFe_{3-x}O_4 + Ni_yFe_{1-y}O + (Cu,Ni,Fe)$ [5324 + Cu] (88)

Initial studies on oxide anodes showed that maximum corrosion resistance was obtained when excess NiO was used in reaction 85, resulting in a sintered anode having a composition of approximately 60 mole percent $Ni_xFe_{3-x}O_4$ and 40 mole percent $Ni_yFe_{1-y}O$. Cermet anodes can be produced by reaction sintering Fe with the oxides of iron and nickel (reaction 86) or by adding metal (either Ni or Cu) to the products of reaction 85 (reactions 87 and 88). One of the primary considerations in the fabrication process was to produce anodes with maximum density for increased corrosion and erosion resistance in the electrolytic cell environment.

a. Raw Material Selection

The selection of raw materials is important to the successful fabrication of inert anodes with maximum density, low impurity content, highest electrical conductivity levels, high strength, and desired microstructures. In general, it was determined that the raw materials used in the production of inert anodes must be one micron or less crystallite size for oxides and 20 microns or less for the metal particles used in cermets. Brief descriptions of the results obtained when various raw materials were used to fabricate $NiFe_2O_4$-NiO, Ni-$NiFe_2O_4$-NiO, and Cu-$NiFe_2O_4$ inert anodes for Hall cell testing follows.

1) $\underline{Fe_2O_3}$

Hematite powders of interest for inert anodes include those which are being used by the ferrite industry such as R-2900[a], a red iron oxide produced by the thermal decomposition of iron sulfate, and Sidmar 015[b], which is a spray roasted iron oxide

[a] R-2900, red iron oxide, Pfizer Inc., New York, NY

[b] 015, spray roasted iron oxide, Sidmar Maritieme, Staalnijverheid N.V.

produced from pickling liquors (acid ferrous chloride solutions) of steel industry by-product waste material. Analytical data on these powders are listed in Table 63. The surface areas range from 3 to 9 m^2/g and the median particle size is larger than 3 microns. However, the individual crystallites are less than one micron. The spray roasted powders are broken remnants of the spherical shells produced during the spray roasting and must be broken down by grinding to distribute uniformly in the inert anode mixture. Figure 187 illustrates the R-2900 and 015 materials. No significant differences were seen in final sintered densities when these two powders were used with similar raw materials in the formulations. Significant differences in microstructure, strength, and electrical properties were not evident in the results when anodes fabricated from the two Fe_2O_3 powders were compared.

2) $\underline{Fe_3O_4}$

Both natural and synthetic magnetite are available for use in inert anode compositions. For example, BK-5000[c], a synthetic, and MO-8029[d], a natural magnetite, are listed in Table 63 along with several other magnetite powders. Surface areas range from 2 to 9 m^2/g and median particles are 3 to 5 microns. The crystallites are submicron as shown in Figure 188. Sintered cermet anodes made with MO-8029 had slightly lower densities than those made with BK-5000. The impurity levels, indicated by Table 63 for these powders, ranged from about 0.7 to 1.2 wt.%. The source of magnetite did not affect the sintered microstructure. All of the hematite powders listed are usable as raw materials for inert anodes.

---

c BK-5000, natural magnetite, Pfizer Inc., New York, NY
d MO-8029, synthetic magnetite, Pfizer Inc., New York NY

TABLE 63

Inert Anode Raw Material Powder Properties - Oxides

Material	Fe_2O_3	Fe_2O_3	Fe_2O_3	Fe_3O_4	Fe_3O_4	Fe_3O_4	Fe_3O_4	Fe_3O_4	NiO	NiO	NiO	NiO	NiO	$NiCO_3$
Designation	R-2900	015	I-1039	BK-5000 Synthetic	MO-8029 Natural	Fine Ox 1000	4498 Natural	I-1062	N-139 Green	N-135 Black	Novamet Green	Black	N-1093 Green	
Supplier	Pfizer	Sidmar	Cerac	Pfizer	Pfizer	Bethlehem Steel	Pfizer	Cerac	Ceramic Color & Chem.	Ceramic Color & Chem.	Inco	United Catalyst	Cerac	Ceramic Color & Chem.
Surface Area, m^2/g	9	3	6	8	6	2	4	9	2	70	-	27	1	-
Particle Size, µm*	Micro	Micro	Micro	Micro	Micro	Micro	Micro	Micro	Micro	Micro	-	Micro	Micro	-
90% Less than	5.7	54.2	5.2	5	5.2	10.9	13	35	13	29	-	27	50	-
50% Less than	3.4	19.0	3.2	3	3.4	4.8	4.8	3.4	6.2	15.2	-	13.4	18	-
10% Less than	2.2	3.5	1.9	1.9	2.1	2.4	2.5	1.8	1.8	7.2	-	6.5	3.4	-
Chemical Analysis**	Spect	Spect	Spect	AA	AA	AA	Spect	Spect	AA	Spect	Spect	Spect	Spect	Spect
Element, wt.%														
Al	.01	.01	.01	.03	.34	.023	.3	.06	.082	.00	.01	.06	.06	-
B	-	-	-	-	-	-	-	-	<.005	-	-	-	-	4
Ca	.04	.01	.05	.20	.06	.012	.07	.2	.066	.1	.01	.02	.03	.02
Co	-	-	-	-	-	-	.01	-	.085	.2	-	.2	.3	.03
Cr	.01	.01	.03	-	-	-	.03	.05	<.005	.02	.00	.02	.01	.01
Cu	-	.01	.00	<.01	<.01	-	.02	.01	<.005	.00	-	.02	.02	.02
Fe	Major	Major	Major	66.2	68.2	74.2	Major	Major	.017	.01	.00	.4	.06	-
Mg	.00	.00	.00	.1	.03	.002	.2	.03	.13	.1	.00	.02	.03	.2
Mn	.01	.1	.01	.47	.03	.68	.01	.2	<.005	.00	-	.00	.00	-
Na	-	.01	-	.06	-	.006	.09	.1	-	-	-	-	-	.2
Ni	-	.02	.02	.01	<.01	<.009	.1	.06	77.5	Major	Major	Major	Major	Major
Pb	-	.01	.01	<.01	.07	-	.01	.01	-	-	-	-	-	-
Si	.00	.01	.00	.02	.07	.00	.3	.01	.20	.1	.00	.03	.03	.04
Tl	-	-	-	<.01	.06	.06	.05	-	-	-	-	-	-	-
Zr	-	-	-	-	-	-	-	-	-	-	-	-	.03	.02

* Micro = Microtrac
Sedi = Sedigraph
** Spect = Qualitative Spectrographic Analysis - Values accurate within factor of 3
AA = Atomic Absorption Analysis

GA 17817.10

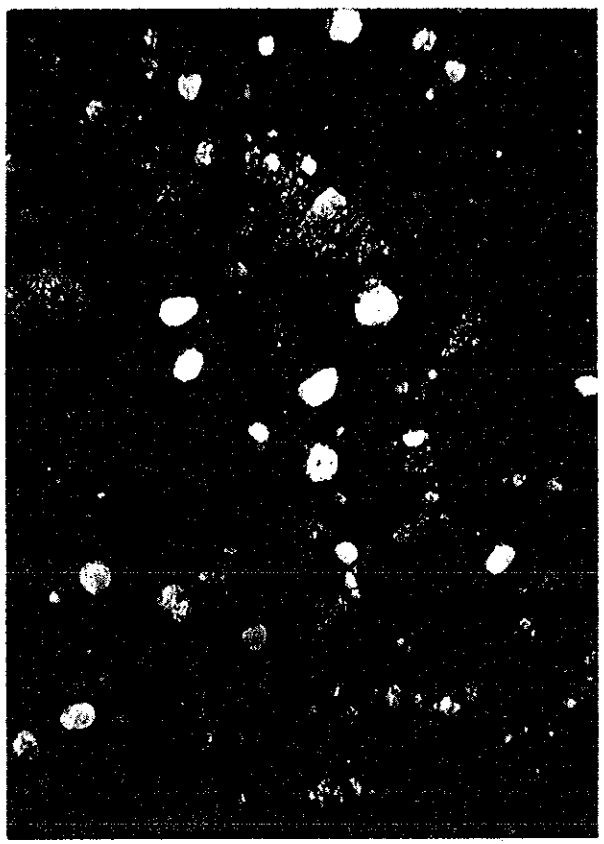

400X 25μm

400X 25μm

Powder: Fe_2O_3
Source: Pfizer
Designation: R-2900

Powder: Fe_2O_3
Source: Sidmar
Designation: 015

Fe_2O_3 Raw Materials
Figure 187

GA 17817.9

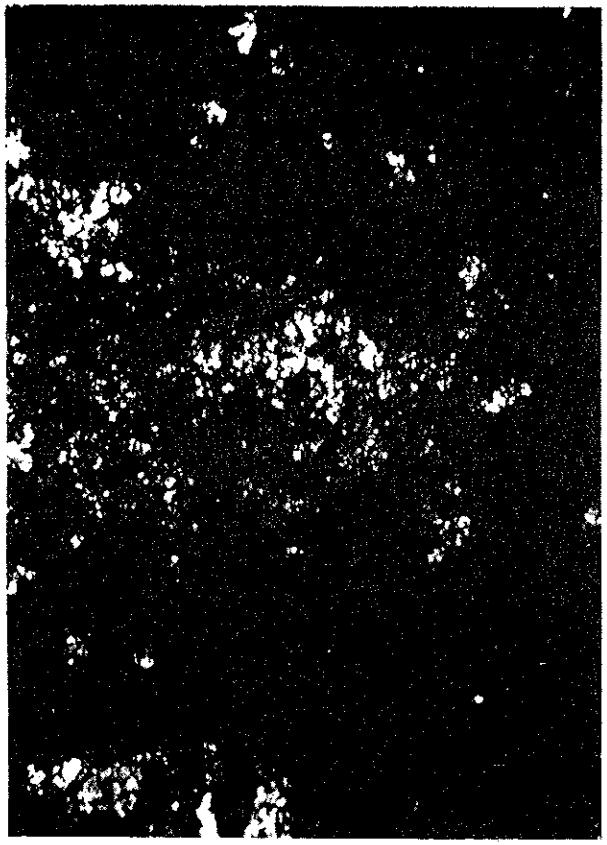

1000X 10μm

Powder: Fe_3O_4
Source: Pfizer
Designation: BK-5000

1000X 10μm

Powder: Fe_3O_4
Source: Pfizer
Designation: 8029

Fe_3O_4 Raw Materials
Figure 188

3) NiO

NiO is available as either green or black. Black NiO is formed by calcination of Ni carbonate or nitrate at 600°C. Black NiO contains excess oxygen and the Ni content ranges between 76 and 77 wt.% (101). Green NiO is produced by firing Ni powder and water in air at 1000°C or by thermal decomposition of Ni carbonate or nitrate at 1000°C. Green NiO is stoichiometric and contains 78.5 wt.% Ni. The black NiO, N-135[a], consists of agglomerates of very small crystallites. The particle size distribution for these powders is relatively narrow with a median particle size of about 14 microns. Green NiO, N-139[b] powder consists of individual crystallites and agglomerated particles. The surface area of the lower temperature processed black NiO is 70 m^2/g compared to 2 m^2/g for the green NiO. The two powders are compared in Figure 189. Sintered densities of inert anodes fabricated using black NiO were much lower than comparable anodes made with green NiO (4.79 vs. 5.79 g/cm^3). The black NiO agglomerates apparently did not break down during processing and hindered the densification process.

4) Fe

Several sources of Fe powder, ranging in median particle diameter of 10 to 74 microns and listed in Table 64, were evaluated. The size of the Fe powder particles has an effect on the microstructure of the sintered anode. Large Fe particles result in remnant pores in the structure. The Fe enters in a displacement reaction with the NiO raw material and ringlets of Ni form around the original Fe particle. This phenomena is illustrated in Figure 190 where a pore, probably the size of the original 74 micron median diameter 1000B Fe particle, is surrounded by a ring of Ni metal. Anodes fabricated with Fe powder of smaller median particle size do not exhibit large pores surrounded by Ni. A 21 micron median diameter Fe powder, Atomet 95, was used in the anode microstructure shown in Figure 191. The sintered anode

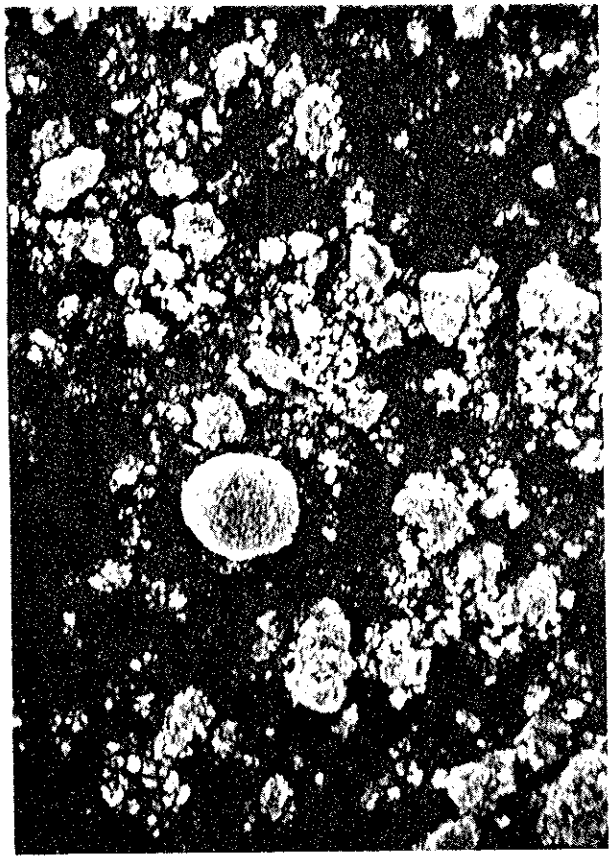

1000X 10μm

Powder: NiO
Source: Ceramic Color and Chemical
Designation: N-139 (Green)

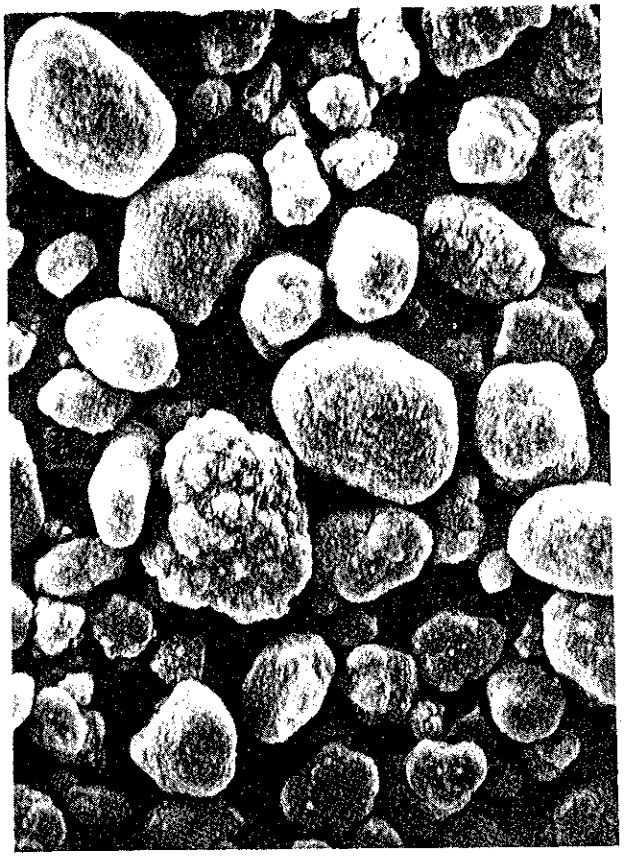

1000X 10μm

Powder: NiO
Source: Ceramic Color and Chemical
Designation: N-135 (Black)

NiO Raw Materials
Figure 189

TABLE 64

Inert Anode Raw Material Powder Properties - Metals

Material	Fe	Fe	Fe	Fe	Ni	Ni	Ni	Cu	Cu	Cu
Designation	1000B	Atomet 95	Lot 528	I-1068	PN-200	HDNP	123	10 μm		1241
Supplier	Hoeganaes	Quebec	Consolidated Astronautics	Cerac	Pfizer	Inco	Inco	Alfa	UMC	Cerac
Surface Area, m^2/g	.1	.3	.4	1.0	0.1	-	0.5	-	-	-
Particle Size	Micro	Micro	Micro	Micro	Micro	Micro	Micro	Sedi	Sedi	Sedi
90% Less than	149	56	66	27	122	128.7	19.8	27	26	26.5
50% Less than	74	21	34	10	60	26.5	8.2	16.2	15	12
10% Less than	30	8	12	4	26	11.2	3.4	7.7	7.6	4.9
Chemical Analysis	Spect	Spect	Spect	Spect	Spect	AA	AA	Spect	Spect	Spect
Element, wt.%										
Ag	-	-	-	-	-	-	-	.00	.02	.00
Al	-	.01	.00	.00	.00	-	<.005	.00	.03	.00
Ca	.00	.02	.03	.00	.00	-	-	.02	nd	nd
Co	-	.03	-	-	.01	-	-	-	-	-
Cr	.03	.4	.02	.03	.7	<.005	<.005	-	-	-
Cu	.03	.02	.04	-	.02	-	-	Major	Major	Major
Fe	Major	Major	Major	Major	.8	<.005	<.005	.01	.04	.00
Mg	.00	.00	.00	.00	.00	<.005	<.005	.01	.00	.00
Mo	-	-	-	-	.06	-	-	-	-	-
Mn	.3	.04	.03	.00	.4	-	-	-	-	-
Na	-	-	-	-	-	-	-	-	-	-
Ni	.03	.1	-	.02	Major	100	100	nd	.03	nd
Pb	.01	.01	.01	.01	-	-	-	.3	.4	.2
Si	.00	.1	.03	.00	.03	<.005	<.005	.01	.00	.00
Sn	-	-	-	-	-	-	-	.3	.06	.09
Ti	-	.3	.01	-	-	-	-	-	-	-
V	-	.5	-	-	-	-	-	-	-	-
Zn	-	-	-	-	-	-	-	nd	nd	.2

* Micro = Microtrac
Sedi = Sedigraph
** Spect = Qualitative Spectrographic Analysis - Values accurate within factor of 3
AA = Atomic Absorption Analysis

GA 17817.7

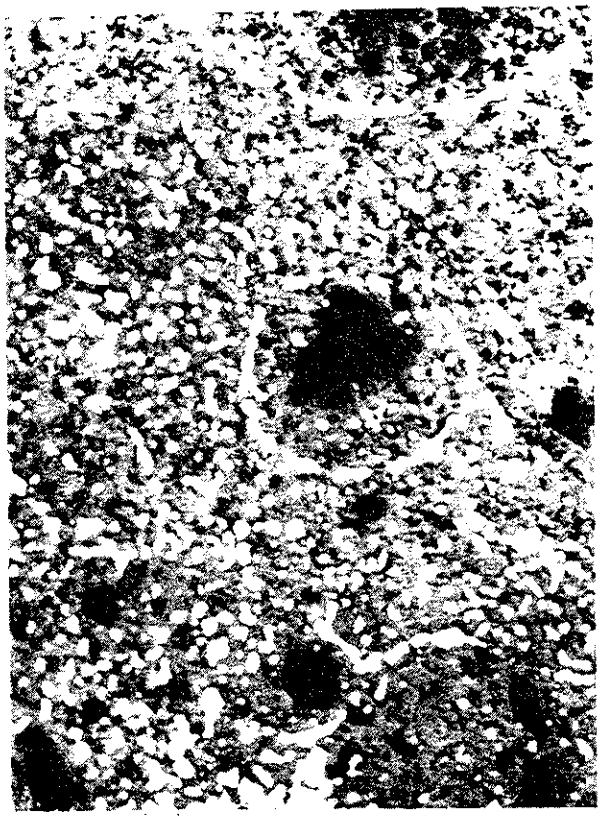

200X 50μm

Sample 94-1

Sintered properties

Bulk density, g/cm^3: 5.62

App. porosity, %: 1.31

H_2O absorption, %: 0.23

Reaction-Sintered Inert Anode Microstructure Using Coarse 74-Micron Median Diameter Fe Powder

Figure 190

GA 17817.6

400X 25μm

Sample 94-2

Sintered properties

Bulk density, g/cm^3: 5.72

App. porosity, %: 0.86

H_2O absorption, %: 0.09

Reaction-Sintered Inert Anode Microstructure Using 21-Micron Median Diameter Fe Powder

Figure 191

density is lowered when coarse Fe powder is used because of the large remnant pores. The morphology of two Fe powders, 21 and 74 median micron diameter, is shown in Figure 192.

5) Ni and Cu

Nickel and Cu powders were added to calcined oxide powders in the manner shown by reactions 87 and 88 and sintered to high densities. These metal powders are listed in Table 64. The highest sintered anode densities were obtained by this method. The size of the dispersed metallic phase in the microstructure is directly dependent on the starting powder size. Powders between 8 and 30 microns were studied. Nickel powders are made by atomization and from nickel carbonyl. Two Ni powders, grades HDNP and 123 made from carbonyl, are shown in Figure 193. These powders have sharp angular corners and are not agglomerated.

The Cu powders evaluated were either irregularly shaped agglomerated particles or atomized spherical particles. These powders are illustrated in Figure 194. A summary of fabricated inert anode densities generated from various raw material combinations is listed in Table 65. These comparisons were made using the reaction sintering approach illustrated by reaction 86. From these data, the preferred raw material combinations for reaction sintered inert anodes was determined to be:

Raw Material Combination	Designation
1. Atomet Fe + BK-5000 Fe_3O_4 + N-139 NiO	94-2
2. Atomet Fe+ R-2900 Fe_2O_3 + N-139 NiO	103-5
3. Atomet Fe + 015 Fe_2O_3 + N-139 NiO	103-7
4. Atomet Fe + NO-8029 Fe_3O_4 + N-139 NiO	94-12

b. Powder Preparation

Preparation of free flowing, dustless, and pressable inert anode powder was completed by agglomeration in a pan pelletizer and in open

GA 17817.8

1000X 10μm

1000X 10μm

Powder: Fe
Source: Quebec
Designation: Atomet 95

Powder: Fe
Source: Hoeganaes
Designation: 1000B

Fe Raw Materials
Figure 192

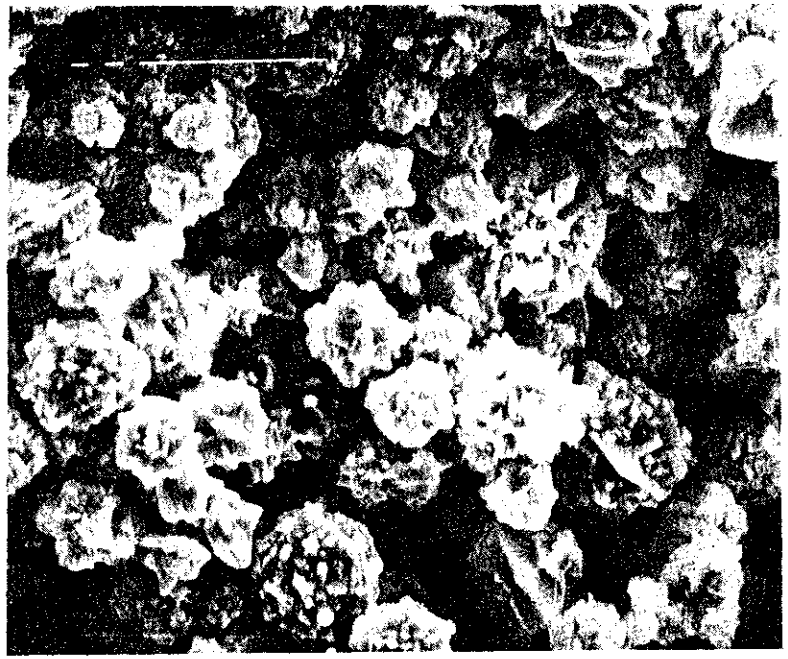

579 2500X

Powder - 123 Grade from INCO

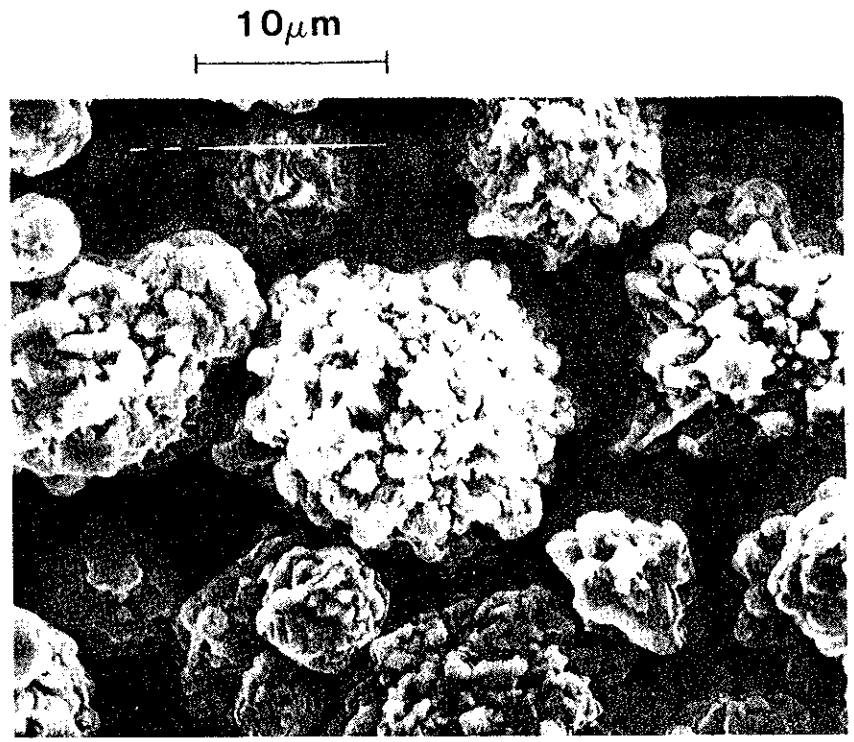

M578 2500X

Ni Powder - HDNP Grade from INCO

Ni Raw Materials

Figure 193

GA 17817.12

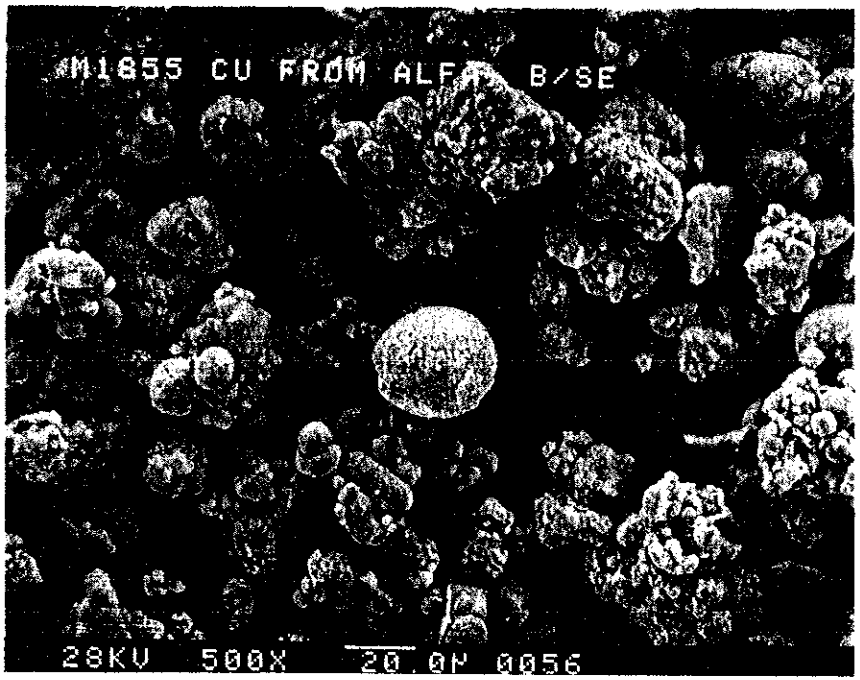

500X 20μm

Copper Metal Powder from Alfa Products

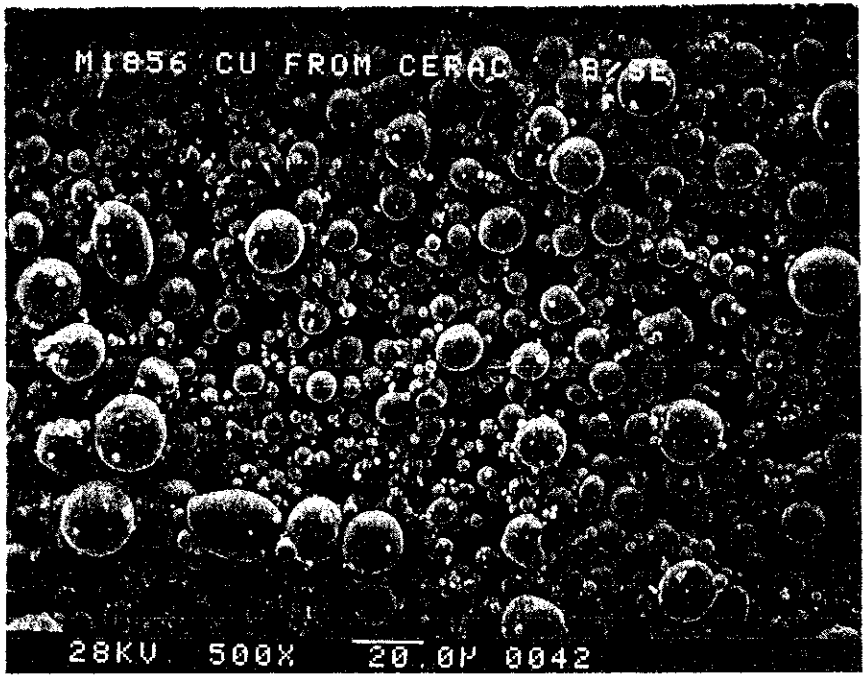

500X 20μm

Copper Metal Powder from Cerac

Cu Raw Materials
Figure 194

TABLE 65

Cermet Fabrication Studies by
Reaction Sintering

Sample Designation	Raw Materials				Green[1] Density g/cm³	Sintered[2] Density g/cm³	Apparent Porosity %
	Fe	Fe_3O_4	Fe_2O_3	NiO			
94-1	1000B	BK-5000		N-139	4.00	5.59	1.06
94-2	Atomet 95	BK-5000		N-139	4.01	5.76	0.53
94-11	Atomet 95	BK-5000		N-139	-	4.75	20.76
94-12	Atomet 95	MO-8029		N-139	4.02	5.49	0.36
103-5	Atomet 95		R-2900	N-139	4.23	5.73	0.26
103-7	Atomet 95		015	N-139	3.93	5.73	0.28
109-1	I-1068	I-1062		N-1093	-	5.40	9.76
109-2	I-1068		I-1039	N-1093	4.67	5.66	3.83
109-3	I-1068		I-1039	N-139	-	5.72	0.45

(1) Pressing Pressure: 103 MPa (15,000 psi)
(2) Sintering Conditions: Temperature - 1250°C
Time - 2 hours
Atmosphere - Argon

and closed spray dryers. A closed system spray dryer was used to prepare the Fe-NiO-Fe_3O_4 composition under an inert cover gas of nitrogen from an isopropyl alcohol solution using a polyvinyl butyral binder. The spray drying was completed with a pressure nozzle using the conditions given in Table 62. Powders were also sprayed with an atomizer wheel, or with a two-fluid nozzle. The pan pelletized 6846 inert anode powder was also prepared with isopropyl alcohol and polyvinyl butyral binder. NiO-Fe_3O_4 oxide powders were spray dried in open systems using water and polyvinyl alcohol as a binder. The agglomerated powder was evaluated for particle size distribution, loose bulk density (LBD), packed bulk density (PBD), flow index (F), pressed green density, and sintered density. A listing of these properties for several agglomerated powders is contained in Table 66. The flow index is calculated from the following equation:

$$F = [(PBD-LBD)/PBD] \times 100 \quad (89)$$

Flow index values above 20 represent powders that will not be free flowing. Spray-dried powders had indices between 5 and 17 compared to 40 for as-blended powder. Coarser spray-dried powders had lower flow indices than the finer spray-dried agglomerates generated using an atomizer wheel. Pan-agglomerated powder had an average flow index of 17. The flowability of as-received blended powder was the same as powder that had been calcined and ground prior to spray drying.

The median particle size for spray-dried powders using a pressure nozzle was about 120 microns compared to 23 to 58 microns for atomizer wheel generated powder. The morphology of raw mix 94-2 closed system spray-dried inert anode powder 6846 is shown in Figure 195. Spray-dried powder from a pressure nozzle is compared to powder spray dried with an atomizer wheel in Figure 196. Note that the atomizer wheel produced more irregular shapes with holes in the agglomerates than the pressure nozzle produced powder. The flow index of the pressure nozzle material was lower (5-6.5 compared to 9.8) indicating better flow properties. Spray-dried agglomerates of the NiO and Fe_3O_4 ingredients of the 94-2 mix of the 6846 cermet were prepared in an

TABLE 66

Powder Characterization - Agglomerated Powders

Powder Type	Process	Sample	Calcined	Ground	Spray Dryer	Binder	Atomization	LBD[2] g/cm³	PBD[3] g/cm³	Index %	Agglomerated Size 90%< µm	50%< µm	10%< µm	Green Density g/c³	Sintered Density g/cm³
Cermet	As Blended	94-2	No	0	No	-	-	1.09	1.81	40	-	-	-	4.0	5.78
Cermet	As Blended	94-2	No	6	No	-	-	1.20	2.74	56	-	-	-	4.4	5.90
Oxide[1]	Spray Dried	1	Yes	Yes	Open	1.5% PVA+	2-Fluid Noz.	1.99	2.28	12.7	-	-	-	-	5.16
Oxide[1]	Spray Dried	5	No	No	Open	1.5% PVA	2-Fluid Noz.	1.59	1.86	14.5	-	-	-	3.87	5.75
Cermet	Spray Dried	NA-4	No	No	Closed	1% PVB*	Pressure Noz.	1.58	1.69	6.5	198	120	64.4	3.78	5.76
Cermet	Spray Dried	NA-8	No	No	Closed	1% PVB	Wheel	1.58	1.75	9.7	98.8	58.4	27.2	3.92	5.70
Cermet	Spray Dried	NA-9	No	No	Closed	0.5% PVB	Wheel	1.65	1.83	9.8	80.0	40.6	11.0	3.99	5.79
Cermet	Spray Dried	NA-10	No	No	Closed	0.5% PVB	Pressure Noz.	1.70	1.79	5.0	235	139	55	3.99	5.80
Cermet	Spray Dried	G-8766	Yes	Yes	Open	1.5% PVA	Pressure Noz.	1.86	1.97	6.0	176.0	104.0	56.0	-	-
Cermet	Pan Pellet.	E7A	No	No	-	0.5% PVB	-	2.31	2.78	17.0	-	-	-	3.96	5.79

(1) PN-200 Ni metal added to oxide mixture after spray drying to make cermet.
(2) LBD = Loose Bulk Density
(3) PBD = Packed Bulk Density
(4) Flow Index = [(PBD-LBD)/PBD] x 100
\+ Polyvinyl Alchol
* Polyvinyl Butyral

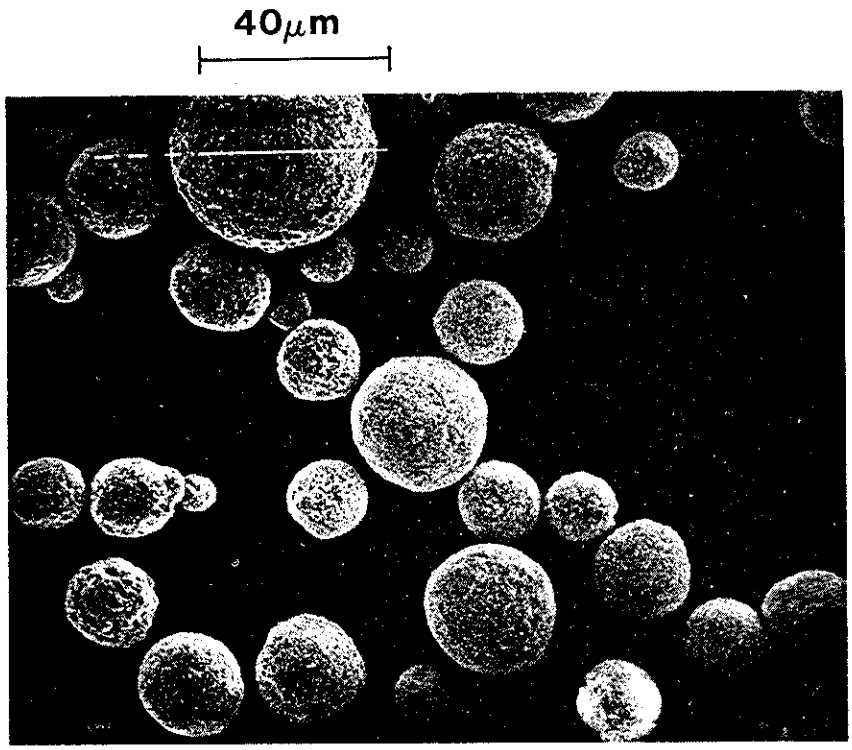

M582 250X

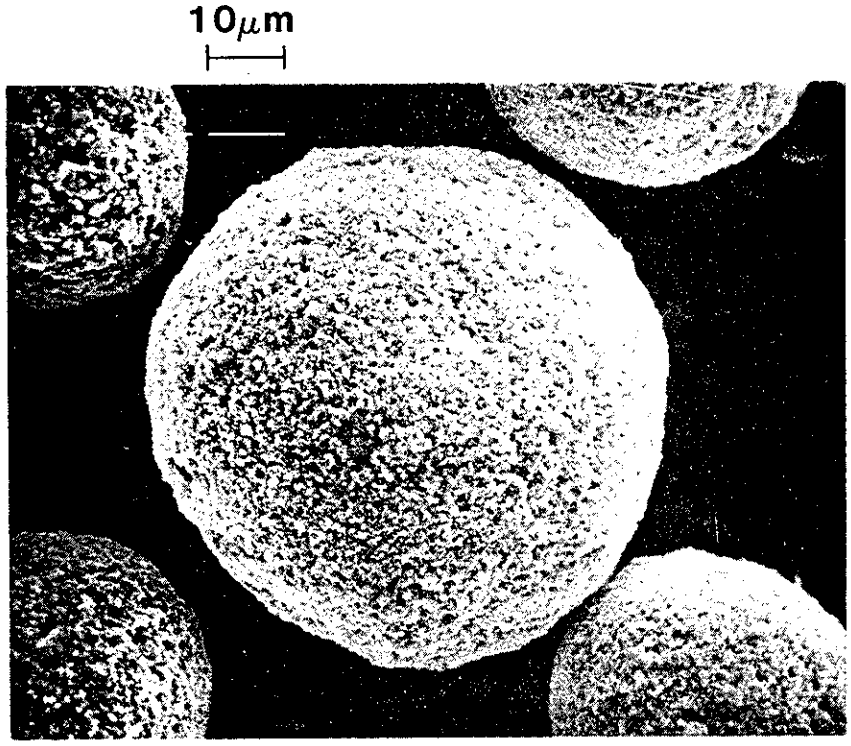

M582 1000X

Closed-System Spray-Dried Inert Anode Powder 6846, 94-2 Mix Unreacted

Figure 195

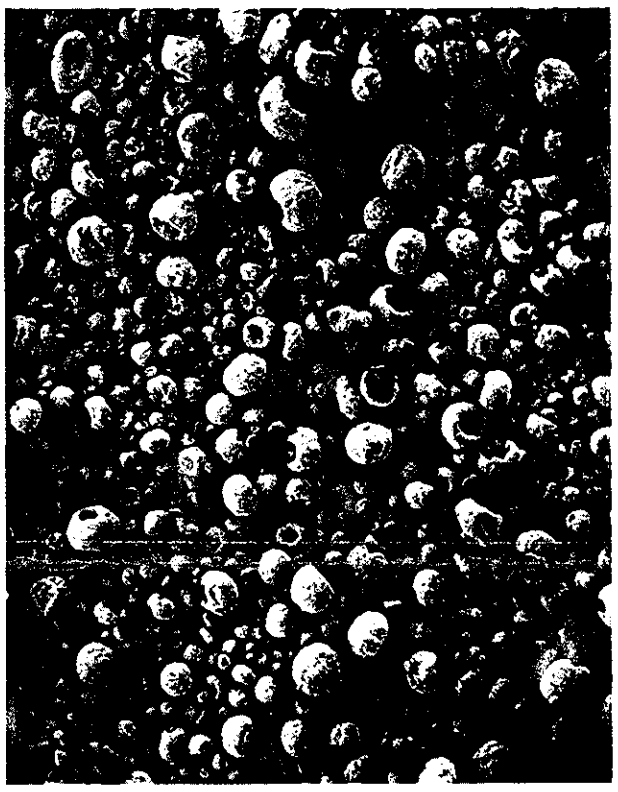

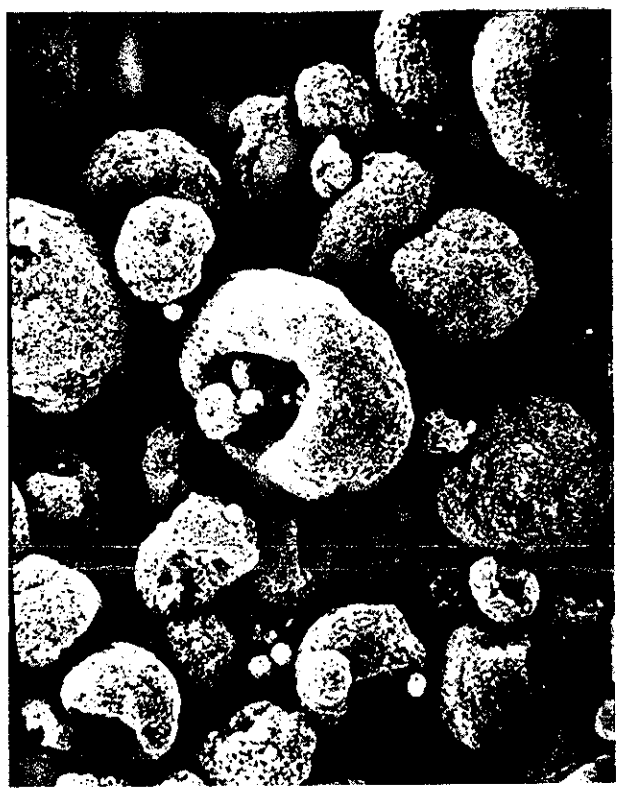

Run 8

58μm

100X

700X

Atomizer wheel

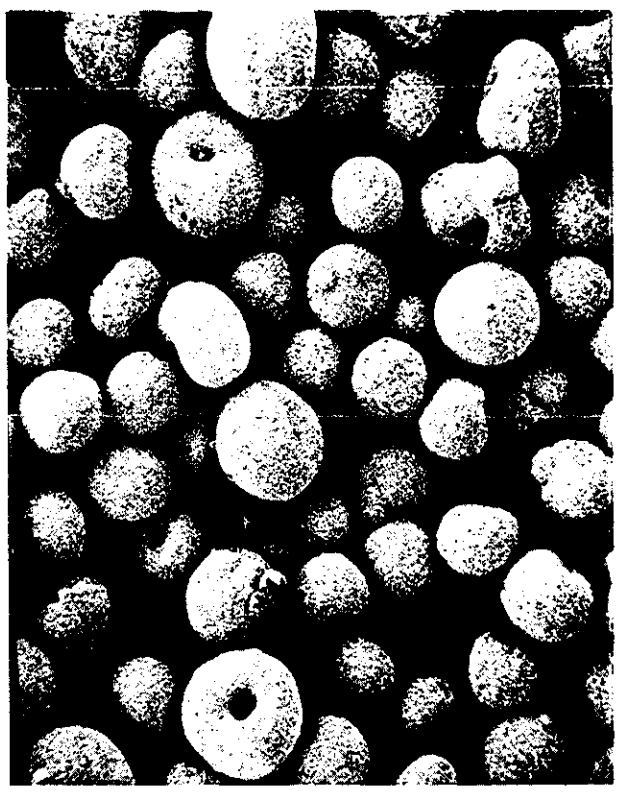

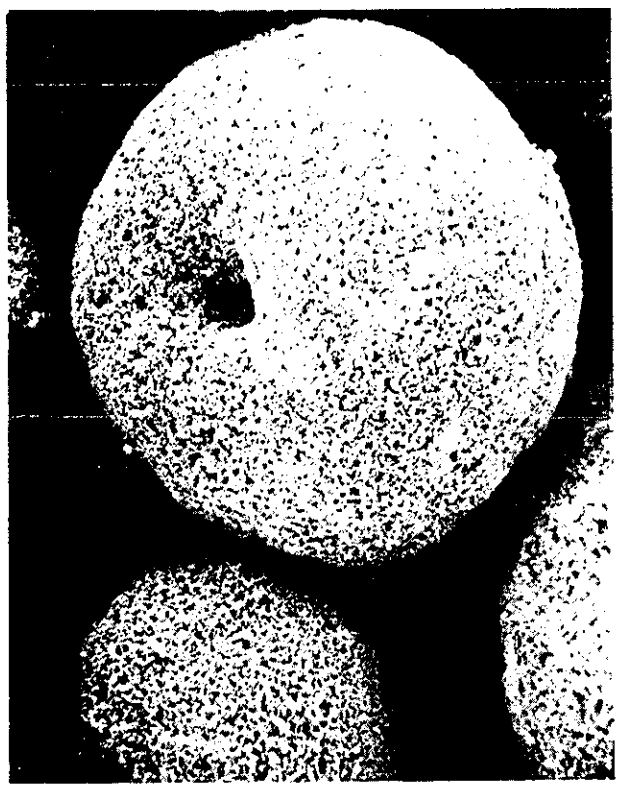

Run 2

117μm

100X

700X

Pressure nozzle

Spray-Dried 6846 Powder Using Atomizer Wheel and Pressure Nozzle

Figure 196

open system with a polyvinyl alcohol-polyethylene glycol system in water with a two-fluid nozzle in a tower spray dryer. The median size for the spray dried agglomerates by this method was only 33 microns as shown in Figure 197. Iron powder, Atomet 95, was added to the spray dried powder by "V" blending to make up the 6846 composition (Figure 197). The flow characteristics of this powder is higher (14.5) than the powders produced in the closed system spray dryer.

Green and sintered bulk densities of inert anode compacts made from either pan agglomerated or spray drying processes did not vary much and do not appear to be dependent on agglomerated particle size. Instead, major increases in density can be realized by changing from the reaction sintering approach to the calcination, grinding, pressing and sintering of inert anode powder.

Dry grinding studies were completed on calcined powder to determine grinding methods and conditions necessary to produce reactive inert anode powder prior to spray drying and sintering. Ball mill grinding powder, for two hours, and fluid energy milling powder at a rate of 40 kg/hour will produce the required reactivity for sintering dense inert anode parts (7). Slower fluid energy feed rates will contaminate the inert anode powder with Cr and Co from the mill liners. Grinding did not significantly improve the reactivity of powders that were blended for reaction sintering but did increase the reactivity of calcined powders.

b. Consolidation Studies

1) Green Compaction and Binder Selection Studies

Green compaction of small samples was done by uniaxial die pressing 9 to 25 mm diameter samples at pressures of 34 to 103 MPa. Larger samples, 50 to 250 mm diameter, were isostatically pressed at pressures of 103 to 207 MPa. Green densities of 57 to 70 percent of theroetical were obtained.

GA 15377

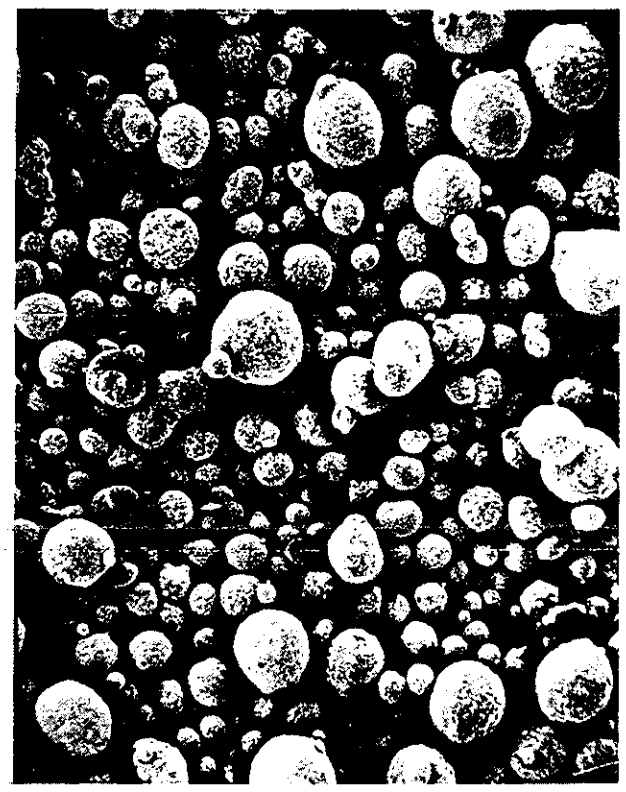

100X

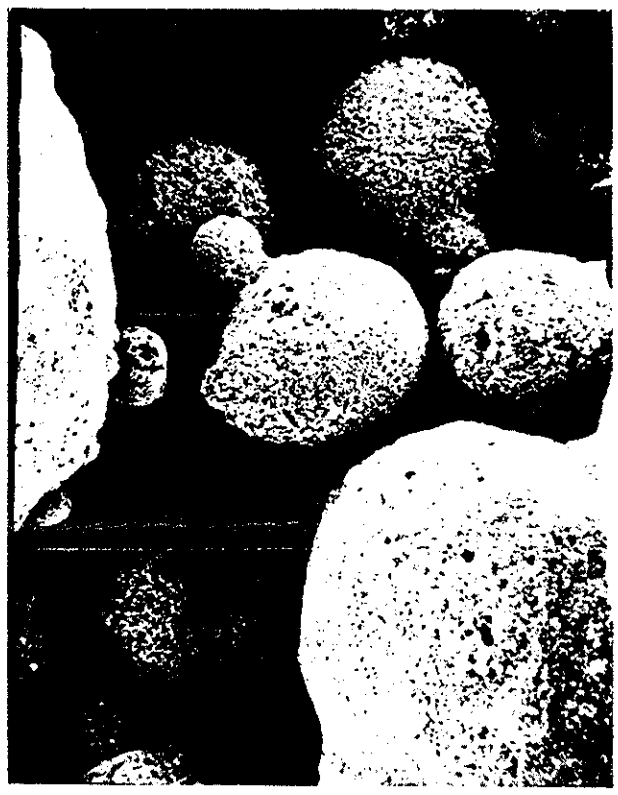

32.9μm

700X

Two fulid nozzle

Fe added by
"V" blending

1000X

Spray-Dried NiO and Fe_3O_4 Oxides 6846 (Top) and with Fe Added (Bottom) Using Two-Fluid Nozzle

Figure 197

f originals have the holes.

Strengths of uniaxially pressed green compacts were tested by diametral loading in order to evaluate binders. The highest strength green compacts were obtained with polyvinyl alcohol in water and polyvinyl butyral in isopropyl alcohol. Strengths of green compacts ranged from 0.1 to 2.5 MPa. Figure 198 illustrates green strength of as-pressed wet and dried compacts. Table 67 lists the binder type, percent binder solution concentration, percent binder solution added, percent binder solids, and resulting diametral strength. Strength results were used to select the polyvinyl alcohol and polyvinyl butyral binders used in anode fabrication. The higher strength compacts can be handled, transported, and machined without chipping and cracking. The binder systems used provided a free flowing powder after spray drying for easy fill of pressing dies and molds. The compacts pressed using these binders were free from laminations, voids, chips, or other pressing flaws. In addition, the compacts, small or large, were strong enough for handling, transport, and green machining on lathes or milling machines.

Compaction studies were conducted on as-blended, as-blended-ground, spray-dried, and pan-agglomerated powders using a mechanical testing machine to obtain pressure-density curves. These compaction curves can be useful for interpretation of the consolidation of inert anode powders. The shape of the consolidation curves should be different for as-blended and agglomerated powders. Lukasiewicz and Reed (102) have shown that the change in slope observed for spray-dried agglomerates corresponds to the pressure at which the granules are being deformed and the intergranular pores are being reduced in size. They also cite a joining pressure where the pressure-density curve of an unagglomerated powder joins the pressure density curve of an agglomerated powder. This occurs when the large intergranular pores are eliminated. Figure 199 illustrates this phenomena for as-blended powder 94-2 and spray-dried powder NA-4. The spray-dried granules start to deform at 1 MPa and the joining pressure occurs at 70 MPa. The loose bulk density of spray-dried

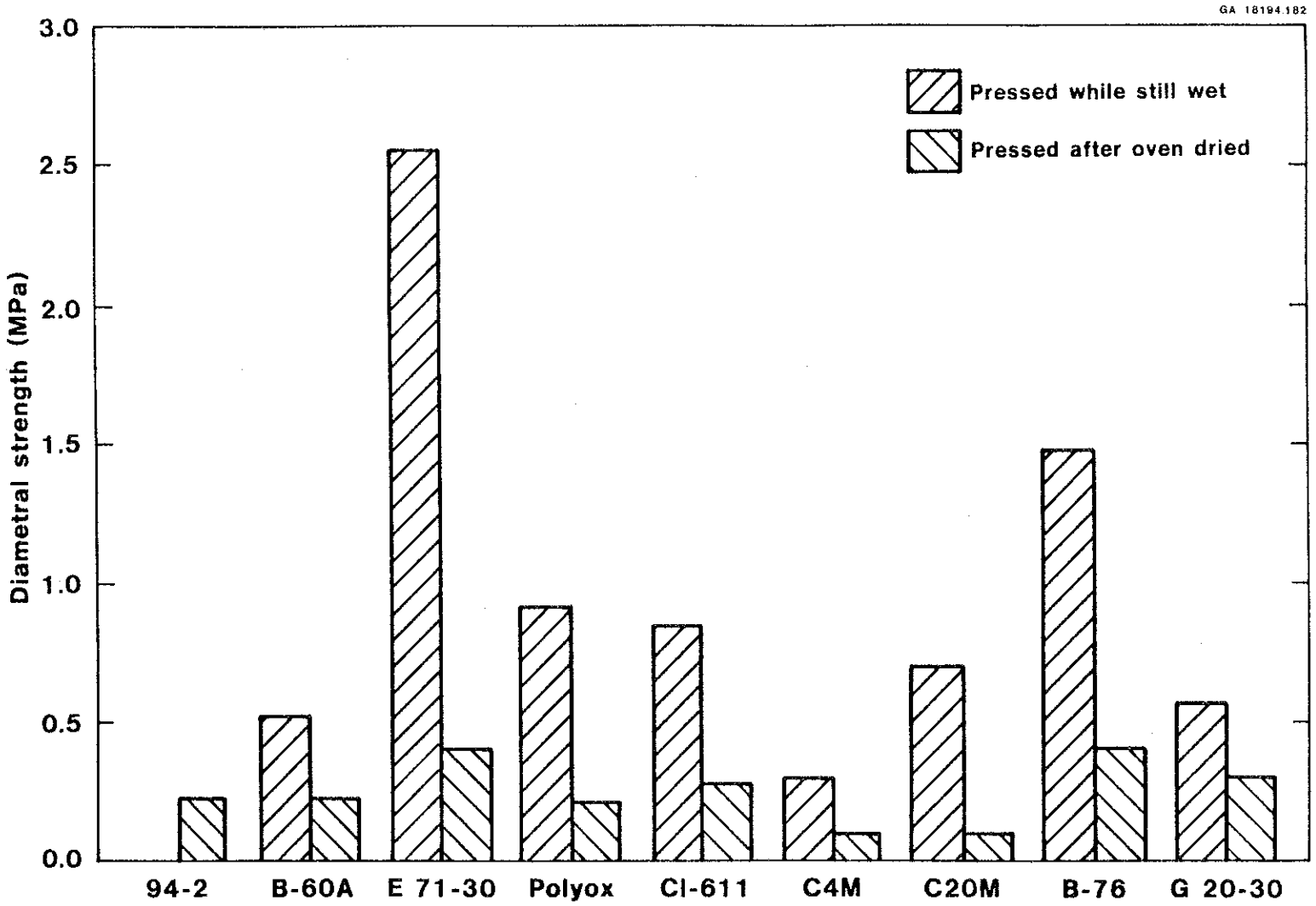

Diametral Strength Tests on Green Compacts Pressed Wet and Dry with Binder Additions
Figure 198

TABLE 67

Organic Binder - Inert Anode Green Compact Strength Evaluation

Binder Designation	Vendor	Binder Composition	Sample Designation	Binder Solution Concentration %	Percent Binder Solution Added %	Powder Status Before Pressing	Diametral Strength MPa	Binder Solids %	Strength Unit Bind MPa
None	--	--	J-116	--	10 H_2O	Wet	1.15	0	--
None	--	--	94-2	--	0 H_2O	Dry	0.21	0	--
Elvanol 71-30	Dupont	Polyvinyl Alcohol	J-119-1A	4	5.61	Wet	1.79	.22	7.97
Elvanol 71-30	Dupont	Polyvinyl Alcohol	J-119-1B	4	5.61	Dry	0.36	.22	1.63
Elvanol 71-30	Dupont	Polyvinyl Alcohol	J-119-2A	4	9	Wet	2.56	.36	7.11
Elvanol 71-30	Dupont	Polyvinyl Alcohol	J-119-2B	4	9	Dry	0.39	.36	1.09
Gelvatol 23-30	Monsanto	Polyvinyl Alcohol	J-116-5A	10	2.84	Wet	.55	.28	1.94
Gelvatol 23-30	Monsanto	Polyvinyl Alcohol	J-116-5B	10	2.84	Dry	.30	.28	1.04
Carbowax 4000	Union Carbide	Polyethylene Glycol	J-118-4A	25	2.63	Wet	.28	.66	.43
Carbowax 4000	Union Carbide	Polyethylene Glycol	J-118-4A	25	2.63	Dry	.10	.66	.15
Carbowax 20,000	Union Carbide	Polyethylene Glycol	J-118-5A	4	6.43	Wet	.68	.26	2.66
Carbowax 20,000	Union Carbide	Polyethylene Glycol	J-118-5A	4	6.43	Dry	.10	.26	.38
Polyox WSRN-12K	Union Carbide	Polyethylene Oxide	J-118-1A	2	4.33	Wet	.91	.09	10.46
Polyox WSRN-12K	Union Carbide	Homopolymer	J-118-1A	2	4.33	Dry	.2	.09	2.30
Avicel CL-611	FMC Corp.	Microcrystalline Cellulose	J-118-2A	2	6.11	Wet	.83	.12	6.84
Avicel CL-611	FMC Corp.	Microcrystalline Cellulose	J-118-2A	2	6.11	Dry	.27	.12	2.20
Avicel CL-611	FMC Corp.	Microcrystalline Cellulose	J-118-3A	2	4	Dry	.73	.08	9.13
Avicel CL-611	FMC Corp.	Microcrystalline Cellulose	J-118-3A	2	4	Dry	.15	.08	1.90
B-60-A	Rohm & Haas	Acrylic Resin	J-116-2A	As Received	5.25	Wet	.51	?	--
B-60-A	Rohm & Haas	Acrylic Resin	J-116-2A	As Received	5.25	Dry	.21	?	--
B-76	Monsanto	Polyvinyl Butyral	J-116-3A	10	2.27	Wet	.32	.23	1.40
B-76	Monsanto	Polyvinyl Butyral	J-116-3A	10	2.27	Dry	.25	.23	1.09
B-76	Monsanto	Polyvinyl Butyral	J-116-4A	5	8.35	Wet	1.48	.42	3.53
B-76	Monsanto	Polyvinyl Butyral	J-116-4A	5	8.35	Dry	.39	.42	.94

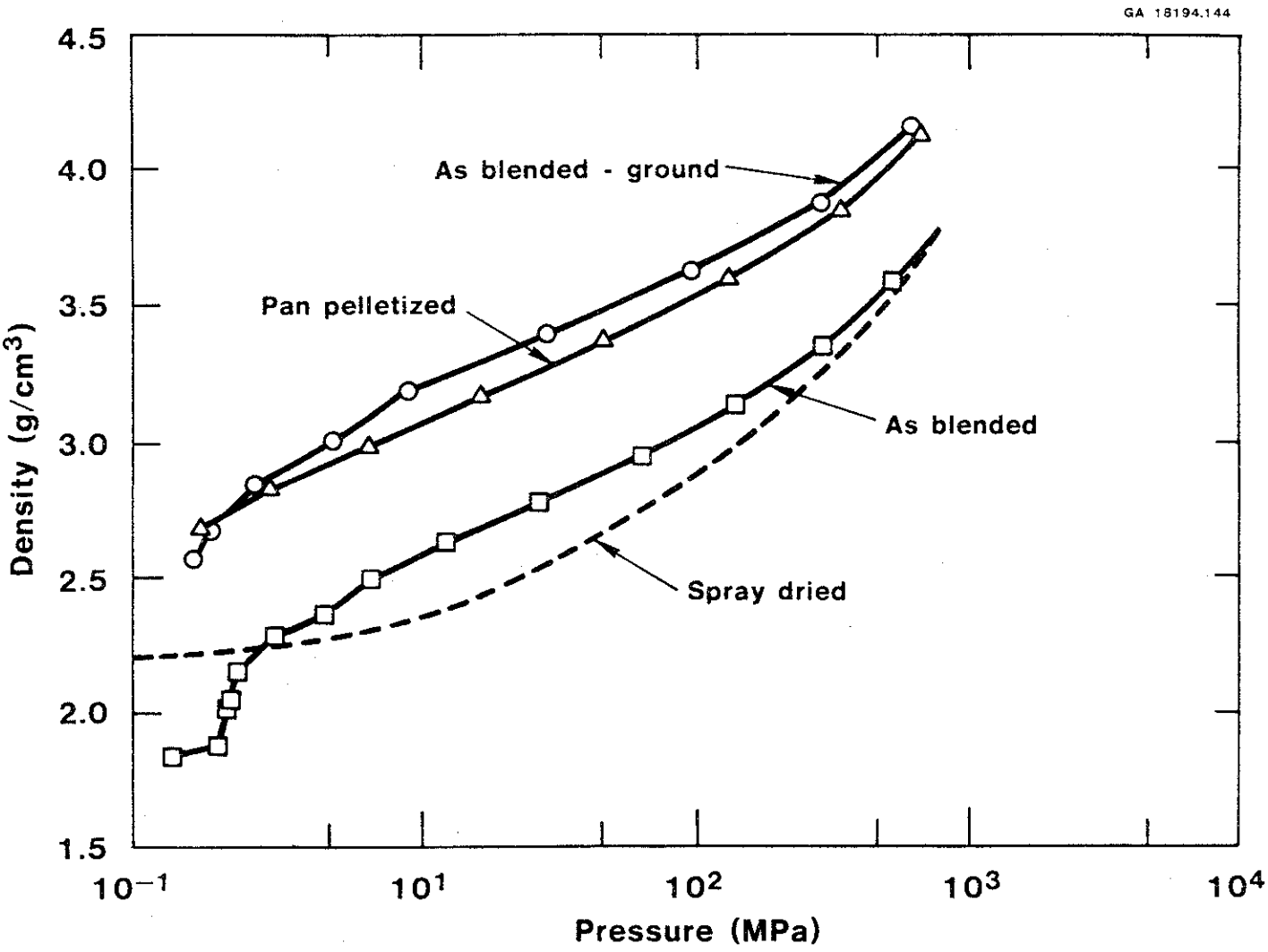

Inert Anode Powder Compaction Curves
Figure 199

powder is higher than the as-blended powder. Grinding the as-blended powder produces a compaction curve with greater densities. Pan-pelletizing of as-blended powder also produces a higher density compaction curve. Breakdown of the pan-pelletized granules does not occur until about 7 MPa. Care has to be taken to characterize these powders under the same humidity, temperature, and pressing conditions.

2) Pressureless Sintering Studies

The sintering behavior of cermet inert anode compositions is influenced by the process method, sintering atmosphere, powder preparation methods, time at temperature, raw materials, and reactivity of the powder.

Green Compact Expansion-Shrinkage Curves: A comparison of the sintering behavior of as-blended and calcined powders was determined using a dilatometer to obtain green compact expansion and shrinkage during sintering. Large expansion and shrinkage differences occur in the as-blended and calcined powder compacts as illustrated in Figure 200. The as-blended green compact undergoes a significant 3.5 percent linear expansion starting at 500°C. This expansion, which calculated to a 10.8 volume percent expansion, is attributed to the displacement reaction:

$$2Fe + 3NiO \rightarrow 3Ni + Fe_2O_3 \qquad (90)$$

Ray and Rapp (15) have noted this reaction previously and Lesniewski et al. (103) note a similar expansion behavior in the reaction sintering of nickel ferrite which they attribute to the formation of $NiFe_2O_4$ from NiO and Fe_2O_3. Reaction (90) leads to an 8.8 molar vol.% expansion. This magnitude of volume expansion during heat up, prior to shrinkage by sintering, may result in cracking of the compact prior to or during sintering (103). These expansions also need to be noted for anode design and composite inert anode assemblies fabricated during one thermal

cycle. A calcined powder compact exhibits normal sintering behavior for a ceramic part as shown by the second curve of Figure 200. Sintering shrinkage begins at approximately 880°C for both the as-blended and calcined 94-2 Ni-nickel ferrite cermet compacts.

Powder Calcination and Compact Sintering Temperatures: Experiments were conducted to densify inert anodes by cold pressing and sintering as-blended (reaction sinter) and calcined cermet powder. Powders were calcined in argon for two hours at temperatures ranging from 600-1200°C. These powders were then ball milled for four hours to make them reactive. Compacts were made by pressing 25 mm diameter right circular cylinders at 138 MPa. Figure 201 shows the density vs. temperature results for these compacts. The maximum density was obtained for 800°C calcined powder sintered to 1350°C. The calcine-sinter process increased fabricated densities from 91 percent of theoretical for reaction sinter processed compacts to 97 percent of theoretical. The optimum temperature appears to be 1350°C.

Effect of Sintering Atmosphere on Densification: Optimum densification of cermet nickel ferrite compositions is dependent upon the sintering atmosphere used. Inert gases such as argon or nitrogen or a buffered gas system must be used to densify inert anodes by the reaction sinter process. These inert gases are necessary to prevent the reaction of free metallic phases such as iron with oxygen, which would preclude the desired displacement reaction of Fe with NiO and Fe_3O_4 to form the mixed oxides of NiO and $NiFe_2O_4$ with an interwoven network of Ni-Fe alloy. An inert cover gas is also necessary, during densification, for the protection of calcined cermet compositions containing free Ni or Cu from oxidation. According to Sticher and Schmalzried (104), reducing atmospheres of 10^{-9} pO_2 or lower should be avoided to keep from reducing the nickel-iron oxide species. Therefore, it was of interest to determine the optimum pO_2 level for the densification of inert anodes.

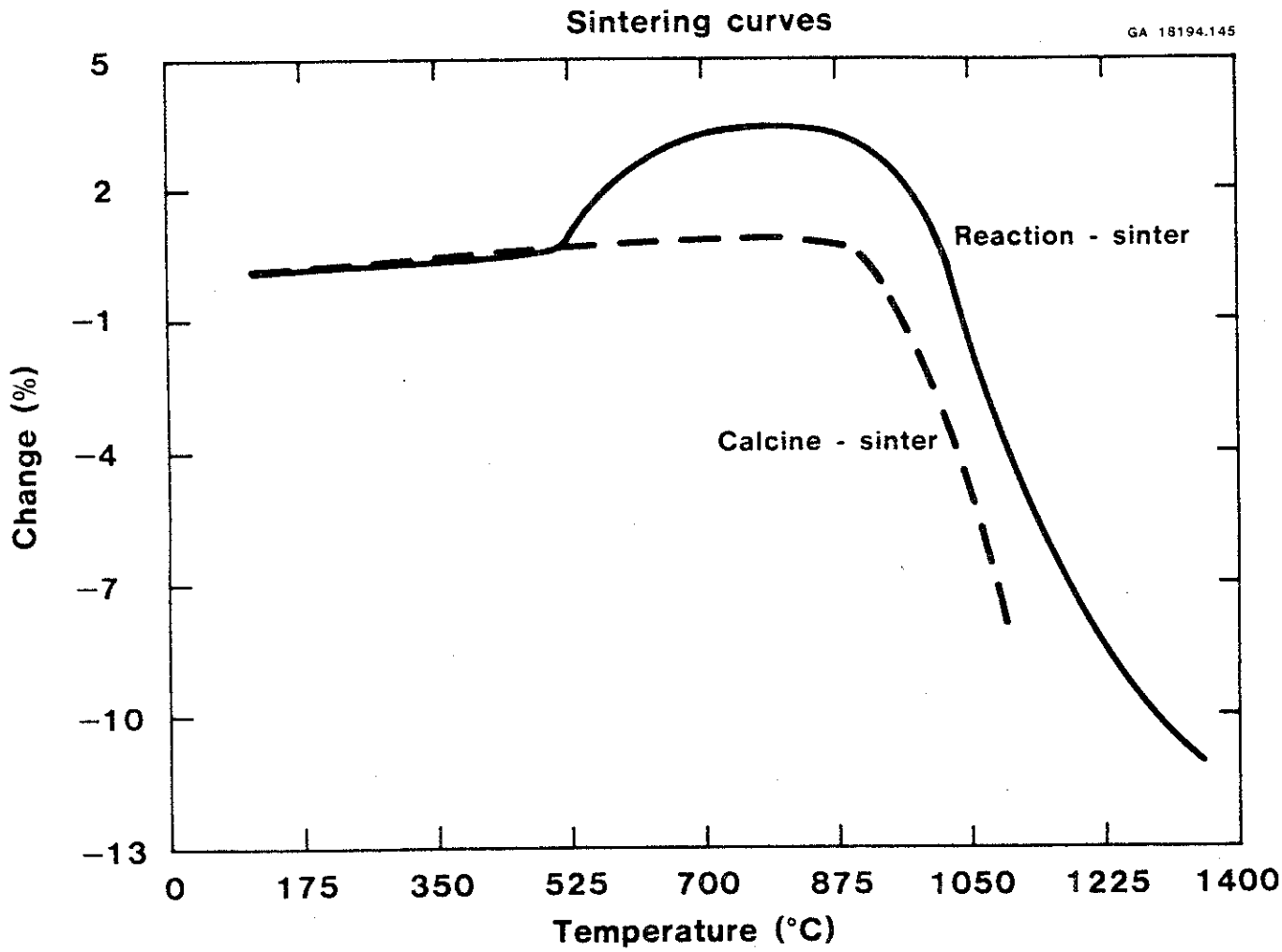

Expansion-Sintering Curves for Reaction-Sintered and Calcine-Sintered Inert Anode Powder Compacts
Figure 200

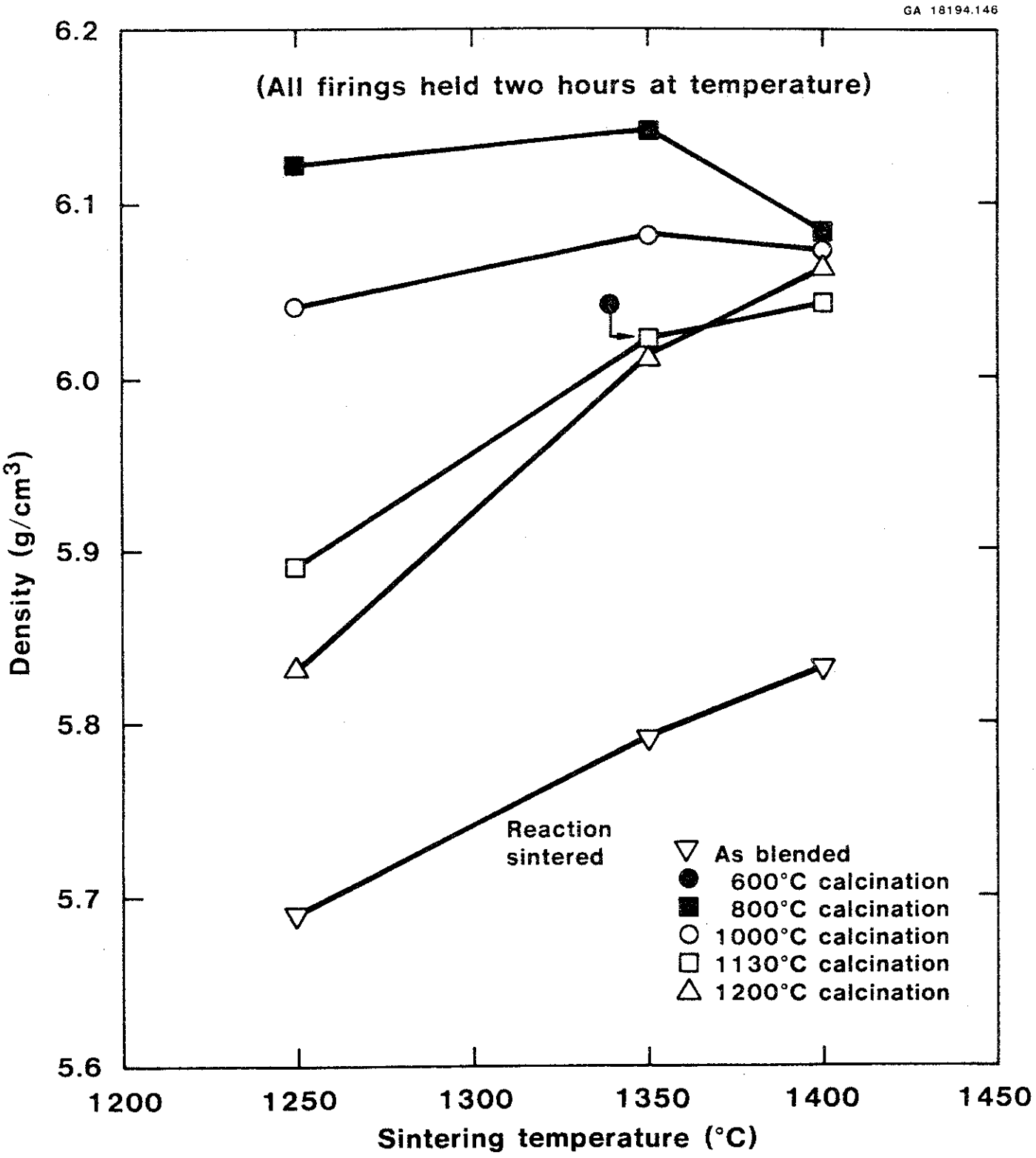

Density Versus Sintering Temperature for Reaction-Sintered, As-Blended, or -Calcined Ground Inert Anode Powder Compacts

Figure 201

The effect of pO_2 ranging from 10^{-2} to 10^{-8} on the densification of reaction sinter and calcined sinter nickel-nickel ferrite compositions was determined. Gas mixtures of argon-oxygen, CO-CO_2, and CO_2 and forming gas (96% N_2 + 4% H_2) were used to obtain the desired pO_2 levels. The density of the reaction-sinter and calcine-sinter powder compacts versus the partial pressure of oxygen is shown in Figure 202. The raw material combinations were the 94-2 and 94-12 mixes listed in Table 65. These results indicate the optimum densification occurs in inert gas atmospheres (pO_2 ~10^{-4} to 10^{-5}) for both the reaction-sinter and the calcine-sinter compacts.

Cold Press and Sinter Calcined Oxide Powders Mixed with Nickel and Copper Metal Powder Additions: An additional cold press sinter method or inert anode fabrication was investigated. Nickel or copper metal powder additions were added to a previously calcined nickel ferrite powder that had been ground and spray dried. This mixture was then cold pressed and sintered in argon to 1350°C for 2 to 4 hours. The highest sintered densities for inert anode compacts were obtained using this process method. Results for a series of nickel or copper additions to a nickel ferrite are shown in Figure 203. Densities of approximately 99 percent of theoretical were obtained by this method. These results are compared in Figure 203 to the other process methods used to fabricate inert anodes.

3) Pressure Sinter Processes

Hot pressing (HP) and hot isostatic pressing (HIP) process methods were also evaluated for densification of inert anodes. Hot press conditions necessary for densification were found to be 15 minutes at 1015°C and 12 MPa pressure. Inert anodes of 6.1 g/cm density, with some local reduction of oxides in contact with graphite pressing dies, were produced under these conditions. HIP'ing experiments were conducted for three hours at 1100°C and 103 MPa pressure. Inert anodes predensified by

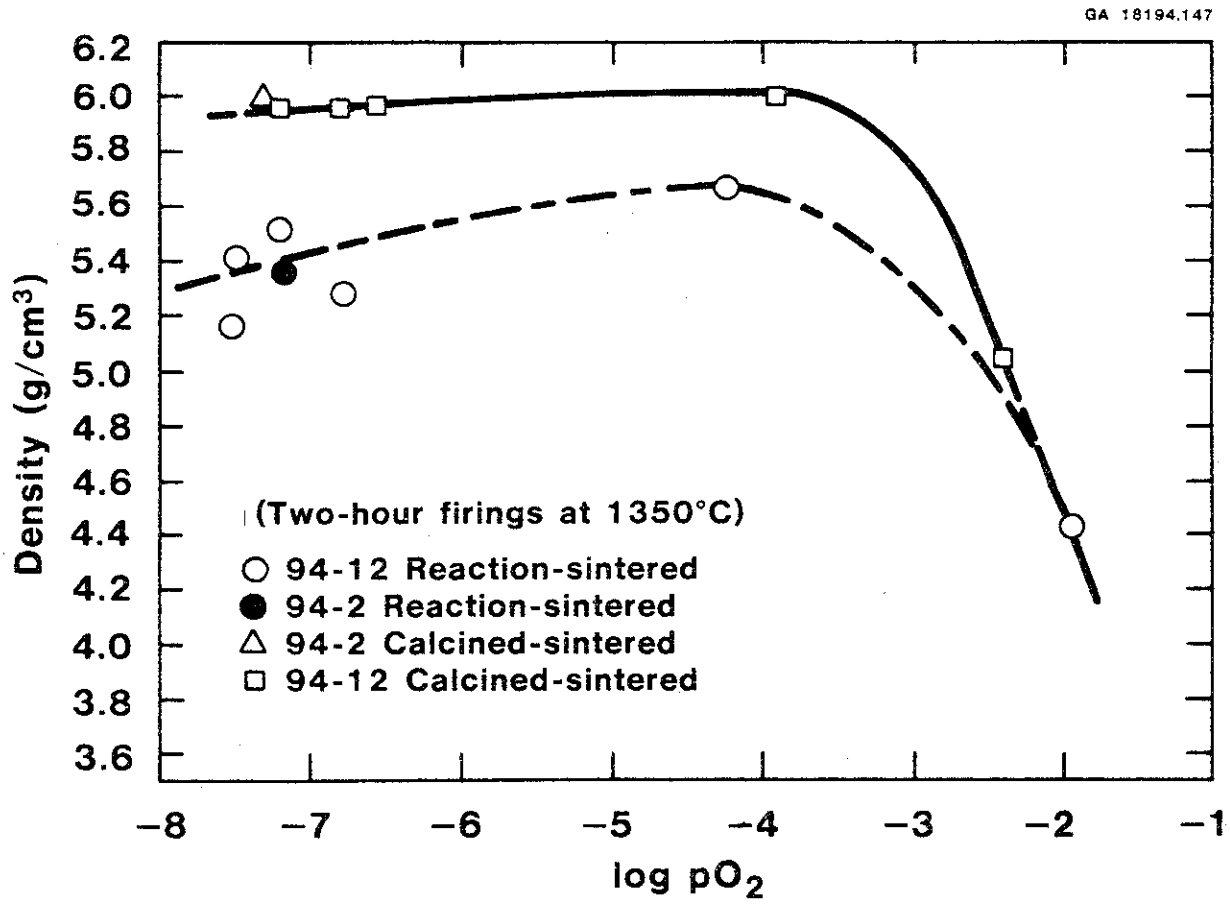

Bulk Density of Inert Anode Versus the Partial Pressure of Oxygen During Sintering

Figure 202

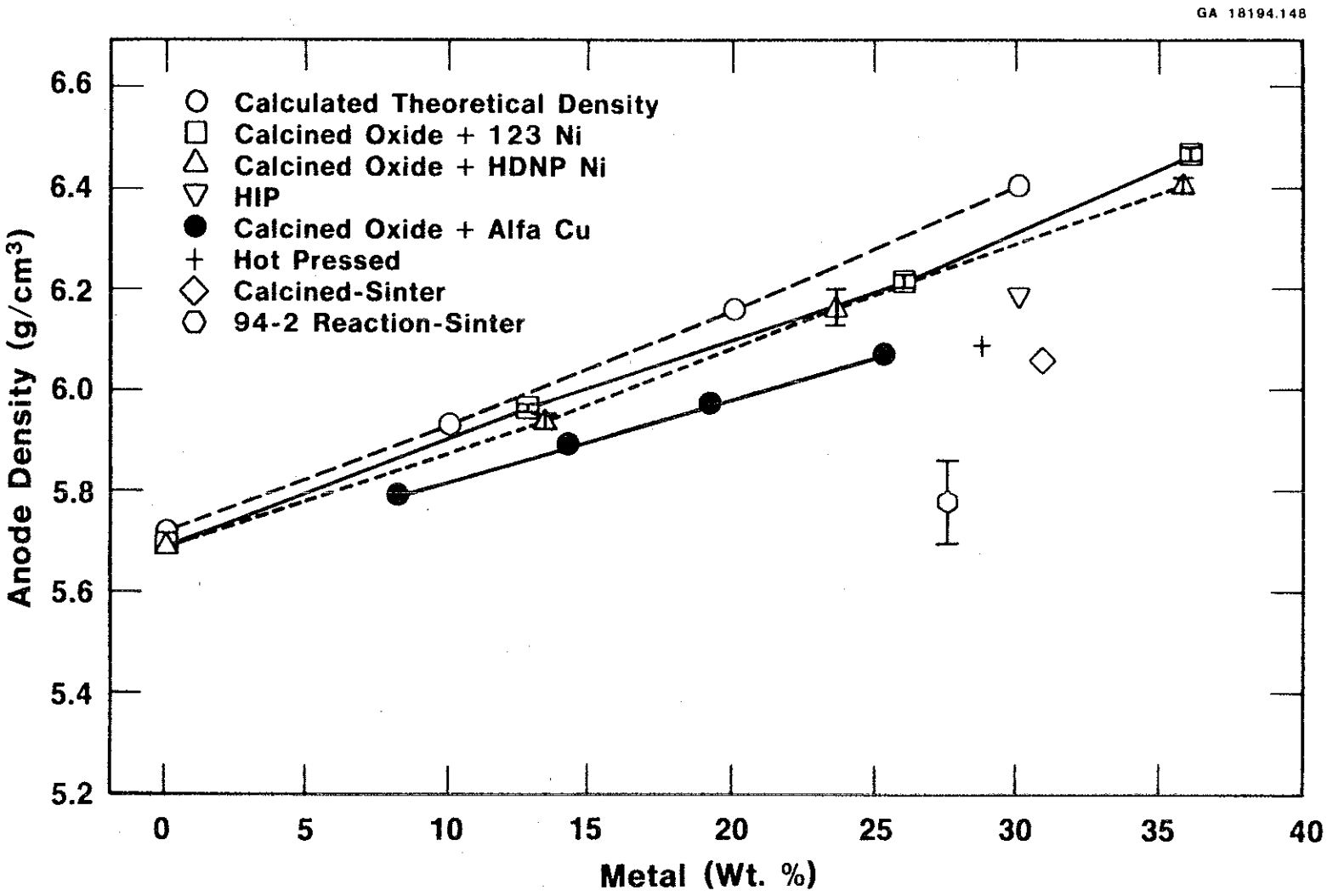

Density of Cermet Inert Anodes Versus Ni or Cu Alloy Content for Several Manufacturing Methods

Figure 203

reaction sintering or by calcine sintering were HIP'ed to densities of 6.1 to 6.2 g/cm^3. These results were obtained for anodes that were HIP'ed with or without containers. These results are shown in Figure 203, and it is obvious that no advantage in densification is obtained by the use of pressure sintering methods.

d. Fabrication Process Methods

Three process flow paths were evaluated in detail. These processes are called the (a) reaction sinter, (b) calcine cermet sinter, and (c) calcine oxide plus metal sinter. The reaction-sinter process follows the sequence where the inert anode raw materials are mixed together; the powder agglomerated, i.e., spray-dried; compact green pressed; and sintered to form the NiO, $NiFe_2O_4$, and Fe-Ni alloy phases in situ. The advantage of this method is that high electrical conductivity anodes are made with a continuous network of wormy metal phase throughout the structure. However, maximum densities of only about 90 percent of theoretical can be realized by this method. In addition, a volume expansion occurs in the compact as displacement reactions occur during the sintering process leading to possible cracking or laminations.

The calcine cermet sinter method consists of mixing all of the raw materials together, calcination of the powder mixture to form the NiO, $NiFe_2O_4$, and Fe-Ni alloy phases in the powder, grinding the powder to make it reactive, agglomeration of the powder, green pressing, and sintering. This method successfully produces sintered compacts of about 97 percent of theoretical density. These compacts have slightly lower electrical conductivity than reaction sintered compacts.

The preferred process method for fabrication of inert anodes is shown in Figure 204. This process is the calcine oxide plus metal sinter and produces anodes with the highest fabricated densities using conventional fabrication methods. In this process the oxide powders

GA 18194.149

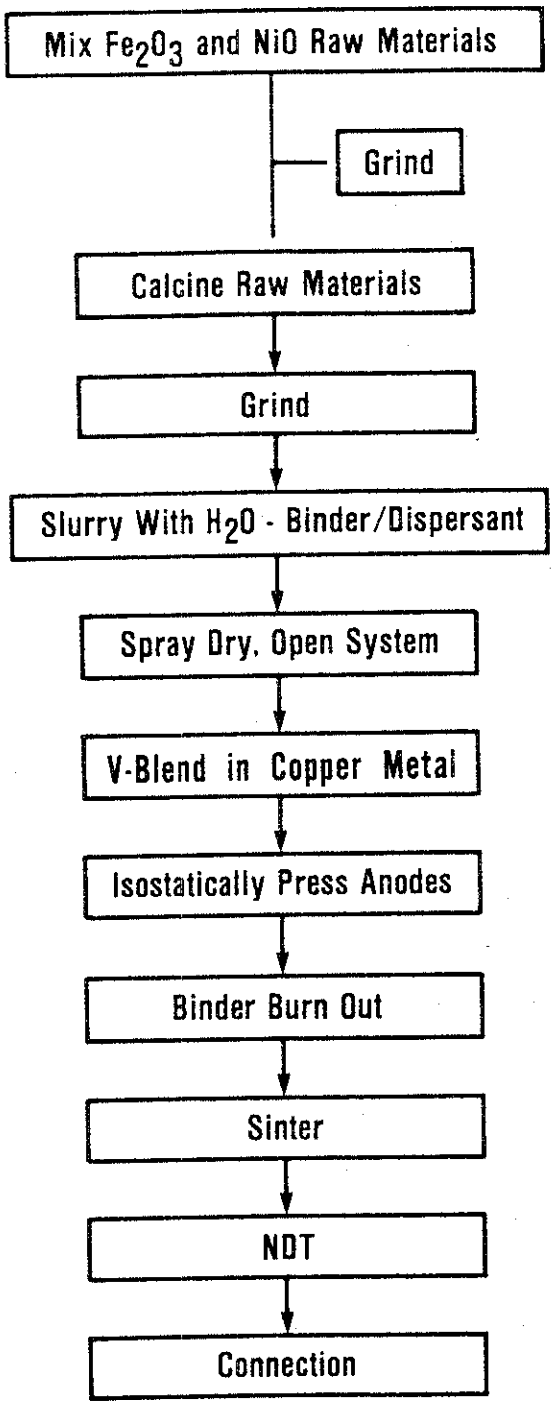

Preferred Inert Anode Manufacturing Process Flow Sheet
Figure 204

are calcined to form $Ni_xFe_{3-x}O_4$ and $Ni_yFe_{1-y}O$ phases in the powder (5324), the reacted powder is ground and spray dried, Cu or Ni metal powder is mixed with the 5324 composition spray-dried agglomerates, the resulting powder mixture is green compacted and then the compact is sintered in a flowing argon atomsphere. An example of a sintering schedule with the Cu added is to slowly heat (2.4°C/min) the compact to 400°C, heat to 1000°C at 5°C/min, hold 2 h at 1000°C, in 2 h heat to 1350°C, hold at 1350°C for 2 h, and cool with the furnace. Sintered densities of 99 percent of theoretical have been achieved by this method. A comparison of a final sintered Ni-cermet inert anode, as shown in Figure 205, with a machined green compact before sintering, illustrates the 38 percent volume shrinkage that occurs on sintering.

e. Microstructural and Physical Property Evaluations

Fabricated inert anode density information has been presented in the previous sections and in Figure 203. Preferred fabricated densities range from 6.1 to 6.25 g/cm. The volume percent porosity, pore distribution, metal particle size and distribution, metal volume percent, and calculated weight percent metal present were determined by image analysis from polished sections. The results from these analyses are contained in Table 68. Reaction sintered inert anodes contain five percent porosity, while calcined sintered compacts contain three to four percent porosity. However, nickel or copper added to calcined oxide powder results in compacts with only 1.5 percent porosity. Metal particle and pore diameters were measured at about 12 and 5 microns median diameter, respectively. The microstructures of the oxide inert anode 5324; Ni-cermet anodes fabricated by reaction sintering, calcine cermet sinter, and calcine oxide plus metal sinter; and Cu-cermet anodes fabricated by calcine oxide plus metal sinter methods are shown in Figures 206 through 210. The effect of HIP'ing on selected samples is also shown in these figures.

GA 16521

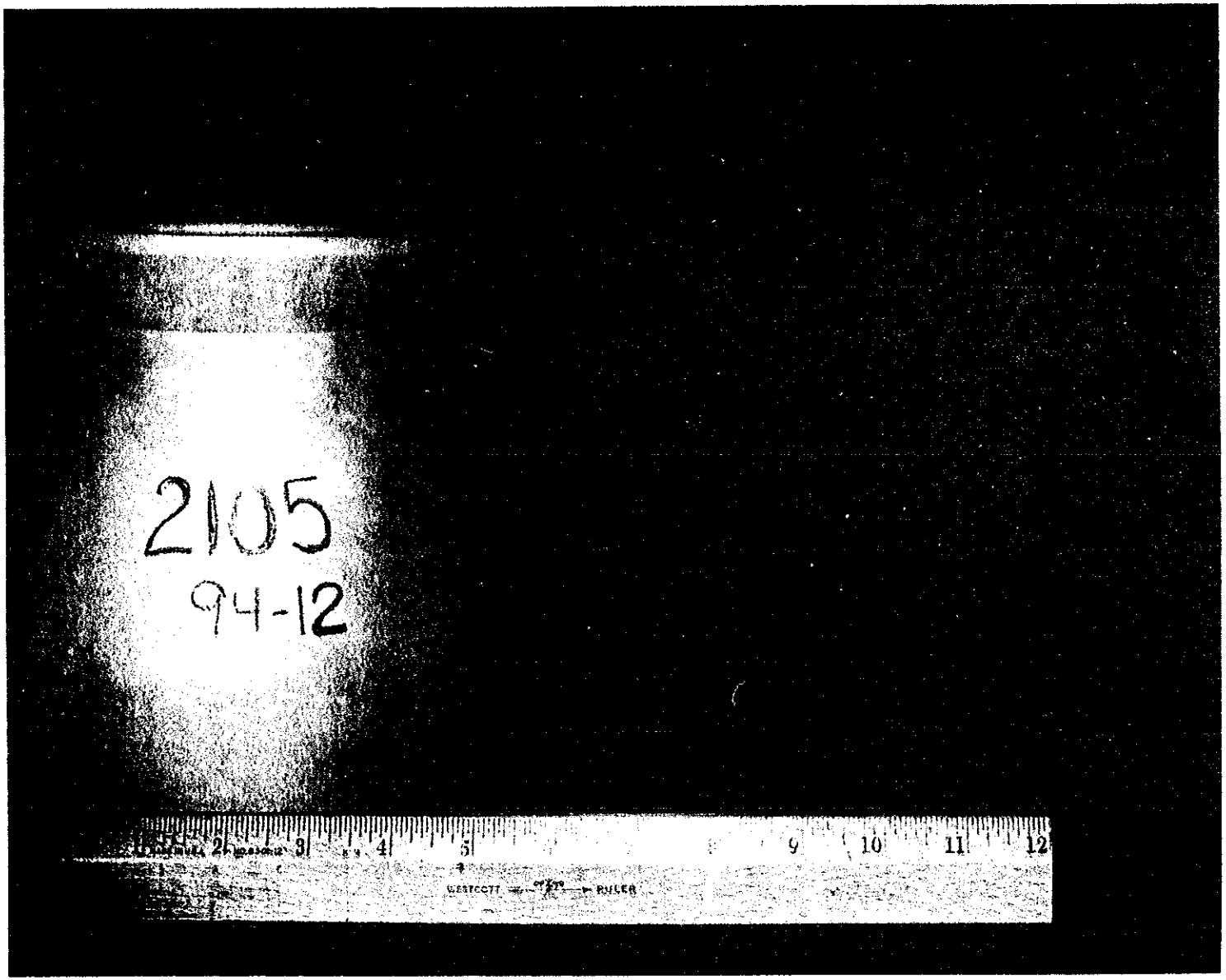

Sintered (Left) and Green (Right) Inert Anodes for 2500-Ampere Cell

Figure 205

TABLE 68

Density and Phase Amounts In Cermet Anodes by Image Analysis

SAMPLE TYPE	WT.% Ni ADDED	NI GRADE	SINTERING FURNACE	HIPed	HIP WITH CONTAINER	ASTM DENSITY	APP. POROSITY	H_2O ABSORPTION
	%					g/cm^3	%	%
5324, Oxide	0	--	Pereny	No	--	5.69	0.16	0.03
	0	--	AT	No	--	5.48	0.37	0.07
	0	--	Pereny	Yes	No	5.43		
	0	--	Pereny	Yes	Yes	5.47	1.16	0.44
	0	--	--	Yes	Yes	5.25	8.72	0.51
6846, Reaction Sinter	0	--	Pereny	No	--	5.89	1.94	0.34
	0	--	Pereny	Yes	No	6.06	4.22	0.20
	0	--	Pereny	Yes	Yes	6.21	0.15	0.08
	0	--	--	Yes	Yes	4.71	23.96	
6846, Calcined Powder	0	--	Pereny	No	--	6.04		
	0	--	Pereny	Yes	Yes	6.19	0.26	0.17
6846, AL-66	0	--	--	Yes	Yes	6.09	0.21	0.04
5324 + NI	10	123	Pereny	No	--	5.97	0.04	0.02
	20	123	Pereny	No	--	6.215	0.09	0.01
	30	123	Pereny	No	--	6.470	0.08	0.01
	10	HDNP	Pereny	No	--	5.940	0.08	0.01
	20	HDNP	Pereny	No	--	6.165	0.06	0.01
	30	HDNP	Pereny	No	--	6.410	0.09	0.01
	10	123	AT	No	--	5.905	0.09	0.01
	20	123	AT	No	--	6.165	0.07	0.01
	30	123	AT	No	--	6.425	0.09	0.01
	10	HDNP	AT	No	--	5.890	0.12	0.02
	20	HDNP	AT	No	--	6.145	0.12	0.02
	30	HDNP	AT	No	--	6.380	0.11	0.02
5234 + CU	5	Alfa	AT	No	--	5.79	0.07	0.01
	10	Alfa	AT	No	--	5.90	0.06	0.01
	15	Alfa	AT	No	--	5.98	0.06	0.01
	20	Alfa	AT	No	--	6.07	0.12	0.02

TABLE 68

Density and Phase Amounts in Cermet Anodes by Image Analysis (Continued)

SAMPLE TYPE	VOL.% NI	±	WT.% NI CALC.	±	AVERAGE METAL PARTICLE, DIAMETER	±	VOL.% POROSITY	±	AVERAGE PORE DIAMETER	±
	%		%		m		%		m	
5324, Oxide	3.82	±1.06	6.02	±1.67	6.07	± 2.41	3.38	±1.19	5.28	±1.98
	--	--	--	--	--	--	--	--	--	--
	0.0	--	0.0	--	--	--	5.46	±3.36	--	--
	0.0	--	0.0	--	--	--	5.67	±1.83	--	--
	2.99	±2.43	5.10	±4.14	10.12	± 2.89	--	--		
6846, Reaction Sinter	24.46	±2.78	35.13	±3.99	11.39	± 7.06	5.29	±1.64	7.55	±5.36
	21.3	±1.16	29.92	±1.63	11.81	± 8.18	1.09	±0.56	4.74	±3.38
	21.45	±1.77	30.24	±2.50	11.25	± 6.76	1.58	±0.64	6.18	±3.75
	7.37	±1.00	19.27	±2.61	7.63	± 3.84	44.60	±6.26	--	--
6846, Calcined Powder	24.31	±1.32	36.64	±1.99	9.67	± 5.19	4.05	±0.64	7.92	±5.28
	20.32	±3.35	29.07	±4.79	10.55	± 6.17	2.54	±0.77	6.54	±3.56
6846, AL-66	19.85	±1.05	28.23	±1.49	9.84	± 5.31	1.65	±0.56	7.33	±3.77
5324 + Ni	8.40	±1.03	12.68	±1.55	9.10	± 5.63	1.61	±0.46	5.27	±2.43
	18.14	±2.08	26.0	±2.98	11.70	± 8.48	1.45	±0.63	4.70	±2.37
	26.20	±2.09	36.0	±2.87	15.04	±12.41	1.51	±0.68	5.02	±2.95
	8.80	±2.81	13.3	±4.52	11.52	±10.43	1.17	±0.32	4.72	±2.24
	16.37	±3.51	23.5	±5.04	13.99	±11.51	1.11	±0.43	4.88	±2.38
	25.99	±5.04	35.8	±6.94	16.24	±13.01	1.52	±0.49	5.10	±3.10
5234 + Cu	5.39	±1.18	8.44	±2.79	7.86	± 5.25	1.01	±0.36	6.16	±3.88
	9.74	±1.78	14.27	±3.6	13.14	± 9.32	1.08	±0.39	5.35	±2.85
	13.5	±2.33	19.32	±4.34	12.1	± 8.0	1.22	±0.39	6.3	±3.6
	18.04	±2.77	25.40	±4.93	13.8	±10.88	2.55	±1.08	---	---

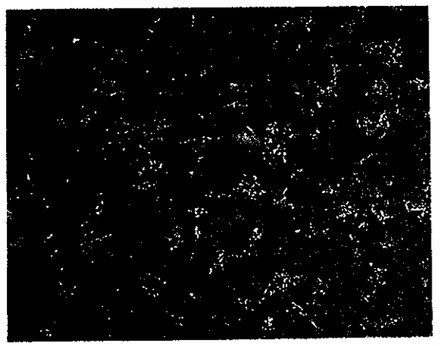

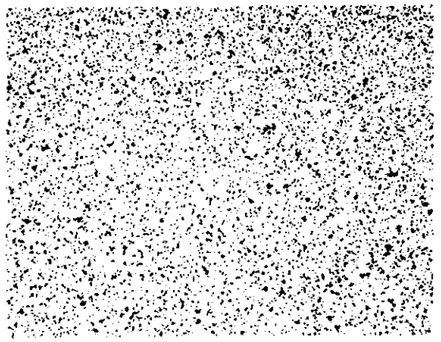

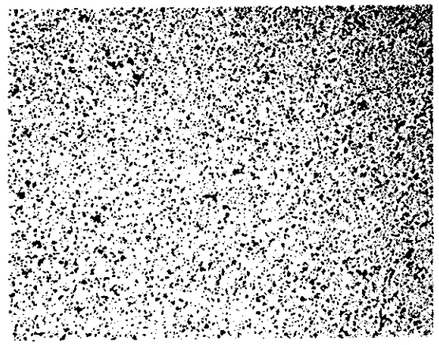

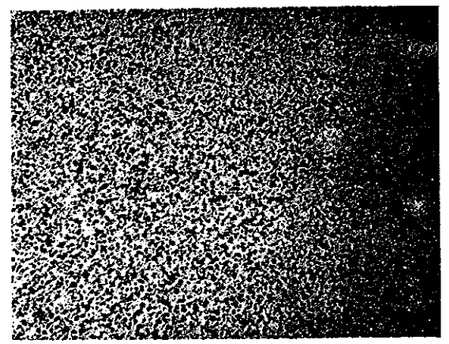

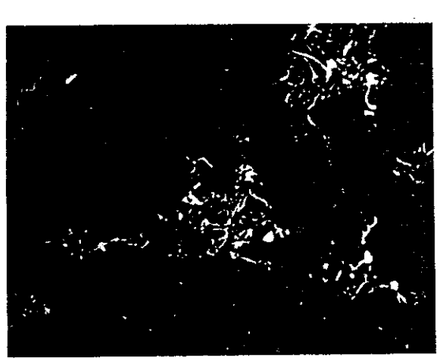

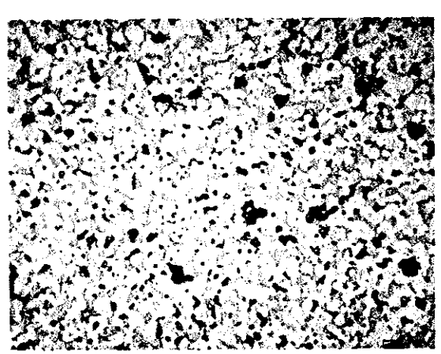

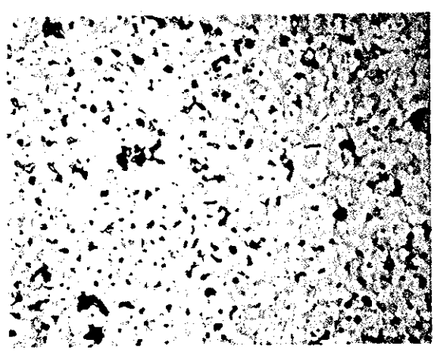

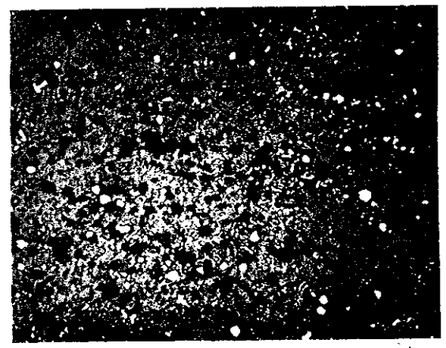

Microstructure and Physical Properties of Oxide Composition 5324 After Hot Isostatic Pressing at 1100°C and 103 MPa Pressure for 3 Hours (Center)

Figure 206

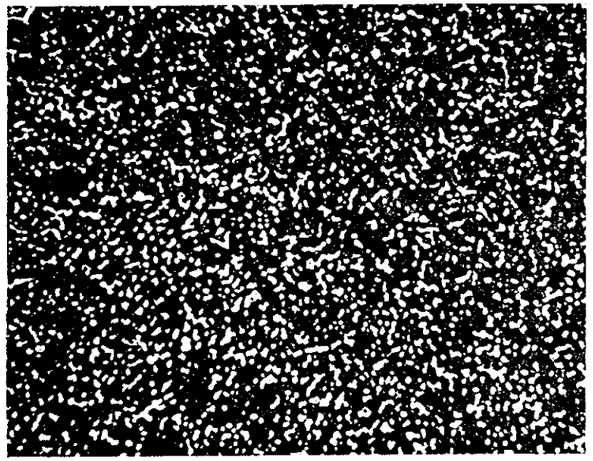

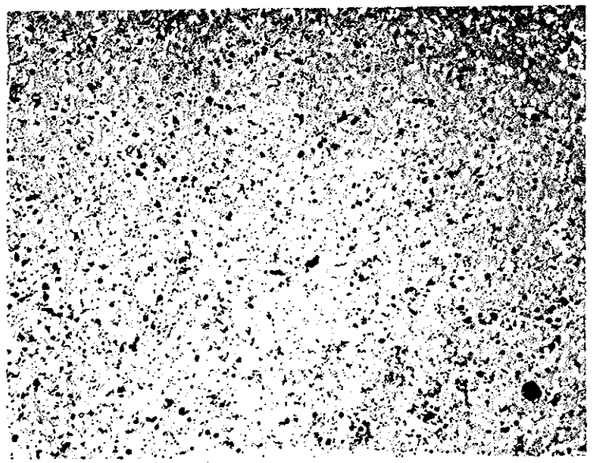

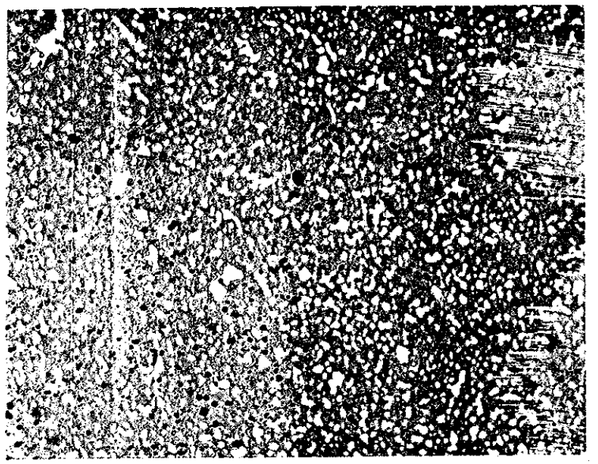

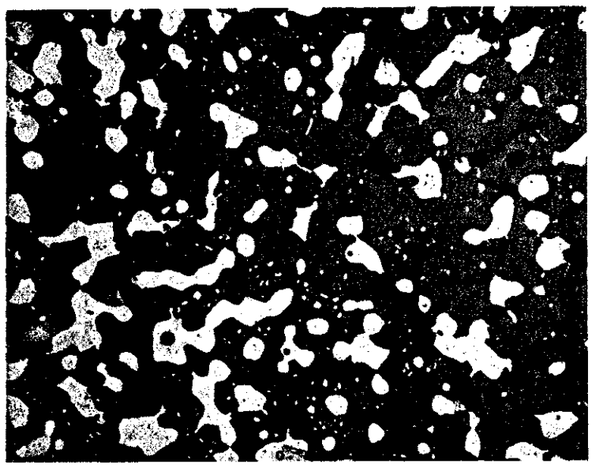

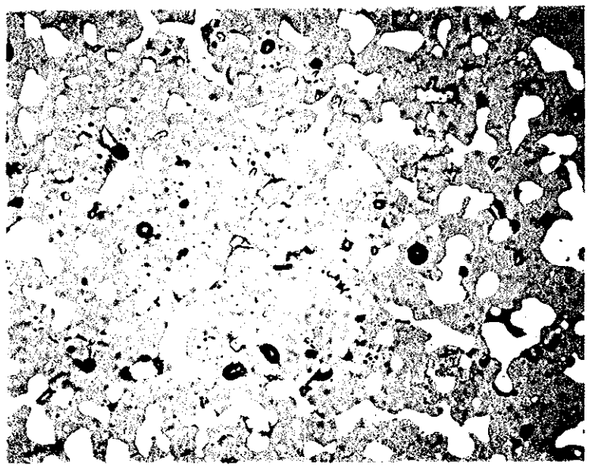

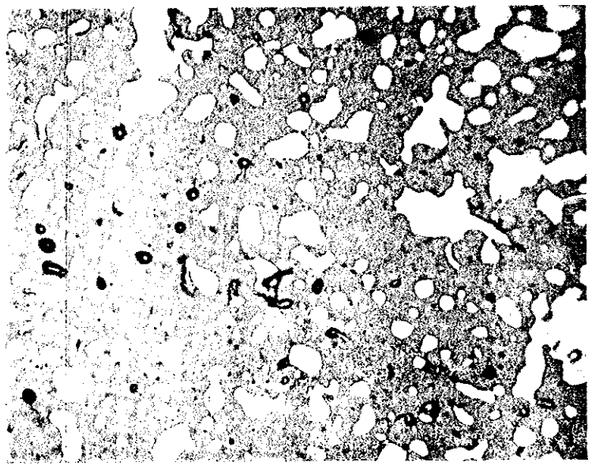

Microstructure and Physical Properties of Cermet Composition 6846 After Calcination, Cold Pressing, Sintering and Hot Isostatically Pressing at 1100°C and 103 MPa Pressure for 3 Hours (Center)

Figure 207

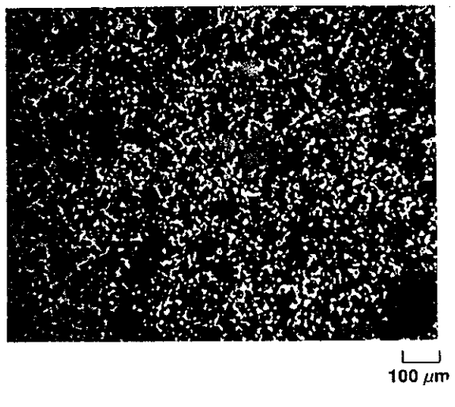

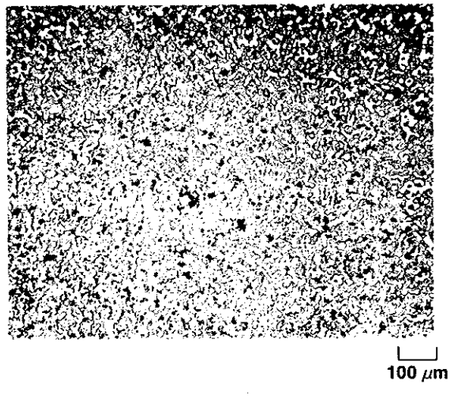

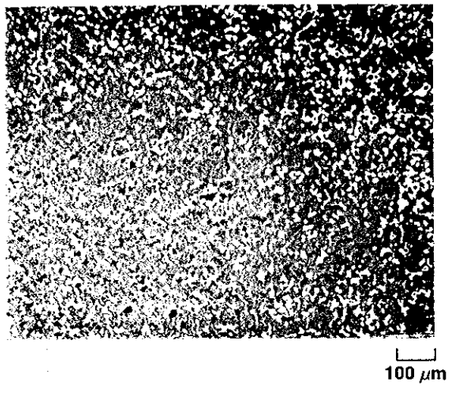

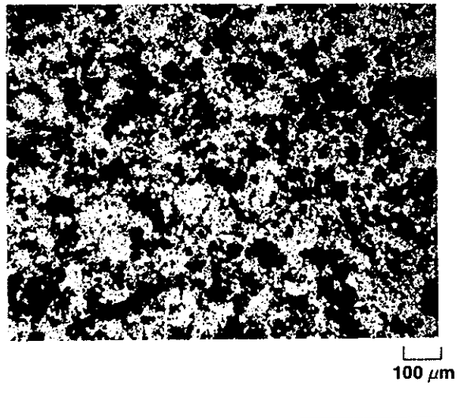

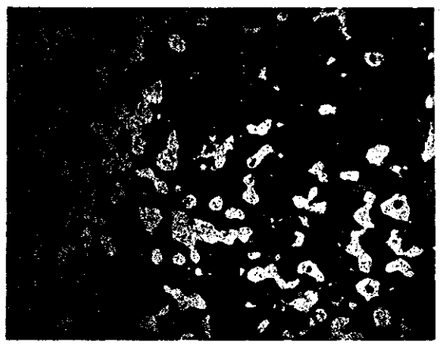

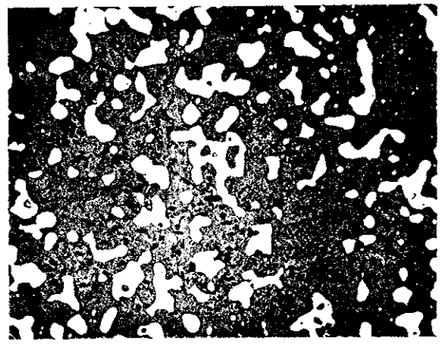

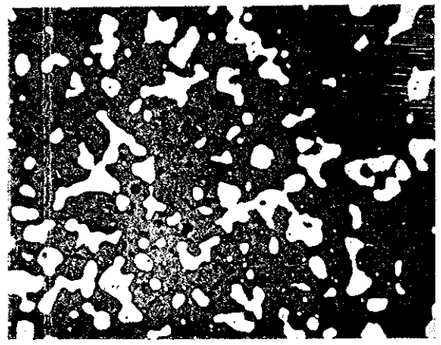

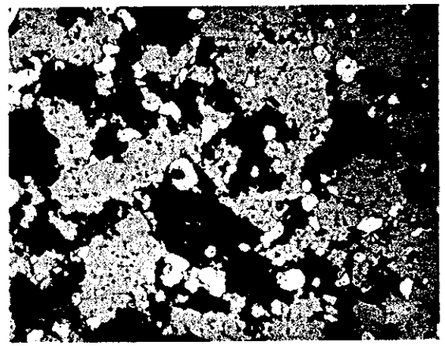

Microstructure and Physical Properties of Cermet Composition 6846 After Hot Isostatically Pressing at 1100°C, 103 MPa Pressure for 3 Hours (Center)

Figure 208

5. Conclusions

Inert anodes of commercial size can be fabricated from commercially available raw materials using conventional powder preparation, pressing, and sintering techniques. The recommended process includes the selection of fine (1 micron median diameter) oxide powders, blending, calcination, and spray drying these powders and then blending with fine (10 micron median diameter) Ni or Cu metal powders. These powders are then isostatically pressed to shape, green machined, and sintered to high densities in atmospheres of flowing inert gas at temperatures of 1200 to 1400°C. Connections can be made to these fabricated inert anodes for successful operation in commercial size (2500-amperes or larger) Hall cells.

V. PHASE III - ANODE-STUB CONNECTION, DESIGN, TESTING AND EVALUATION

1. Objectives

Objectives of this phase of the project were to develop a stable connection between the metallic electrical stub material and the inert anode of proper materials and design, evaluate the anode and the anode stub connection performance in pilot size Hall cells, and perform detailed analysis on the anodes after testing to evaluate inertness of the material and to predict anode life.

2. Introduction

Areas of investigation included: (a) anode and anode connection designs, (b) finite element analysis of anode-anode connection designs, (c) Hall cell testing and performance of bench and pilot sized anodes, and (d) evaluation of anode properties after Hall cell testing. Performance of anode assemblies is expected to be dependent upon many variables, including Hall cell operating parameters and practices, anode fabrication practices and variables, and raw material selection. The purpose of the experiments conducted in this phase of the project was to determine important factors that influence anode performance and life.

Patent literature makes reference to various conceptual and experimental techniques that could be utilized to join the current conductor from the bus with a nonconsumable anode body--usually a semiconductive oxide material. A 1973 patent (29) describes proposed connections using liquid silver, silver or platinum coatings with a nickel alloy wire mesh, and a nickel powder as joint materials.

Two more recent patents (30,105) discuss materials that can be used as a current distributor within the ceramic anode body. Metals such as nickel, copper, cobalt, molybdenum, and molten silver; nonmetallic electrically conductive materials such as carbides, nitrides, and borides were suggested. It is stated that the current distributor should be "built into the anode" and that it "must not react with the ceramic material at the operating temperature, e.g., at 1000°C."

The pure metals listed above may fulfill conductivity requirements of a current distributor, but in general they lack elevated temperature mechanical strength, oxidation resistance and will not have coefficients of thermal expansion matching that of the ceramic anode body.

The Sumitomo Chemical Co., Ltd. (28) suggested conductive substrate materials such as titanium, nickel, copper, carbon, graphite, carbides, nitrides, borides, silicides, molybdenum, and tungsten on which the oxide ceramic could be coated. The oxidizing atmosphere which is generated in a Hall cell with inert anodes will erode carbon or graphite, so this material is not a likely candidate as a current distributor. Other approaches were to utilize an alloy that will produce a spinel and/or perovskite structure oxide upon oxidation. Thus, a coherent interface between the current distributor and the conductor could be established.

3. Anode Connection Design - 60-A Cell Testing

Many anode-to-stub connection designs were considered and evaluated during the initial years of the project (3). Initial studies were conducted with an all-oxide 5324 anode material (NiO 51.3, Fe_2O_3 48.7 wt.%) exhibiting low electrical conductivity and resistance to thermal shock. Designing and demonstrating a stable, low-resistance connection assembly with this material was most difficult, and all attention switched to the newer 6846 reaction sintered cermet material (NiO 60 wt.%, Fe_2O_3 20 wt.%, Fe 20 wt.%) with improved electrical conductivity and thermomechanical properties.

With this material, a diffusion welding technique was found to be most promising. The technique involved prereducing the anode surface in the joint area with carbon at 1000°C, followed by diffusion welding the reduced layer to a nickel 201 stub rod at 380 kPa pressure in an argon atomosphere.

A series of anodes with diffusion welded connections were evaluated in 60-A and 2500-A Hall cells during the project. Billet shaped solid anodes, approximately 65 mm diameter, were run in the 60-A bench Hall cell; and crucible shaped inert anodes, approximately 180 mm diameter, were run in the 2500-A pilot Hall cell. Control of the Hall cell variables during

operation with inert anodes proved to be most important. One of the objectives of the project was to develop an inert anode material and a connection that had a two-to-three-year-lifetime stability. Any change in microstructure of the connection to the anode and of the anode itself was considered detrimental to performance.

Inert anode test No. IA-96 (6846 material) is typical of results obtained in the 60-A cell (Figure 211). Raw material combinations used to fabricate the anode consisted of 20 wt.% Atomet 95 Fe, 20 wt.% Pfizer BK-5000 Fe_3O_4, and 60 wt.% N-139 green nickel oxide (6846). The anode was isostatically pressed at 138 MPa and reaction sintered at 1350°C in argon. The 60-A cell is shown in Figure 213, and was controllable according to the following parameters:

Bath Temperature	960°C
Bath Ratio	1.12
Anode-Cathode Distance	25-38 mm
Cell Current	30-35 A
Current Density	1 A/cm^2 (anode bottom)

Alumina feed was adjusted for the assumed current efficiency of the cell. Figure 212 is a photograph of a polished cross-section of anode IA-96 following the 96-hour test. This photograph clearly shows the oxidation zone that occurs in the anode due to anodic dissolution during electrolysis. The diameter of the anode has not been reduced to any measurable extent. Two samples, M-316 and M-317, were extracted from the sample for microstructural investigations. Figures 213 and 214 are photomicrographs of the connection area of this anode. The two photomicrographs clearly show the zones that occur in the anode from the nickel stub through the diffusion weld, reduced cermet and the transition zone to the normal cermet. Note that a layer of oxide occurs in the transition zone between the reduced cermet and the cermet.

Phases present in the cermet region are nickel oxide, nickel ferrite and Ni-Fe alloy. As expected for the unaltered material, phases present in the reduced cermet phase next to the diffusion welded connections are Ni-Fe alloy, iron-aluminum fluorides, cryolite bath and an iron-fluorine-silicon-oxygen compound. Figure 215 is a photomicrograph of the bottom of the

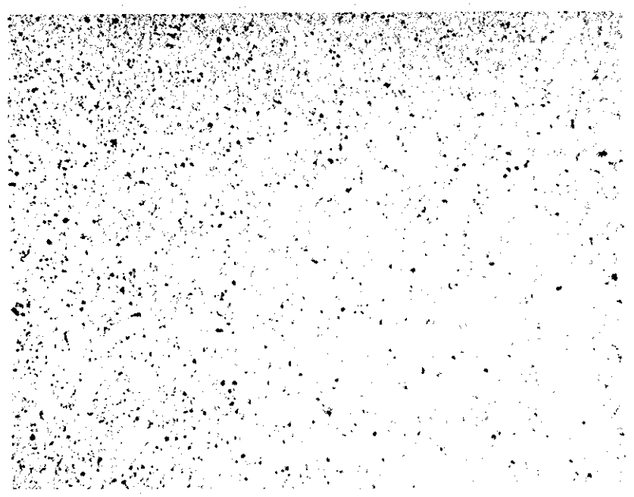

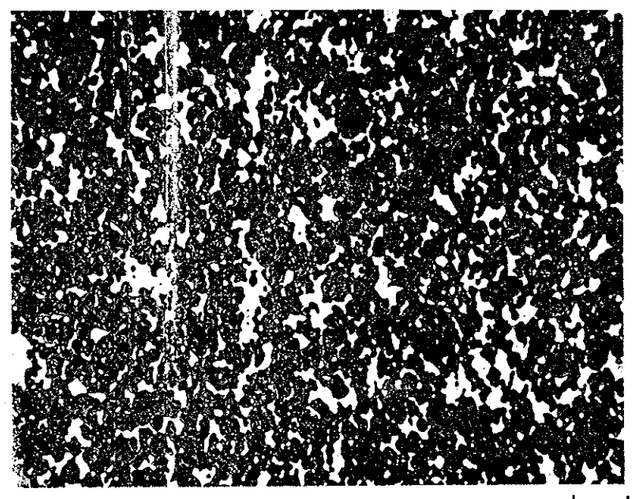

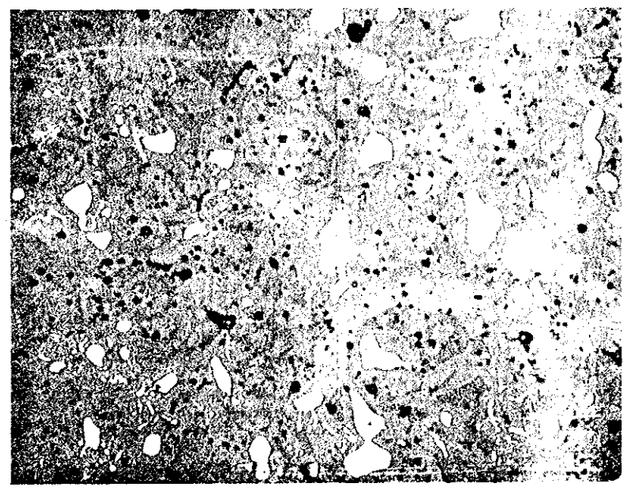

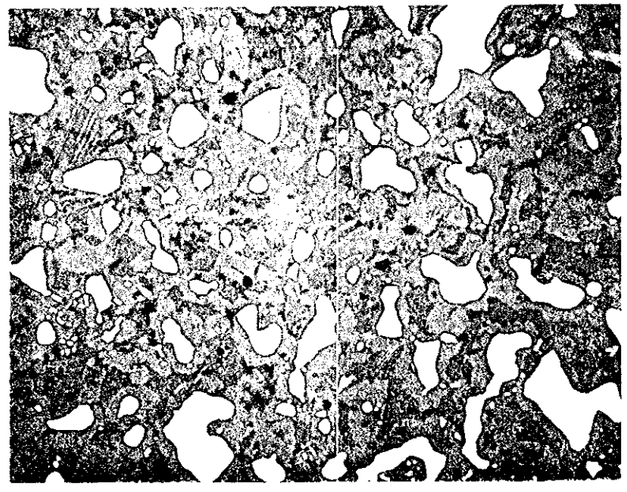

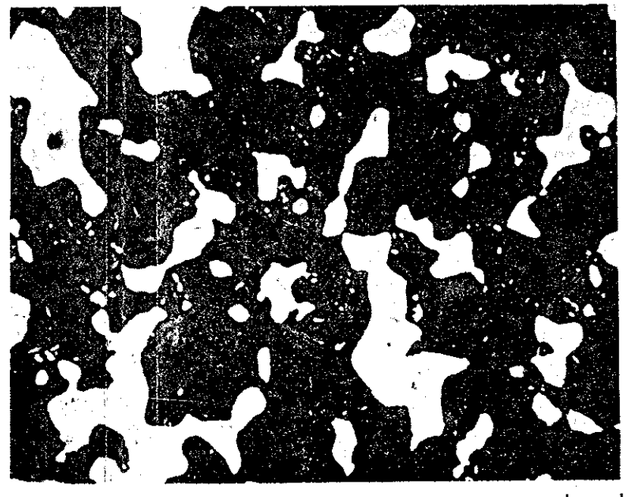

Microstructure of Cermet Anodes Fabricated by Addition of Grade 123 - Ni Metal to 5324 Oxide Powder, Cold Pressing and Sintering

Figure 209

GA 17323

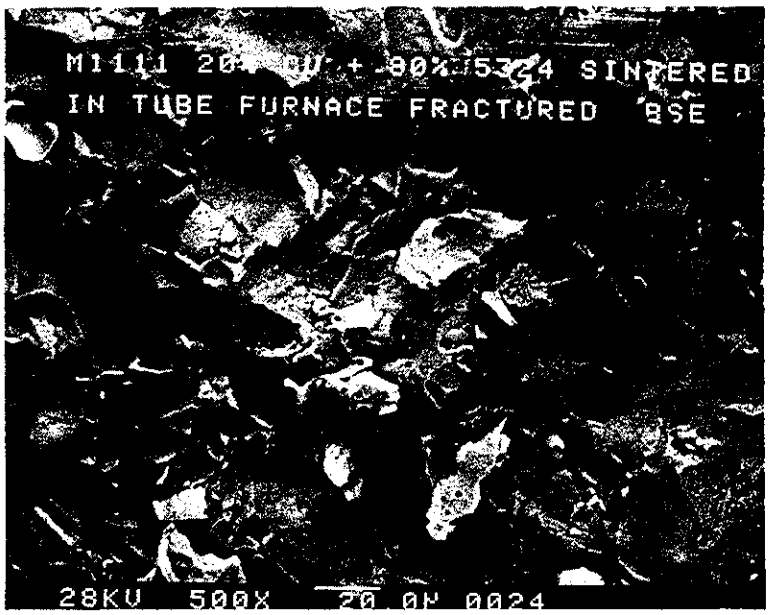

500X M1111 20μm

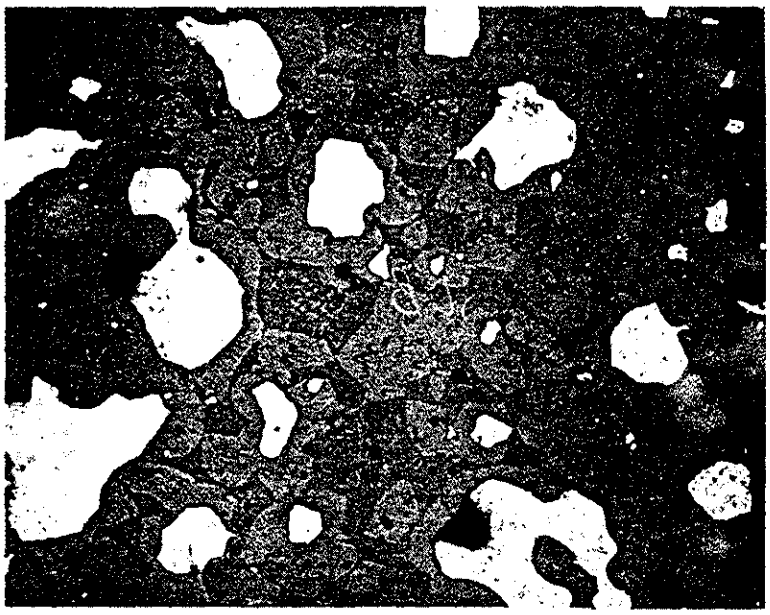

400X M1111 25μm

Fractured (top) and Polished Surfaces of 5324 + 20% Alfa Cu Cermet Inert Anode

Figure 210

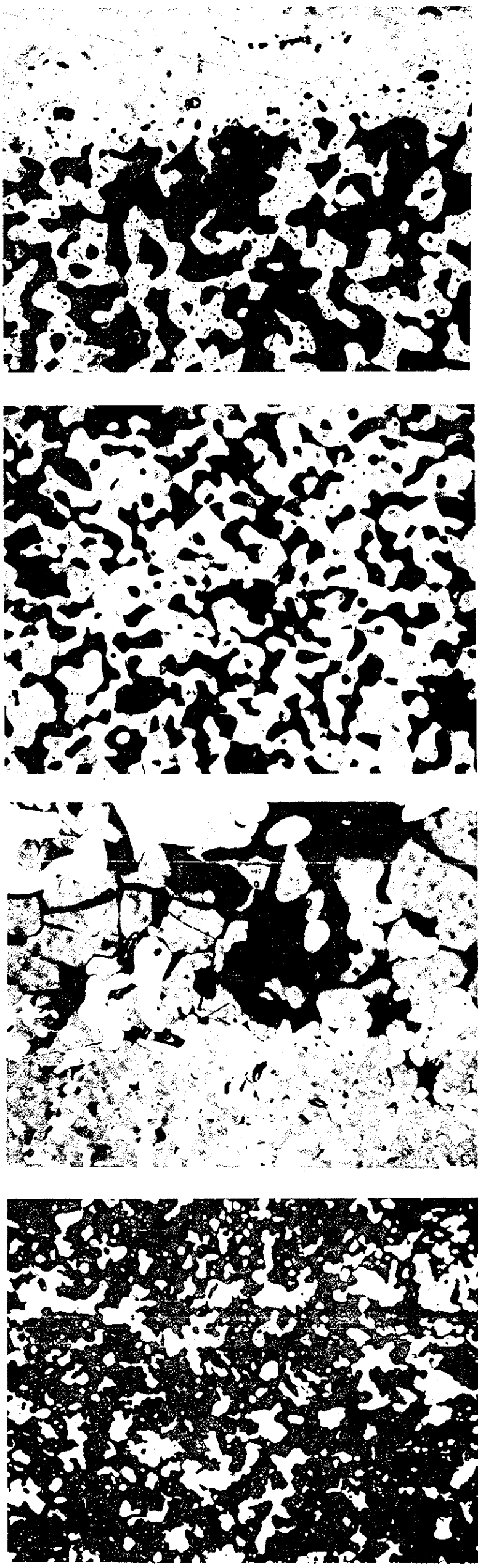

Anode 94-2, Test 1A-96 Sample M-316 (200X)

Figure 213

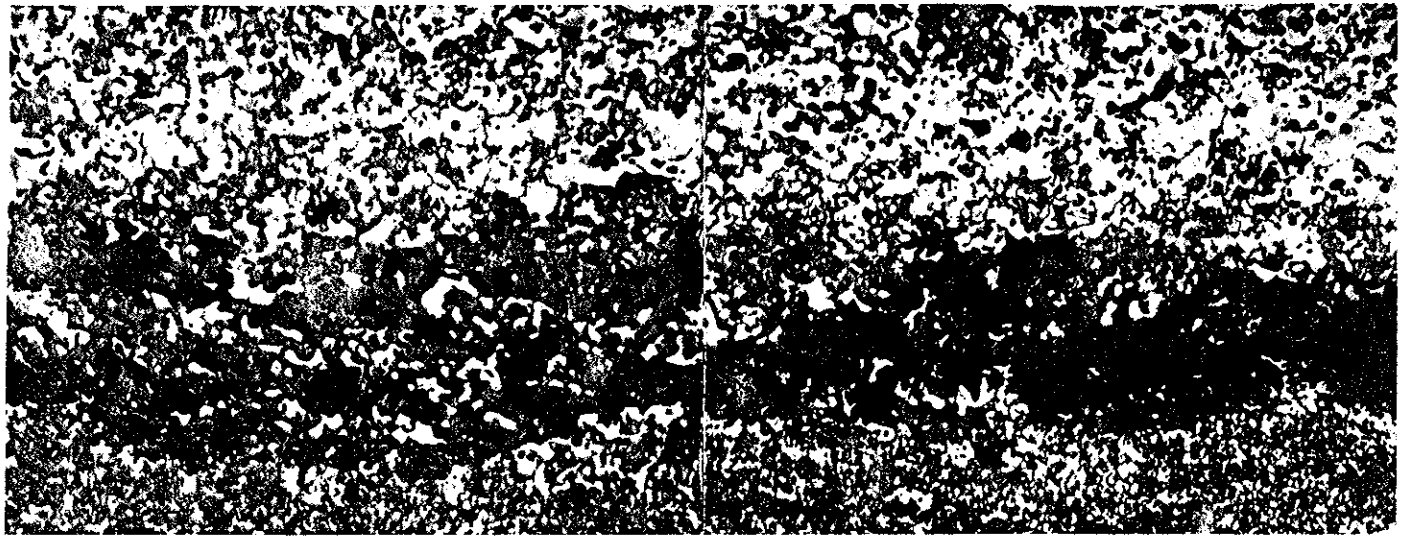

M-316 50X

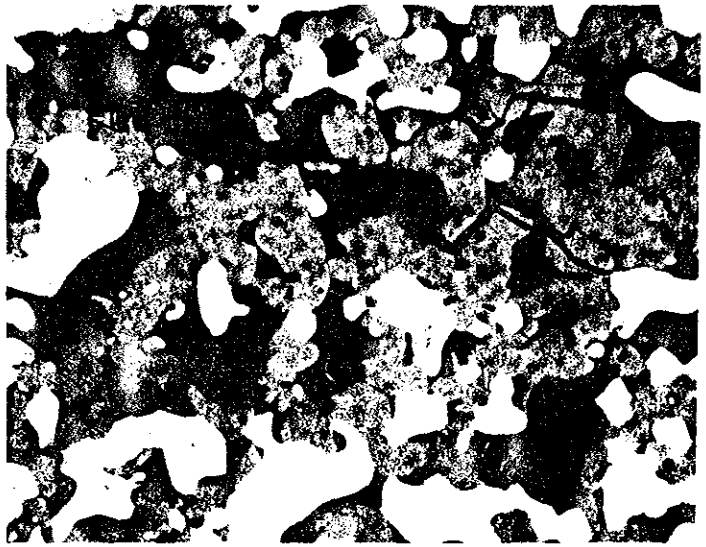

M-316 200X

Test 1A-96, Top of Billet, Below Diffusion Weld

Figure 214

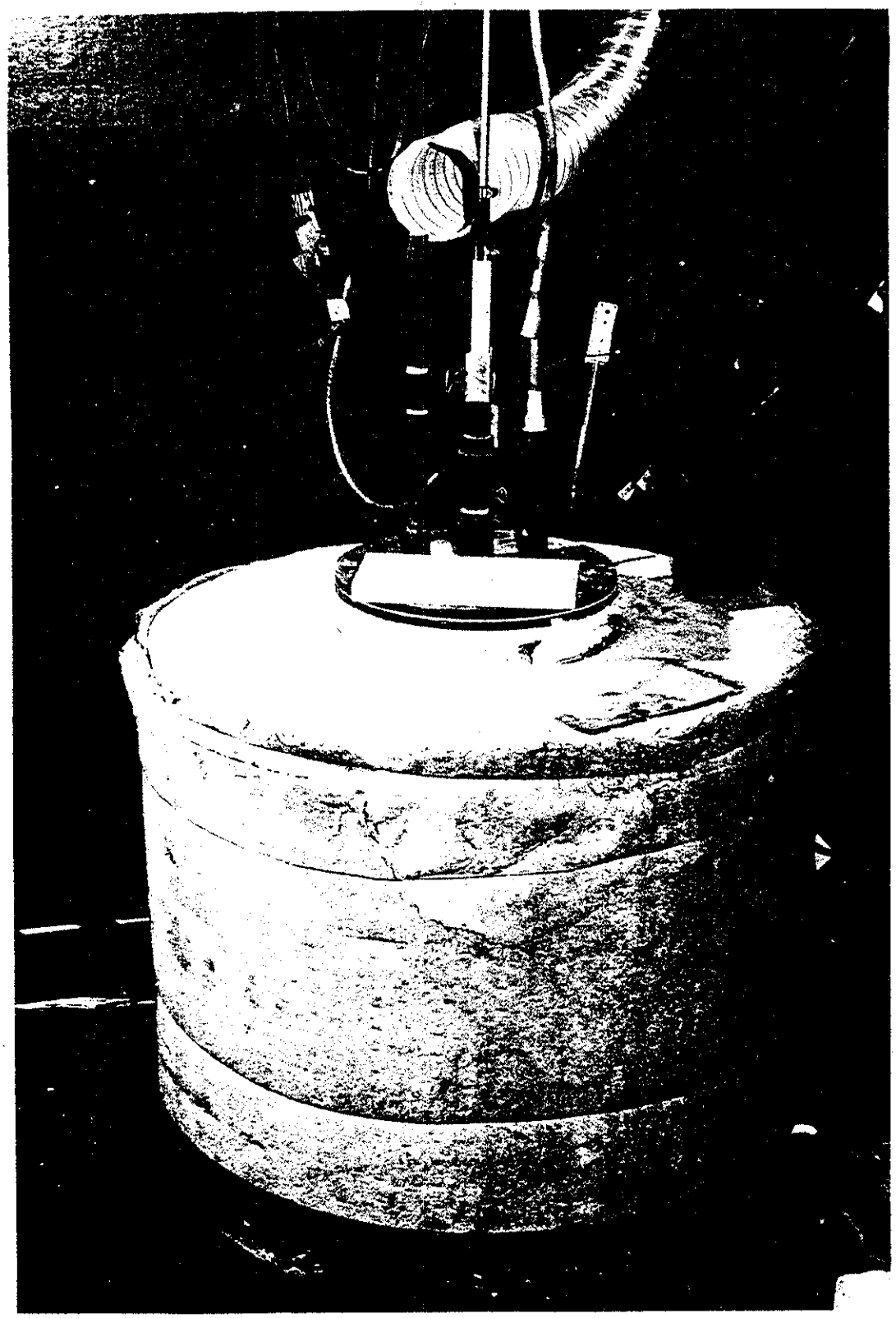

60-Ampere Bench Scale Reduction Cell
Figure 211

GA 17859.9

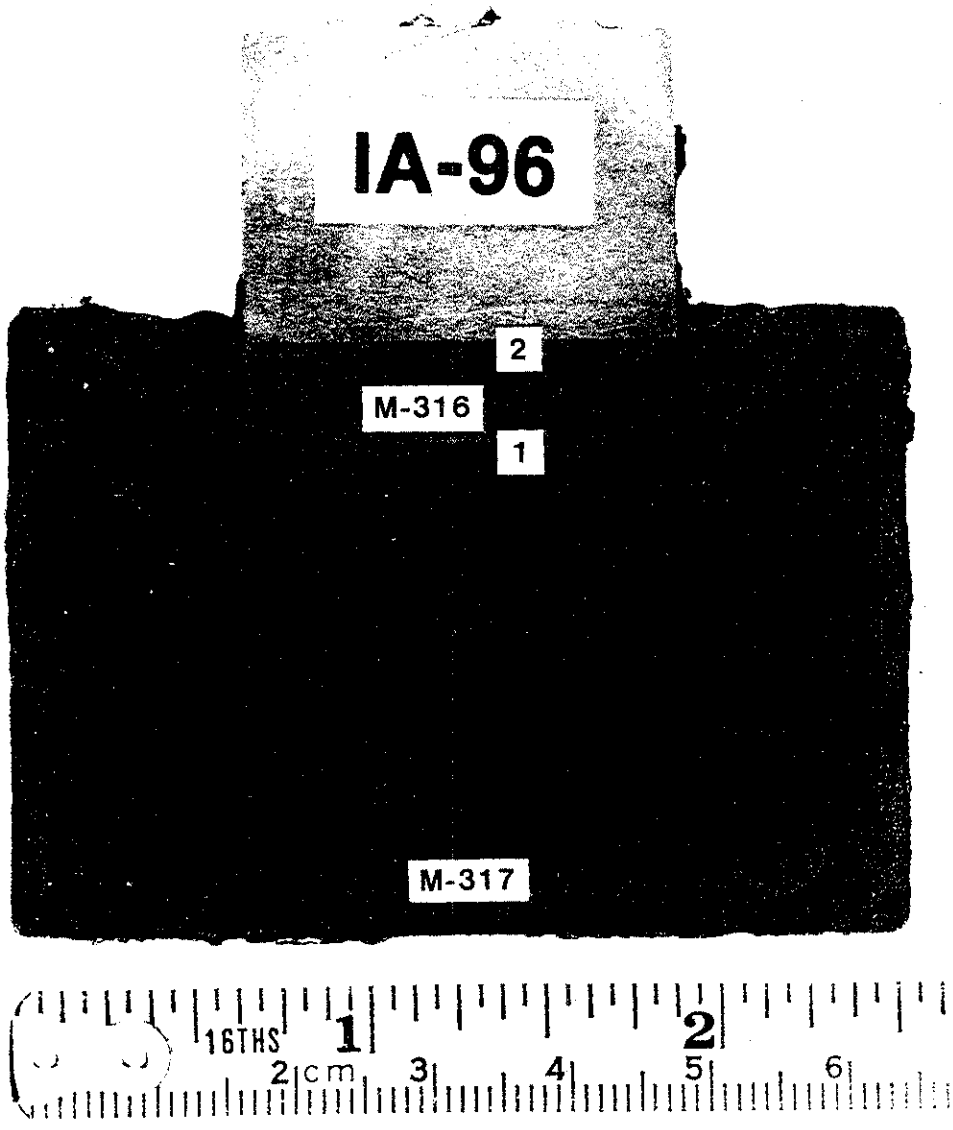

Anode 94-2-2, Test 96, 96 Hours in 60 Ampere Cell
Figure 212

GA 16521

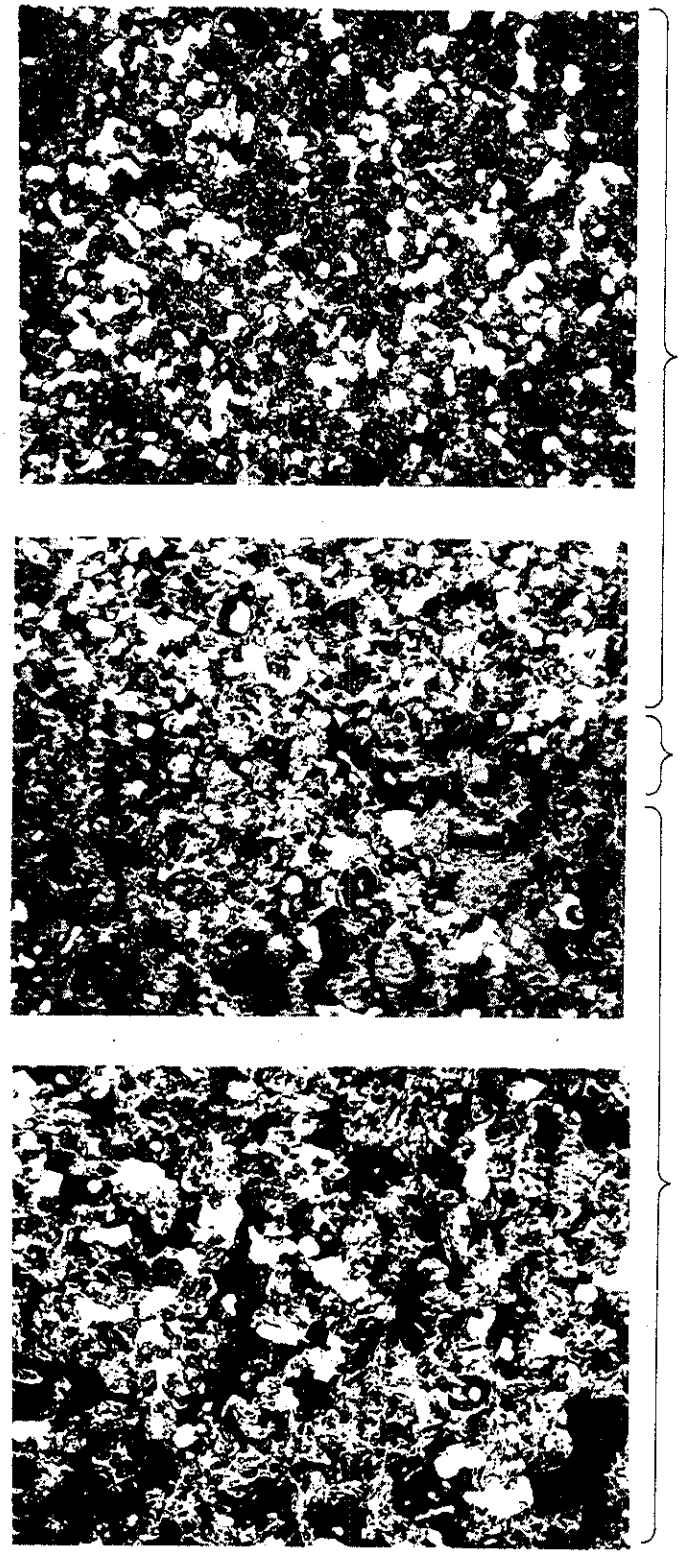

Test IA-96, 96 Hours, Bottom of Exposed Billet, 94-2 6846 Material

Figure 215

anode showing the oxidation or reacted layer due to anodic dissolution during electrolysis.

Results from these early tests in the 60-A cell showed that the 6846 cermet composition was not stable due to changes in the microstructure upon exposure to electrolysis and bath. The Ni-Fe alloy metal phase was removed generating porosity for bath penetration and continued degragation. The diffusion welded connection was penetrated by both species together with microstructural changes during electrolysis. Gaps formed in the connection area that eventually would lead to failure.

Recognizing these problems, results were sufficiently encouraging to continue testing in the larger 2500-A cell while corrosion studies and material development programs continued to produce oxide materials with improved stability and life.

4. 2500-A Pilot Cell Design and Testing

Testing of inert anode assemblies in a 2500-A pilot cell was included in this research program to demonstrate the ability to fabricate large inert anode shapes and make connections to metallic stub materials for preheating and transferring into molten bath. Operation of this size cell conserves material and labor as compared to larger cells, while providing critical information leading to the use of inert anodes in commercial cells.

Experience has demonstrated that operation of a small, self-heated cell is difficult with regard to temperature control and the ability to maintain a frozen ledge on sidewalls. The cell must be heavily insulated to conserve heat and maintain an operating temperature of 960°C. The required heat is generated by maintaining an interelectrode spacing of approximately 100 mm. Cell operation is usually limited to approximately ten weeks due to deterioration and penetration of the lining with molten bath and metal. This time period was considered sufficient for the tests planned on inert anodes.

A photograph of the 2500-A cell is shown in Figure 216. The cell was

GA 17742-1

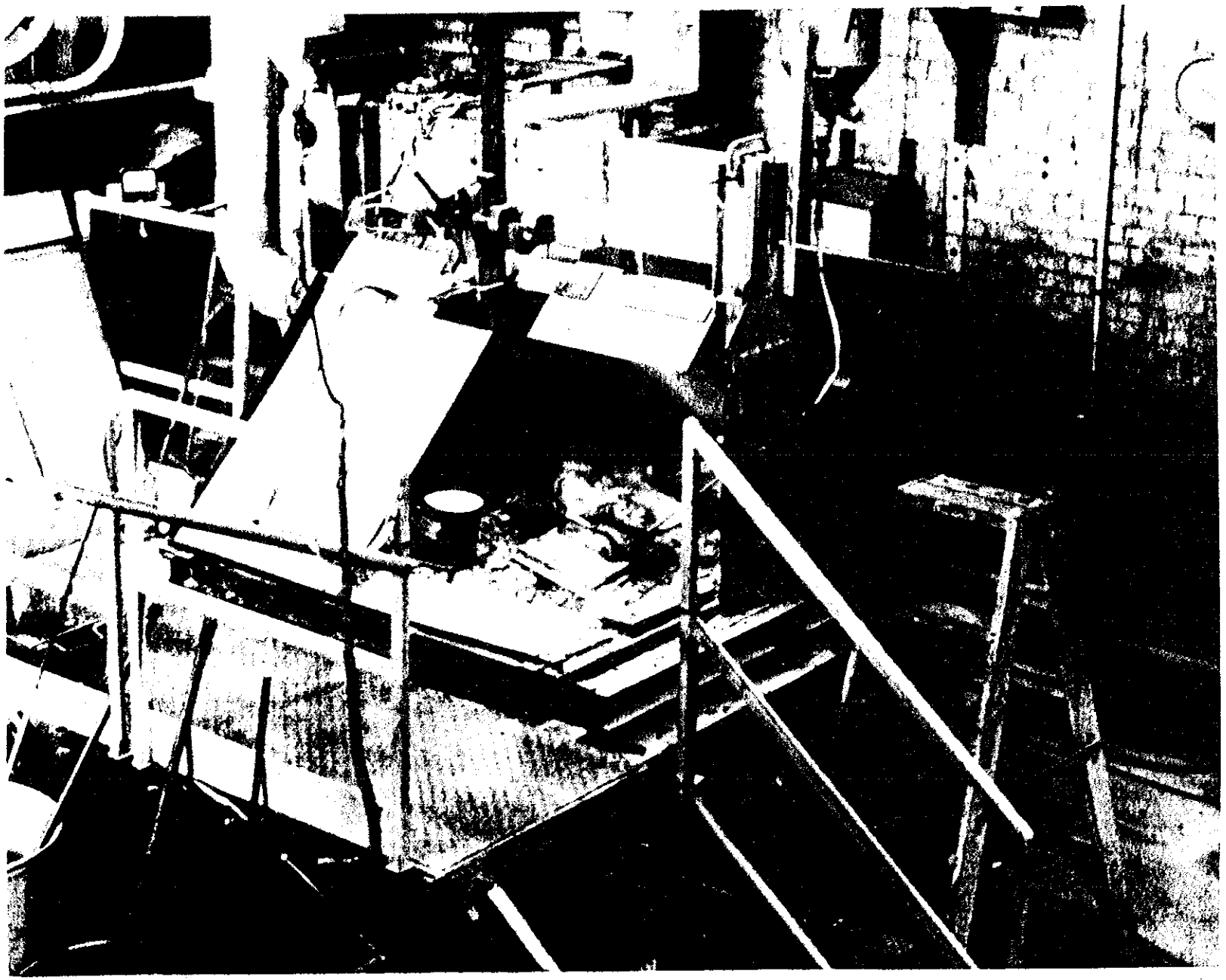

2500-A Hall Cell
Figure 216

started with a single carbon anode placed on carbon resistor blocks, with power applied to provide the initial heat. When the temperature under the anode reached 850°C, the sides were packed with crushed bath half way up the anode. When the temperature reached 977°C, liquid bath, tapped from another cell, was added and electrolysis started.

As with any new cell, bath ratio was constantly changing due to sodium intercalation in the lining, requiring constant additions of sodium fluoride. Current efficiency during this startup period was approximately 50 percent and not considered unusual based upon the dusty condition of the cell.

Operation with the carbon anode continued for several days to stabilize cell operating parameters prior to removal of the carbon anode and introduction of the inert anode assembly. Bath temperature was targeted for 960°C with a bath ratio (NaF/AlF_3) of 1.15. Al_2O_3 content varied considerably in initial runs as attempts were made to minimize mucking or sludging while still operating at near saturation levels.

The inert anode materials selected for these tests consisted of NiO (60 wt.%), Fe_3O_4 (20 wt.%), and Fe (20 wt.%) powders which were mixed, spray dried, isostatically pressed and reaction sintered to produce a three-phase cermet material consisting of $NiFe_2O_4$ spinel, $Ni_{i-x}Fe_xO$ oxide, and Ni/Fe alloy metal phases.

Two anode configurations were used in these pilot studies. The first was a flower pot type configuration joined to the nickel stub by diffusion welding (Figure 217). The second was a flask type configuration joined to the stub with a mechanical connection (Figure 218). Many connections for joining the inert anode to the metallic stub material were designed and tested in smaller bench scale studies prior to scale-up and operation in the 2500-A cell. The high temperature and severe environment associated with Hall cell operation precluded the use of conventional oxide-to-metal joining systems. Diffusion welding emerged as the leading candidate for the cermet anode material and was therefore selected for pilot cell testing. The process involves pre-reducing the anode surface in the joint

GA 18194.150

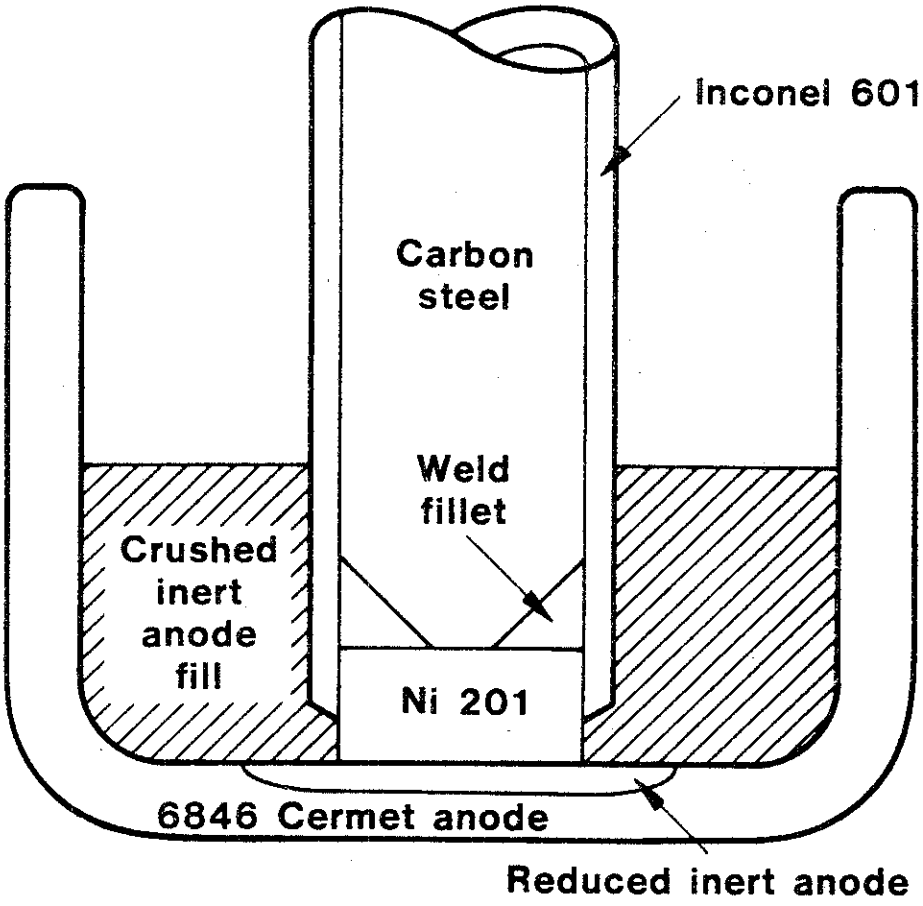

Materials:
1. Carbon Steel
2. Inconel 601
3. Ni 201
4. Weld Fillet: Incoweld A
5. Reduced Inert Anode
6. 6846 Inert Anode
7. 6846 Crushed Anodes

Materials of Construction in Anodes for the 2500-Amp Cell
Figure 217

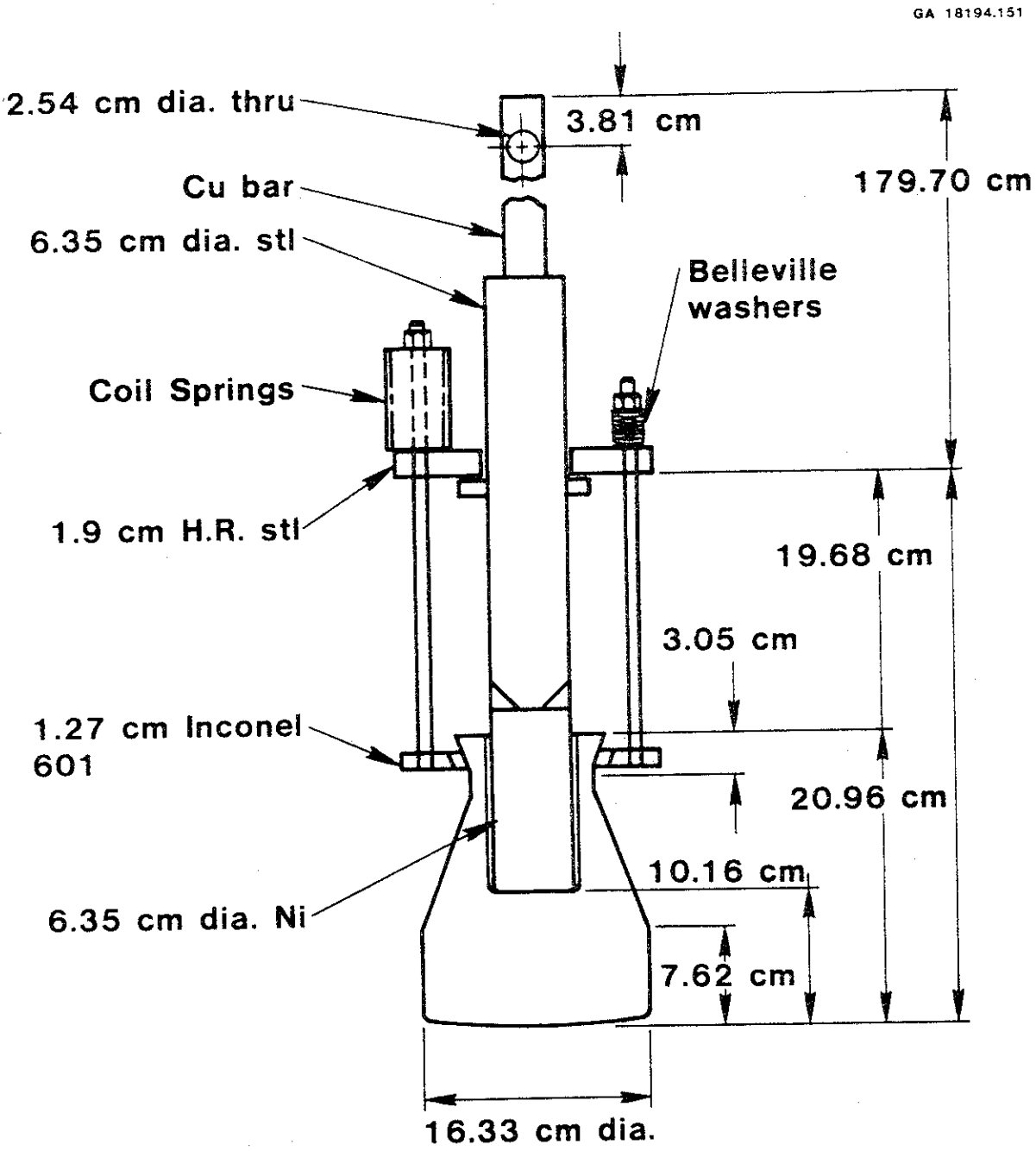

Anode to Bus Mechanical Connection
Figure 218

area with carbon at 1000°C, followed by diffusion welding the reduced layer to a Nickel 201 stub rod at approximately 380 kPa pressure in an argon atmosphere. This process was developed through experimentation until a system was developed producing joints with adequate strength. Ultimately, the strength of the joint was found to be stronger than that of the inert anode material itself. A four-anode assembly representing the flower pot design and diffusion welded connection is shown in Figure 219. The stability of this joint was suspect for long-term performance in Hall cell environments due to bath penetration, nickel stub corrosion, void creation and creep. Therefore, an anode with a thick bottom joined mechanically to the metallic stub as shown in Figure 218 was also evaluated. It was anticipated that the connection area would operate at a lower temperature thereby extending life of the assembly.

a. Anode Preheat

A furnace was constructed to preheat four anodes prior to transfer to the electrolytic cell. A schematic of this furnace is shown in Figure 220. Even heating of the anode assembly was provided by a radiation shield on the grating holding the anode assembly, and by installing a flat plate on top of the grating so that no part of any anode was in direct line of sight with the heating elements used in the furnace. The anodes were elevated above the steel plate allowing convective rather than conductive heating. Thermocouples were installed in the furnace and a test run conducted to check temperature uniformity and heat-up rates. A variation of no more than 10-20°C was found throughout the furnace in the vicinity of the anodes during heat-up.

b. Anode Transfer and Early Life in the Cell

Experiments were performed and calculations made to determine how the anode assembly should be transferred. A procedure was developed, consisting of wrapping the anodes before preheating with 50 mm of a high alumina fiber blanket and preheating the assemblies to 1000°C, for transfer to the cell in less than 90 seconds.

GA 17742.5

4-Anode Assembly

Figure 219

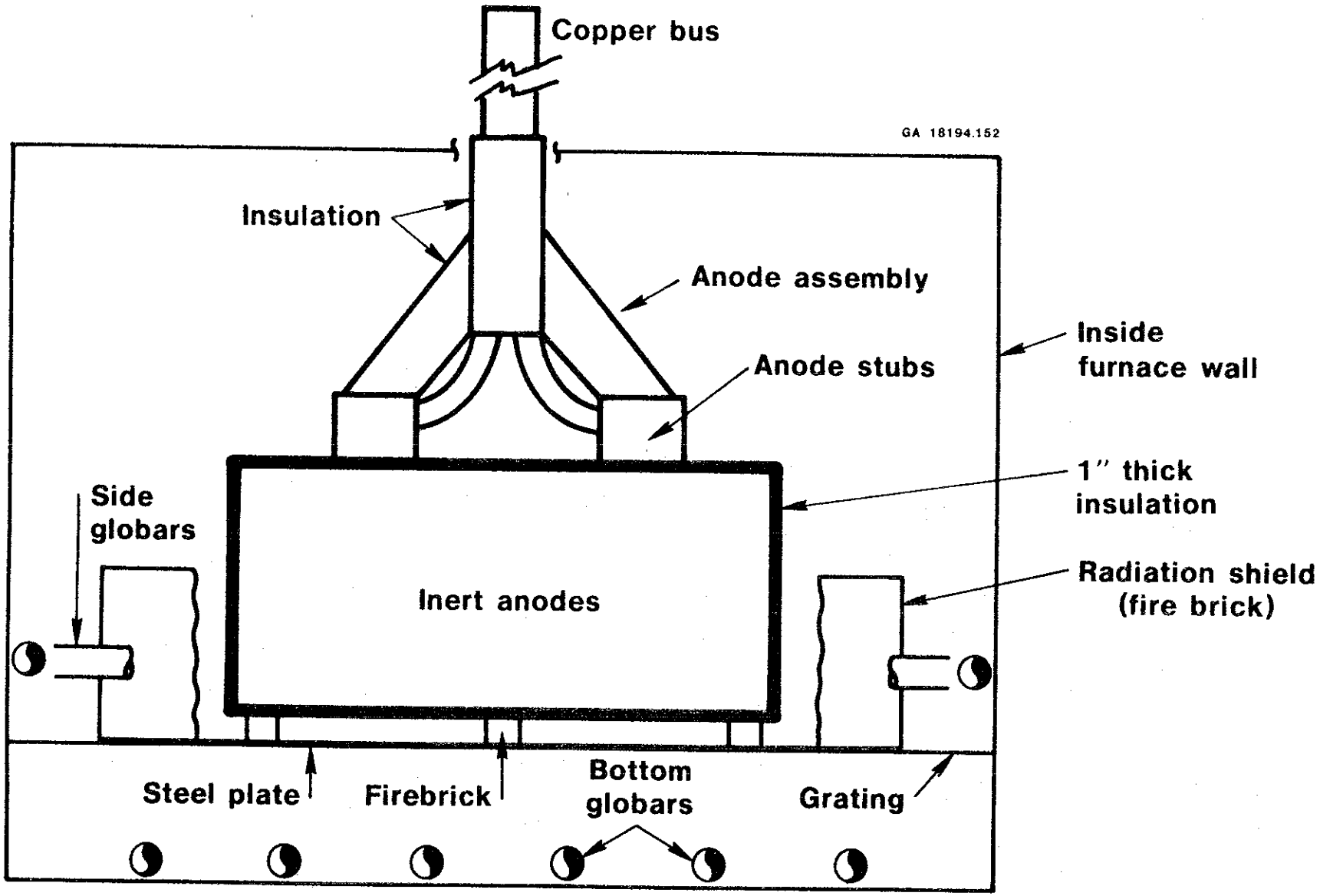

Anode Preheat Furnace
Figure 220

Temperatures were measured on one anode of each of two anode clusters transferred to the cell, and on another anode cluster that was subjected to a simulated transfer. The anodes in all cases represented the flower pot configuration diffusion welded to the metallic stub. Thermocouples were placed at five locations as shown in Figure 221 for one of the transfers. The thermocouples were 1/8-in. diameter, ungrounded Chromel-Alumel with an Inconel sheath. Thermocouples on the outside of the anode were held in place with hose clamps. Thermocouples 3 and 4 were installed 6.35 mm into the steel stub. Temperature differentials through the anode wall and along the length of the anode are shown in Figures 222 and 223. Stresses calculated from these ΔT's are summarized in Table 69. These stresses are not high enough to cause failure.

Finite element analyses were conducted on a flask anode configuration to also establish preheat and transfer practices. Procedures were developed to minimize thermal gradients during preheat and operation, establish steady state preheat temperatures and stresses and protect the anode during transfer. Previous studies demonstrated that at least 50 mm of a fiber blanket insulation was necessary to protect the anodes from thermal shock during transfer. Analyses showed that it was further necessary to insulate the stub at least 100 mm above the top of the anode to reduce the thermal gradient through the anode bottom.

Finite element models of the anode were also used to steady the effects of stub depth and undercut geometry at the cylindrical corner of the connection recess well. The boundary conditions shown in Figure 224 were used for all cases. It was assumed the anode was placed 50 mm into the bath with 25 mm of crust above the bath. The anode was insulated 180 mm above the bottom in most cases. Material properties and convection heat transfer coefficients are listed in Table 70. Calculated temperatures agreed well with measured temperatures as shown in Figure 224.

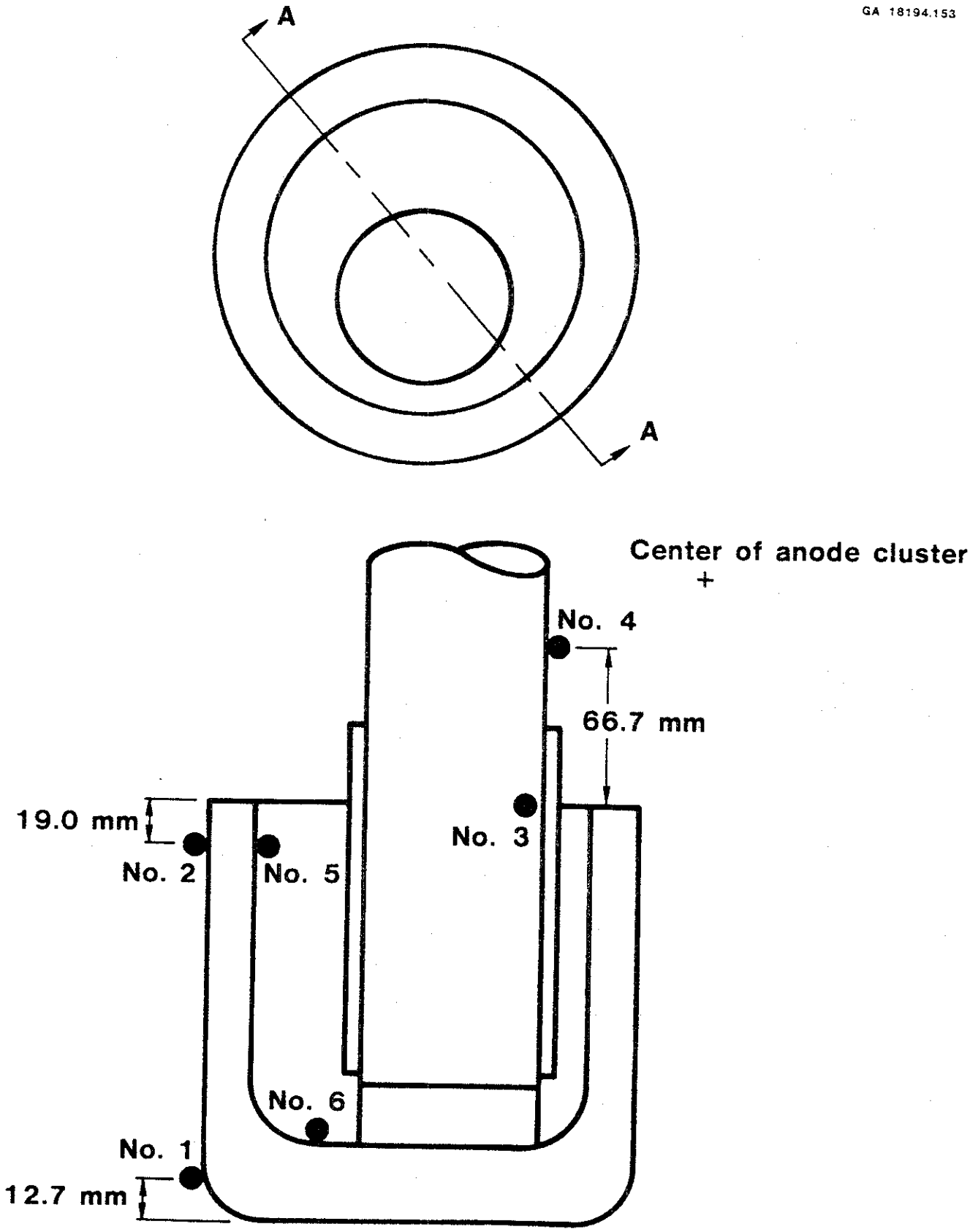

Thermocouple Locations
Simulated Inert Anode Transfer

Figure 221

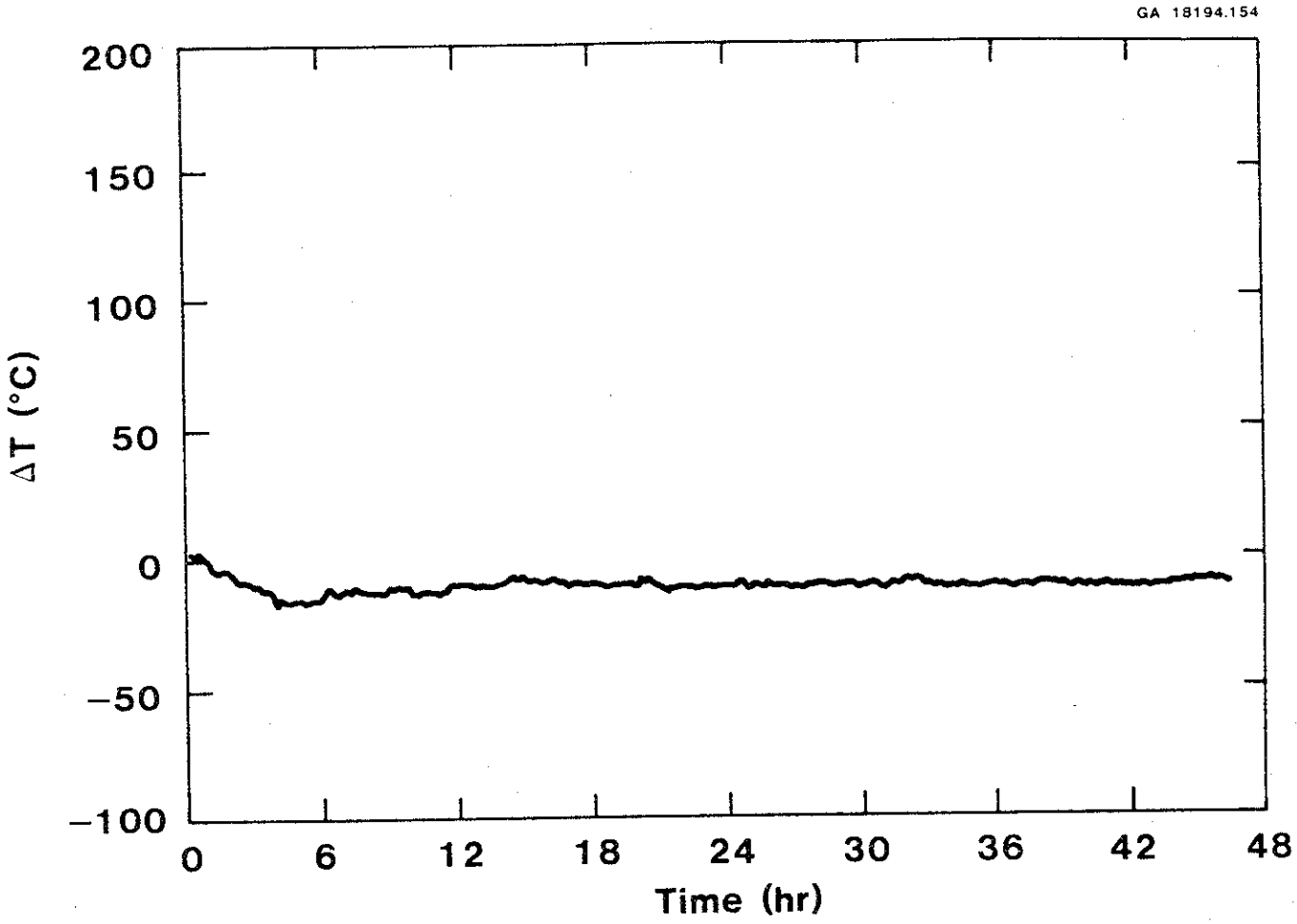

ΔT Through Wall
Figure 222

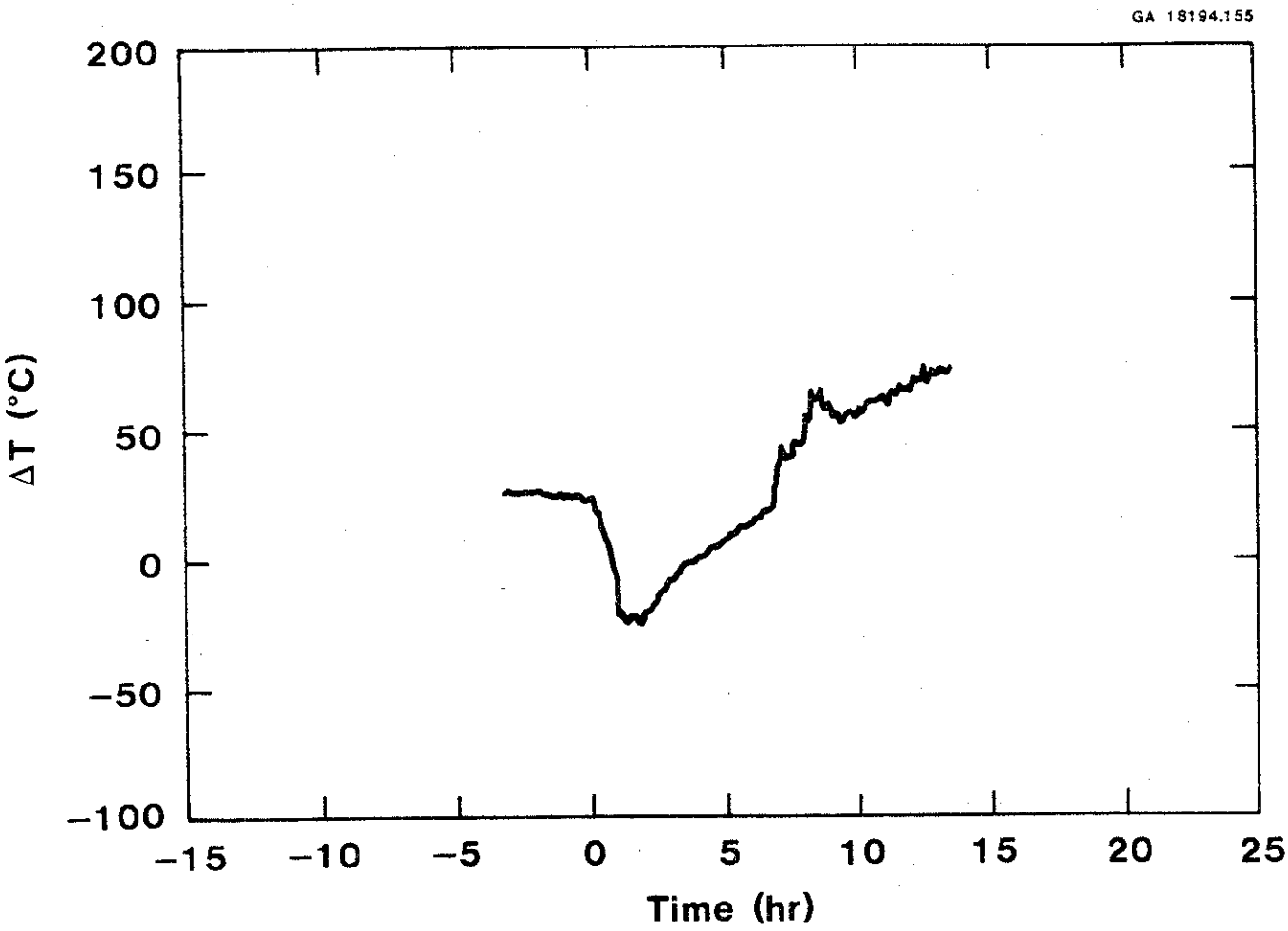

ΔT Along Length

Figure 223

TABLE 69

Calulated Stresses in Inert Anode
Resulting from Thermal Gradients

Location	Side of Anode	Wall Surface	Stress, MPa (Tension +, Compression -) Axial	Circumferential
Top of Anode	Outer	Outside	0	+22.8
		Inside	0	-22.8
	Inner	Outside	-	-
		Inside	-	-
At Bath Line	Outer	Outside	+32.4	+17.9
		Inside	-32.4	-17.9
	Inner	Outside	-	-
		Inside	-	-

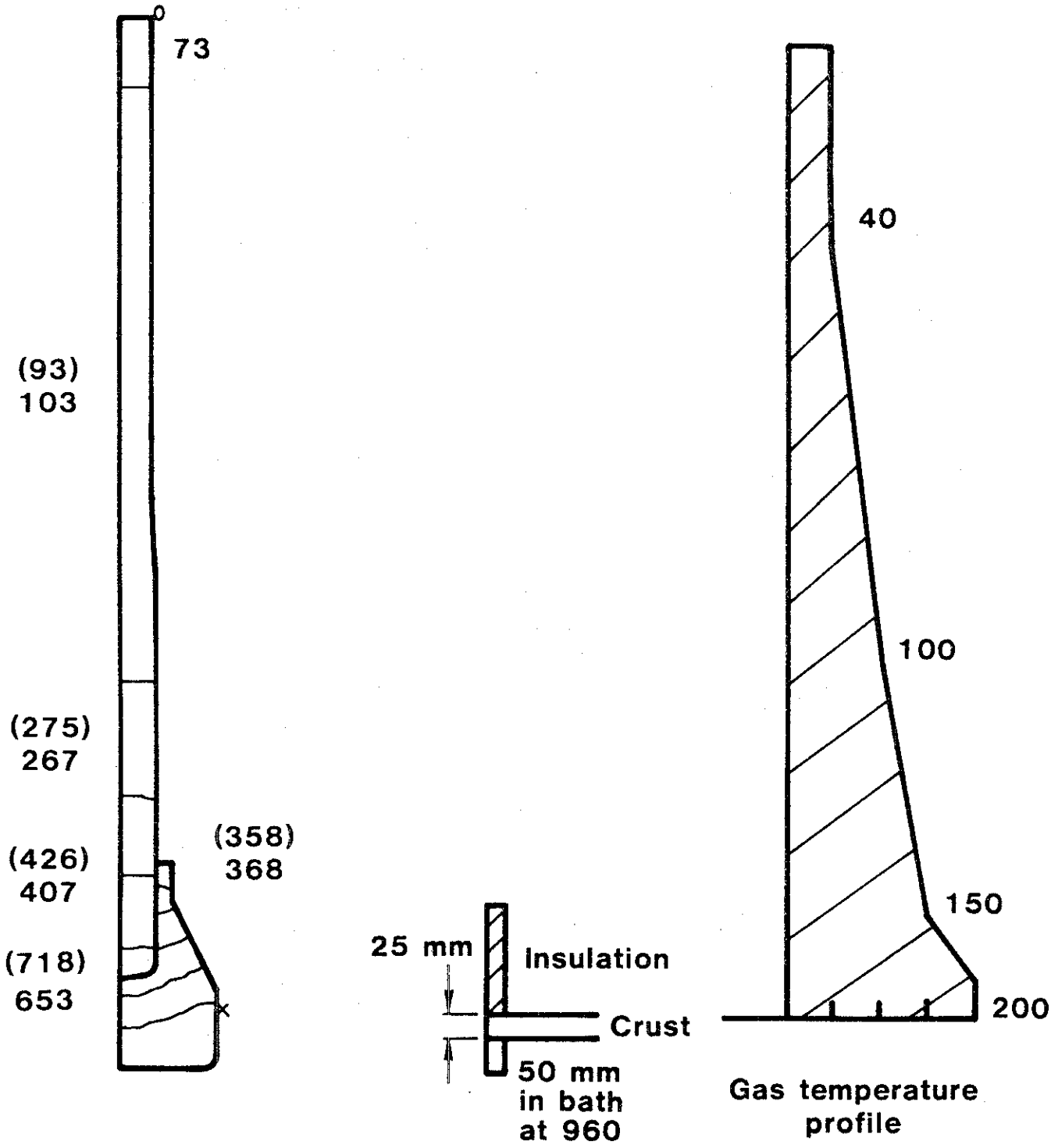

Note: Temperatures in parentheses are measured temperatures, others are calculated.

Comparison of Analytical and Experimental Temperatures in Anodes

Figure 224

TABLE 70

Material Properties Used in Finite Element Analyses

Property	20°C	300°C	600°C	900°C
Thermal Conductivity, BTU-in./in^2-hr-°C				
Inert Anode (6846)	9.35	6.23	4.73	5.08
Nickel	72.2	56.3	58.8	58.8
Steel	63.5	48.5	-	-
Copper	400.	400.	-	-
Heat Transfer Coefficient, J/mm^2 • K				
30 mm Fiber Blanket	0.0021	0.0047	0.0067	0.0092
Stub to Air	0.029	0.088	0.180	0.294
Modulus of Elasticity, GPa				
Inert Anode (6846)	51.0	-	-	-
Coefficient of Thermal, Expansion, 10^{-5}/°C				
Inert Anode (6846)	0.81	1.11	1.27	1.27

The analyses conducted did not include effects of creep and relaxation, which reduce stresses with time. In this study, stresses are generated due to material expansion incompatibility, with room temperature as the reference point. A model that includes time dependent effects would be considerably more complicated and would require additional material testing. This additional data is not available since the material was changing due to corrosion.

The results from Case 4 (Table 71) show that stresses at point B are reduced approximately 30 percent by increasing the distance between stub and cermet base. The temperature drop for this case is 555°C and the average axial gradient at the center line is 3.6°C/mm. This compares with a temperature drop of 406°C and an average gradient of 4.0°C/mm. in Case 2. The increased thermal resistance due to the thicker cermet base reduces heat flow.

In general, no direct relation is evident between temperature drop (ΔT) or axial gradient at the center line to stress. The nonlinear temperature distribution resulting in gradient changes in both radial and axial directions, coupled with changes in material properties with temperature, make the correlation difficult.

The result of Case 3, Table 71, shows a 15 percent drop in radial and axial stresses and a 7 percent drop in hoop stresses due to undercutting of the end of the stub.

Insulating the stub decreases the stresses about 70 percent (Case 1 vs. Case 2) and reduces total heat flow by a factor of 3. Insulation was removed from the stub during operation in an effort to freeze bath before reaching the connection.

The stresses in Table 71 can be compared to the mean failure stresses shown in Table 72 (83.2 MPa for material tested at 1000°C). Stresses are high enough to cause cracking of the anode at the corner on the inside where the nickel stub contacts the anode. Reducing the stress concentration at the corner reduces the stresses somewhat, as shown above.

TABLE 71

Stresses in Anode

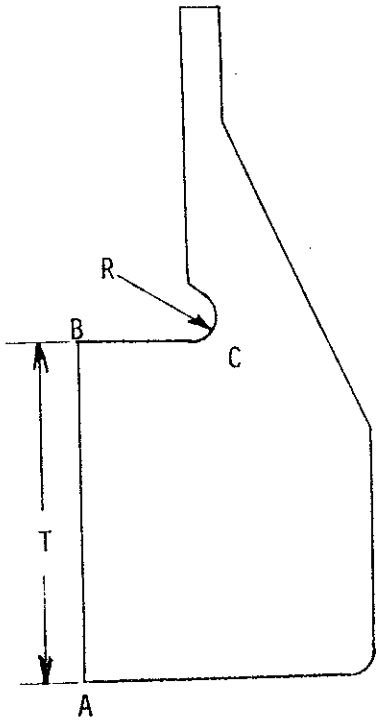

Delt = Temperature Change
= TA - TB

Gradient = Delt/Thickness(T)

R = Fillet Radius

Case	T, mm	R, mm	Insulation, mm	Delt, °C	Gradient, °C/mm	Stresses-Point B SX	SY	SZ	Stresses-Point C SX	SY	SZ
						MPa			MPa		
1	100	0	Top	124	1.2	19.7	0.2	19.6	34.7	16.2	23.7
2	100	0	180	406	4.0	64.9	0.3	64.9	114.6	61.2	70.3
3	100	25x10	180	406	4.0	62.4	0.2	62.3	94.0	44.7	64.5
4	150	0	180	552	3.6	45.3	0.1	45.1	60.0	36.9	45.3

TABLE 72

MOR Strength of Inert Anode 6846

Test Temp °C	No. of Specimens	Mean Failure Stress, σ_{Mean} MPa	Standard Deviation, MPa	Correlation Coefficient, r	Weibull Modulus, m	Characteristic MOR, MOR_o (2)
23	44	103	12.3	0.9782	9.49	108
1000	42	83.2	10.3	0.9772	9.02	87.7

(1) Tested in 3-point bending.

(2) $MOR_o = \sigma_{Mean} \left[\frac{1}{\Gamma \left(\frac{1}{m} + 1 \right)} \right]$

The voltage drop through a flask was calculated to be 0.159 volts from a point on the steel stub at the top of the anode to the bottom. This includes voltage drops through part of the nickel stub and the anode. Measurements of contact voltage drop for the mechanical connection were 0.08 volts, showing good agreement with calculations.

c. Cell Operation with Inert Anodes

The bath in the 2500-A cell was quite dirty with carbon dust during operation with the carbon anode. This dusting was attributed to both the anode and carbon lining. After one day of operation with inert anodes, the bath was snow white or clear, indicating that the objectionable carbon dust was burned by the oxygen generated at the anode surface. It was also observed that gas at and near the inert anodes was in the form of foam vs. separate individual bubbles. This duplicates observation on the smaller bench scale cells and is encouraging with regard to reducing interelectrode spacing.

The alumina content was maintained as close to saturation level as possible while attempting to minimize mucking or sludging. Probing of the sides indicated that a frozen ridge did exist on the sidewalls; however, it is questionable whether this ridge was maintained 100 percent of the time due to alumina concentration fluctuations and temperature control. The absence of normal anode effects with inert anodes made it difficult to adjust alumina feed rates. The cell was very sensitive to temperature changes. Opening a hole in the crust for bath additions and/or temperature measurements would quickly lower bath temperature 10-15°C in only minutes. Temperature was controlled by raising or lowering current. Cell current efficiency would vary and was never as high as that achieved in commercial cells due to the aforementioned control problems. At times, aluminum was made on the bare carbon sidewalls and subsequently back-reacted with oxygen, reducing current efficiency. Data collected during cell operation is listed in Table 73. Bath ratios were obtained every eight hours, or more often if required. Bath samples were also taken for XRD analysis for ratio and Al_2O_3 content every eight-hour shift. Due to

TABLE 73

Data Collected from 2500-A Cell

---

1. Cell Voltage
2. Cell Amps
3. Bath Temperature
4. Bath Ratio (NaF/AlF_3
5. Al_2O_3 Concentration
6. lb. Al_2O_3 fed to bath
7. 16. NaF fed to bath
8. 16. AlF_3 fed to bath
9. Bath analysis
10. Amp-hours
11. Volt-hours
12. Volt-Amp data
13. Wt. of Aluminum tapped
14. Analysis of Aluminum tapped
15. Shell temperature
16. Anode immersion depth
17. Stub current load
18. Bath depth

initial problems with alumina control and the necessity to operate near saturation levels, a continuous feeder was installed, minimizing alumina concentration fluctuations. A larger cell would be much easier to control when attempting to simulate commercial operation on a continuous basis.

4. Results and Discussion

Two separate four-inert-anode assemblies were operated for 12 and 21 days during 1983, representing the longest inert anode test periods up until that time. Both runs were terminated due to stub failure, although subsequent autopsy of the anodes revealed objectionable corrosion and material changes precluding extended operation. Bath alumina concentration for the 12- and 21-day runs is shown in Figures 225 and 226, respectively. For the 12-day run, Al_2O_3 concentration decreased with time, while the concentration was fairly constant and close to saturation for the 21-day period. It should be noted that at one point during the 12-day run, the concentration dropped to almost 3 percent.

Bath ratios are illustrated in Figures 227 and 228. Bath ratio was determined by the pyrotitration method and by X-ray diffraction (XRD); a comparison of the results from the two methods is given in Figure 229. Pyrotitration results are approximately 0.04 higher than XRD results. Control of bath ratio was tighter in the 21-day run than during the 12-day operation. Also, there was a bath ratio low of approximately 0.875 in the 12-day run. Earlier bench-scale results showed that operation at ratios this low caused fluorination and dissolution of the anode material.

Additions of NaF and AlF_3 to the cell were made throughout to adjust bath ratio. More NaF was needed than AlF_3, indicating the cathode block and sidewalls were continually intercalating sodium.

The analysis of the aluminum produced during both runs is shown in Figures 230 and 231. In both cases, the concentrations of iron and nickel were far above commercial limits.

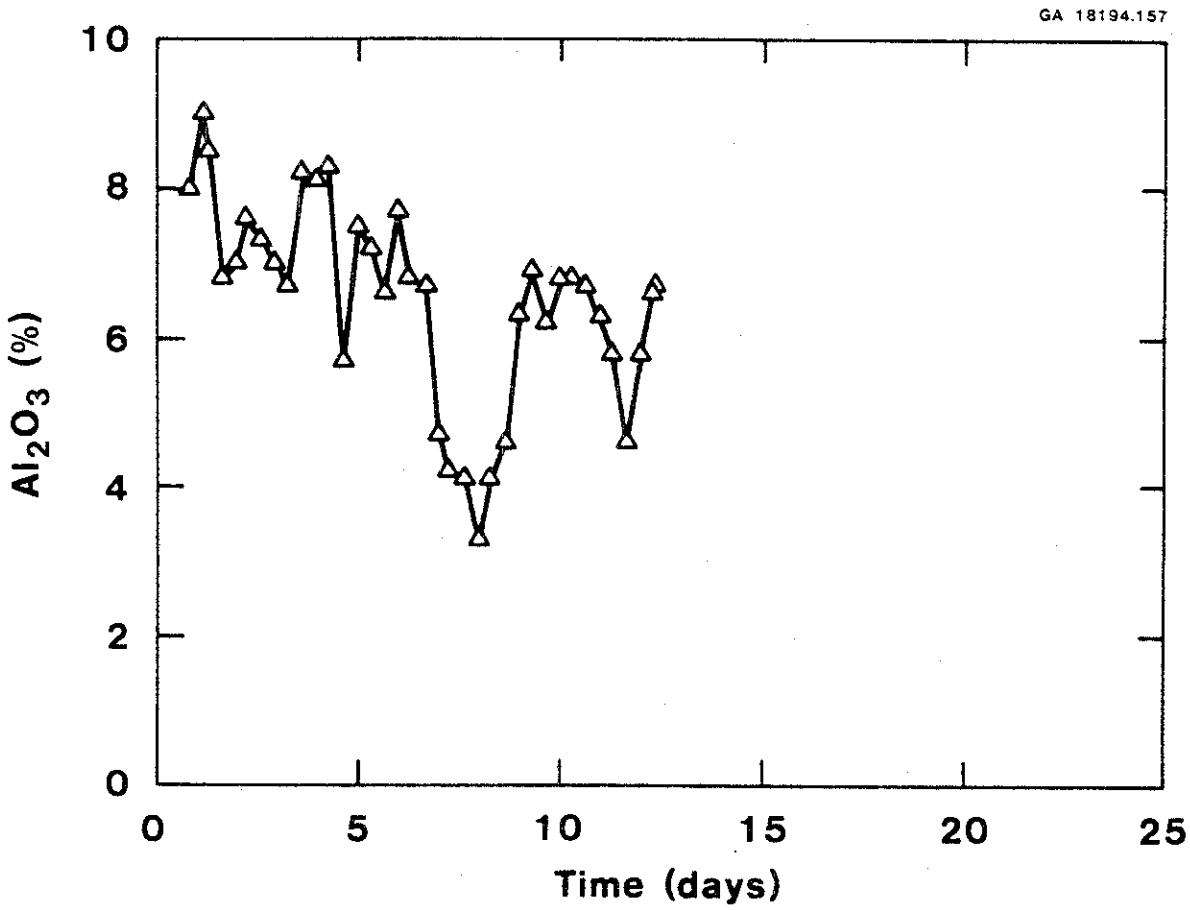

Alumina Concentration in Bath for 12-Day Run
Figure 225

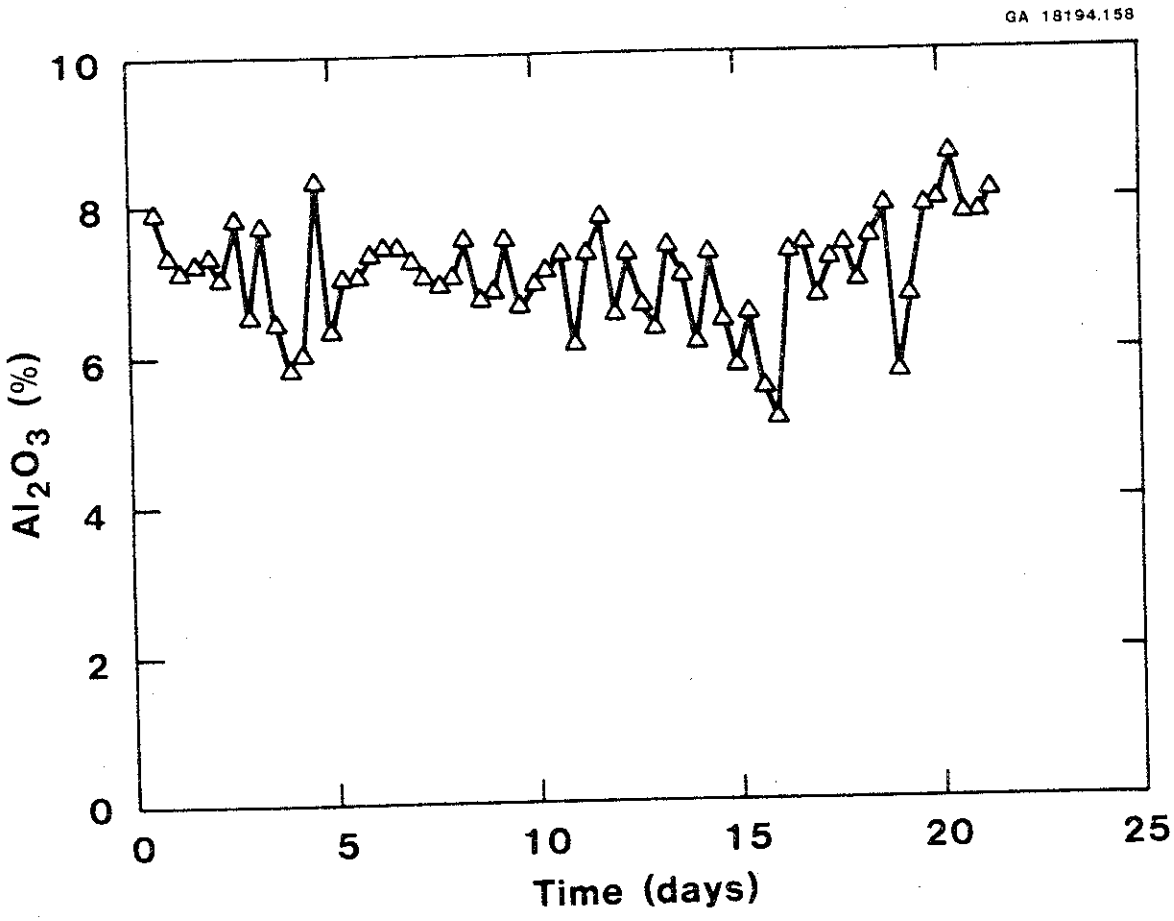

Alumina Concentration in Bath for 21-Day Run
Figure 226

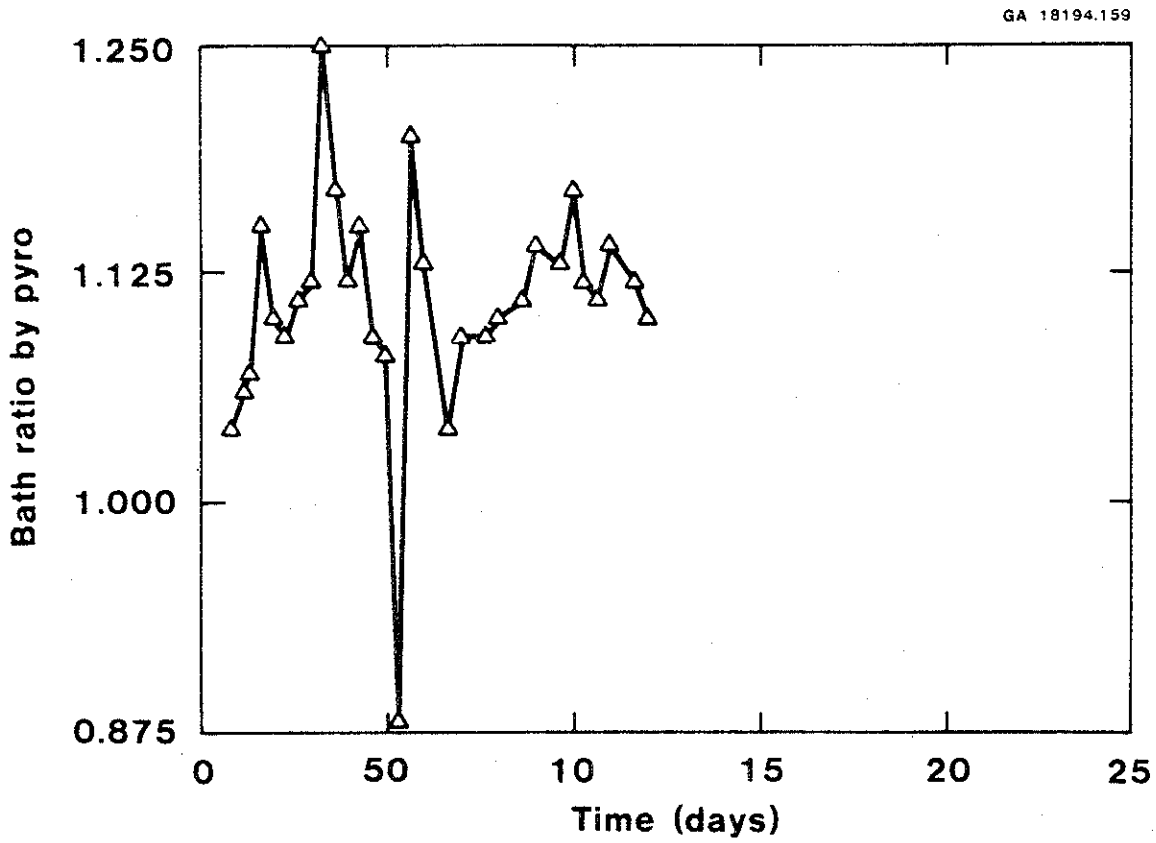

Bath Ratio as Determined by Pyrotitration for 12-Day Run
Figure 227

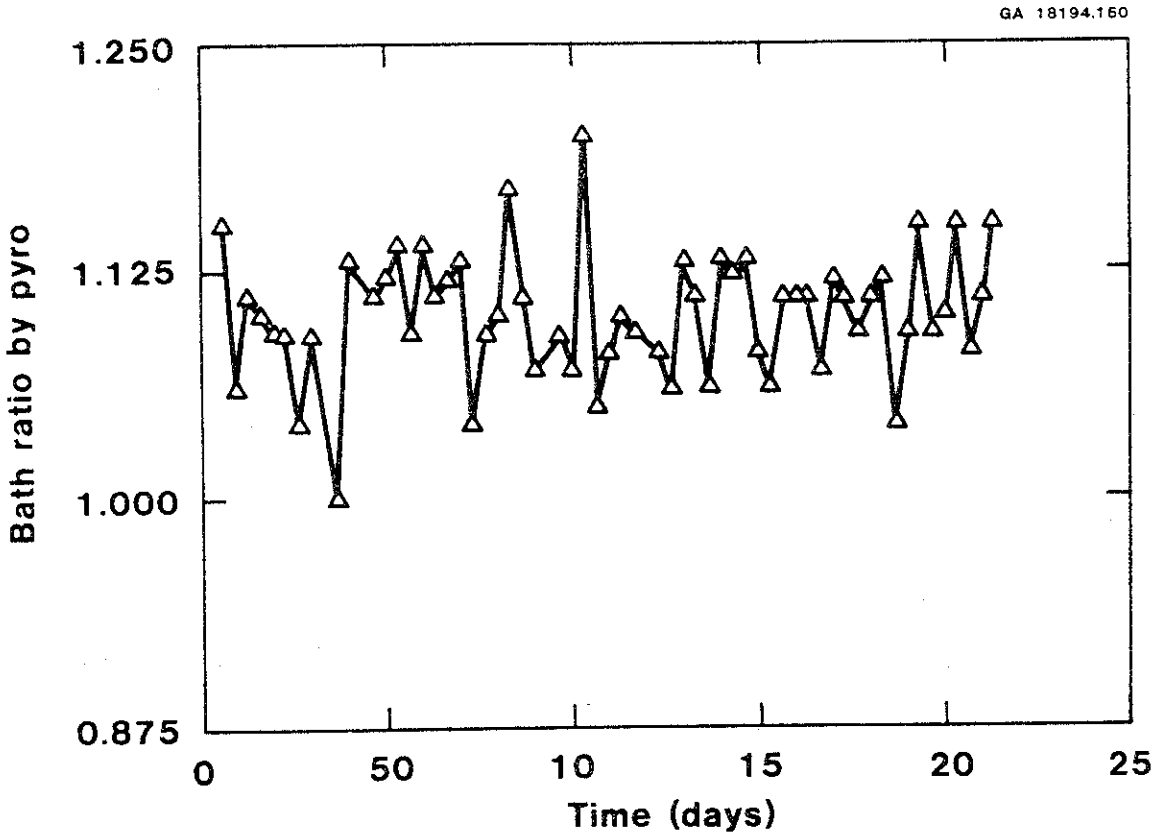

Bath Ratio as Determined by Pyrotitration for 21-Day Run
Figure 228

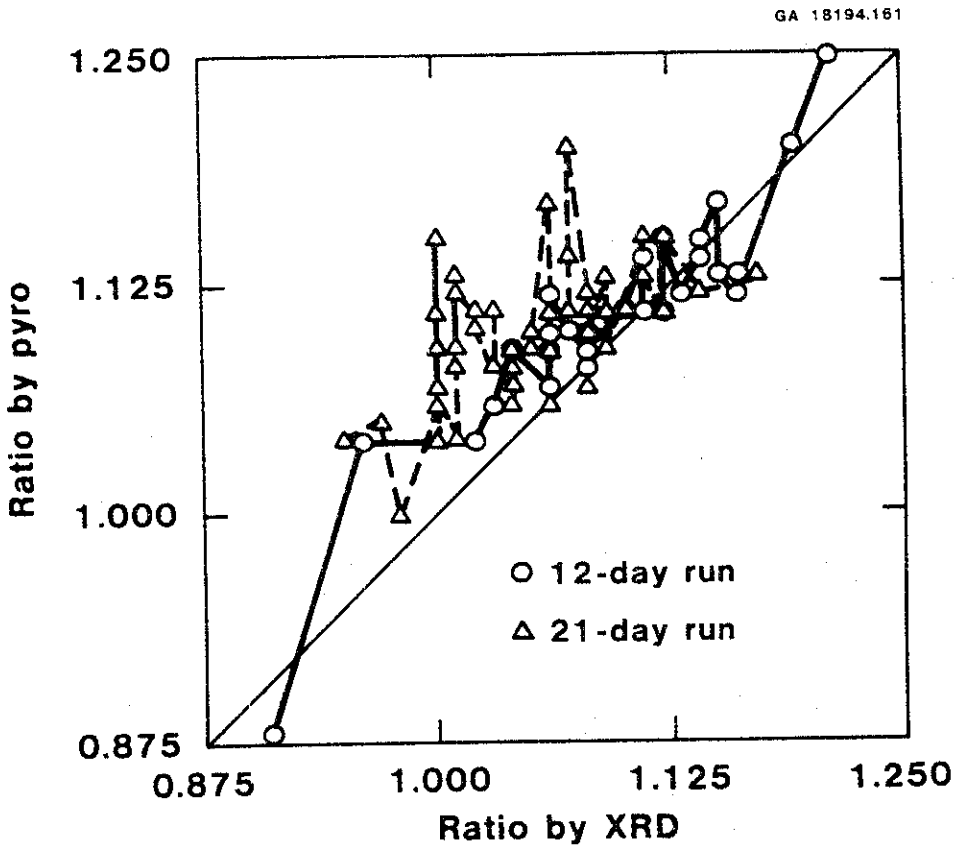

Comparison of Bath Ratio Determination by Pyrotitration to the Determination by X-Ray Diffractions

Figure 229

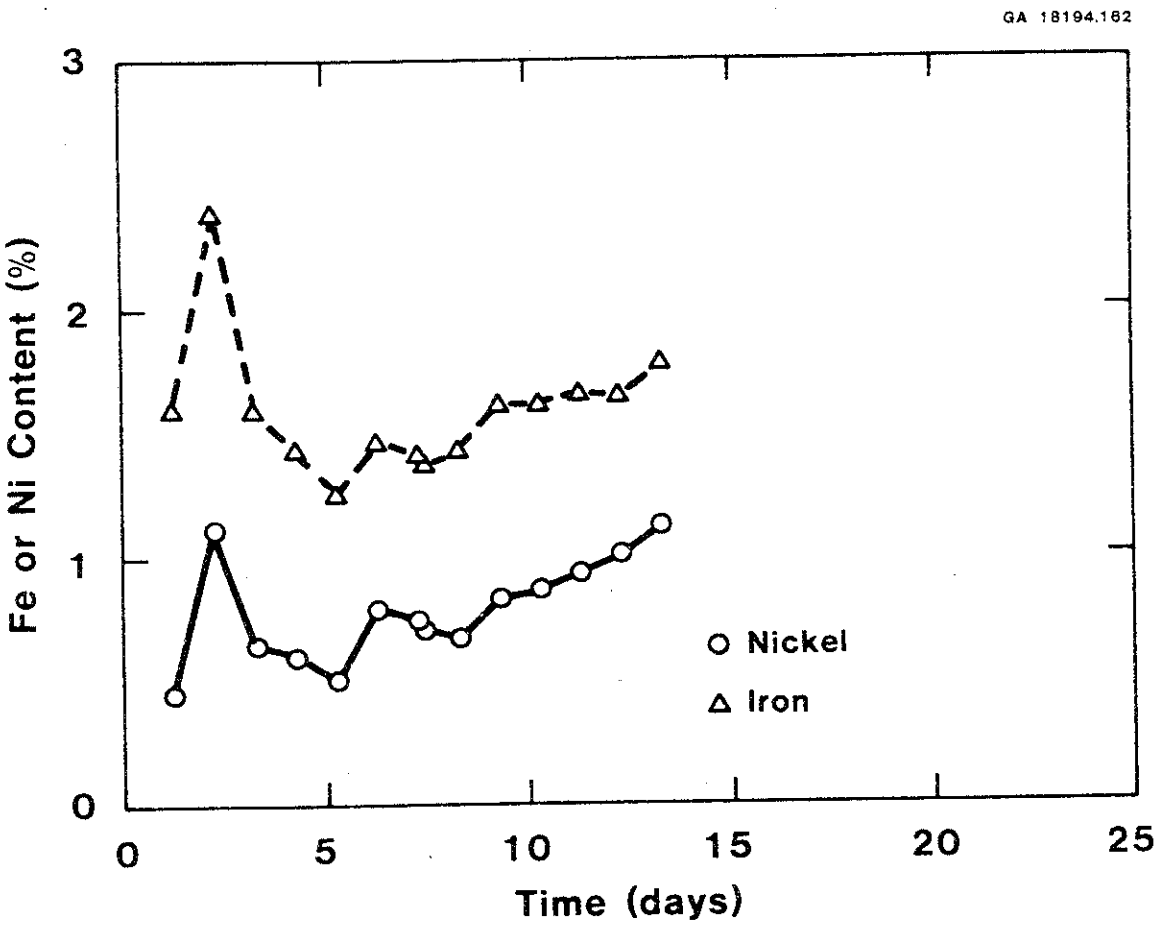

Metal Analysis During 12-Day Run
Figure 230

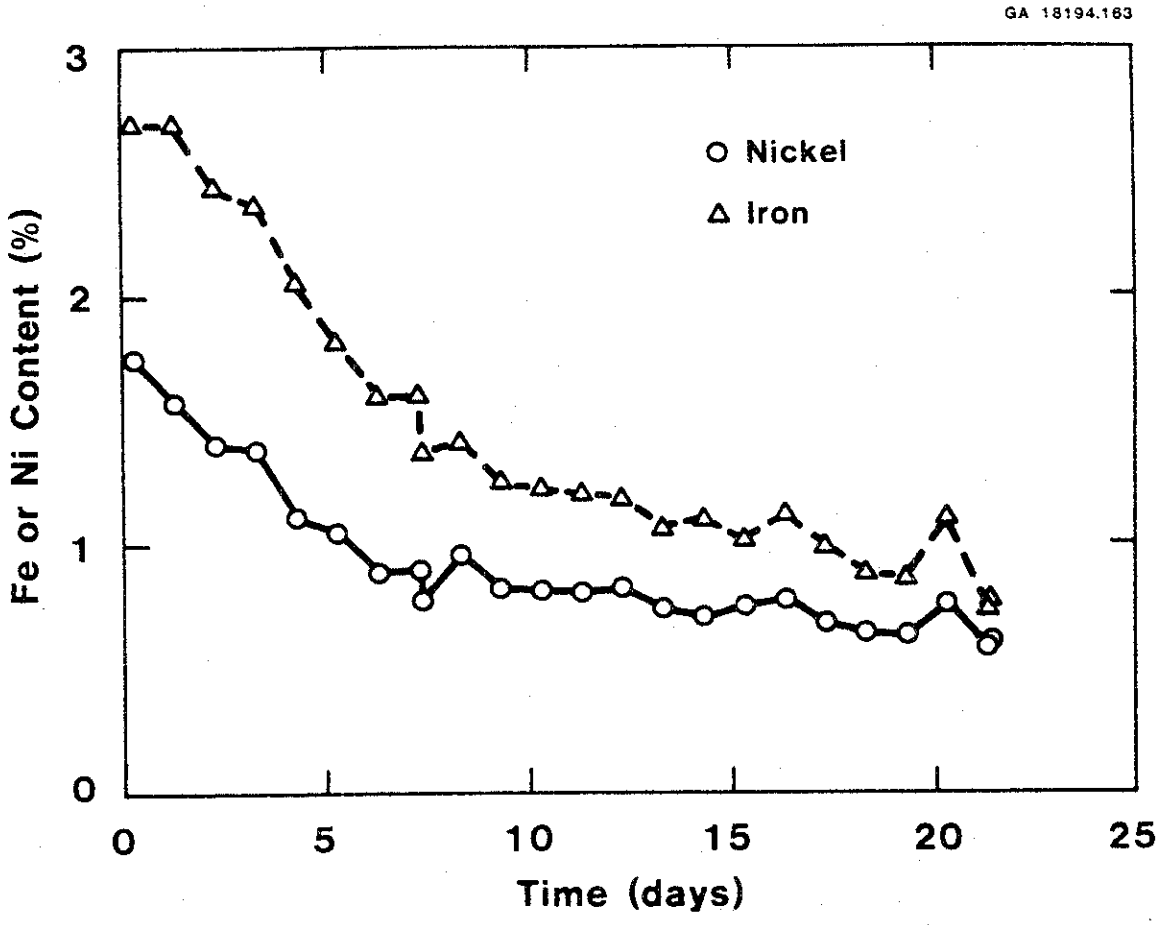

Metal Analysis During 21-Day Run
Figure 231

5. Evaluation of Inert Anodes Tested in the 2500-A Cell

Autopsies of inert anodes included examination of the microstructure of as-fabricated anodes and the microstructural changes that occur as a result of electrolysis. A cross-section of one anode after fabrication, reduction, and diffusion welding to a nickel stub is shown in Figure 232. The cut anode surface has been grit-blasted to reveal the different materials. The depth of the reduced zone is approximately 9.5 mm. The interface zone between the reduced cermet and the unaltered cermet is soft, and material is easily removed by grit-blasting, indicating higher porosity in this area. Vertical cracks are present in the anode and originate at the surface boundary between the reduced cermet and the unaltered material, indicating circumferential cracking.

A cross-section of an anode after testing in the cell for 21 days is shown in Figure 233. Although intact, material has been removed, reducing wall thickness in the area of the anode exposed to bath. Also, considerable microstructural changes have occurred as a result of electrolysis. Later studies demonstrated that oxidation and/or electrolysis of the Ni alloy metal phase occurs with this material, resulting in the altered microstructure that is darker than the unaltered region. This altered microstructure has coarser metal and oxide grains present, higher porosity, less metal, and has been penetrated by bath. A wide gap also developed in the original interface region between the reduced and unaltered cermet material. This gap has been observed to grow with length of service and would eventually lead to anode-connection failure. The circumferential crack does not appear to have propagated to the anode bottom. The bottom layer is nearly void of metal; however, a small band of apparently normal cermet still exists in the anode region between the oxidized and reduced layers of the anode-connection structure.

The cross-section of another 6846 cermet anode following 185 hours of electrolysis is shown in Figure 234. Again, the microstructure of the anode has been altered, and both components are present in the reacted area. The flask shape of this anode with a thick bottom was selected to raise the stub-to-anode connection above bath level in an attempt to keep bath from entering the connection area.

1759

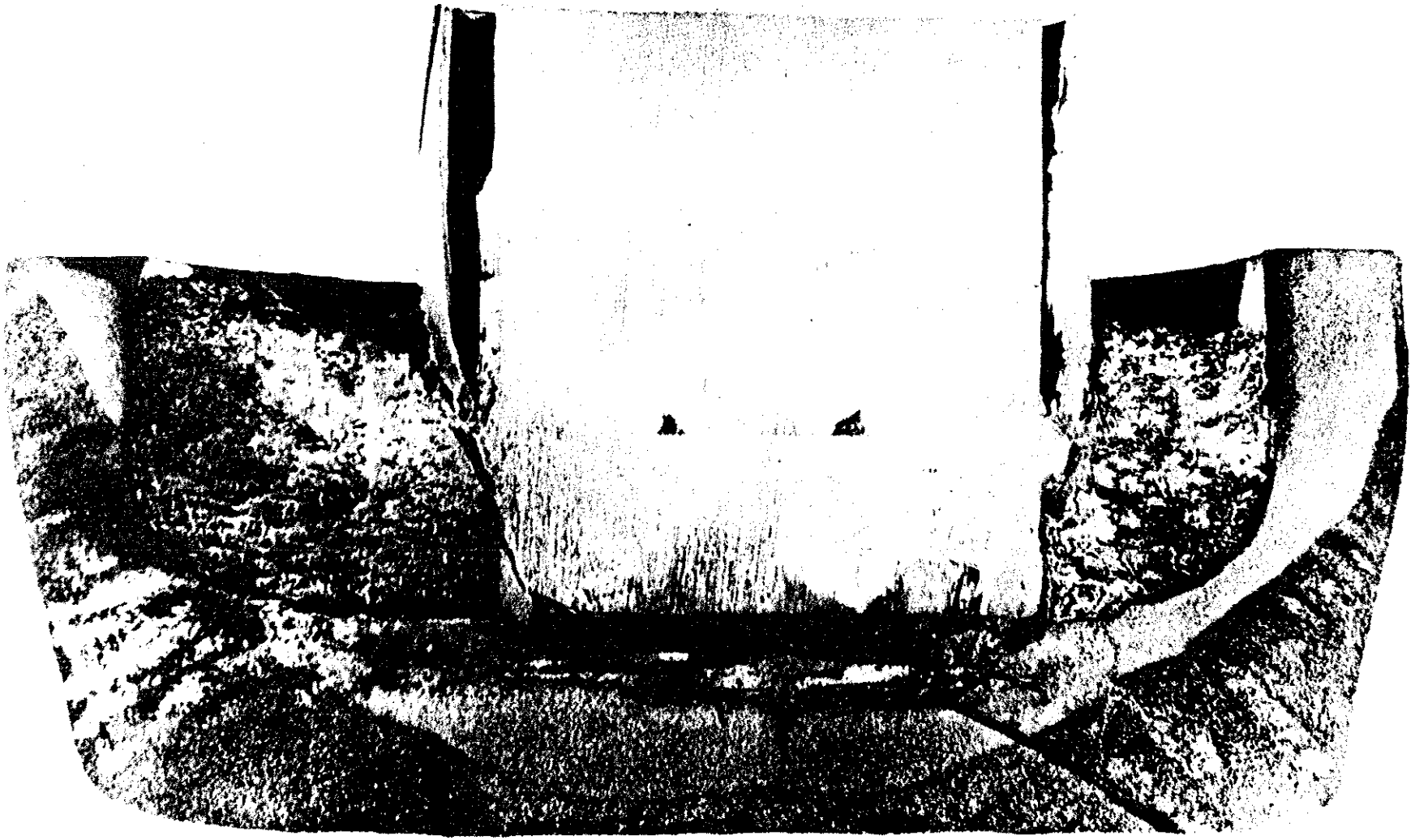

94-2 Anode Tested 21 Days in 2500-Amp Cell
Figure 233

GA 17742.18

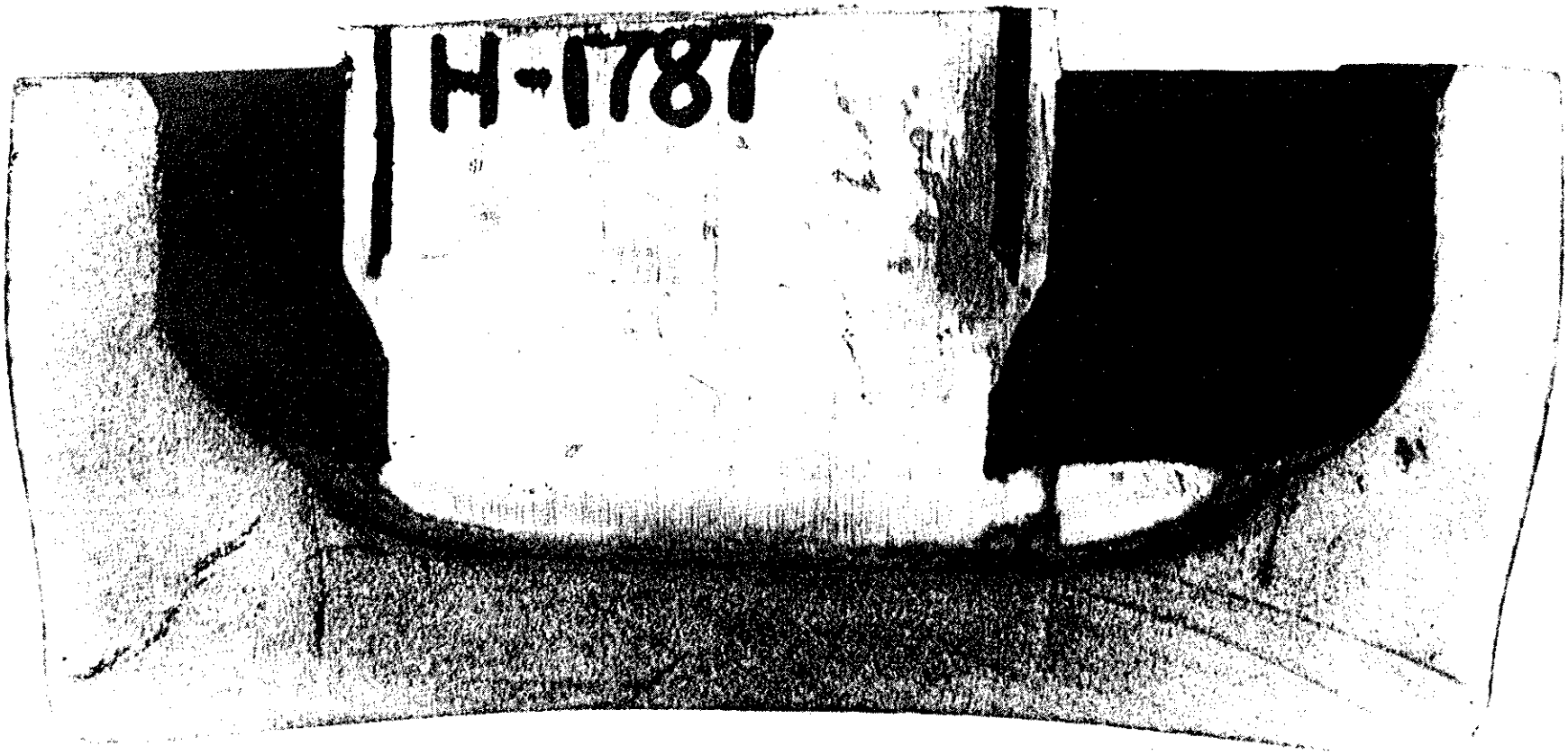

94-2 Anode As-Fabricated

Figure 232

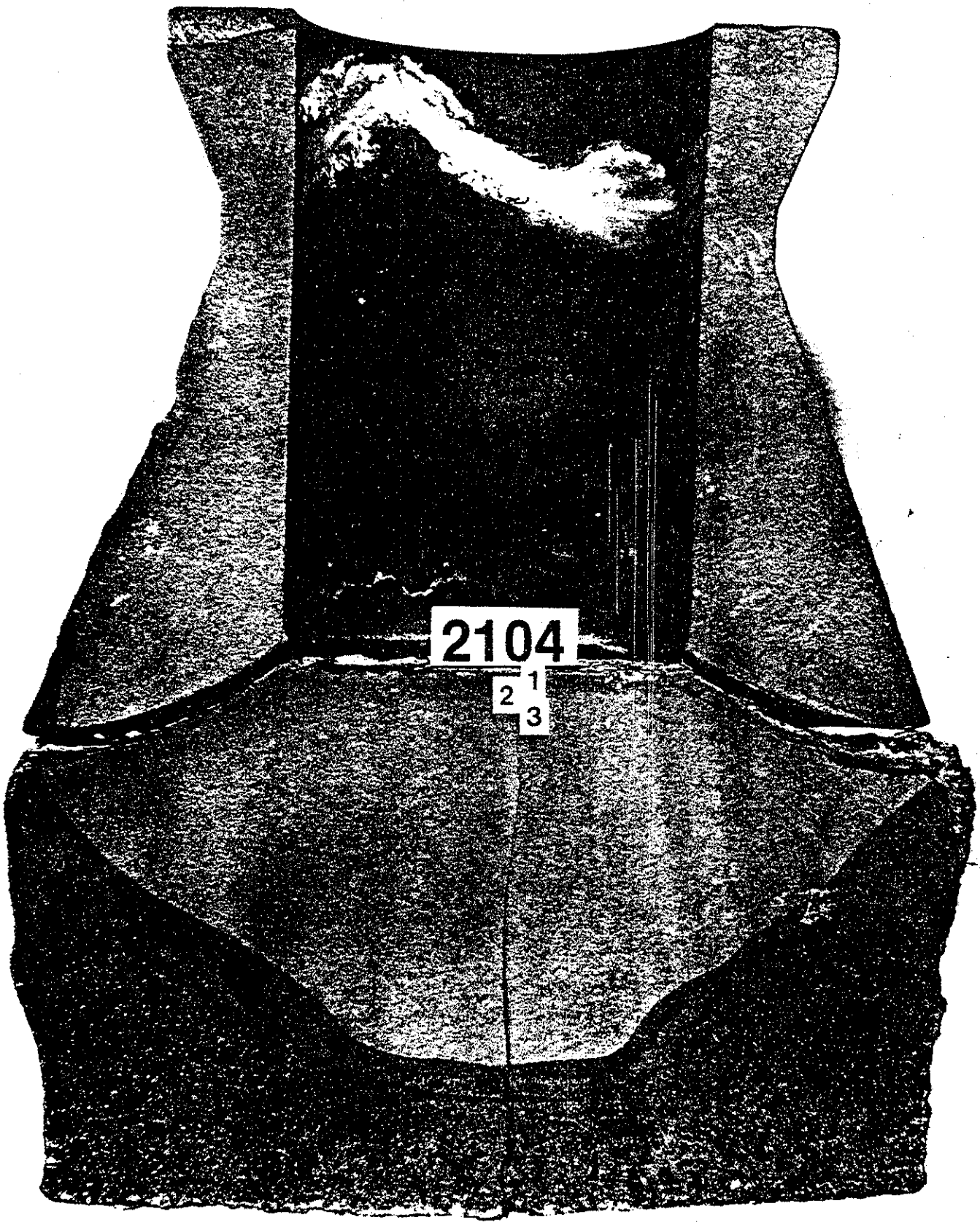

Inert Anode 2104, 94-12, After 185 Hours, 1984 March-April

Figure 234

It was apparent that the performance of inert anodes fabricated from the aforementioned cermet material was directly related to the corrosion resistance of the material as demonstrated by microstructural examination and chemical analyses. Bath penetration due to corrosion resulted in objectionable dissolution of anode material and ultimate failure of the connection. The flask anode design as shown in Figure 234, was evaluated in an attempt to raise the anode-to-stub connection interface above bath level and develop a bath freeze line in the thicker bottomed anode. These attempts were unsuccessful as liquid bath was found to penetrate above bath level during electrolysis. Bath penetration was at least partially driven by capillary forces.

While the mechanical connection performed well, sensitivity of the flask design to thermal shock was demonstrated by cracking of one anode when crust was removed and insulation then replaced too quickly around the anode.

6. Conclusions and Recommendations

Although the 2500-A cell was originally included in the program to develop preheat and transfer procedures of inert anode assemblies for subsequent use in larger cells, the small self-heated cell also proved effective in providing an opportunity to develop cell operating parameters for testing the cermet anode material and connection designs for days and weeks at a time. Improved anode materials are required to eliminate the objectionable corrosion of the metal phase in the cermet material used in the pilot-cell tests. Improved cermet compositions, as described in other sections of this report, exhibit excellent performance in bench scale studies with no evidence of objectionable corrosion. The viability of this new material to perform well for extended periods of time should be demonstrated in other pilot-cell evaluations. It is suggested that these tests be conducted in an even larger size pilot-cell, precluding control problems with the small self-heated cell used in the tests described. Additional testing with these new materials is needed to establish reliable preheat, transfer, and operating procedures leading to commercial evaluation. Properties of the material in an operating environment and how they vary

with time are needed to establish probability of survival of candidate anode materials. Mechanically joining the inert anode to the mechanical stub looks promising; however, this design can be further optimized to minimize stresses and increase life. Preheat and transfer methods developed to date and discussed above will probably not need to be changed. Slight changes in type and thickness of insulation may be made as additional material property data becomes available.

VII. REFERENCES

1. K. Grjotheim, C. Krohn, M. Malinovsky, K. Matiasovsky, and J. Thonstad in "Aluminum Electrolysis Fundamentals of the Hall-Heroult Process," 2nd Edition, Aluminum-Verlag, Dusseldorf (1982).

2. K. Horinouchi, N. Tachikawa, and K. Yamada, "DSA in Aluminum Reduction Cells," Proceedings of the First International Symposium on Molten Salt Chemistry and Technology, Kyoto, Japan, April 20-22, 1983.

3. F. W. Baker, Inert Anodes for Aluminum Smelting, First Annual Technical Report, DOE-CONS-40158-1, 1983 January.

4. F. W. Baker, Inert Anodes for Aluminum Smelting, Tenth Interim Technical Report, DOE-CONS-40158-10, 1983 October.

5. F. W. Baker, Inert Anodes for Aluminum Smelting, Eleventh Interim Technical Report, DOE-CONS-40158-11, 1983 November.

6. F. W. Baker, Inert Anodes for Aluminum Smelting, Twelfth Interim Technical Report, DOE-CONS-401548-12, 1985 March.

7. F. W. Baker, Inert Anodes for Aluminum Smelting, Thirteenth Interim Technical Report, DOE-CONS-40158-13, 1985 March.

8. J. D. Weyand et al., Inert Anodes for Aluminum Smelting, Fourteenth Quarterly Technical Report, DOE-CONS-40158-14, 1984 November.

9. J. D. Weyand et al., Inert Anodes for Aluminum Smelting, Fifteenth Quarterly Technical Report, DOE-CONS-40158-15, 1985 April.

10. J. D. Weyand et al., Inert Anodes for Aluminum Smelting, Fourth Annual Technical Report, DOE-CONS-40158-16, 1984 November.

11. J. D. Weyand et al., Inert Anodes for Aluminum Smelting, Seventeenth Quarterly Technical Report, DOE-CONS-40158-17, 1985 May.

12. J. D. Weyand et al., Inert Anodes for Aluminum Smelting, Eighteenth Quarterly Technical Report, DOE-CONS-41058-18, 1985 July.

13. J. D. Weyand et al., Inert Anodes for Aluminum Smelting, Nineteenth Quarterly Technical Report, DOE-CONS-40158-19, 1985 October.

14. S. P. Ray, "Inert Electrode Compositions," U.S. Patent 4,374,050, February 15, 1983.

15. S. P. Ray and R. A. Rapp, "Composition Suitable as Inert Electrode Having Good Electrical Conductivity and Mechanical Properties," U.S. Patent 4,454,015, June 12, 1984.

16. S. P. Ray and R. A. Rapp, "Composition Suitable for Inert Electrode," U.S. Patent 4,455,211, June 19, 1984.

17. W. H. Haupin and J. Metals, "A Scanning Reference Electrode for Voltage Contours in Aluminum Smelting Cells," Vol. 23, p. 46, October 1971.

18. S. Y. Shen, Energy and Materials Flows in the Production of Primary Aluminum, ANL/CNSV-21, October 1981.

19. N. Jarrett, W. B. Frank, and R. Keller in "Metallurgical Treatises, USA-China Bilateral Conference, Beijing, China, 1981," K. L. Tien and J. F. Elliot, ed., Met. Soc. AIME (1981).

20. K. Billehaug and H. A. Øye, "Inert Anodes for Aluminum Electrolysis in Hall-Heroult Cells (I)," Aluminum, 57, 146 (1981).

21. T. G. Pearson, "The Chemical Background of the Aluminum Industry," The Royal Institute of Chemistry, Lectures, Monographs and Reports No. 3, (1955).

22. A. I. Belyaev and Y. Y. Studentsov, "Electrolysis of Alumina in Fused Cryolite with Oxide Anodes," Legkie Metal, 6 (3), 17-24, (1937).

23. A. I. Belyaev, "Electrolysis of (Fused) Alumina with Ferrite Anodes," Legkie Metal 7 (1), 7-20, (1938).

24. B. Marincek, "Electrolytic Cell," U.S. Patent 3,562,135, February 9, 1971.

25. B. Marincek, "Electrolytic Process," U.S. Patent, 3,692,645, September 19, 1972.

26. H. J. Klein, H. Lehman, B. Marincek, J. K. Leers and W. Schmidt-Halting, Tonindustrie Zeitung, 100 (3), 255 (1976).

27. K. Yamada, T. Hashimoto, K. Horinoichi, German Patent Appl. 2547168 (1976).

28. K. Yamada, T. Hashimoto, K. Horinoichi, "A Method for Producing Aluminum," British Patent 1,461,155, January 13, 1977.

29. H. Klein, "Process for the Electrolytic Production of Aluminum," U.S. Patent 3,718,550, February 23, 1973.

30. H. Alder, "Electrolysis of a Molten Charge Using Nonconsumable Electrodes," U.S. Patent 3,960,678, June 1, 1976.

31. V. V. Stender and V. V. Trofimenko, Khimicheskaya Teknologiya (Karleov), No. 12, p. 41-45 (1969).

32. H. Alder, "Inconsumable Electrodes," U.S. Patent 4,057,480, November 8, 1977.

33. H. Alder, "Process for the electrolysis of a Molten Charge Using Inconsumable Bi-Polar Electrodes," U.S. Patent 3,930,967, January 6, 1976.

34. M. Rolin, in Les Equilibres Chimiques Das Les Bains D'Electrolyse De L'Aluminum, Institut National Des Sciences Appliques De Lyon, Villeubanne, France (1973).

35. R. A. Rapp, A. Ezis, and G. J. Yurek in Met. Trans., v. 4, 1283 (1973).

36. C. Tangehitvittaya, R. A. Rapp, and J. P. Hirth, Met. Trans. A, 13A 585 (1982).

37. A. D. Dalvi and W. W. Smeltzer, J. Electrochem Soc., 117, 11, 1431 (1970).

38. W. C. Dunlap, Jr., in Methods of Experimental Physics, p. 32, v. 6, Part B; K. Lark-Horovitz and V. A. Johnson, ed., Academic Press, New York (1959).

39. R. A. Rapp in Techniques of Metal Research. Vol. 4, Book 2, Wiley, New York, eds. R. A. Rapp and D. A. Shores (1970).

40. D. H. DeYoung, "Solubilities of Oxides of Inert Anodes in Cryolite Based Melts," Light Metals (1986).

41. S. P. Ray, "Composition for Inert Electrodes," U.S. Patent 4,399,008, August 16, 1983.

42. C. F. Jefferson, C. K. Baker, IEEE Transactions on Magnetics, Vol. Mag. 4, No. 3, p. 460-64 (1968).

43. L. G. VanUitert, J. Chem. Phys., 23, p. 1883-87 (1955).

44. D. Elwell, B. A. Griffiths and R. Parker, Brit. J. Appl. Phys., 17, p. 587 (1966).

45. R. Parker and M. S. Smith, J. Phys. Chem. Sci., 21, p. 76 (1961).

46. G. P. Tarcy in "Corrosion and Passivation of Cermet Inert Anodes in Cryolite Type Electrolytes," Light Metals (1986).

47. C. Wagner, J. Phys. Chem. Solids, Vol. 33, 1050-1059 (1972).

48. J. C. Maxwell as quoted by R. E. DeLaLue and C. W. Tobias In J. Electrochem. Soc., 106, 829-932 (1959).

49. V. B. Tare and J. B. Wagner, J. Appl. Phys., 54, 252 (1983).

50. F. W. Baker, Inert Anodes for Aluminum Smelting, Second Annual Technical Report, DOE-CONS-40158, 1983 September.

51. F. W. Baker, Inert Anodes for Aluminum Smelting, Ninth Interim Technical Report, DOE-CONS-40158-9, 1983 May.

52. A. I. Belyaev, M. B. Rapoport, and L. A. Firsanova, Elektrometallurgiya Alyuminiya, Metallurgizdat, Moscow (1953).

53. M. Rolin and M. Bernard, "Solubilite des oxydes dans la cryolithe fondue," Bull. Soc. Chim. France, (1963) 1035-1038.

54. H. G. Johansen,"Jern Som Forurensningselement I Aluminiumelektrolysen" (Dr. ing. Dissertation, The University of Trondheim, Norway, 1975).

55. E. W. Dewing, "Thermodynamics of the System NaF-AlF Part III: Activities in Liquid Mixtures," Met. Trans. 3 (1972) 495-501.

56. O. Kubaschewski, "The Thermodynamic Properties of Double Oxides," High Temperatures - High Pressures, 4 (1972) 1-12.

57. D. F. Weill and W. S. Fyfe, "The 1010° and 800°C Isothermal Sections in the System Na_3AlF_6-Al_2O_3-SiO_2," J. Electrochemical Soc., 111 (1964) 582-585.

58. W. E. Haupin and W. B. Frank: "Bath Properties Computer Program (BPROP)," Process and Chemistry and Physics Division Letter Report No. 7-82-10.

59. V. E. Shvaiko-Shvaikovskii, B. F. Yudin, and A. I. Leonov, "Thermodynamic Properties of Cerium Chromite," Izvestiya Akademii Nauk SSSR, Neorganicheskie Materialy, 4 (1968) 925-930.

60. J. Gerlach, U. Hennig, and H-D. Potsch, "Dissolution Kinetics of Alumina in Cryolite Melts with Al_2O_3, AlF_3, CaF_2LiF, of MgF_2 Additives," Erzmetall 31 (1978) 496-504.

61. P. M. Shurygin, L. N. Barmin, and V. N. Boronenkov, "Kinetics of Dissolution of Al_2O_3, MgO, and SiO_2 in Cryolite," Izvestiya Vysshikh Uchebnykh Zavedenii Tsvetnaya 5, No. 4 (1962) 106-112.

62. J. Gerlach, U. Hennig, and K. Kern, "The Dissolution of Aluminum Oxide in Cryolyte Melts," Metallurgical Transactions B, Vol. 6B, March 1975, 83-86.

63. A. R. Cooper and W. D. Kingery, "Dissolution in Ceramic Systems: I, Molecular Diffusion, Natural Convection and Forced Convection Studies of Sapphire Dissolution in Calcium Aluminum Silicate," J. Am. Ceramic Soc. 47 (1964) 37-43.

64. A. R. Cooper and W. D. Cooper, "Dissolution in Ceramic Systems: II, Dissolution of Alumina, Mullite, Anorthite, and Silica in a Calcium-Aluminum-Silicate Slag," J. Am. Ceramic Soc. 47 (1964) 249-254.

65. C. A. Natalie and J. W. Evans, "Influence of Lime Properties on the Rate of Dissolution in CaO-SiO_2-FeO Slags," Ironmaking and Steelmaking (1979) 101-109.

66. Y.-U. Kim and R. D. Pehlke, "Mass Transfer During Dissolution of a Solid into Liquid in the Iron-Carbon System," Met. Trans. 5 (1974) 2527-2532.

67. L. Reed and L. R. Barrett, "The Slagging of Refractories, Part 1. The Controlling Mechanism in Refractory Corrosion," Trans. Brit. Ceram. Soc. 54 (1955) 671-676.

68. G. J. Yurek, "Mechanisms of the Corrosion of Refractories by Slags involving the Formation of Solid Reaction Products," Progress Report to National Science Foundation, 1 Nov. 1981 to 31 April 1984, Contract No. DMR-8106986, 15 May 1984.

69. G. J. Yurek, M.I.T., private communication.

70. D. A. Weirauch, "Review of the Literature Pertaining to the High-Temperature Corrosion of Ceramics," Alumina, Chemicals, and Ceramics Division Report No. 03-85-18, Alcoa Laboratories, 1985 April.

71. W. G. Cochran, "Flow Due to a Rotating Disk," Proc. Cambridge Phil. Soc. 30 (1934) 364-375.

72. V. G. Levich, "Physiochemical Hydrodynamics," Prentice-Hall, Englewood Cliffs, New Jersey (1962).

73. B. Levich, "The Theory of Concentration Polarization," Discussions of the Faraday Society, No. 1 (1947) 37-49.

74. M. Eisenberg, C. W. Tobias, and C. R. Wilke, "Mass Transfer at Rotating Cylinders," Chemical Engineering Progress Symposium Series, 51, No. 16 (1955).

75. A. J. Bard and L. R. Faulkner, Electrochemical Methods, John Wiley and Sons, New York (1980).

76. E. W. Dewing, "The Solubility of Aluminum Carbide in Cryolite Melts," Trans AIME, 245 (1969) 2181-2184.

77. K. Grjotheim, C. Krohn, M. Malinovsky, K. Matiasovsky, and J. Thonstad: Aluminum Electrolysis, p. 181, Aluminum-Verlag, Dusseldorf (1982).

78. Ibid, p. 167.

79. J. R. Selman and C. W. Tobias, "Mass-Transfer Measurements by the Limiting Current Technique," Advances in Ceramic Engineering, 10 73 (1978) 211-318.

80. Macdonald, Digby D., "Transient Techniques in Electrochemistry," (New York: Plenum Press, 1977) 17-19.

81. Chizmadzhev Yu. A. and Chirkov Yu. G., Chapter 5, Porous Electrodes, in COMPREHENSIVE TREATISE ON ELECTROCHEMISTRY, Vol. 6, Electrodics, Transport, edited by Yeager E. et al. (New York, 1983) 317-391.

82. Grjotheim K. et al., Aluminum Electrolysis, 2nd ed., 1982.

83. DeYoung, D. H., private communication with inert anode team.

84. Keller, R. H., private communication with inert anode team.

85. Tarcy, G. P. to Jacobs, S. C., Heavy Metals in Hall Cell Fume Collection System, Internal Memo, Alcoa Laboratories, August 18, 1984.

86. "Flexural Strength of High Performance Ceramics at Ambient Temperature," MIL-STD-1942A, Department of the Army, Washington, D.C. 20310, 21 November 1983.

87. D. G. S. Davies, "The Statistical Approach to Engineering Design in Ceramics," Proc. Br. Ceram. Soc., 22, 1973, 429-52.

88. J. J. Petrovic, L. A. Jacobson, P. K. Talty, A. K. Vasudevan, "Controlled Surface Flaws in Hot Pressed Si_3N_4," J. Am. Ceram. Soc. 58, 1975, p. 113.

89. M. Baker, "Short Rod K_{Ic} Measurements of Al O_2"$_3$Fracture Mechanics of Ceramics, Vol. 3, ed. by R. C. Bradt, D. P. H. Hasselman, and F. F. Lange, Plenum Pub. Co., pp. 483-494 (1978).

90. A. G. Evans, A. H. Heuer, and D. C. Porter, "The Fracture Toughness of Ceramics," Fracture 1977, Vol. 1, Fourth International Conference on Fracture, Waterloo, Canada, June 19-24, 1977 pp. 529-556.

91. W. R. Buessem and A. Dorf, "The Thermal Expansion of Ferrites at Temperatures Near the Curie Point," Proceedings Thirteenth Annual Meeting Metal Powder Association, 1957, pp. 196-204.

92. Thermophysical Properties of Matter, TPRC, Lafayette, IN, Y. S. Touloukian, Director, IFI/Plenum, New York-Washington, 1978, Vol. 4, p. 149 - Ni.

93. Ibid, Vol. 5, p. 174 - NiO.

94. Engineering Properties of Selected Ceramic Materials, J. F. Lynch, et al., editors, American Ceramic Society, Inc., 1966, p. 5.5.5-4 - $NiFe_2O_4$.

95. Williard E. Hauth III and Stephen D. Stoddard, "State-of-the-Art--Alumina Ceramics for Energy Applications," American Ceramic Society Bulletin, 57 (2) 181-182 (1978).

96. L. H. Farmer, "Slip Casting of Large Refractory Shapes," for abstract see 1978 Am. Ceram. Soc. Bull. 57, [3] 378 (1978).

97. T. M. Wehrenberg, E. R. Begley, and R. F. Patrick, "Isostatic Pressing Large Refractory Blocks," American Ceramic Society Bulletin 47, 642-645 (1968).

98. Corhart, "T-1185 Tin Oxide Refractory, Properties Brochure," Corhart Division of Corning Glass Works (1978).

99. J. D. Weyand and S. P. Ray, "Inert Anodes for Aluminum Smelting," for abstract see Am. Ceram. Soc. Bull. 59 [3] 378 (1980).

100. H. J. Van Hook in Phase Diagrams - Materials Science and Technology, A. M. Alper, ed., Academic Press, New York (1976) Vol. 6, pp. 201-03.

101. D. H. Antonsen, "Nickel Compounds," Kirk-Othmer: Encyclopedia of Chemical Technology, Vol. 15, 3rd Ed. 801-819, (1981).

102. S. J. Lukasiewicz and J. S. Reed, "Character and Compaction Response of Spray Dried Agglomerates," American Ceramic Society Bulletin, 57 (9) (1978), 798.

103. A. Lesniewski, S. Gosiorak and R. Moskalewicz, "The Use of Dilatometry to Evaluate the Ferrite Formation Process with Respect to Research and Production Technology," Science of Ceramics, Proceedings of the Eleventh International Conference, ed. R. Carlsson and S. Karlsson (Klippan, Sweden: Swedish Ceramic Society), 99-104 (1981).

104. J. Sticher and H. Schmalzried, "The Geometric Representation of Thermodynamic Variables in Multicomponent Systems Based on Iron," Report to the Institute for Theoretical Metallurgy and Physical Chemistry at the Technical University of Clausthal, (1975 May).

105. H. Alder, British Patent 1,138,208.